AD-A186 492 UNITED STATES AIR FORCE RESEARCH INITIATION PROGRAM 1/11
1985 TECHNICAL REPORT VOLUME 2(U) UNIVERSAL ENERGY
SYSTEMS INC DAYTON OH R C DARRAH APR 87
UNCLASSIFIED AFOSR-TR-87-1718 F49620-85-C-0013 F/G 15/3 NL

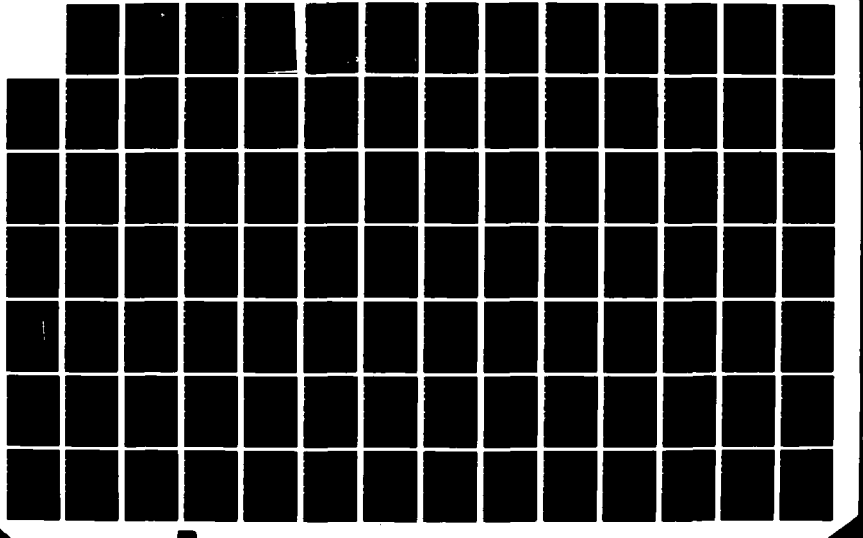

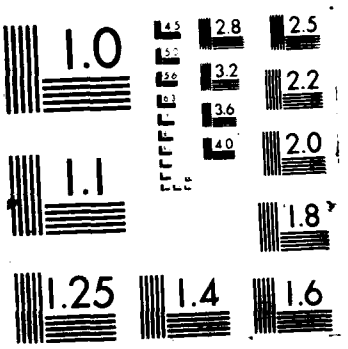
1.0
1.1
1.25
1.4
1.6
1.8
2.0
2.2
2.5
2.8
3.2
3.6
4.0

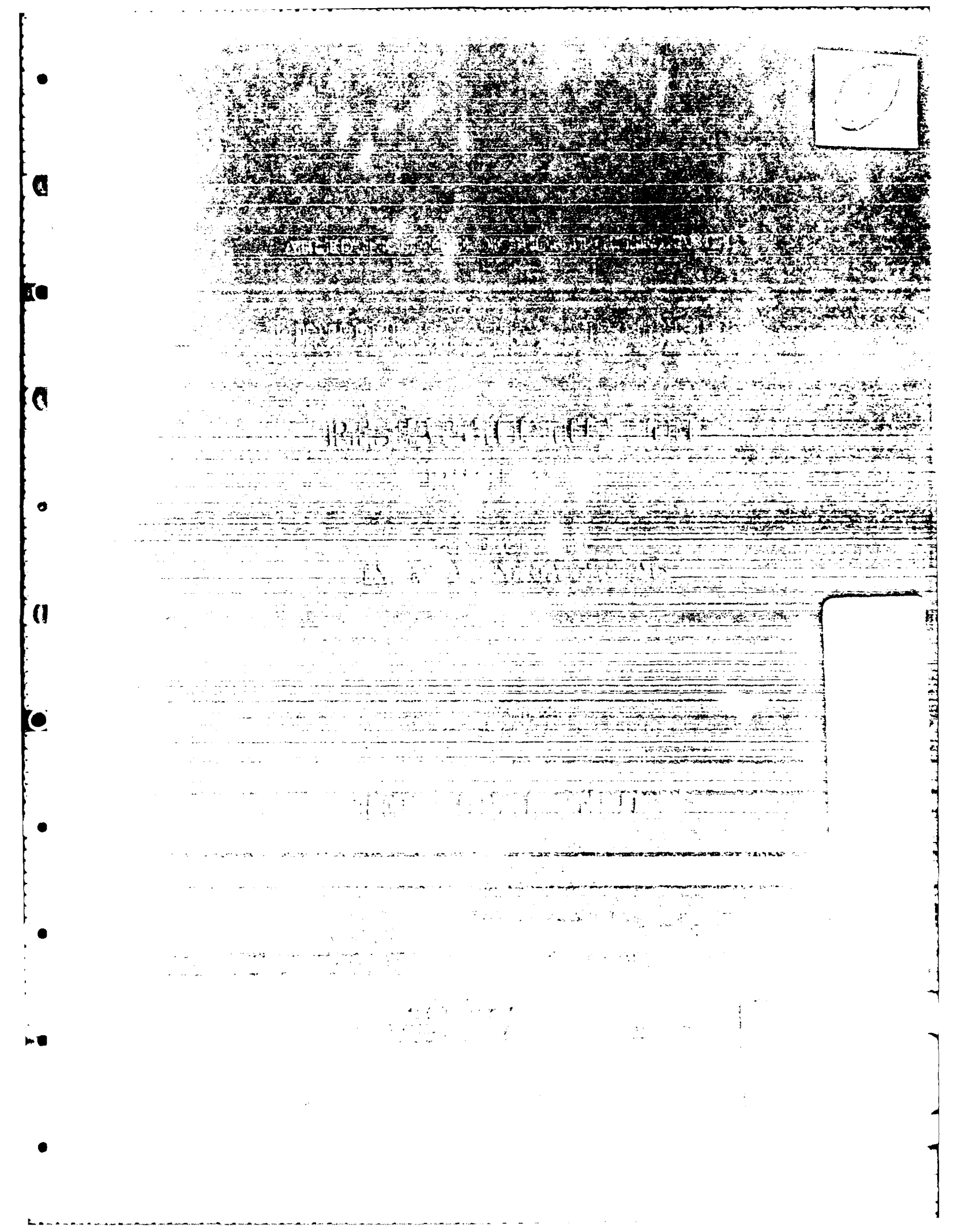

UNCLASSIFIED
SECURITY CLASSIFICATION OF THIS PAGE

REPORT DOCUMENTATION PAGE

Form Approved
OMB No. 0704-0188

1a. REPORT SECURITY CLASSIFICATION UNCLASSIFIED	1b. RESTRICTIVE MARKINGS
2a. SECURITY CLASSIFICATION AUTHORITY	3. DISTRIBUTION/AVAILABILITY OF REPORT Approved for public release; distribution unlimited.
2b. DECLASSIFICATION/DOWNGRADING SCHEDULE	
4. PERFORMING ORGANIZATION REPORT NUMBER(S)	5. MONITORING ORGANIZATION REPORT NUMBER(S) AFOSR-TR- 87-1718
6a. NAME OF PERFORMING ORGANIZATION UNIVERSAL ENERGY SYSTEMS INC.	6b. OFFICE SYMBOL (If applicable)
6c. ADDRESS (City, State, and ZIP Code) 4401 Dayton Xenia Rd Dayton OH 45432	7a. NAME OF MONITORING ORGANIZATION Air Force Office of Scientific Research/XOT
8a. NAME OF FUNDING/SPONSORING ORGANIZATION AFOSR	8b. OFFICE SYMBOL (If applicable) XOT
8c. ADDRESS (City, State, and ZIP Code) Building 410 Bolling AFB, DC 20332	7b. ADDRESS (City, State, and ZIP Code) Building 410 Bolling AFB DC 20332
	9. PROCUREMENT INSTRUMENT IDENTIFICATION NUMBER F49620-85-C-0013
	10. SOURCE OF FUNDING NUMBERS

PROGRAM ELEMENT NO.	PROJECT NO.	TASK NO	WORK UNIT ACCESSION NO.
61102F	3396	D5	

11. TITLE (Include Security Classification)
USAF Research Initiation Program Volume 2

12. PERSONAL AUTHOR(S)
Program Director Rodney C. Darrah

13a. TYPE OF REPORT	13b. TIME COVERED	14. DATE OF REPORT (Year, Month, Day)	15. PAGE COUNT
Interim	FROM _____ TO _____	April 1987	

16. SUPPLEMENTARY NOTATION

17. COSATI CODES			18. SUBJECT TERMS (Continue on reverse if necessary and identify by block number)
FIELD	GROUP	SUB-GROUP	

19. ABSTRACT (Continue on reverse if necessary and identify by block number)

(SEE REVERSE)

20 DISTRIBUTION/AVAILABILITY OF ABSTRACT ☒ UNCLASSIFIED/UNLIMITED ☐ SAME AS RPT ☐ DTIC USERS	21. ABSTRACT SECURITY CLASSIFICATION UNCLASSIFIED
22a. NAME OF RESPONSIBLE INDIVIDUAL Richard Kopka, Major, Program Manager	22b. TELEPHONE (Include Area Code) (202) 767-4971
	22c. OFFICE SYMBOL XOT

INTRODUCTION

Research Initiation Program - 1985

AFOSR has provided funding for follow-on research efforts for the participants in the Summer Faculty Research Program. Initially this program was conducted by AFOSR and popularly known as the Mini-Grant Program. Since 1983 the program has been conducted by the Summer Faculty Research Program (SFRP) contractor and is now called the Research Initiation Program (RIP). Funding is provided to establish RIP awards to about half the number of participants in the SFRP.

Participants in the 1985 SFRP competed for funding under the 1985 RIP. Participants submitted cost and technical proposals to the contractor by 1 November 1985, following their participation in the 1985 SFRP.

Evaluation of these proposals was made by the contractor. Evaluation criteria consisted of:

1. Technical Excellence of the proposal
2. Continuation of the SFRP effort
3. Cost sharing by the University

The list of proposals selected for award was forwarded to AFOSR for approval of funding. Those approved by AFOSR were funded for research efforts to be completed by 31 December 1986.

The following summarizes the events for the evaluation of proposals and award of funding under the RIP.

A. Rip proposals were submitted to the contractor by 1 November 1985. The proposals were limited to $20,000 plus cost sharing by the universities. The universities were encouraged to cost share since this is an effort to establish a long term effort between the Air Force and the university.

B. Proposals were evaluated on the criteria listed above and the final award approval was given by AFOSR after consultation with the Air Force Laboratories.

C. Subcontracts were negotiated with the universities. The period of performance of the subcontract was between October 1985 and December 1986.

Copies of the Final Reports are presented in Volumes I through III of the 1985 Research Initiation Program Report. There were a total of 82 RIP awards made under the 1985 program.

i

(1)

AFOSR-TR- 87-1718

Approv
distri ... release;
... d.

DTIC
ELECTE
NOV 17 1987
S D
E

This document has been approved for public release and sale; its distribution is unlimited.

87 11 17 ...

UNITED STATES AIR FORCE

1985 RESEARCH INITIATION PROGRAM

Conducted by

UNIVERSAL ENERGY SYSTEMS, INC.

under

USAF Contract Number F49620-85-C-0013

RESEARCH REPORTS

VOLUME II OF III

Submitted to

Air Force Office of Scientific Research

Bolling Air Force Base

Washington, DC

By

Universal Energy Systems, Inc.

April 1987

INTRODUCTION

Research Initiation Program - 1985

AFOSR has provided funding for follow-on research efforts for the participants in the Summer Faculty Research Program. Initially this program was conducted by AFOSR and popularly known as the Mini-Grant Program. Since 1983 the program has been conducted by the Summer Faculty Research Program (SFRP) contractor and is now called the Research Initiation Program (RIP). Funding is provided to establish RIP awards to about half the number of participants in the SFRP.

Participants in the 1985 SFRP competed for funding under the 1985 RIP. Participants submitted cost and technical proposals to the contractor by 1 November 1985, following their participation in the 1985 SFRP.

Evaluation of these proposals was made by the contractor. Evaluation criteria consisted of:

1. Technical Excellence of the proposal
2. Continuation of the SFRP effort
3. Cost sharing by the University

The list of proposals selected for award was forwarded to AFOSR for approval of funding. Those approved by AFOSR were funded for research efforts to be completed by 31 December 1986.

The following summarizes the events for the evaluation of proposals and award of funding under the RIP.

A. Rip proposals were submitted to the contractor by 1 November 1985. The proposals were limited to $20,000 plus cost sharing by the universities. The universities were encouraged to cost share since this is an effort to establish a long term effort between the Air Force and the university.

B. Proposals were evaluated on the criteria listed above and the final award approval was given by AFOSR after consultation with the Air Force Laboratories.

C. Subcontracts were negotiated with the universities. The period of performance of the subcontract was between October 1985 and December 1986.

Copies of the Final Reports are presented in Volumes I through III of the 1985 Research Initiation Program Report. There were a total of 82 RIP awards made under the 1985 program.

MINI-GRANT RESEARCH REPORTS

1985 RESEARCH INITIATION PROGRAM

Technical Report Number	Title and Mini-Grant No.	Professor
Volume I		
1	Individual Differences in Abilities, Learning, and Cognitive Processes 760-OMG-027	Dr. Phillip L. Ackerman
2	Maximum Voluntary Hand Grip Torque for Circular Electrical Connectors 760-OMG-068	Dr. Samuel Adams
3	Temperature Dependence of Ion-Molecule Association Reactions: Halide Ion Addition Reactions 760-OMG-105	Dr. Lucia Badcock
4	Report Not Received In Time. Will Be Provided When Available. 760-OMG-095	Dr. Richard Bertrand
5	Metaphor and Machines: A New Look at Case Theory 760-OMG-031	Dr. Peter J. Binkert
6	Speech Produced at Various Acceleration Levels 760-OMG-033	Dr. Zinny S. Bond
7	Creating Projected Images 760-OMG-001	Dr. Kevin W. Bowyer
8	Computer-Based Instruction: Effect of Cognitive Style, Instructional Format, and Subject-Matter Content 760-OMG-085	Dr. Linda J. Buehner
9	Nonlinear Feedback Controls for Two-Link Robotic Manipulators 760-OMG-097	Dr. Connie K. Carrington

Volume II

78	Report Not Received In Time. Will Be Provided When Available. 760-OMG-071	Dr. Yin-min Wei
79	Development of High Strength Beta Titanium Alloys Via Rapid Solidification Processing - The Coarsening of Erbium Oxide in Ti-15V-3Al-3Sn-3Cr Beta Titanium Alloy 760-OMG-086	Dr. Isaac Weiss
80	Report Not Received In Time. Will Be Provided When Available. 760-OMG-038	Dr. Jesse Williams
81	Labeling the Topographic Features of an Infrared Image 760-OMG-003	Dr. David Wilson
82	Radiation from Flying Through Nuclear Debris Clouds 760-OMG-035	Dr. Arthur Woodrum

1245s

OPTIMUM DESIGN OF STRUCTURES WITH MULTIPLE CONSTRAINTS

R.V. Grandhi
Assistant Professor
Mechanical Systems Engineering
Wright State University
Dayton, Ohio 45435

Final Report AFOSR/UES Mini Grant

Contract No. F49620-85-C-0013

Summary

This report presents a design optimization algorithm for structural weight minimization with multiple frequency constraints. An optimality criterion method based on uniform Lagrangian density for resizing and a scaling procedure to locate the constraint boundary were used in optimization. Multiple frequency constraints of equality and inequality types were addressed. The effectiveness of the algorithm was demonstrated by designing a number of truss structures with as many as four hundred and eighty nine design variables. No attempt was made to reduce the number of design variables by such procedures as linking and/or invoking symmetry conditions. The design examples include a ten bar truss, two hundred bar truss, a modified ACOSS - II and COFS (Control of Flexible Structures) mast truss. All the structures contain nonstructural mass besides their own mass. The algorithm is extremely stable and in all cases the optimum designs were obtained in less than twenty iterations regardless of the size of the structure and the number of design variables.

Acknowledgement

This research work was performed in collaboration with the Analysis and Optimization Group at Air Force Wright Aeronautical Laboratories, Dayton, Ohio. The Principal Investigator sincerely acknowledges the technical support of Dr. V.B.Venkayya, Dr. N.S.Khot, Lt. R.A. Canfield, Ms. Victoria Tischler, and finally the Group Leader Mr. Nelson Wolf for providing the excellent research facilities.

Introduction

The optimal design of structures with frequency constraints is extremely useful in manipulating the dynamic characteristics in a variety of ways. For example, in most low frequency vibration problems the response of the structure to dynamic excitation is primarily a function of its fundamental frequency and mode shape. In such cases the ability to manipulate the selected frequency can significantly improve the performance of the structure. Similarly the aeroelastic characteristics of an aircraft wing are primarily governed by its torsional and bending properties which can best be studied by the lower torsional and bending modes. In fact, in most narrow-band excitation problems control of the frequencies in the critical range is tantamount to control of the dynamic response.

A large amount of literature related to the optimization of structures with frequency constraints is available. Most of these papers present design algorithms based on a single frequency constraint which uses only the information about the fundamental frequency and the associated vibration mode [1-5]. A few papers however, consider multiple frequency constraints [6-9]. A brief description of the previous research work is given below. This is by no means the complete literature on frequency optimization.

Miura and Schmit [1] minimized the structural mass of a cantilever beam and a wing structure with a fundamental frequency constraint. A mathematical programming method based on an interior penalty function was used. This method can be used in conjunction with design variable linking for optimizing practical structures. Refs. [2-7, 9] employed optimality criteria methods in designing minimum weight structures. Minimization of structural mass subject to a fundamental frequency constraint and maximization of the fundamental frequency for a given structural mass has been considered in the design of rods and trusses by Venkayya and Tischler [5]. Elwany and Barr [6] presented results for the minimum mass design of a cantilever beam subjected to multiple (up to three) torsional frequency constraints. A variational procedure was used in deriving the neces-

sary conditions of optimal design. The resulting integral equations and their solution are continuous function of spatial variables. Fleury and Sander [7] used a generalized optimality criteria method for designing beams with multiple frequency and buckling constraints. Basically the method is an extension of the conventional optimality criteria approach or it can be viewed as a linearization in mathematical programming. Pedersen [8] has addressed beam problems with constraints on the first four frequencies using a Linear Programming method. Khot [9] has considered a truss structure with two frequency constraints and found interesting anomalies in the convergence. Olhoff [10] presented results for maximizing a higher order frequency subject to a given volume constraint. He uses a variational approach and derives the optimality condition in an integral form. The resulting optimum shape is a continuous function of the spatial variable.

This research work examines the problem of finding the minimum weight structure satisfying the frequency constraints. The design problems considered are optimization (i) with a single (fundamental or higher) frequency constraint (an equality constraint) and (ii) with constraints on multiple frequencies (treated as equality and inequality constraints). The optimality criterion method in conjunction with a scaling procedure has been used to design a minimum weight structure with frequency constraints. The algorithm developed by Venkayya and Tischler [5] has been used as the basis for the development of the present multiple frequency constraint formulation.

This algorithm based on an optimality criterion approach is very efficient and reliable even in the presence of a large number of design variables. The optimality criterion is derived by differentiating the Lagrangian with respect to the design variables and the minimum weight design should satisfy this criterion. The essence of the optimality criterion is that at the optimum the weighted sum of the Lagrangian energy density must be the same in all the elements. The optimality condition consists of the gradients (constraints and objective function) and Lagrangian multipliers. The gradients of the frequency con-

straints and objective function can be derived analytically from the dynamic equilibrium equations and the expression for the objective function. In the case of a single constraint, the evaluation of the Lagrangian multiplier is simple and straight forward. However, in the case of multiple (active) constraints determination of the Lagrangian multipliers requires approximations. The basic equations are nonlinear and also the inadmissibility of non-positive Lagrangian multipliers presents additional difficulties. In this work, Lagrangian multipliers are approximated using simple expressions derived from single constraint conditions. The optimization consists of three basic steps. The first step is analysis of the structure followed by scaling and resizing. Analysis gives information about feasibility or nonfeasibility of the design. Scaling is for obtaining the feasible design. A simple scaling procedure is developed for multiple frequency constraints. An estimate of the scale factor is obtained iteratively to reach the frequency constraint boundary. The resizing algorithm is derived from optimality conditions.

This report discusses the optimality algorithm, resizing procedure, and scaling techniques for multiple frequency constraints. The effectiveness of the algorithm is demonstrated by using large structural design applications with hundreds of design variables and multiple frequency constraints.

Problem Statement

The structural optimization problem is stated as follows:

Minimize structural weight

$$W(\mathbf{x}) = \sum_{i=1}^{n} \rho_i x_i l_i \tag{1}$$

subject to behavior constraints

$$g_j(\mathbf{x}) = \omega_j{}^2 - \bar{\omega}_j^2 = 0 \qquad j = 1, 2, \ldots . k \tag{2}$$

$$g_j(\mathbf{x}) = \omega_j{}^2 - \bar{\omega}_j^2 \geq 0 \qquad j = k+1, k+2, \ldots, m$$

and side constraints on the design variables

$$x_i \geq x_i^{\ell} \tag{3}$$

where ρ_i is the density, l_i is the length, x_i is the design variable, x_i^{ℓ} is the lower limit on the design variable, ω_j is the j^{th} natural frequency, $\bar{\omega}_j$ is the specified value of the j^{th} frequency, n is the number of design variables, and m is the number of design constraints.

Optimality Method

The optimality method consists of two steps. The first step involves derivation of the optimality conditions and associating them with an energy condition in the structure. In the second step, an iterative algorithm is derived with the help of the energy condition to achieve the optimality condition.

The Lagrangian formulation for the above stated problem is written as:

$$L(\mathbf{x}, \lambda) = W(\mathbf{x}) - \sum_{j=1}^{m} \lambda_j g_j(\mathbf{x}) \tag{4}$$

where $L(\mathbf{x}, \lambda)$ is the Lagrangian function and the λ's are the Lagrangian multipliers. The unknowns are the design variables x_i and the Lagrangian multipliers λ_j.

Minimization of the Lagrangian L with respect to the design variable vector $\mathbf{x}$ gives the condition for the stationary value of the objective function as:

$$\frac{\partial L}{\partial x_i} = \frac{\partial W(\mathbf{x})}{\partial x_i} - \sum_{j=1}^{m} \lambda_j \frac{\partial g_j}{\partial x_i} = 0 \tag{5}$$

From equation 5, the optimality condition can be written as

$$\sum_{j=1}^{m} e_{ij} \lambda_j = 1 \qquad i = 1, 2, \ldots, n \tag{6}$$

where

$$e_{ij} = \frac{\partial g_j / \partial x_i}{\partial W / \partial x_i} \tag{7}$$

Equation 7 represents the ratio of the constraint to the objective function gradients with respect to the design variables. These ratios can be associated with special forms of energy densities depending on the type of constraints. For the case of frequency constraints, e_{ij} is computed as follows.

The eigenvalue problem corresponding to the undamped linear system is written as

$$\mathbf{K}\phi_j = \omega_j^2 \mathbf{M}\phi_j \tag{8}$$

where ω_j is the j^{th} natural frequency, ϕ_j is the j^{th} eigenvector or natural mode of the structure, and $\mathbf{K}$ and $\mathbf{M}$ are the stiffness and mass matrices respectively. The mass matrix $\mathbf{M}$ is a combination of the structural mass, $\mathbf{M}_s$, and the nonstructural mass, $\mathbf{M}_c$.

In this research work, the natural frequencies are calculated using the Sturm Sequence method [11,12] in conjunction with a bisection procedure. By using this method any desired frequencies and the corresponding modes can be computed without computing any of the remaining frequencies and modes.

The square of the j^{th} natural frequency of the structure can be defined by a Rayleigh quotient as:

$$\omega_j^2(\mathbf{x}) = \frac{\phi_j^t \mathbf{K} \phi_j}{\phi_j^t \mathbf{M} \phi_j} \tag{9}$$

where superscript t denotes the transpose. Substitution of equation 9 in 7 gives the expression for e_{ij} as:

$$e_{ij} = \frac{\{\phi_j\}^t \ \mathbf{k_i} \ \{\phi_j\} - \omega_j^2 \{\phi_j\}^t \ \mathbf{m_i} \ \{\phi_j\}}{\rho_i x_i l_i} \tag{10}$$

where $\mathbf{k_i}$ and $\mathbf{m_i}$ are the i^{th} element stiffness and mass matrices respectively in the global coordinate system. The eigenvectors were normalized using the expression

$$\phi_j^t \mathbf{M} \phi_j = 1 \tag{11}$$

In deriving the e_{ij} expression, the stiffness and structural mass matrices were assumed to be linear functions of the design variables. This is true for truss and membrane elements, and needs minor modification for bending and other types of finite elements.

The solution of the optimization problem involves $(n + m)$ unknown quantities, where n is the number of design variables and m is the number of Lagrangian multipliers corresponding to m constraints. The optimality condition described in equation 6 gives n equations. The additional m equations can be computed by writing the original constraint conditions as follows:

From the Rayleigh's quotient in equation 9, the derivative of the frequency with respect to the design variables can be written as

$$\frac{d\omega_j^2}{dx_i} = \gamma_j \frac{\omega_j^2}{x_i} \tag{12}$$

where γ_j is the ratio of the nonstructural modal mass to the total modal mass and is given by

$$\gamma_j = \frac{\phi_j^t \mathbf{M}_c \phi_j}{\phi_j^t \mathbf{M} \phi_j} \tag{13}$$

Substituting equation 12 in equation 7 gives,

$$e_{ij} = \frac{\partial g_j / \partial x_i}{\partial W / \partial x_i} = \frac{\gamma_j \omega_j^2 / x_i}{\rho_i \ell_i} \tag{14}$$

Equation 14 for active constraints takes the form

$$\sum_{i=1}^{n} e_{ij} \rho_i x_i \ell_i = \gamma_j \tilde{\omega}_j^2 \qquad j = 1, 2, \ldots, m \tag{15}$$

Combining equations 6 and 15 provides the necessary equations for determining the Lagrangian multipliers as follows:

$$\sum_{i=1}^{n} e_{ij} \rho_i x_i \ell_i e_{ij} \lambda_j = \gamma_j \tilde{\omega}_j^2 \qquad j = 1, 2, \ldots, m \tag{16}$$

or

$$\mathbf{H}\lambda = \hat{G} \tag{17}$$

where the matrix $\mathbf{H}$ is given by

$$\mathbf{H} = \mathbf{e}^t \mathbf{D} \mathbf{e} \tag{18}$$

$\mathbf{H}$ is of the order mxm since it involves multiplication of mxn, nxn, and nxm matrices, and $\hat{G}$ is a vector of $\gamma_j \tilde{\omega}_j^2$. $\mathbf{D}$ is a diagonal matrix and its i^{th} diagonal element is given by

$$D_{ii} = \rho_i x_i \ell_i \tag{19}$$

The elements of matrix $\mathbf{H}$ can not be determined explicitly because the $\mathbf{e}$ and $\mathbf{D}$ matrices are functions of the design variable vector which is itself unknown. Equations 6 and 17 are nonlinear sets of equations, and they have to be solved by iterative methods.

Optimization Technique

1. Resizing Algorithm

The optimality condition for multiple frequency constraints can be stated as, "The weighted sum of the Lagrangian energy densities corresponding to multiple frequency constraints should be equal to unity in all the elements". This can be achieved by satisfying the condition given in equation 6. By multiplying both sides of Eq. 6 by x_i^p and taking the p^{th} root ($\alpha = \frac{1}{p}$), we obtain

$$x_i^{k+1} = x_i^k \left[\sum_{j=1}^{m} C_j e_{ij}^k \right]^{\alpha} \tag{20}$$

where α controls the step size, and C_j contains the weighting parameters which can be approximated as functions of the Lagrangian multipliers. Superscripts k and $k+1$ are introduced to denote the iteration numbers. The iteration scheme is repeated until the set convergence criterion is satisfied. If there is no minimum size constraint for an element, then the quantity within the parenthesis is equal to unity at the optimum.

The design is started with an initial value of α as 0.5. After a design cycle (i.e., scaling the design to a feasible region and resizing the design using equation 20) if the objective function increases from the previous iteration, then the α value is reduced adaptively. The smaller α value avoids larger changes in the design when it is closer to the optimum and gives a stable convergence. It acts like move limits on the design variables. The lowest value for α is taken as 0.001. If α becomes smaller than 0.001, then the resizing is terminated.

2. Scaling Procedure

In the optimization scheme after each resizing, the design variables are normalized to have a maximum value of unity. The normalized design vector may not be acceptable, thus scaling it to the feasible region is essential, otherwise some of the constraints may be violated. This helps monitoring the progress of each design cycle and also finding the active

constraints. At the end of each resizing the normalized design variables are multiplied by a scaling factor Λ, and it is computed as follows:

The Rayleigh quotient for the j^{th} frequency at the current design is written as

$$\omega_{jo}^2 = \frac{\phi_j^t \mathbf{K} \phi_j}{\phi_j^t (\mathbf{M}_s + \mathbf{M}_c) \phi_j} \tag{21}$$

where ω_{jo} is the unscaled frequency. By scaling the design variables by a factor Λ_j, the desired frequency ω_{jd} is obtained. Then the Rayleigh quotient becomes

$$\omega_{jd}^2 = \frac{\Lambda_j \phi_j^t \mathbf{K} \phi_j}{\phi_j^t (\Lambda_j \mathbf{M}_s + \mathbf{M}_c) \phi_j} \tag{22}$$

In this equation, it is assumed that scaling the structural members by Λ_j implies that $\mathbf{K}$ and $\mathbf{M}_s$ are scaled in a similar way. This is certainly true in membrane elements and needs modification for bending elements. The nonstructural mass $\mathbf{M}_c$ does not depend on the design variables, and hence it is not multiplied by Λ_j. Equation 22 can be further simplified to relate the desired frequency, ω_{jd} with the unscaled frequency, ω_{jo} as

$$\omega_{jd}^2 = \frac{\Lambda_j}{\Lambda_j \eta_j + \gamma_j} \omega_{jo}^2 \tag{23}$$

where η_j is the ratio of the structural modal mass to the total modal mass and is given by

$$\eta_j = \frac{\phi_j^t \mathbf{M}_s \phi_j}{\phi_j^t \mathbf{M} \phi_j} \tag{24}$$

also,

$$\eta_j + \gamma_j = 1 \tag{25}$$

Now the ratio r_j^2 is defined as

$$r_j^2 = \frac{\omega_{jd}^2}{\omega_{jo}^2} = \frac{\Lambda_j}{\Lambda_j \eta_j + \gamma_j} \tag{26}$$

Then the scaling parameter corresponding to the j^{th} frequency becomes

$$\Lambda_j = \frac{\gamma_j r_j^2}{1 - r_j^2 \eta_j} \qquad for \qquad r_j^2 \eta_j < 1 \tag{27}$$

and

$$\Lambda_j = r_j^2 \qquad for \qquad r_j^2 \eta_j \geq 1 \tag{28}$$

One scaling parameter Λ_j is computed for each constraint, and from these values one value is selected based on the type of constraints. If there are all inequality constraints, then Λ is selected such that the most violated constraint becomes active. If any one of the constraints is an equality type, then the scaling parameter corresponding to that one is used. This formulation handles only one equality constraint, and the rest have to be inequality constraints. This is so, because after scaling more than one constraint can never be made active unless it is a repeated frequency. Besides, if there are more than one equality type constraint, there may not exist a feasible solution. Since the frequency constraints are nonlinear functions of the design variables, repetition of the scaling procedure may be necessary in some design cycles.

3. Role of the Lagrangian Multipliers/Active and Passive Constraints

The Lagrangian multipliers are computed by using simple approximations. Here the λ's are considered merely as weighting parameters, and they are computed as if there is only one constraint.

The optimality condition for a single constraint is written as

$$e_i \lambda = 1 \qquad i = 1, 2, ..., n \tag{29}$$

Substituting $e_i = \frac{1}{\lambda}$ in equation 15 gives:

$$\frac{1}{\lambda} \sum_{i=1}^{n} \rho_i x_i f_i = \gamma_j \omega_j^2 \tag{30}$$

where λ takes the form

$$\lambda = \frac{W}{\gamma_j \bar{\omega}_j^2} \tag{31}$$

and W represents weight of the structure. The j^{th} Lagrangian multiplier corresponding to the j^{th} frequency constraint can be approximated as:

$$\lambda_j = \frac{W}{\bar{\omega}_j^2(1-\eta_j)} \tag{32}$$

It is evident from Eq. 32 that in the absence of nonstructural mass the value of the Lagrangian multiplier becomes indefinite. The structure can not be optimized for frequency constraints alone unless some nonstructural mass is associated with the system. As a matter of fact, nonstructural mass is the major part of the total mass in most of the aerospace structures. The nonstructural masses are due to aircraft engines, payloads, actuators, hinges, *etc.* Optimization in the absence of nonstructural mass is only possible when additional constraints such as static displacements or stresses are present.

The concept of active and passive constraints is crucial in the multiple frequency constraint problem. The active constraints are those within a certain percentage from their respective limits. The remaining ones are passive constraints. The resizing formula (Eq. 20) uses the Lagrangian multipliers corresponding to the active constraints. The active and passive constraints decision was made at the outset (after the first iteration) of the design and no changes were made during rest of the design. The iteration was continued as long as there was improvement in the design (reduction in weight, for example). It is worthwhile pointing out some characteristics of the emerging designs during the iterations. If only a single Lagrangian multiplier (corresponding to one active constraint) is participating in the iteration, the weight of the structure reduces rapidly and the step size adjustments (α value) have to be made very early in the design. This happens because the inactive frequencies tend to cluster toward the active frequency and mode switching can destroy smoother convergence. However, by adjusting the value of α, the optimum design can be

approached more smoothly. The price of reducing α is reflected in an increased number of iterations. In the other extreme when the number of active constraints are more because of the larger percentage specifications around the limiting values, then more Lagrangian multipliers participate in the resizing. Iterations using more Lagrangian multipliers produce two interesting characteristics: first, the problem tends to be overconstrained, and the resulting optimum corresponds to an upperbound solution. The second characteristic is that the clustering of frequencies (at least among the active ones) is significantly reduced. Also the inequality constraints stay away from the constraint boundary. The step size (α) adjustments do not play a significant role, because the iteration converges quite smoothly. The percentage value for finding the active constraints varies from problem to problem, but usually within 5-10% from the constraint limit would be adequate.

4. Optimization Algorithm

An outline of the design optimization procedure is given as follows:

(i) The design starts with uniform sizes for all the design variables.

(ii) At the current design, the desired natural frequencies and the corresponding mode shapes are calculated using the Sturm Sequence method.

(iii) The design variables are scaled to the constraint boundary in order to satisfy all the behavior constraints. The Lagrangian multipliers are evaluated.

(iv) The Lagrangian energy is computed for each mode in each element. $\sum e_{ij}\lambda_j$ is evaluated for all the elements. The design variables are resized using equation 20.

(v) The design variables are normalized with the maximum value of the design variables.

Repeat steps (ii) to (v) until the set convergence requirements are satisfied. The steps (ii) to (v) constitute one iteration. In Eq. 10, e_{ij} can become negative for some elements, if the nonstructural mass is substantial, i.e., the square of the natural frequency multiplied by the modal kinetic energy is larger than the modal potential energy. In this case, the

corresponding design variable takes its lower limit value and the e_{ij} contribution in Eq. 20 is zero. This creates aberrations and takes a few extra iterations in converging to the optimal solution. So, whenever there is a substantial amount of nonstructural mass, it is better to use only the modal potential energy for e_{ij} in all the elements. This provides a stable convergence in design optimization. All the problems solved in this work employed just the modal potential energy because of substantial nonstructural mass.

Numerical Results

The effectiveness of the optimality algorithm is demonstrated by using a ten bar truss (Fig. 1), a two hundred bar truss (Fig. 4), a modified ACOSS - II (Fig. 7) and a COFS model (Fig. 10) as design examples. The emphasis here is in solving large scale structural design problems with hundreds of design variables.

1. Ten bar truss

The structure shown in Fig. 1 is made up of aluminum with Young's modulus, 10^7 *psi* and weight density, 0.1 lb/in^3. At each of the four free nodes 2.588 $lb\text{-}sec^2/in$ nonstructural mass is added. One design variable was assigned to each structural element. At the initial design, all the cross-sectional areas were 1.0 in^2 for each member. The design was scaled by a factor of 9.5318 to obtain a 4000 lb initial weight. The lower limit on the design variables was 0.1 in^2.

Ref. 5 presents optimization studies with different fundamental frequency limits. In this work, first the structure was designed with a higher order frequency constraint alone. The structural weight was optimized with the second natural frequency constrained to six different values. The second frequency was required to be 10, 15, 20, 25, 27.08 and 30 Hz in six different cases. Ten design variables and one frequency constraint were considered. Table 1 presents all the frequencies and the structural weight at the optimum design in all these cases. Table 2 gives the optimum design variables. The variation of the optimum weight with the second frequency limits is shown in Fig. 2. From the results obtained, it is clear that the optimality algorithm can be effectively used in designing structures with a higher order frequency constraint.

After this, the ten bar truss was designed with multiple frequency constraints. The structural weight was minimized such that the fundamental, second and third frequencies were constrained. Tables 3 and 4 present the results obtained under different constraint

conditions. The first set was with $\omega_1 = 7.0$ Hz, the second with $\omega_1 = 10.0$, the third with $\omega_1 = 7.0$, and $\omega_2 \geq 15.0$, the fourth with $\omega_1 = 10.0$, $\omega_2 \geq 15.0$, the fifth with $\omega_1 = 7.0$, $\omega_2 \geq 15.0$, and $\omega_3 \geq 20.0$, and finally all inequality constraints, $\omega_1 \geq 3.5$, $\omega_2 \geq 10.0$, and $\omega_3 \geq 14.0$ Hz were considered. Table 3 gives all the frequencies at the initial and optimum designs, and Table 4 consists of all the design variables at the optimum. The iteration history for $\omega_1 \geq 3.5$, $\omega_2 \geq 10.0$, and $\omega_3 \geq 14.0$ Hz is shown in Fig. 3. It took seven iterations to reach the optimal solution. In the last three iterations there was not much change in the objective function. As explained in earlier sections, at the most one equality constraint was considered in any set and the rest were inequality types.

2. Two hundred bar truss

The two hundred bar truss was formulated by Venkayya, *et. al.* [13] for demonstrating the computational efficiency of the optimality method in designing very large structures. The structure shown in Fig. 4 has 77 nodes, 200 bar elements, and 150 degrees of freedom. At each of the 75 free nodes 0.5 $lb\text{-}sec^2/in$ nonstructural mass was considered. The structure is made up of steel with Young's modulus, 30.0 x $10^6 psi$ and a weight density of 0.283 lb/in^3. 200 design variables were assigned to the 200 bar elements in structural weight optimization. At the initial design all the cross-sectional areas were 10.0 in^2. The lower limit on the design variables was 0.1 in^2. The initial weight of the structure was 99634 lb, and the first five frequencies at the initial design were 2.87, 13.02, 13.72, 31.92, and 37.68 Hz. First, the structure was designed with a fundamental frequency constraint. Various fundamental frequency limits were considered starting from 2.0 to 8.0 Hz. Table 5 presents the first five frequencies and the optimum weight for different fundamental frequency limits. Fig. 5 shows the variation of the optimum weight as the frequency limit is increased. The structural weight increases very rapidly at the higher frequency limits. Beyond a certain frequency limit, it is not possible to design a practical structure. Next, this truss was designed with two frequency constraints, $\omega_1 = 3.0$ Hz and $\omega_2 \geq 9.0$ Hz. The

optimum weight of 5226.5 lb. was obtained in seven iterations and the iteration history is given in Fig. 6. The first five frequencies at the optimum were 3.0, 9.01, 9.41, 14.39, and 14.78 Hz. Also, the same structure was designed with $\omega_1 = 4.0$ Hz and $\omega_2 \geq 10.0$ Hz. The optimum weight was 9220.9 lb. and the first five frequencies at the final design were 4.0, 10.0, 11.04, 14.46, and 15.78 Hz. In both the cases the second frequency constraint was satisfied as if it was an equality constraint. The design variables at the optimum for both the cases are given in Ref. 14.

3. Modified ACOSS - II

The ACOSS (Active Control of Space Structures) model II was developed by the C.S. Draper Laboratory [15]. The structure consists of two subsystems: the optical support structure and the equipment section, which are connected by springs at three points to allow vibration isolation [Fig. 7]. In this work, ACOSS - II was modified to have only the optical support structure, and it is fixed at the three springs locations. Also, a couple of nodes were removed from the original model. The modified ACOSS - II consists of the upper mirror support truss, the lower mirror support truss, and the metering truss. The finite element model is shown in Fig. 8; it has 33 nodes and 113 truss elements. All the elements are made up of graphite/epoxy with Young's modulus, $18.5 \times 10^6 psi$ and weight density, $0.055\ lb/in^3$. The lower limit on the design variables was $0.1\ in^2$. The initial cross-sectional areas were taken as $10.0\ in^2$. At the initial design the weight was 18709.8 *lb* and the first five frequencies were 1.21, 2.71, 4.21, 10.33, and 10.48 Hz.

The modified ACOSS - II was designed with 113 design variables under two different sets of frequency constraints. In the first set, the structural weight was minimized such that the fundamental frequency was equal to 2.0 Hz. The optimum weight was 11687.3 *lb* and the first five frequencies were 2.00, 2.04, 2.39, 5.19, and 5.68 *Hz*. The second frequency is very close to the fundamental frequency. In the second set, the constraints were $\omega_1 = 2.0$ Hz and $\omega_2 \geq 3.0$ Hz. The optimum weight was 11820.2 *lb* and the first five

frequencies were 2.00, 3.72, 4.46, 6.78, and 7.22 Hz. The structural weight was increased by 133 *lb* (approximately 1%) to separate the second frequency from the fundamental one. All the five frequencies were well separated. Fig. 9 shows the iteration history for this case. A large reduction in the weight was obtained in the first four iterations, and afterwards the reductions in weight were very small. Ref. 14 presents the design variable values at the optimum. In this example, the second frequency tries to approach the first one very rapidly, so both the Lagrangian multipliers were used throughout the optimization.

4. COFS (Control of Flexible Structures) Model

The Mast Flight System [16] is composed of several subsystems. The primary structural component is the beam assembly (Fig. 10) which is called the COFS model. The beam cross section is triangular with the longerons located at the vertices of an equilateral triangle. The truss structure repeats itself in two-bay segments. There are 27 two-bay segments for a total of 54 bays. A typical two-bay segment of the truss structure is shown in Fig. 11.

The structure consists of 489 truss elements thus 489 design variables were considered in the design optimization. All the elements are made up of graphite/ epoxy with Young's modulus, 18.5 x 10^6 *psi* and weight density 0.055 lb/in^3. The initial cross sectional areas were taken as 1.0 in^2, and the lower limit on the design variables was 0.1 in^2. The structural weight was minimized such that the fundamental frequency was equal to 0.18 Hz. At the initial design the weight was 1407.42 *lb* and the first five frequencies were 0.2058, 0.2058, 1.4570, 1.4570 and 3.6524 Hz. Fig. 12 gives the mode shapes corresponding to the first, third and fifth frequencies. The second and fourth modes are similar to the first and third respectively due to the symmetry in the structure. The optimum weight was 258.35 *lb*, and the first four frequencies were 0.1800, 0.1802, 1.1068, and 1.1221 Hz. The second frequency is not equal to the first one, and similarly the fourth one is not equal to the third one. The optimization algorithm created unsymmetry in the structure, thus the repeated frequency

condition is eliminated. Most of the design variables reached their lower limit, and mostly the longerons contributed to the weight. The bottom longerons are much stronger than the top ones. The details of the optimum design are given in Ref. 14.

Conclusions

In this research work the minimum weight design of structures with multiple frequency constraints was obtained using an optimality method. A simple resizing scheme in conjunction with a scaling procedure has been used. Once again the optimality criterion method has shown to be very efficient in designing large practical structures with a small number of iterations. The number of design variables considered was very large. All the structures contain nonstructural mass besides their own mass. Whenever the nonstructural mass is smaller compared to the structural mass, aberrations occurred in reaching the optimal design. Also, if there were two frequencies very close to each other, the switching of modes caused abrupt changes in the distribution of the variables, and hence caused oscillations in the structural weight. It took a few iterations to get a stable convergence.

References

1. Miura, H. and Schmit, L.A., "Second Order Approximation of Natural Frequency Constraints in Structural Synthesis," Intl. J. for Numerical Methods in Engineering, Vol. 13, 1978, pp. 337-351.

2. Kiusalaas, J., and Shaw, R.C., "An Algorithm for Optimal Structural Design with Frequency Constraints," Intl. J. for Numerical Methods in Engineering, Vol. 13, 1978, pp. 283-295.

3. Levy, R., and Chai, K., "Implementation of Natural Frequency Analysis and Optimality Criterion Design," Computers and Structures, Vol. 10, 1979, pp. 277-282.

4. Khan, M.R., and Willmert, K.D., "An Efficient Optimality Criterion Method for Natural Frequency Constrained Structures," Computers and Structures, Vol. 14, No. 5-6, 1981, pp. 501-507.

5. Venkayya, V.B., and Tischler, V.A., "Optimization of Structures with Frequency Constraints," Computer Meth. for Nonlinear Solids and Structural Mech., ASME, AMD-54, 1983, pp. 239-259.

6. Elwany, M.H.S., and Barr, A.D.S., "Minimum Weight Design of Beams in Torsional Vibration with Several Frequency Constraints," J. of Sound and Vibration, Vol. 62, No. 3, 1979, pp. 411-425.

7. Fleury, C., and Sander, G., Generalized Optimality Criteria For Frequency Constraints, Buckling Constraints and Bending Elements, AFOSR-TR-80-107, 1980.

8. Pedersen, P., "Design with Several Eigenvalue Constraints by Finite Elements and Linear Programming," Journal of Structural Mechanics, 10(3), 1982-83, pp. 243-271.

9. Khot, N.S., "Optimization of Structures with Multiple Frequency Constraints," Computers and Structures, Vol. 20, No. 5, 1984, pp. 869-876.

10. Olhoff, N., "Optimization of Vibrating Beams with Respect to Higher Order Natural

Frequencies," J. of Structural Mechanics, 4(1), 1976, pp. 87-112.

11. Gupta, K.K., "Free Vibrations of Single - Branch Structural Systems," J. of the Institute of Mathematics and its Applications, Vol. 5, No. 3, 1969.

12. Peters, G., and Wilkinson, J.H., "Eigenvalues of $Ax = \lambda Bx$ with Band Symmetric A and B," Computer Journal, Vol. 12, 1969, pp. 398-404.

13. Venkayya, V.B., Khot, N.S., and Reddy, V.S., "Optimization of Structures Based on the Study of Energy Distribution," Proc. of the Second Conf. on Matrix Methods in Structural Mechanics, AFFDL-TR-68-150, 1968, pp. 111-154.

14. Grandhi, R.V., and Venkayya, V.B., OPTFREQ: Optimization of Structures with Multiple Frequency Constraints, Technical Report, AFWAL-TR-87-XXX-FIBR, 1987.

15. Handerson, T., Active Control of Space Structures (ACOSS) Model 2, Report C-5437, The Charles Stark Draper Laboratory, Inc., September 1981.

16. Lenzi,D.C., and Shipley, J.W., "MAST Flight System Beam Structure and Beam Structural Performance," Proceedings of the NASA/DOD Control/Structures Interaction Technology, 1986, NASA-CP 2447, Part 1, pp. 265-279.

Table 1 Ten Bar Truss
Initial and Final Frequencies for a Specified Second Frequency (Hz)

Frequency No.	Initial Design	$\omega_2 = 10.0$	$\omega_2 = 15.0$	$\omega_2 = 20.0$	$\omega_2 = 25.0$	$\omega_2 = 27.08$	$\omega_2 = 30.0$
1	8.96	3.26	4.92	6.64	8.40	9.17	10.34
2	27.08	10.00	15.00	20.00	25.00	27.08	30.00
3	27.45	10.19	15.07	20.13	25.00	27.11	30.13
4	51.25	16.01	15.30	21.51	27.66	30.96	35.42
5	58.00	18.08	22.21	30.39	39.34	43.96	50.73
6	64.73	22.96	24.28	32.81	41.32	45.54	51.39
7	66.87	25.21	39.49	52.53	65.35	70.40	78.90
8	80.85	27.25	41.64	55.89	70.49	76.84	87.71
Weight (lb)	4000.0	304.5	637.0	1251.5	2243.8	2865.9	4143.9

Table 2 Ten Bar Truss

Optimum Design Variables (in^2) for a Specified Second Frequency (Hz)

Frequency Limit	10.0	15.0	20.0	25.0	27.08	30.0
Element No.						
1	0.910	2.313	4.435	7.699	9.598	13.720
2	0.821	2.154	4.140	7.224	8.979	12.866
3	0.910	2.313	4.435	7.697	9.598	13.720
4	0.821	2.154	4.140	7.223	8.979	12.866
5	0.768	0.602	1.223	2.195	2.905	3.907
6	0.570	0.353	0.760	1.382	1.850	2.774
7	0.712	1.723	3.413	6.211	7.898	11.075
8	0.712	1.723	3.413	6.211	7.898	11.075
9	0.581	1.037	2.114	4.017	5.431	8.460
10	0.581	1.036	2.114	4.003	5.431	8.460
Weight (lb)	304.5	637.0	1251.5	2243.8	2865.9	4143.9

Table 3 Ten Bar Truss
Initial and Final Frequencies (Hz) in Different Constraint Conditions

Frequency No.	Initial Design	$\omega_1 = 7.0$	$\omega_1 = 10.0$	$\omega_1 = 7.0$ $\omega_2 \geq 15.0$	$\omega_1 = 10.0$ $\omega_2 \geq 15.0$	$\omega_1 = 7.0$ $\omega_2 \geq 15.0$ $\omega_3 \geq 20.0$	$\omega_1 \geq 3.5$ $\omega_2 \geq 10.0$ $\omega_3 \geq 14.0$
1	8.96	7.00	10.00	7.00	10.00	7.00	4.40
2	27.08	10.96	13.73	15.58	19.16	15.61	12.14
3	27.45	16.27	22.29	16.93	24.52	20.17	14.00
4	51.25	18.21	25.19	18.75	27.16	20.77	17.89
5	58.00	27.39	38.04	29.13	38.71	28.76	19.58
6	64.73	29.55	42.21	30.30	40.53	29.76	22.96
7	66.87	47.92	65.79	46.93	67.66	53.88	34.01
8	80.857	50.34	69.93	49.67	71.38	56.03	35.72
Weight (lb)	4000.0	1137.3	2614.0	1172.6	2736.3	1308.4	489.17

Table 4 Ten Bar Truss

Optimum Design Variables (in^2) in Different Constraint Conditions

Element No.	$\omega_1 = 7.0$	$\omega_1 = 10$	$\omega_1 = 7.0$ $\omega_2 \geq 15.0$	$\omega_1 = 10.0$ $\omega_2 \geq 15.0$	$\omega_1 = 7.0$ $\omega_2 \geq 15.0$ $\omega_3 \geq 20.0$	$\omega_1 \geq 3.5$ $\omega_2 \geq 10.0$ $\omega_3 \geq 14.0$
1	6.045	13.965	5.511	13.147	5.672	2.306
2	1.969	4.437	1.937	5.683	3.823	1.304
3	6.045	13.965	5.511	13.147	5.672	2.306
4	1.969	4.437	1.937	5.683	3.823	1.304
5	0.100	0.100	0.207	0.488	0.646	0.639
6	0.100	0.100	0.414	0.517	0.321	0.557
7	3.206	7.579	3.616	9.093	4.191	1.029
8	3.206	7.579	3.616	9.093	4.191	1.029
9	2.226	5.009	2.414	4.110	1.604	0.800
10	2.226	5.009	2.414	4.110	1.604	0.800
Weight (lb)	1137.3	2614.0	1172.6	2736.3	1308.4	489.17

Table 5 Two Hundred Bar Truss
Initial and Final Five Frequencies (Hz) for a Specified
Fundamental Frequency

	ω_1	ω_2	ω_3	ω_4	ω_5	Weight (lb)
Initial Design	2.87	13.02	13.72	31.92	37.68	99634.0
Frequency Limit						
2.0	2.00	6.24	6.66	10.69	12.64	2365.7
3.0	3.00	8.19	8.92	13.67	13.81	5004.7
4.0	4.00	9.79	10.90	14.43	15.66	9198.4
5.0	5.00	11.24	12.71	15.13	17.17	15500.9
6.0	6.00	12.61	14.28	15.90	18.13	24830.6
7.0	7.00	13.93	15.86	16.90	19.65	38683.3
8.0	8.00	16.74	19.08	20.15	24.16	61186.7

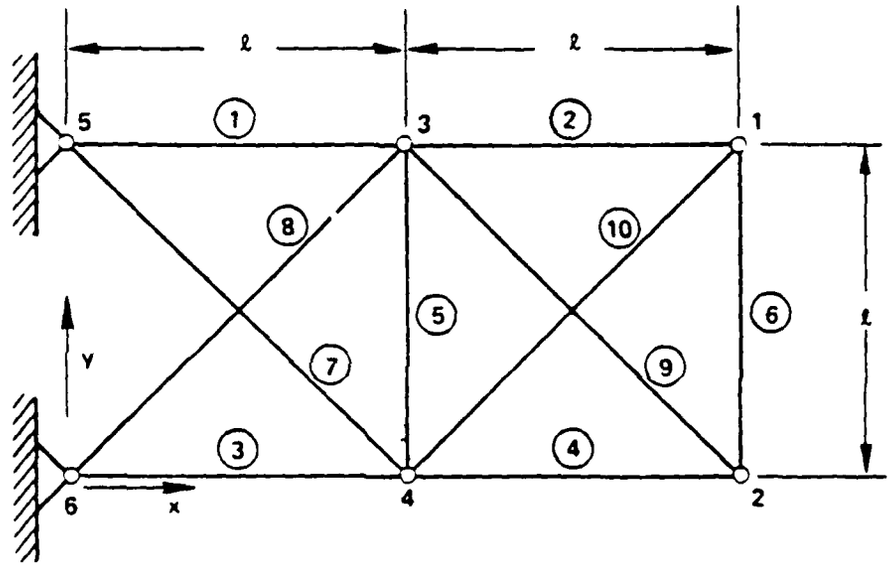

ℓ = 360 in.

Fig. 1 Ten Bar Truss Structure

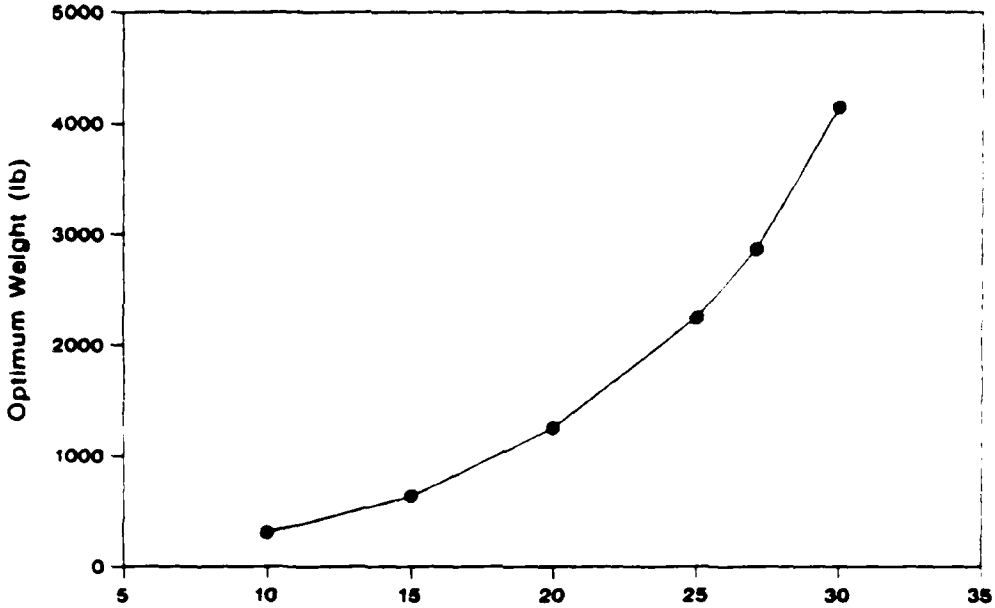

FIG 2 Ten Bar Truss - Specified Second Frequency

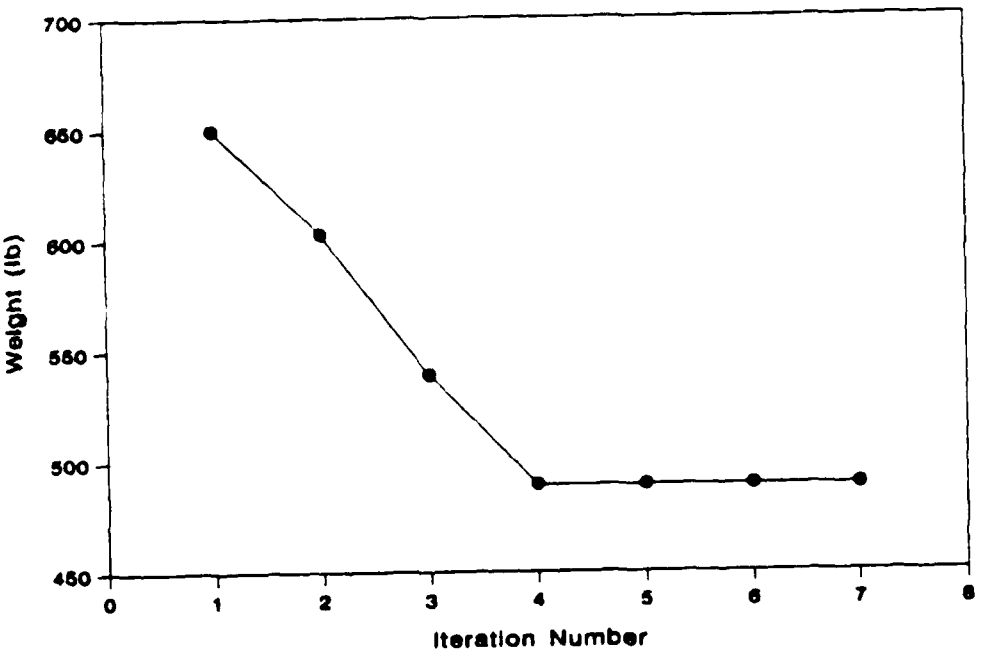

Fig. 3 Ten Bar Truss - Three Inequality Constraints

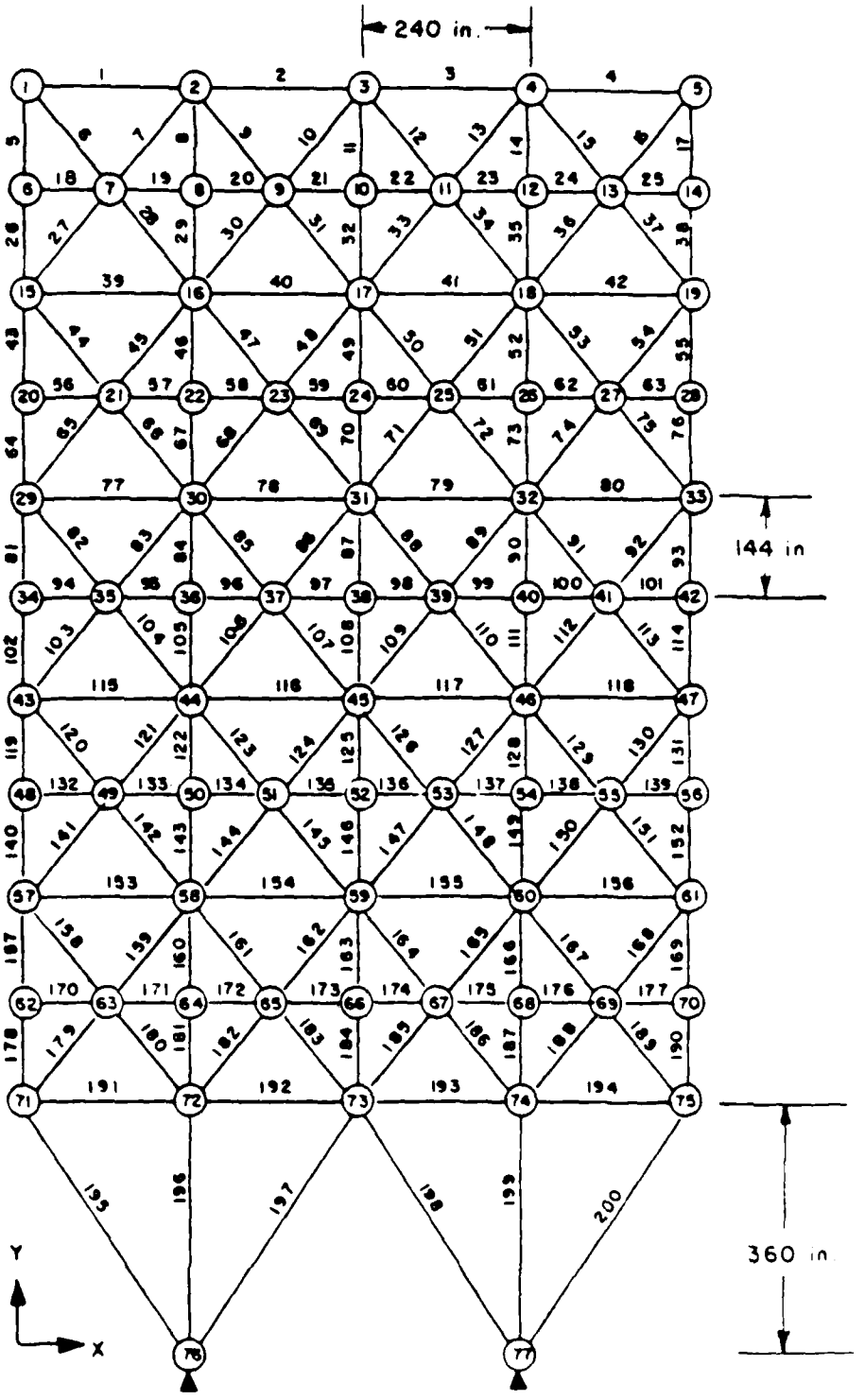

Fig. 4 Two Hundred Bar Truss Structure

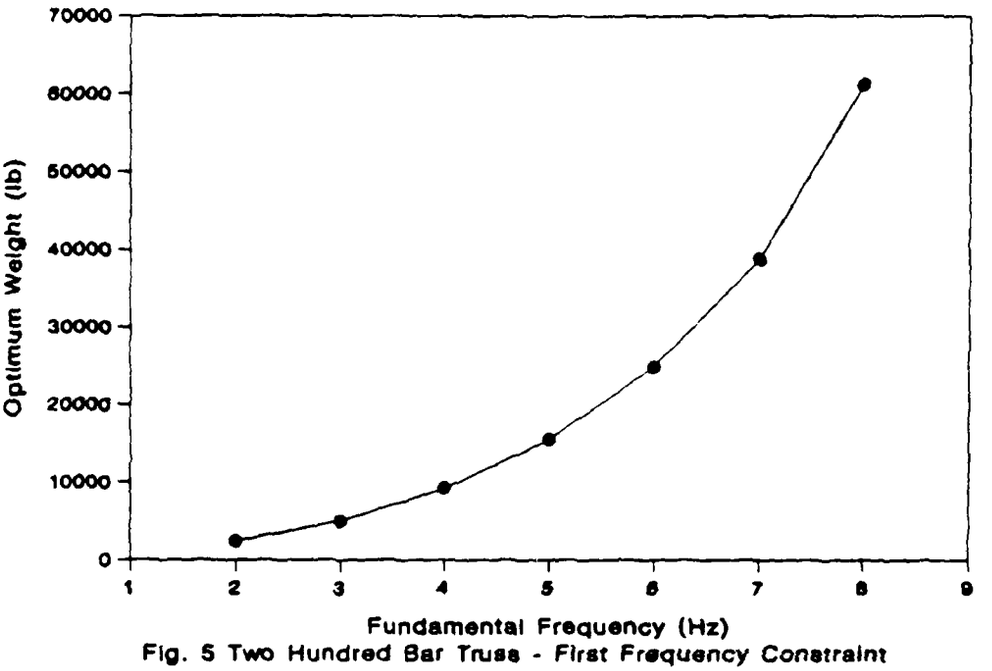

Fig. 5 Two Hundred Bar Truss - First Frequency Constraint

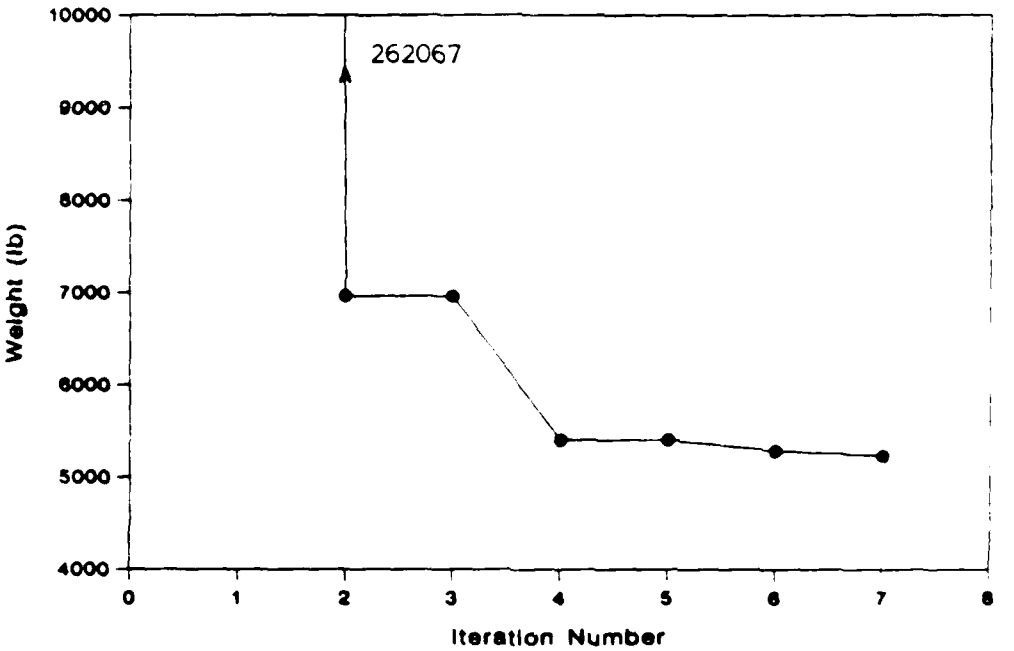

Fig. 6 Two Hundred Bar Truss - Two Constraints

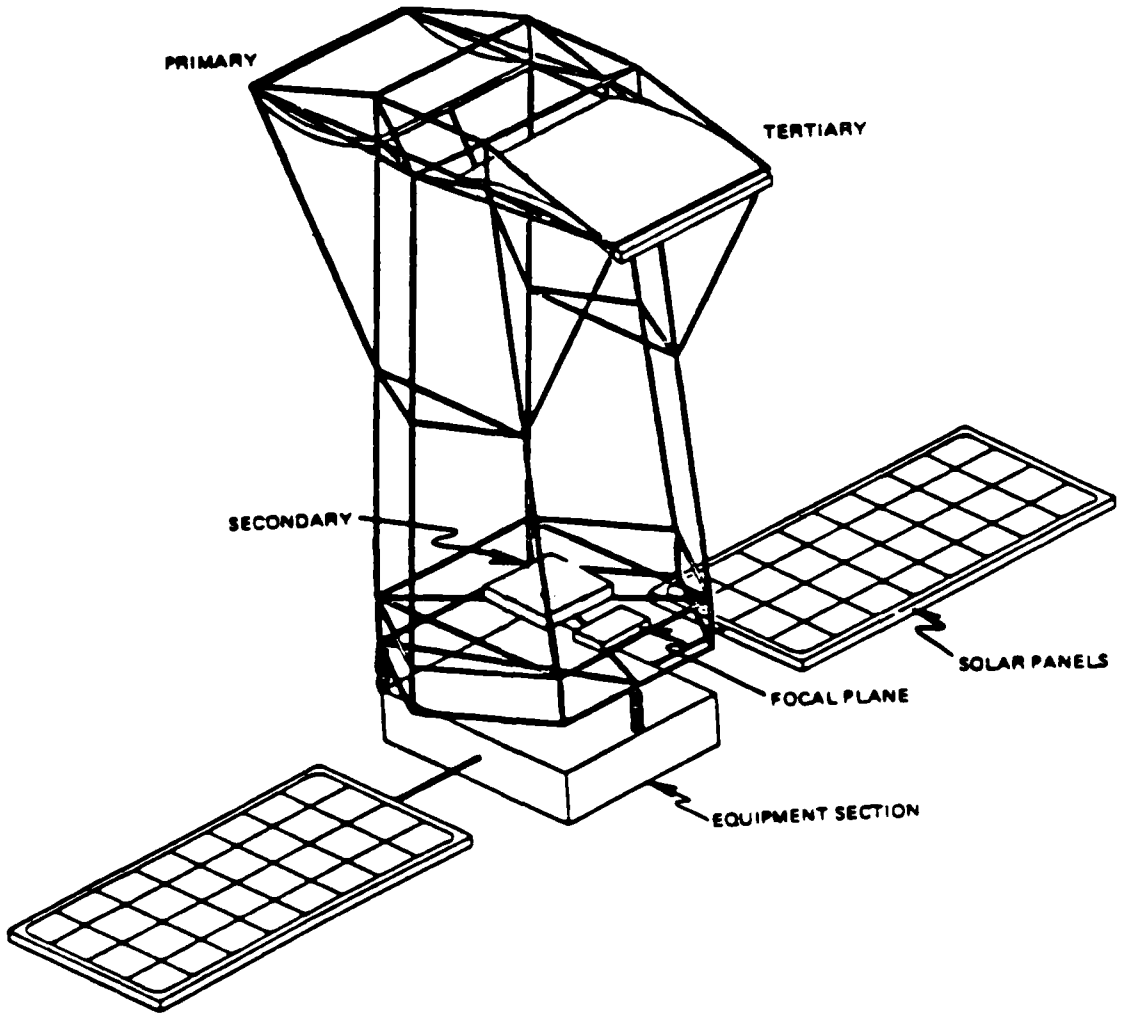

Fig. 7 ACOSS Model II

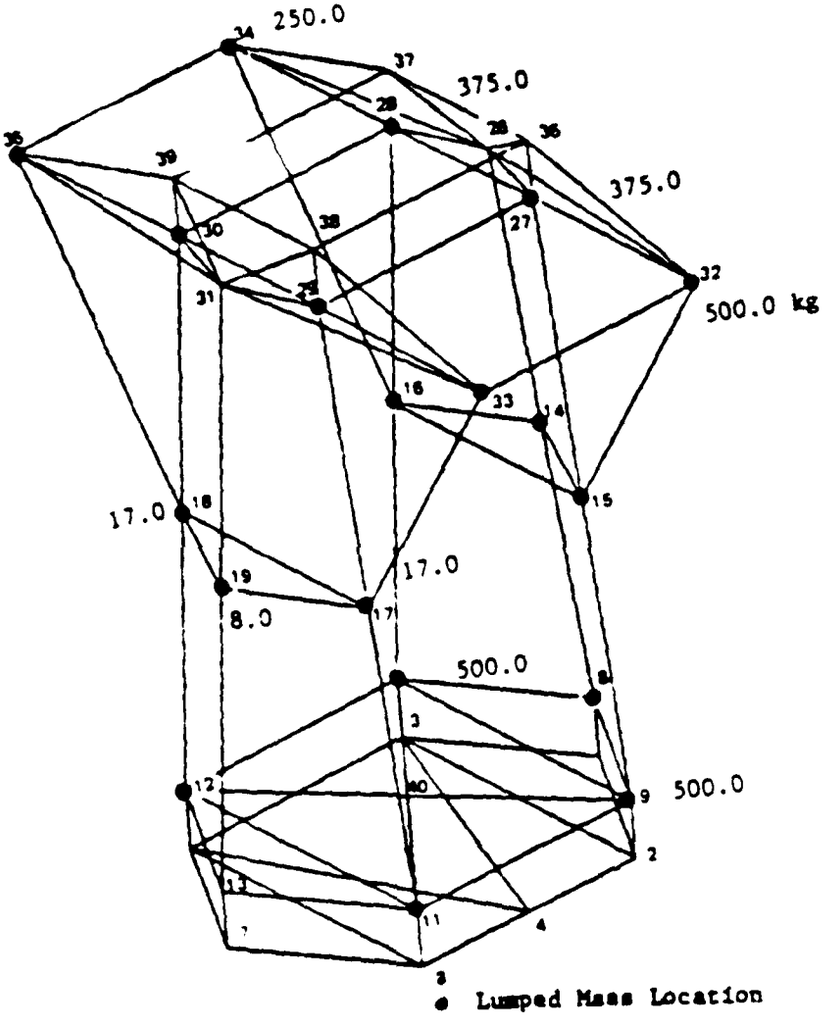

Fig.8 Finite Element Representation of ACOSS II

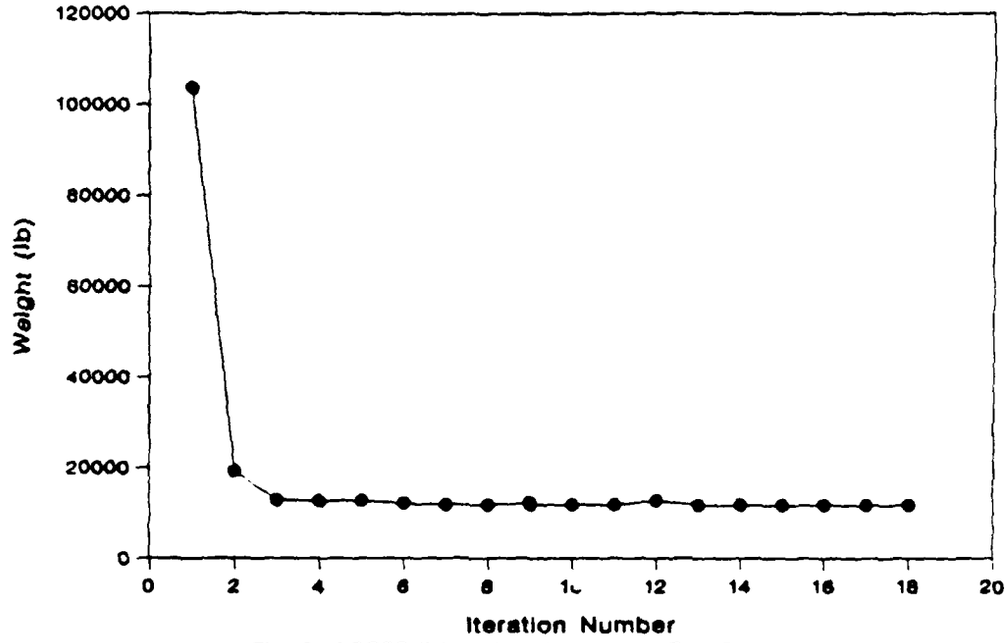

Fig. 9 ACOSS II Iteration History with Two Constraints

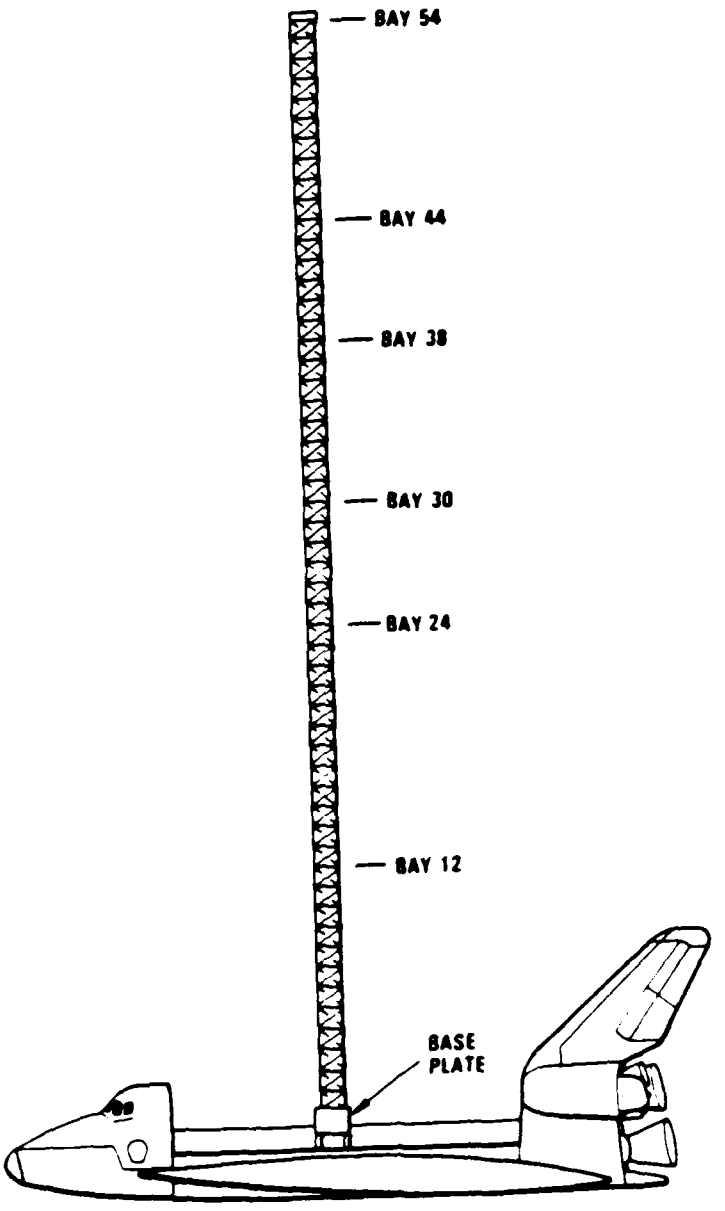

Fig.10 COFS Model

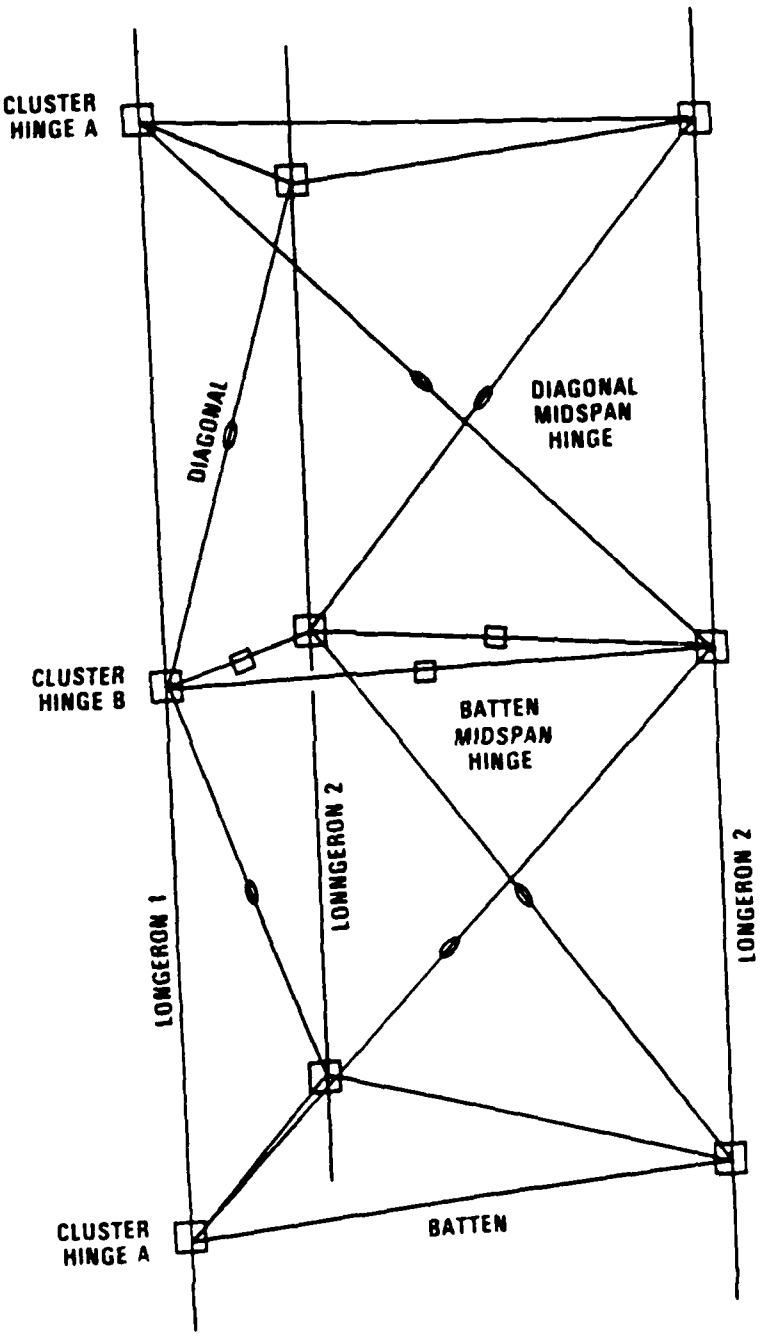

Fig.11 Two Bay Representation

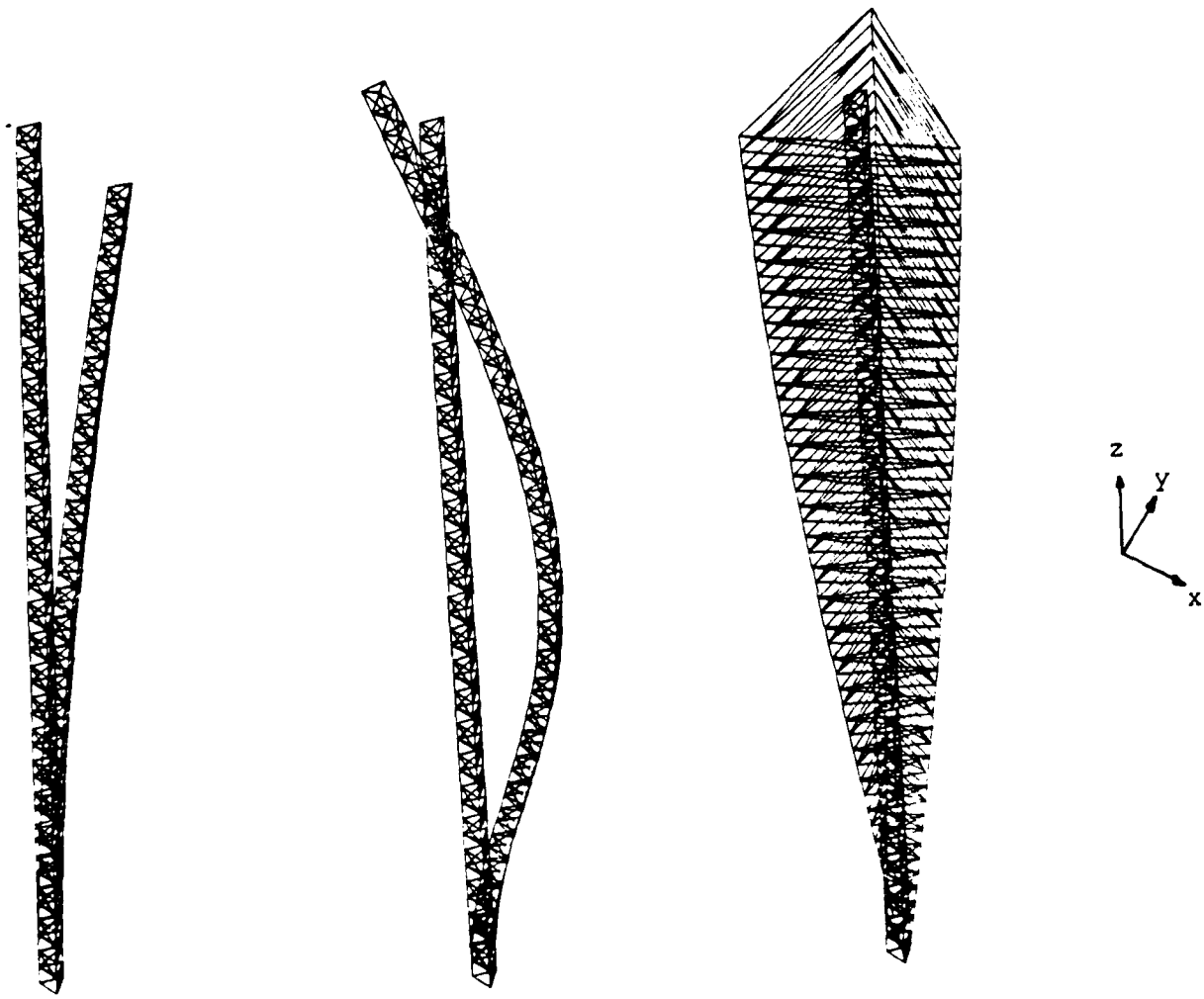

Mode 1 Mode 2 Mode 3

Fig. 12 Mode Shapes

List of Publications Under this Sponsorship

Journal Papers

"Structural Optimization with Frequency Constraints" submitted to AIAA Journal, February, 1987.

"Optimal Structural Design with Control Gain Norm Constraint," submitted to AIAA Journal, February, 1987.

"Optimum Design of Large Structures with Multiple Constraints," Accepted for publication in AIAA Journal, 1987.

Conference Proceedings

"Effect of Passive Damping on Optimum Structural Design," ASME Design Engineering Technical Conference, Boston, MA, October 1987.

"A Combined Optimality Criteria/Mathematical Approach to Design Large Structures," AIAA/ASME/ASCE/AHS Structures, Structural Dynamics and Materials Conference, Montery, CA, April 1987.

"Structural and Control Optimization of Space Structures," AIAA/ASME/ASCE/AHS Structures, Structural Dynamics and Materials Conference, Montery, CA, April 1987.

"Structural Optimization with Frequency Constraints," AIAA/ASME/ASCE/AHS Structures, Structural Dynamics and Materials Conference, Montery, CA, 1987.

"Optimal Structural Design with Control Gain Norm Constraint," AIAA 25th Aerospace Sciences Meeting, Reno, Nevada, January, 1987.

"Improving the Active Vibrational Control of Large Space Structures through Structural Modifications," 37th International Astronautical Congress, Innsbruck, Austria, 4-11 October, 1986.

"An Integrated Approach to Structure and Control Design of Space Structures," Recent Developments in Structural Optimization, (Ed. F.Y. Cheng), ASCE Publication, 1986.

"Optimum Design of Large Structures with Multiple Constraints," AIAA/ASME/ASCE/AHS Structures, Structural Dynamics and Materials Conference, Part 1, pp. 398-408, San Antonio, Texas, 1986.

Report

"Comparison of Optimization Algorithms for Large Structures," AFWAL-TM-86-204-FIBR, May 1986.

Abstracts

"Structural and Control Optimization of Space Structures," Aerospace Sciences Mini Symposium, 1987.

"Optimum Design of Large Structures with Multiple Constraints," Society of Engineering Science 22nd Annual Meeting, Pennsylvania State University, October 1985.

SOLID FUEL RAMJET COMBUSTOR FLOW

Mahesh S. Greywall
Mechanical Engineering Department
Wichita State University
Wichita, Kansas 67208

UES Project 760
Mini-Grant 019

Submitted to
PORT, Aero Propulsion Laboratory
U.S. Air Force Wright Aeronautical Laboratory

December 1986

ABSTRACT

A study of the flow through a solid-fuel (75 % hydroxylterminated polybutadiene and 25 % cross-linked polystyrene) ramjet combustor is presented. The computations were carried out using both the infinite reaction rate kinetic model and the global reaction rate kinetic model. Also included in the study is the effect of an added mixing zone on the combustion efficiency.

I. INTRODUCTION

Solid-fuel ramjet has gained interest in the recent years as a propulsion device for specific defense applications. As the use of this device receives increasing attention, it becomes increasingly important to develop theoretical models to describe flow through the various ramjet components: in particular, the complex flow through the dump (sudden-expansion) type combustors. Theoretical studies of the combustor flow field, especially the parametric type, will lead to a better understanding of what goes on in the combustor, and thus to a better design. The insight gained by these studies will also help in planning the combustor test programs and in better understanding the test results.

Much of the analysis of SFRJ combustors in the past has dealt with correlating the fuel regression data with mass flux through the combustor. A discussion of the various correlation formulae is given in Ref. 1 (section 4.3.4). This reference also has a discussion of the more recent formulae that include, guided by one-dimensional analysis, the dependance of regression ratres on the chamber pressure and the combustor inlet air temperature.

Almost all of the two-dimensional calculations of the SFRJ combustor flow, up till now, have been carried out by Netzer, and by Netzer in cooperation with others (see, for example, Refs. 2-5). These calculations were carried out by adapting the 2-D elliptic flow codes developed by the Imperial College (6,7) to the SFRJ geometry. In Ref. 2 calculations of combustor flow were carried out using vorticity and stream function as the dependent variables. Radiation was neglected and fast chemical reaction (mixing limited combustion) was assumed. The results of calculations were in good qualitative agreement with the experimental data (also obtained by the author) for plexiglas. In Ref. 3 calculations were repeated for an all-hydrocarbon fuel. The regression rates were too low and were arbitrarily increased by 30% to obtain a more realistic value of the blowing parameter. As pointed out by the author, radiation plays a dominant role in all-hydrocarbon fuel combustors, and the neglect of radiation in his calculations was the reason for his low regression rates. Stevenson and Netzer (4) repeated the calculations of Ref. 2 using primitive variables, the results were similar to those otained earlier with the use of vorticity-stream function variables. Metochianakis and Netzer (5) modified the earlier work (3) to include the effects of radiation. The amount of radiation striking the fuel surface depended strongly on an empirical constant C appearing in their formulation. The constant was selected to match

the results of their calculations with the experimental data. Results of the calculations, carried out for plexiglas, were similar to those obtained earlier without the radiation effects. As pointed out by the authors, radiation plays an unimportant role in combustors using plexiglas fuel.

An interesting approach to the modeling of liquid-fuel dump ramjet combustors, called "modular" modeling, is presented by Edelman, et.al. (8). The model makes use of the modular concept, in which the combustor flow field is broken down into various interacting components, each with its own distinct flow characteristics. This approach allows rapid calculation of the combustor flow, thus making it feasible to conduct parametric studies. Our approach to compute flow through the solid-fuel dump ramjet combustor, presented in this report, is based on this modular concept.

Flow through the solid-fuel dump ramjet combustor is considered as made up of three interacting flow regions, P, R1, and R2 as shown in the figure below.

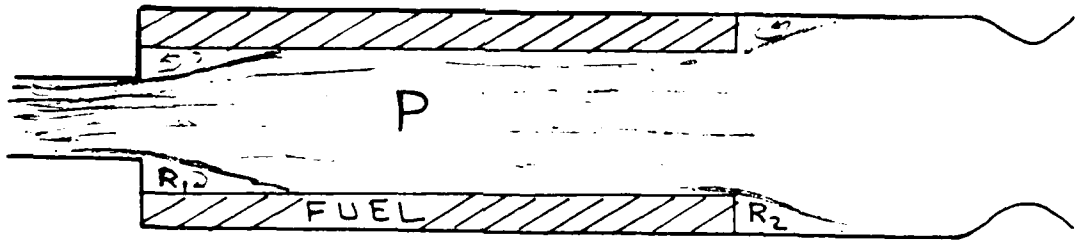

Regions R1 and R2 represent, respectively, the recirculating zones at the combustor inlet step and the aft-fuel-grain step. Region P represents the rest of the combustor-nozzle flow. Flow through region P is a directed flow and, thus, can be computed using parabolic codes. Flow in regions R1 and R2 need to be calculated either using elliptic codes, or modeled empirically. The work presented in this report does not include regions R1 and R2. Thus, it models flow only through that portion of the combustor where the directed flow is in contact with the fuel grain. Even so, the work provides some insight into the diffusion limitations of the combustor efficiency and how the computations of the combustor efficiency are effected by the use of finite reaction rate models. It also show

how the combustor efficiency is effected by the mixing zones that are appended to the combustor.

In section II is given the basic intoductory information. This section includes information about the computational method, the solid fuel and its properties, the combustor geometry, and the defination of some basic terms used in this report.

The Ramjet Technology Branch, PORT, of AFWAL Aero Propulsion Laboratory has an active research and development program in the area of solid-fuel ramjet combustors (see, for example, Refs.9, 10). The present work is conducted to provide theoretical support to the PORT's exerimental efforts.

II. INTRODUCTORY INFORMATION

COMPUTATIONAL METHOD:

All the computations were carried out using a modified version of the computer code given in Refs.11 and 12. The original code computes the mass, momentum, and energy transport of a single species for two-dimensional 'parabolic' (boundary layer type) turbulent flows without any chemical reaction. The code was modified,

(i) to compute the transport of four species; N2, O2, Fuel, and the combustion products.

(ii) to include chemical reaction; two kinds of chemical reaction models were used. (1) infinite reaction rate, and (2) global finite reaction rate.

(iii) to incorporate fuel evaporation from the surface; the rate of of fuel evaporation from the surface, $\dot{m}_f$, was calculted from the equation,

$$\dot{m}_f \bar{h} = \dot{Q}$$

where $\dot{Q}$ is the heat transfered to the fuel grain surface and $\bar{h}$ is defined later on. All the wall fluxes (mass, momentum, and energy) were corrected to take into account the effect of mass addition (blowing) from the surface.

The computations were carried out using 21 streamlines (grid points normal to the flow) and an axial integration step equal to one-tenth of the combustor diameter.

FUEL AND ITS PROPERTIES:

The solid fuel and its properties used in the computaions were as follows:

Fuel: 75% Hydroxylterminated polybutadiene (HTPB) &

25% crosslinked polystyrene (CLPS),

Heat of combustion = 45,760 kJ/kg,

Stoichiometric Air/Fuel ratio = 13.31,

$h = h_{vap} + h_w$ = 1,760 kJ/kg,

where h_{vap} is the latent heat of evaporation and h_w is the enthalpy needed to heat the fuel grain to the specified wall temperature.

These fuel properties were supplied by PORT and are very close to those given in Ref. 1 (Table 2-III).

COMBUSTOR GEOMETRY AND FLOW PARAMETERS:

All the computations, except those given in section VI, were carried out for flow through a 10 cm port diameter combustor (see the figure below).

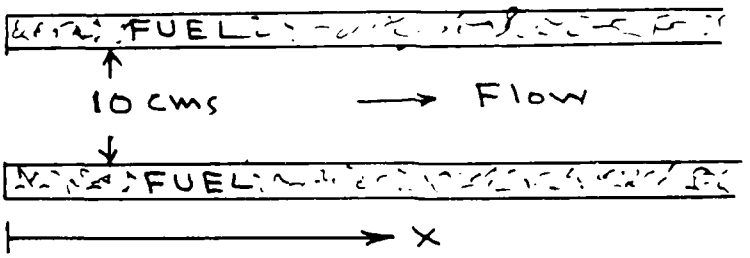

The flow was started with the following parameters.

Velocity = 170 M/s

Temperature = 1200 K

Pressure = 7 atm.

Fuel wall temperature = 980 K.

In all our calculations, we used ideal gas law, fixed constant pressure specific heat equal to 1.338 kJ kg-C (air at 2000 K), and both Prandtl and Schmidt numbers equal to one for all the species. The combustor geometry and the starting values of the flow parameters were selected to simulate the experimental conditions of Schadow et. al. (Ref.13).

DEFINATIONS OF SOME BASIC TERMS USED IN THE REPORT

Combustion Efficiency: Combustion efficiency at an axial location x is defined as

$$\eta_f(x) \quad \frac{M_f(x) \quad \dot{\omega}_f(x)}{M_f(x)}$$

where M_f is the rate (in kg/s) at which the fuel is evaporating from the begining of the combustor upto the axial location x, and $\dot{\omega}_f$ is the flux (in kg/s) of the unburnt fuel at the axial location x. Note, if there was no combustion at all, $\dot{\omega}_f$ will be equal to M_f, and the combustion efficiency as defined above will be zero.

Radial Flame Location: Radial flame location is defined by the position of maximum in the radial temperature distribution.

III. INFINITE REACTION RATE COMPUTATIONS

During this set of computations the combustion was considered to be mixing limited with a simple one-step chemical reaction (infinite reaction rate kinetic model). Thus, 1 kg of fuel and r kg of O_2 (r is the stoichiometric ratio of O_2 mass to fuel mass) produced (1 + r) kg of combustion produts, and fuel and oxygen could not co-exist.

Results of the computation of the combustion efficiency as a function of the axial distance are shown in Fig.1. The solid curve shows the actual computed results and the dotted curve is a smooth approximation to it. We note that the combustion is diffusion limited. The axial distance is shown normalized by the combustor diameter. However, since the radial diffusion transport of the fuel and the oxygen is not scaled linearily with the radial distance, these results may not apply to a combustor of different size diameter.

The wiggles in the computed results are due to the finite grid size normal to the flow direction. Within a given grid cell there is complete mixing and, thus, there is no diffusion limitation on the combustion. Figure 2 shows the effect of the grid size normal to the flow on computed combustion efficiency. We note that reducing the grid size reduces the wavelength and the amplitude of the wiggles.

In Fig.3 are shown the computed radial variations of temperature, O_2 and the fuel at an axial distance of 62 cms from the start of the calculations. These distributions are what one would expect with a one-step chemical reaction model. They are in qualitstive agreement with the experimental data. The predicted flame temperature of 4000 K is much too high compared with the experimental value (Ref.13) of approximately 2500 K. The predicted flame temperature is close to the local adiabatic flame temperature. Also shown in this figure is the flame temperature calculated with the heat of reaction reduced artificially by 25%.

Fig. 1 Axial variation of the combustion efficiency using infinite reaction rate kinetic model (I.R.R.).

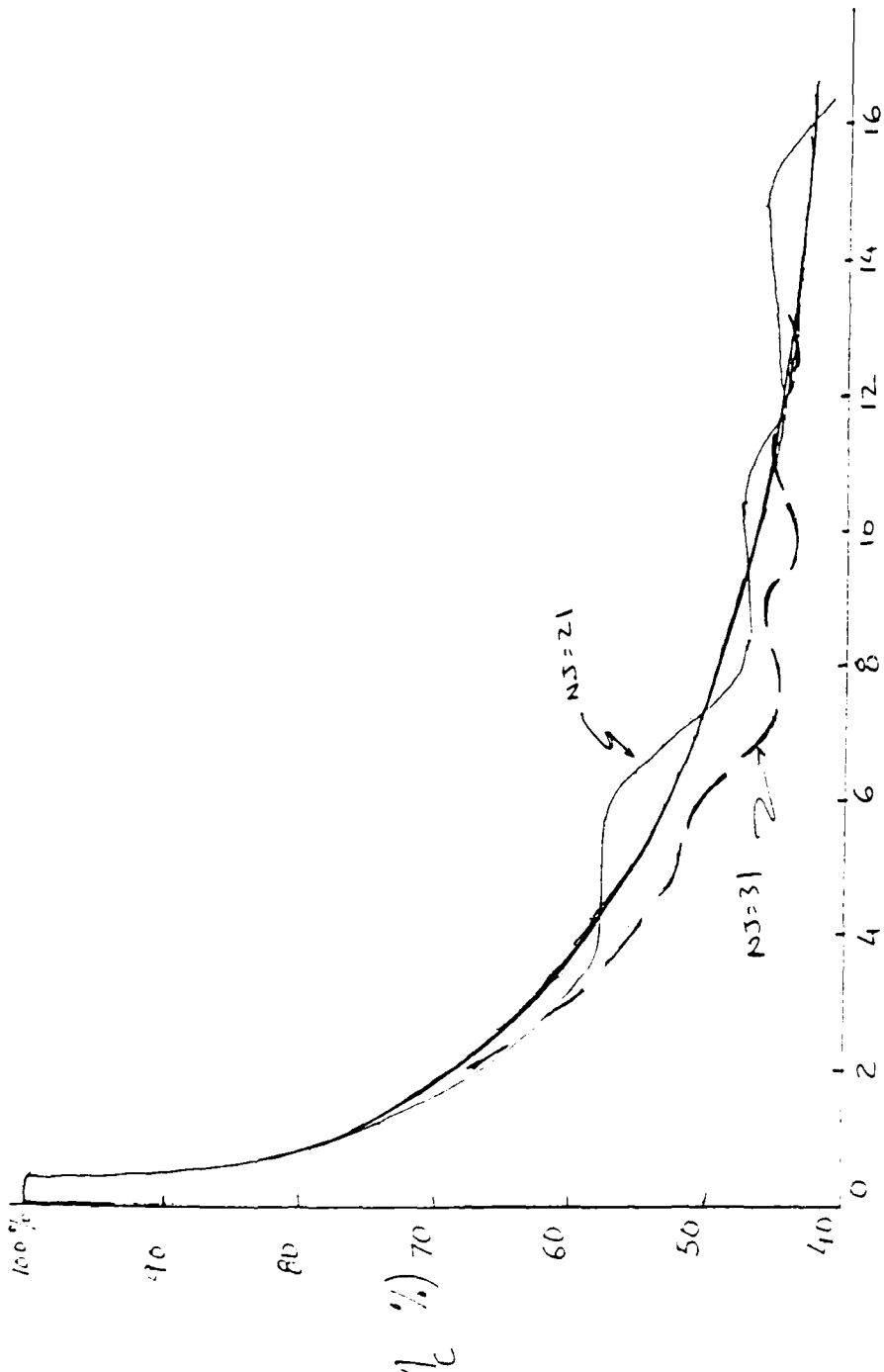

Fig 2 Effect of the grid size normal to the flow on the computed axial variation of the combustion efficiency (infinite reaction rate kinetic model). NJ represents the number of grid points between the wall and the centerline.

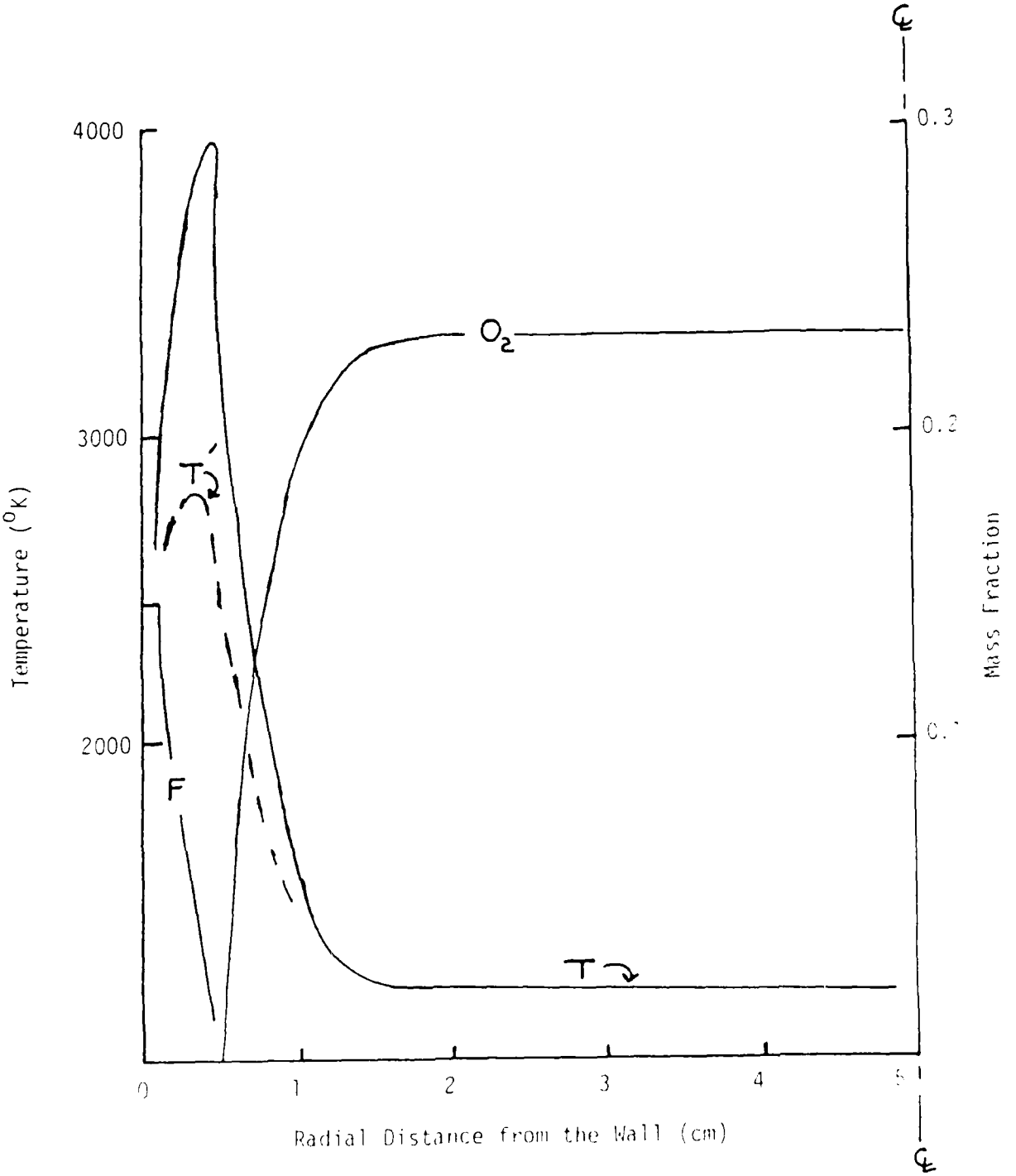

Fig.3 Radial distributions of combustor temperature (T), and oxygen (O_2) and fuel (F) mass fractions. Also shown is the radial temperature distribution (T') with the heat of combustion reduced by 25%.

IV. FINITE REACTION RATE COMPUTATIONS

Detailed reaction mechanisms have been so far developed and tested for only a limited number of relatively simple fuels such as: $H_2, CO, CH_4, CH_3OH, C_2H_2, C_2H_6$. The present state of art is far from poroviding a detailed finite reaction model for the kind of fuel used in the present study (Hydroxyl-terminated polybutadiene - $C_{73}H_{103}O$). For complex fuels in the parafin family Edelman and Fortune have developed a quasi-global reaction rate model. This model uses for the first step the chemical reaction,

$$C_nH_m + \frac{n}{2}O_2 \rightarrow \frac{m}{2}H_2 + nCO,$$

and, from there on uses the detailed reaction mechanisms for H_2 and CO (along with O_2 and N_2 of the combustion air).

In the present study a global reaction rate model was used. A general form of the global reaction rate model is given by,

$$\frac{dC_f}{dt} = -A\, f(p,T)\, C_f^{\alpha_1}\, C_{O_2}^{\alpha_2}\, e^{-(E/RT)}$$

where C_f and C_{O_2} are molar concentrations of *fuel* and O_2, A, α_1, and α_2 are constants; 'f' a function of pressure and temperature; and, (E/R) the activation energy. All the coefficients appearing in the global reaction rate model are determined empirically. All our attempts (literature survey and private comunications) to obtain information about these coeeficients (or of some simpler global reaction rate model) for the fuel used in the present study were fruitless. Thus, the computations were carried out with the simplest version of the global reaction rate model, i.e., with $f(p,T) = \alpha_1 = \alpha_2 = 1$. With the mole fractions C_f and C_{O_2} converted into mass fractions, X_f and X_{O_2}, the global reaction rate model used in the present study is given by,

$$\frac{dX_f}{dt} = -A\, X_f\, X_{O_2}\, e^{-(E/RT)}$$

Since A and E are still unknown , the computations were carried out with A and E R as parameters. For a given value of E/R, A was varied from a high value where the finite reaction rate results were almost same as the infinite reaction rates results, to a low value below which there was no combustion. The results obtained for different values of E R were qualitatively similar. Thus, we have presented the results only for E R = 10,000.

In Fig.4 is shown the combustion efficiency, η_c, as a function of the axial distance, x, for $E/R = 10.000$ and for $A = 10^7$, 10^6, and 3×10^5. For A greater than 10^7 the results were very close to those obtained with the the infinite reaction rate model. And, for A less than 3×10^5 there was practically no combustion. From Fig.4 we note that for small values of x, η_c is higher for higher values of A, as expected. However, for large values of x, η_c approaches roughly the same value for all values of A. This limiting value is close to the one obtained with the infinite reaction rate model. This implies that for large axial distances the combustion is diffusion limited.

In Fig.5 is shown the radial distribution of temperature at the axial distance $x = 1.02$ meters from the start. The curve for the case $A = 10^7$ was too close to the infinite reaction rate curve, and therefore is not shown. From this figure we note that as A decreases the flame temperature decreases and the flame becomes broader. For $A = 3 \times 10^5$ the predicted flame temperature is comparable to the observed experimental value (Ref.13).

In Fig.6 is shown the axial variation of the radial location of the flame. Once again we note that for $A = 10^7$ the global reaction rate model approaches the infinite reaction rate model. From this figure we also note that penetration of the flame into the core flow decreases as A decreases.

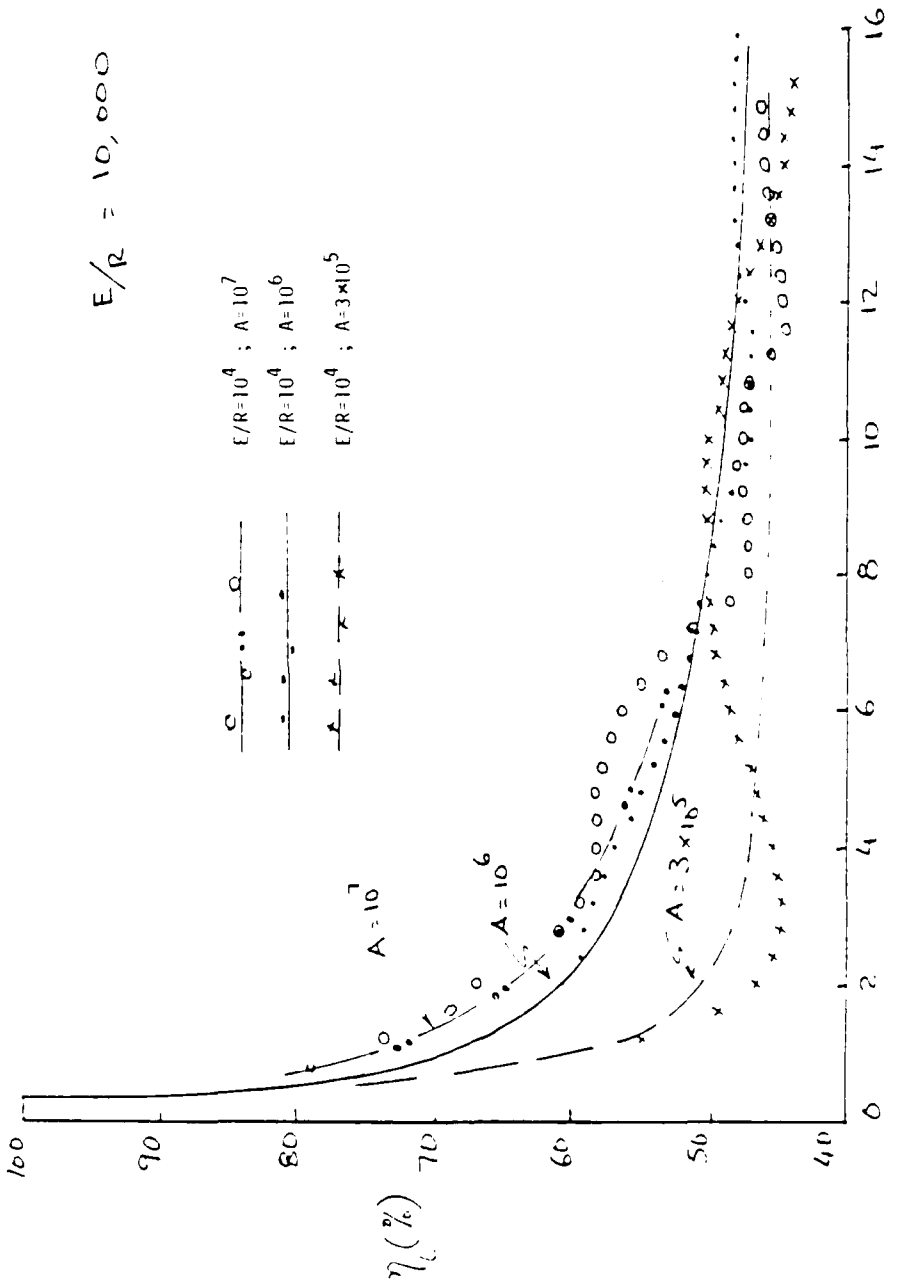

Fig 4 Axial variation of the combustion efficiency using global finite rate kinetic model (G.F.R).

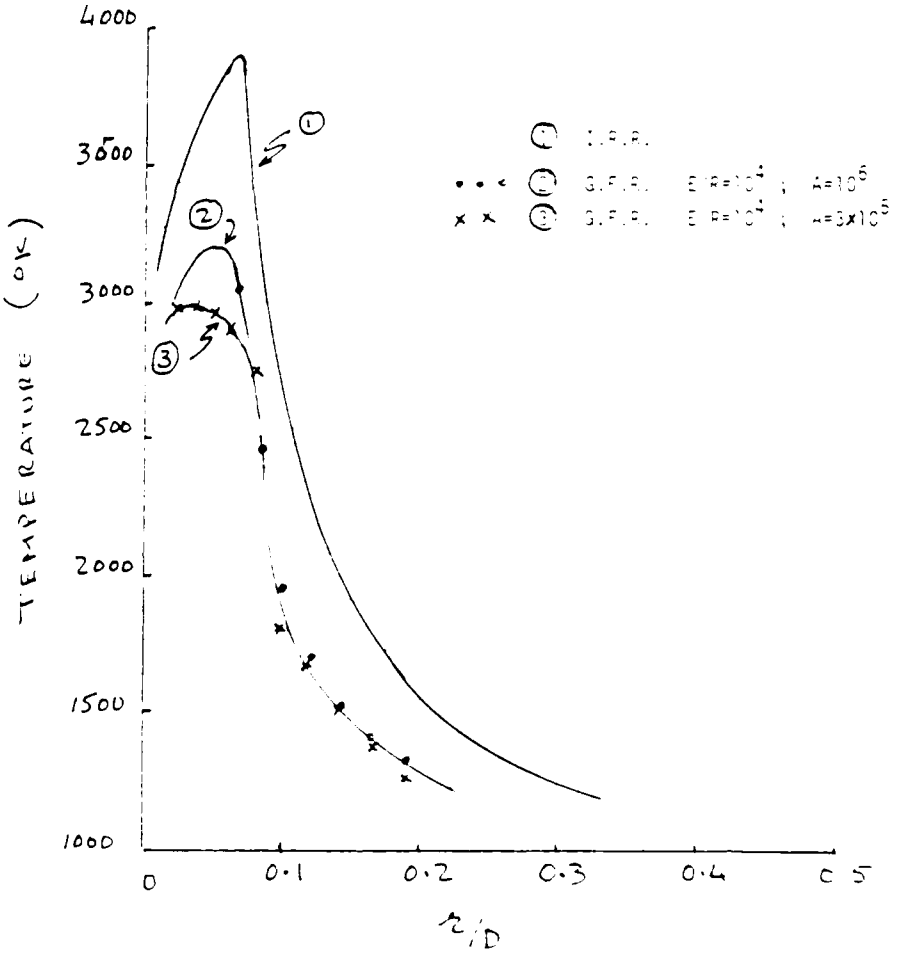

Fig.5 Radial distribution of the temperature at the axial distance x d=10.2.

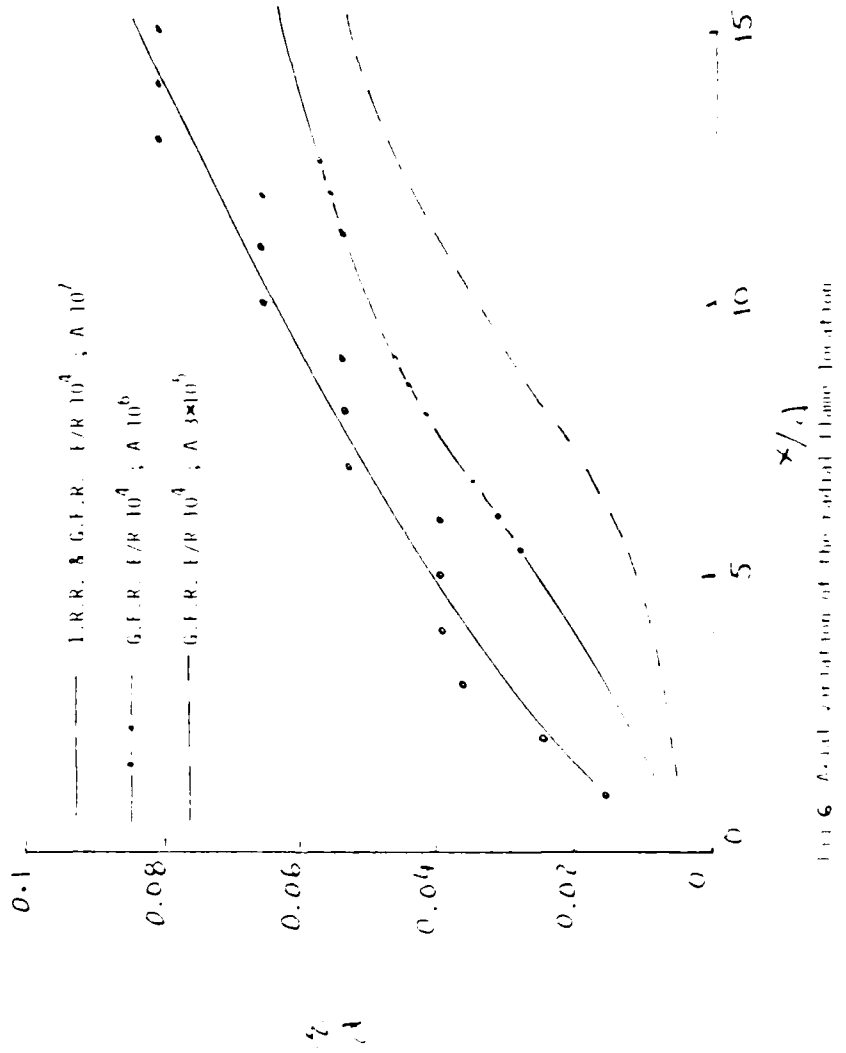

Fig 6 Axial variation of the radial flame location

V. EFFECT OF AN ADDED MIXING ZONE

In the previous section we have seen how the combustion is limited by diffusion. It is of some interest to investigate how the unburnt fuel (accumulated adjacent to the fuel grain) will diffuse and burn if the combustor was extended beyond the end of the fuel grain; that is, if we were to add a mixing zone to the combustor.

In this section we have studied the combustion efficiency of a combustor with mixing zones of various lengths added to it. The computations were carried out by modifying the code so that beyond a specified axial distance the fuel evaporation rate was set equal to zero. The radius of the mixing zone was set equal to the combustor radius; and, thus there is no step expansion. The figure below shows the geometry of the combustor with a mixing zone.

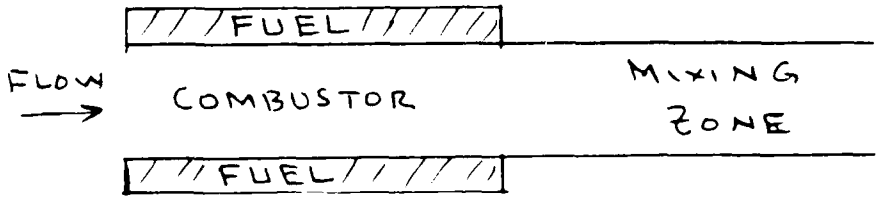

In Fig.7 are shown the results of the computations. The computations were carried out for the case of infinite reaction rate. Three sets of computation were carried out with the following parameters

Combustor length = 5D	Mixing length = 30D
Combustor length = 10D	Mixing length = 25D
Combustor length = 15D	Mixing length = 20D

Where D = the combustor port diameter. The solid curve in Fig.7 for the case [illegible] mixing zone. The solid curve intersects the axis at [illegible] the case of [illegible] Fig.7 [illegible] the axial variation of combustion efficiency [illegible] Section 2 and 3 along with appropriate portions of the

solid curve are for cases (ii) and (iii), respectively. From these figures we note that the combustion efficiency increases in the mixing zone rather rapidly for short combustors followed by mixing zones (case (i) indicated above); but it rises more gradually for long combustors followed by a mixing zone.

Calculations were repeated this time using global finite reaction rate model with $A = 5 \times 10^{11}$ and $E/R = 10{,}000$. The results are shown in Fig.8. Comparing these results with those given in Fig.7, we note that the rise of combustion efficiency in the mixing zone markedly slows down when the reaction proceeds at a finite rate. An interesting point to note in Fig.8 is that the curve marked 1 never reaches 100% but flattens out at about 94%. A look at the radial temperature outputs revealed that this flattening out of the η_c curve is associated with the flame having practically gone out.

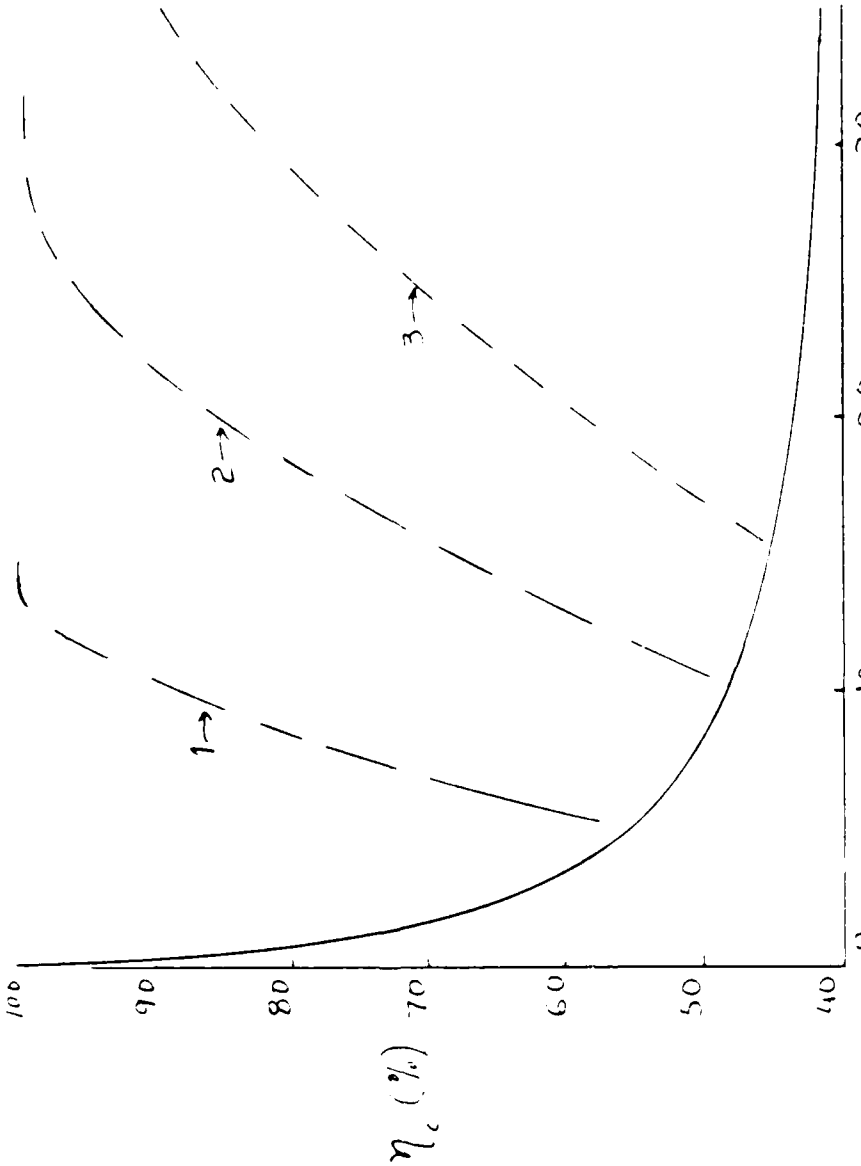

Fig. 7 Effect of upwelling at inlet and zone for a cooling fan on the conjugate effectiveness, for both cases with and without the model.

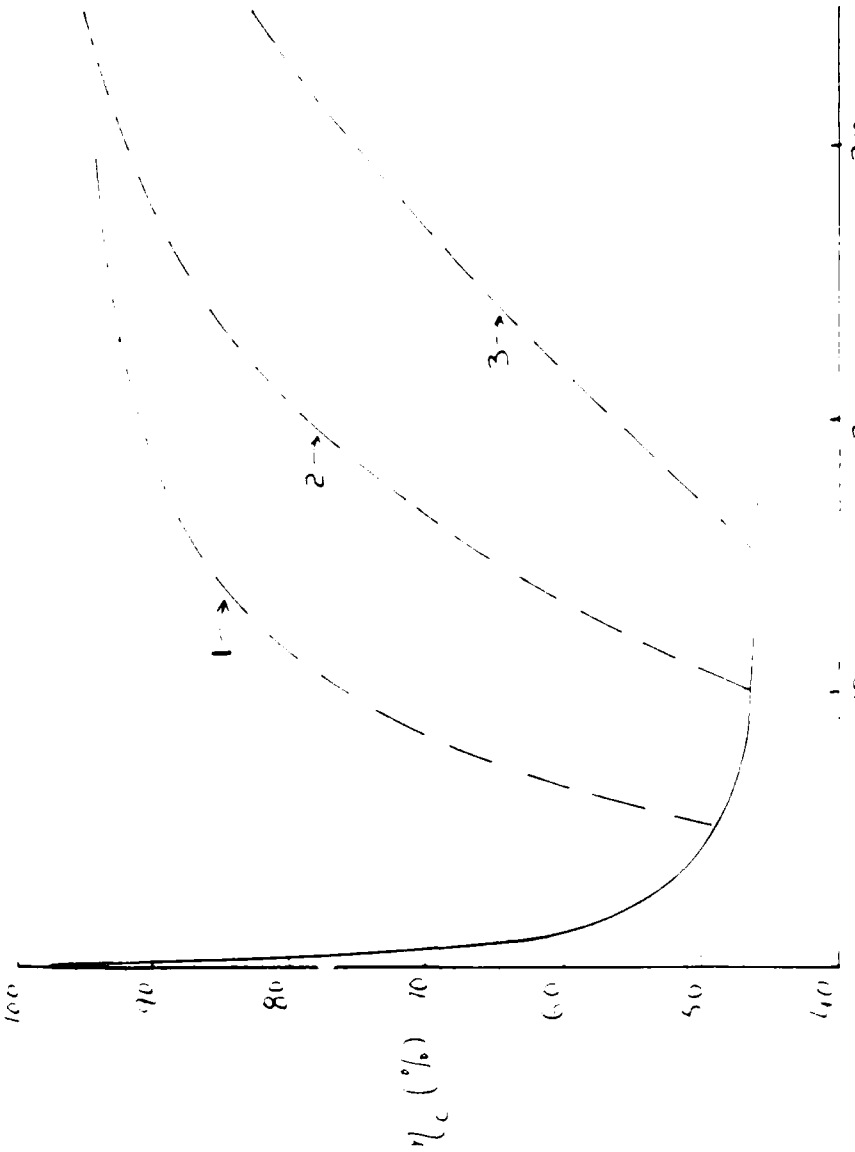
100
90
80
70
60
50
40
η_c (%)
10
20
30
X / D
1
2
3

VI EFFECT OF COMBUSTOR PORT DIAMETER

All the computations presented so far were for a combustor with a port diameter of 10 cms. The results of these computations were presented with the axial distance z normalized by $\frac{1}{2}$ the combustor port diameter. However, since the combustion is diffusion limited it is not scaled by z/R. To study how the axial variation of the combustor efficiency is effected by the port diameter, calculations were carried out with port diameter set equal to 5 cms. All the other variables (inlet velocity, inlet temperature, fuel, etc.) were kept same as in the previous computations. In Fig.9 are shown the results of these computations using the infinite reaction rate model. They are compared with the results for the 10 cms port diameter combustor. Fig.10 compares the results for 5 cms and 10 cms port diameter combustors using global finite reaction rate model. From both the Figs.9 and 10 we see what was expected, that the axial variation of the combustion efficiency is not scaled by z/R.

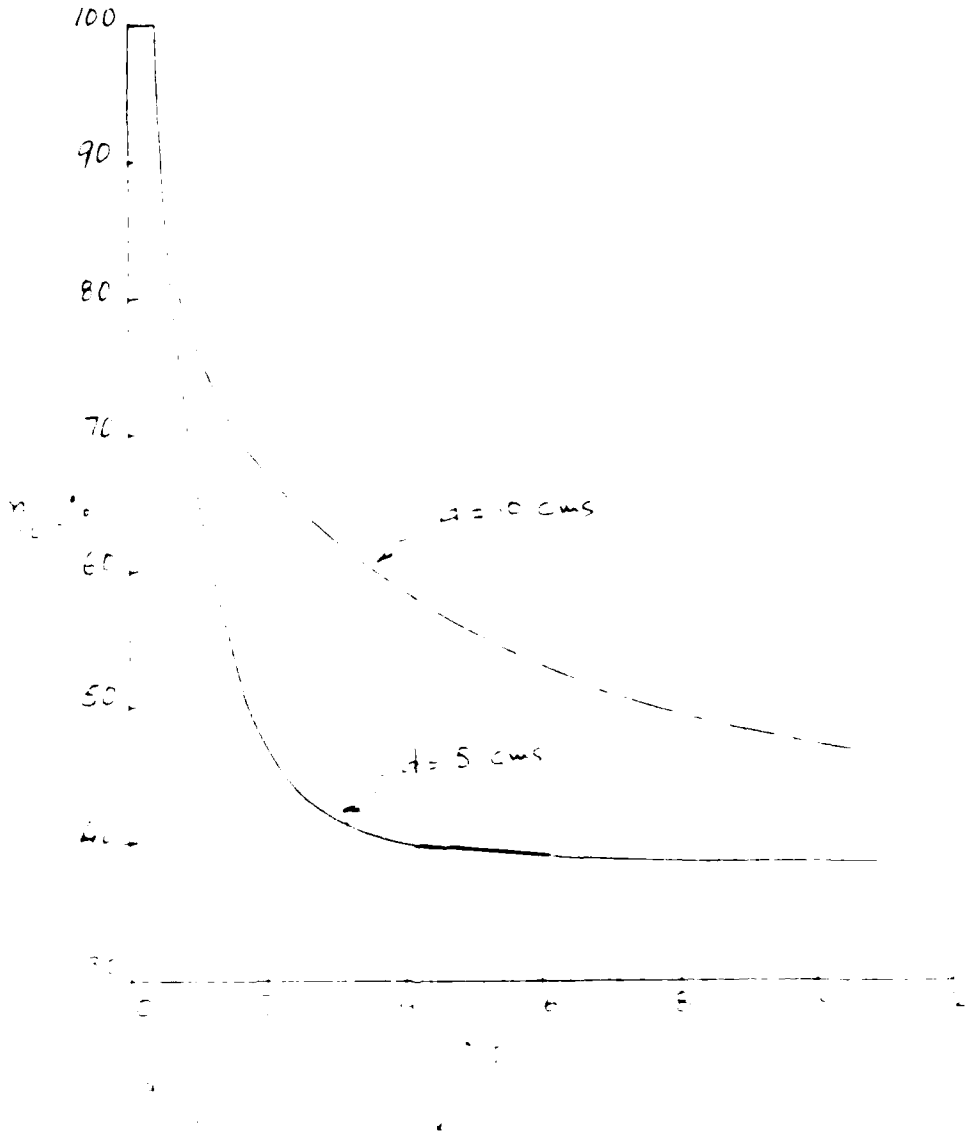
100
90
80
70
60
50
40
30
v = 10 cms
v = 5 cms

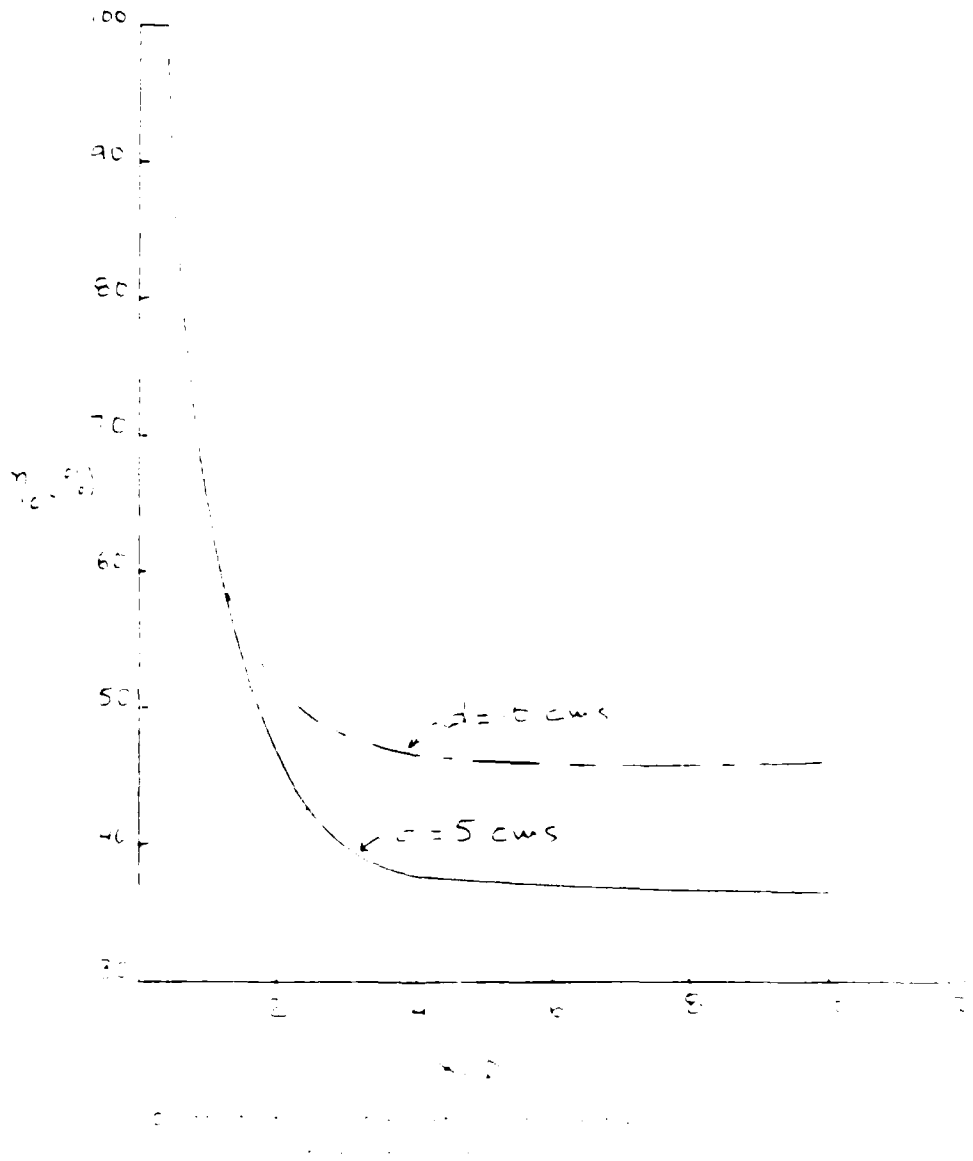
100
90
80
70
60
50
40
30
d = 5 cms
d = 5 cms

ACKNOWLEDGEMENTS

I would like to thank Mr. P.L. Buckley, Dr. F.D. Stull, and Dr. R. Boray for their help during the course of these investigations. I am also beholden to the rest of the PORT members for lending a helping hand and their courtesy during my 1985 summer stay at the laboratory.

The work was supported by AFOSR partly through the 1985 USAF-UES summer faculty program, and partly through the follow-up program.

REFERENCES

1. Fundamental Combustion Technology for Ramjet Applications," CPIA 363, Vol. II, Sept. 1982.

2. Netzer, D.W., "Modeling Solid-Fuel Ramjet Combustion," Journal of Spacecraft and Rockets, Vol. 14, [illegible] pp. [illegible].

   Netzer, D.W., "Modeling Applications to Solid Fuel Ramjet Combustion," Journal of Spacecraft and Rockets, Vol. [illegible], Sept. [illegible], pp. 263-264.

3. [illegible] and Netzer, D.W., "Modeling Solid-Fuel Ramjet Combustion," Journal of Spacecraft and Rockets, Vol. [illegible], Jan.-Feb. 1981, pp. 83-84.

4. [illegible] and Netzer, D.W., "Modeling Solid-Fuel Ramjet Combustion, Including Radiation [illegible]," Journal of Spacecraft and Rockets, Vol. 20, No. 4, July-Aug. 1983, pp. 405-406.

5. [illegible], A.D., Knight, A.M., Runchal, A.K., Spalding, D.B., and Wolfshtein, M., "Heat and Mass Transfer in [illegible] Flows," Academic Press, New York, 1969.

6. Pratt, A.M., and Spalding, D.B., "A General Computer Program for Two-Dimensional Elliptic Flows," [illegible], Imperial College of Science and Technology, London, Report HTS-76-2, Aug. 1977.

7. [illegible], and [illegible], N., "Modeling Techniques for the Analysis of Ramjet [illegible]," AIAA Journal, Vol. [illegible], May 1984, pp. [illegible].

8. [illegible], "[illegible] Ramjet Dump Combustor," Fourth [illegible], AIAA, Vol. [illegible], pp. [illegible].

9. [illegible]

10. [illegible]

AUTOMATED IMAGE PROCESSING TECHNIQUES FOR LANDSAT THEMATIC MAPPER DATA

Barry N. Haack and Miles R. Roberts

George Mason University

Fairfax, Virginia 22030

FINAL REPORT

SUBCONTRACT S-760-OMG-093

Universal Energy Systems

Dayton, Ohio

Prepared for the

AIR FORCE OFFICE OF SCIENTIFIC RESEARCH

BOLLING AFB, WASHINGTON DC

December, 1986

ABSTRACT

This report identifies and evaluates automated image processing techniques for the segmentation of Landsat Thematic Mapper data for a set of earth surface conditions of interest to the U. S. Air Force. A review of basic techniques and developments in image processing strategies is included as is documentation on the existing and anticipated operational global earth surface spaceborne remote sensing systems.

For each of the conditions of interest, a review of previous segmentation activities, a consideration of signature extension possibilities and suggested strategies for successful automated image processing techniques is presented. In addition, appropriate Thematic Mapper data and associated ancillary information which include the conditions of interest are identified.

1.0

INTRODUCTION

Current, reliable information on conditions at the earth's surface are necessary for many U. S. Air Force activities. Those conditions may be dynamic or static and may include such features as population density, land use or cover, topography, transportation networks and soil parameters. Information on those features are important for Air Force navigation, reconnaissance and intelligence interests.

One tool of increasing importance in obtaining earth surface information is remote sensing. Remote sensing has recently been expanded greatly by the use of new platforms such as earth orbiting satellites and the Shuttle Missions to acquire information; the use of sensors in more portions and combinations of the electromagnetic spectrum such as active microwave, thermal infrared and multispectral scanners; and the incorporation of computers in the handling and processing of remotely sensed data.

Because of the potential need by the Air Force for information at essentially any point on the surface of the earth, it is important to determine what utility can be made of data from operational, ongoing, essentially global spaceborne remote sensing systems. The data most suitable for this need are from the Thematic Mapper (TM) sensor of the Landsat series of

satellites. TM is a seven band multispectral scanner with 30 m spatial resolution collecting data at a sixteen day repeat cycle for all areas between 81 degrees north and south latitude.

Because the informational needs of the Air Force may require a short response time and must be very accurate, automated computer image processing techniques may be the best methodology to obtain the necessary information. This study has identifed and evaluated the application of various automated image processing techniques applied to TM data for segmentation of a specific set of earth surface conditions of interest to the Air Force. The set of conditions is listed in Table 1.

Section 2 of this report briefly reviews some of the basic image processing strategies important in remote sensing of earth surface features. This review includes various signature extraction techniques, both per pixel and contextural, and strategies incorporating multitemporal, multisensor and ancillary data sets. The concept of ancillary data is extended to the development and utilization of geographic information systems (GIS). In addition, the possible use of expert systems or artificial intelligence in image processing is considered.

Section 3 documents the orbiting parameters and sensor and data characteristics of the Landsat based TM sensor. Other current or planned spaceborne sensing systems which meet the requirements of operational and near-global coverage are also presented. These systems include the older Landsat based Multispectral Scanner

(MSS), the new French Systeme Probatoire d'Observation de la Terre (SPOT), the NOAA based Advanced Very High Resolution Radiometer (AVHRR) and future developments of the Landsat and SPOT series of spaceborne sensors.

TABLE 1. SURFACE CONDITIONS TO BE EVALUATED

PHYSIOGRAPHIC

- Slope
- Surface roughness
- Streams
- Lakes and reservoirs
- Wetlands
- Snow accumulation
- Boundary demarcations (walls, fences, hedgerows)
- Loose soil
- Sand
- Coastal beaches

VEGETATIVE

- Pasture
- Mixed cropland
- Brush
- Forest (evergreen, mixed, deciduous)
- Height and density of vegetation
- Orchards
- Agriculture
- Wildlife habitat

Section 4 assesses the likelihood of sucessfully delineating the conditions in Table 1 using automated image processing techniques applied to TM data. This section includes an extensive review of previous attempts to identify these features as presented in the open literature and when appropriate, identifies the most successful techniques or suggests new strategies. Problems of both temporal and spatial signature extension difficulties due to climatic and site factors are presented for selected conditions. Section 5 is a summary of the possible success of automated image processing by parameter of interest and suggests future research efforts.

Appendix 1 identifies TM data sets for geographic locations in the United States which contain combinations of the parameters of interest. In addition to the availability and quality of TM and MSS data for those sites, appropriate ancillary data which would be useful in developing processing strategies or assessing the accuracies of processing results are documented. These ancillary data include topographic maps, land use and land cover maps or digital data, digital elevation data and aerial photography.

There were several assumptions or limitations made based on requirements of the Air Force which were considered in this study. One of these was the possible need for data on a near global basis. This limited the range of possible sensing systems which could be evaluated. A second assumption was the possibility of needing data on a near real time basis. In

actuality this is a very difficult constraint with existing systems as currently configured. However, this constraint may be ameliorated by the use of the existing archive of data and selecting data within the climatic time frame of interest.

It was also assumed that there would be some limits on the availability of ancillary data for many areas of possible interest and that traditional methods of field checking for training site selection or cluster signature identification may not be possible. Finally, it was determined that the spatial domain of typical interest would be on the order of 25 km per side.

2.0

IMAGE PROCESSING

Image processing techniques for remotely sensed digital data can be divided into two basic areas. First is image enhancement which is simply a range of data manipulations, both geometric and radiometric, to provide an image product which can be more easily, rapidly, and accurately interpreted by an analyst. Some of the commonly employed image enhancement techniques include edge enhancement, density stretching, and scale matching.

The second method of image processing, and the focus of this study, is data classification. These techniques involve using a computer to examine or manipulate the digital data using a variety of algorithms to eventually classify the data, usually on a pixel by pixel basis, into themes or categories of interest such as land cover or occasionally land use. While image enhancement assists a human interpreter, image classification is more generally viewed as data manipulation without a human interface. While removing the human component in classification is frequently the goal of artificial intelligence or expert systems, image classification as it is currently utilized includes a significant amount of human interaction. An important issue in information extraction from remotely sensed data is the relative amount of man-machine interaction. The task of this effort was to evaluate various automated image classification

techniques with extremely limited human interface for the specified list of parameters. For most of those parameters, image enhancement techniques for analyst interpretation may be equally or more effective than classification. The purpose of this section is to briefly review some of the techniques, problems, and developments in automated image classification.

2.1 SIGNATURE EXTRACTION

The traditional techniques of image classification depend upon the use of multispectral digital information and the concept of unique spectral signatures. The basic premise is that features of interest will have unique spectral signatures and that a computer can be trained to recognize those signatures and then classify the digital data. Initially in the development of classification techniques, spectral signatures were collected in the field or laboratory for matching with the digital values collected by remote sensors. This technique was generally ineffective for a variety of reasons including complexities of the energy flow profile. Currently most spectral signatures are obtained or extracted from the remotely sensed data itself by either supervised on unsupervised methods prior to classification.

One method of signature extraction is supervised or training field selection. This assumes the analyst can identify one or more homogeneous areas of the features or land covers of interest within the data or image set. The computer is then directed to

those training sites and calculates the digital statistics which are considered to be the spectral signature for that theme. This technique relies upon the ability to identify reliable training sites either by ancillary data or field visits. For many areas of potential interest to the Air Force, the ability to identify training sites may be difficult because of limited access or ancillary data.

A second method of signature extraction is unsupervised or clustering. This technique does not rely initially on ground information. Computer based algorithms are employed which based upon a statistical sampling of the image data, group the pixels into spectrally similar clusters. It is assumed that these clusters are representative spectral signatures for unique surface land covers. The task of the analyst then becomes one of assigning the proper land cover to each cluster signature. This can sometimes be done based on recognizable reflectance curves such as water, green vegetation, and bare soil or some knowledge of the surface conditions. Frequently, a combination of supervised and unsupervised methods of signature extraction are combined in hybrid signature extraction prior to classification.

A significant problem in classification directly related to the differences between image enhancement and classification is theme or feature categorization. It is important to recognize that themes identifiable by the image analyst may not be identifiable in automated image classification. One of the common aspects

this problem is the difference between land cover and land use. Automated image classification can generally delineate land covers such as grass or forest but not land use such as is the forest being used as timber or recreation. It is the inferential ability of the image analyst to incorporate more than simply the tonal or digital values available for automated image classification which allows the determination of land use in addition to land cover.

This categorization problem is evident within this study where some of the conditions of interest, such as pasture, are land use categories which can more easily be delineated by an analyst and image enhancement and not a land cover such as grass recognizable by automated classification. Classes used by an analyst cannot always be extended to automated classification; this problem may necessitate a new classification system.

3.2 CLASSIFICATION

After a reasonable set of signatures are extracted for the data set of interest, algorithms are employed to classify all pixels within the scene into one of the spectral signatures based on various statistical rules. There are a number of classification algorithms including minimum distance, parallelepiped and maximum [illegible] among others. Which classification system to employ may depend on the [illegible] of the hardware/software system, [illegible] the [illegible], and the [illegible]. There [illegible]

classification system employed.

Frequently in classification, the output products are either statistical information, such as the number of hectares of corn or deciduous forest, or as mapped information. Any output product should be assessed for accuracy which may be difficult depending on the ability to have "truth" against which to determine the accuracy. It is more difficult to achieve mapped accuracy than statistical accuracy. With mapped output there is generally employed a smoothing or filtering algorithm to generalize the information into more useful and identifiable map units. This study is to obtain mapped information. For many areas of interest to the Air Force, it may be difficult to assess the map accuracy because of the lack of ground truth.

2.3 DATA SELECTION

A significant issue in classification is what input data to utilize. This includes common parameters as seasonality and scale considerations, amount and type of preprocessing and possible data transformations. For multispectral data it is sometimes advisable to only select certain available bands to reduce the complexity of data manipulations. A common band selection technque is transformed divergence calculations.

Data transformations may also be employed prior to signature extraction to enhance data analysis or to provide new data

These transformations may include band ratios, indexes such as green vegetation indexes or principal components.

Input data may also include multitemporal or multisensor data. Multitemporal data sets are extremely useful for change detection and for classification of seasonally dynamic phenomena such as vegetation. Sometimes two or more dates are necessary to obtain the feature separation desired. With the availability of sensors in many regions of the electromagnetic spectrum, there are attempts to spatially register data from different sensors for classification. This has been done with multispectral scanner data such as MSS or TM and radar.

Because of problems associated with per pixel classification, there have been numerous suggestions to incorporate contextural or texture information in classification strategies. Visual interpretation of remotely sensed images relies on pattern and association. However, typically with per pixel automated classification, the only inputs are the reflectance or emittance values for each pixel. There are many land covers which might be more easily identified if contextural information, the relationship of one pixel to its neighbors, could be utilized in automated classification. Various texture measures based on digital value changes from pixel to pixel have been utilized as input data values in signature extraction and classification.

Another possibility to increase classification accuracy is to incorporate other types of ancillary data. If elevation, slope,

suitable vegetation or soil types are known and can be assigned with reliability to each pixel, they can be incorporated in the classification process. For example, frequently two forest types may not be spectrally separable but they may occur at different elevations. If elevation information are known, they can be used to separate the forest class into separate types after initial categorization. This may be part of a hierarchical classification strategy.

The incorporation of ancillary information with remotely sensed raw data values or classified theme information is essentially the construction of a geographic information system (GIS). A GIS historically was and still may be a set of scale and projection matched thematic maps for an region on transparent material so that they can be overlaid to produce new maps. More frequently, a GIS is computer based and can be an extremely powerful tool for many applications. In the context of the study, a GIS may be a method to increase classification accuracy or to use remotely sensed classification results in other information collection or analysis efforts.

2.4 SIGNATURE CONFUSION

There are many [illegible]
accurate [illegible]
system [illegible]

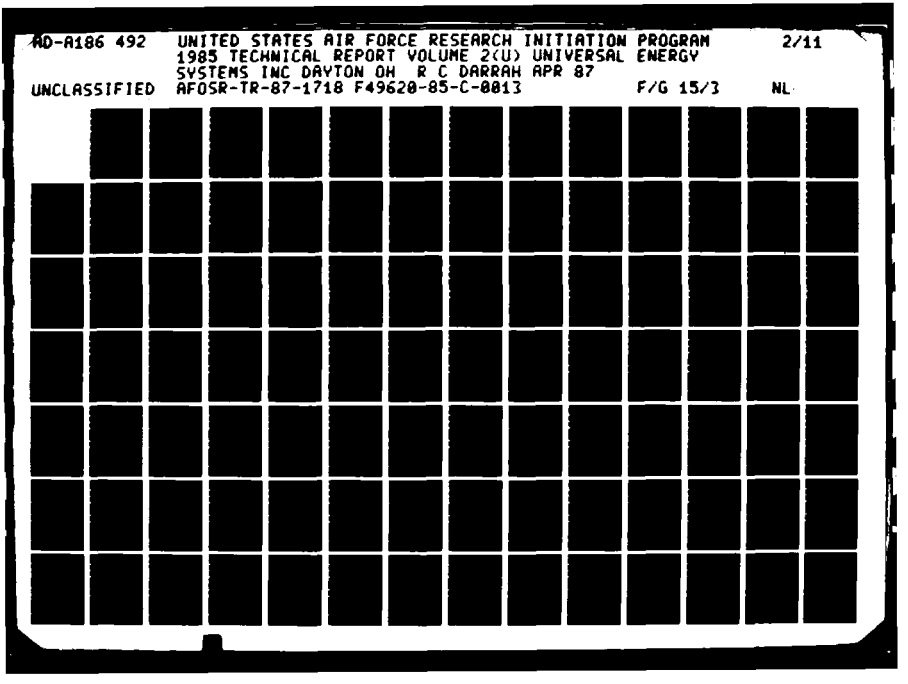
AD-A186 492 UNITED STATES AIR FORCE RESEARCH INITIATION PROGRAM 2/11
1985 TECHNICAL REPORT VOLUME 2(U) UNIVERSAL ENERGY
SYSTEMS INC DAYTON OH R C DARRAH APR 87
UNCLASSIFIED AFOSR-TR-87-1718 F49620-85-C-0013 F/G 15/3 NL

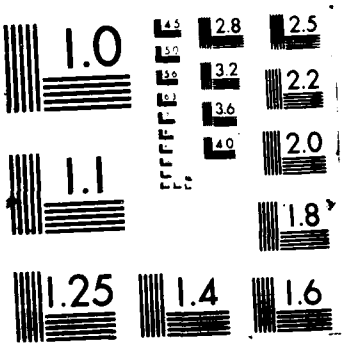
1.0
1.1
1.25
1.4
1.6
1.8
2.0
2.2
2.5
2.8
3.2
3.6
4.0
4.5
5.0
5.6
6.3
7.1
8.0
9.0
10.0

mixed pixels, too unique signatures or not sufficiently unique signatures.

Mixed pixels are non-homogeneous pixels where there are several land covers or features within each pixel. In some cases this is a function of too small a spatial resolution and in others, the complexity of the natural or cultural environment. Complex natural environments may be transitional areas between ecosystems. Cultural complexity is typified by most tropical agricultural areas where the field sizes are very small, there is a highly overlapping crop calender and a mixture of crops within fields by intercropping. It is arguable as to how beneficial smaller spatial resolution data may be in solving this problem. Smaller resolution data rapidly increases data handling problems and in some areas, may create too many signatures. Certainly in extremely heterogeneous areas, smaller pixel size will not be an asset in automated classification but it will be an asset for image enhancement and interpretation.

Too unique a spectral signature occurs when a feature of interest produces many different signatures. For example, fields of corn many have many different signatures as a function of soil type, stage of development, moisture availability, topographic slope or orientation, and row compass orientation among others. It is not expected that there will only be one signature per classification theme but there is a threshold of too many signatures.

Signatures which are not sufficiently unique frequently occur

among vegetation types which can not be separated based upon the available spectral information. Sometimes this can be resolved by; 1) a different date of data or multitemporal processing, 2) incorporation of ancillary data and a hierarchical classification strategy, 3) the collection of more spectral bands, or 4) multisensor data sets.

A significant problem with image classification is temporal and spatial signature extension. Signatures obtained from one data set may very likely not be usable in another data set collected for the same geographic area at a different time (temporal extension) on for a different geographic area (spatial extension). The reasons for these difficulties are due to both changes in the surface conditions or changes within other portions of the energy flow profile.

Changes in surface conditions may be a function of seasonal vegetation phenology, moisture changes due to precipitation events or cultural activities such as crop harvesting, deforestation or grassland burning. Energy flow profile changes may include different sun angles or sensor direction or more likely, atmospheric changes. There are various strategies, such as atmospheric modeling which are usually extremely complex and rely upon a variety of ancillary information, to compensate for signature extension problems. These strategies have varied degrees of success. There are no universal ways to resolve these difficulties and in an operational context, such as is being

considered in this study, it may be advisable not to depend on signature extension but rather consider each data set independently.

2.5 ARTIFICIAL INTELLIGENCE

Artificial intelligence (AI) is an aspect of computer science of considerable current interest and potential which may have applicability to remote sensing. Artificial intelligence can be defined as that part of computer science concerned with symbol manipulation processes that produce intelligent action. Intelligent action is a decision making and implementation process that is goal oriented and based upon a logical reasoning path. A general knowledge base is expected to guide this reasoning process. The basic problem when attempting to implement AI is the exact form of the computer input/output (I/O) and internal data structures. The nature of human reasoning and memory is not perfectly understood and thus it is impossible for a programmer to write computer code that emulates human thinking.

The re'ationships betwen AI and its various subfields such as natural language processing and expert systems are not clearly understood. Natural language processing allows the machine to accept queries and deliver responses in ordinary, or close to ordinary, English. This removes the necessity of having to translate commands, questions, and database information into a programming language and thus greatly reduces programming time. Natural language processing is far from perfected. Operational

systems do exist, but the operator must use a limited vocabulary list and closely adhere to a simplistic grammar structure. The problem of word context and subtle implications so pervasive in English language use has yet to be dealt with in a robust manner. Natural language interfaces work well in a constrained universe where all concepts (as expressed by words) and all relationships (as expressed by grammar) are limited and can be well defined. In image interpretation, this ability to precisely define all possible conditions does not currently exist.

Expert systems codify human experience in a set of rules that can be followed by a computer. Classically, this is done by extensively debriefing a human expert, and constructing a computer program for use by a non-expert. This program "interrogates" the non-expert, prompting him with a branching series of questions. These questions lead the program logic through the path of rules from the expert's knowledge base. As with natural language interfacing, expert systems work well in a closed universe where all possible conditions can be accounted for in a branching rule based logical structure.

A primary problem with expert system construction is data acquisition and structuring. This is the establishment of a database structure that is simple enough to be queried, yet complex enough to utilize all the interlocking rules of thumb as set out by the expert. The exact method of debriefing the expert has been found to affect the final expert system to a significant

degree. A problem with this debriefing is that the computer programmer involved in constructing the expert system must be competent in the subject material as well. Special computer languages have been written to make this task easier such as Prolog and Lisp.

Computers are capable of making near instantaneous decisions when sufficient evidence is present to make a logically clear cut decision. Humans are able to make probabalistic decisions based on fragmentary evidence. Slight indications that a condition is true may sum up to a definite conclusion on the part of the human expert. At the same time, these indications (evidence) may be meaningless if considered individually. The ability of humans to make decisions in this way is often called "fuzzy logic", or "fuzzy set theory". Problems in this realm may have several partial solutions or multiple ways to arrive at a single solution that is probably correct. The logical structure of such decision rules is currently imperfectly understood and cannot be performed by a computer.

Human experts also learn throughout a problem. After solving (or even failing to solve) a problem, humans are more able to examine a more difficult problem. This concept of self-teaching through problem solving is called heuristic reasoning. At the present time, computers do not possess this ability.

Automated image understanding is an advanced AI function important in many disciplines. It is considered a vital

objective in national defense research where the speed of new weapons systems does not allow sufficient time for human response to potential threats. Currently, image understanding (or interpretation) is still in a very basic research mode. In the defense community, there is extensive work on the automated recognition of aircraft and missles. These shapes are graphically "primitive"; they can be decomposed into simple squares, cones, and circles. This has been a requirement for machine recognition of objects. The object must be able to be described mathematically so that an image can be compared with a mathematical "template".

In remote sensing of the natural world, this mathematical description is virtually impossible because of the diversity in form and type of materials. This can be readily seen in the signature extension problem. The extension of spectral signatures developed for one geographical area into another has not been very successful. Ground truth must be established for the new area before accurate classification can take place. This is a result of the great diversity of the earths cover and that very few places on earth are identical. If the climate is the same, then the elevation and vegetation are often different; if the elevation is the same, then the soil moisture is probably different. All of these factors dramatically affect the spectral reflectance of the terrain and severely limit the automated recognition of earth surface features or conditions.

Despite the great amount of discussion and prognostications concerning the universal applicability of artificial intelligence applications in image processing, there has been little application of these techniques found in the literature of environmental remote sensing. Although there is not a clearly documented reason for this trend, two factors can be identified:

1) SPEED. A large emphasis has been placed in AI development upon processing speed; often, this is a stipulation of defense applications. In remote sensing of the environment, there is little need for real-time processing.

2) COST. The development of an operational AI system is extremely costly. Thousands of hours of time are required for specialists to program every possible option and parameter into the machine. This level of effort is not easily available in environmental remote sensing.

There are possible applications of aspects of AI in automated image processing for environmental conditions such as considered in this study. Those applications will be most successful initially in some combination of man-machine interaction where a sequence of analysis keys will be considered for various locations and ancillary information.

3.0

SPACEBORNE REMOTE SENSING SYSTEMS

The focus of this study was to examine those remote sensing systems within the civilian sector providing data which might be segmented to identify the specific features of interest. The limitations on the data systems included being near-global, operational or near-operational, and providing accessible data. The primary systems of interest are the sensors of the United States Landsat series of satellites, the French SPOT satellite and the NOAA meteorological sensor AVHRR. The orbiting and sensor characteristics of these systems are described in this section.

3.1 LANDSAT

The primary operational spaceborne remote sensing systems for land surfaces have been the Landsat series of satellites and associated sensors. The first of these satellites, the Earth Resources Technology Satellite 1 or ERTS 1 (which was renamed Landsat 1), was launched by NASA in July, 1972. It contained a four-band Multispectral Scanner (MSS) and a three-band Return Beam Vidicon (RBV) sensor. The RBV never collected a significant amount of data to be considered an operational sensor. Two other satellites also carrying the MSS and RBV have been launched (Landsats 2 and 3, in 1975 and 1978, respectively) and have

successfully provided data for multiple earth resources purposes. The modified RBV of Landsat 3 was a single band system of 40 m spatial resolution. Unlike the previous RBV sensors, it did function properly but the sensor was not included in latter Landsats because it was replaced by improved sensors.

The second generation of Landsat satellites began with Landsat 4 in 1982, followed by Landsat 5 in 1984. These satellites contain the MSS and a new sensor called the Thematic Mapper (TM). The TM is a more advanced scanner that provides improved spectral, radiometric, and spatial resolution data than the MSS. The MSS and TM sensors are the systems of concentration in this study and particularly the TM because of its improved resolutions.

The General Electric Company has served as spacecraft manufacturers and system integrator for Landsat under the direction of NASA/GSFC. After launch and performance verification, the responsibility for operation of Landsats 4 and 5 was changed form NASA to NOAA. Commercialization of these and future Landsats was accomplished under a contract agreement beginning in September, 1985 between the Earth Observation Satellite Company (EOSAT) and the U. S. Department of Commerce.

The Landsat satellites have near circular, repetitive, sun-synchronous polar orbits with descending nodal times of roughly 9:30 a. m. local sun time. Landsats 1-3 are at a slightly higher altitude (905 km) than Landsats 4 and 5, so they have a cycle of 251 orbits which repeat every 18 days, as compared with a 233-

revolution and 16-day-repeat cycle for the more recent satellites. The Landsat 1-3 orbital coverage creeps westward by one orbit swath each day providing adjacent coverage on consecutive days, whereas adjacent coverage occurs every seven or nine days with Landsats 4 and 5.

For Landsats 1-3, the distance between corresponding orbit paths on consecutive days at the equator is 159 km. This results in a swath overlap of 14 percent at the equator, for the nominal swath of 185 km, with greater amounts of overlap at higher latitudes. This consecutive-day coverage increases the possibility of cloud-free coverage for sites in the overlap zones. Landsats 4 and 5 have lesser amounts of overlap, e. g., seven percent at the equator, on their adjacent (7/9 day interval) paths.

3.1.1 MULTISPECTRAL SCANNER

The Multispectral Scanner (MSS) is a line scanning device which continually scans the Earth in a 185 km swath nominally perpendicular to the orbital path. Scanning is accomplished by an oscillating mirror; six lines are scanned simultaneously by six detectors in each of the four different visible and near-infrared spectral bands during each West-to-East mirror sweep. On Landsat 3, a fifth (thermal) band was also scanned but its data proved to be unreliable. MSS system characteristics are summarized in Table 2.

The nadir resolution of the MSS is 79 x 79 m for Landsats 1-3 and 82 x 82 m for Landsats 4 and 5. The maximum scan angle of Landsats 4 and 5 is slightly larger than that of Landsats 1-3, so that the 185 km swath width is maintained from the lower altitude.

TABLE 2. CHARACTERISTICS OF THE LANDSAT MSS

	Landsats 1-3	Landsats 4-5
Spectral Band Pass (Nominal, micrometers)	Band 4: 0.5-0.6 5: 0.6-0.7 6: 0.7-0.8 7: 0.8-1.1	Band 1: 0.5-0.6 2: 0.6-0.7 3: 0.7-0.8 4: 0.8-1.1
Number of Detectors/Band	6	6
Altitude (km)	905	705
Nadir Footprint of IFOV (m)	79x79	82x82
Scan Angle (degrees)	5.78	7.46
Swath width (km)	185	185
Ground Sample spacing (m)		
scan direction	57	57
line to line	79	57
Bits/Band (telemetered)	6	6
Levels/Band (CCT)	128 (bands 4,5,6) 64 (band 7)	128 (all bands)

MSS data are over-sampled at a rate that produces a 57 m ground sample distance at nadir in the scan direction. The line-to-line sample distance of 79 m is maintained for Landsats 1-3. Resampling is performed for geometrically corrected digital tapes. For Landsats 4 and 5, a 57 x 57 m sample grid is

produced, to make the data compatible with the 28.5 x 28.5 m sample spacing of geometrically corrected Landsat TM data. Cubic-convolution is the standard method used for resampling.

The Landsat MSS signals are quantized at the spacecraft into 64 levels (six bits) before being telemetered to the ground. A non-linear function is used for the first three bands and a linear function for the fourth. On the ground, the non-linear responses are expanded (decompressed) onto a linear scale having 128 levels. Computer-compatible tapes (CCTs) produced for Landsats 1-3 before 1979 had levels 0-127 for the first three bands (called bands 4,5 and 6), and levels 0-63 for the fourth (Band 7); after 1979, the fourth band also was expanded to the 0-127 range. Beginning with Landsat 4, the MSS bands were numbered 1-4, each spanning a 0-127 data range on CCTs.

Both relative and absolute radiometric calibration procedures are applied to Landsat MSS data. These and other factors affect the overall quality of the MSS data that are available to users. Pre-launch and post-launch calibration procedures have been employed for the Landsat MSS systems. There has been some evolution in the post-launch procedures, as knowledge of system characteristics increased and new problems were encountered. The pre-launch procedure employed a large-aperture integrating-sphere calibration source. It was stepped through a representative range of intensities. The dynamic range of each channel was determined and the least-responsive channel in each band (except

faulty detectors) was identified and used to establish the dynamic range to be used for the calibrated output of the band.

Each MSS also has an internal calibration lamp which is viewed by each detector through a variable-density filter. This produces a calibration-wedge signal which is sampled at several different positions at the end of every other mirror sweep. Regression coefficients are established during preflight calibrations, based on individual channel responses to the calibration-wedge samples.

In post-launch ground processing of image data, the channel responses to the calibration sources are used with the preflight regression coefficients to compute individual channel gains and offsets. These gains and offsets are computed every other scan line and are filtered along the satellites track to smooth any variation in the values (Thomas, 1975). The filtered gains and offsets are then used with look-up tables to equalize the responses of the individual detectors in each band, produce the desired dynamic ranges, and radiometrically correct raw image data values. Adjustments in dynamic range and/or equalizations are made occasionally during the satellite lifetimes through use of additional multiplicative and additive modifiers.

These procedures produced variable consistency in removing striping and banding artifacts from Landsat MSS data. Therefore, an additional step was added in the Landsat Multispectral Image Processing System (MIPS) developed for Landsats 4 and 5. It is a histogram calibration process which adjusts the channel gains and

offsets so that, within each band, the channel means and standard deviations become the same as the average band value (Alford and Imhoff, 1985). Each image is divided into segments with revised gain and offset values being determined for each segment. These values are blended between segments before being applied, with updates typically being made every 200 lines.

The radiometrically corrected digital values can be converted to absolute radiance values through use of maximum and minimum radiance values, called Lmax and Lmin. Lmax is the radiance value corresponding to the maximum number of video quantum levels on the output CCT, while Lmin is the radiance value corresponding to zero counts. Values for Lmax and Lmin differ from satellite to satellite and from time to time for a given satellite. It is important to note that the specific values may be for the date of processing or the date of acquisition. Also all tapes produced since 1979 have a 0-127 count range for all bands, so a recently processed Landsat-2 CCT will have an expanded Band 7 range even though a similar tape processed earlier would have a 0-63 range.

Two other cautions are also in order. First, the absolute accuracy of the radiometric calibration is not measured after launch. Second, the system response may change with time but not have this fact reflected in the published Lmax values.

This information applies to MSS products obtained through the EROS data center. Products obtained through other ground

stations may have different calibration procedures and different formats.

Only limited resources have been allocated to monitoring the post-launch performance of the Landsat MSS systems. For the first two or three systems, spectral signatures were extracted quite regularly over a few selected sites in the Western United States, mainly at or near White Sands, New Mexico. These provided some inputs to the ground processing procedures at that time. More recently, Nelson (1985) reanalyzed those data and quantified the previously observed decline of Landsat-1 MSS responses relative to those of Landsat-2.

Other investigators have made comparisons of the relationships between various pairs of MSS systems. Rice and and Malila (1983) summarize the available data and give transformations between the various combinations. Richardson (1982) also has examined such relationships and made comparisons. Both Markham and Barker (1985b) and Murphy et al. (1985) have indicated that the Landsat-4 MSS calibration appears to be slightly anomalous in comparison to the other Landsat MSSs.

Generally, the Landsat MSS has produced data of good quality. As one might expect, however, with a series of sensors that have been in operation for more than a decade, a number of problems have developed from time to time. A comprehensive account of system changes, improvements, and anomalies encountered during the first ten years of Landsat was prepared by Clark (1982).

Volume I of the Landsat-4 Science Characterization Early Results Symposium (Barker, 1985a) contains several papers documenting more recent events and anomalies. Other related papers include Tilton et al. (1985) and Malila et al. (1984).

Landsat data are archived in both film and digital tape form at the NOAA/NESDIC Landsat Customer Service Facility at Sioux Falls, South Dakota. The EOSAT Corporation recently assumed rights to collect new data and to market both new data and past data less than ten years old. This service will continue to be handled through the Sioux Falls Facility for two or three years.

Both black and white or false color composite images can be purchased in a variety of forms. Computer compatible tapes (CCTs) are also available in several formats. Fully processed tapes, CCT-PM, are both radiometrically and geometrically corrected, many with ground control data. The standard geometric projection is Space Oblique Mercator (SOM), although UTM projections are an option. CCT-AM data are radiometrically corrected, but not geometrically corrected. Tape formats may place spectral band values either interleaved or sequentially on the tape.

The MSS sensor is not currently planned to be continued on Landsat 6 (1989) or Landsat 7 (1991 expected). Rather a multispectral scanner emulater (EMSS) will be placed on the space platform and reprocess TM data on-board to replicate MSS data

with an improved spatial resolution of 60 meters. This will provide a continuation of the MSS data collected since 1972.

3.1.2 THEMATIC MAPPER

The Thematic Mapper (TM) is an advanced multispectral imaging sensor carried by Landsats 4 and 5. This improved sensor is the primary sensor considered in this study. Landsat 4 was launched in 1981 and Landsat 5 in 1984. Characteristics of the TM are summarized in Table 3. This sensor has improved spectral, spatial and radiometric resolution in comparison to the MSS.

TABLE 3. CHARACTERIZATIONS OF THE LANDSAT THEMATIC MAPPER

	Spectral Region	
Spectral Band Pass (micrometers)	Band 1: 0.45-0.52 2: 0.53-0.61 3: 0.62-0.69 4: 0.78-0.91 5: 1.57-1.78 7: 2.10-2.35	Band 6: 10.4-12.4
Number of Detectors /Band	16	16
Altitude (km)	705	705
Nadir Footprint of IFOV (m)	30	120
Active Scan Angle (degrees)	7.7	7.7
Ground Sample Spacing scan direction (m) line to line (m)	 28.5 28.5	 28.5 28.5
Levels/Band	256	256

The linear resolution of the TM is about 2.7 times finer than that of the MSS, the IFOV of the TM is 30 x 30 m as compared with 82 x 82 m for the MSSs on Landsat 4 and 5. Greater radiometric sensitivity of the TM over the MSS is achieved by utilizing eight-bit quantization (256 levels) in the analog-to-digital conversion process. The TM has better signal to noise specification and utilizes linear response functions. The TM has more spectral bands than the MSS, seven instead of four. Spectral bands have been added in the blue (0.45 to 0.52 micrometer) region, the mid-infrared (1.55 to 1.75 and 2.08 to 2.35 micrometers) and the thermal-infrared region (10.4 to 12.5 micrometers). The TIR band has 120 m spatial resolution. Three TM bands approximate the four MSS bands. The visible green and red bands are narrower than their predecessors in order to improve their ability to distinguish phenomena in this region. The reflective infrared band is narrower than the combined bands of the MSS in this region, having its center in a region of maximum sensitivity to plant vigor.

The TM sensor is active during mirror sweeps in both directions, 16 scan lines per mirror sweep (four detectors for the thermal band). A scan-line corrector mirror compensates for overlap and underlap which would occur from this scanning motion.

TM data are sampled at a rate of one sample per 30 m at nadir in the scan direction. Line-to-line spacing also is nominally 30 m on tapes that are only radiometrially corrected; scan lines on

successive sweeps are displaced on these tapes by a substantial number of pixels relative to each other in the scan-line direction (Beyer, 1985). Since the thermal band (Band 6) has a coarser 120-m resolution, each data value is repeated in a 4 x 4 array of the high-resolution 30-m pixels on radiometrically corrected tapes.

Geometrically corrected tapes are resampled to a 28.5 x 28.5 m grid. The standard resampling procedure is cubic convolution which results in some smearing of spatial detail. Nearest neighbor sampling is also an option. The standard geographic projection is Space Oblique Mercator. UTM is an option when the scene center is between 65 degrees north and south latitude and Polar Stereographic at higher latitudes (Beyer, 1985).

Both pre-launch and post-launch calibration procedures are employed for the Landsat TM systems. The pre-launch procedure employs large-aperture integrating-sphere calibration sources (Barker et al., 1985, and Lansing and Barker, 1985). Each is stepped through a representative range of intensities under several different operating temperatures. The dynamic range of each channel is determined and the least-responsive channel in each band is identified and used for the calibrated output for the band.

Radiometric correction takes place when each high density tape (R-tape) containing raw date is used to produce an archival high density tape (A-tape) which contains only radiometrically

corrected data, but has all the geometric correction parameters appended. Any geometric correction takes place in a subsequent process and results in a P-tape. The radiometric correction process has three phases (Singh, 1985; and Irons, 1985). The first phase screens the R-tape and extracts, accumulates, and saves calibration, shutter, and subsampled histogram data, for each channel, from each scan. The second phase computes radiometric gains and biases for all channels and generates lookup tables which are applied to raw data during the third phase.

Each TM contains three calibration lamps which are viewed by all reflective-band detectors once during each scan. Up to eight different combined lamp intensity levels can be produced. These lamp levels are cycled through slowly and the corresponding detector outputs are monitored.

Least-square fits are first produced after the pre-flight measurements to relate the channel outputs to the 20 different integrating-sphere radiated levels that were tested. These result in a derived gain and offset for each detector (Barker et al., 1985). Similarly, these radiated values are related to the calibration lamp response through regression analysis. For each band, maximum and minimum radiance values are determined. Barker et al. (1985) and Malila and Anderson (1986) discuss these values.

The individual detector calibrations for TM were not expected to satisfactorily equalize the responses of detectors within each band, so a histogram normalization option was implemented for TM as well. The procedure employed matches histogram means and standard deviations extracted from the scene being processed, and is described by Irons (1985). To expedite processing, the radiometric correction steps are combined into radiometric lookup tables which are used to map raw digital counts into radiometrically corrected values.

Each radiometrically corrected digital value can be converted to a spectral radiance value (Malila and Anderson, 1986). The necessary coefficients are provided for each band in tape headers.

Because thermal infrared radiation differs from the reflective radiation sensed by the other TM bands, a different calibration procedure is used for Band 6. A two-point internal calibration function is used. One point is from the temperature-controlled blackbody reference source on the calibration shutter and the other is from measured temperature of another portion of the calibration shutter.

The dynamic range of Band 6 initially was 260 to 320 degrees K, but was changed to a range of 200 to 340 degrees K. Tape header coefficients for Band 6 can be used to convert calibrated counts into spectral radiance. However, since the observed radiance is a function of both the true temperature of the object and its

spectral emittance, as well as atmospheric effects; variable spectral emittances can cause apparent temperatures to differ substantially from true temperatures.

This discussion applies to TM products obtained through the EROS data center. Products from other ground stations may have different calibration procedures and different formats.

The TM sensors have produced data of very good quality. Their data have been analyzed extensively under the Landsat-4/5 Image Data Quality Analysis (LIDQA) program. Artifacts which have been discovered and described include scan-corrected level shifts, bright-target saturation, and between-sensor calibration differences. Most of these are correctable. Sources detailing the TM data quality include Salomonson (1984), Barker (1985b), and Markham and Barker (1985a). Barker (1985b) gives a comprehensive discussion of TM reflective band radiometry and analyses the sources and magnitudes of error and estimates overall accuracy.

TM image products can be obtained in the same range of formats as the MSS data from EOSAT and EROS. Similarly TM CCTs can be obtained in several formats and corrections as the MSS CCTs.

The first seven band TM data for Landsat 4 were obtained on 22 August 1982. Until the first TDRS (Tracking and Data Relay Satellite) satellite was launched and became operational, TM data

could only be acquired in the range of ground receiving stations. Failure in 1983 of two of four solar panels that power the TM and MSS sensors have kept the Landsat 4 TM off operational status. Landsat 5 was launched in March, 1984 and began routine collection of TM data in April.

There are several anticiapted changes in future Landsat platforms, TM sensors and additional Landsat sensor packages. The Landsat platform for the next two systems, Landsat 6 in 1989 and Landsat 7 in 1991, will be called OMNISTAR. It will have a twenty year life expectancy. It may be launched either by the Shuttle or by expendable rocket and is also expected to be serviced by the Shuttle. The TM on Landsat 6 is expected to include a panchromatic band (0.5 to 0.86 micrometers) with a 15 m spatial resolution. In addition, the TM projected for Landsat 7 may replace the current 120 m thermal channel with up to four TIR bands at 60 m spatial resolution.

Other sensor packages being considered for future Landsat missions include a low cost, low resolution sensor (500 m) with increased temporal frequency. Also a Multispectral linear array system with selectable channels and off-nadir pointing to provide stereoscopic imagery is under discussion.

3.2 SPOT

The French earth resources Systeme Probatoire d'Observations de la Terre (SPOT) was sucessfully launched in February, 1986. This

essentially global, near-polar sun-synchronous satellite has local sun time crossings of approximately 10:00 am. It is at an orbit altitude of 832 km and has a normal repeat cycle of 26 days.

The satellite carries two identical high resolution visible (HRV) sensors with multispectral linear arrays. Each HRV has a swath of 60 km and combined provide a swath of 117 km. The sensors are capable of collecting 10 m spatial resolution data in a panchromatic mode and 20 m data in a three channel multispectral mode. In addition, the sensors have off-nadir, pointable viewing capability. This off-nadir viewing provides stereoscopic coverage which could produce topographic information with approximately 10 m contour spacing. The pointable sensor also provides revisit capabilities of up to 7 visits at the equator within a normal 26 day cycle. The number of possible revisits increases with higher latitudes.

The French Government has committed to a continuation of the SPOT program with plans for SPOTs 2, 3 and 4 through the 1990s. SPOT 2 will be identical to SPOT 1. SPOTs 3 and 4 are expected to have an additional multispectral band in the mid-infrared (1.5 to 2.7 micrometers) for vegetative assessment. The SPOT platform may very well add an additional sensor for large area, broad resolution vegetative analysis. This sensor would have four spectral bands, a 2000 km swath, 1 km spatial resolution and near daily repeat coverage.

3.3 AVHRR

An operational global remote sensing system which has been receiving increased utilization for earth surface information is the Advanced Very High Resolution Radiometer (AVHRR) sensor carried on the United States NOAA series of meteorological satellites. This sensor is the most recent of a series of orbiting satellites and sensors which have evolved since the launch of the first meteorological satellite, TIROS, in 1960.

The AVHRR sensor has five channels including one visible, one NIR, one MIR and two TIR. The swath width of the sensor is 2700 km and the spatial resolution is 4 km off nadir and about 1 km at the nadir. One of the primary reasons for the increased utilization of this sensor is the high temporal resolution of two passes per day, day and night, and four passes when there are the normally operating two satellites.

Several of the non-meteorological applications of AVHRR data include monitoring dust and sandstorms, volcanic monitoring with the thermal bands, marine oil spill analysis, flood demarkation, forest and grassland burning assessment, various geologic lithologic determinations, and vegetation biomass using vegetative indexes. The high temporal resolution of these sensors and the near real time availability of data are extremely important for some applications. However, the limited spatial resolution makes it an unlikely data source for the parameters of

this study.

REFERENCES

Alford, W.L., M.L. Imhoff, 1985. Radiometric Accuracy Assessment of Landsat-4 Multispectral Scanner Data, Landsat-4 Science Characterization Early Results, Volume 1: Multispectral Scanner (MSS), NASA Conference Publication 2355, Goddard Space Flight Center, Greenbelt, Maryland, pp. 1-9 through 1-21.

Barker, J.L., Editor, 1985a. Landsat-4 Science Characterization Early Results, NASA Conference Publication 2355, Goddard Space Flight Center, Greenbelt, Maryland.

Barker, J.L., 1985b. Relative Radiometric Calibration of Landsat TM Reflective Bands, Landsat-4 Science Characterization Early Results, Volume III: Thematic Mapper(TM), Part 2, NASA Conference Publication 2355, Goddard Space Flight Center, Greenbelt, Maryland, pp. III-1 through III-219.

Barker, J., D. Ball, K. Leung, J. Walker, 1985. Prelaunch Absolute Radiometric Calibration of the Reflective Bands on the Landsat-4 Protoflight Thematic Mapper, Landsat-4 Science Characterization Early Results, Volume II: Thematic Mapper(TM), Part 1, NASA Conference Publication 2355, Goddard Space Flight Center, Greenbelt, Maryland, pp. II-277 through II-372.

Beyer, E.P., 1985. An Overview of the Thematic Mapper Geometric Correction System, Landsat-4 Science Characterization Early Results, NASA Conference Publication 2355, NASA Goddard Space Flight Center, Greenbelt, Maryland, pp. II-87 to II-145.

Clark, B.P., 1982. Ten Years of Landsat, 1972-1982, An Historical Perspective of Spacecraft and Ground Processing Anomalies, CSC/TR-82/60008, Computer Sciences Corporation, Silver Spring, Maryland.

Irons, J.R., 1985. An Overview of Landsat-4 and the Thematic Mapper, Landsat-4 Science Characterization Early Results, Volume II: Thematic Mapper, Part 1, NASA Conference Publication 2355, NASA Goddard Space Flight Center, Greenbelt, Maryland, pp. II-15 to II-46.

Lansing, J.C., J.L. Barker, 1985. Thermal Band Characterization of the Landsat-4 Thematic Mapper, Landsat-4 Science Characterization Early Results, Volume III: Thematic Mapper, Part 2, NASA Conference Publication 2355, NASA Gooddard Space Flight Center, Greenbelt, Maryland, pp. III-233 to III-256.

Malila, W.A., D.A. Anderson, 1986. Satellite Data Availability and Calibration Documentation for Land Surface Climatology Studies, ISLSCP Report No. 5, Boulder, Colorado.

Malila, W., M. Metzler, D. Rice, E. Christ, 1984. Characterization of LANDSAT-4 MSS and TM Digital Image Data, IEEE Transactions on Geoscience and Remote Sensing, Vol. GE-22 (3), pp. 177-191.

Markham, B.L., J.L. Barker, 1985a. Spectral Characterization of the Landsat Thematic Mapper Sensors, Landsat-4 Science Characterization Early Results, Volume II: Thematic Mapper, Part 1, NASA Conference Publication 2355, NASA Goddard Space Flight Center, Greenbelt, Maryland, pp. II-234 to II-276.

Markham, B.L., J.L. Barker, 1985b. Spectral Characterization of the Landsat-4 MSS Sensors, Landsat-4 Science Characterization Early Results, Volume I: Multispectral Scanner, NASA Conference Publication 2355, NASA Goddard Space Flight Center, Greenbelt, Maryland, pp. I-23 to I-56.

Murphy, J., F. Ahern, P. Duff, A. Fitzgerald, 1985. Assessment of Radiometric Accuracy of Landsat-4 and Landsat-5 Thematic Mapper Data Products from Canadian Production Systems, Photogrammetric Engineering and Remote Sensing, Vol. 51(3), pp. 1359-1369.

Nelson, R.F., 1985. Sensor Induced Temporal Variability of Landsat MSS Data, Remote Sensing of Environment, pp. 35-48.

Rice, D.P., W.A. Malila, 1983. Investigation of Radiometric Properties of the Landsat-4 Multispectral Scanner, Report Number 162300-3-F, Environmental Research Institute of Michigan, Ann Arbor, Michigan.

Richardson, A.J., 1982. Relating LANDSAT Digital Count Values to Ground Reflectance for Optically Thin Atmospheric Conditions, Applied Optics, Vol. 21 (8), pp. 1457-1464.

Salomonson, V.V., 1984. Special Issue on Landsat-4, IEEE Transactions on Geoscience and Remote Sensing, GE-22(3).

Singh, A., 1985. Thematic Mapper Radiometric Corrrection Research and Development Results and Performance, Photogrammetric Engineering and Remote Sensing, Vol. 51(9), pp. 1379 -1383.

Thomas, V.L., 1975. Generation and Physical Characteristics of the Landsat 1 and 2 MSS Computer Compatible Tapes, Report X-563-75-223, NASA Goddard Space Flight Center, Greenbelt, Maryland.

Tilton, J., B. Markham, W. Alford, 1985. Landsat-4 and Landsat-5 MSS Coherent Noise: Characterization and Removal, Photogrammetric Engineering and Remote Sensing, Vol. 51(9), pp. 1263-1279.

4.0

ANALYSIS OF SURFACE CONDITIONS

This section evaluates the ability to locate and evaluate the surface features of interest listed in Table 1 by automated processing of remotely sensed data, primarily Landsat TM data. Several of the listed conditions are combined in a single presentation because of definitional difficulties such as between brush, forest, and the height and density of vegetation or because of a similar remote sensing perspective such as streams, lakes and reservoirs, all of which require the recognition of water.

For each condition, there is included a review of prior efforts to evaluate the condition with remotely sensed data and when appropriate, additional processing strategies are presented. In addition, problems associated with the analysis of the condition such as temporal and spatial signature extension are presented.

4.1 SLOPE

Slope and aspect information are most easily obtained from existing topographic maps or elevation data bases. Most elevation information is obtained from photogrammetric measurements of stereoscopic remotely sensed photographs or images. If stereoscopic pairs are available, then elevation and slope information can be obtained. However, until quite

recently, 1986, there was no systematic collection of spaceborne stereoscopic data.

There are techniques for single image slope determination in areas of homogeneous surficial cover that have relatively uniform albedo. While these conditions may be found locally within a scene, it is rare for this to be the case over broad areas. Therefore, slope detemination of a local area may be much simpler than slope determination over the entire image.

While remotely sensed data are often the sources of elevation and slope information, elevation data can also significantly increase the accuracy of classification of vegetation using remotely sensing data (Foote et al., 1981). In one study, Hoffer et al. (1979) found that elevation data improved vegetation classification by 15 percent. Vegetation density and type are often dependent on elevation, slope and orientation primarily due to climatic changes such as altitude zonation.

Generally, most researchers in remote sensing who need to access elevation information have overlaid the imagery onto existing topographic maps or have registered the image data to a digital elevation model (DEM). A DEM is a matrix of numbers representing elevation values at points that are uniformly spaced. This spacing is the resolution of the DEM. DEM data for the United States are currently being compiled and released by the U.S. Geological Survey (see Appendix A). The Defense Mapping Agency

is in the process of constructing a world wide digital elevation database with 30 meter resolution. If sufficiently detailed data are available from these sources it would be much quicker, and probably more accurate to overlay the imagery data onto a terrain model constructed from the USGS or DMA digital elevation data than to attempt to extract elevation information from currently available spaceborne remotely sensed imagery.

However, despite a general preference for DEM data if available, there is interest and research into obtaining slope and elevation data from non-stereoscopic remote sensing. For some applications, currently available DEM data may be of too coarse a resolution to differentiate small terrain features of interest such as gullied landscapes.

If ground cover is homogeneous and a standard albedo can be established, then reflectance from the scene varies only with topography and is proportional to the cosine of the illumination angle. This relationship can be of use in forested or grassland terrain where the vegetative canopy is essentially homogeneous, or in unvegetated areas of similar rocks or soils. If this approach is used, it would be possible to determine a slope amount for every pixel that is illuminated by the sun. The use of multitemporal imagery would provide various angles of illumination that should provide data for all but the most frequently shadowed mountainsides. In addition, the slope calculations from one image can be compared with the slope calculations of another as consistency checks.

Single image spacecraft data have been found to be of use in localized slope analysis. Watson (1968) has cautioned against using any single image to create a complete model because the scene illumination is dependent on both the vertical and horizontal angle to the illumination source. Watson also noted that photometric slope from brightness measurements are more reliable if the illumination is perpendicular to any linear landforms.

Slope may also be assessed by processing the image data to create a differential image; that is, an image that is the first differential of the original scene reflectance. This is achieved by passing a series of digitally weighted filters over the data (Jensen, 1986). A first differential image will show the overall trend of the slope and is also useful for edge identification, particularly of ridgelines. Any abrupt change in spectral values results in a drastic change in the first differential. It must be stressed that this type of image shows the differential of the image reflectance values, not of the configuration of the terrain itself. They can only be correlated well if a relatively homogeneous surface cover exists.

A similar technique has been used to identify gullies from digital elevation models. This technique passes a three by three digital filter over the data, and if the central pixel is found to be a minima critical point, then a "saddle" is identified.

This process looks for these points in four directions passing through the center point (E-W, N-S, NW-SE, NE-SW). When the product of these operations is displayed, it is found that the gullies are well delineated by strings of oriented saddle points (Carroll, 1983).

Another method has been developed for obtaining an estimate of local slope in hilly or mountainous areas from TM images. This method requires that the valley bottoms and ridge lines be identified. An estimate is then made of the approximate maximum relief; this estimate can be made from existing maps. The slope in any area is then determined by dividing the estimate of local relief by the horizontal image distance between a ridgeline and the center of the valley (Wang, 1984). Wang uses a linear model in this procedure which is appropriate for old mountain chains. In glaciated areas or newer mountains, cartographic logic would require the use of curvilinear models because the slope generally becomes much steeper nearer the top of the landforms. Alpine glacial horns are a perfect example of this topographic principle.

In some situations multiple Landsat images may be available and conventional stereoscopy may be applied to analyse the data. Shadowing can result in useable stereoscopic effect if images are available with disparities in inclination or azimuth of the sun illumination. Gregory and Moore (1983) reported that large vertical exaggerations exist if multiple Landsat images possessing these characteristics are available. Thus, it is

possible that elevation information can be extracted without parallax for particular scenes. However, Gregory and Moore found that this vertical exaggeration is non-uniform over the entire image and varies with the latitude of the images used. If images are available meeting the required criteria (illumination direction and azimuth are standard information in scene retrieval data from EROS), this effect may be useful on a local scale for relative slope determination via visual examination.

In orbital globally imaging systems there is some amount of overlap in the scenes. Therefore, stereoscopic information is contained in the overlap areas. However, the height of the imaging system above the topography may require the digital enhancement of the scene data in order to make this effect visible except in areas of extreme vertical relief. Platform stability, imaging system resolution, geometric correction and image matching accuracy have also been found to be highly important if elevation information is to be extracted in this fashion (Welch and Ehlers, 1985). Although attractive intuitively because the information is present in the imagery, this method presents difficult technical problems.

Experimental, operational and future spaceborne remote sensing systems have been directed towards the acquisition of elevation information. The Shuttle based Large Format Camera and Metric Camera missions have collected stereoscopic photography of segments of the earth's surface on an experimental basis. More

Importantly, the recent operational SPOT satellite offers stereoscopic coverage of the earth (see Section 3.2). Evaluation of the accuracy of this stereoscopy has not been well established as yet because most of technical evaluation of the SPOT data has been based on airborne scanner data resampled and degraded to SPOT image resolution. However, it is expected that 10 m contour information will be extracted from the SPOT data. Geospectra Corporation of Michigan has already announced software that will produce topographic maps from SPOT stereopairs. It is claimed that these maps will meet U.S. Geological Survey standards for 1:50,000 scale topographic maps (Vincent et al., 1984). Several future spaceborne remote sensing systems, including Landsat, may also contain stereoscopic capabilities.

In summation, DEM databases are a more reliable and faster way to obtain slope information in specific areas than non-stereoscopic satellite data analysis. However, if DEM or SPOT data are not available for a specific area, then there are both digital and visual techniques available to possibly determine slope information solely from TM imagery. Unfortunately, these techniques require very specific conditions and have generally not been duplicated and utilized by other researchers, so the speed, accuracy, and global applicability of them remains to be more fully evaluated. Either DEM or stereoscopic data from SPOT and similar future systems will be the best methods to obtain slope information.

REFERENCES

Carroll, R., 1983. Automated Gully Delineation using Digital Elevation Data, Technical Papers, 49th Annual Meeting, American Society of Photogrammetry, pp. 144-151.

Foote, H.P., S.C. Blair, G.W. Wukelic, V.L. Coburn, 1981. Analysing and Mapping Regional Land Use Trends by Combining Landsat and Topographic Data, International Geoscience and Remote Sensing Symposium (IGARSS), p. 1437.

Gregory, A.F., H.D. Moore, 1983. Non-parallactic Stereoscopy Using Shadow Disparity, Technical Papers of the 49th Annual Meeting, American Society of Photogrammetry, pp. 160-169.

Hoffer, R.M., M.D. Fleming, L.A. Bartolucci, S.M. Davis, R.F. Nelson, 1979. Digital Processing of Landsat MSS and Topographic Data to Improve Capabilities for Computerized Mapping of Forest Cover Types, Purdue University Laboratory for Applications of Remote Sensing (LARS) Technical Report 011579.

Jensen, J.R., 1986, Introductory Digital Image Processing, Prentice-Hall.

Vincent, R.K., P.K. Pleitner, D.H. Coupland, H. Schulz, E.R. Oshel, 1984. New Digital Elevation Mapping Software Applied to SPOT Simulation Stereo Data, SPOT Simulations Applications Handbook, Proceedings of the 1984 SPOT Symposium; p.92.

Wang, L., 1984. Relative Elevation Determination using Landsat, Photogrammetria, Vol. 39.

Watson, K., 1968. Photoclinometry from Spacecraft Images, U.S. Geological Survey Professional Paper 599-B.

Welch, R., M. Ehlers, 1985. Digital Image Processing Techniques For Deriving Terrain Coordinates From Satellite Image Data, (Abstract only), Technical Papers of the 51st Annual Meeting, Vol. 2, American Society of Photogrammetry, p. 875.

4.2 SURFACE ROUGHNESS

Local surface roughness is a difficult condition to quantify; in fact, there does not even exist a standard measure that expresses a "surface roughness factor". In addition, roughness is a quality that varies with scale. It is a known problem in military terrain analysis that an area can appear on the map to have little relief, and therefore be assumed to be easily traversable by vehicles; but, in actuality, the land may be gullied and crossed by small intermittent streams that make vehicle movement difficult or impossible. Desert surfaces such as in the Sahara are yet another example of this scale problem. In some areas, the desert surface consists of small grain sands that exist in dunes of highly variable sizes; while in other areas, the desert surface consists of cobble to boulder sized rocks. Both of these areas often appear indistinguishable on topographic maps and can appear very similar on satellite imagery.

Surface roughness results from the complex geomorphological interaction of vegetation, wind, and water eroding and weathering different types of bedrock. In sedimentary rock, if an area is predominantly sandstone or limestone, then extensive cobbles are not expected in the erosional surface material. However, if the bedrock consists of coarse conglomerates, then the opposite is expected. In areas of recent volcanism, lava fields provide some of the roughest surfaces found on earth. Locally, a river channel that possesses significant gradient will generally be

floored with boulders and cobblestones. Thus, at some scales surface roughness of an area can be inferred from specific knowledge of local geography (location of streams, amount of slope) and geology (bedrock type).

Some of this knowledge can be obtained from remotely sensed data. Considerable progress has been made is the discrimination of some rock types in arid areas using only spectral data. Ratios between different combinations of TM bands have proven to be particularly useful because a ratioed image removes the effects of differential illumination of the topography (Rowan and Lathram, 1980). However, in vegetated areas multispectral data are frequently insufficient to determine the bedrock type and other measures must be used in conjunction with radiometric pixel values. It is thought that texture measures such as the Hsu classifier can assist considerably in determining bedrock types (Kirakofe, 1984). An operational system to reliably ascertain surface roughness from geologic and other secondary indicators would have to rely upon a consistent set of data which might be incorporated into a GIS from a variety of sources in addition to remote sensing.

A theoretical approach that has yet to be applied to surface roughness is the fractal description of image reflectance. Fractals were first extensively discribed by mathematician Benoit Mandelbrot (1977). Mandelbrot applied fractals to various geomorphological processes, the most quoted being the description

of coastlines. Since that time fractals have found application in computer graphics, physics, and other fields as a method of describing the results of some natural processes.

Pentland (1984) suggests that fractals are a superior method of describing rough earth surfaces. Pentland also recognizes several important constraints to the indiscriminate use of fractal based descriptions. One constraint is that the surface must be a result of a fractal process in order for the fractal description to be meaningful. An example of a fractal process (that is, one that is scale independent within broad limits) is erosion; it is reasonable that small scale gullys are similar in form to larger scale valleys (Haggerstone, 1983). Another constraint is that the image area subjected to fractal analysis must be consistent in that all of the area must have been subjected to the same process. This requires careful image segmentation to obtain fractally heterogeneous areas. An example of segmentation difficulty might be found in satellite images that span the divide of the Sierra Nevadas. On one side of this mountain chain there is a significant amount of rainfall, while the other side is desert. These two areas have been subjected to significantly different erosional regimes and, if analysed together, could not be assumed to have any meaningful fractal dimension. Fractal based description of image data is a promising and intuitively attractive idea. However, much work remains to be done before it is an operationally reliable technique to describe the three dimensional roughness of a scene from the two dimensional image data.

Because surface roughness is difficult to quantify and is scale dependent, there has been little related empirical work with TM data. Visual interpretation and prior knowledge of the landforms in the scene allow the analyst to make some estimates of the local surface roughness. The 30 m spatial resolution of the TM is too coarse to permit quantization of localized surface roughness or ground particle size. Even the 10 m resolution of the SPOT satellite will not allow the analyst to directly assess the surface roughness in a particular area. If a landslide area consists of 3 meter boulders (rendering it virtually impassable except with great difficulty) the SPOT imagery will not be able to show this fact directly. Examination of a low angle illumination scene might reveal shadow patterns amenable to texture analysis; but no work was found that utilized this approach.

Most investigations of surface roughness have been with radar because radar returns are highly dependent upon the roughness of the surface. Although the modeling of radar returns from different reflectors is extremely mathematical and complex, there are general guidelines available.

When using radar to examine surface roughness, a surface is "radar rough" (bright reflection) or "radar smooth" (low reflectance) depending on the relationship of the root mean particle size on the ground to the wavelength. A surface will be

"radar rough" if the average particle size is larger than the wavelength of the sensor, and "radar smooth" if the particle size is smaller (Dozier and Strahler, 1983).

Bryan (1981) reports that the relationship between rough and smooth terrain in imaging radars can be expressed as:

rough > Wavelength of radar/8 * (sin depression angle of radar);
smooth < Wavelength of radar/8 * (sin depression angle of radar).

However, this simple equation is not universally agreed upon, as the nature of radar backscatter from complex reflectors is not well understood.

An investigation of surface qualities using Shuttle Imaging Radar-A (SIR-A, L band, 23 cm wavelength, resolution 40 m) was conducted using data covering Las Cruces, New Mexico (Teng, 1985). The results of this investigation showed that qualitative examination of radar returns from an orbital platform are useful in determining surface roughness, at least in non-vegetated areas. Teng found that regional SIR-A image patterns generally correspond to the amount of surface dissection; and that locally the image brightness corresponds to differences in surface roughness due to desert pavement, dunes, scarps, and small amounts of vegetation. Arroyos were found to stand out clearly because of the diffuse scatter produced by their coarse grained materials. Arroyos were distinguished that were smaller than the approximately 40 m resolution of the imagery if they were oriented orthagonal to the radar look direction. This effect is due to the taller and denser amount of vegetation (due to the

greater availability of water in the arroyo bottom) and the steep to vertical walls of most arroyos. Both of these factors result in higher radar backscatter.

In a similar study, King (1985) reported that it was difficult to distinguish even between flat, undulating, or hilly landscapes using SIR-A radar returns in highly vegetated Indonesia; only mountainous areas could be identified with certainty. This scale of information is not directly related to surface roughness except that local relief determines drainage gradients. King indicates that the surface of the land cannot be directly imaged with available radar data if the surface is covered with vegetation. These two studies indicate different results about the capabilities of SIR-A radar returns as a function of the amount of vegetative cover.

A "multispectral" approach to radar analysis has been advocated. In this technique, radars of different wavelengths and polarizations are used to multiply image the target area, and multispectral classification techniques are used to classify the terrain. In a pilot study of Death Valley, California, Daily (1980) found that different desert surfaces were identifiable utilizing this approach combining airborne and SEASAT radar data. Daily also acknowledged the difficulty in terrain interpretation where ground truth is not readily obtained. Radar speckle, an unavoidable problem with radar images, renders many conventional pixel classifiers inoperable (although median value filters are

recommended). In other areas, lava flows were easily discernable by very bright returns on the SEASAT images, but this is an abnormally rough earth surface condition. Karst topography of low (10 meter) relief also had high reflectance in SEASAT images of the Dominican Republic but it is uncertain whether this is due to the vegetation cover or the surface itself.

In another study of Death Valley using cross- and like-polarization radar (Evans et al., 1986), cross-polarization brightness returns corresponded well with rough alluvium of younger geologic age while older deposits had significantly lower returns. L band returns diminished when the average particle size became less than one tenth the size of the wavelength. Cross-polarized radar was more dependent on the surface rouhness than like-polarized radar. Evans concluded that multipolarization radar imagery should be acquired in order that the maximum information be extracted from the scene.

Radar contains much information about the condition of the imaged surface. However, the complex nature of natural reflectors has resulted in confusing results on radar returns and utilizations. The difficulty in using radar lies not only in the analysis, but also in the accurate geometric transformation of the radar data onto a "flat" map projection for registration with other remotely sensed imagery or maps (Wu, 1983). Any radar data available for an area of interest should be visually examined; there is no tool better for rapid perception of terrain relief except possibly a reliable large scale topographic map.

The ability of remote sensing techniques to evaluate surface roughness is a function of the type and particularly the scale of surface roughness information desired. Automated determination of surface roughness directly from TM data will be very difficult because of the 30 m spatial resolution of the sensor. Possible exceptions to this may be texture measures or the use of fractals. Secondary indicators of texture, such as bedrock or geomorphology, can be obtained via remote sensing or more likely by the incorporation of a variety of ancillary information in a GIS. A sensor which can be indicative of roughness is radar but there are currently no global programs to systematically collect radar data appropriate to this study.

REFERENCES

Bryan, M.L., 1981. Urban Land Use Using Synthetic Aperture Radar, Proceedings of the PECORA VII Symposium, pp. 124-143.

Daily, M., 1980. The Use of Imaging Radar for Geology and Archeology, Technical Papers of the Fall Meeting, American Society of Photogrammetry, pp. DA-1-B-1 to DA-1-BB-13.

Dozier, J., A.H. Strahler, 1983. Ground Investigations In Support of Remote Sensing, in the Manual of Remote Sensing, American Society of Photogrammetry.

Evans, D.L., T.G. Farr, J.P. Ford, T.W. Watson, C.L. Werner, 1986. Multipolarization Radar Images for Geologic Mapping and Vegetation Discrimination, IEEE Transactions on Geoscience and Remote Sensing, Vol. GE-24(2), p. 247.

Haggerstone, B., 1983. Drainage Pattern Delineation: A Function of Image Scale, Technical Papers of the 49th Annual Convention, American Society of Photogrammetry, pp. 529-533.

King, R.B., 1985. Comparison of SLAR, SIR, and Landsat Imagery for Mapping Land Systems in Kalimantan, Indonesia, Proceedings of the International Conference of the Remote Sensing Society and the Center for Earth Resources Management, pp. 381-390.

Kirakofe, B.E., 1984. The Effect of Surficial Properties on Lithological Dicrimination Using Landsat Digital Data, Technical Papers of the 50th Annual Meeting, American Society of Photogrammetry, pp. 187-195.

Mandelbrot, B.B., 1977. Fractals: Form, Chance, Dimension, Freeman.

Pentland, A.P., 1984. Fractal Based Description of Natural Scenes, IEEE Transactions on Pattern Analysis and Machine Intelligence (PAMI) No. 6, p. 661.

Rowan, L.C., E.H. Lathram, 1980. Mineral Exploration, in Remote Sensing of Geology, Siegal, Gillespie ed. .

Schaber, G.G., G.L. Berlin, W.E. Brown, 1976. Variations in Surface Roughness within Death Valley, California: Geologic Evaluation of 25cm Wavelength Radar Images, Geolological Society of America Bulletin No. 87, pp. 29-36.

Teng, W.L., 1985. An Analysis of SIR-A Imagery for Mapping Soils in the Las Cruces Area of New Mexico, Technical Papers of the 51st Annual Meeting, American Society of Photogrammetry, pp. 341-351.

Wu, S.C., 1983. Geometric Corrections of Side Looking Radar Images, Technical Papers of the 49th Ann. Meeting, American Society of Photogrammetry, pp. 354-364.

4.3 WATER

The discrimination of water from land is one of the earliest and best understood applications of remote sensing. Water absorbs

almost all energy in the infrared part of the electromagnetic spectrum. On infrared aerial photography, open water appears almost uniformly black, except water heavily laden with sediments which is generally a pale blue.

To delineate the water/land interface, any spectral information in the .75 to 1.1 micrometer range may be used (Schowengerdt, 1983). Various scientists have used MSS band 7 and TM band 4 to obtain excellent results in the identification of water bodies. A land cover assessment in South Dakota utilizing low resolution MSS data achieved a 93 percent accuracy of identification of water covered areas (Ripple and Miller, 1982). The remaining 7 percent error was probably due to small ponds and creeks of less that 1 pixel size. Schowengerdt (1983) has illustrated the cartographic precision obtainable for locating water using low spatial resolution MSS data. With a simple thresholding operation, the convoluted edges of Lake Anna, Virginia were almost perfectly delineated. With such easily achieved and accurate identification of water covered areas, it will be desirable to use TM data for the greater resolutions offered.

4.3.1 STREAMS

Small streams are the most difficult water bodies to identify with satellite imagery. This is particularly true if they are significantly smaller than the ground resolution or pixel size of the sensor. Another problem with stream identification in vegetated areas is that a small stream is often obscured by

overhanging vegetation. In some environments, these gallery forests can be secondary indicators of a stream.

It is possible to infer the existence of a stream without actually seeing the stream itself. If an area is well vegetated, it can be assumed that water is necessarily present. Topographic valleys are also usually the result of water erosion. The exact position of a small stream may change as it undergoes evolution but the position of the floodplain or stream valley is generally stable over a long period of time.

Even if a stream is smaller than the resolution limit of the image, this fact can be used to give an upper limit to the size of the stream. If gradient information (see SLOPE) is available, it may be used to approximately infer the width and flow rate of a stream, because, in areas of steep gradient, it can be assumed that the stream is relatively rapid and has a narrow floodplain, while flat or rolling land can be assumed to have streams that are slower, shallower, and generally have wide floodplains.

Vegetation density is almost invariably greater near waterways. This vegetation discrimination may be accomplished either digitally or by visual enhancement. Blanchard and Frick (1982) reported that contrast stretching techniques applied to TM band 3 data significantly aided the visual identification of the woodlands along creek valleys in Oklahoma. The authors of this study felt that their results were not sufficiently precise

because some other areas of vegetation were erroneously included in their classification of the creekside woodland. However, inspection of their maps shows that the creeks can be inferred reasonably well by "connecting the dots" between mapped areas of creekside woodland. Outlying areas classified as creekside woods are visually identifiable as not being part of any "connectable" linear series. These outlying areas are where the classification fails but human visual interpretation based of spatial relationships can easily discern that they are not part of the desired class. Thus, the presence of a creek can be inferred from the other image data available, even if the creek is too small to show up on the resolution of the image.

Digital edge finding techniques can also be employed to locate small streams. These techniques are probably much more useful in difficult areas of low topography and nearly uniform vegetation density. First derivative filters accentuate gradients but in this application, it would be preferable to use second derivative filters because they enhance maxima (data value peaks). Jensen (1986) showed how Laplacian (second derivative) filters enhanced the delineation of small streams in wetlands. Jensen reports that if the Laplacian filtered image is added back into the original image, the combination is very effective in wetland detail enhancement.

Wetlands are the most difficult type of area in which to directly identify small streams. In these areas there are no topographic clues, and the vegetation is generally dense everywhere so the

technique used by Blanchard and Frick cannot be expected to achieve satisfactory results. These areas also show the vegetation overhang effect to a high degree. However, it can generally be inferred that wetland areas will contain streams.

Because small streams may be best identified by the vegetation changes that occurs near them, a vegetative enhancement approach might well be the best processing strategy to identify them. The tasselled cap transformation (Kauth and Thomas, 1976) has been found to be very useful in the discrimination of different vegetative types. Data transformation onto "greenness" and "brightness" axes extracts an optimal amount of vegetative information from the raw multispectral data (Jensen, 1986). Therefore, if the image under investigation was first transformed via this method, and then a second derivative filter was applied (in order to identify maxima "greenness" edges) the small scale streams should be optimally identified. This processing strategy for the identification of small streams has not been found in the literature but logically it should result in the desired results.

4.3.2 LAKES AND RESERVOIRS

As discussed in the introduction to this section, there has been no difficulty in the identification of large bodies of water from satellite image data. Research involving large bodies of water has generally taken for granted that these bodies can be identified and plotted accurately. Work has now progressed into

water quality assessment and volumetric estimation. This latter objective has made extensive use of multitemporal imagery to determine lake shrinkage and expansion.

Ground survey information is still generally employed for water depth values necessary for volumetric estimates but some amount of depth information may be present in the imagery. The best penetration of water occurs in the spectral region 0.3 to 0.6 micrometers (TM bands 1 and 2). Penetration of water is also dependent upon the amount of suspended solids in the water (Salomonson et al., 1983). It is possible to extract quantitative depth information from satellite imagery in some limited situations but on an operational basis, and particularly for inland waters, this is a very limited and difficult process.

An interesting example of the identification and mapping of large to medium scale water bodies is Woldai's (1983) study of hydrological projects in the Jiangjan plain of China. Despite the fact that no ground truth or maps were available, Woldai analysed the progress of Chinese flood control efforts in this valley by mapping drainage canals, dikes and lakes. Identifications were made through multitemporal imagery of basins used primarily for agriculture but available for water storage in times of high precipitation. These basins are characterized by agricultural patterns most of the year but in the winter flood season they can become large lakes almost overnight. Woldai's work is indicative of the ability of satellite remote sensing to locate and monitor large water bodies. Information about weekly

or even daily changes in the size and location of these features is easily obtained from satellite data.

Essentially any open water area larger than the pixel size of the sensor can be reliably delineated with multispectral digital data by simple single band density slice techniques. Smaller water bodies can occasionally be inferred by other features such as vegetation or topography. This inference may require the incorporation of ancillary data and can be best accomplished by trained interpreters. Information on water depth or flow rates may also be inferred by ancillary information but cannot be reliably obtained by remote sensing.

REFERENCES

Blanchard, W.A., A. Frick, 1982. Identification and Mapping of Riparian Woodlands From Simulated Thematic Mapper Data, Technical Papers of the 1982 ACSM-ASP Fall Convention, pp. 50-61.

Jensen, J.R., 1986. Introductory Digital Image Processing, Prentice-Hall.

Kauth, R.J., G.S. Thomas, 1976. The Tasseled Cap-A Graphic Description of the Spectral-Temporal Development of Crops as seen by Landsat, Proceedings of the Symposium on Machine Processing of Remotely Sensed Data, pp. 41-51.

Ripple, B.J., S.B. Miller, 1982. Remote Sensing and Computer Modelling for Water Quality Planning in South Dakota, in Remote Sensing for Resource Management, Soil Conservation Society of America.

Salomonson V.V., T.J. Jackson, J.R. Lucas, G.K. Moore, A. Rango, T. Schmugge, D. Scholz, 1983. Water Resources Assessment in the Manual of Remote Sensing, American Society of Photogrammetry.

Schowengerdt, R.A., 1983. Techniques for Image Processing and Classification in Remote Sensing, Academic Press.

Woldai, T., 1983. Major Water Conservation And Reclaimation Projects in the Jianghan Plain and Surroundings, Hubei Province, China, Proceedings of the EARSeL/ESA Symposium on Remote Sensing Applications for Environmental Studies, pp. 93-110.

4.4 WETLANDS

There exists a sizeable body of published work on the remote sensing of wetlands. This interest has been widespread for a number of reasons. From an environmental viewpoint, wetlands have become recognized as important fish and wildlife breeding grounds. Wetlands are also currently disappearing due to drain and fill development operations. From a terrain or transportation perspective, wetlands are an important obstacle. Remote sensing has been found to be an invaluable tool for the mapping of wetlands for two reasons. One reason is that temporal change in wetlands can be quite rapid and imagery can be obtained with high temporal frequency. The second is that wetland areas tend to be difficult to survey on the ground due to limited accessibility.

One frequent problem in the analysis of wetlands is the many different types of wetlands, each of which has specific terrain and vegetation characteristics. A salt marsh in the tidal zone is usually characterized by extensive grasses; this is a very different wetland than the cane brakes of the Louisiana Delta

country, or the cypress groves of Georgia's Okefenokee swamp. A wetland classification system for use with remotely sensed data has been devised to address this problem by the U.S. Fish and Wildlife Service (Cowardin et al., 1979). It is hoped that more workers will adapt this system so that the results of one study can be meaningfully compared with the results of another. To date, most wetland research using remotely sensed imagery has used data specific classification systems. Often, wetland is not differentiated into type, the classification system simply specifies wetland versus non-wetland. This has lead to difficulties in the extension of an apparently successful image processing strategy to a different area. Depending on the vegetation present and the amount of open water, the spectral signatures of two wetlands may be very different.

From a remote sensing standpoint, wetlands are very interesting because they are transitional areas between land and water. As seen before, there is little difficulty discriminating the land from the water (provided the spatial resolution is sufficient); however, in swampy, muddy lowland areas that are often periodically inundated by tides, this discrimination is often difficult.

The vegetation present also confuses the classification of wetlands. In some areas of the earth, standing water occurs underneath 100 percent tree cover. This condition can be found in the cypress swamps of Georgia and the mangrove swamps of the tropics. An image taken from space and analysed visually will

show healthy vegetation in these areas, leading the analyst to infer that the vegetation exists on solid land. As an extension, it might be thought that a man might possibly traverse that land, albeit with some difficulty. However, many wetlands of this type are almost impossible to cross on foot. The combination of bottomless mud, water that can be deeper than a man can walk in, tangled above and below water vegetation, and the omnipresence of daunting amounts of insects and reptiles render this type of country virtually impassable to foot travellers. In most of these areas boats are necessary for transit. Thus, it is highly important to be able to distinguish wetland from other vegetated areas.

Generally, only wetland or non-wetland classification with varied degrees of accuracy has been achieved using only spectral data from satellite imagery (Carter, 1982). In order to achieve reliable subclassifications of the wetlands, it has been necessary to visually analyse texture and landscape associations (Finley et al., 1981). These classification strategies are more accurate than using purely spectral data.

Because of the transitional nature of wetlands and the dense, mixed vegetation so often found in these areas, it will probably be necessary to use ancillary information to fully delineate wetlands using satellite data. A significant amount of wetland delineation can be done with fairly rudimentary geographic knowledge. If a wetland is identified directly adjacent to

coastal dunes, then it can be reasonably inferred that it is a salt marsh primarily comprised of high grasses and reeds with little or no trees. Site, situation, and climatic zone are important factors in determining wetland vegetation assemblages.

Another approach has been suggested to deal with the low spatial resolution of Landsat data when classifying wetlands. Essentially, this approach advocates that the Landsat data be used to extract a statistical picture of the wetland under investigation, and that the statistics be used to infer detail that is generally only visible in higher resolution aerial photography. In other words, the image is not treated as a map (as is normally the case); instead, the image is treated as a set of samples of the wetland. Thus, if 25 percent of the wetland image was classified as pure water pixels, and 10 percent pure tree cover, then pixels that are spectrally mixed and not readily classified into a "pure" category are treated as though they were 25 percent open water and 10 percent tree covered (Roller, 1981). This approach implies scale independence with certain limits, and this model may be very effective if the image is properly segmented into grossly homogenous areas (to the limits of the image resolution). A similar approach was used in a study of land cover in Idaho (Anderson et al., 1982). Although this study concerned irrigated lands, a field check of the the land cover estimated from statistical treatment of the Landsat MSS data showed an accuracy of 89 percent.

Airborne radar has been used in the discrimination of salt marsh

areas. Shuchman et al., (1981) have reported that a multiband radar approach clearly identified coastal marshes in Florida. They hypothesized that X band radar reflects off the top of marsh grass (yielding "radar rough" bright returns) while the longer wavelength L band penetrates to the water, which is smooth in comparison to the wavelength (yielding "radar smooth" dark reflectances). This multiband approach may be applicable to other areas. In another study, L band radar was shown to identify standing water underneath tree cover in Georgia (Evans et al., 1986). Both HH (like) polarization and VH (cross) polarization were found to be effective in revealing the standing water.

There has been a considerable amount of research and discussion about the ability of radar to penetrate vegetative cover and image the surface underneath. Unfortunately, theoretic models of imaged phenomena have not been sufficiently developed for radar analysis of natural surfaces to be reliable except when the imagery can be extensively checked against ground truth. The combination of MSS or TM data to locate vegetation and radar to locate water below the vegetation may be an effective multisensor approach for automated image processing of wetlands. For the purposes of this study, the lack of globally available radar data makes this only a speculative strategy.

The ability to locate wetlands with automated processing of TM data is situation dependent. In some environments, the wetlands

may have a sufficiently unique spectral signature that reliable discrimination can be obtained. In other environments or during other temporal windows, wetlands may not be uniquely identified. Multitemporal data may be an effective processing strategy particularly if during one date, the water of the wetlands may be observed either because of leaf-off or flooding conditions. Multisensor processing using vegetation penetrating radar with TM may be effective when globally available radar systems exist. GIS based ancillary information such as topography and proximity to water may also be useful in locating wetlands.

REFERENCES

Anderson, H., M. Gross, S. Manning, 1982. Regional Aquifer System Assessment through Landsat Digital Image Analysis, Proceedings of the RNRF Symposium of Remote Sensing Applications to Resource Management, p.70.

Carter, V., 1982. Applications of Remote Sensing to Wetlands, in Remote Sensing for Resource Management, ed. C.J. Johansen, J.L. Sanders, Soil Conservation Society of America.

Cowardin, L.M., V. Carter, F.C. Golet, E.T. LaRoe, 1979. Classification of Wetlands and Deep Water Habitats of the United States, U.S. Fish and Wildlife Service.

Evans, D.L., T.G. Farr, J.P. Ford, T.W. Thompson, C.L. Werner, 1986. Multipolarization Radar Images For Geologic Mapping and Vegetation Discrimination, IEEE Transactions on Geoscience and Remote Sensing, Vol GE-24(2), p. 247.

Finley, R.J., S. McCullock, P. Harwood, 1981. Landsat Classifications of Coastal Wetlands in Texas, Proceedings of the PECORA V Symposium.

Roller, N.E., 1981. Strategies for Information - Directed Wetlands, Proceedings of the Symposium on the Machine Processing

Of Remotely Sensed Data Symposium, p.231.

Shuchman, R.A., E.S. Kasischke, G.A. Meadows, 1981. Detection of Coastal Zone Environmental Conditions using Synthetic Aperture Radar, International Geoscience and Remote Sensing Symposium (IGARSS), p.756.

4.5 SNOW DEPTH

Considerable effort has been expended attempting to establish snow cover conditions through satellite and air photo analysis. The majority of these snow studies are for assessment of the extent of cover and not snow depth because of the complexity of how the snow interacts with the sensor used. This interaction is dependent of the density and water equivalence of the snow. In addition, partial melt of the snowpack has been found to significantly affect the spectral reflectance of the snow. A number of theoretical models have been developed to model snow reflectance with radiative transfer theory; however, none of these models have been found to be valid for all purposes (Wiscombe and Warren, 1980).

In examining snow with remotely sensed images, the first issue is the discrimination of snow from cloud cover. In the visible range, snow and clouds both have high reflectance values, very unlike almost any other natural surface. In TM bands 4,5 and 7, snow reflectance digital values were reported to average 198, 226, and 220, respectively; the variance for all three bands was around 40 (Izadpanah, 1985). TM band 5, 1.55-1.75 micrometers, allows discrimination between clouds and snow. In this band the

snow will have a much lower reflectance than clouds (Rango, 1983; Salmonson et al., 1983). By the use of thresholding values, two masks can be created that will discriminate the snow covered areas from non-covered areas. The first mask, using a high threshold value and preserving the pixels above this value, combines the snow and clouds, eliminating all other areas of the image. The second mask is applied to the 1.55-1.75 mm band, using only the pixels remaining from the first mask. This mask uses a low threshold value and preserves the pixels below the threshold which will be snow. If sufficiently cloud free data can be obtained on suitable dates, TM data can effectively show the extent of snow cover. Snow depth is much more difficult.

Rango (1983) reported that the visual snow line in non-forested terrain corresponds roughly to a snow depth of approximately 2.5 cm. This snowline is defined as a line within which the snow has a consistently high brightness on the image. Snow patches that appear mottled are usually of less depth than 2.5 cm. He also recognized that significant tree cover in snowy areas and the presence of shadowing caused by topography requires that the analyst be knowledgeable about the local terrain before a reliable snow line determination can be made.

Snow depth charts are published for both hemispheres by the Global Weather Control of the U.S. Air Force using a computer program that calculates this information from ground stations, precipitation, and temperature data. The generalization of the

snow covered areas and consistent overestimation of lightly covered areas on these charts coupled with the high variability of local snow depth due to topography and elevation renders these charts inadequately accurate for determining localized snow depth (Kukla and Robinson, 1981).

In one study of open land, average snow brightness increases up to a depth of about 10 inches (McGinnis et al., 1975). However, Kukla and Robinson (1981) found that snow brightness varied according to the land cover in a mixed woodland/farmland area of Ohio. This study determined that differences in snow reflectance were mostly due to the varying amounts of the different land covers in the scene. To utilize this technique to assess snow depth, it might be necessary to create a mask for the forested areas and only analyse the consistency and range of the snow brightness values for the cleared land in the image.

The difficulty in determining snow depth from reflectance data has led to model based research that uses imagery data to determine the extent of the snowfall; the snowfall line is then overlaid on the topography. Bagchi (1983) has proposed a model for the Hymalayas that shows some promise in determining the snow depth in mountainous areas with very limited ground monitoring capabilities. Bagchi's model incorporates the orographic increase effect relating elevation to greater amounts of snowfall. The percentage of rain to snow in the local precipitation is a function of temperature which is controlled by the elevation. The amount of snow is modelled as linearly

increasing with height. A linear relationship may not be strictly correct and fieldwork would need to be done to establish this relationship more precisely. In addition, it is thought that the latitude of the area in which this model is applied might also be a significant factor. Bagchi stresses that the general approach of his model should be valid in other areas but that area specific parameters would have to be investigated for application to other mountainous areas of the world.

This approach is especially attactive because it uses known geographic information with image data to evaluate ground conditions at a specific site. Much of the available research in the remote sensing of snow attempts to determine snow parameters only with image data, without consideration of the topographic and climatic situation of the site.

Unfortunately, there is no confirmation of Bagchi's results from ground stations because of the inaccessibility of the Himalayan terrain. He does state that the results are reasonable in comparison to the outflow of the basin as measured at a river monitoring station. Although Bagchi's model is applied only for mountainous areas where the orographic effect is in operation, this type of terrain is precisely where other workers have claimed that the determination of snow depth is most difficult (Kukla and Robinson, 1981). Models and other attempts to estimate snow depth using remote sensing can possibly provide estimates of average snow depth but not local variations due to

drifting and topographic factors.

Both active and passive microwave remote sensing of snow and ice has been attempted because of the microwave ability to penetrate cloud cover that often obscures snowy and mountainous areas. The presence of operational satellite passive microwave radiometers aboard the NOAA (coverage every 12 hours) and GOES (coverage normally every 30 minutes) satellites have promoted research in snow and ice remote sensing. This high temporal coverage is of importance in snow conditions because of the rapid change that snow cover can undergo in a few days of warm weather or, conversely, during a storm. The low spatial resolution of satellite microwave radiometers is a serious restriction to determine local snow conditions except in flat, grassy or poorly vegetated regions where the snow can be assumed to be consistent over a large area (Salmonson, 1983). Chang et al. (1980) developed linear relationships between snow depth and microwave brightness using data from the NOAA-7 radiometer. In flat, unforested areas, snow depth was negatively correlated with the 37 gHz microwave brightness under dry snow conditions, but this sensor has a resolution of only 28 km by 17 km. Chang (1981) also found that the microwave brightness decreased more rapidly with snow depth in a short (0.8 cm) wavelength than in a longer (6 cm) wavelength, a difference attributed to a scattering effect of the snow crystals. Tiuri (1981) noted a similar effect for well controlled experimental conditions in Finland. Chang advocates a multispectral approach for snow depth investigation

that would exploit different microwave wavelengths.

The ability of active microwave sensors such as radar to penetrate or reflect from the snow surface is highly dependent on the amount of water and ice present in the snow, the angle of incidence of the radar wave, the surface roughness of the snow, and the underlying material. This complexity of signal return makes interpretation very difficult. Additionally, global radar coverage is not available at present, although this may change in the future. Radar analysis of snow is generally found to be extremely difficult and full of uncertainty. Considerable current effort is occurring to model the reflectance of the snow at various frequencies. Styles et al. (1981) reported that radar return generally increases with increasing water equivalence, decreases with the presence of liquid water, increases with crystal size, and is sensitive to the roughness of the underlying material if the snow is dry. Stiles concludes that snow interaction with radar is not yet sufficiently understood to permit radar analysis of snow with accuracy and precision. The potential of accurate snowpack monitoring may be greatly increased once optimal combinations of microwave frequencies are found.

Salmonson (1983) suggests that reliance upon a single sensor to remotely assess snow conditions would be in error. Instead, he advocates the integration of data from different sources to gain the most information possible. Visible spectrum data from the TM can assess local conditions on a periodic basis while near-

infrared data delineates areas of surface melting and permits snow/cloud discrimination. Nighttime thermal observations, while of low spatial resolution, double the number of TM observations available, thus increasing the opportunity of cloud free scenes. Passive radiometers yield a regional view and their penetrating characteristics can provide information about the snow condition and depth over homogeneous areas. However, for small basins and mountainous areas, active microwave sensor data will probably be required.

The extent of snow cover can easily be accomplished with currently operating spaceborne sensors. The high temporal resolution provided by the meteorological platforms are capable of providing a higher probability of cloud-free and near real-time data than Landsat. Currently, there are no reliable systems to determine snow depth with remote sensing but some modelling approaches like that of Bagchi, and microwave sensors may provide that information on a regional, average basis.

REFERENCES

Bagchi, A.K., 1983. Estimation of Depth of Snow from Landsat Imagery, Technical Papers of the 49th Annual Meeting, American Society of Photogrammetry, pp. 551-555.

Chang, A.T.C., J.L. Foster, D.K. Hall, A. Rango, 1980. Monitoring Snowpack Properties by Passive Microwave Sensors Onboard Aircraft and Satellites, Proceedings of a Workshop on Microwave Remote Sensing of Snowpack Properties, NASA Conference Pub. No. 2153.

Chang, A.T.C., 1981. Microwave Radiometry Approaches to Snow Property Determination, International Geoscience and Remote Sensing Symposium (IGARSS), pp. 669-671.

Izadpanah, A., 1985. Remote Sensing Application in Spatial Planning: A Case Study, in Proceedings of the Regional Symposium on Remote Sensing Applications of Socio-Economic Aspects of the Environment, pp. 21-25.

Kukla, G., D. Robinson, 1981. Accuracy of Operational Snow and Ice Charts, International Geoscience and Remote Sensing Symposium (IGARSS), pp. 974-979.

Kukla, G., D. Robinson, 1980. Climatic Value of Operational Snow and Ice Charts, Proceedings of Snow Watch 1980 Conference, National Science Foundation.

McGinnis, D., J. Pritchard, D. Weisnet, (1985). Snow Depth and Snow Extent using VHRR data from the NOAA-2 Satellite, NOAA Technical Memorandum NESS 63.

Rango, A., 1983. Operational Applications of Remote Sensing for Snow Hydrology, RNRF Symposium on the Application of Remote Sensing to Resource Management, pp. 977-988.

Salmonson, V.V., ed., 1983. Water Resources Assessment, in the Manual of Remote Sensing, American Society of Photogrammetry.

Styles, W.H., F.T. Ulaby, A.K. Kung, A. Aslam, 1981. Radar Spectral Observations of Snow, International Geoscience and Remote Sensing Symposium (IGARSS) pp. 654-660.

Tiuri, M., 1981. Microwave Emission Signatures of Snow in Finland, International Geoscience and Remote Sensing Symposium (IGARRS), pp. 670-677.

Wiscombe, W.J., S.G. Warren, 1980. A Model for the Spectral Albedo of Snow, 1: Pure Snow. Joural of the Atmospheric Sciences, Vol. 37, pp. 2712-2728.

4.6 BOUNDARY DEMARCATIONS

Most satellite remote sensing has focused on the classification of areal phenomena such as the identification of corn fields, floodplains, or urban areas. Little work has been published on the classification of linear or point phenomena. These three basic types of data (area, linear, point) represent increasingly difficult identification tasks from automated processing of orbital data. With area data, enough homogeneous pixels are usually available that signature extraction and classification can be accomplished. With linear or point data, this is not possible. Even with 10 m resolution SPOT data, classification of linear features will still be difficult, since many linear features are not 10 meters wide. This is not to say that many linear features will not be visible; on the contrary, a highly reflectant concrete road will often dominate the neighboring pixels and show up clearly on satellite imagery. The difficulty in automated classification is that virtually all of the road pixels will show a mixed reflectance that is a combination of road and neighboring vegetation and there will be few, if any, "pure" road pixels for signature extraction. Many linear features are visible on satellite imagery and can be enhanced by edge detection and lineament tracing algorithms but precise identification is difficult unless morphological clues provide a basis for visual interpretation (Pelletier, 1983).

Improved roads are one of the easiest linear visual

classifications to make with satellite image data. Paved roads generally have very different reflectances from the surrounding land cover and can often be recognized because they are relatively long, straight, and possess geometrically simple curves. Dirt roads are virtually indistinguishable even on enhanced satellite imagery. Walls, fences and hedgerows are also indistinguishable on commercially available satellite imagery at the present time. No studies were found that directly address the identification of these features. The possible location of these features may be obtained by edge detection enhancements based on changing land covers from one field to another but the existence of a wall, fence or hedgerow at these locations cannot be determined with TM data. There are some approaches that may prove more feasible in the future.

High resolution TM or SPOT imagery may be of use to identify linear features if the illumination is of a sufficiently low angle so as to cast long shadows. This implies the use of early morning and seasonally low sun angle images in relatively flat terrain. With this technique, an extensive process would be necessary to reliably identify most of the linear features of interest in the scene because the illumination for any one scene will tend to reveal stuctures only in an alignment perpendicular to the illumination and not shadowed by other, larger topographic features. The use of edge enhanced multitemporal imagery in a GIS context allows the successive addition of edge extractions from a series of scenes, thus assembling a map of the linear features revealed from a number of different sun orientations.

A promising approach to linear feature identification has been found in the literature on artificial intelligence. Witkin (1982) and others (Fischler et al., 1982) at the Fairchild Artificial Intelligence Laboratory have developed a classification of edges found in images. This classification is based on numerical intensity data from the images. Various edge types are recognized including shadow, material boundary, surface marking, and surface intersection.

Since linear features of interest in this study (walls, fences, hedgerows) are too small to be seen with conventional satellite imagery resolution, a shadow edge holds promise for their identification. Material boundary edges (like agricultural field boundaries) may infer from prior regional geographic knowledge that some boundary demarcation may be present but does not classify the edge in terms of a specific feature. In Fischer et al. (1982) it is recognized that "we would not want to use shadows as features; on the other hand, shadow edges are very important cues in looking for ...thin raised objects." Knowledge of the sun angle and the shadow dimensions therefore can allow calculations about the size of the object casting the shadow. The size information of the shadow, it's thickness, consistency and statistical characterization may allow the subclassification of shadow edge types and infer what is casting the shadow. To accomplish this, it is necessary to know if it is a shadow or some other kind of edge. Intensity based edge

classification may be useful.

Two approaches have been taken to identify shadow edges. Fukue et al. (1981) compared small areas on either side of the suspected edge; if the standard deviation was the same on either side of the edge, and the difference between mean values for each of the two areas could be attributed to a single scale factor, then the edge was determined to be a shadow edge (in other words, there was no difference in albedo between one side to another). In a more detailed approach, Witkin (1982) reports that shadow edges show good linear correlation across the shadow boundary if a small strip is considered on either side of the shadow edge. To confirm a suspected shadow edge, it is "imbedded" in a series of parallel curves on either side of the edge, and correlation is checked between opposing pairs of curves (one on either side). Sustained high correlation with some disturbance in one or both of the regression parameters (slope and intercept) are thought to strongly indicate a shadow edge.

In order to reduce the computational time to find all image shadows cast by thin raised objects, Fischler et al. (1982) applied a series of enhancements to isolate shadows of interest. A thin line detector oriented parallel to illumination direction is passed over the image, and the lines found by it are enhanced. The shadow lines are thinned, and added back onto the original image; as a result, the base of each shadow now points to the object casting the shadow. The use of multitemporal imagery allows the intersections of shadow lines to locate objects more

precisely and also more shadows are added.

Many algorithms exist for edge or line detection (Schulz, 1983). Loew et al. (1981) provide a method that was found to be particularly useful in locating straight edges. A Sobel filter was employed to identify edge points, and a Hough tranformation to identify lines from the disconnected edge segments. This sort of approach would be particularly useful in low spatial resolution satellite data, because linear feature extraction often results in a bewildering array of small disconnected line segments. The Hough transform allows for minimum and maximum line tolerances to be specified. It is also useful to identify corner points for image registration (Fang and Huang, 1982).

Several other methods of line detection were tested by Hall and Mertz (1983). Their study is of particular interest because they applied it successfully to simulated TM data to determine agricultural boundaries. They reported that Laplacian (second differential) high pass filtering was superior to Sobel (gradient) filtering. Shaw et al. (1981) obliquely supports this conclusion. In the Hall and Mertz study, spatial frequency "notch" filtering utilizing the Fast Fourier transformation was found to be more versatile to enhance different types of edges. Hall and Mertz also reported that normalized TM bands 2 and 3, unnormalized 2 and 3, the 4/3 band ratio, and the first principal component were the most useful in automated line extraction.

With MSS data, MacDonald et al. (1981) reported that human interpretation found the most linear features on Band 7 imagery, while the least variation between three human interpreters was found using Band 6 data. It is also recommended that cross polarized radar be used in tandem with Landsat data whenever possible. VH synthetic aperture radar aligned orthagonal to the Landsat illumination was found to be the best combination for small linear feature detection.

In conclusion, the precise location and identification of walls, fences and hedgerows on satellite imagery is still very much theoretical. There are numerous ongoing studies to determine the best possible way to extract lines from an image. A possible approach for locating boundary demarcations using shadow information has been outlined but this requires either excessively long shadows or increased spatial resolution data. There is no strategy known that even approaches operational status. Much research still remains to be done in this area. There are two basic difficulties: the subpixel nature of the targets, and the difficulty in classification of linear objects that do not possess enough pixels to allow signature extraction. Edge classification techniques currently being developed in artificial intelligence offer the best approach to the problem, but, at the present time, there has not been any association of edge types with specific features on satellite imagery.

REFERENCES

Fang, J.Q., T.S. Huang, 1982. A Corner Finding Algorithm For Image Analysis and Registration, Proceedings of the National Conference on Artificial Intelligence, pp. 46-54.

Fischler, M.A., S.T. Barnard, R.C. Bolles, M. Lowry, L. Quam, G. Smith, A. Witkin, 1982. Modeling and Using Physical Constraints In Scene Analysis, Proceedings of the National Conference On Artificial Intelligence, pp. 30-38.

Fukue, K., H. Shimoda, T. Sakata, 1981. Complete Lineament Extraction With the Aid of Shadow Free Landsat Image, Machine Processing of Remotely Sensed Data Symposium, pp. 94-101.

Gillespie, D.A., D.L. Civco, W.C. Kennard, 1986. Identification of Forest and Agricultural Edges Using Landsat Thematic Mapper Data: Preliminary Results, Technical Papers. ACSM-ASPRS Annual Convention. pp. 279-289.

Hall, J.R., F.C. Mertz, 1983. Edge Discrimination as Applied to Thematic Mapper Data, International Geoscience and Remote Sensing Symposium (IGARSS) pp. 7.1-7.4.

Loew, W.H., R.L. Pickholtz, L. Goldman, 1981. Image Processing for Cartographic Applications, Machine Processing of Remotely Sensed Data Symposium, pp. 447-457.

MacDonald, H., W.Waite, C. Elachi, M. Borengasser, D. Tolman, 1981. Exploration For Fractured Petroleum Reservoirs using Radar/Landsat Merge Combinations, International Geoscience and Remote Sensing Symposium (IGARSS), Vol. I; pp. 312-324.

Pelletier, R.E., 1985. Identification of Linear Features In Agricultural Landscapes Through Spatial Analyses of Thermal Infrared Multispectral Scanner Data, Technical Papers of the 51st Annual Meeting Vol. I, Am. Soc. Photogrammetry, pp. 381-390.

Schulz, B.S., 1983. Algorithms for Data Smoothing, Edge and Line Detection and Vectorization, International Geocience and Remote Sensing Symposium (IGARSS), pp. 8.1-8.3.

Shaw, R., L. Sowers, E. Sanchez, 1981. A Comparative Study of Linear and Nonlinear Edge Finding Techniques For Landsat Multspectral Data, Proceedings of the Pecora VII Symposium, pp. 529-542.

Witkin, A.P., 1982. Intensity Based Edge Classification, Proceedings of the National Conference on Artificial Intelligence, pp. 36-41.

4.7 LOOSE SOIL

It is difficult to define loose soil such that it would be identifiable with remote sensing. This difficulty is because of the variety of conditions under which loose soil could occur. Bare soil can be located with automated image processing but not all bare soil is loose soil. Since loose soil is frequently a function of large soil size particles (sand size texture), it is to a considerable extent discussed in Section 4.8 on sand. This section specifically considers loose soil areas subject to saturation.

Saturation of the topsoil can occur for a variety of reasons. The soil can be subjected to river valley flooding, snow melting, rising watertable, or rainfall. All of these conditions can lead to saturated soil. If the soil is continually or frequently in a saturated state, then the area can be called a wetland (see Section 4.4). This section is concerned with the recognition of normally dry areas subject to intermittent periods of wetness causing miry conditions and inhibited ground movement.

Most studies of remote sensing for soil moisture are in soil

identification, agricultural soil moisture estimation and the location of wetlands. Wet ground appears dark on both natural color and infrared photography or FCC imagery (Salomonson et al., 1983). The reflectance curves for wet versus dry soils deviate most sharply between 0.57 and 0.75 micrometers (Myers et al., 1983). If the vegetation coverage dominates the image reflectance, moist ground is often characterized by lush vegetation that is dark green in natural color and bright red in the infrared.

Although miry ground can feasibly be identified on a single image (Tommervik, 1986), it is highly advisable that multitemporal imagery be used with climatic data to examine both wet and dry season conditions. Change detection techniques can then be utilized to find areas that are intermittently wet. If weather records are available, then an image can be obtained that follows a period of heavy rainfall.

Millington et al. (1986) experimented with several change detection techniques. In this study of playa geomorphology, TM band 7 ratioing (band 7 from two different dates) worked well for the identification of wet ground. The third principal component image also revealed areas of hydrologic change. Highly localized areas may not be visible with these processing strategies; rather the change detection image primarily reveals seasonal changes.

Tommervik (1985) reported that TM and SPOT imagery were both

about equal in the identification of Alpine valley mires. The high spatial resolution of SPOT compensated for the high spectral and radiometric resolution of the TM. Haas and Waltz (1983) reported that TM band 5 was useful in the identification of wet prairie grasslands. Wet meadows were found to be identifable with few errors of omission except when located in dry basins containing agricultural activities (Koeln et al., 1985).

In areas of high vegetation and rainfall, it may be difficult to obtain cloud free TM imagery for dates of interest. A limited amount of information about ground conditions can be inferred from change detection techniques applied to coarse spatial resolution vegetation index images. A study in Kenya (van der Brink, 1986) used a normalized difference index on AVHRR multidate imagery (red and infrared bands) to monitor ephemeral stream growth. These are subpixel sized features inferred from the growth of the vegetation. Imagery was used for rainy and dry periods to locate these streams. Although AVHRR data are low resolution (1.1 km), the floodplains of these streams were evident in the processed imagery. The high temporal resolution of AHHRR makes it an attractive sensor for large scale soil moisture estimation (Ormsby, 1981). Heilkema (1981) used AVHRR imagery on a moisture reconnaissance of desert locust breeding grounds.

The vegetation change noted in the stream study by van der Brink is significant because it indicates that the ground is wet in these areas. In dry areas, vegetation growing on miry ground may

be the only vegetation dense enough to show up on Landsat imagery (Carter, 1982). AVHRR data may be more appropriate for heavily vegetated areas of the world where there may be extensive miry ground, while TM or SPOT data may be more appropriate for dry or mountainous areas where miry ground is expected to occur on a much smaller extent, and be generally associated with less vegetation.

Thermal remote sensing also shows promise in the identification of miry areas. Experiments with airborne scanners have shown that differential cooling rates can be measured between wet and dry meadows. Wet meadows are cool during both night and day measurements, while dry meadows become hot during the day. Thermal measurements taken at both times were found to discriminate between wet and dry meadows on this basis (Haberl and Stock, 1983). This technique has not been applied to satellite imagery.

Additional information about potentially miry areas can be determined with the aid of detailed topographic information. This can be image derived (see SLOPE, 4.1), or from existing maps. Geomorphology often determines if the ground can be saturated. More mire is expected in floodplains than on steep sloping mountainsides. Robinove (1979) showed in an integrated terrain classification study using Landsat imagery in Queensland that a high correlation exists between upland areas and dry vegetation, and between valley areas and wet vegetation. Image

classifications are generally improved by the addition of terrain data and processing time can be reduced (Likens and Maw, 1982). This latter benefit occurs because large areas can often be "masked" out of the image if it is known that the ground condition could not exist in the masked area.

An integrated GIS approach is recommended to identify occasionally miry terrain. Vegetative indications of soil saturation have been found to be useful to identify areas where the groundwater is near or at the surface. Radar, particularly L band (Benton et al., 1983; also, see WETLANDS, 4.4) can identify areas of standing water under vegetative cover. Terrain data indicates where miry areas can be logically located, meteorological data can provide a qualitative estimate of the amount of recent precipitation, and thermal data can provide information about snow melting. All of these input data sources are useful in determining if a local area is miry. Small spatial resolution data are not as important as temporal or radiometric resolution, except in the identification of very small miry areas. Multitemporal imagery is highly important. Historical imagery can show maximum and minimum ground wetness conditions. All of these techniques, particularly if included into a GIS, can indicate possible areas of saturated soils. However, the definitional problems between loose soil, saturated areas, wetlands and sand make this a difficult condition to reliably evaluate.

REFERENCES

Benton, A.R., A.J. Blanchard, R.W. Newton, 1983. Multifrequency Radar Interpretation Techniques Applied to the Coastal Zone, Technical Papers of the 1983 ACSM-ASP Convention, pp. 157-166.

Carter, V., 1982. Applications of Remote Sensing to Wetlands, in Remote Sensing for Resource Management, Ed. C.J. Johannsen, J.L.Sanders, Soil Conservation Society of America, pp. 284-300.

Haas, R.H., F.A. Waltz, 1983. Evaluation of Thematic Mapper Data For Natural Resource Assessment, Proceedings of the PECORA VIII Symposium, pp. 122-133.

Haberl, S., P. Stock, 1983. The Synthesized Climatic Function Map, Proceedings of the EARSel Symposium on Remote Sensing Applications for Environmental Studies, pp. 273-281.

Heilkema, J.U., 1981. Landsat Monitoring of Desert Locust Breeding Grounds in Africa, the Near East, and Southwest Asia, International Geoscience and Remote Sensing Symposium (IGARSS), pp. 1168-1170.

Koeln, G.T., J.E. Jacobson, C.L. Hill, 1985. The Use of Landsat's Thematic Mapper For Wetlands Inventory, Proceedings of the PECORA 10 Symposium, pp. 441-446.

Likens, W., K. Maw, 1982. Updating Landsat-derived Land Cover Maps Using Change Detection and Masking Techniques, Technical Papers of the 1982 ACSM-ASP Fall Convention, pp. 256-271.

Millington, A.C., A.R. Jones, N. Quarmby, J.R. Townsend, 1986. Monitoring Geomorphological Processes In Desert Marginal Environments Using Multitemporal Satellite Imagery, Proceedings of the 7th International Symposium, ISPRS, pp. 631-637.

Myers, V.I., M.E. Bauer, H.W. Gausman, W.G. Hart, J.L. Heilman, R.B. MacDonald, A.B.Park, R.A. Ryerson, T.J. Schmugge, F.C. Westin, 1983. Remote Sensing Applications in Agriculture, in the Manual of Remote Sensing, American Society of Photogrammetry.

Ormsby, J.P., 1981. Land Surface Features as Indicators of Surface Characteristics for Input to Large Scale Hydrological Models, International Geoscience and Remote Sensing Symposium

(IGARSS), pp. 103-115.

Robinove C.J., 1979. Integrated Terrain Mapping with Digital Landsat Images in Queensland, Australia, USGS Professional Paper 1102.

Salomonson,V.V., T.J. Jackson, J.R. Lucas, G.R. Moore, A. Rango, T. Schmugge, D. Scholz, 1983. Water Resources Assessment, in the Manual of Remote Sensing, American Society of Photogrammetry.

Tommervik, H., 1986. Comparison of SPOT Simulated and Landsat-5 TM Imagery in Vegetation Mapping, Proceedings of the 7th International Symposium, ISPRS, pp. 525-529.

van den Brink, J.W., 1986. A Study with NOAA-7 AVHRR Imagery in Monitoring Ephemeral Streams in the Lower Catchment Area of the Tana River, Kenya, Proceedings of the 7th International Symposium, ISPRS, pp. 783-785.

4.7 SAND

The location of sandy areas from satellite imagery is generally not considered to be a difficult task. One reason is that sand has an unusually high spectral reflectance for natural surface material. It is not as highly reflective as snow or clouds, but in all visual bands it is enough to dominate the pixel reflectance value if it comprises a significant portion of the pixel. This is true even where 90-100 percent of the pixel is vegetation (Satterwhite and Henley, 1982).

In addition to showing a high spectral reflectance, sandy areas are generally found in a relatively few specific environments such as deserts, riverbanks and beaches. Coastal beaches were a separate condition in Table 1 but because a primary identifying

factor of these environments is the presence of sand near water, they are incorporated into this section. Gross environmental clues provide information about where sand might be expected and high spectral reflectance in the visible wavelengths will identify where the sand actually occurs. Many of the environmental clues that are associated with sand deposition are themselves relatively easy to locate. Lakes and waterways have been discussed elsewhere in this report. If larger than the data pixel size these features are relatively easy to delineate. Beaches are almost invariably associated with bodies of water of image size greater than one pixel.

Because of the high spectral reflectance of sand, beach areas are very obvious even on coarse resolution MSS imagery. Chong et al. (1983) devised a modified band ratio using MSS bands 5 and 7 to discriminate beaches and roads in an unsupervised classification procedure. A false color composite image of Florida shows clear and nearly continuous beach delineation, even where the beach is considerably less wide than the pixel width (USGS, 1973). In a study using TM data, all bands except 4 (near-infrared) and 6 (thermal) were found to be good for beach identification (Troiler et al., 1986).

In automated classification procedures coastal roads can be confused with beaches (Chong et al., 1983; Troiler et al., 1986). Visually, the characteristic regular linearity of roads should discriminate them from beaches. Automated road/beach discrimination would be difficult to implement using spectral

signatures or textural measures, because most linear features do not present enough "pure" pixels in the image to be amenable to statistical characterization.

Although the subject of black sands has not been found in the literature, it should be remarked upon that all sand is not uniformly white or tan. Some sandy beach areas may not appear with the clarity that white, primarily quartzitic beaches do. Black basaltic sand can be found on beaches in direct proximity to volcanoes. The island of Hawaii possesses beaches of this type. Any analyst of sand beach areas should be aware that these black basaltic sands may be present near recently active volcanoes.

Deserts are also relatively easy to identify on remotely sensed imagery. On standard false color infrared imagery, there will be a pronounced lack of reddish tones on the imagery indicating a lack of vegetation. The question in desert areas is whether the image consists of sand or rougher desert pavement. This question is addressed elsewhere in this report (see SURFACE ROUGHNESS, 4.2). Generally, it appears that even in high albedo desert areas, sand will have the highest albedo of the scene components and appear as light tan to white. Schmidt and Bernstein (1978) reported that rocks of high sulfate content may be confused with sandy areas but other contextural data such as topography or the presence of lineations in the exposed sulfate outcrops may be used to discriminate sand from the sulfates.

Additional visual clues that often indicate sandy areas are the presence of dunes in the image, or perceptible localized "blurring" of boundaries (Myers et al., 1983). This blurring due to migrating sands may obscure linear features that are visible and continuous elsewhere on the image. Medium to large scale dune fields are usually recognizable in satellite imagery; a good example can be found on the USGS Landsat image mosiac of Tunisia (USGS, 1983).

Radar has been used to analyse rapidly changing beach geomorphology and desert environments. Radar is probably more useful in beach sand identification and morphology than in the analysis of deserts because the linearity of the beach structures can be relatively easily determined. Optimal radar information extraction requires radar image data from a platform imaging perpendicular to linear features. For longshore dunes this requires a side scanning radar platform moving parallel to the beach.

In a study using airborne SAR data, many small transient beach features were identified including inlets, sandbars, and dune "blowouts" where the linear beach dunes had been swept out by winds (Wedler and Taylor, 1984). Wedler and Taylor also indicated that X band, HH polarized radar signals provided the best overall image detail but C band, HH polarization radar was inexplicably better for the identification of beach foredunes. The best dune delineation occurs when the radar depression angle

approaches the angle of the dune faces.

Radar imagery of deserts have proved considerably more difficult to interpret. Some information can be determined about the texture of the surface (see SURFACE ROUGHNESS, 4.2). In the recognition of dune fields Huadong et al. (1986) reported that the geometry of the dunes is a dominant factor in the brightness shown on the radar image. If the slipfaces are oriented perpendicular to the radar look direction, the dunes will be very bright in the image. Brightness decreases when the slipfaces move away from this orientation, reaching extinction when the dune slipfaces are oriented 180 degrees away from the radar look direction. Therefore, it would be necessary to know the predominant orientation of the dunefield prior to radar signal interpretation. This information might be inferred if a predominant wind direction is known from meteorological data.

Dune structure is variable depending upon sand availability and the amount of fluctuation in wind direction. If local wind direction is bimodally distributed, dunes can be oriented linearly parallel to mean wind direction; if wind direction is highly variable, then nonlinear "star" dunes can result that have no preferred orientation (Fryberger, 1979). To identify small dunefields the radar look direction should be in direct opposition to prevalent wind direction. This would place the slipfaces (the dune side away from the wind direction) directly perpendicular to the radar look direction for maximum

backscatter.

In site analysis from aerial photography, geomorphologists have recognized that specific features can assist in determining the granularity or texture of the surface material. V-shaped gullies indicate granular soils (Way, 1973). The angle of repose of these sands (the angle of the gully side to horizontal) is generally about 30 degrees (Mintzer et al., 1983). In many regions, drainage density is related to the coarseness of the surface materials. Sandy areas have a relatively coarse drainage network because precipitation is absorbed rapidly into coarse grained materials (Williams et al., 1983). Most available water sinks directly into the ground water table, resulting in little surface runoff and the resultant drainage patterns.

Some knowledge of the geomorphology of an area is helpful in the recognition of sandy areas. Mintzer et al. (1983) qualitatively charted how the maturity of a watercourse is related to the particle size of the sediment that is deposited along it's course. Essentially, "young" or immature streams and rivers are associated with coarse sediments while mature streams and rivers accumulate much finer sediment (clays and muds) along the banks. Young watercourses have high slope gradients, relatively straight, braided stream channels, shallow depth, narrow floodplains, and proximity to source areas. Of these characteristics, braided channels and narrow floodplains are both easily discriminated visually from satellite imagery. Therefore, if highly reflective (tan to white) areas are observed in the

false color composite image, and these areas are in the proximity of, and roughly oriented in the direction of, a "young" stream or river, it is highly likely that they are sandy areas.

No great difficulties are presented in the spectral classification of sandy beaches along coastlines with the possible exceptions of dark volcanic sand beaches and potential confusion with roads. Of these two problems, roads would be the most important because of the relative rarity of recent volcanoes in direct proximity to beaches. The separation of coastal roads from beach areas presents a difficult problem from an automated viewpoint but is relatively easily resolved by visual examination, particularly if linear enhancement filtering is applied to the image. Texture differences between hard surface roads and granular beaches might also be seen on radar imagery.

Desert sand is usually indicated by dune structures and high reflectance material in all but TM bands 4 and 6. Radar is not advised for the identification of local sandy areas in deserts because of the slope aspect problem associated with dunes. Misclassification of sulfate bearing rocks (and other rocks of very high albedo) as sandy areas could present some problems, but these rocks are most likely to be rarely observed as small patches enclosed in a much more massive bedrock exposure. Unlike sands, these rocks are also very stable in any multitemporal data set.

REFERENCES

Chong, Y.K., V.K. Vong, A.C. Yeo, 1983. Landsat Study of Changes in Surface Cover, 8th Canadian Symposium on Remote Sensing, pp. 718-726.

Fryberger, S.G., 1979. Dune Forms and Wind Regime, in A Study of Global Sand Seas, ed. E.D. McKee, USGS Professional Paper 1052.

Huadong, G., G.G. Schaber, C.S. Breed, A.J. Lewis, 1986. Shuttle Imaging Radar Response from Sand Dunes and Subsurface Rocks of the Alashan Plateau in North-Central China, Proceedings of the Seventh International Symposium, ISPRS, pp. 137-144.

Mahmood, N.N., H.L. Men, M. Breneau, 1985. Landcover Mapping of Parts of Peninsular Maylaya Using Digital Landsat Data, 3d Asian Agricultural Remote Sensing Symposium TOKAI/ESCAP/NCRT; pp. 141-153.

Mintzer, O., S.Khorram, R.Ryerson, A.S. Benson, J.E. Colcard, R. Colwell, P. Howarth, G. Lawrence, B. Mathur, J. Mollard, H. Rib, R. Thomas, J. Scherz, S. Wall, J. Wardlow, R. Welch, 1983. Engineering Applications, in the Manual of Remote Sensing, American Society of Photogrammetry.

Myers, V.I., M.E. Bauer, H.W. Gausman, W.G. Hart, J.W. Heilman, R.B. MacDonald, A.B. Park, R.A. Ryerson, T.J. Schmugge, F.C. Weston, 1983. Remote Sensing Applications in Agriculture, in the Manual of Remote Sensing, American Society of Photogrammetry.

Satterwhite, M.B., P. Henley, 1982. Effects of Ground Cover and Leaf Area on the Spectral Reflectance of Vegetation-Soil Targets, Technical Papers of the ACSM-ASP Fall Convention, pp. 352-363.

Schmidt, R.G., R. Bernstein, 1978. Evaluation of Improved Digital Processing Techniques of Landsat Data for Sulfide Mineral Prospecting, in Digital Image Processing for Remote Sensing, ed. R. Bernstein, IEEE.

Troiler, L.J., W.R. Philipson, W.D. Philpot, 1986. Landsat Thematic Mapper Images for Hydrologic Land Use and Cover, Technical Papers of the ACSM/ASPRS Annual Convention, pp. 269-278.

USGS, 1973. Satellite Image Mosaic of Florida from NASA ERTS-1 Imagery. Printed scale 1:2,000,000 reduced from 1:500,000 image scale.

USGS, 1983. Satellite Image Mosaic of Tunisia, published by the Office of Topography and Cartography, Tunis, in cooperation with the Laboratory of Teledetection, Ministry of Agriculture, France.

Way, D.W., 1973. Terrain Analysis - A Guide to Site Selection Using Aerial Photographic Analysis, Dowden, Hutchinson, Ross.

Wedler,E., R.B. Taylor, 1984. X- and C-Band SAR Image Response over Malpeque Barrier System Prince Edward Island, Canada, Technical Papers of the 50th Annual Meeting, Vol. 1, ASP-ACSM Convention, pp. 21-31.

Williams R.S., J.M. Aaron, M.J. Abrams, R.W. Birnie, H.W. Blodget, D.R. Bowley, T. Brewer, R.L. Brooks, W.D. Carter, P.S. Chavez, M.M. Clark, D.H. Coupland, W.E. Davies, M. Deutch, J.I. Ebert, C.D. Elvidge, J.P. Ford, J.R. Francica, J.D. Friedman, A.F. Goetz, D.P. Gold, W.R. Hemphill, Y.W. Isachsen, A.B. Kahle, M.J. Kingston, W.S. Kowalik, S.P. Leatherman, B.K. Luchitta, R.J. Lyon, T.R. Lyons, N. Malmula, S.E. Marsh, C.L. Molnia, E.C. Morris, J.T. Neal, D.W. O'Leary, S. Onyosko, D.G. Orr, M.W. Podwysocki, L.C. Rowan, D.B. Segal, S.L. Simpson, C.S. Southworth, D.D. Stellar, R.W. Stnigelin, H. Svensson,A.F. Thiesen, C.M. Trautwein, R.K. Vincent, B. Voight, R.D. Watson, 1983. Geological Applications, in the Manual of Remote Sensing, American Society of Photogrammetry.

4.9 AGRICULTURE

In the original list of surface conditions (Table 1), there were several variations on food production. These conditions included pasture, mixed cropland, orchards and agriculture. Because these conditions are normally spatially contiguous from a remote sensing perspective they frequently are examined together and often create problems of separation from each other. For this reason, these food production conditions are all considered within this section.

A common problem with these cover types is differentiating between active and inactive agriculture. Frequently, fields and pastures have periods of inactivity because of seasonality, agricultural practices such as a fallow period, livestock migrations such as transhumance or changing land use patterns particularly at urban/rural interfaces. In some situations, these periods of inactivity are periodic, in others permanent. Areas of inactive agriculture are extremely difficult to reliable delineate with remote sensing techniques, particularly automated processing. In addition, the importance of locating inactive agriculture is a function of the problem being considered.

Pasture is a very difficult land use to classify. This is because of the active/inactive problem and also because of the tremendous variations in the livestock density of lands being utilized as pasture such as intensive feedlot and extensive rangeland. Mixed cropland can be defined in many ways such as

various combinations of croplands, orchards and pasture; heterogeneous agricultural fields due to intercropping; or fields of homogeneous crops but where adjacent fields may be different crops. Because of these various definitions, mixed cropland will not be discussed as a separate condition. From spaceborne remotely sensed data, orchards generally appear similar to cropland as a relatively honogeneous green vegetation spectral signature depending on the spatial resolution of the sensor and the crown closure of the trees. For this reason, orchards will be treated as essentially another crop type.

Areas of food production in a regional sense are generally known from ancillary data such as climatic, population density or maps of economic geography. More specifically, agricultural areas can be generally recognized visually from spaceborne imagery by distinctive land use patterns associated with fields. An exception to this are extensive, generally subsistence, agricultural practices in areas of low population density such as tropical rainforest and steppe environments. In these locations, the existence of this type of activity could be extracted from ancillary information but site specific active agriculture might only be inferred from remotely sensed data. This possible indication would be additionally hampered by shifting cultivation practices which would necessitate current data. While there are exceptions as noted, generally areas of food production can be located by visual analysis of remotely sensed data. Automating this process may be possible by an expert system or artificial

intelligence approach. A more difficult task than locating areas of food production, and the focus of much of this section, is the identification of specific crops.

An extensive review of the literature concerning the identification of cropland type and pasture from satellite imagery has led to the conclusion that reliable specific classification of these areas on a global basis will be a difficult task. Although there are literally hundreds of studies that deal with the classification and assessment of ground cover, the spatial extension of multispectral classification techniques from original study areas to other regions is an unresolved problem.

The reasons for this difficulty are manifold and before exploring some techniques that have been applied to the many area specific analyses that appear in the literature, it will be useful to consider the major problems that have been encountered in the spatial and temporal extension of multispectral signatures. Consideration will also be made of some global crop and field distribution patterns.

While variations in climate, terrain, vegetation and land use patterns have often hindered the extension of multispectral signatures in the past, it is increasingly emerging in the literature that the proper consideration of these site specific variables may conversely assist in the classification of land cover as well (De Sachy et al., 1986). The integration of these

factors with remotely sensed information may well prove to be an excellent application for artificial intelligence or GIS techniques to solve a problem that has proved to be relatively intractable, often simply because of the great amount and diverse types of data that need to be used.

While much research has been published concerning the remote sensing of agriculture, unfortunately most of the studies concern areas in the United States where the major crops in the image are generally known beforehand and good ground truth is readily obtainable from maps or recent large scale aerial photography. Thus, many studies are available of well inventoried areas of known crop distributions; corn, soybeans and wheat are extensively covered in the literature. For taro, rice, potatoes, tea and many other crops this is unfortunately not true. In addition, there are different hybrids of most crops. Konijnenburg and Irsyam (1986) identified 26 different types of rice in Indonesia. In Canada and Russia, both winter and spring wheat are planted. These hybrid strains possess climatic, locational, and seasonal differences. Spectral differences from satellite images between hybrids are seldom addressed in the literature.

A related problem to the global identification of crops is that usually the basic methodology of agricultural remote sensing studies has relied upon aerial photography, ground truth and multilevel sampling schemes. Few efforts have used only satellite imagery to identify crops and pasture in poorly mapped

areas of unknown crop assemblages. However, in any attempt to identify agricultural vegetation worldwide, many instances will be found where there is limited ancillary data. Globally, there are also many regions where ground truth is simply not rapidly obtainable, either because of sheer remoteness or because of access restrictions. Before examining specific remote sensing agricultural applications, it is useful to review variations in agricultural practices.

4.9.1 GLOBAL AGRICULTURAL PATTERNS

The structure of regional agriculture systems plays an important part in the ability of spaceborne sensors to determine what is in a particular area. The township and range system of the midwestern United States is perhaps the most intelligible land division system; the square pattern is clearly visible from most types of orbital imagery. This type of land system is optimal for multispectral analysis because the fields can be easily differentiated. Consequently, signature extraction training sites are easily defined and a classification technique can be evaluated in a preliminary fashion by the ability of the classifier to be consistent inside the delineated fields.

The metes and bounds system of land division found in the earlier settled areas of the United States is characterized by small, irregular parcels of land that usually can be seen oriented to the terrain. Fields in these areas are often linear along streams, rivers, and mountain valleys. This system of land

division is similar to what is found in much of Europe, Africa, and non-Communist Asia. It is indicative of agriculture that is controlled at the family or village level. A land division pattern of this type is more difficult to classify. The reduced number of pixels per field and the increased number of border pixels results in signature statistical complexity. In areas of very small fields and mixed agricultural practices, field segmentation into discrete crops for supervised signature extraction is difficult. Alternatively, an unsupervised classification of these mixed agricultural areas may yield far too many clusters to be useful. Areas of small field sizes such as normally occur in tropical, densely populated, developing countries where subsistent agriculture is practiced, create many problems for spectral classification. These problems include complex crop calenders where a single crop may be in many stages at a given time, and heterogeneous fields due to intercropping and other similar practices.

In the Soviet Union and some other Communist countries, classification is considerably eased because land parcels tend to be very large and homogenously cropped as a result of collectivization of the land. This results in individual fields that are clearly visible even on MSS imagery (O'Malley, 1983). Other regions that would normally be associated with small farming parcels can also have large areas under single crop cultivation. This occurs in some parts of Africa, where ex-colonial plantations are now operated by the state in a

collective fashion (Haack, 1986).

Modernization of farm practices usually leads to an increase in field size. Major capital investments such as large irrigation projects or the introduction of farm machinery tends to promote the homogenization of the agricultural landscape by moving the farm away from individual management into agribusiness. This is an ongoing process in more technologically advanced countries of the world.

Larger fields facilitate the identification of crop and pastureland because there are more "pure" field pixels available for statistical analysis, fewer fields are present, and fewer crops are represented. Field size will also determine the type of data that can be used to obtain a reliable analysis of the agricultural land use. If the large fields of the collective farms are to be analysed, then low spatial resolution MSS data may be sufficient. In areas of small fields, TM or SPOT data will be much more effective (DeGloria, 1983). A National Academy of Science report (1977) on the capabilities of remote sensing in developing countries identified a threshold of 60 pixels necessary to obtain a good radiometric measurement of a field.

Climate type should also be known prior to data analysis. Drier and colder climates are associated with fewer crop types, more pasture, and shorter growing seasons. These attributes result in remotely sensed data that are relatively easy to classify multispectrally. Tropical agriculture can be extremely difficult

to analyse because the growing season is essentially year round and many different crops can be grown. Few seasonal or climatic constraints are placed upon the farmer about when or what he must plant; consequently, many different crops at many different phenological stages are often present at the same time in tropical areas (Haack, 1986).

The climatic regime also has impact upon both the short and long term agricultural variation to be found in a particular area. High latitude, cold environment vegetation is relatively stable. It is homogeneous over broad areas and has a well defined seasonality. This tendency can be observed with winter wheat in the Soviet Union or Canada. In addition, these northerly areas are not prone to land use change from year to year. Classification performed for one year will very likely be applicable to other years; similarly, available land cover/land use maps can be expected to be reasonably accurate, even if somewhat dated. Wet tropical environments may be much more subject to change; consequently historical data and maps may not be as useful.

In summary, the cooler and the more technologically advanced the farming practices of an area are, the easier it will be to arrive at a reliable multispectral classification of the agriculture in the image. The inverse is also true. This trend has implications on the complexity of the statistical measures required to perform the analysis, and also on the resolution of

the imagery that is to be employed. It is unfortunate that the tropical areas where we expect to experience the most difficulty in classification also tend to evidence a higher amount of cloud cover, reducing the total imagery available for a particular site.

From the above discussion of some of the considerations that must be weighed in the analysis of agricultural scenes, it should be apparent why classification results reported in the literature can vary widely. From a multispectral classification viewpoint, corn in Kansas is not corn in Russia; and corn in Nigeria might also be very different. If all of these considerations can be welded into a coherent geographic picture of a particular landscape and integrated into multispectral classification techniques, then the capability of global identification of crops and pasture might be attainable. At the current time, no sufficiently robust analytic model has been put forth that is capable of this task.

4.9.2 PASTURE RECOGNITION

One of the most recurrent problems in remote sensing is the failure of many scientists to establish a clear division between what is actually seen or measured from the image data and what is inferred about the scene itself. This basic division of the information extraction process is very important in the [illegible] of the Earth's surface from satellite imagery; the [illegible] difference between land cover and land use must be [illegible]

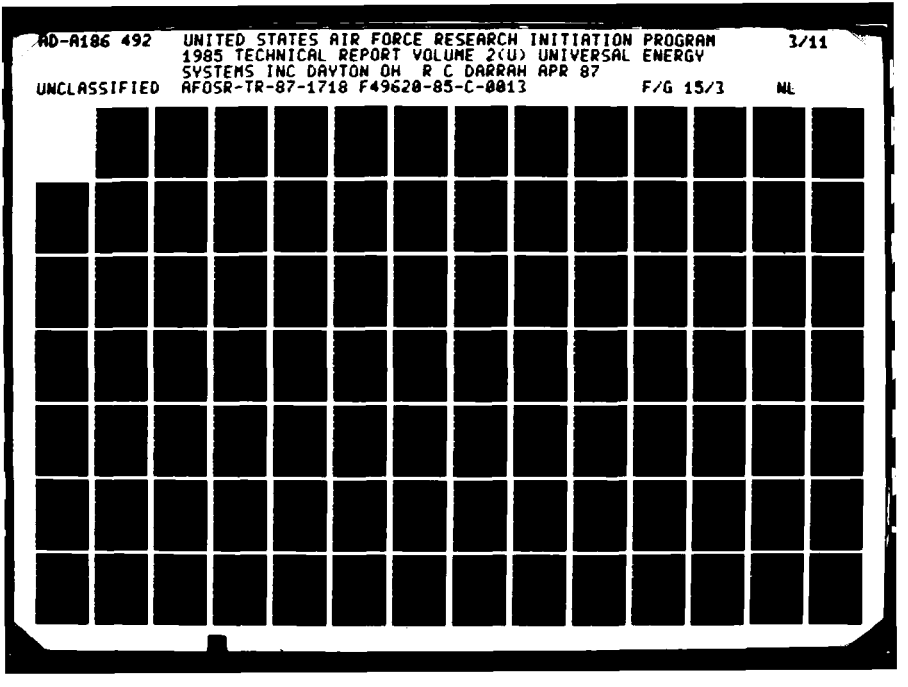
AD-A186 492 UNITED STATES AIR FORCE RESEARCH INITIATION PROGRAM 3/11
1985 TECHNICAL REPORT VOLUME 2(U) UNIVERSAL ENERGY
SYSTEMS INC DAYTON OH R C DARRAH APR 87
UNCLASSIFIED AFOSR-TR-87-1718 F49620-85-C-0013 F/G 15/3 NL

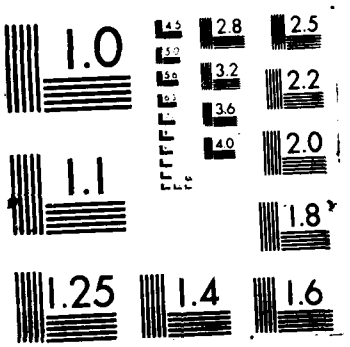
1.0
1.1
1.25
1.4
1.6
1.8
2.0
2.2
2.5
2.8
3.2
3.6
4.0

understood. The automated classification of image reflectance values is often very useful in the determination of many land cover categories, but the determination of land use is largely an inferential process (Smith, 1986). Sometimes, the inference is very obvious; if rows of plants are observed in a polygonal field, then obviously this land is being used for agriculture. Unfortunately, in many areas a land use classification has no such obvious interpretation keys. Also, the presence of useful keys in the image is very dependent upon image date and resolution (both spectral and spatial).

A good example of this interpretational difficulty is the identification of pastures. A non-pasture field may appear identical to areas of known pasture in all but the largest scale imagery. A land use classification category like pasture rather than a more easily obtained land cover grass classification may lead to difficulties. If a grassy field is classified as pastu based upon spectral similarity to known pasture, and this designation is in turn transferred to a map, then a later analyst with no knowledge of the original classification methodology may incorrectly conclude that food in the form of livestock is available in this area.

There are many examples to illustrate the importance of this land cover/land use distinction (Merchant, 1981; Wilson and Thompson, 1981). In the midwestern corn belt of the United States, fields are allowed to lie fallow in order to restore the soil condition

after a period of intense cultivation. Since fallow fields are frequently planted with grass or alfalfa that is subsequently plowed under to increase nitrogen levels in the soil, it would seen reasonable to possibly use these fields as pastureland in the fallow periods. On a remotely sensed image, these grassy fields may be interpreted as pasture. However, in some areas of the midwest, the economy is not based upon livestock production, and consequently few of these fields are utilized as pasture. An analyst must be aware of the agricultural practices and the economic production of a region before attempting to identify pastureland with remotely sensed data. In the dairyland state of Wisconsin, any non-wooded, non-cropped land is very likely to be used as pastureland. However, the Delmarva Penisula of eastern Maryland primarily produces vegetables and fowl; consequently, most similar land remains unused as pasture.

The difficulty in interpreting pasture from remotely sensed images is recognized by Anderson, et al. (1976). The Anderson land use and land cover classification system for use with remotely sensed data has achieved wider acceptance in remote sensing than any other classification system. A significant aspect of this classification system is that pasture and cropland are grouped together at the Level II class. Many remote sensing studies indicate that Level II classification is the most detailed classification that can be reliably achieved with high altitude aerial photography or space imagery without ground truth. In foreign areas of poor a priori knowledge, Level II classification of ground cover probably is the best that can be

done without complex numerical analysis of the image data or the inclusion of ancillary data to partially fulfil the role of ground truth.

In addition to the pasture/land use, versus grass/land cover, classification difficulty is the problem of the variability of land covers used for pasture. Pastureland can be defined as ground used for the grazing of livestock; but in various regions of the world, livestock is grazed upon very different kinds of land. In the eastern United States, pasture is often fallow fields and can be readily recognized in large scale aerial photographs by a number of clues including shape (which identifies the area as a field), the absence of field crops (which shows that the land is not actively used at the present time for production), fences, and often the presence of grazing paths. All of these clues are a function of these pastures usually being well vegetated and intensively grazed. Australian range serves as sheep pastureland even though the vegetation is relatively sparse. These Australian pastures are what most eastern American farmers would consider to be too arid and unsuitable for animal grazing. So, in some instances, a pasture is an intensely grazed, relatively lush fallow field or bottomland while in other cases, a pasture is a relatively arid and sparsely vegetated rangeland that may only support one sheep per 500 acres. These two types of areas obviously will not have the same, or even similar, multispectral signatures. Thus, in the identification of pasturelands, we also have a definitional

problem with pasture.

In this study pasture will be divided into two broad types; 1) rangeland used for grazing, and 2) delineated areas associated with farms that are used for grazing. The latter category includes river bottomlands and hilly slope pastures as well as fallow fields occasionally used for grazing. Additionally, a pasture will be considered to be predominantly grasses. While the above classes of pastureland cover the majority of pasturelands on the Earth, it should be borne in mind that virtually any vegetated land can be (and, somewhere in the world, probably is) utilized for the grazing of animals.

These definitional problems become very important in per pixel classification because pasture is frequently transitional between organized cultivation and sparse vegetation or woodland. Pasture is often an example of the "mixed pixel" problem in classification because no single vegetation type dominates the pixel reflectance value. An individual pasture pixel may include green grasses, an old field in transition to brush, and part of of a neighboring irrigated field. Farmers in the densely populated Far East will graze water buffalo upon sub-pixel areas unused for other purposes, including roadsides and rice paddy dikes. In the latter case, it is highly doubtful that a classification of pasture can be assigned to any single area of the image because grazing is a secondary land use superimposed upon a primary use. The vegetation, road and field patterns can be expected to only reflect the primary land use.

Because delineated pasture fields are usually in close proximity to croplands, it is difficult to discuss one without involving the other. In general, past work in the classification of pasture using remotely sensed imagery has been approached largely as a problem of differentiating pasture from actively producing crop fields. In areas where fallow fields are used for pasture, it is important to realize that this is a temporal, and most likely an annual, phenomenon; last year's crop fields can be this year's pasture. This is more of a problem in mid and low latitude moist climates where vegetation is more active and consequently land use/land cover is less temporally stable.

Short term temporal changes can also be seen in areas where the location of grazing can change with the season. In a study of the Sudd in Sudan, Yath and van Gils (1986) classified grasslands as seasonal pasturage where a "wave" effect can be seen between the upland wet season pasturelands and the river valley dry season pastures. East (1965) termed this migratory practice "transhumance" and identified it as primarily being found in primitive or poor cultures. As cropping becomes established in an area, transhumance is reduced by the introduction of stored animal feed.

In crop classification, multitemporal data frequently improves classification. A simple differentiation of soybeans and wheat in Iowa determined that crop classification accuracy can approach

100 percent using 6-date TM imagery (Pitts et al., 1983). Several studies have also specifically identified the importance of imagery dates when attempting to recognize pasturelands. Gillespie et al. (1986) reported consistent confusion in spectral classification between hay (a harvest crop) and pasture fields in a TM analysis of an autumn Connecticut scene. It was felt that plant senescence (the onset of old age and brownness) results in homogenizing of the spectral signatures of these land covers at this time of year.

Troiler et al. (1986) experienced similar difficulties in classifying pasturelands near Rochester, New York using July TM imagery. In this study a later date was recommended when other crops have been harvested. This would leave only bare harvested fields and pasture in the scene, considerably easing the multispectral classification problem. Proper date selection or a multitemporal classification strategy may be necessary to identify pasture but the exact dates to use in the classification may be difficult to identify. Historical data could be utilized but it must be borne in mind that short term weather will be the driving force behind both plant emergence and senescence.

Some studies have used single image analysis for pastures with good success. In a visual interpretation study, Troiler et al. (1986) determined that pasture is best discriminated visually using TM band combination 3,5,4. Miller et al. (1985) reported that pastureland could be discriminated from alfalfa and grain stubble fields in California's San Joaquin Valley. This

classification was performed without multitemporal coverage. With the exception of harvested grain fields, pasturelands had the highest reflectance in TM band 5 of all crops present in the scene. The harvested fields were differentiated from the pasturelands because they were much more reflective in the visible bands. TM band 4 was found to be useful in agricultural crop identification, but alfalfa fields were similar to pastures in this band. Graphs accompanying this report show a high variance of the pasture pixels, particularly in band 5.

Miller's (1985) determination that TM bands 4 and 5 are most useful in the identification of grassy pastures is supported by other studies. Troiler et al. (1986) and Haas and Waltz (1983) found that band 5 was best for grassland and range evaluation. Riechert (1984) reported that the TM bands 5/4 ratio was good for crop, bottomland, and rangeland classification.

The U.S. Dept. of Agriculture routinely performs detailed land use classification based upon aerial photography. Satellite images are also used to stratify the area under investigation. In this procedure, pasturelands are identified by "a spotty pale red appearance" in the standard FCC satellite image (Good, 1986). This description is similar to that appearing in the USGS land use/land cover photointerpretation keys (Loelkes et al, 1984). These identifying characteristics of pale color (low vegetation reflectance) and spottiness are because much of the pastureland associated with farms in the United States is non-irrigated,

usually not fertilized, and often possesses a variable amount of trees. The lack of water and nutrients together with grazing pressures results in a CIR photo or standard FCC image with vegetation redness less than that of nearby cultivated fields or forests. Similarly, Mueller et al. (1985) found that the infrared reflectance of pasturelands in Florida was between that of bare soil (very low IR reflectance) and the surrounding pine plantations (high IR reflectance). The presence of some trees and variable water availability (causing irregular vegetation patterns) leads to the spotty texture. However, it is significant that USDA workers make no attempt to determine if the land parcel is actually used as pasture; land is classified as pasture only on the basis that it could reasonably serve as such (Good, 1986).

Several sources, including the USDA and Troiler et al. (1986), report that pasture areas are easily confused with tended grass areas such as parks or parcels of land surrounding farm houses. This problem stems from the land cover and land use inference difficulty. Caution is therefore indicated when interpreting pastureland in the immediate vicinity of human settlement.

Grass areas are often best identified early in the growing season before full crop development (Ripple, 1986). Grass usually emerges and becomes green before almost all other plants but later in the season the grass reflectance can be overwhelmed by nearby plants with much larger LAI (Leaf Area Indexes) and consequently much higher IR reflectances. A possible approach to

multitemporal classification of grassy areas might be a delineation of the grasslands in an early season scene; this delineation could be used to refine the classification via image differencing of a late season image that would show the harvested grasslike crops (alfalfa or hay) as bare or stubbled soil. Areas within a specified radius of dwellings could also be masked out. In this fashion, farmyard areas and harvestable hay fields might be discriminated from unharvested grassy areas. It will still be difficult to ascertain if these grassy areas actually contain livestock.

Another pasture recognition approach based on seasonality was suggested by Howes (1984) utilizing multitemporal images of the Nicaraguan savanna. This study reports that the optimal image date for classification can vary as much as a month due to climatic fluctuations. An interesting finding in this study is that near the end of the wet season, pastures located on thin, dryer topsoils lose their infrared spectral reflectance a few weeks earlier than croplands on thicker, moister soils. Therefore, pasturelands can possibly be identified by a comparison between wet season and end of wet season data. This approach might be very valuable in the lower latitudes where field delineations are generally much more difficult to determine due to consistently lush and highly reflectant vegetation across the entire landscape.

In higher latitudes, it may be easier to obtain good pasture

classifications. A study of vegetative land cover near Green Bay, Wisconsin obtained 85 percent accuracy. This study used only a TM7/TM5 ratio procedure in an unsupervised classification (Lo et al., 1984). Suprisingly, poorer results were obtained for the same data set when a tasseled cap transformation was employed. It is speculated that the transformation of the data set resulted in too many spectral clusters. Essentially, the complexity of the information made available by the tasselled cap technique grossly exceeded the level of information needed to classify a relatively simple landscape.

These results suggest that land cover classification in areas of relatively simple landscape may be best done with coarser spatial resolution MSS data. If there are only a few major cover types in a specific area, then the inherently higher variance in TM data (Crist, 1984) might prove to be a hindrance rather than a help in automated classification. Using TM or SPOT imagery in an unsupervised classification may result in numerous spectral clusters that do not reflect significant ground cover differences.

The use of MSS to classify simple landscapes is supported by Merchant and Roth (1981). In a classification of Kansas grasslands, 85 percent accuracy was achieved in determining ground cover. The classes employed in this study were woodland, bare ground, and 25, 50, 75, 100 percent grass covered. If precise field delineation is required, then TM or SPOT data might still be required for edge definition.

Although the increased TM within field variance can be more complex than needed for simple landscape classifications, it can conversely aid classification accuracy by providing additional information about complex and difficult to classify scenes. Haas and Waltz (1983) reported that variance was increased approximately 10 percent in the TM compared to MSS data for both cropland and grazed rangeland. This increased variance can lead to improved evaluation of crop and grassland conditions such as total amount of ground cover.

One way that the image relectance components of soil and vegetation can be separately analysed is by use of the Knauth-Thomas Tasseled Cap transformation. In this procedure, the image reflectance values are rotated through n-dimensional spectral space onto another set of axes by use of a sensor specific formula. No data are lost because the coordinate system is merely reoriented. This new set of axes is oriented so that vegetation reflectance (the greenness component) is orthogonal to the soil reflectance (the brightness component). This 90 degree separation of reflectance components theoretically maximizes the separability of the two components prior to further analysis, and thus the evaluation of the vegetation by itself is simplified. An additional benefit is that computer data handling and storage requirements are lessened by the reduction in data dimensionality. The tasseled cap transformation has different coefficients that rotate the data onto the appropriate axes for

both MSS and TM (Jensen, 1986). However, some work suggests that the soil brightness axis may be a series of soil line segments of different slopes. The line segment slope may be dependent upon the soil type of the region under analysis (Huete et al., 1986). If this is true, then careful image segmentation is recommended prior to grassland evaluation using the tasseled cap transformation.

Rangeland areas used for pasture have been reported to be identifiable on satellite imagery. Several studies have indicated that rangeland useage may be feasibly determined by differences in spectral reflectance between areas that have been grazed and those that have not. Robinove (1979) using MSS data noted differences between grazed and ungrazed arid Australian rangelands on dry season imagery. Klumph and Adams (1985) discuss how the Alberta Public Lands Division utilize special "rangeland enhanced" satellite image products to study the condition of the range; from these enhancements grazed land may be distinguished from ungrazed land.

Klumph and Adams (1985) indicate that the absence of "litter" on the ground in grazed areas leads to noticable textural differences on the Landsat imagery. Thus, texture is indicated as a primary clue in the automated recognition of actively grazed areas. This is supported by the USGS photointerpretation guide (Loelkes et al, 1983) specifying spotty appearance as an interpretation key to pasture identification. Mueller et al. (1985) found that pastures were visually identifiable in a study

of Northern Florida by a distinct rough texture apparent in TM bands 1, 2 and 3. The study by Miller et al. (1985) of the San Joaquin Valley cited previously had similar observations.

If texture differences are present between grazed and ungrazed range, then this characteristic might be useful on a global basis for the discrimination of range used as pastures. This technique might be particularly useful in third world regions because land management practices have often not been implemented to prevent overgrazing. In some third world countries, grazing pressure may be due to either livestock or wildlife and could probably not be separated without ground truth or supporting ancillary information.

The use of texture measures to analyse rangeland will require prior segmentation of the image into relatively homogeneous areas. This will reduce rangeland variance due to non-vegetative factors and allow the histogram stretched values to primarily show very small changes in the range. Therefore, an initial segmentation must be performed so that rangeland is separated from non-rangeland. The masking of crop fields prior to pasture classification is excellently discussed in Miller, et al. (1985). Also, from the studies by Huete et al. (1984) and Ezra et al. (1984) cited earlier, areas of different soil type would probably need to be analysed separately. With such factors as different vegetative regime and regional soil type accounted for, texture measures can then be applied to the apparently homogenous

rangeland. Examination of the second order statistics of the rangeland may reveal a bimodal distribution of interpixel relationships within this visually homogeneous rangeland if part of the range is used as pasture.

In arid range areas, difficulties may be encountered in determining if vegetation is present to any significant degree. Some soils can have reflectances that are very similar to the reflectances of non-green plants such as senescent grasses. These areas may actually be sparse pasturelands and afford some degree of vegetation cover.

Satterwhite (1984) attempted to address this problem for arid sites in Nevada. Analysis of only TM infrared bands may not be sufficient because brown or grey vegetation (grass or brush) does not offer sufficient infrared reflectance to differentiate vegetated from non-vegetated lands. Satterwhite reported some success using different combinations of visible band and near IR band ratios to identify sparse vegetation. A visible red/near IR band ratio proved to be the most effective in differentiating yellow-green vegetation. Near IR/visible band ratios were also well correlated with the amount of ground cover. Band ratios quickly stratified the scene into color types; the image could be segmented into bare soil, yellow, and green vegetation with relative ease. This could be an effective "first look" technique to quickly stratify a scene prior to textural or other in-depth analysis. Satterwhite stated that some grey vegetation was not detected on dark soils nor was senesced vegetation in gravelly

areas.

An alternative approach to optimizing rangeland information is the use of more complex vegetation indices than simple ratios. A number of such vegetation indexes are available. A good review of exactly how they may be calculated from the image data is found in Jensen (1986). Miller et al. (1985) effectively assessed pasture canopy using the Transformed Vegetation Index (TVI) of TM bands 3 and 4. A good review of different indices used with success for arid land and rangeland vegetation studies can be found in McCoy (1981). Five different indices including the TVI had correlation coefficients of approximately .86 with leaf area index. Vegetation indices can be indicative of actual ground cover but the exact date of the imagery remains the least understood variable in rangeland evaluation using only remotely sensed imagery.

Potential pasture areas can frequently be determined by automated land cover classifications. However, if potential pasture currently contains livestock is unlikely to be determined from remotely sensed data. Because of the large variability in grazing practices and lands utilized for grazing, the location of potential pasture areas should be attempted on a region specific basis and will be most successful where ancillary information exists on livestock practices.

4.9.3 CROP IDENTIFICATION

Although agricultural field patterns are readily evident on all high or medium resolution satellite imagery, the exact contents of a particular field are difficult to ascertain without ground truth. Classification based only upon matching the spectral reflectance of crops at a particular time to known signatures has generally been found to yield insufficient accuracy. Other factors such as soil brightness, atmospheric conditions, and the exact phenological stage of the plants at the time of imaging have been found to alter the spectral reflectance of any particular crop to the extent that no constancy exists between the same type crop fields in different regions and at different times (Myers et al., 1983).

In visual interpretation, the identification of crop types on remotely sensed imagery begins with the acquisition of climatic and seasonal data. The primary crops are identified and crop calenders are compiled that show the planting, growth, and harvesting times of each crop (Avery, 1985). The analyst is then cognizant of emergence and harvest patterns of the major crops. With this information, the analyst can examine imagery of different periods during the growing season and identify the crops from their chronological phenology. This can be accomplished with single date imagery if the date of image acquisition is well chosen.

This basic methodology is operationally performed with small

variations for both airborne and satellite imagery. For domestic sites, most of these steps are not particularly difficult because the analyst is often very knowledgable about the expected crop assemblages and distributions. The Department of Agriculture and individual county agricultural offices can be called to clarify particular questions about planting and harvesting dates and information is readily obtained about the past production of different areas.

Much of this knowledge will not be available for foreign areas. Without ground truth, and without a good knowledge of the assemblage of crops and vegetation present in the scene, the analyst is faced with severe difficulties in identifying crop types. At the present time, this cannot be done reliably using only satellite data.

Considerable effort has been expended to automate the crop recognition process so that reliable statistical estimates of crop production can be obtained over broad areas. It would seem fundamental that accurate field recognition is prerequisite to accurate crop production estimates but this is not necessarily the case. Crop estimates can accept some degree of error in field identification as long as it is predictable. It is satisfactory that only a certain percentage of fields are identified from the remotely sensed data, because the identified acreage (the dependent variable) is statistically regressed onto final production (the independent variable) in order to obtain a

predictive model. Regional crop prediction does not directly address the problem dealt with in this study: the accurate recognition of individual crops. However, crop recognition algorithims developed for regional agricultural assesssments may be applicable for specific pixel or field recognitions.

Possibly the most extensive investigation of global crop recognition and evaluation strategies has been a series of United States funded projects for operational useage of satellite data to identify and predict yields for specific crops over broad geographical areas. CITARS, terminating in 1975, was developed to compare different techniques of automated crop discrimination using MSS data. The target crops were corn and soybeans and the test sites were primarily in Illinois and Indiana. A maximum classification accuracy of 75 percent was obtained with late August data when the crops had attained full canopy and when within field variance was lowest. For this data set, the best classifier used a single representative signature for each crop and not multiple training sites. This study also demonstrated the failure of signature extension to other areas. When the recognition algorithim was used in other test areas, a 22 percent loss of accuracy was incurred (Myers et al., 1983).

The Large Area Crop Inventory Experiment (LACIE) attempted to evaluate agricultural production of wheat over wide areas of the Soviet Union and the United States. Crop identification was achieved through a supervised classification where analysts (using multitemporal imagery and ancillary data) labelled

approximately 100 pixels per scene as wheat; approximately 40 of these pixels were subsequently used for training statistics. The remaining unused pixels designated by the analyst were used to test the maximum likelihood classifier prior to use over the whole image. Although useful aggregate agricultural figures were produced from LACIE, no information was found that analyses the per pixel accuracy of wheat identification.

The AGRISTARS program was created in 1980 to expand LACIE developments into evaluation of five more crops: barley, corn, rice, cotton, and soybeans. AGRISTARS sought to further automate the crop identification process over a greater extent of the earth. Initial AGRISTARS classification of croplands was executed using a conventional supervised classification process similar to that employed in LACIE. An unsupervised clustering classification was developed to replace this process early in the program. This algorithim, termed CLASSY, was used to delineate different types of crops on single date imagery. A notable feature of CLASSY was that only the interior of the fields were used for the classification. The use of interior pixels greatly reduced the mixed pixel problem found along field edges. Consequently, the interiors provided a more representative statistical data set for individual crop classification (NASA, 1981). This procedure is relatively easy to implement automatically if edge information can be extracted from the image; essentially, it is the reverse of conventional line thinning.

A number of other interesting methods and results were reported by AGRISTARS researchers. A model was created of seasonal changes in plant reflectivity so that the CLASSY algorithim could be extended into multitemporal classification. This model fitted a bell-shaped curve to the image reflectance of a particular field as charted over time. Decision parameters for crop identification were the maximum peak value (corresponding to crop growth climax), the time of this peak value, and the inflection points of the fitted curve to either side of the peak value. These inflection points were thought to roughly correspond to initial greening of the plant and plant senescence. This model was found to work well (86 percent accuracy) in the identification of five different crops for a test site in Argentina (NASA,1982).

AGRISTARS also reported that generally mixed croplands can be characterized as either small grain assemblages or not small grain assemblages. This is important for scene characterization prior to classifcation. Different bands of the MSS were reported to be better for different crops; no single band or band combination was found to be to be optimal for all crop identifications. Band 4 discriminated corn from soybeans, while band 5 was best to identify late planted corn. Overall, MSS bands 5 and 7 were the most useful in crop identification (NASA, 1983).

Evaluations of TM Simulator (TMS) data were also undertaken as part of AGRISTARS. The principal components transformation of

the TMS data showed that components 1 and 2 were roughly equivalent to greenness and brightness indexes derived from MSS data. The TMS data had the additional benefit of reducing the mixed pixels in the scene by a 3:1 ratio. Classification of crops using TMS bands 1,2,3, and 4 provided the best accuracy of any combination of TMS bands. This combination had a crop identification accuracy of between 75 and 90 percent for a number of crops in a multitemporal classification test in Missouri. AGRISTARS researchers reported that image stratification is very important in the classification of general vegetation types but that stratification is not recommended if only crop identification is desired.

If current locations of agricultural fields are important, it may be efficient to use historical, possibly multitemporal data, to assess areas of agriculture and then determine areas of change with more recent data. A review of several agricultural change detection techniques can be found in Burns and Joyce (1981). This study reports no significant difference in any of the four techniques compared; differencing, composite classification, radiance shift, and regression. Image differencing is probably to be preferred because it is computationally simple. Principal components analysis has also been found to be useful for change detection. Richards (1984) reported that the changed areas are often highlighted in the first or second principal component.

Radar is also indicated as being of some use in the AGRISTARS

research. Experiments using SEASAT data over Kansas determined that corn and soybean fields may be discriminated early in the season by using radar texture differences (NASA, 1983). Also, field edge information was found to be very good on radar images, suggesting that radar may be used to find field boundaries prior to the employment of the CLASSY algorithim. There is considerable interest in using radar to classify croplands because of its all-weather and day-night capabilities but crop/radar interaction is not sufficiently well understood to be operationally useful for crop classification (Meyers et al., 1983). Factors such as row direction and soil wetness can have a dramatic effect on crop backscatter (NASA, 1983).

Other, less comprehensive attempts to reliably identify crop types are also available in the literature. Like the federal research discussed above, these reports generally suffer from many of the problems treated at the beginning of this section. In particular, it was found during the literature review that the lack of small field identification techniques and the lack of third world crop identification reports would severely limit the extendability of the CITARS, LACIE, or AGRISTARS methods over a great deal of the world. None of these latter efforts even attempt to address tropical agriculture, where the greatest difficulties in reliable identification of crop types are expected.

Some recent studies have focused on these problems. A supervised classification using TM data of the St. Lawrence River area in

Canada was attempted to undertake identification of the crops contained in relatively small (100 meter width) fields. Optimal image acquisition time was established through prior research as late August. Single date data were limiting in this study because hay was often misclassified as corn and cereals (14 percent and 50 percent misclassification, respectively), while sugar beets and soybeans were accurately classified to within acceptable limits (Cihar et al., 1985). A working knowledge of regional crop patterns may be of great assistance in areas where crop classification is difficult because of the presence of small, mixed crop fields or the confusion reported by several studies between small grain crops (Belward and Taylor, 1986).

Another approach to the small field problem was taken by Menenti et al. (1986) using various vegetative indexes. This study demonstrated that multiple index values may be useful if the area to be analysed is composed of a wide variety of crops. Data from selected dates within the regional crop calendar may be optimized by using target specific index values. Menenti et al. attempted to extend spatial signatures of diverse Mediterranean crops between the Po Valley and Argentina using this technique. The TVI and a TM band 5/7 "greenness" ratio were found to be useful. Of the nine different crops, excellent classification results were obtained for all except alfalfa. An interesting result of this study is that the index values are traced through time and intercropping practices are revealed because the time "track" of an intercropped area is shown to lie between the time "tracks" of

the two component agricultural types. The use of vegetation index tracking over time is supported indirectly by Pitts et al. (1983) who reported that classification accuracy of croplands was increased by tracking values of the fields using both the tasseled cap and principal component transformations.

Menenti's approach appears to be well worth pursuing for several reasons. One reason is that low latitude, spatially small areas of diverse useage are apparently classified with some success; this type of agriculture that often includes intercropping presents one of the most difficult challenges in agricultural remote sensing. In addition, this pattern is often what is encountered in third world countries. In a broader application, the statistical treatment of the well known mixed-pixel problem in the light of geographic associations and multitemporal imagery promises to be a much more robust approach than statistical analysis of purely spectral values.

The more relevant ancillary data that can be introduced into the classification process, the better the final classification results can be expected to be. In addition, more image data than just the multispectral pixel values should be employed. As demonstrated earlier, texture data may prove to be useful to separate crops and pastures. To identify crops in areas of mixed agriculture, multitemporal tracking of vegetation indexes and/or coordinate transformations would seem to be the most promising approaches. Climate data will be necessary to determine the optimal dates of image acquisition for a region. All of these

factors need to be considered in any attempt to reliably identify the type and growth stage of a crop in many areas of the world. Thus, in order to optimize the image informational content, it is desirable to approach the classification procedure from a Geographic Information System (GIS) standpoint (Merchant and Roth, 1981) relying not only on image data but also on other forms of data that can be incorporated to improve the classifier performance. Satellite imagery can frequently determine the qualitative land cover of an area but a reliable determination of land use must depend upon the integration of ancillary data (Smith, 1986). An additional benefit of the GIS approach is that the computational problems of multitemporal image analysis are eased by the fundamental data structure versatility of most modern systems (Harrington, 1981).

The potential use of GIS-assisted classification can be illustrated by the consideration of conventional photointerpretation keys. For example, topographic information can assist in the identification of pasture areas. Loelkes et al. (1983) indicate that cropland is generally not found in delineated fields having slopes greater than 10 percent. Thus if detailed topographic models are available in a GIS format, the overlay of an edge-enhanced space image should reveal areas of delineated fields on slopes too steep for cultivation. If it is known that livestock are present in this area, then these areas can reasonably be inferred to be pasture.

A good demonstration of the GIS approach to arid land vegetation classification is found in Yool et al. (1984). This study emphasizes that basic vegetation type and density can be determined from orbital imagery but for a more detailed picture of local conditions it is necessary to incorporate ancillary data in a GIS based approach to classification. Slope and sun aspect information were found to be particularly important to obtain higher accuracy in the classification of percent live/dead standing foliage and percent of total vegetation coverage. A useful and basic stratification of vegetative cover types for an arid site was found by creating a texture image band from the multispectral bands. This texture image was generated by passing a 3 x 3 window over the vegetation sensitive MSS band 5. The standard deviation of the data within the window was written to the GIS texture file. There are several forms of texture-based image segmentations that operate in a similar fashion (Rosenfeld, 1984).

While image classification in a GIS format is potentially much more reliable than pixel spectral value derived classifications, this type of automated processing does not fully emulate the mental processes of a skilled image interpreter. A GIS-based classifier is analogous to placing a series of maps in addition to the image in front of the interpreter. The maps are of great assistance, but still do not supply the complete knowledge base utilized by the skilled photointerpreter.

A step beyond GIS-assisted classification is the employment of an

artificial intelligence (AI) or expert system to achieve classification accuracy equal to or exceeding that performed by human experts. GIS systems are operational at the present time but artificial intelligence image analysis systems are still in the research phase. It has proven very difficult to model human decision making processes for use in an automated classification system. The causes of this fact are complex, and cannot be dealt with in significant detail in this report. However, we can examine various inputs and decision processes used by the skilled photointerpreter and tentatively show what additional skills an artificially intelligent machine classification system must use in order to fully emulate the human expert.

Two immediately noticable characteristics of manual photointerpretation methods of crop discrimination are that they are fundamentally multitemporal and ancillary data are incorporated. Any attempt in automating crop identification through artificial intelligence techniques must utilize these types of information in the classification process. In addition, any AI application must utilize feature shape and textural information because these are very important keys in manual photointerpretation (Avery, 1985). Currently, the numerical analysis of pixel specific spectral data is achieved via a wide variety of methods; unfortunately, the analysis of texture and shape information is not nearly so advanced. At the present time, there is not even a widely accepted measure of either of these two image feature attributes.

A major problem also exists with the modeling of human decision making processes. AI specialists have recognized that humans tend to reason on a hierarchical, or sequentially logical basis, while computers generally operate on what might be called a simultaneous basis; that is, a single list is considered and the object in question is classified according to what category fits best. The advantage of human processing is the ability to freely go up and down the hierarchical decision tree as hypotheses are tested and rejected; computers traditionally have a difficult time doing this. An illustration of this can be seen in the logic used in conventional GIS analytical mapping operations.

The Boolean logic used in GIS operations is quite unlike the probablistic thinking exercised by humans. Humans are able to follow a long decision tree process based upon additive probabilities. In this process a great many different kinds of decision input data are used. In image analysis, some of these inputs (or interpretation keys) are absolute identifiers, while others are more or less reliable indicators about which other keys should be sought for confirmatory evidence. In contrast, most computer programs treat all keys as equal; in addition, either a condition is absolutely true or it is not. This Boolean logic is an incomplete model of human probablistic decision making processes. It is extremely important for a programmer attempting to automate pattern/texture based feature recognition to recognize the different levels of clues that drive the

decision making process. Unfortunately, the theoretical structure of this process tends to be difficult to ascertain because it is approached in the literature many different ways, depending upon the application. For image analysis of the earth's surface, the Department of Defense Interservice Committee on Photointerpretation Keys and Techniques has done extensive work on classifying keys; an excellent review of this work as applied to vegetation recognition can be found in Williams (1984).

One classification strategy that has used a probabalistic logical structure is the use of a priori information. The basis of a priori classification is that if an area has had under cultivation in the past 60 percent crop A, 30 percent crop B, and 10 percent other crops, then this information is integrated with the classification rule. Usually, these probabilities are used to assist the classifier in deciding which category to place pixels that are not clearly identified by their reflectance alone.

A priori data were used in a classifier for a CITARS crop identification effort. Although it did not prove to be significantly useful for that effort (Myers et al., 1983), its use is still advocated. The failure of historical a priori data to improve crop classification accuracy in the CITARS evaluation was thought to have been caused by the mismatching of the statistical sampling units on the imagery and the crop reporting

districts. A difficulty frequently encountered in a priori classification strategies is the exact structure of the association between the a priori data and areal units.

A good example of the potential use of a priori information to aid classification can be seen in Indonesia. Statistically, 60 percent of all land under cultivation in this country is wetland rice (Konijnenburg and Irsyam, 1986). Therefore if a field is identified from an image it can be assigned a probable classification of wetland rice even prior to any numerical spectral analysis. If multitemporal imagery is available for the site, the certainty of identification can increase greatly because wetland rice progresses through a very identifiable phenologic progression that is summarized well by Konijnenburg and Irsyam (1986). Two very different types of clues (one image derived, one non image derived) can be combined logically to provide near certain identification in a relatively poorly mapped area of the world.

If past production figures are not available or judged to be unreliable for the purposes of a priori classification, it may be possible to estimate a priori probabilities from regional food supply figures. Although this approach was not found in the literature, a logical justification for it may be constructed rather easily. A benefit of this approach is that this type of tabular statistical data are available for much of the world because of the current international concern with food shortages in third world countries (USDA 1981, 1985). It is these same

areas where we expect to find a shortage of good agricultural statistics to aid in a priori image classification.

In third world countries food import and redistribution is usually marginal, and people generally eat what they can grow nearby. If the residents of a particular region primarily eat taro (a root crop) during much of the year, and if it is also known that significant crop import or export does not exist, then it is a logical inference that small fields surrounding villages in this region are most likely taro fields.

The above example is relatively simplistic; as mentioned earlier, a more robust model is probably needed that can incorporate land cover image data, land use statistics, crop and livestock production, climate, and other types of data as needed. Models of this sort have been developed by geographers working on regional studies; good examples may be found for India, Russia, and England in Bayliss-Smith (1983). Image data have not been integrated with most of these models and they have not been implemented on computers. However, if these tasks can be undertaken, and valid data structures for decision making can be implemented, there is a good chance that the resultant analytical model may be versatile enough to classify agricultural land accurately worldwide.

Locating areas of crop production can be generally accomplished quite easily with visual analysis of remotely sensed data

primarily by looking at field patterns. Automating this process could be attempted but it is questionable if it could be accomplished more reliably than by a trained analyst. Specific crop identification by automated processing is a very difficult problem, particularly in areas of small field sizes and complex cropping practices and areas of limited ancillary data or ground truth accessibility.

Several possible processing strategies for improved crop identifications have been presented in this section. The most useful strategies are those incorporating ancillary data such as a priori crop types and acreages, crop calenders and GIS construction.

REFERENCES

Anderson, J.R., E.E. Hardy, J.T. Roach, R.E. Witmer, 1976. A Land Use and Land Cover Classification System for Use With Remotely Sensed Data, USGS Professional Paper 964.

Avery, 1985. The Interpretation of Air Photographs, 4th ed., Burgess.

Bayliss-Smith, T.P., 1983. The Ecology of Agricultural Systems, Cambridge University Press.

Belward, A.S., J.C. Taylor, 1986. The Use of Multitemporal Landsat Data for Improving Crop Mapping Accuracy, Proceedings of the 7th International Symposium, ISPRS, pp. 381.

Burns, G.S., A.T. Joyce, 1981. Evaluation of Land Cover Change Detection Techniques Using Landsat MSS Data, Proceedings of the Pecora VII Symposium, pp. 252-260.

Cithar, J., F.J. Ahern, M. Bernier, K.P. Thomson, 1985. Thematic

Mapper Evaluation for Agriculture and Forestry in Canada, Technical Papers of the 1985 ACSM-ASPRS Fall Convention, pp. 902-913.

Crist, E.P., 1984. Comparison of Coincident Landsat-4 MSS and TM Data Over an Agricultural Region, Technical Papers of the 50th Annual Meeting, American Society of Photogrammetry, pp. 508-517.

DeGloria, S., A.S. Benson, R.N. Colwell, 1983. Evaluation of Landsat-4 Image Quality for the Interpretation of Vegetation Cover Proceedings of the Pecora 8 Symposium, pp. 147-161.

DeSachy, J., S. Castan, G. Fisse, 1986. Introduction of Thematician Knowledge in Remote Sensing Imagery Interpretation, Proceedings of a Symposium of the International Society for Photogrammetry and Remote Sensing, ISPRS, pp. 418-429.

East, W.G. 1965. The Geography Behind History, W.W. Norton Co..

Ezra, C.E., L.R. Tinney, R.D. Jackson, 1984. Considerations for Implementing Vegetation Indices For Agricultural Applications, Technical Papers of the 50th Annual Meeting, American Society of Photogrammetry, pp. 526-534.

Gillespie, D.A., D.L. Civco, W.C. Kennard, 1986. Identification of Forest and Agricultural Edges using Thematic Mapper Data: Preliminary Results, Technical Papers of the 1986 ACSM-ASPRS Convention, Vol. 5, pp. 279-289.

Good, K., 1986. Verbal communication.

Haack, B.N., 1986. Verbal communication.

Haas, R.H., F.A. Waltz, 1983. Evaluation of Thematic Mapper Data for Natural Resource Assessment, Proceedings of the Pecora 8 Symposium, pp. 122-135.

Harrington, J.A., 1981. The Effects of Seasonal Differences in Climatic Conditions on Landsat Spectral Signatures and Associated Land Cover Classifications, Proceedings of the Pecora VII Symposium, pp. 262-267.

Henderson, L., 1983. Agricultural Applications of TM Data,

Proceedings of the Pecora 8 Symposium, pp. 134-146.

Howes, D.W., 1984. Crop Phenology Variance and the Accuracy of Landsat Tropical Savanna Cropland Inventories, Technical Papers of the 50th Annual Meeting, American Society of Photogrammetry, pp. 414-424.

Huete, A.R., D.F. Post, R.D. Jackson, 1984. Soil Spectral Effects on 4-space Vegetation Discrimination, Remote Sensing of the Environment, 1984.

Jensen, J., 1986. Introductory Digital Image Processing, Prentice Hall.

Klumph, S.G., B.W. Adams, 1985. The Use of Landsat "Rangeland Enhancements" to Monitor Public Rangelands in Southern Alberta, Proceedings of the Pecora 10 Symposium, pp. 109-113.

Konijnenburg, R.V., M. Irsyam, 1986. Monitoring of Renewable Resources in Equatorial Countries, Proceedings of the 7th International Symposium, ISPRS, pp. 335-340.

Lo, H.C., F.L. Scarpace, T.M. Lillesand, 1984. Multitemporal Analysis of Landsat Data for Agricultural Land Use/Land Cover Pattern Analysis, Technical Papers of the 50th Annual Meeting, American Society of Photogrammetry, pp. 288-302.

Loelkes, G.L., G.E. Howard, E.L. Schwertz, P.D. Lampert, S.W. Miller, 1983. Land Use/Land Cover and Environmental Photointerpretation Keys, U.S.G.S. Bulletin No. 1600.

McCoy, R.M., 1981. Models in Remote Sensing: An Approach to Mapping Vegetation in Arid Lands, Proceedings of the Pecora VII Symposium, pp. 427-441.

Menenti, M., S. Azzali, D. Collado, S. Leguizamon, 1986. Multitemporal Analysis of Landsat Multispectral Scanner (MSS) and Thematic Mapper (TM) data to Map Crops in the Po Valley (Italy) and in Mendoza (Argentina), Proceedings of the 7th International Symposium, ISPRS, pp. 293-299.

Merchant, J.W., E.A. Roth, 1981. Inventory and Evaluation of Rangeland in the Cimarron National Grassland, Kansas, Proceedings of the Pecora VII Symposium, pp. 104-113.

Merchant, J.W., 1981. Employing Landsat MSS Data in Land Use Mapping: Observations and Considerations, Proceedings of the Pecora VII Symposium, pp. 71-91.

Miller, L.D., Y.K. Yang, T. Cheng, M. Unverferth, 1985. Assessing Dynamic Forage Conditions in Individual Ranch Pastures Using Thematic Mapper Imagery and an IBM Personal Computer, Proceedings of the Pecora 10 Symposium, pp. 179-188.

Mueller, P.W., D.F. Lozano-Garcia, R.M. Hoffer, 1985. Interpretation of Forest Cover on Microwave and Optical Satellite Imagery, Proceedings of the Pecora 10 Symposium, pp. 578-592.

Myers, V.I., Bauer M.E., Gausman, H.W., Hart, W.G., Heilman, J.L. MacDonald, R.B., Park, A.B., Ryerson, R.A., Schmugge, T.J. Westin, F.C., 1983. Remote Sensing Applications in Agriculture, in the Manual of Remote Sensing, American Society of Photogrammetry.

NASA, AGRISTARS FY 1981, 1982, 1983 Research Reports.

National Academy of Sciences, 1977. Resource Sensing from Space: Prospects for Developing Countries.

O'Malley, J.R, 1983. Application of Remote Sensing in the Analysis of Rural Cultural Landscape, in Introduction to Remote Sensing of the Environment, 2d ed., B.J. Richason, editor, Kendall-Hunt.

Pitts, D.E., R. Bizzell, K. Henderson, D. Thompson, C. Sorenson, D. Carnes, 1983. Agricultural Applications of TM Data, Proceedings of the Pecora 8 Symposium, pp. 134-146.

Riechert, P. 1984. Recent Developments and Trends of Relevance to Multi-Level Remote Sensing, Proceedings of the ESCAP/NRMC Regional Conference on Multi-Level Remote Sensing for Forestry Application, pp. 219-231.

Richards, J.A., 1984. Thematic Mapping from Multitemporal Image Data Using the Principal Components Transformation, Remote Sensing of the Environment, 16:35-46.

Ripple, R.J., 1986. Phenological Effects on Grass Canopy/Spectral

Relationships, Technical Papers of the 1986 American Society of Photogrammetry-ACSM Convention, Vol. 5, pp. 69-79.

Robinove, C.J., 1979. Integrated Terrain Mapping With Digital Landsat Images in Queensland, Australia, USGS Professional Paper No. 1102.

Rosenfeld, A., 1984. Image Analysis, in Digital Image Processing Techniques, M.P. Ekstrom, ed., 1984, Academic Press.

Satterwhite, M.B., 1984. Discriminating Vegetation and Soils Using Landsat MSS and Thematic Mapper Bands and Band Ratios, Technical Papers of the 50th Annual Meeting, American Society of Photogrammetry, pp. 479-490.

Smith, G.S., 1986. Techniques for Deriving Land Use Information From Landsat Data through the Use of a Geographic Information System, Technical Papers of the 1986 ACSM-ASPRS Annual Convention, Vol.5, pp. 243-249.

Troiler, L.J., W.R. Phillipson, W.D. Philpot, 1986. Landsat Thematic Mapper Images for Hydrologic Land Use and Cover, Technical Papers of the American Society of Photogrammetry-ACSM Convention, Vol. 5, pp. 269-278.

U.S. Dept. of Agriculture, 1981. World Indices of Agricultural and Food Production, Econ. Research Service Statistical Bulletin No. 669.

U.S. Dept of Agriculture Economic Research Service, 1985. World Food Needs and Availabilities.

Williams, D.L., 1984. Numerical Taxonomic Methods for Construction of Image Interpretation Keys, Technical Papers of the 50th Annual Meeting, American Society of Photogrammetry, pp. 231-242.

Wilson, C.L., F.J. Thomson, 1981. Integration and Manipulation of Remotely Sensed and Other Data in a Geographic Information System, Proceedings of the Pecora VII Symposium, pp. 303-317.

Yath, Y.A., H.A. van Gils, 1986. Multitemporal Landsat for Land Unit Mapping on the Project Scale of the Sudd-floodplain, Southern Sudan, Proceedings of the 7th International Symposium ISPPS, p. 531.

Yool, S.R., D.W. Eckhardt, M.J. Consentino, J.E. Estes, 1984. A Geographic Information System Approach to Quantitative Assessment of Wildland Fuels, Technical Papers of the 49th Annual Convention, American Society of Photogrammetry, pp. 792-801.

4.10 FOREST

The brush, forest, height and density of vegetation and orchard conditions in Table 1 are all related from a remote sensing, and particularly from an automated processing, perspective. The separation of these conditions is difficult because of frequent similarities in spectral and phenological characteristics. In addition, there are definitional problems such as between brush and forest.

These conditions can best be differentiated by sufficient climatic, vegetative and land cover ancillary information because they frequently do not conexist. Under natural environmental conditions, brush is not associated with forest except for localized areas of forest succession. Brush is generally confined to semiarid environments such as the chapparal of mediterranean climates. Similarly, orchards are found in limited areas often associated with other agricultural activities.

Orchards generally cannot easily be delineated from forests by automated processing unless spectrally unique or by the incorporation of texture measures. In this study orchards are included as another crop type in section 4.9 with other available food sources.

Brush is extremely difficult to separate from forest with spaceborne remote sensing and also definitionally. Where brush is successional to forest, the lack of shadows and lesser crown

closure of brush may provide spectral differences. Because brush and forest seldom are found in the same locations naturally, ancillary data are frequently necessary to locate areas of possible brush. For these reasons, brush is not considered separately in this study.

There are many remote sensing methods to evaluate vegetation density as indicated by biomass, leaf area index and green vegetative indices (GVI). These measures are presented in several sections of this study (see particulary 4.9 on agriculture). Relative biomass is very much controlled by vegetative phenology, moisture availability and other vegetative controlling factors. An interest of the Air Force is vegetative height which cannot be reliably determined from existing automated processing techniques of spaceborne remotely sensed data. Biomass or GVI measures can be misleading. Young grasses can have a higher GVI than just emerging forest foliage. Height of vegetation can best be ascertained by the use of ancillary data to determine what natural or cultural vegetation may exist in a region of interest. This study will not additionally consider the height and density of vegetaion directly. This section is focused on forests.

As early as 1973 forests could be classified on MSS imagery into deciduous and coniferous with 80 percent accuracy (Heller et al, 1983). Accuracy has since risen for this relatively simple level of classification. Forest areas of significant size can

generally be identified from MSS, TM or SPOT imagery. As was the case in agricultural areas, the exact description of the forest is considerably more difficult, especially using low resolution MSS imagery in areas of complex vegetation. TM imagery provides a more useful product for forest characterization (Bradbury et al., 1985) and the integration of the SPOT monochrome 10 m resolution data with the multispectral mode 20 m data yields airphoto-like quality for the examination of very small areas (Cliche et al., 1985). While this latter technique is attactive, the merging of SPOT data is currently computationally complex because of different resampling algorithims for the visible and IR bands due to SPOT scanner problems.

Although many different forest conditions and characteristics have been analysed using satellite imagery, this report is interested in only a few of the variables discussed in the literature of the satellite remote sensing of forests. These variables are the basic type of tree (coniferous or deciduous), the density of the forest, and the amount of ground cover provided by the forest.

This latter quantity is crown closure. With 100 percent crown closure, no ground is visible between the trees, while at 25 percent crown closure, 75 percent of the pixel reflectance is from the ground between trees. Crown closure is a measure of horizontal tree density having great bearing upon aerial observation but little bearing upon the ease of ground traverse because the density of the trees is essentially measured at tree

top level. Some tree types (e.g., oak) can have a sparse understory, while many pines and cedars are very dense at ground level. At the present time it is impossible to discern the brushiness of the understory vegetation without much higher resolution or ancillary data that describes the basic character of the forest.

Some research has used crown closure as the basic classification parameter for forested lands. Heller et al. (1983) considered woodland to be areas of 25 to 60 percent crown closure and closed forest to be 60 to 100 percent crown closure. Pure tree stands are those where 70 percent of the crown closure consists of a single species or type of tree. This basis for classification is justified because crown closure of the forest is the dominant spectral reflectance characteristic of forests on vertical angle remotely sensed imagery. This conclusion is supported by many studies. For example, Klock et al. (1985) found crown closure as determined from MSS imagery to agree with ground truth 94 percent of the time. Classification into four equal classes of crown closure was used in a recent study in India and was found to be 90 percent accurate, even in mountainous terrain (Singh, 1986). A post classification smoothing filter also increased accuracy slightly by eliminating classification outliers. The use of such a filter is essentially incorporating contextual data in a very crude fashion because neighboring pixels have an influence over the classification of the pixel in question.

For any classification procedure, signature extraction is more important than the classification algorithm. Hoffer et al. (1979) tested several forest classification algorithims of MSS data of a forested site in Colorado. These algorithims included Gaussian maximum likelihood, minimum distance to cluster mean, and a hierarchical (layered) classifier. Virtually no difference was found between the classifier performances in this study. Accuracy for all three was around 93 percent for an Anderson (1976) level II classification, and around 76 percent for level III.

Error associated with classification is often caused by some degree of mixing in the forest population. Often, this mixing is of different types of trees that coexist in the same habitat. If mixing is suspected in the tree population, and this mixing is important to quantify, then unsupervised classification is recommended because small changes in the forest population mixture will be evident as spectrally distinct clusters. A study of South Carolina forests indicated that while supervised classification of sites with poor prior ground truth gave the analyst more control over the classification, unsupervised classification yielded a higher overall accuracy in characterizing the forest (Kelton et al., 1985). Forest/ nonforest discrimination was achieved with 97 percent accuracy in the unsupervised classification procedure, while the supervised procedure yielded 93 percent accuracy. However, excessive numbers of clusters may indicate tree diversity but still not be readily identifiable as specific species. Both classification

procedures essentially failed at an Anderson Level III classification.

Khorram and Katibah (1981) performed a comparison between two forms of unsupervised classification for the same test site in California. Essentially the question addressed was, should the training sites be statistically analysed as part of a single population of pixel reflectance values, or should each training site be considered independently. In practice, this makes considerable difference in the number of clusters generated from the unsupervised clustering procedure. If forty clusters are specified to the algorithm, then in the first case, there will be forty clusters while the second case will generate forty clusters for each training site. Khorram and Katibah reported that the results of the second case were superior because small vegetation differences are contained in the additional clusters. An ensuing difficulty is that good ground truth is required to assign meaningful labels to the great numbers of generated clusters.

The use of unsupervised classification for forest characterization is also advocated by other studies. In an area of diverse forest types in Florida, unsupervised classification was applied to TM data. While some extraneous classes were generated, most classes reflect actual differences in the forest (Echols et al., 1986). TM bands 2,3,5, and 7 were the most useful data for the unsupervised classification procedure. Bands 4 and 5 were useful in discriminating between pines and hardwoods

in river bottom areas.

Other reports recommend similar band combinations for the analysis of forests using satellite digital data. Troiler, et al. (1986) recommend using all visible bands and band 7 for digital analysis, or the 3,5,4 composite image for visual interpretation of forests.

The use of a texture image as another spectral band is recommended by Consentino and Estes (1981) in their seminal GIS fire fuels model of Southern California. The standard deviation of a 3 by 3 pixel window passed over the band 5 image data was written to the texture channel. An identical procedure was used by Strahler (1983) in another study of forests. In the latter study, the resulting texture image was smoothed by requiring that image-derived texture pixels exist in clusters no smaller than 6 pixels, or else be merged with the largest contiguous cluster. The smoothed pixels usually reflect actual differences on the ground and are only smoothed to create a better regional forest map.

Strahler considers texture to be an orthagonal data set to the spectral image data because the texture band is poorly correlated with any of the spectral bands. This indicates that additional data are present in the texture band that are not obvious in the spectral data. High texture values are reported to correspond to forest edges, intermediate values are found in young tree stands with gaps in the crown closure, and low texture values are found

in old stands with complete canopy coverage of the ground. Strahler also advocates the use of unsupervised clustering and the retention of many clusters for later analyst labeling because these clusters usually represent real differences on the ground.

A highly automated procedure for examining forest succession was used by Merola (1984). Good results were reported in this study using MSS data covering a structurally complex forest in Utah. Principal components analysis was used to reduce data dimensionality by eliminating cross correlation between spectral bands, followed by cluster analysis to generate unsupervised classes. Discriminant analysis was then used to examine the statistical content of the clusters. Discriminant analysis was also used by Howarth and Wickware (1983) and Tom and Miller (1984) to examine statistical context of clusters generated in an unsupervised classification. An advantage of Merloa's methodology is that all of these numerical analysis procedures can be invoked using common statistical packages; SPSS was used in this case.

Analysis of the two principal components of the MSS shows that the first is essentially the visible information, while the second is the infrared information. It is also reported by Merola (1984) that this procedure is quite good for identifying landscape units that have characteristic vegetation associations. From the view of classical geographical analysis this is important. A landscape (or regional) unit should be identified

prior to examination of its specific attributes. This is essentially a top-down approach. However, many studies in remote sensing approach terrain analysis in a bottom-up fashion, taking great effort to examine individual attributes when a clear idea of the terrain as a whole can answer many specific questions without time consuming numerical image analysis. If a bottom up study is required, then it may be advisable to apply canonical analysis to determine the reliability of the lower hierarchical classes which are the components of the landscape (Menon and Hopkins, 1984).

Other current research indicates that complex numerical techniques of data handling and transformation are not required to classify forests accurately. Principal components was found to be of little use in forest analysis because it is not suited for contrast enhancement among dense vegetation (Chiao et al., 1986; Epp and Reed, 1986). This conclusion is supported by Dury et al. (1986). Ratios were not found suitable because slight albedo differences are suppressed. In the study by Dury et al., a mean value 3 by 3 smoothing filter enhanced later classification, justified by essentially the same logic as that used by Strahler. Dury et al. also advocated supervised and unsupervised classification procedures both be utilized in any forest study.

Radar has been used to examine forested areas; however, the consensus of research reviewed indicated that is it not as useful as multispectral scanner data. Campbell (1981) used K-band SLAR,

Seasat L-band SAR, and MSS imagery to visually classify land cover in southeastern Pennsylvania. MSS imagery were recommended as best for the accurate (90 percent) classification of forest. Similarly, C-band radar was found by Leckie (1983) to be of poor use in forest identification, although he does report that forest generally has a rougher texture than cleared land or brush on the radar image.

Hoffer et al. (1985) conducted a comprehensive study using multiband (X anf L) and multipolarization data over forested areas. This study illustrates the classic diffficulty of interpreting radar data without ground truth. X-HH imagery was found to show conifers dark and deciduous light, while the pattern revealed in X-HV is exactly the reverse. The report concludes that X-HH has higher tonal contrast than any other band/polarization tested, but L band is useful for its ability to detect water under tree cover.

Radar data may be useful in defining the edge of the forest, particularly where the edge is oriented parallel and facing the sensor. Low look angle (28 degrees) SIR-B imagery was found to show these type of edges better than high angle data of the same area in Florida (Mueller et al., 1985). Texture measures applied to TM imagery have also been used for this purpose (Gillespie et al., 1986). Classification of the different types of edges resulting from the TM image edge extraction process led to computational complications. Radar appears to be more suitable

for edge information, especially if multiple look directions are available. Radar data may be a useful asset in image segmentation prior to more detailed forest characterization.

Segmentation of forest/nonforest areas prior to detailed forest characterization is recommended by many researchers. In a study of Pennsylvania forest resources, good segmentation was achieved using a Baysian maximum likelihood classifier (Russo and Stauffer, 1983). In a similar study of habitats in Louisiana, Bands 5 and 7 were useful to segment the study area manually. Band 7 was most useful for general vegetation regionalization but band 5 was especially useful in delineating regional boundaries caused by land use change (Evans and Burns, 1983).

Some studies recommend that classification take place in a sequential decision tree, so that not all of the image pixels are classified at the same stage. This approach is often called "layered", or hierarchical classification. It is an extension of a masking procedure where only the pixels classified as forest are used in the second, more detailed classification. The logical extension of this type of approach leads to lengthy decision tree structures where some pixels are identified at each step and eliminated from further consideration. This approach is advocated strongly in Loranzo-Garcia and Hoffer (1985). A primary advantage of this procedure is that different classification algorithims and different band combinations can be used at each stage. These can be target specific for particular classes. Loranzo-Garcia reported 98 percent accuracy in

forest/nonforest classification and 95 percent accuracy in deciduous/coniferous classification using multitemporal MSS imagery. This approach has a weakness in that extensive time is usually required to construct the decision tree and extensive CPU time is required to run the various algorithims used at different stages of the process. Hierarchical decision tree structures are often found in AI applications because they are thought to more closely emulate human decision processes than "one rule" classifiers.

Multitemporal data are clearly useful when making deciduous/coniferous classifications. Early spring data are recommended by Gillespie et al. (1986). Data for coniferous vegetation has often been obtained in the winter while deciduous trees are usually imaged in the leaf-on condition. Deciduous/coniferous differentiation can be readily performed using imagery with moderate to heavy ground snow cover. Hudson and Lusch (1985) reported in a study of Michigan that level slicing can be employed to visually separate forest types in an area covered by 21cm of snow. The conifers are very dark in all visual bands. The mass of branches and trunks caused the deciduous areas to be somewhat dark compared to the extremely high digital values of everything else in the scene.

In areas of mixed timber types, a GIS approach using multitemporal and slope data layers was found to significantly assist accurate characterization of the forest (Stibig and

Schardt, 1996). Sadler and Joyce (1985) claim that multisensor data are usually needed in any heavily vegetated area because the leaf reflectance in these areas can reach a saturation point and mask out differences in the vegetative canopy. It is also indicated in this report that the near-infrared/red band ratio of TM simulator data is useful for differentiating old, mature, and regenerated forests. If this is true, inferences can be made about the level of brush and availability of clearings in the forest of interest. To do this, ancillary data will be required to characterize these different ages of forests. In most areas, there are very definite differences between these types of forests. For example, North American forests tend to be very brushy and thick when they are young or regenerating, while older forests are relatively clear below a closed canopy due to the lack of sunlight. On the other hand, tropical rainforests have a thick understory despite full development of the canopy. The density of the understory can be a direct result of the availability of water. The use of topographic information in a GIS approach to classification would be very useful to discriminate lowland swamps and river valleys where this may occur.

Although gross characterization of forests is readily performed with MSS data, a more detailed portrait of a local landscape will emerge if higher resolution SPOT or TM data is utilized. This is particularly true in diverse landscapes. An analysis of Northern Florida using TM data and a maximum likelihood classifier resulted in classes that were more numerous and more useful to

ground investigators than those produced by an identical procedure using MSS data (Echols et al., 1986). Confusion was high between pine plantations and hardwood bearing wetlands because the characteristically low spectral reflectance of the conifers was similar to that of the water/deciduous mixture.

Generally, forest can be delineated using traditional automated processing techniques. Multitemporal, texture, hierarchical classifiers and ancillary data can also increase accuracies in specific situations and contribute to improved recognition of forest subcategories.

REFERENCES

Anderson, J.R., E.E. Hardy, J.T. Roach, R.E. Wittmer, 1976. A Land Use and Land Cover Classification System for Use With Remotely Sensed Data, USGS Professional Paper No. 964.

Bradbury, P.A., R.H. Haines-Young, P.H. Mather, A. Macdonald, 1985. The Use of Remotely Sensed Data for Landscape Classification in Wales: The Status of Woodlands in the Landscape. Proceedings of the International Conference of the Remote Sensing Society and the Center for Earth Resources Management, pp. 401-411.

Campbell, J.B., 1981. Comparisons of Land Cover Classifications from Selected Remote Sensing Systems, Technical Papers of the 47th Annual Meeting, American Society of Photogrammetry, pp. 618-626.

Chiao, K., Y. Chen, H. Shieh, 1986. Digital Processing of Airborne MSS Data for Forest Cover Type Classification, Proceedings of the 7th International Symposium ISPRS, pp. 15-18.

Cliche, G., F. Bonn, P. Teillet, 1985. Integration of the SPOT Panchromatic Channel into its Multispectral Mode for Image

Sharpness Enhancement, Photogrammetric Engineering and Remote Sensing, vol. 51, No. 3.

Cosentino, M.J., J.E. Estes, 1981. Use of Landsat Data to Develop A Fuels Database for a Wildland Fire Simulation Model, Proceedings of the Pecora VII Symposium, pp. 590-599.

Dury, S.J., W.G. Collins, P.D. Hedges, 1986. The Use of SPOT Simulation Data in Forestry Mapping, Proceedings of 7th International Symposium, ISPRS, pp. 425-428.

Echols, P.F., B.E. Ruth, D.M. Jordan, J.D. Degner, 1986. Landsat Thematic Mapper Data Within the Suwannee River Basin, Technical Papers of the 1986 ACSM-ASPRS Annual Convention, Vol. 5, pp. 162-171.

Epp, H., R. Reed, 1986. Spruce Budworm Infestation Detection Using an Airborne Pushbroom Scanner and Thematic Mapper Data, Proceedings of the 7th International Symposium ISPRS Commission VII, pp. 429-434.

Evans, D.L., P.Y. Burns, 1983. Landsat Imagery for the Interpretation of Louisiana Forest Habitat Regions, Technical Papers of the 49th Annual Meeting, American Society of Photogrammetry, pp. 33-42.

Gillespie, D.A., D.L. Civco, W.C. Kennard, 1986. Identification of Forest and Agricultural Edges Using Landsat Thematic Mapper Data: Preliminary Results, Technical Papers of the 1986 ACSM-ASPPS Annual Convention, Vol. 5, pp. 279-289.

Heller, R.C., J.J. Ulliman, R.C. Aldrich, G. Hildebrandt, R.M. Hoffer, D.T. Lauer, L. Sayn-Witgenstein, D.A. Stellingwerf, 1983, Forest Resource Assessments, in the Manual of Remote Sensing, American Society of Photogrammetry.

Hoffer, R.M., M.D. Fleming, L.A. Bartolucci, R.F. Nelson, 1979. Digital Processing of Landsat MSS and Topographic Data to Improve Capabilities For Computerized Mapping of Forest Cover Types, LARS Technical Report, The Laboratory for Applied Remote Sensing, Purdue University.

Hoffer, R.M., S.E. Davidson, P.W. Mueller, D.F. Lozano-Garcia, 1985. Comparison of X and L Band Radar Data for Discriminating Forest Types, Proceedings of the Pecora 10 Symposium, pp. 439-440.

Howarth, P.J., C.W. Wickware, 1983. Multivariate Analysis Techniques for Land Cover Classification Using Multispectral Scanner Data, 8th Canadian Symposium on Remote Sensing, pp. 463-473.

Hudson, W.D., D.P. Lusch, 1985. Leaf-Off Remotely Sensed Data as a Source of Forest Resource Information, Proceedings of the Pecora 10 Symposium, pp. 68-77.

Kelton, K., W.A. Shain, L. Nix, 1985. Supervised and Unsupervised Methods of Spectral Classification of Vegetative Types in the South Carolina Coastal Plain, Technical Papers of the 1985 ACSM-ASP Fall Convention, pp. 440-449.

Khorram, S., E.F. Katibah, 1981. Use of Landsat Multispectral Scanner Data in Vegetation Mapping of a Forested Area, Technical Papers of the 47th Annual Meeting, American Society of Photogrammetry, pp. 383-392.

Klock, G.O., P.Gum, L.E. Jordan, 1985. Developing a Resource Management Data Base for the Okanogan National Forest from Multispectral Imagery and the Use of GIS, Proceedings of the Pecora 10 Symposium, pp. 144-152.

Leckie, D.G., 1983. Preliminary Results of an Examination of C-Band Synthetic Aperture Radar for Forestry Applications, Proceedings of the 8th Canadian Symposium on Remote Sensing, pp. 151-164.

Lozanzo-Garcia, D.F., R.H. Hoffer, 1985. Hierarchical Classification of Multitemporal/multispectral Scanner Data, Proceedings of the 11th International Symposium on Machine Processing of Remotely Sensed Data, pp. 162-169.

Menon, S., P.F. Hopkins, 1984. Investigation of Spectral Separability and of the use of Canonical Analysis for Forest Type Mapping In Central New York, Technical Papers of the 50th Annual Meeting, American Society of Photogrammetry, pp. 553-561.

Merola, J.A., 1984. Contextual Analysis of Landsat Spectral Signatures, Technical Papers of the 50th Annual Meeting, American Society of Photogrammetry, pp. 278-287.

Mueller, P.W., D.F. Lozano-Garcia, R.M. Hoffer, 1985.

Interpretation of Forest Cover on Microwave and Optical Satellite Imagery, Proceedings of the Pecora 10 Symposium, pp. 578-592.

Russo, S.A., M.L. Stauffer, 1983. The Statewide Forest Classification of Pennsylvania using Landsat MSS Data, Technical Papers of the 49th Annual Meeting, American Society of Photogrammetry, pp. 43-52.

Sadler, S.A., A.T. Joyce, R.B. Waide, W.T. Lawrence, 1985. Monitoring Tropical Forests from Satellite and Aircraft Platforms: Some Limitations and New Approaches, Proceedings of the Pecora 10 Symposium, pp. 473-482.

Sadler, S.A., A.T. Joyce, 1985. Global Tropical Forest Monitoring, Proceedings of the International Conference of the Remote Sensing Society and the Center for Earth Resources Management, pp. 41-50.

Singh, A., 1986. Tropical Forest Cover Classification using Landsat Data in Northeastern India, Proceedings of the 7th International Symposium ISPRS Commission VII, pp. 513-516.

Stibig, H.J., M. Schardt, 1986. Digital Classification of Forested Areas using Simulated TM and SPOT and Landsat 5/TM Data, Proceedings of the 7th International Symposium ISPRS, Commission VII, pp. 79-85.

Strahler, A.H., 1983. Timber Inventory Using Landsat, 8th Canadian Symposium on Remote Sensing, pp. 665-673.

Tom, C.H., L.D. Miller, 1984. An Automated Land Use Mapping Comparison of the Bayesian Maximum-Likelihood and Linear Discriminant Analysis Algorithms, Photogrammetric Engineering and Remote Sensing, Vol. 50(2), pp. 193-207.

Troiler, L.J., W.R. Phillipson, W.D. Philpot, 1986. Landsat Thematic Mapper Images for Hydrologic Land Use and Cover, Technical Papers of the 1986 ACSM-ASPRS Annual Convention, Vol. 5, pp. 269-278.

4.11 WILDLIFE HABITAT

With a maximum resolution of 10 meters available from civilian

remote sensing imagery, it is clearly impossible to identify or track any individual animals from orbital platforms. However, satellite remote sensing imagery has been used in a number of studies to evaluate the quality of wildlife habitat if ancillary information indicates wildlife are present in the scene. Also, a number of studies using aerial photography for habitat evaluation present techniques that can be adapted for use with satellite imagery.

Prior to discussion of specific strategies used for habitat evaluation, it is useful to consider some basic properties of habitats. Possibly the most fundamental property is that habitats are not absolute; animals will tend to seek locations that have the best conditions for them in a local area (Mead et al., 1981). Identical ground conditions at pixel locations in two different areas that both contain the same wildlife types will not necessarily dictate that the wildlife is present at both sites. Deer provide a good illustration of this point. These animals will generally avoid human habitation whenever possible. In areas of extensive human settlement the deer have little choice but to inhabit relatively small patches of woodland because this is the best habitat available. In areas of less human settlement, there is a much wider range of habitats available, and deer consequently will tend to be in more extensive woodlands at some distance from settlements.

The implication of this for image processing is that habitats

cannot be identified from a specific spectral reflectance. Surface conditions as outlined in other sections of this paper can be evaluated for habitat optimality within a region, but this must always be done relative to what other conditions and combinations of conditions are available to the wildlife elsewhere in the area.

Another important principle in wildlife habitat evaluation is that animals, and particularly mammals, usually need different types of land cover for different purposes. Woodlands are good for shelter, while clearings and agricultural fields are necessary for feeding. Animals tend to be populous near the intersection of different land cover types or ecotones (Mead et al., 1981). Image edge extraction and classification have been identified as important processes prior to habitat evaluation (Murray and Leckenby, 1985). Evans and Burns (1983) used TM band 5 for edge extraction because of its sensitivity to cultural boundaries. In particular, band 5 data delineated cleared fields from forest. This type of edge provides ideal conditions for many mammals because of the availability of open field forage in combination with woodland shelter.

Several aspects of habitat identification using remotely sensed data have been reported in the literature. Brooks (1985) and Carnegie et al. (1983) advocated that the image analyst attempting habitat identification should be knowledgeable about the subject. Many seemingly insignificant facts can be important in habitat location, and therefore a specialist is needed who can integrate

diverse types of information from many sources. In addition, the analyst will need a flexible image processing system so that different types of algorithms can be employed to conduct information inquiries of diverse types.

The land cover classification system must also be versatile and be adaptable to many different environments. Meyer-Arendt and Wicker (1981) found that neither the U.S. Fish and Wildlife Service wetlands classification or the U.S.G.S. land cover classification system were adequate for a detailed habitat mapping in Louisiana. Rather a hierarchical scheme was developed that allowed increasingly detailed information to be appended to the class type as required. Open water or upland forest needed very few modifiers while marsh classes were quite complex. The need for "fuzzy" or transitional classes is also outlined; many habitat boundaries are gradational instead of abrupt changes.

Because small climatic and vegetative differences are important in wildlife location, unsupervised classification is recommended. Supervised classification tends to obscure transitional and small ground cover differences. Often, regions that are thought to be relatively homogeneous prove to be very diverse. Mead et al. (1981) found that a study area in the Great Dismal Swamp contained 43 different canopy classes and 243 fairly distinct vegetative communities.

With these generalities in mind, remotely sensed imagery can

provide the analyst with a useful technique of rapidly ascertaining where significant numbers of native wildlife can most probably be found in a region of interest.

Treadwell et al. (1985) provided a list of important habitat evaluation parameters that can be evaluated using remote sensing imagery. Although this study reported on the use of ultralight aircraft for habitat evaluation, the parameter list is useful as a guideline to the construction of a quantitative evaluation procedure to identify optimal wildlife habitats.

Remote sensing imagery can be utilized to assist habitat evaluation in the following ways (adapted and abridged for satellite imagery from Treadwell et al.):

1) To develop definitions of habitat types based on landform, soil, and vegetation communities;

2) To determine the spatial distribution and juxtaposition of these habitat types;

3) To calculate indices of interspersion or proximity between types;

4) To perform areal measurements of habitat types;

5) To obtain varying degrees of floral information;

6) To obtain some data regarding the quality of forage and the location of seasonally early greening areas;

7) To determine the seasonal location of watering locations;

8) To recognize special habitat features associated with particular species.

In most habitat studies, a stratification process is employed. If animals are known to exist in a region, then satellite imagery can be used to determine where are the landscape conditions most favorable for the wildlife. For example, ducks favor small bodies of water like ponds and inlets which can be located by thresholding techniques applied to remotely sensed data. Exclusionary evidence is also utilized. Very little wildlife will be found in arid environments of little vegetation and distant from water locations.

This logical inference procedure is a parametric approach; that is, certain conditions are identified as desirable (or undesirable) wildlife habitats. The presence or absence of these parameters at a particular location (pixel) are used in an overlay GIS to determine the likelihood or suitability of the location for a specific wildlife type. A combination of certain parameters is identified as essential for the existence of wildlife in a particular location. Skaley (1990) provided an example of this methodology in his location of bird habitats using aerial photography. Certain topological features of forest cover were associated with specific species. The habitat of the species was then presumed to be located where these features were present, and the converse was presumed to be also true.

Poller (1978) located geese habitats by monitoring with satellite imagery the recession of snow cover. If snow cover was present in areas of known geese habitat, then the geese would not be

found there until a later date. Multitemporal MSS imagery for a several year span was used to monitor these northward-moving habitats. Multitemporal imagery is also useful in identifying seasonal habitat areas where wildlife concentrations are associated with initial vegetation greening providing food early in the spring (Treadwell et al., 1985).

A more complex and useful GIS analysis can be undertaken by introducing ranking of the parameters according to importance, and also using classes within each parameter. An index can then be calculated for each pixel that assesses the habitat optimality of that location. An example of this parameter ranking can be found in Dixon et al. (1983) where land cover classes are graded from most to least preferred by Canadian moose herds. Deciduous was more preferred that upland coniferous, which was in turn better than lowland coniferous. An example of classes within each parameter can be found in a study of elk habitat by Murray and Leckenby (1985). In this study, weighted distance from forage and cover was used to develop an index value for each pixel that reflects habitat suitability. Cover/forage ratios were also found to be a meaningful input to the habitat index value calculations. Some parameters such as road density are recognized to be of variable impact, and thus difficult to account for in numerical models.

Mead et al. (1981) detail the use of a computer program that calculated individual indexes for land cover class interspersion, juxtaposition, and an overall measure of spatial diversity. The

relative importance of each was thought to be dependent upon species and area. By calculating all of these indices individually, the model is potentially more useful for multiple species habitat evaluation without extensive recomputation.

GIS-based habitat models have been developed that can significantly assist in the location of optimal animal habitats. A major difficulty in implementing these models is the necessity of obtaining detailed ancillary data to create a model for globally diverse habitats and species. The weights applied to each parameter in the habitat index calculations are very dependent upon the region and the species (Mead et al., 1981). Remotely sensed data can be an important source for some of the information needed. These habitat models can indicate optimal wildlife habitats but not wildlife presence.

REFERENCES

Brooks, W.T., 1985. Implementation of an Integrated Resource Information System and Its Application in the Management of Fish and Wildlife Resources in Alaska, Proceedings Auto-Carto 7, pp. 46-51.

Carnegie, D.M., B.J. Schrumpf, D.A. Mouat, 1983. Rangeland Applications, in the Manual of Remote Sensing, American Society of Photogrammetry.

Dixon, R., L. Bowles, B. Knudsen, 1983. Moose Habitat Analysis in North-Central Manitoba from Landsat Data, 8th Canadian Symposium on Remote Sensing, pp. 623-629.

Evans, D.L., P.Y. Burns, 1983. Landsat Imagery for the Interpretation of Louisiana Forest Habitat Regions, Technical

Papers of the 49th Annual Meeting, American Society of Photogrammetry, pp.33-42.

Mead, R.A., T.L. Sharik, S.P. Prisley, J.T. Heinen, 1981. A Computerized Spatial Analysis System for Assessing Wildlife Habitat from Vegetation Maps, Technical Papers of the 47th Annual Meeting, American Society of Photogrammetry, pp. 212-220.

Meyer-Arendt, K.J., K.M. Wicker, 1981. Classification and Mapping Habitats within the Mississippi River Deltaic Plain Region, Proceedings of the Pecora VII Symposium, pp. 163-174.

Murray, R.J., D.A. Leckenby, 1985. Elk Habitat Evaluation Using Distance Mapped Landsat Data, Proceedings of the Pecora 10 Symposium, pp. 346-355.

Roller, N.E., 1978. Quantitative Evaluation of Deer Habitat, Proceedings of the 4th Annual Pecora Symposium, pp. 137-146.

Skaley, J.E., 1980. From Landforms to Avian Habitat - A Look at Topology, Technical Papers of the Fall Meeting, American Society of Photogrammetry, pp. RS-2-E1 to RS-2-E8.

Treadwell, B.D., P.L. Warren, S. Berwick, 1985. Emerging Technologies for the Assessment and Monitoring of Wildlife Habitat in Developing Countries, Proceedings of the Pecora 10 Symposium, pp. 362-379.

5.0

SUMMARY

This study has evaluated the ability to identify a set of surface conditions of interest to the Air Force using automated processing of primarily Landsat Thematic Mapper digital data. This evaluation had several restrictions imposed upon it. One of those restrictions was the emphasis on automated processing rather than image enhancement. A second restriction is the possibility of Air Force interest in virtually any surface area on the globe. It is much easier to develop region specific processing strategies than consider the possible variations of a single condition, such as wetlands, on a global basis. The necessity of considering areas of limited accessibility and ancillary information was an added restriction.

A brief, generalized summary of the results of the evaluation of the conditions of interest follows. These conditions are ordered as found in Table 1 which differs slightly from this document because some conditions were presented together.

SLOPE. The availability of digital terrain model data and the current availability of SPOT stereoscopic spaceborne data makes it unnecessary to attempt to obtain this information from TM data.

SURFACE ROUGHNESS. Generally the scale of surface roughness information needed is unavailable from TM or other current spaceborne data. Radar may be a more appropriate sensor.

STREAMS. Water can be easily identified with TM digital data.

Therefore, streams larger than the TM spatial resolution can be identified. Smaller streams may be located by secondary vegetative indicators or other ancillary data.

LAKES AND RESERVOIRS. These water features can easily be identified unless subpixel in size.

WETLANDS. This condition is highly variable and thus the ability to locate wetlands will vary spatially and temporally. Generally, reasonable processing strategies can be identified to locate wetlands. These strategies may be region specific. Multitemporal, multisensor and ancillary data strategies are among the most successful.

SNOW ACCUMULATION. Snow extent can be easily obtained. The use of AVHRR data may be advantageous because of the high temporal resolution. No operational techniques for determining snow depth have been identified, but promising approaches are available with models and other sensors.

BOUNDARY DEMARCATIONS. Edge enhancement techniques provide an image analysis procedure to locate possible areas of boundary demarcations. The limited spatial resolution of TM does not permit the determination of if walls, fences or hedgerows actually exist in these possible locations.

LOOSE SOIL. Loose soil can be defined in many different ways. Frequently loose soil is a function of large soil texture and is therefore considered in the sand section. Other loose soils may be considered as wetlands. Loose soil subject to saturation is difficult to locate only with TM data. These areas may be easier to locate within a GIS and with microwave sensors.

SAND. Sand, because of its high reflectivity, can be located quite reliably with automated processing of TM data.

COASTAL BEACHES. Assuming most coastal beaches contain sand in proximity to water, they can be located using the techniques for delineating sand and water.

PASTURE. Pasture is very difficult to locate accurately because it is a land use and not a land cover, and because of the multiplicity of conditions under which pasture occurs. Generally, land covers which are possible pasture locations can be segmented with TM data but the actual presence of livestock is only problematic.

MIXED CROPLAND. This condition can be defined in many ways and because of that was not considered separately. Agricultural areas can be determined via image enhancement but not easily by fully automated techniques.

BRUSH. Brush is definitionally and spectrally difficult to separate from forests. Brush is normally found in different climatic regions than forest and if this can be ascertained from ancillary climatic data, the same techniques for location may be applicable as used for forest.

FOREST. Forest areas can be spectrally delineated with TM data particularly with texture measures and multitemporal data sets. The differentiation of various forest communities and species types is more difficult.

HEIGHT AND DENSITY OF VEGETATION. There are many effective remote sensing measures for biomass estimation. These measures can be correlated with vegetative density but not height.

ORCHARDS. Orchards are similar to agricultural fields and as

such, can be located as possibly being in areas of agricultural production but only occasionally spectrally separated from other crops.

AGRICULTURE. Agricultural areas can be located with image enhancement techniques by their distinctive patterns. The specific identification of crop type by spectral classification is much more difficult, especially in areas of small fields and heterogeneous cropping practices.

WILDLIFE HABITAT. There are successful models, generally based on GIS techniques, to locate areas of possible wildlife. Many of the necessary inputs to these models can be extracted from remotely sensed data. The location of wildlife habitat is not the same as the location of wildlife.

Remotely sensed data can be extremely useful in the location and analysis of many of the conditions of interest to the Air Force. This study, because of the restrictions applied and the difficulty of considering each condition independently in one study, was limited in the depth of analysis provided and the ability to test various analysis techniques. Assuming the same interests and restrictions utilized in this study continue, there are several areas of additional examination recommended.

1. Additional condition by condition examination by automated processing of TM data could be tested using the suggested most promising techniques. These techniques include texture, GIS, fractals and multisensor data sets among others, possibly in an

artificial intelligence framework. There are many interesting and promising analysis strategies which should be explored. These strategies may be more fully developed in a regional or data specific context. The spatial and temporal extendability of these techniques is an additional area of needed study.

2. This study made a distinct separation between image enhancement and automated processing techniques, as is typical of most remote sensing studies. This study restricted itself to automated processing strategies. A less limiting and more successful operational system would incorporate a mix of man-machine interactions. This mix could include a sequence of automated processing strategies for features easily identified by classification such as snow, water, bare soil, sand, and green vegetation in association with image enhancements to assist trained interpreters for other features such as agricultural areas, lineaments, and wetlands among others. A major advantage of this systems approach is that all conditions are examined together rather than independently. The exploration of various man-machine interfaces and the development of sequential strategies and keys could be extremely productive. These strategies will be most effective if region specific and with analysts familiar with those regions. These regions may be areal or thematic; for example South East Asia or tundra climates.

3. A common problem presented in this study is the need for ancillary information in most delineations. An important area for further research is to ascertain what ancillary information

is available for potential areas of interest and incorporate that information in a systems approach to condition assessment. It is a mistake to utilize remotely sensed data as a sole informational source. It is only one possible data source and most useful when combined with other data such as elevation, climate, vegetation, geology, and economic geography. This availability of information should be done on a regional basis and incorporated into a sequential processing strategy. The construction and utilization of a GIS will be a logical approach to this data integration. One aspect of this data integration will be the availability of remotely sensed data, how historical remotely sensed data can be accessed and utilized and a realistic appraisal of the necessity and availability of recent or real-time remotely sensed data.

Remote sensing is an extremely useful technique for information acquisition. It is a rapidly expanding technique both in its applications and the availability of new data and processing strategies. There is a great amount which is not known about how to maximize the extraction of information from remotely sensed data. This study has indicated the potential of a particular type of data, Thematic Mapper, for a specified set of conditions. Certainly this technique merits considerable more utilization and analysis.

APPENDIX A

SELECTED THEMATIC MAPPER AND ANCILLARY DATA AVAILABILITY

Landsat TM scenes were identified which collectively contain the conditions of interest for this study. The relevant digital data and images for those areas were obtained. For each scene, this appendix briefly describes the areas, lists the parameters of interest contained in each area and identifies selected ancillary information for utilization in the analysis of those scenes.

The ancillary data included the availability of National High Altitude Photography (NHAP), USGS 1:250,000 topographic and Land Use/Land Cover maps or digital data, USGS Digital Terrain Model elevation data (DTM), and the availability of other Landsat MSS or TM data which may be of interest for multitemporal analysis stratigies.

The USGS NHAP program collects excellent quality aerial photography for essentially the entire United States. This program was initiated in the early 1980's and has nearly completed the first nation-wide collection and in some areas has begun a second collection effort. The photos are obtained in two formats; color infrared (CIR) at a scale of 1:58,000 and normal black and white at 1:80,000. This excellent photography was collected under cloud-free and leaf-off conditions. The second cycle of this program will be leaf-on conditions. The photos are indexed on microfiche copies of reduced 1:250,000 scale

topographic maps. The photography is relatively inexpensive and easily obtained in various scales and formats. These photos provide valuable ancillary data for developing spectral signatures for classification of TM data or for accuracy assessments.

Other photographic data can be identified using the Aerial Photography Summary Record System (APSRS) of the National Cartographic Information Center (NCIC). ASPRS is a frequently updated listing of available photography for the United States indexed on microfiche by 1:24,000 scale topographic maps. Frequently, small scale CIR photography can be obtained directly from the USGS EROS Data Center in Sioux Falls, South Dakota.

Topographic maps of the United States are available at a variety of scales. An appropriate scale for working with TM or MSS data is 1:250,000. For specific studies larger scale maps may be desirable. The USGS has also created Land Use and Land Cover maps at both 1:100,000 and 1:250,000 scales. Most of the United States has been completed at the 1:250,000 scale but much remains to be finished at the larger scale. The land use/cover maps are created from aerial photography and contain Level II information as listed in the Anderson, Hardy, Roach and Witmer (1976) system. These maps are being digitized by the USGS and can be purchased for selected areas of the country in that format. The maps are helpful ancillary data for the TM data and the digitized information is potentially very useful as one component in a GIS.

Digital Elevation Models (DEM's) are digital records of terrain elevation for ground positions at regularly spaced horizontal intervals. Elevation data are available for some USGS 7.5-minute (1:24,000) topographic quadrangles and all United States 1 degree by 2 degrees (1:250,000) maps. For the 7.5 minute data, the ground distance between each pair of digitized points is 30 meters. The 1:250,000 scale DEM data are available in two forms: 1 degree by 1 degree blocks with a 3-arc second distance between each pair of digitized points; or in 1 degree blocks with a ground distance between points equal to approximately 200 feet. These elevation data are very useful as ancillary data in classification strategies and as components in a GIS.

A search was also conducted for other available MSS or TM data for each study site. Other Landsat data may be useful in multitemporal analysis techniques.

1. IMPERIAL VALLEY, CALIFORNIA

A. Data and site description

The TM scene was collected on 12 December 1982 and has scene number E-40149-17444. This area in Southern California has frequently been the subject of remote sensing studies in part because of the interesting mix of land covers and also because of the general availability of good quality data in this arid environment.

The primary land covers in this region are agricultural fields, mostly irrigated, and desert landscapes including some bare sands and xerophytic vegetated areas. Water areas are represented by a portion of the Salton Sea, a small playa, the New and Alamo Rivers passing through the agricultural area and various irrigated canals such as the All American and East Highland. Rock outcrops in a portion of the Chocolate Mountains are located in the northeastern corner of the study site.

The warm climate, relatively fertile soils and availability of water for irrigation from the Colorado River allows the Imperial Valley to be a very productive agricultural area for a wide range of crops. Among the prominent crops are lettuce, sugar beets and cotton. Feed lot beef cattle are also found here because the continuous growing season allows for up to seven cuttings of alfalfa per year. The United States and Mexican border is very evident in the TM image because of the changes in field sizes and patterns. Scattered within the agricultural areas are a number of towns including Brawley, El Centro, Calexico and Mexicali.

B. Contained parameters

surface roughness
streams,canals
lakes
boundary demarcation
sand

mixed cropland

agriculture

C. Ancillary data

NHAP CIR collected in 1984 and 1985.

Topographic and Land Use/Cover (1:250,000)

Salton Sea	Topographic	1969	
	Land use/cover	1980	(not digital)
El Centro	Topographic	1977	
	Land use/cover	1979	(not digital)

Additional Landsat

A total of 41 Landsat TM data takes have been made for this path/row (39/37). Of these, 19 are of good to excellent quality. There are also 43 scenes of similar quality MSS data available for this area since 1981.

3. MIAMI, FLORIDA

A. Data and site description

This TM scene (identification E-40157-15181) was collected on 21 January 1983. The subscene study area was approximately 4000 square kilometers centered on Miami, Florida. The primary land cover in this region is urban and near-urban features in and around the cities of Miami, Hollywood, Hialeah, Fort Lauderdale, and their extensive suburbs. Water features include numerous

reservoirs, portions of the Atlantic Ocean, and Biscayne Bay, where some shallow shoal areas are evident.

A significant portion of the area contains wetlands along the eastern edge of the Everglades. There are also limited areas of evergreen and deciduous forests and rangelands. Extensive areas of agriculture, including croplands, orchards and pastures are located in the south and west portions of this region. Topographically this area is extremely flat. There are, however, some coastal beaches.

B. Contained parameters

lakes and reservoirs
wetlands
boundary demarcations
sand
coastal beaches
pasture
mixed cropland
brush
forest
vegetation
orchards
agriculture
wildlife habitat

C. Ancillary data

NHAP CIR collected in 1985.

Topographic and Land Use/Cover (1:250,000)

West Palm Beach	Topographic	1972	
	Land use/cover	1976	(digital)
Miami	Topographic	1971	
	Land use/cover	1976	(digital)

Additional Landsat

There have been 47 TM scenes collected for path/row 15/42. Of these only five are of good to excellent quality. Since 1981, 30 good or better MSS scenes have also been acquired.

3. LOS ANGELES, CALIFORNIA

A. Data and site description

This TM scene collected on 10 December 1982 has identification E-40147-17565. This subscene contains extensive urban areas in the northeastern portion of the Los Angeles Basin. Reservoirs and a very limited amount of agriculture are found within this area.

The more important features for this study are the San Gabriel Mountains in the north and other mountainous areas within the scene. These areas provide extensive variations in slope and roughness and are primarily covered by brush vegetation (chapparal).

B. Contained parameters

slope

roughness

reservoirs

brush

vegetation

wildlife habitat

C. Ancillary data

NHAP CIR not available under NHAP.

Topographic and Land Use/Cover (1:250,000)

Los Angeles	Topographic	1975
	Land use/cover	1977 (digital)

Additional Landsat

There have been 41 TM scenes obtained for path/row 41/36. Of these scenes, 14 have 30 percent of less cloud cover and band quality ratings of 5 or higher. There have also been 38 MSS scenes collected since 1981 for this area of the same quality.

4. DELEWARE COUNTY, INDIANA

A. Data and site description

TM scene E-40103-15505 was collected on 27 October 1982. The primary land cover in this area is agricultural fields in the

traditional township and range land division format of the midwest. The primary crops in this area are corn, soybeans and miscellaneous grains. There is an extensive amount of livestock activity, primarily feedlot but with some open pasture, for hogs and cattle. Scattered within the agriculture fields are broadleaf deciduous forest woodlots, some reservoirs and wetlands. There are also several towns. The topography is extremely flat.

B. Contained parameters

streams
reservoirs
wetland
boundary demarcations
pasture
forest
vegetation
agriculture
wildlife habitat
snow (different date)
orchards

C. Ancillary data

NHAP CIR collected in 1983.

Topographic and Land Use/Cover (1:250,000)

Muncie Topographic 1978

Land use/cover 1981 (digital)

Additional Landsat

Forty-eight TM scenes have been collected for path/row 21/32. Of these only seven are of good to excellent quality. In addition, 31 MSS scenes of similar quality have been acquired since 1981.

5. WASHINGTON, DC

A. Data and site description

This scene was collected on 2 November 1982 and has image identification E-40190-15140. The subscene of interest is located to the west of Washington, DC. Included in this area are extensive urban developments and a variety of transportation networks. The major river is the Potomac and there are a number of smaller streams and several reservoirs. The general system of land division is complex and the resulting land cover patterns are highly irregular. There are numerous areas of broadleaf deciduous forest, very limited amounts of needleleaf evergreen trees and some wetlands. There are frequent areas of agriculture. The area is gently rolling with some areas of steeper terrain towards the Appalachian Mountains on the west.

B. Contained parameters

slope

streams

boundary demarcations

brush

forest

orchards

wildlife habitat

snow (different date)

C. Ancillary Data

NHAP CIR collected in 1981 and 1982.

Topographic and Land Use/Cover (1:250,000)

Washington	Topographic	1979	
	Land use/cover	1976	(digital)
Baltimore	Topographic	1978	
	Land use/cover	1977	(digital)

Ancillary Landsat

There have been 49 TM scenes obtained for this path row (15/33). Of these 10 are of good quality. Since 1981 there have also been 20 MSS scenes of similar quality obtained for this area.

Contractor Report-RF 5408

EFFECT OF HIGH FREE-STREAM TURBULENCE ON TURBULENT BOUNDARY LAYER FLOW AND HEAT TRANSFER

J.C. Han and C.D. Young

Mechanical Engineering Department

Texas A&M University

College Station, Texas 77843

Prepared for

AFOSR through UES

Subcontract No. S-760-OMG-018

December, 1986

ABSTRACT:

Experiments were performed to investigate the effect of high free-stream turbulence on the turbulent boundary layer flow and heat transfer. The high turbulence intensity was produced by a wind tunnel jet-grid system. An electrically heated, thin foil flat plate test section, with 0.75" thick, 12" wide, and 60" long, was placed at the immediate downstream from the jet-grid location. In the jet-grid system, the compressed air flowing inside the hollowed biplanar square-mesh grids was oriented to blow (through small injection holes uniformly distributed on the grid surface) in the downstream direction with a controllable flow rate. The grid (circular tube) diameter and the grid mesh length was 0.25" and 1", while the injection hole diameter and spacing was 0.052" and 1", respectively. For the grid with an 5% injection ratio, the turbulence intensity was about 15% at 20 grid diameters downstream, while the corresponding value was about 7.5% for the grid without injection. The boundary layer velocity/turbulence intensity profiles were measured along the midplane of the flat plate at four axial locations, 20, 40, 80, and 120 grid diameters, under two mainstream velocities, 50 and 100 fps, respectively. The distributions of the local heat transfer coefficient on the flat plate were also determined. The results showed that the Stanton number increased with increasing turbulence intensity due to grid injection. At the fully turbulent downstream regions ($Re_x \cong 10^6$), the Stanton numbers with and without injections were about 50% and 25%, respectively, higher than that the standard turbulent correlation, whereas at the very first turbulent upstream regions ($Re_x \cong 10^5$), the corresponding values were about 180% and 70% higher. More measurements are required in order to

conclude the combined effects of turbulence intensity, length scale, and Reynolds number on the turbulent flow heat transfer.

ACKNOWLEDGEMENTS:

This mini grant contract was funded by the Air Force Office of Scientific Research (AFOSR) and was monitored by the Universal Energy Systems, Inc., under Subcontract No. S-760-OMG-018. Their support is greatly appreciated.

NOMENCLATURE:

b	turbulence grid diameter
C_f	friction factor, $\tau_w/[(1/2)\rho U^2]$
C_p	specific heat at constant pressure
h	heat transfer coefficient
I	electric current through foil
J	injection ratio, injection mass flow rate/(injection mass flow rate + mainstream flow rate)
K	thermal conductivity
Pr	molecular Prandtl number, $\mu C_p/K$
Pr_t	turbulent Prandtl number
q"	heat transfer rate per unit surface area
R	foil resistance
Re_x	length Reynolds number, UX/ν
Re_θ	momentum thickness Reynolds number
St	Stanton number, $h/(\rho U C_p)$
T	local temperature
T_w	flat plate surface temperature
T_∞	mainstream air temperature
TU	streamwise turbulence intensity, $(\bar{u'^2}/U)^{1/2}$; also local streamwise turbulence intensity, $(\bar{u'^2}/u)^{1/2}$
U	mean streamwise velocity
u	local streamwise velocity
u'	local streamwise fluctuating velocity
v	local normal velocity
v'	local normal fluctuating velocity
u'v'	Reynolds stress

$v'T'$	Reynolds flux
X	streamwise distance from flat plate leading edge
Y	normal distance from flat plate surface
ξ	unhead starting length from flat plate leading edge
ν	kinematic viscosity
ρ	mainstream air density
τ_w	wall shear stress

I. INTRODUCTION:

The effect of free-stream turbulence on turbulent boundary layer heat and momentum transfer have been recognized as one of the critical problems in turbine airfoil design. In the case of adiabatic turbulent boundary layer flow over a flat plate, many studies [1-2] have consistently confirmed that increases of skin friction are caused by increased free-stream turbulence levels. However, the impacts of free-stream turbulence on the turbulent boundary layer heat transfer were contradictory as indicated by Simonich and Bradshaw [6]. Some studies [3-5], which based on low Reynolds number (Re_θ) flow experiments (transitional boundary layer flow) or used coarse boundary layer trips or unconventional free-stream turbulence generating devices (large length scale of turbulence), showed that the heat transfer rates were not affected by free-stream turbulence levels. Recently, Simonich and Bradshaw [6] and Hancock and Bradshaw [7] indicated that the free-stream turbulence effect depends upon the free-stream turbulence intensity and length scale. Based on wind tunnel grid-generated turbulence with turbulence intensity up to 6% and length scale ratio up to 5, they found that the Stanton number increases with increasing free-stream turbulence and the increased rate of Stanton number is larger than the increased rate of skin friction which implies that Reynolds-analogy factor ($2\ St/C_f$) increases. They also concluded that the Stanton number at given turbulence intensity decreases as the length scale increases, while the maximum impact of the free-stream turbulence obtained for cases where the boundary layer thickness and streamwise dissipation length scale are about the same.

Blair [8-10] conducted extensive experiments to determine the

influence of free-stream turbulence on flat plate turbulent boundary layer heat transfer and mean profile development with wind tunnel grid-generated turbulence intensity ranging from 0.25 to 7 percent. Free-stream multicomponent turbulence intensity, longitudinal integral scale, and spectral distributions were obtained for the full range of turbulence levels. In general, Blair's data support Simonich, Hancock, and Bradshaw's conclusions in which both the skin friction and heat transfer were substantially increased for increased levels of free-stream turbulence, and the Reynolds-analogy factor is shown to linearly increase with increasing free-stream turbulence level. The skin friction and the Stanton number correlations was respectively obtained to account for the effects of turbulence intensity, length scale, and boundary layer Reynolds number (Re_θ). He also found that the logarithmic region of the mean velocity and temperature profiles were not affected by free-stream turbulence levels and the turbulent Prandtl number (Pr_t) increases with increasing free-stream turbulence intensity in most region of the boundary layer except that near the wall (sublayer) region where the Pr_t decreases with increasing turbulence intensity.

In the aforementioned studies [6-10], the effect of free-stream turbulence on turbulent heat transfer were based on the wind tunnel grid-generated turbulence with a maximum turbulence intensity of up to 6%. It is noted that the turbulence level, at the nozzle guide vane (after combustor) and the second stage stator (after rotor), can be as high as 15-20% in engine conditions. It is interesting to know whether the results obtained in [6-10] can be extended to the very high turbulence condition. In other words, the Stanton number and the

Reynolds-analogy factor will continue to increase with further increasing turbulence intensity or they will reach a plateau at certain high levels of intensity. However, it is very difficult to obtain very high free-stream turbulence with the simulated length scale in engine conditions by using classic wind tunnel grid-generated turbulence experiments. Recently, Moffat [11] investigated the effect of very high free-stream turbulence produced by a free jet on the turbulent boundary layer heat transfer sponsored by NASA HOST programs. In a progress report by Moffat [11] at 26 and 48% turbulence intensities, Stanton numbers in the margin of a free jet were 85 and 350%, respectively, higher than the standard zero percent free-stream turbulence condition. Detailed boundary layer velocity and temperature profiles, integral length scale, and the Reynolds analogy factor have not been reported yet.

A long term engine research program was initiated by the Air Force Wright Aeronautical Laboratories (AFWAL), Aero propulsion Laboratory, Turbine Engine Component Division (POTC). Under the 1985 USAF-UES Summer Faculty Research Program, Han [12], suggested by Dr. Richard Rivir of AFWAL/POTC, studied the effect of high free-stream turbulence from a free-jet on the flat plate turbulent boundary layer flow and heat transfer. Some preliminary velocity/turbulence intensity profiles, friction factor and Stanton numbers were measured. The results showed that the Reynolds analogy factor was much greater than one for turbulence intensity up to 20%. MacMullin [13] followed up the research effort at AFWAL/POTC. Detailed boundary layer velocity/turbulence intensity and temperature profiles, integral length scale, and spectra were measured for turbulence intensity up to 18%. The results indicated

that the Stanton number and friction factor increased with increasing turbulence intensity. The Reynolds analogy factor increased up to 12% of turbulence intensity, then became constant and decreased after 15% of turbulence intensity. However, the influence of length scale, as found by previous researchers, was inconclusive at the conditions tested. Further research is required.

Another technique which had been used to produce high turbulence was the wind tunnel jet-grid system [14-15]. In the jet-grid system, the jets flowing inside the hollowed grids can be oriented to blow in the upstream or downstream direction with a controllable flow rate. The turbulence intensity can be as high has 15% while maintaining isotropy and homogeneity. Recently, O'Brien and Vanfossen [16] applied the same technique to study the influence of jet-grid turbulence on heat transfer from the stagnation region of a cylinder in cross flow. They found that the jet-grid provided turbulence intensity of 10 to 12 percent, for downstream blowing with the blowing rate adjusted to an optimal value for flow uniformity, while the heat transfer was 37 to 53 percent higher than that the zero-turbulence case. In the present investigation, the similar jet-grid system was employed to study the effect of high free-stream turbulence on the boundary layer flow and heat transfer. Detailed velocity/turbulence intensity profiles and the Stanton numbers were taken through a flat plate placed at the downstream of the wind tunnel jet-grid system. The turbulence levels could be as high as 15% at 20 grid diameters downstream from the jet-grid device.

II. OBJECTIVES OF THE RESEARCH EFFORT:

This study is aimed to investigate the effect of high free-stream turbulence from a wind tunnel jet-grid on flat plate turbulent boundary

layer flow and heat transfer.

There are two types of objectives: long range and immediate. For the present investigation, the immediate objectives are restricted to the following:

1. Design and construction a wind tunnel jet-grid flat plate test apparatus.

2. Instrumentations the test section for velocity (hot wire anemometer) and temperature (thermocouples) measurements.

3. Calibrations and preliminary measurements for the mainstream flow mean and fluctuating velocity profiles across the boundary layer at several downstream locations from the jet-grid; calculations the turbulence intensity, log-law velocity, and friction factor distributions on the corresponding measurements.

4. Wall temperature and mean temperature profile measurements; calculations the log-law temperature and heat transfer coefficients.

The long range objectives are as follows:

1. Detailed measurements on mean and fluctuating velocity and temperature profiles, u, v, T, u'v', v'T', to construct log-law velocity and temperature, and turbulent Prandtl number Pr_t distributions in the boundary layer. Detailed measurements on length scale distributions.

2. Calculate the combined effects of high turbulence intensity, length scale, and Reynolds number on the friction factor and heat transfer coefficients.

3. Do the similar measurements as items 1 and 2 with one row and two rows film cooling.

III. EXPERIMENTAL APPARATUS:

A. Wind Tunnel/Jet Grid System: A schematic of the low speed wind

tunnel/jet-grid system is shown in Figure 1. The wind tunnel had an inlet cross section of 24" x 12" and a contraction ratio of 4:1. The test channel was 6" high, 12" wide, and 60" long. The wind tunnel was operated at the suction mode by a 7 1/2 hp axial blower. The jet-grid was placed between the end of the wind tunnel straight section and the test channel. For the jet-grid system, air from a 1200 scfm compressor passed through a pressure regulator (air pressure downstream of the regulator was about 110 psig), an orifice flow meter (the pressure drop was determined by Validyne transducer and demodulator), a control valve, and entered injection chambers. The air was then injected from the injection chambers through small injection holes uniformly distributed on the surface of a biplanar square-mesh grid of circular tubes, as shown in Figure 2. The grid (aluminum tubes) diameter and the grid mesh length was 1/4" and 1", while the injection hole diameter and spacing was 0.052" and 1", respectively. The injection was directed in the downstream direction of the grid. The injection rate was about 3-5% in order to produce the maximum isotropic turbulence. For comparison, the turbulence can be produced by the biplanar square-mesh grid with no air injection (passive grid) and by the same biplanar square-mesh grid with air injection (jet-grid).

B. Flat Plate Test Section/Instrumentation: A sharp edge flat plate test section was placed at the downstream from the jet-grid device as shown in Figure 3. The distance between the flat plate leading edge and the jet-grid surface was about 0.625". The flat plate was 0.75" thick, 12" wide and 60" long and had a 1.375" unheated sharp leading edge. The plate was composed from a 1/8" thick formica sheet at the top, a 1/2" thick asbestos foam in the middle, and another 1/8" thick

formica sheet at the bottom. The space between the plate top surface and the channel ceiling, and the gap between the plate bottom surface and the channel floor was about 4.5" and 0.75", respectively. Twenty seven pieces of stainless steel foils connected in series by buss bars were cemented on the top surface of the formica plate to complete the flat plate test section. Each piece of thin foils had 0.001" thick, 2" wide and 12" long. The fin foil was powered (A.C.) by a variac through buss bars to provide a nearly uniform surface heat flux during the heat transfer tests. A 1/16" gap, which filled up with packing material, was provided between every two foils. The foil was instrumented by 55, 30-gauge, copper-constantan thermocouples in the strategic locations to measure the local surface temperature distributions, as shown in Figure 3. The thermocouples were soldered underneath the foil through holes in the flat plate. Several thermocouples were soldered along the bottom surface of the flat plate in order to determine the heat losses through the flat plate during the steady state heat transfer tests. Thermocouples were also used to measure the mainstream air temperatures at the leading and the trailing edges of the flat plate, and the injection air temperature at the injection chambers. A Beckman multimeter was used to determine the power input to the foil by measuring the electric current, the voltage drop, and the resistance across the foil. A 60-channels Fluke 2285B data logger was used for temperature readings and data storages. An A to D converter was connected between the data logger and the T.I. microcomputer.

C. Automatic Traversing/Hot Wire Anemometer: A computer-controlled traversing device, which was located on the top of the test channel, was designed to hold the hot wire probe (TSI 102, or DISA 55 p.

11) for the boundary layer velocity/intensity/temperature profile measurements. This device could also be moved manually to different streamwise and spanwise locations for the similar measurements. The device was made of a Ball Screw (0.2" pitch) driven by a Sanyo stepping Motor (40 oz-in, stepping angle 1.8°, 200 steps per turn, 0.025" per step) through a T.I. microcomputer. A 4-channels TSI IFA 100 constant temperature anemometer, a 2-channels DISA 55D-05 constant temperature anemometer, and 2 HP 3478A precision multimeters were employed along with an A to D converter to the T.I. microcomputer for hot wire signal analysis and data acquisition. The true RMS based on 200 samples per 10 sec was obtained for the turbulence intensity calculations. The turbulence intensity was calculated based on the method suggested by [17] for the TSI wire and based on the method provided by [18] for the DISA wire. All the data were reduced through a VAX 8300 microcomputer. The hot wire was calibrated through an ASME calibrator (with a chamber diameter of 8" and a nozzle diameter of 0.5"). A pitot tube probe was insert at the downstream location in the test channel to check the mainstream air velocity.

IV. EXPERIMENTAL RESULTS:

The preliminary experimental results will be presented in this section. Data were taken based on a specific jet-grid design, as described in the previous section, for two free-stream (mainstream) velocities, U = 50 fps and 100 fps. The free-stream turbulence intensity profiles produced by different injection ratios will be described first. The boundary layer velocity/turbulence intensity profiles along several streamwise locations will then be presented for the cases of without injection and with injections, respectively.

Finally, the effect of free-stream turbulence (due to injection) on the turbulent boundary layer heat transfer (Stanton number) will be discussed.

Maximum Turbulence Intensity: In reference [16], an isotropic turbulence could be obtained at X/b = 16 downstream from the jet-grid device. They found that the maximum turbulence intensity was produced under a 1 to 2% injection ratio. In the present investigation, the free-stream turbulence intensity vs injection ratio at X/b = 20 are shown in Figure 4 for two free-stream velocities. The results show that the free-stream (the potential core) turbulence intensity increases from 11.6 to 19.5% when the injection ratio changes from 0 to 5% for the case of the low free-stream velocity, whereas it increases from 10.4 to 11.7% when the injection ratio changes from 0 to 3.2% for the case of the high free-stream velocity. Therefore, a 3% to 5% injection ratio was used to produce the maximum turbulence intensity for the cases of low and high mainstream velocities in the present investigation. The injection ratio (J) was defined as the ratio of the injection mass flow rate to the sum of the injection mass flow rate and the mainstream mass flow rate.

Turbulence Intensity Decay: In order to understand the turbulence intensity decay rate in the streamwise direction, the Tu vs X/b are shown in Figure 5 for both TSI and DISA Hot Wire measurements. At each streamwise location, data were based on the averages of 10 points measurements in the central core region. In general, the results from both systems are very similar except that the Tu obtained by DISA are slightly lower than that obtained by TSI at X/b < 40. Both results show that the streamwise turbulence intensity decreases with increasing distance from the jet-grid location. The results indicate that the

turbulence intensity with injection (jet-grid) is higher than that without injection (passive-grid) and the former has a slightly faster decay rate than the latter for both mainstream velocities. The results also indicate that the turbulence intensity with the lower mainstream velocity is slightly higher than that with the higher mainstream velocity. With the low mainstream velocity, the intensity decreases from 15% to 6% and from 7.5% to 4%, respectively, for the cases of with and without injections when the distance (X/b) increases from 20 to 80, while with the high mainstream velocity, the corresponding values are from 11.5% to 4.5% and from 6.5% to 3.5%, respectively. It is interesting to note that, in the case of without injection (passive circular tube-grid), the intensity decay rates agree well with that obtained by Blair et al. [19], i.e., $Tu = 0.78\ (X/b)^{-5/7}$, but they are lower than that proposed by Baines and Peterson [20] for the square bar-grid, i.e., $Tu = 1.12\ (X/b)^{-5/7}$.

Velocity/Intensity Profiles: The boundary layer velocity/turbulence intensity profiles for the cases of with and without injections were measured along the tunnel midplane at four axial locations (X/b = 20, 40, 80, and 120) for both low and high mainstream velocities. At each location, a total of 45 points was measured from near the flat plate (y ≅ 1/8") to the centeral core region (y = 2.25"). The results are show in Figures 6-7 for the high speed (U ≅ 100 fps) and in Figures 8-9 for the low speed (U ≅ 50 fps), respectively. For two mainstream velocities, the boundary layer velocity/turbulence intensity profiles are very similar at the same downstream locations. The streamwise local velocity increases from the flat plate surface to the free-stream core region, while the corresponding streamwise local

turbulence intensity decreases from the wall region. The local turbulence intensity was based on the local fluctuation velocity and the local mean velocity. At the upstream location, X/b = 20, the velocity profiles are distorted by the injection. However, at the downstream locations, X/b = 40, 80, and 120, the velocity profiles become uniform. It is noted that the hot wire was traversed in-line with the injection holes (in the normal direction). It is seen that the turbulence intensity profiles for the case with injection are bigger than that without injection.

Heat Transfer Results: The local heat transfer coefficient was calculated from $h = (q'' - q''_{loss})/(T_w - T_\infty)$, where q'' = uniform surface heat flux determined by the electric current and the foil resistance (I^2R) and check with the electric current and the voltage drop across the foil (IV); q''_{loss} = the heat loss from the flat plate top wall (foil) to the flat plate bottom wall by conduction and the heat loss from the foil surface to the channel walls by radiation; T_w = local wall temperature (about 105°F); and T_∞ = mainstream air temperature (about 75°F) at the leading edge of the flat plate. It was found that the heat losses due to heat conduction and radiation were about 10 and respectively, for the cases of the high and the low mainstream The local heat transfer coefficient, h, was then converted local Stanton number, $St = h/(\rho C_p U_\infty)$, where ρ, C_p, and air density, specific heat, and velocity, respectively. the local Stanton number vs Reynolds number, Figures 10 and 11. The flat plate laminar correlations with zero percent turbulence with 6% turbulence intensity [8].

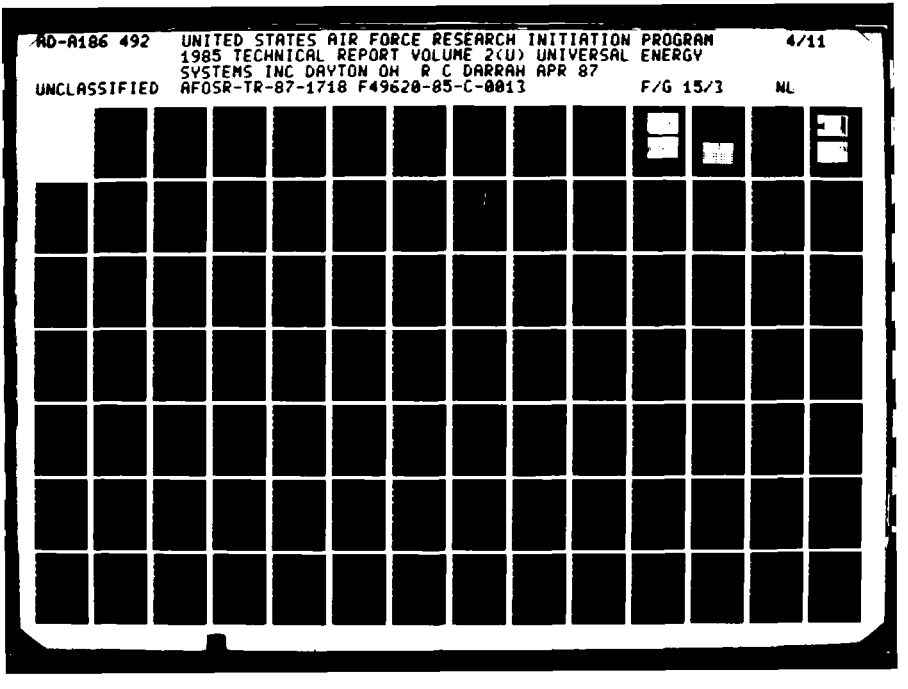
AD-A186 492
UNITED STATES AIR FORCE RESEARCH INITIATION PROGRAM 1985 TECHNICAL REPORT VOLUME 2(U) UNIVERSAL ENERGY SYSTEMS INC DAYTON OH R C DARRAH APR 87
4/11
UNCLASSIFIED
AFOSR-TR-87-1718 F49620-85-C-0013
F/G 15/3
NL

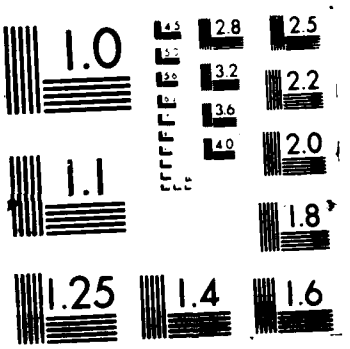
1.0
1.1
1.25
1.4
1.6
2.8
3.2
3.6
4.0
2.5
2.2
2.0
1.8

comparisons. Laminar correlation: $St = 0.453\ Pr^{-2/3}\ Re_x^{-1/2}\ [1 - (\xi/x)^{3/4}]^{-1/3}$; Turbulent Correlation: $St = 0.0307\ Pr^{-0.4}\ Re_x^{-0.2}\ [T_w/T_\infty]^{-0.4}$.

The local Stanton numbers along three axial lines are shown in Figure 10 for the case of the high streamwise velocity without injection. The results show that the Stanton numbers are fairly uniform in the spanwise direction and decrease with increasing Reynolds number. It is seen that Blair's data with 6% nominal turbulence intensity is about 18% higher than that the standard turbulent correlation [8], while the present data is about 5-10% higher than that Blair's at the fully turbulent region, $Re \cong 10^6$. It should be noted that the present flat plate was placed immediately downstream from the grid, therefore, the turbulence intensity was very high (about 20-30%) at the leading edge of the flat plate then decay to about 7% at X/b = 20 and to about 4% at the trailing edge of the plate, X/b = 120. The nominal turbulence intensity was about 8% over the entire plate. In contrast, the Blair's flat plate was placed far downstream from the grid and the turbulence intensity was varied from 8% at the leading edge to about 4% at the trailing edge of the plate, i.e., a nominal turbulence intensity of 6% over the entire plate. This may be the reason why the present Stanton numbers are very much higher than Blair's at the upstream high turbulence intensity region (which corresponding to $Re \cong 10^5$), and are still about 5-10% higher at the downstream region ($Re_x \cong 10^6$). It is suggested that, in the near future, data should be taken by moving the flat plate far downstream from the grid (X/b = 20). Meanwhile, in order to understand the combined effects of the turbulence intensity and the length scale on the boundary layer heat transfer, the integral length scale should be taken simultaneously with the velocity/intensity profile measurements.

The local Stanton numbers along the axial centerline of the flat plate are shown in Figure 11 for the cases of low and high mainstream velocities with and without injections. In general, for two mainstream velocities studied, the Stanton numbers with injection are about 40% and 25%, respectively, higher than that without injection at the leading edge ($Re_x \cong 10^5$) and the trailing edge region ($Re_x \cong 10^6$). The increased Stanton numbers are contributed by the high turbulence intensity produced by the injection. The results also show that, at the upstream region, the Stanton numbers in the case of the high mainstream velocity are slightly higher than that the low velocity case. But, at the downstream region, the results are found to be reversed.

V. CONCLUSIONS:

Within the past 12 months, the wind tunnel with jet-grid flat plate test rig was constructed and instrumented. Based on a specific jet-grid design, the preliminary results for velocity/intensity/heat transfer profiles were obtained for two mainstream velocities and for the cases of with and without injections. The following conclusions could be drawn:

1. The maximum turbulence intensity (central core region), up to 15% at X/b = 20, could be produced from the jet-grid device by using an approximately 5% injection ratio.

2. The turbulence intensity (central core region) with injection was about 80-100% and 30-50%, respectively, higher than that without injection at X/b = 20 and X/b = 80. The turbulence intensity decay rate with injection was slightly faster than that without injection.

3. The detailed boundary layer velocity/intensity profiles were documented. The local turbulence intensity decreased from the flat

plate surface to the central core region. The local velocity profile was distorted by the injection at X/b = 20. But the effect diminished at larger X/b ratios.

4. The detailed heat transfer coefficient distributions were obtained. The Stanton number increased with increasing turbulence intensity due to injection. At the fully turbulent downstream regions ($Re_x \cong 10^6$), the Stanton numbers with and without injections were about 50% and 25%, respectively, higher than that the standard turbulent correlation, whereas at the very high turbulent upstream regions ($Re_x \cong 10^5$), the corresponding values were about 180% and 70% higher.

VI. RECOMMENDATIONS:

Based on this preliminary results, the jet-grid technique seems to be promising to study the high turbulence heat transfer problems. However, in order to conclude the combined effects of high turbulence intensity, length scale, and Reynolds number on the Stanton number and the friction factor, the following investigations are recommended for the immediate future:

1. Design several jet-grid devices in order to optimize the maximum turbulence intensity produced by the grid injection.

2. The flat plate should be placed far downstream from the jet-grid (X/b ≅ 20) in order to have an uniform (isotropic) turbulence approaching the test section.

3. Measure the length scales, spectra, and velocity profiles simultaneously across the turbulent boundary layer.

4. Constract the turbulent Prandtl number (Pr_t) distributions by measuring the mean and the fluctuating quantities, u, T, u'v', and v'T', in both streamwise and spanwise directions.

5. Measure the film cooling effectiveness and the heat transfer coefficient with film cooling under the high turbulence conditions.

VII. REFERENCES:

1. Sugawara, S., Sato, T., Hirosyasa, K., and Osaka, H., "The Effect of Free-Stream Turbulence on Heat Transfer from a Flat Plate," NACA Tech. Memo 1411, 1958.
2. Feiler, C.E., and Yaeger, E.B., "Effect of Large-Amplitude Oscillations on Heat Transfer," NASA Tech. Report R-142, 1962.
3. Kestin, J., "The Effect of Free-Stream Turbulence on Heat Transfer Rates," Advanced in Heat Transfer, Vol. 3, Academic Press, London, 1966.
4. Junkhan, G.H., and Serovy, G.K., "Effects of Free-Stream Turbulence and Pressure Gradient on Flat-Plate, Boundary-Layer Velocity Profiles and on Heat Transfer," ASME Journal of Heat Transfer, Vol. 89, 1967, pp. 169-176.
5. Reynolds, W.C., Kays, W.M., and Kline, S.J., "Heat Transfer in the Turbulent Incompressible Boundary-Layer-1-Constant Wall Temperature," NASA Memo 12-1-58W, 1958.
6. Simonich, J.C., and Bradshaw, P., "Effect of Free-Stream Turbulence on Heat Transfer Through a Turbulent Boundary Layer," ASME Journal of Heat Transfer, Vol. 100, 1978, pp. 671-677.
7. Hancock, P.E., and Bradshaw, P., "The Effect of Free-Stream Turbulence on Turbulent Boundary Layers," ASME Journal of Fluids Engineering, Vol. 105, 1983, pp. 284-289.
8. Blair, M.F., "Influence on Free-Stream Turbulence on Turbulent Boundary Layer Heat Transfer and Mean Profile Development, Part I - Experimental Data," ASME Journal of Heat Transfer, Vol. 105, 1983, pp. 33-40.
9. Blair, M.F., "Influence of Free-Stream Turbulence on Turbulent

Boundary Layer Heat Transfer and Mean Profile Development, Part II - Analysis of Results," ASME Journal of Heat Transfer, Vol. 105, 1983, pp. 41-47.

10. Blair, M.F., "The Effects of Free-Stream Turbulence on the Turbulence Structure and Heat Transfer in Zero Pressure Gradient Boundary Layers," United Technologies Research Center Report: R82-915634-2, E. Hartford, CT, November 1982.

11. Moffat, R., and Maciejewski, P.K., "Heat Transfer with very High Free-Stream Turbulence," NASA Grant NAG 3-522. Proceedings of the 1985 Turbine Engine Hot Section Technology Conference, NASA conference publication 2405, 22 October 1985, pp. 203-215.

12. Han, J.C., "Effect of High Free-Stream Turbulence from a Free Jet on Flat Plate Turbulent Boundary Layer Flow and Heat Transfer," 1985 USAF-UES Summer Faculty Research Program, Contract No. F49620-85-C-0013, 30 August 1985.

13. MacMullin, R., "Effects of Free-Stream Turbulence from a Circular Wall Jet on Flat Plate Heat Transfer and Boundary Layer Flow," M.S. Thesis, the Air Force Institute of Technology, AFWAL/POTC, December 1986.

14. Gad-El-Hak, M., and Corrsin, S., "Measurements of the Nearly Isotropic Turbulence Behind a Uniform Jet Grid," Journal of Fluid Mechanics, Vol. 62, Part 1, January 8, 1974, pp. 115-143.

15. Tassa, Y., and Kamotani, Y., "Experiments on Turbulence behind a Grid with Jet Injection in Downstream and Upstream Direction," Physics of Fluids, Vol. 18, No. 4, April 1975, pp. 411-414.

16. O'Brien, J.E., and VanFossen, G.J., "The Influence of Jet-Grid Turbulence on Heat Transfer from the Stagnation Region of a

Cylinder in Crossflow," ASME paper 85-HT-58, August 1985.

17. Rivir, R.B., Research Engineer, Personal Communications, AFWAL/POTC, WPAFB, Ohio, February 1986.

18. DISA Instruction and Service Manual for Type 55D05 Battery-Operated CTA.

19. Blair, M.F., Bailey, D.A., and Schlinker, R.H., "Development of a Large-Scale wind Tunnel for the Simulation of Turbomachinery Airfoil Boundary Layers," ASME Journal of Engineering for Power, Vol. 103, October 1981, pp. 678-687.

20. Bainess, W.D., and Peterson, E.G., "An Investigation of Flow through Screens," Trans. ASME, Vol. 73, 1951, pp. 467-480.

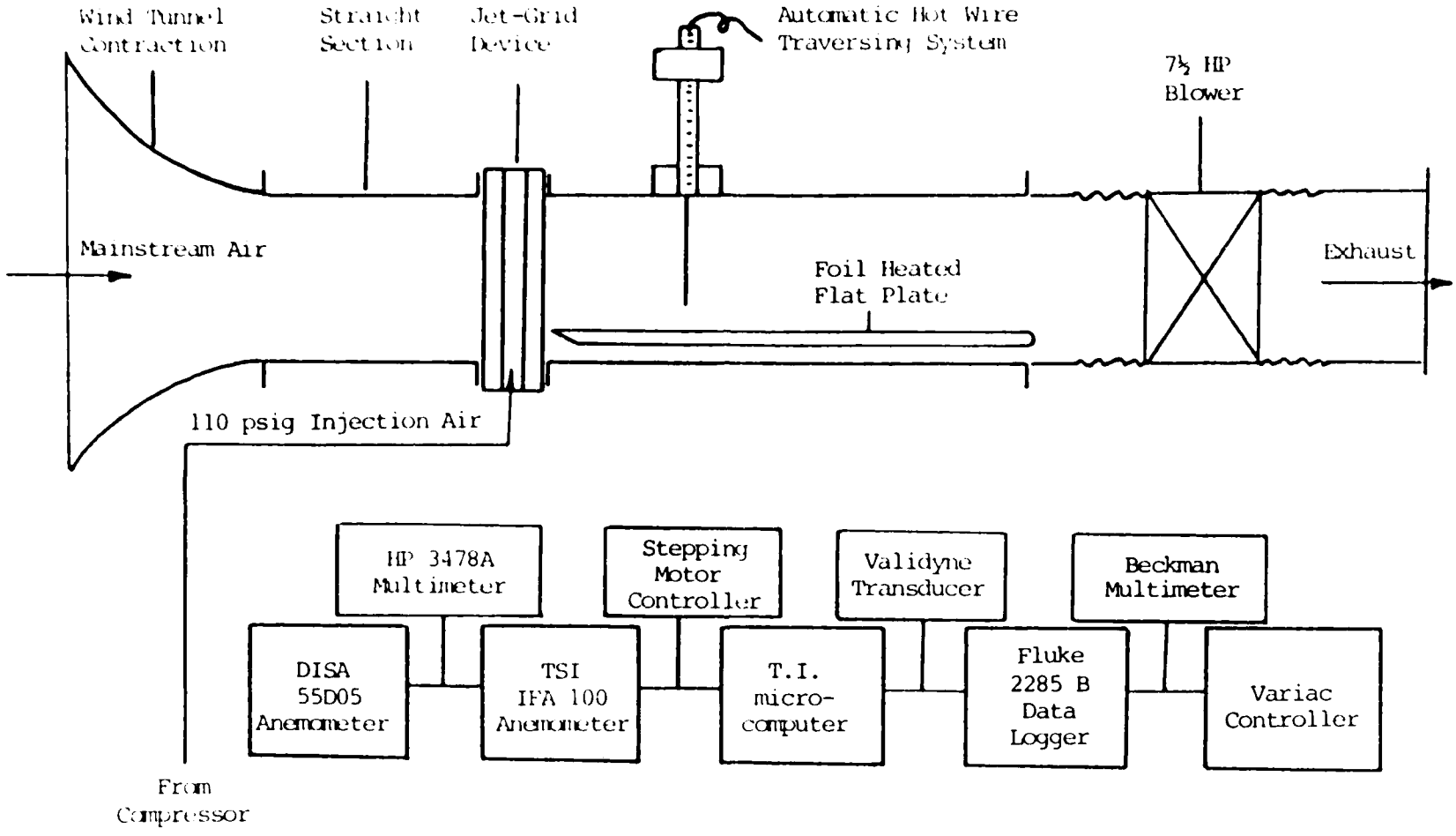

Figure 1. A Schematic of the Test Apparatus and Instrumentations.

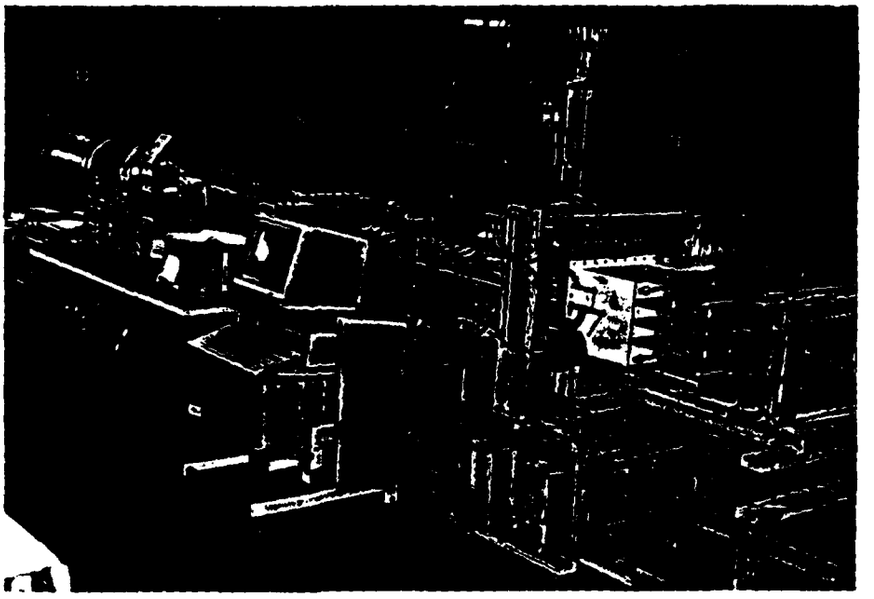

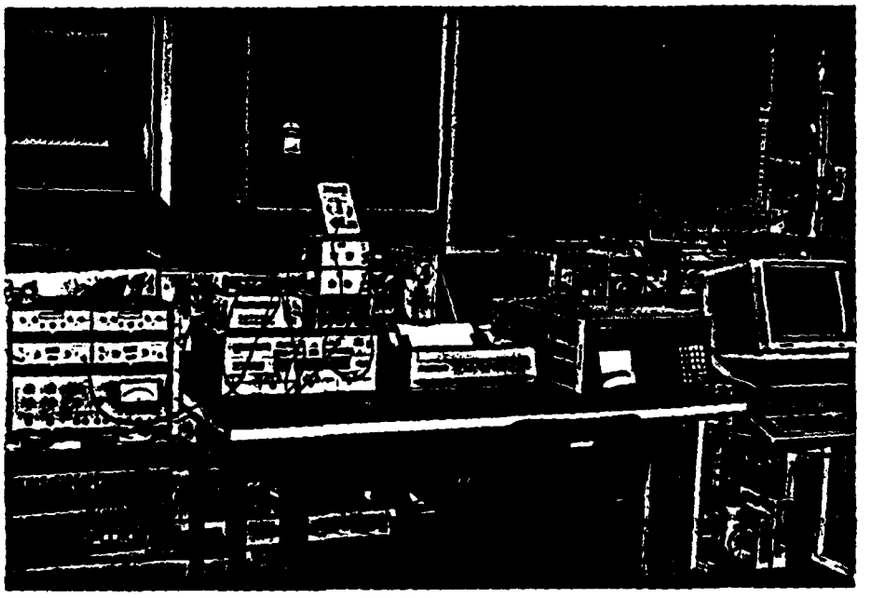

Figure 1-(a). Photos for the Test Rig and Instrumentations.

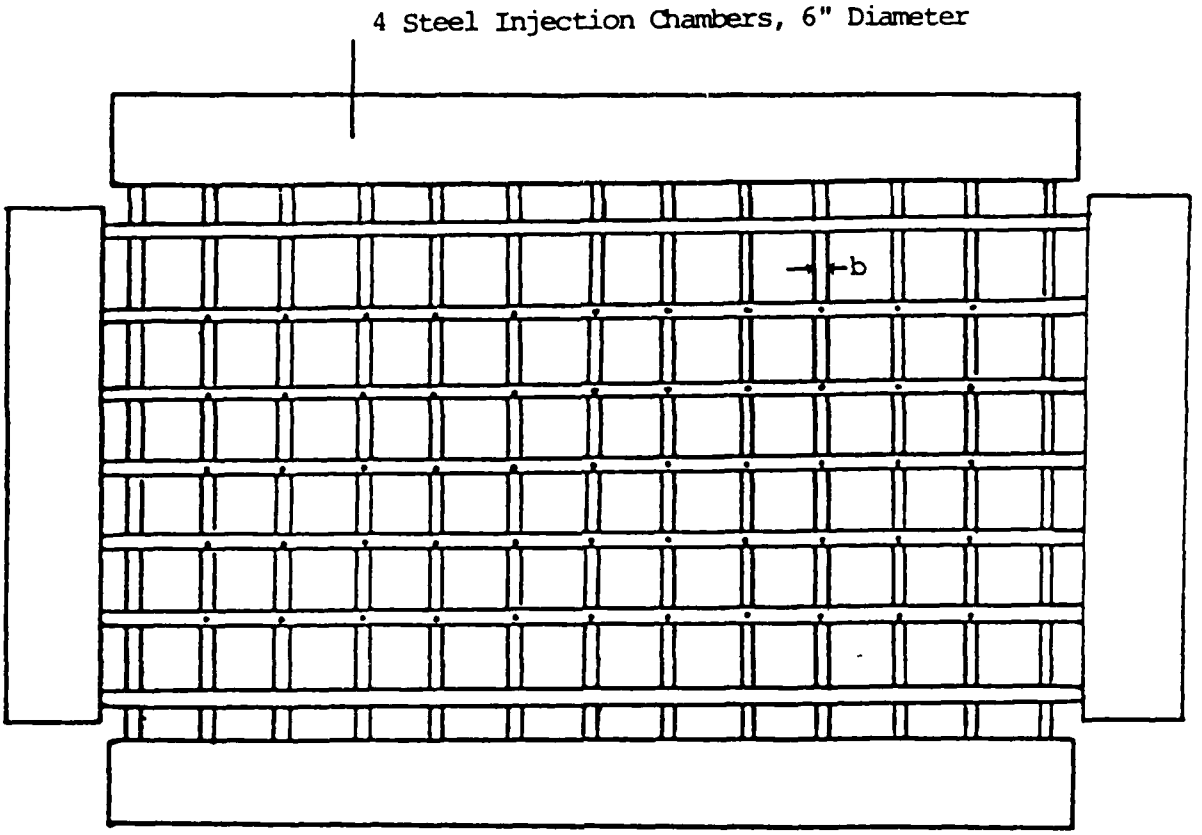

Grid Diameter (b) = 0.25"
Grid Mesh Length = 1.0"

Injection Hole Diameter = 0.052"
Injection Hole Spacing = 1.0"

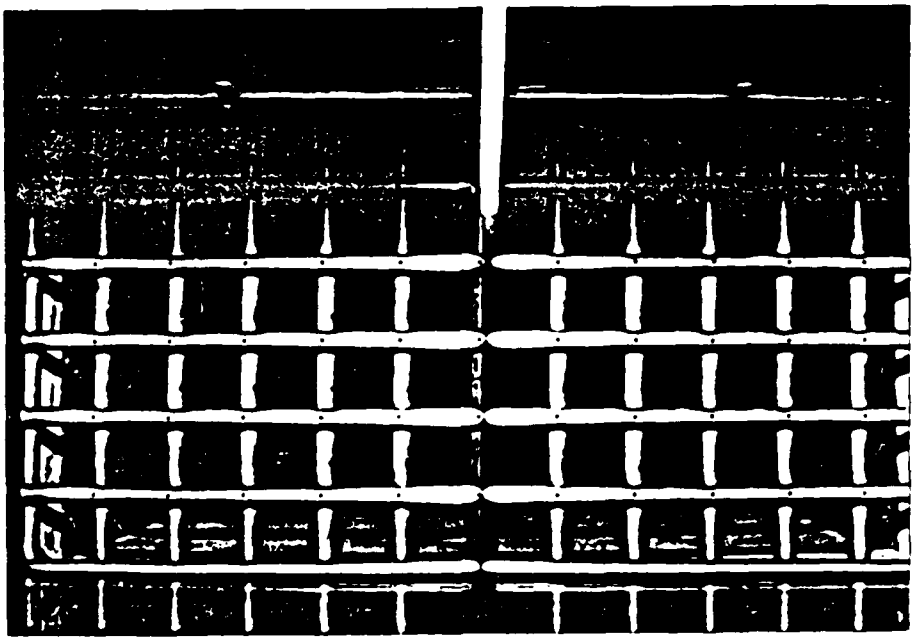

Figure 2. Jet-Grid Device and Its Dimensions.

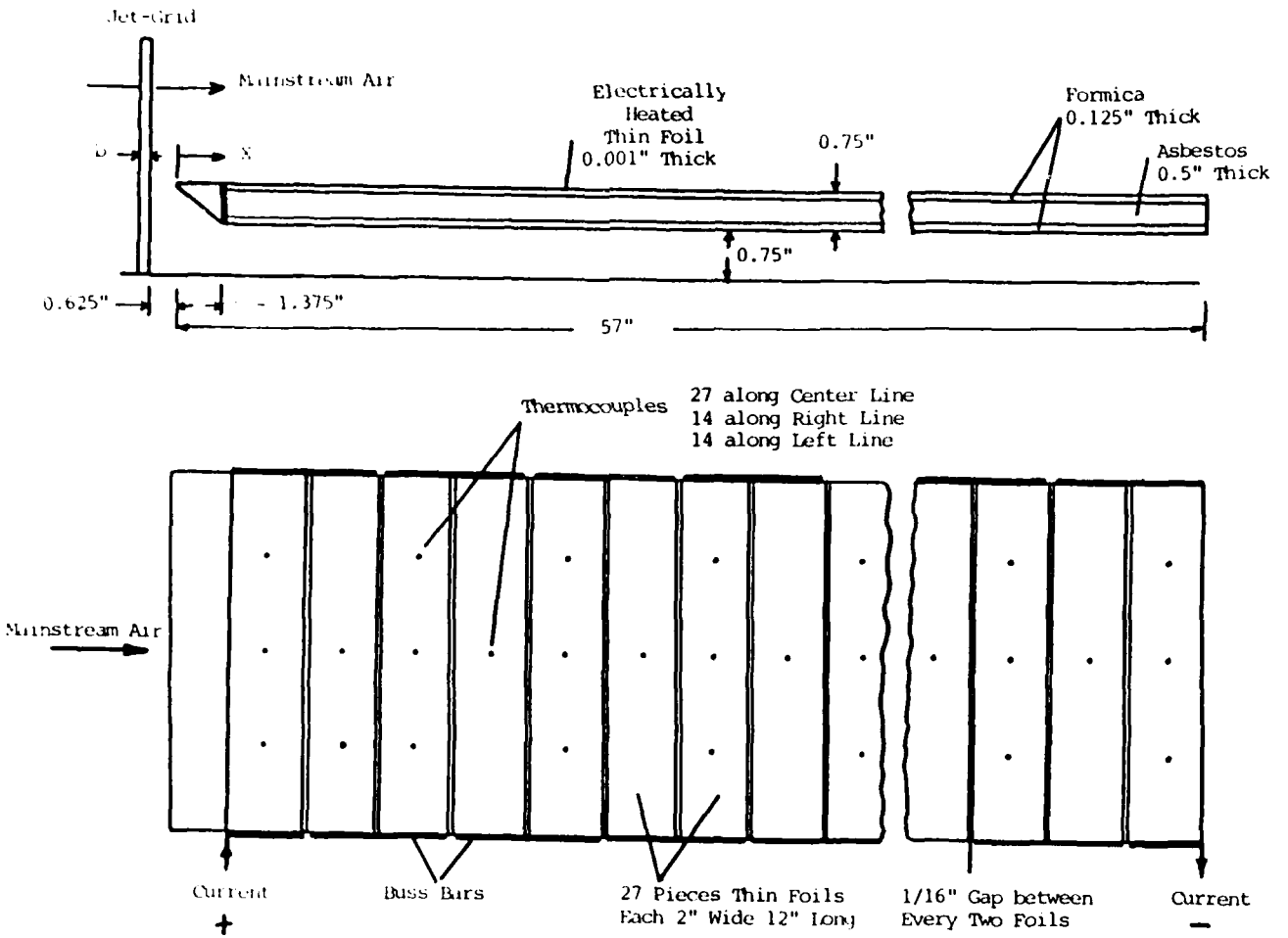

Figure 3. Electrically Heated Foil Flat Plate and Thermocouple Locations.

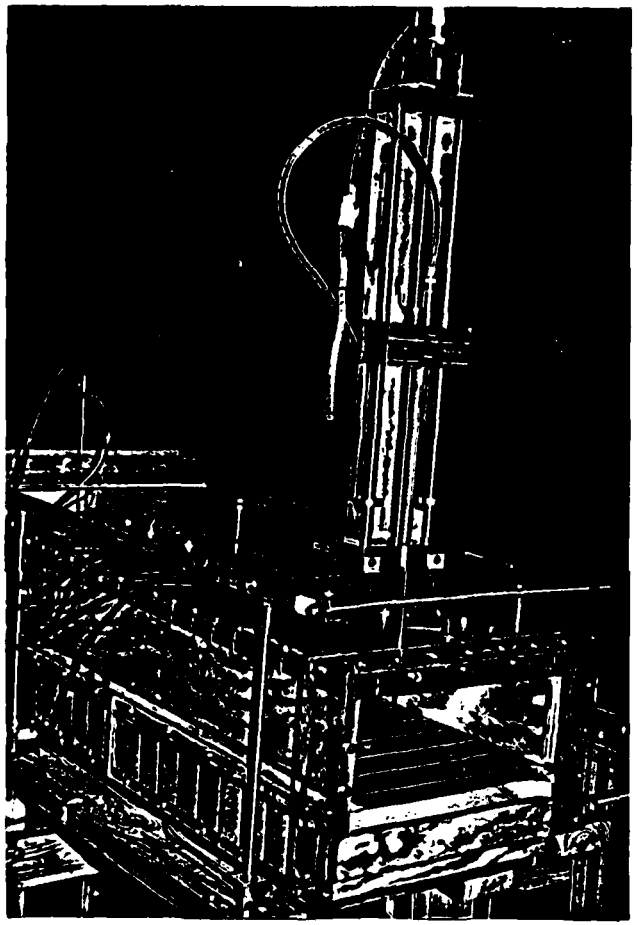

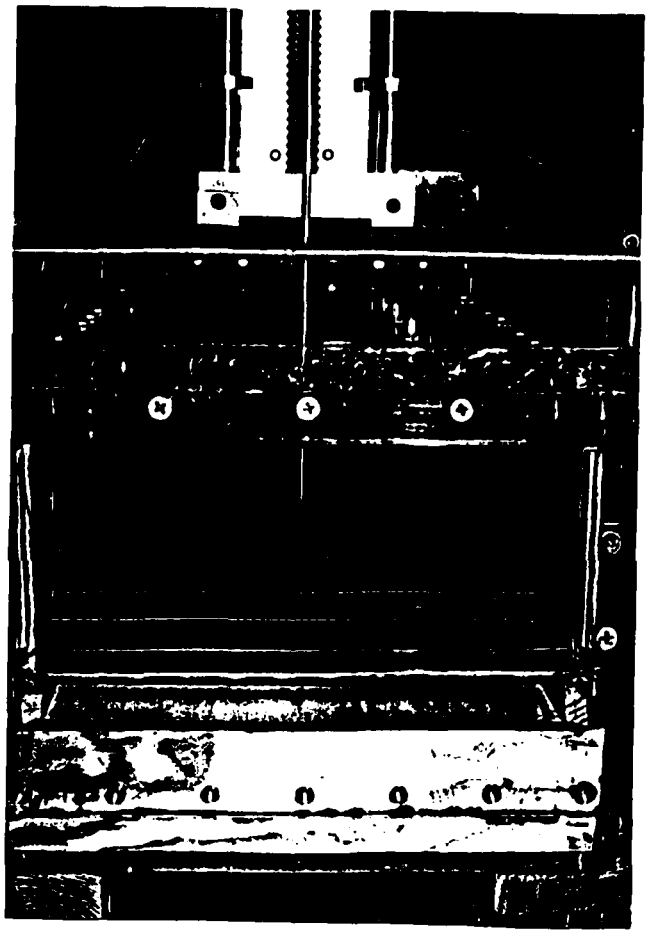

Figure 3-(a). Photos for the Traversing System and Foil Heated Test Section.

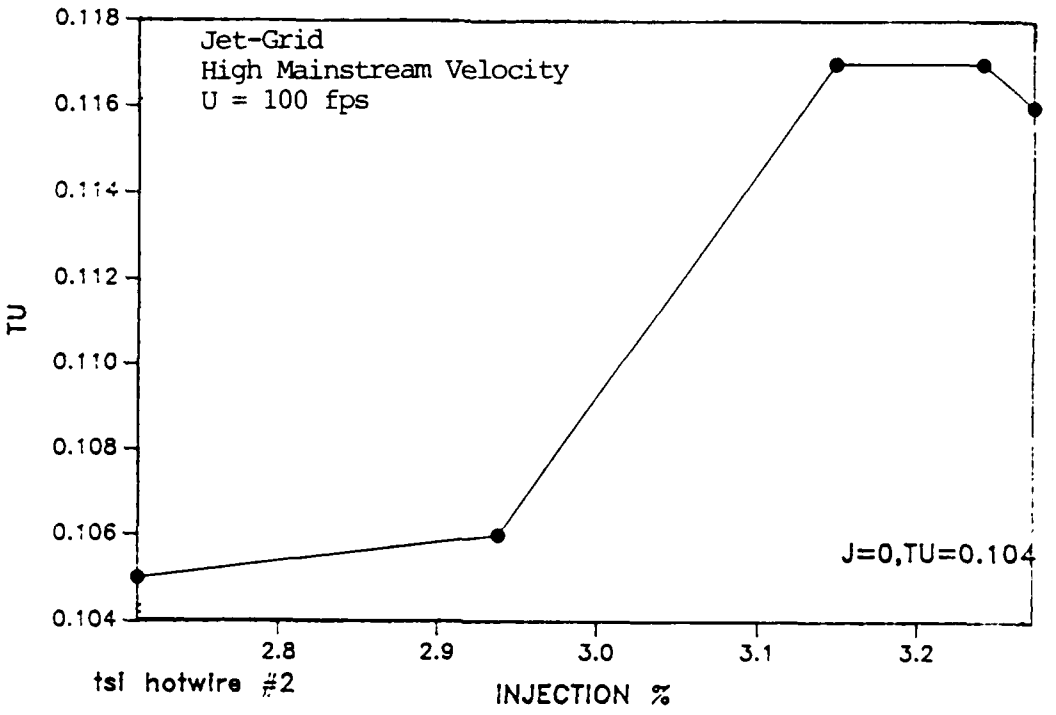

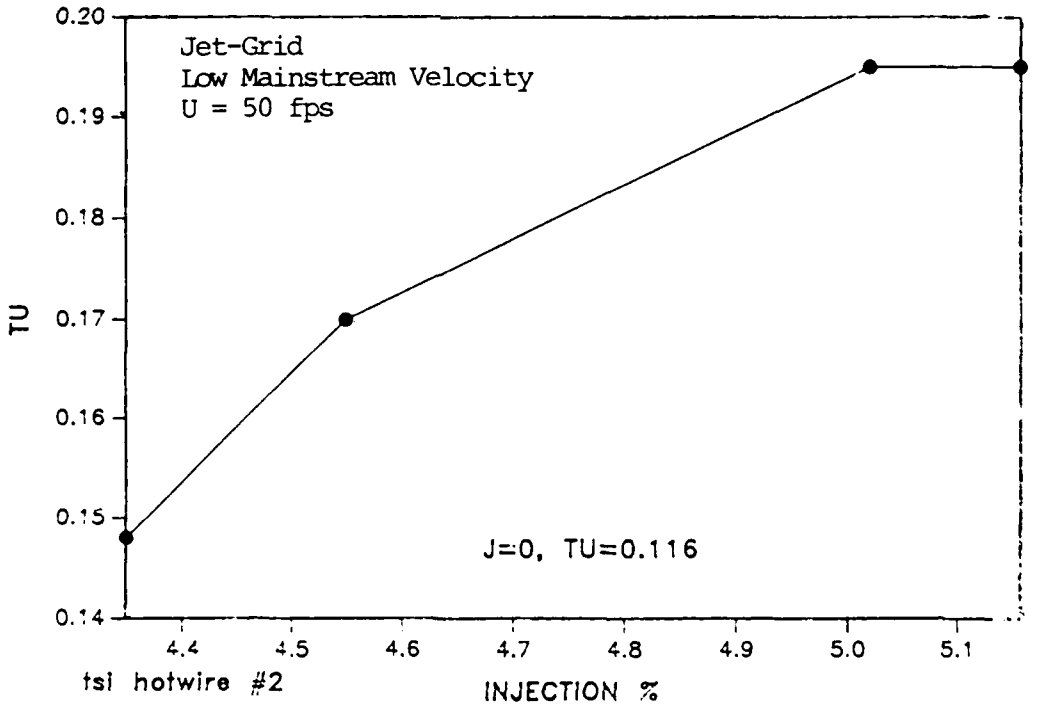

Figure 4. Turbulence Intensity vs Injection Ratio at X/b = 20.

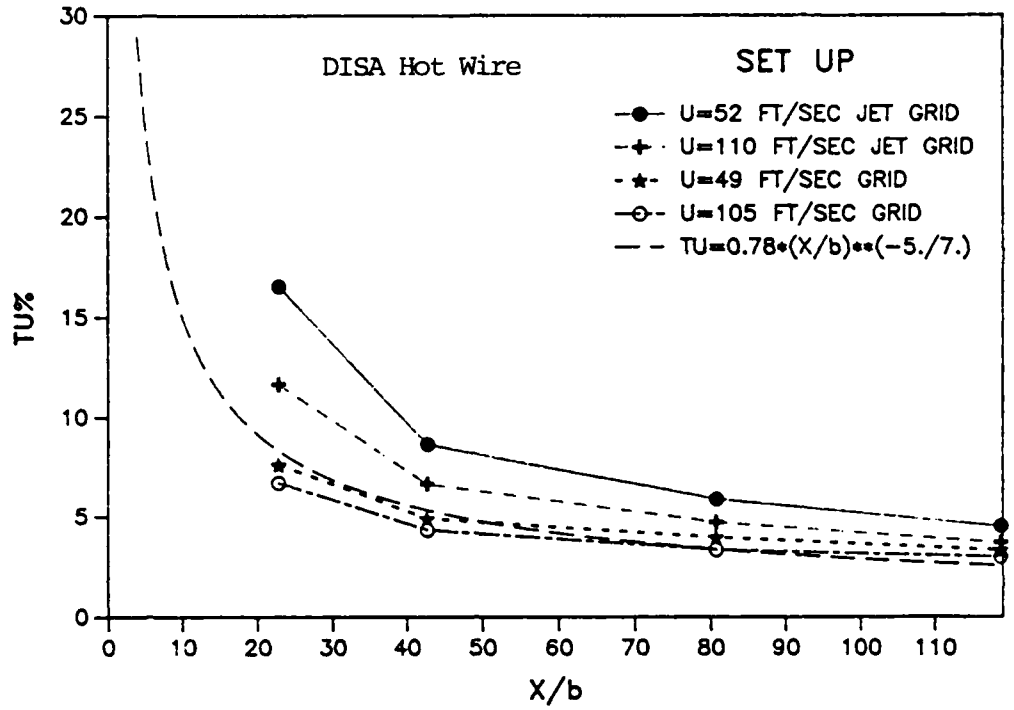

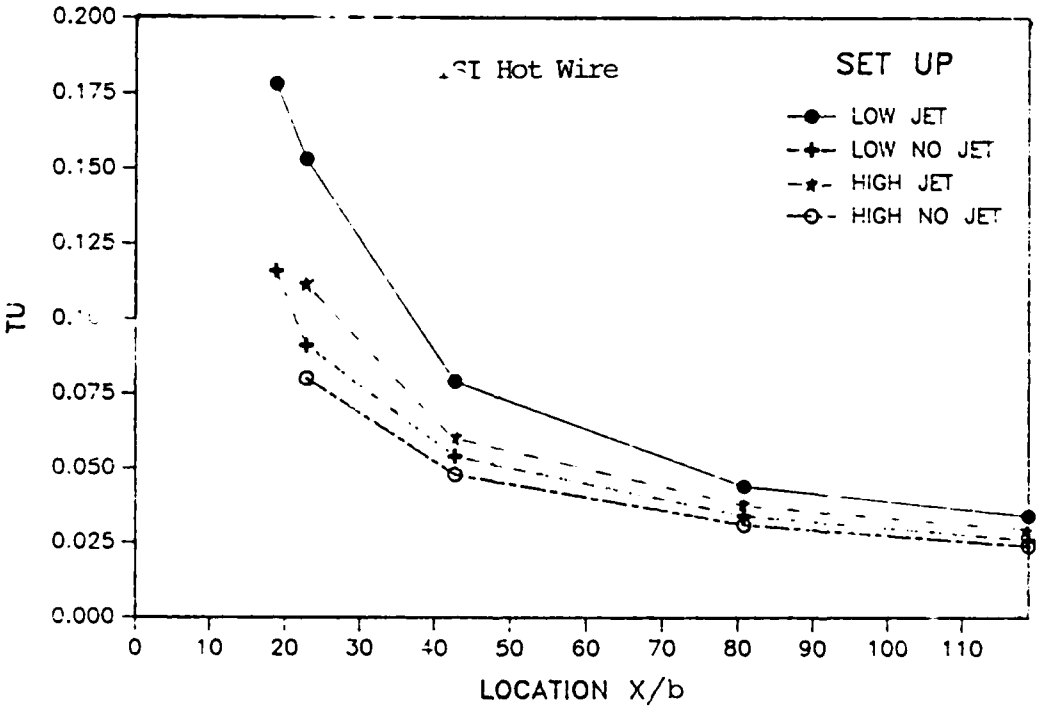

Figure 5. Turbulence Intensity Decay Rate.

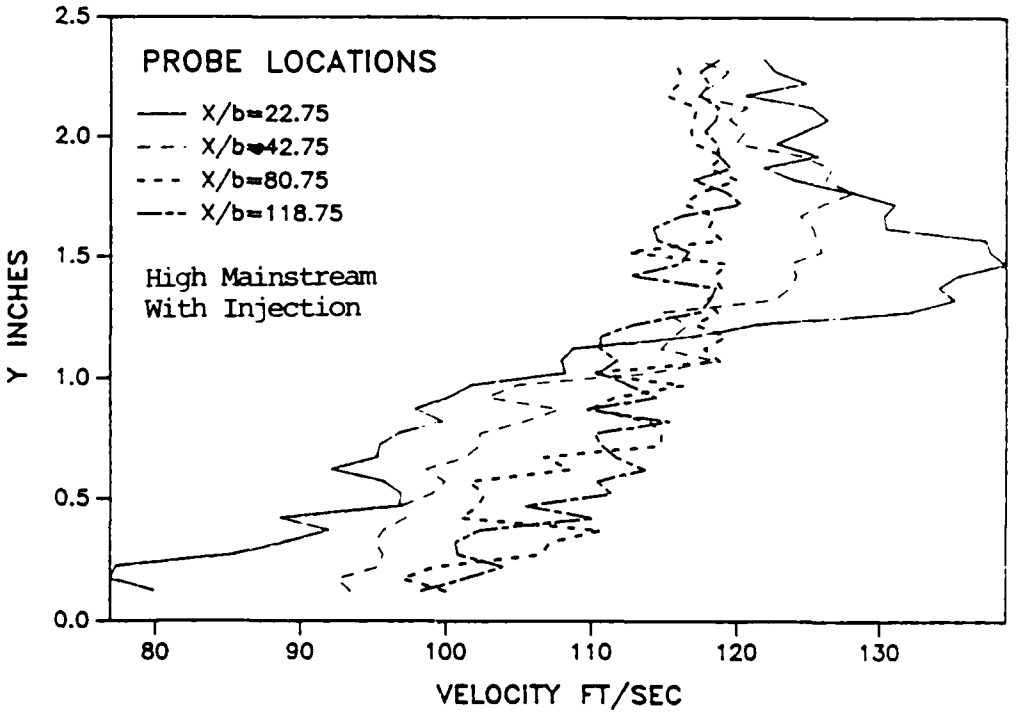

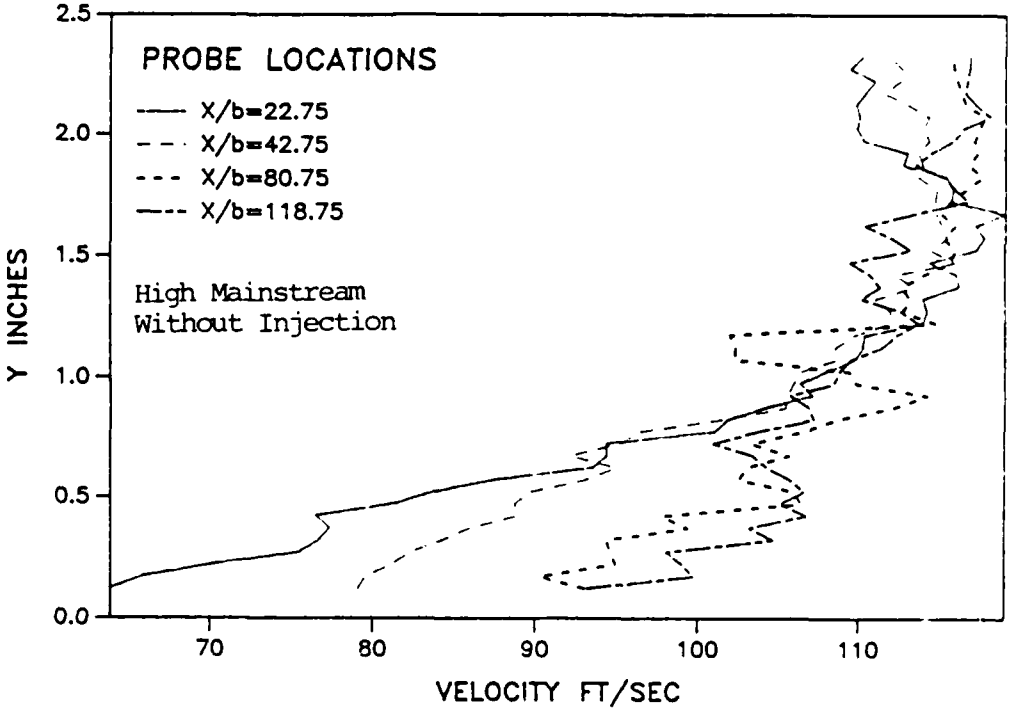

Figure 6. Boundary Layer Velocity Profiles at Four Axial Locations.

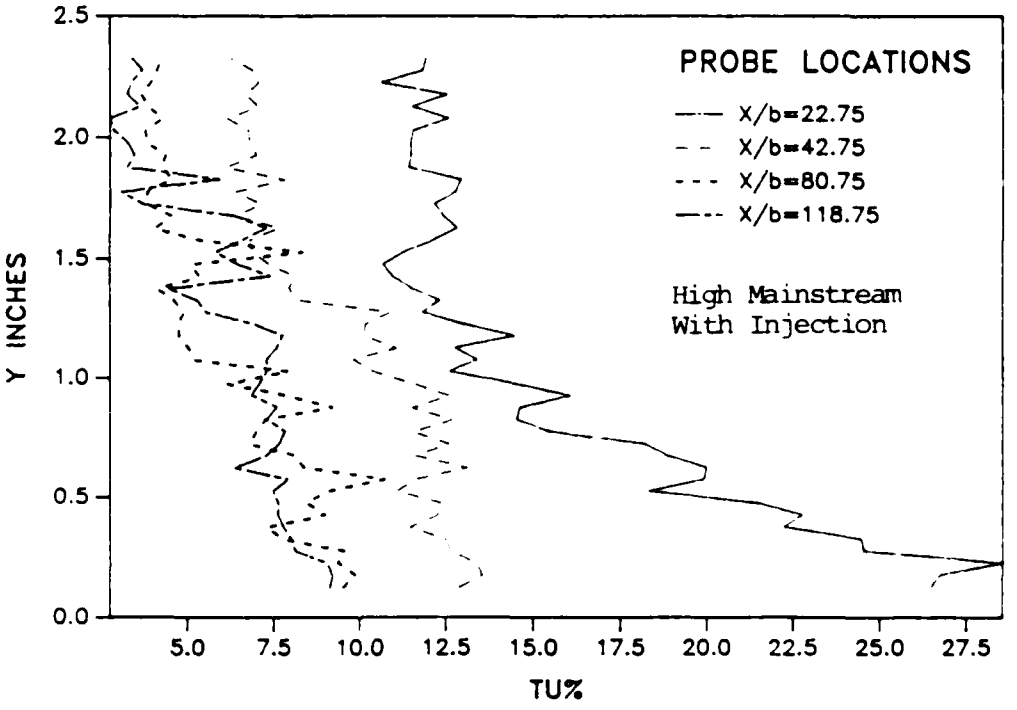

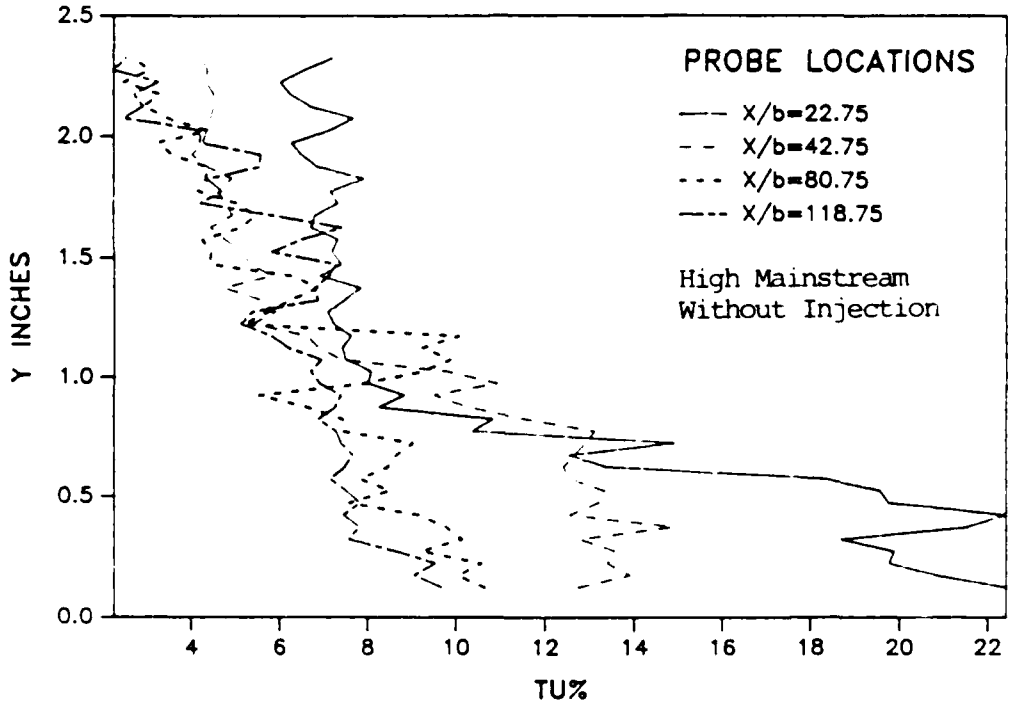

Figure 7. Boundary Layer Turbulence Intensity Profiles at Four Axial Locations.

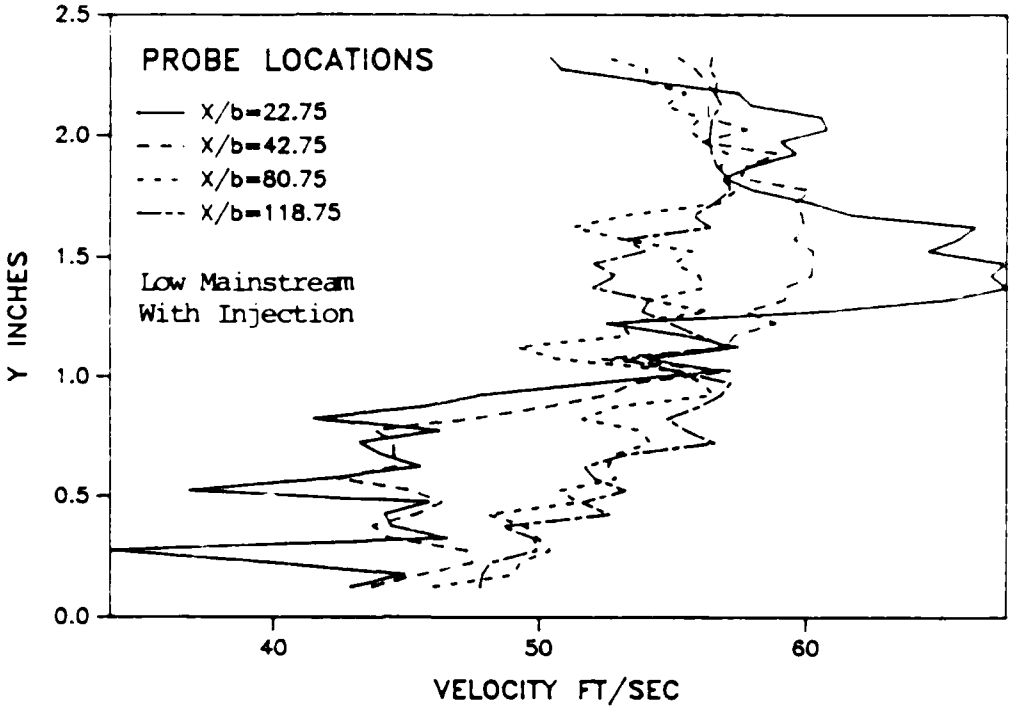

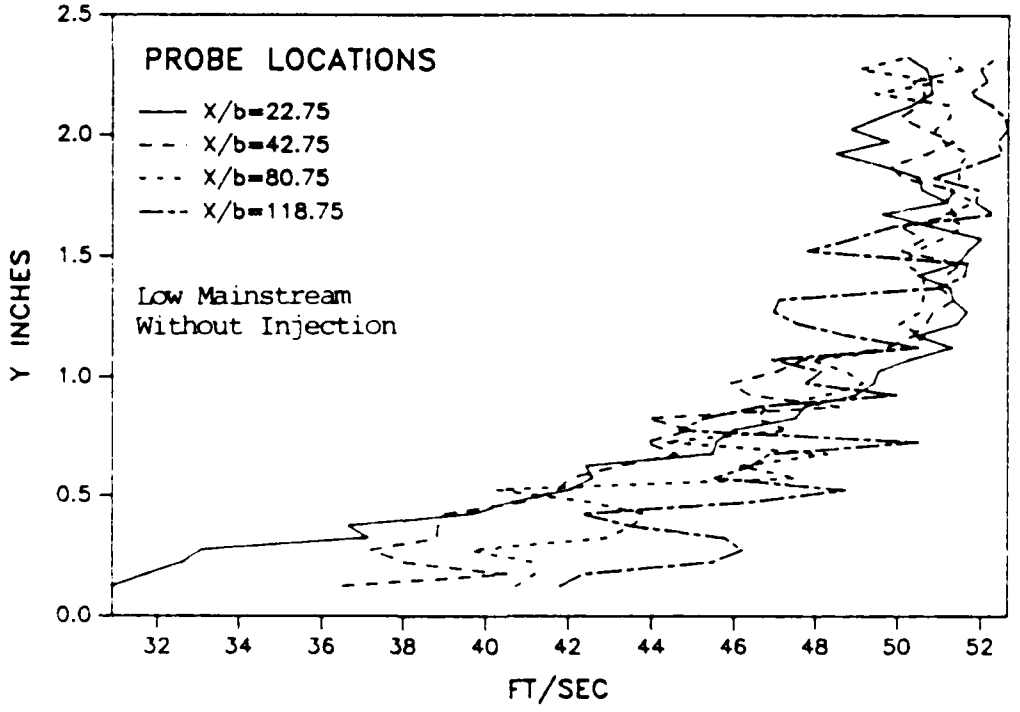

Figure 8. Boundary Layer Velocity Profiles at Four Axial Locations.

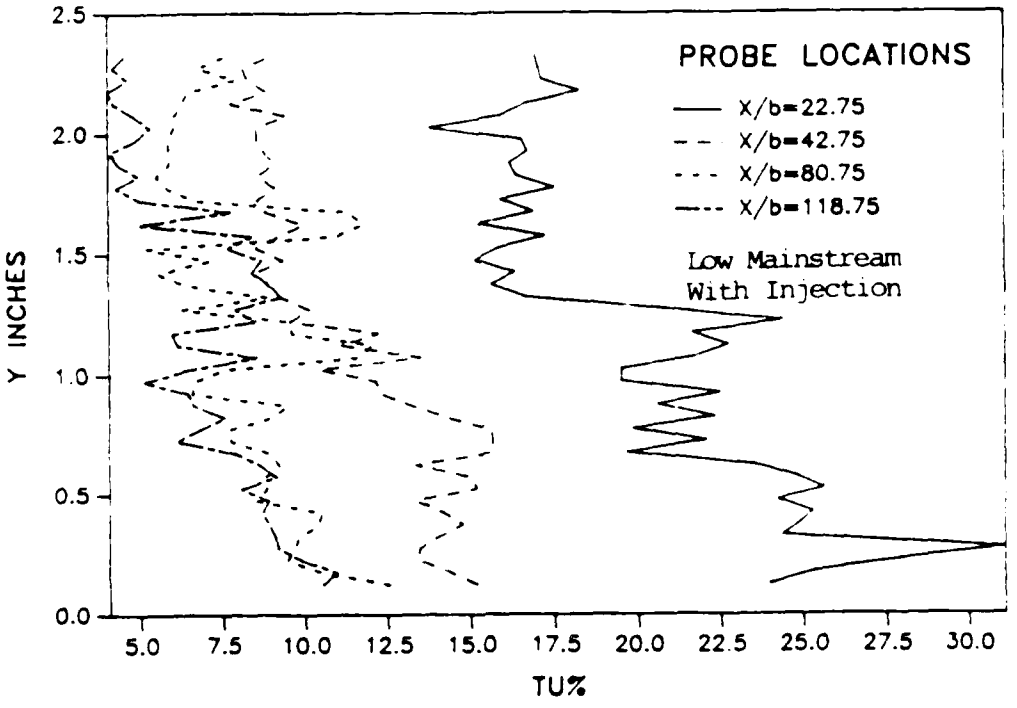

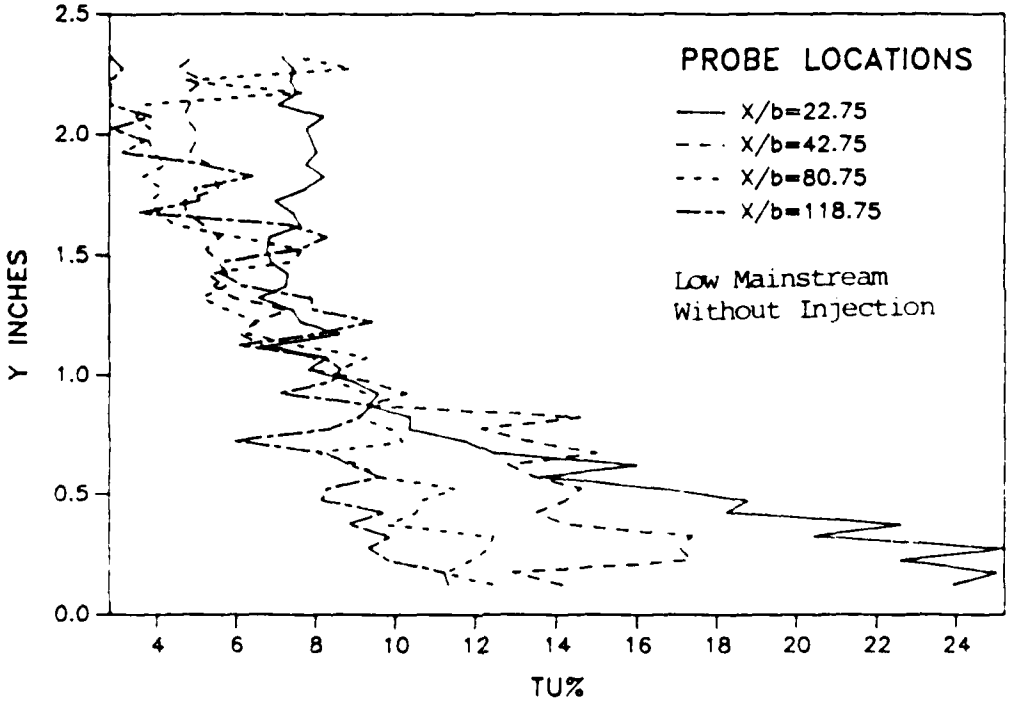

Figure 9. Boundary Layer Turbulence Intensity Profiles at Four Axial Locations.

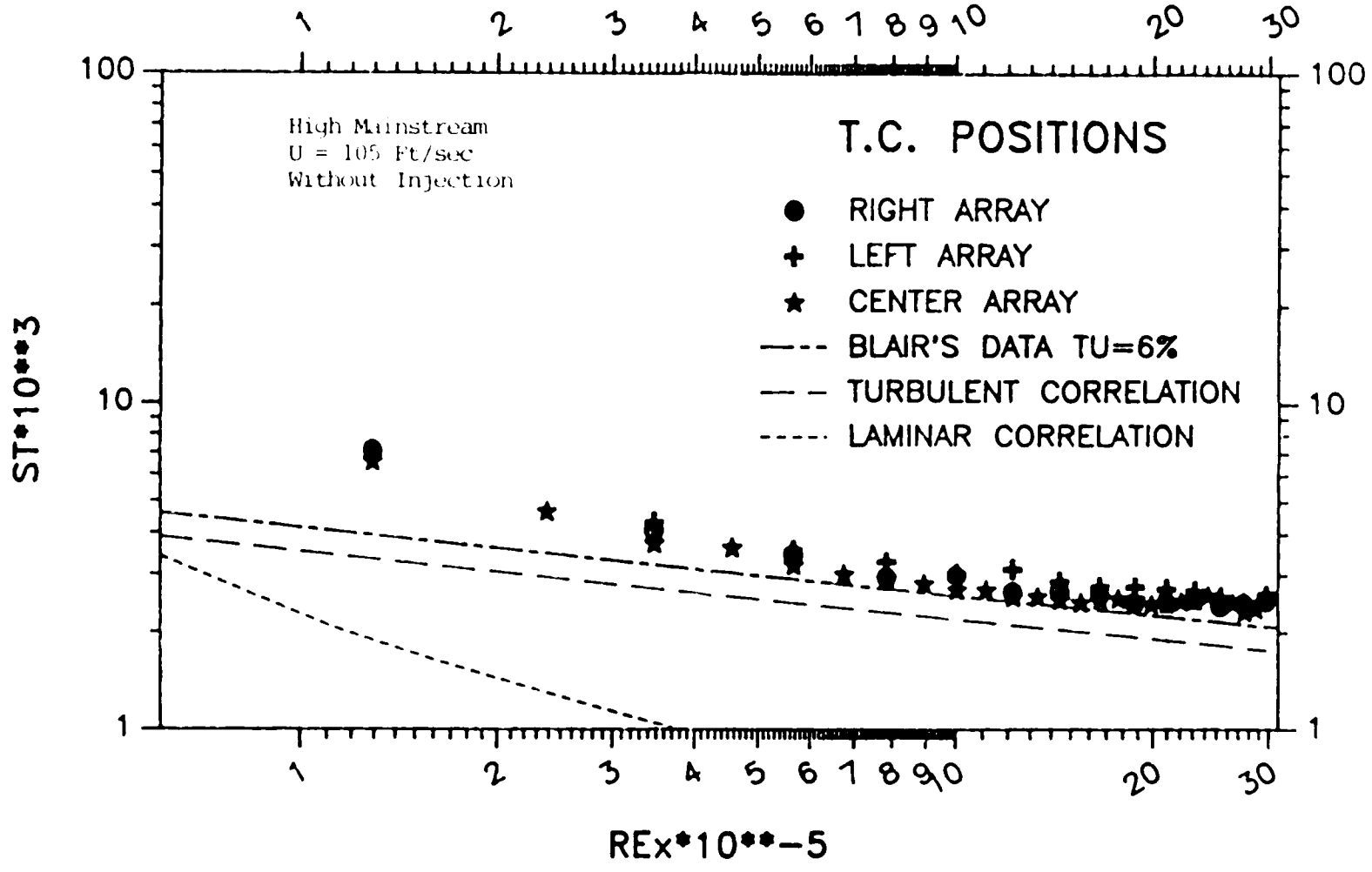

Figure 10. Spanwise Stanton Number vs Reynolds Number and Comparison With Previous Investigations for the Case of High Mainstream Velocity Without Injection.

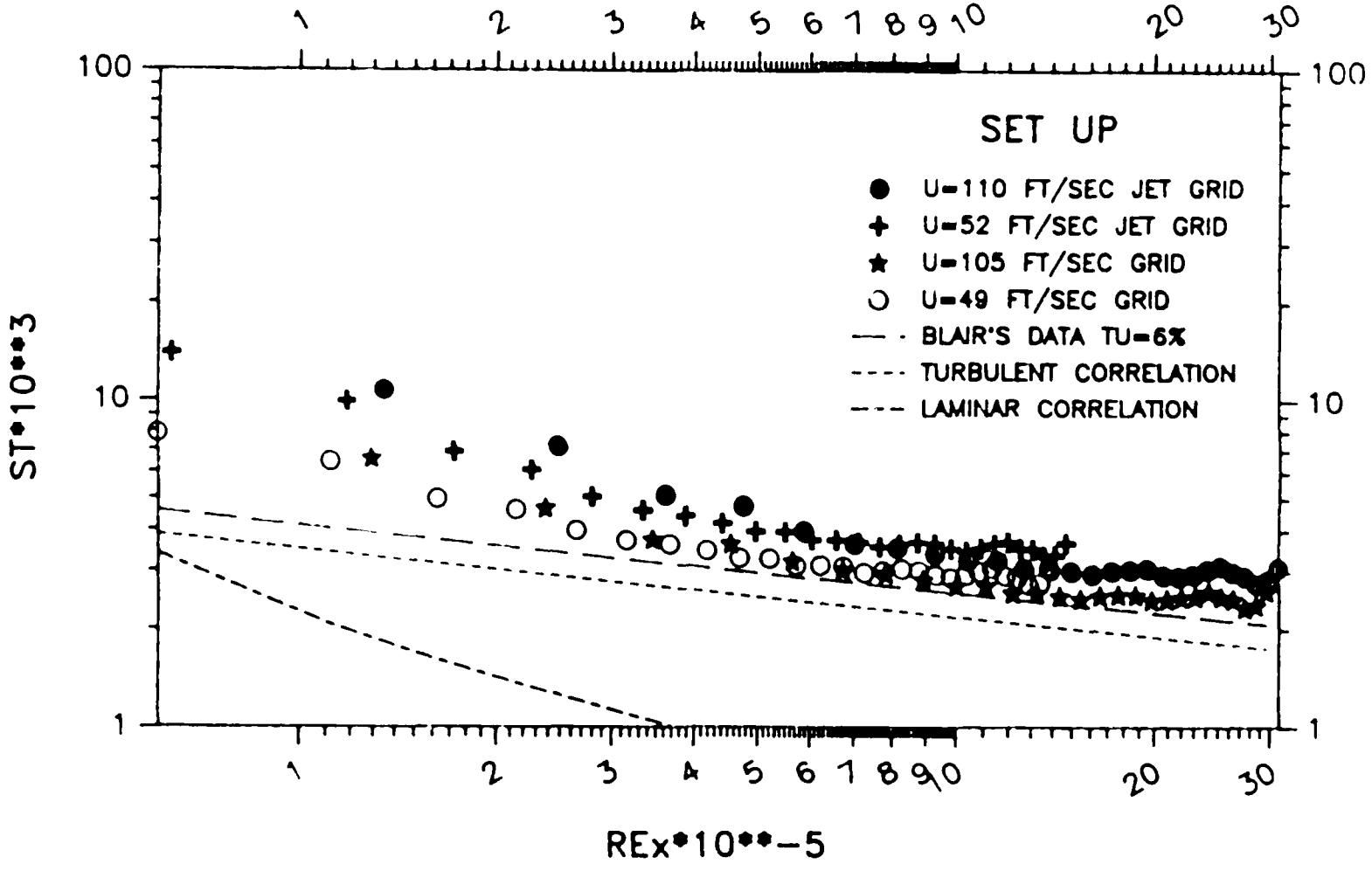

Figure [illegible] Turbulence Intensity (Produced by Jet-Grid) on the St- [illegible]

Appendix

1. Fluid Flow Data
2. Heat Transfer Data

FLUID FLOW DATA
U=110. FT/SEC JET GRID X/b= 22.75

NO	Y	VEL	TU%
1	0.125	79.868	26.474
2	0.175	76.816	26.715
3	0.225	77.233	28.539
4	0.275	85.447	24.514
5	0.325	88.928	24.446
6	0.375	91.968	22.222
7	0.425	88.560	22.754
8	0.475	96.823	21.449
9	0.525	96.898	18.287
10	0.575	95.728	19.918
11	0.625	92.116	19.975
12	0.675	95.297	18.832
13	0.725	95.426	18.163
14	0.775	96.749	15.486
15	0.825	99.761	14.518
16	0.875	97.873	14.594
17	0.925	100.209	16.049
18	0.975	101.761	14.455
19	1.025	108.212	12.585
20	1.075	107.964	13.378
21	1.125	108.735	12.730
22	1.175	116.990	14.456
23	1.225	121.399	12.994
24	1.275	132.099	11.804
25	1.325	135.261	12.303
26	1.375	134.156	11.488
27	1.425	135.482	10.946
28	1.475	138.784	10.663
29	1.525	137.697	11.249
30	1.575	137.402	12.130
31	1.625	130.437	12.787
32	1.675	130.243	12.335
33	1.725	131.[illegible]	12.144
34	1.775	128.[illegible]	12.[illegible]
35	1.825	124.313	12.924
36	1.875	121.889	11.411
37	1.925	125.[illegible]00	11.474
38	1.975	122.741	11.473
39	2.025	124.[illegible]71	11.539
[illegible]	[illegible]	[illegible]	[illegible]
41	2.125	126.256	11.511
42	2.175	120.547	12.521
43	2.225	124.795	10.620
44	2.275	122.[illegible]92	11.831
45	2.325	121.871	11.911

FLUID FLOW DATA
U=110. FT/SEC JET GRID X/b= 42.75

NO	Y	VEL	TU%
1	0.125	93.392	12.880
2	0.175	92.486	13.540
3	0.225	95.435	13.357
4	0.275	95.641	12.612
5	0.325	95.134	12.465
6	0.375	95.697	11.423
7	0.425	97.207	12.247
8	0.475	96.944	12.367
9	0.525	99.053	11.061
10	0.575	99.899	11.592
11	0.625	98.608	13.104
12	0.675	101.322	11.605
13	0.725	102.331	12.585
14	0.775	102.329	11.532
15	0.825	105.358	12.671
16	0.875	107.778	11.506
17	0.925	102.820	12.596
18	0.975	104.854	11.560
19	1.025	113.960	10.404
20	1.075	118.629	9.798
21	1.125	114.769	11.057
22	1.175	115.591	10.134
23	1.225	116.610	10.146
24	1.275	114.739	10.886
25	1.325	122.605	8.146
26	1.375	123.716	7.938
27	1.425	124.144	8.079
28	1.475	123.698	7.364
29	1.525	125.917	6.872
30	1.575	125.536	6.792
31	1.625	125.302	7.[illegible]28
32	1.675	124.394	6.[illegible]46
33	1.725	126.[illegible]04	7.[illegible]11
34	1.775	128.[illegible]65	7.[illegible]41
35	1.825	126.[illegible]41	7.[illegible]11
36	1.875	126.535	7.[illegible]76
37	1.925	124.[illegible]24	7.[illegible]22
38	1.975	119.86[illegible]	7.[illegible]47
39	2.025	124.[illegible]99	7.[illegible]47
[illegible]	[illegible]	[illegible]	[illegible]
41	2.125	120.[illegible]74	7.[illegible]47
42	2.175	117.071	8.678
43	2.225	118.488	7.267
44	2.275	119.402	8.883
45	2.325	117.150	8.248

FLUID FLOW DATA
U=110. FT/SEC JET GRID X/b= 80.75

NO	Y	VEL	TU%
1	0.125	99.929	9.510
2	0.175	96.923	9.867
3	0.225	99.326	9.339
4	0.275	106.581	9.527
5	0.325	107.141	7.765
6	0.375	110.665	7.262
7	0.425	100.939	8.967
8	0.475	102.232	8.420
9	0.525	102.635	9.069
10	0.575	101.557	10.720
11	0.625	108.535	8.343
12	0.675	106.709	8.100
13	0.725	114.762	6.795
14	0.775	114.832	6.972
15	0.825	114.015	7.240
16	0.875	109.872	9.203
17	0.925	111.588	7.821
18	0.975	116.339	6.143
19	1.025	109.912	7.924
20	1.075	118.815	5.213
21	1.125	117.750	5.025
22	1.175	119.255	4.754
23	1.225	117.054	4.732
24	1.275	118.652	4.878
25	1.325	117.914	4.600
26	1.375	118.901	4.118
27	1.425	118.400	5.326
28	1.475	119.312	5.099
29	1.525	112.440	8.327
30	1.575	118.955	5.332
31	1.625	118.033	4.033
32	1.675	118.389	4.512
33	1.725	116.308	3.844
34	1.775	117.444	3.824
35	1.825	120.029	4.544
36	1.875	118.041	4.255
37	1.925	118.998	4.367
38	1.975	117.025	3.826
39	2.025	116.756	3.784
40	2.075	116.356	4.281
41	2.125	117.163	3.861
42	2.175	115.082	3.669
43	2.225	115.916	3.938
44	2.275	116.011	4.122
45	2.325	115.496	4.228

FLUID FLOW DATA
U=110. FT/SEC JET GRID X/b=118.75

NO	Y	VEL	TU%
1	0.125	98.321	9.138
2	0.175	101.224	9.196
3	0.225	103.909	9.036
4	0.275	100.802	8.111
5	0.325	100.641	8.000
6	0.375	102.341	7.768
7	0.425	110.119	7.616
8	0.475	105.450	7.617
9	0.525	111.361	7.469
10	0.575	110.364	7.905
11	0.625	113.702	6.343
12	0.675	111.663	7.266
13	0.725	110.662	7.660
14	0.775	110.231	7.824
15	0.825	115.368	7.277
16	0.875	109.675	7.587
17	0.925	114.446	6.854
18	0.975	112.625	7.085
19	1.025	110.481	7.298
20	1.075	111.763	7.300
21	1.125	110.583	7.591
22	1.175	110.608	7.762
23	1.225	112.872	6.872
24	1.275	117.446	5.534
25	1.325	118.147	5.281
26	1.375	118.544	4.414
27	1.425	112.602	7.394
28	1.475	116.096	6.430
29	1.525	116.691	5.804
30	1.575	114.477	6.589
31	1.625	114.195	7.262
32	1.675	116.119	6.334
33	1.725	120.302	3.733
34	1.775	119.227	3.203
35	1.825	117.000	5.319
36	1.875	119.593	3.263
37	1.925	118.784	3.485
38	1.975	118.588	3.301
39	2.025	117.772	2.928
40	2.075	118.525	2.783
41	2.125	118.694	3.647
42	2.175	117.406	3.285
43	2.225	118.053	3.387
44	2.275	117.446	3.711
45	2.325	118.744	3.405

FLUID FLOW DATA
U=105. FT/SEC GRID X/b= 22.75

NO	Y	VEL	TU%
1	0.125	63.758	22.412
2	0.175	65.799	20.819
3	0.225	70.217	19.759
4	0.275	75.487	19.872
5	0.325	76.707	18.671
6	0.375	77.334	21.510
7	0.425	76.494	22.408
8	0.475	81.350	19.743
9	0.525	83.791	19.557
10	0.575	87.528	18.283
11	0.625	93.562	13.364
12	0.675	94.398	12.524
13	0.725	94.360	14.913
14	0.775	101.021	10.374
15	0.825	101.800	10.822
16	0.875	104.098	8.249
17	0.925	107.118	8.838
18	0.975	106.348	8.004
19	1.025	107.916	8.074
20	1.075	109.741	7.496
21	1.125	110.269	7.418
22	1.175	110.367	7.613
23	1.225	114.039	7.218
24	1.275	114.292	7.087
25	1.325	114.010	7.469
26	1.375	116.286	7.833
27	1.425	116.110	6.906
28	1.475	114.427	7.397
29	1.525	117.372	7.188
30	1.575	117.810	7.316
31	1.625	117.307	6.707
32	1.675	119.094	6.743
33	1.725	115.777	7.315
34	1.775	115.894	7.145
35	1.825	115.496	7.910
36	1.875	112.759	6.840
37	1.925	113.043	6.491
38	1.975	110.257	6.285
39	2.025	109.851	7.144
40	2.075	110.017	7.683
41	2.125	109.801	6.698
42	2.175	110.394	6.246
43	2.225	110.978	6.026
44	2.275	109.424	6.571
45	2.325	110.186	7.213

FLUID FLOW DATA
U=105. FT/SEC GRID X/b= 42.75

NO	Y	VEL	TU%
1	0.125	79.042	12.736
2	0.175	79.469	13.905
3	0.225	81.094	13.388
4	0.275	82.281	13.560
5	0.325	84.222	12.765
6	0.375	85.936	14.877
7	0.425	88.859	12.538
8	0.475	88.702	13.202
9	0.525	89.694	13.333
10	0.575	93.059	12.523
11	0.625	94.924	12.407
12	0.675	92.087	12.660
13	0.725	95.175	12.900
14	0.775	96.267	13.117
15	0.825	101.254	11.562
16	0.875	105.407	10.265
17	0.925	105.534	9.502
18	0.975	105.896	10.917
19	1.025	106.379	9.776
20	1.075	108.515	7.386
21	1.125	108.515	6.864
22	1.175	109.649	6.603
23	1.225	111.858	5.383
24	1.275	112.000	5.892
25	1.325	110.973	5.548
26	1.375	113.425	4.719
27	1.425	112.287	5.829
28	1.475	116.015	5.331
29	1.525	114.504	5.120
30	1.575	115.492	4.756
31	1.625	115.184	4.429
32	1.675	114.810	4.928
33	1.725	114.765	4.725
34	1.775	114.857	4.637
35	1.825	113.728	4.929
36	1.875	113.990	4.357
37	1.925	113.689	4.025
38	1.975	114.381	4.283
39	2.025	114.031	4.375
40	2.075	114.362	4.453
41	2.125	113.097	4.524
42	2.175	111.523	4.520
43	2.225	112.552	4.355
44	2.275	112.716	4.373
45	2.325	111.940	4.249

FLUID FLOW DATA
U=105. FT/SEC GRID X/b= 80.75

NO	Y	VEL	TU%
1	0.125	92.938	10.639
2	0.175	90.177	10.036
3	0.225	94.878	10.567
4	0.275	94.558	9.204
5	0.325	94.308	10.131
6	0.375	99.335	9.779
7	0.425	97.734	9.147
8	0.475	106.415	7.568
9	0.525	105.994	8.513
10	0.575	102.508	7.811
11	0.625	102.995	8.466
12	0.675	105.657	8.656
13	0.725	103.298	9.033
14	0.775	106.480	7.442
15	0.825	108.632	7.433
16	0.875	112.184	6.644
17	0.925	114.329	5.526
18	0.975	109.845	7.896
19	1.025	109.400	9.228
20	1.075	102.215	9.867
21	1.125	102.243	9.236
22	1.175	101.914	10.063
23	1.225	114.803	5.168
24	1.275	112.766	5.724
25	1.325	113.198	6.238
26	1.375	112.725	6.839
27	1.425	114.102	6.324
28	1.475	115.774	4.410
29	1.525	116.045	4.449
30	1.575	115.347	4.243
31	1.625	116.021	5.123
32	1.675	115.156	5.451
33	1.725	115.722	5.021
34	1.775	116.727	4.160
35	1.825	117.701	4.342
36	1.875	116.889	4.377
37	1.925	117.403	3.567
38	1.975	117.217	3.267
39	2.025	117.524	4.390
40	2.075	117.863	3.475
41	2.125	116.667	2.939
42	2.175	116.396	3.296
43	2.225	116.163	2.501
44	2.275	115.962	3.074
45	2.325	115.846	2.728

FLUID FLOW DATA
U=105. FT/SEC GRID X/b=118.75

NO	Y	VEL	TU%
1	0.125	93.159	9.681
2	0.175	99.665	9.053
3	0.225	98.971	9.530
4	0.275	97.970	8.632
5	0.325	104.644	7.567
6	0.375	103.182	7.811
7	0.425	106.730	7.444
8	0.475	105.076	7.826
9	0.525	106.585	7.504
10	0.575	105.705	7.141
11	0.625	104.259	7.481
12	0.675	103.371	7.666
13	0.725	100.907	7.391
14	0.775	103.675	7.277
15	0.825	107.171	6.871
16	0.875	106.859	7.255
17	0.925	105.699	7.399
18	0.975	108.449	6.896
19	1.025	108.794	6.695
20	1.075	109.490	6.935
21	1.125	111.449	6.183
22	1.175	112.370	5.808
23	1.225	113.750	5.105
24	1.275	112.607	5.360
25	1.325	110.135	6.873
26	1.375	111.317	6.785
27	1.425	110.665	7.116
28	1.475	109.407	7.277
29	1.525	113.288	5.812
30	1.575	112.001	6.473
31	1.625	110.332	7.404
32	1.675	113.385	5.841
33	1.725	116.840	4.217
34	1.775	116.023	4.689
35	1.825	115.364	4.378
36	1.875	113.527	5.552
37	1.925	114.550	5.586
38	1.975	115.937	4.202
39	2.025	116.532	4.231
40	2.075	118.157	2.496
41	2.125	117.289	2.934
42	2.175	116.643	2.726
43	2.225	116.752	3.269
44	2.275	116.895	2.281
45	2.325	116.943	2.567

FLUID FLOW DATA
U= 52. FT/SEC JET GRID X/b= 22.75

NO	Y	VEL	TU%
1	0.125	42.891	23.981
2	0.175	44.940	25.307
3	0.225	39.772	27.954
4	0.275	33.813	31.100
5	0.325	46.577	24.380
6	0.375	44.439	24.885
7	0.425	44.192	25.290
8	0.475	45.869	24.219
9	0.525	36.797	25.623
10	0.575	41.926	24.793
11	0.625	45.547	23.499
12	0.675	44.050	19.651
13	0.725	43.223	22.074
14	0.775	46.273	19.832
15	0.825	41.455	22.318
16	0.875	45.709	20.589
17	0.925	47.842	22.513
18	0.975	52.156	19.485
19	1.025	56.683	19.506
20	1.075	54.025	21.760
21	1.125	57.430	22.737
22	1.175	55.359	21.628
23	1.225	52.456	24.399
24	1.275	60.600	20.773
25	1.325	65.322	16.632
26	1.375	67.499	15.641
27	1.425	66.919	16.360
28	1.475	67.421	15.176
29	1.525	64.569	15.868
30	1.575	65.702	17.246
31	1.625	66.319	15.258
32	1.675	61.697	16.925
33	1.725	60.124	15.934
34	1.775	57.976	17.552
35	1.825	56.851	16.403
36	1.875	57.933	16.196
37	1.925	59.608	16.747
38	1.975	59.006	16.579
39	2.025	60.777	13.811
40	2.075	60.560	15.979
41	2.125	57.876	16.733
42	2.175	57.388	18.296
43	2.225	53.958	17.180
44	2.275	50.791	17.084
45	2.325	50.399	16.983

FLUID FLOW DATA
U= 52. FT/SEC JET GRID X/b= 42.75

NO	Y	VEL	TU%
1	0.125	43.718	15.177
2	0.175	45.609	14.391
3	0.225	47.522	13.424
4	0.275	47.281	13.462
5	0.325	44.356	14.093
6	0.375	43.723	14.786
7	0.425	45.430	14.174
8	0.475	46.357	13.345
9	0.525	45.146	15.187
10	0.575	42.448	15.027
11	0.625	44.663	13.344
12	0.675	44.533	15.686
13	0.725	44.533	15.677
14	0.775	43.806	15.637
15	0.825	47.479	14.260
16	0.875	50.270	13.247
17	0.925	52.556	12.285
18	0.975	53.523	12.157
19	1.025	57.138	10.440
20	1.075	52.340	13.531
21	1.125	56.972	11.090
22	1.175	57.287	12.226
23	1.225	58.864	9.574
24	1.275	57.722	10.158
25	1.325	59.222	9.279
26	1.375	59.219	8.902
27	1.425	60.205	8.534
28	1.475	60.267	9.380
29	1.525	60.277	8.529
30	1.575	59.538	9.225
31	1.625	59.924	9.398
32	1.675	59.845	8.841
33	1.725	59.582	8.593
34	1.775	60.177	9.132
35	1.825	57.483	8.612
36	1.875	57.722	9.109
37	1.925	58.917	8.811
38	1.975	56.042	8.582
39	2.025	57.749	8.555
40	2.075	56.303	9.482
41	2.125	56.260	9.284
42	2.175	56.559	8.856
43	2.225	56.171	8.309
44	2.275	55.800	8.165
45	2.325	55.134	9.044

FLUID FLOW DATA
U= 52. FT/SEC JET GRID X/b= 80.75

NO	Y	VEL	TU%
1	0.125	46.025	12.526
2	0.175	49.058	10.477
3	0.225	49.288	9.455
4	0.275	50.406	9.644
5	0.325	49.947	9.830
6	0.375	49.506	10.400
7	0.425	48.067	10.502
8	0.475	51.480	8.494
9	0.525	50.759	8.826
10	0.575	52.864	8.783
11	0.625	52.569	9.212
12	0.675	52.757	8.933
13	0.725	54.114	7.741
14	0.775	53.839	7.686
15	0.825	51.597	9.011
16	0.875	52.788	9.471
17	0.925	56.505	6.585
18	0.975	56.050	6.611
19	1.025	55.206	7.535
20	1.075	50.686	11.664
21	1.125	49.163	12.051
22	1.175	53.380	9.613
23	1.225	53.022	9.516
24	1.275	56.303	6.263
25	1.325	54.057	8.872
26	1.375	56.154	6.379
27	1.425	55.948	5.571
28	1.475	55.009	7.114
29	1.525	55.687	5.215
30	1.575	53.099	10.951
31	1.625	51.244	11.805
32	1.675	53.227	11.323
33	1.725	56.767	6.638
34	1.775	57.305	5.860
35	1.825	56.766	5.500
36	1.875	56.763	5.876
37	1.925	57.023	5.900
38	1.975	56.080	5.859
39	2.025	55.553	6.031
40	2.075	56.007	6.058
41	2.125	54.640	6.298
42	2.175	55.430	6.467
43	2.225	53.913	7.952
44	2.275	53.988	6.778
45	2.325	52.449	7.628

FLUID FLOW DATA
U= 52. FT/SEC JET GRID X/b=118.75

NO	Y	VEL	TU%
1	0.125	47.780	10.534
2	0.175	47.859	10.962
3	0.225	48.168	9.896
4	0.275	49.893	9.179
5	0.325	49.828	9.101
6	0.375	48.633	8.906
7	0.425	52.623	8.707
8	0.475	51.610	8.889
9	0.525	53.227	8.039
10	0.575	52.082	9.140
11	0.625	51.703	8.624
12	0.675	53.134	7.891
13	0.725	56.527	6.087
14	0.775	55.501	6.805
15	0.825	54.741	7.569
16	0.875	55.936	6.625
17	0.925	56.787	6.442
18	0.975	57.132	5.113
19	1.025	55.032	6.494
20	1.075	53.130	8.567
21	1.125	57.034	6.142
22	1.175	55.917	5.958
23	1.225	54.863	8.524
24	1.275	53.825	7.892
25	1.325	54.090	9.299
26	1.375	51.980	8.978
27	1.425	52.835	8.426
28	1.475	52.020	8.720
29	1.525	53.923	7.673
30	1.575	53.250	8.393
31	1.625	56.365	4.950
32	1.675	55.717	7.752
33	1.725	56.523	5.046
34	1.775	57.091	4.297
35	1.825	57.052	4.991
36	1.875	56.601	4.331
37	1.925	56.423	4.140
38	1.975	56.326	4.882
39	2.025	56.373	5.322
40	2.075	56.437	4.867
41	2.125	56.273	4.248
42	2.175	56.554	4.053
43	2.225	56.507	4.665
44	2.275	56.348	4.215
45	2.325	56.413	4.573

FLUID FLOW DATA
U= 49. FT/SEC GRID X/b= 22.75

NO	Y	VEL	TU%
1	0.125	30.888	23.932
2	0.175	31.762	25.019
3	0.225	32.646	22.575
4	0.275	33.096	25.209
5	0.325	37.131	20.424
6	0.375	36.653	22.614
7	0.425	39.659	18.227
8	0.475	40.685	18.768
9	0.525	42.048	16.558
10	0.575	42.596	13.631
11	0.625	42.435	15.991
12	0.675	45.490	12.449
13	0.725	45.576	11.755
14	0.775	45.977	10.340
15	0.825	47.517	10.384
16	0.875	47.750	9.339
17	0.925	49.000	9.572
18	0.975	49.434	8.918
19	1.025	49.542	7.802
20	1.075	50.304	8.282
21	1.125	51.319	6.800
22	1.175	50.449	8.609
23	1.225	51.436	7.619
24	1.275	51.666	7.431
25	1.325	51.333	6.567
26	1.375	51.257	7.274
27	1.425	50.470	7.312
28	1.475	51.455	6.878
29	1.525	51.693	6.796
30	1.575	52.005	6.842
31	1.625	50.805	7.633
32	1.675	49.612	7.443
33	1.725	51.189	6.980
34	1.775	50.575	7.735
35	1.825	50.513	8.205
36	1.875	49.568	7.772
37	1.925	48.474	8.030
38	1.975	49.764	7.907
39	2.025	48.853	7.766
40	2.075	49.564	8.194
41	2.125	50.336	7.045
42	2.175	50.826	7.534
43	2.225	50.737	7.382
44	2.275	50.689	7.449
45	2.325	50.234	7.153

FLUID FLOW DATA
U= 49. FT/SEC GRID X/b= 42.75

NO	Y	VEL	TU%
1	0.125	36.524	14.138
2	0.175	40.523	12.916
3	0.225	38.000	17.369
4	0.275	37.201	17.065
5	0.325	38.834	17.386
6	0.375	38.851	14.225
7	0.425	39.018	13.497
8	0.475	40.923	14.239
9	0.525	41.766	14.614
10	0.575	42.059	13.438
11	0.625	43.227	12.798
12	0.675	44.624	14.988
13	0.725	43.850	13.268
14	0.775	44.985	12.136
15	0.825	43.896	14.598
16	0.875	48.597	9.299
17	0.925	46.393	10.286
18	0.975	45.904	9.319
19	1.025	47.052	7.855
20	1.075	47.698	7.982
21	1.125	49.733	6.591
22	1.175	50.367	6.100
23	1.225	50.682	6.520
24	1.275	50.857	7.300
25	1.325	51.370	5.922
26	1.375	51.038	5.438
27	1.425	51.152	5.774
28	1.475	51.546	5.543
29	1.525	50.071	5.242
30	1.575	50.645	5.584
31	1.625	50.041	5.171
32	1.675	51.418	4.737
33	1.725	51.135	4.682
34	1.775	51.387	5.544
35	1.825	50.097	5.441
36	1.875	49.843	5.302
37	1.925	50.709	4.843
38	1.975	51.352	4.996
39	2.025	50.671	4.951
40	2.075	50.058	4.663
41	2.125	50.513	4.812
42	2.175	50.651	4.785
43	2.225	50.354	5.154
44	2.275	51.549	4.544
45	2.325	51.245	4.408

FLUID FLOW DATA
U= 49. FT/SEC GRID X/b= 80.75

NO	Y	VEL	TU%
1	0.125	40.721	12.425
2	0.175	41.186	11.263
3	0.225	41.112	11.869
4	0.275	39.620	12.367
5	0.325	42.885	12.452
6	0.375	43.538	9.793
7	0.425	43.832	10.531
8	0.475	42.501	10.691
9	0.525	40.245	11.510
10	0.575	47.564	9.616
11	0.625	46.134	9.124
12	0.675	48.296	8.049
13	0.725	44.279	10.182
14	0.775	47.333	9.932
15	0.825	46.555	9.059
16	0.875	46.814	9.425
17	0.925	48.243	9.271
18	0.975	49.161	8.485
19	1.025	48.753	8.587
20	1.075	47.864	9.282
21	1.125	50.226	7.601
22	1.175	50.651	6.259
23	1.225	50.023	6.518
24	1.275	50.522	5.761
25	1.325	50.607	5.110
26	1.375	50.620	5.748
27	1.425	50.621	5.275
28	1.475	50.159	7.435
29	1.525	50.400	7.662
30	1.575	51.047	6.050
31	1.625	51.576	4.448
32	1.675	51.127	4.063
33	1.725	51.832	3.861
34	1.775	51.256	4.153
35	1.825	51.470	3.655
36	1.875	51.458	4.250
37	1.925	51.699	3.930
38	1.975	51.115	3.802
39	2.025	50.880	3.824
40	2.075	51.243	3.477
41	2.125	51.273	3.605
42	2.175	49.424	7.643
43	2.225	51.042	4.659
44	2.275	49.038	8.903
45	2.325	50.171	7.508

FLUID FLOW DATA
U= 49. FT/SEC GRID X/b=118.75

NO	Y	VEL	TU%
1	0.125	41.792	11.336
2	0.175	42.365	11.228
3	0.225	45.485	9.833
4	0.275	46.215	9.326
5	0.325	45.793	9.874
6	0.375	43.515	8.816
7	0.425	42.327	9.722
8	0.475	46.432	8.151
9	0.525	48.739	8.289
10	0.575	45.505	9.634
11	0.625	46.417	8.850
12	0.675	46.886	8.232
13	0.725	50.520	5.926
14	0.775	44.679	8.343
15	0.825	45.279	9.127
16	0.875	46.607	9.391
17	0.925	49.979	7.106
18	0.975	47.751	8.413
19	1.025	48.138	8.612
20	1.075	46.922	8.222
21	1.125	50.503	6.055
22	1.175	48.856	8.055
23	1.225	47.563	9.431
24	1.275	46.970	7.918
25	1.325	47.090	7.880
26	1.375	50.998	6.169
27	1.425	51.620	5.634
28	1.475	51.679	5.709
29	1.525	47.780	7.594
30	1.575	48.915	8.296
31	1.625	49.875	7.381
32	1.675	52.306	3.570
33	1.725	51.880	5.064
34	1.775	51.942	4.959
35	1.825	50.847	6.420
36	1.875	51.758	5.134
37	1.925	52.509	3.140
38	1.975	52.405	3.710
39	2.025	52.648	2.854
40	2.075	52.566	3.848
41	2.125	52.256	2.814
42	2.175	51.735	2.825
43	2.225	52.151	2.872
44	2.275	51.443	3.447
45	2.325	52.376	2.851

HEAT TRANSFER DATA:
U=110 FT/SEC JET GRID

NO	X	H	Rex	ST
1	2.44	0.763554E+02	0.134664E+06	0.107559E-01
2	4.50	0.511811E+02	0.248611E+06	0.720969E-02
3	6.56	0.363630E+02	0.362558E+06	0.512232E-02
4	8.63	0.336780E+02	0.476505E+06	0.474409E-02
5	10.69	0.282768E+02	0.590452E+06	0.398325E-02
6	12.75	0.257917E+02	0.704399E+06	0.363319E-02
7	14.81	0.250958E+02	0.818346E+06	0.353516E-02
8	16.88	0.240766E+02	0.932292E+06	0.339158E-02
9	18.94	0.229545E+02	0.104624E+07	0.323352E-02
10	21.00	0.229853E+02	0.116019E+07	0.323786E-02
11	23.06	0.217399E+02	0.127413E+07	0.306243E-02
12	25.13	0.218041E+02	0.138808E+07	0.307147E-02
13	27.19	0.213468E+02	0.150203E+07	0.300705E-02
14	29.25	0.208881E+02	0.161597E+07	0.294242E-02
15	31.31	0.213521E+02	0.172992E+07	0.300779E-02
16	33.38	0.215049E+02	0.184387E+07	0.302932E-02
17	35.44	0.216975E+02	0.195781E+07	0.305645E-02
18	37.50	0.207101E+02	0.207176E+07	0.291736E-02
19	39.56	0.205311E+02	0.218571E+07	0.289215E-02
20	41.63	0.208480E+02	0.229965E+07	0.293678E-02
21	43.69	0.215892E+02	0.241360E+07	0.304119E-02
22	45.75	0.221456E+02	0.252755E+07	0.311957E-02
23	47.81	0.211794E+02	0.264150E+07	0.298347E-02
24	49.88	0.205743E+02	0.275544E+07	0.289823E-02
25	51.94	0.195408E+02	0.286939E+07	0.275264E-02
26	54.00	0.200233E+02	0.298334E+07	0.282061E-02
27	56.06	0.219592E+02	0.309728E+07	0.309332E-02

U=105 FT/SEC GRID

NO	X	H	Rex	ST
1	2.44	0.447779E+02	0.128994E+06	0.659503E-02
2	4.50	0.317069E+02	0.238143E+06	0.466990E-02
3	6.56	0.254751E+02	0.347291E+06	0.375205E-02
4	8.63	0.247091E+02	0.456440E+06	0.363924E-02
5	10.69	0.218839E+02	0.565589E+06	0.322312E-02
6	12.75	0.205246E+02	0.674738E+06	0.302292E-02
7	14.81	0.200443E+02	0.783886E+06	0.295219E-02
8	16.88	0.192285E+02	0.893035E+06	0.283203E-02
9	18.94	0.184294E+02	0.100218E+07	0.271434E-02
10	21.00	0.184336E+02	0.111133E+07	0.271496E-02
11	23.06	0.175375E+02	0.122048E+07	0.258298E-02
12	25.13	0.175660E+02	0.132963E+07	0.258717E-02
13	27.19	0.171775E+02	0.143878E+07	0.252996E-02
14	29.25	0.168516E+02	0.154793E+07	0.248196E-02
15	31.31	0.171923E+02	0.165708E+07	0.253214E-02
16	33.38	0.173171E+02	0.176623E+07	0.255051E-02
17	35.44	0.172668E+02	0.187537E+07	0.254310E-02
18	37.50	0.166629E+02	0.198452E+07	0.245416E-02
19	39.56	0.167434E+02	0.209367E+07	0.246602E-02
20	41.63	0.169799E+02	0.220282E+07	0.250086E-02
21	43.69	0.171234E+02	0.231197E+07	0.252198E-02
22	45.75	0.177021E+02	0.242112E+07	0.260722E-02
23	47.81	0.171038E+02	0.253027E+07	0.251909E-02
24	49.88	0.167801E+02	0.263942E+07	0.247142E-02
25	51.94	0.158002E+02	0.274856E+07	0.232710E-02
26	54.00	0.161189E+02	0.285771E+07	0.237404E-02
27	56.06	0.177934E+02	0.296686E+07	0.262066E-02

HEAT TRANSFER DATA:
U=52 FT/SEC JET GRID

NO	X	H	Rex	ST
1	2.44	0.471058E+02	0.641986E+05	0.139703E-01
2	4.50	0.335334E+02	0.118520E+06	0.994506E-02
3	6.56	0.234227E+02	0.172842E+06	0.694650E-02
4	8.63	0.206283E+02	0.227164E+06	0.611777E-02
5	10.69	0.170828E+02	0.281486E+06	0.506626E-02
6	12.75	0.155395E+02	0.335808E+06	0.460859E-02
7	14.81	0.149306E+02	0.390130E+06	0.442801E-02
8	16.88	0.141948E+02	0.444452E+06	0.420977E-02
9	18.94	0.134194E+02	0.498774E+06	0.397982E-02
10	21.00	0.133803E+02	0.553096E+06	0.396823E-02
11	23.06	0.126572E+02	0.607418E+06	0.375376E-02
12	25.13	0.126085E+02	0.661739E+06	0.373932E-02
13	27.19	0.124144E+02	0.716061E+06	0.368175E-02
14	29.25	0.120257E+02	0.770383E+06	0.356648E-02
15	31.31	0.122701E+02	0.824705E+06	0.363895E-02
16	33.38	0.124158E+02	0.879027E+06	0.368217E-02
17	35.44	0.123423E+02	0.933349E+06	0.366038E-02
18	37.50	0.119120E+02	0.987671E+06	0.353277E-02
19	39.56	0.116593E+02	0.104199E+07	0.345783E-02
20	41.63	0.119012E+02	0.109631E+07	0.352956E-02
21	43.69	0.122699E+02	0.115064E+07	0.363892E-02
22	45.75	0.124622E+02	0.120496E+07	0.369592E-02
23	47.81	0.119211E+02	0.125928E+07	0.353545E-02
24	49.88	0.118627E+02	0.131360E+07	0.351813E-02
25	51.94	0.113050E+02	0.136792E+07	0.335275E-02
26	54.00	0.113632E+02	0.142225E+07	0.337001E-02
27	56.06	0.124039E+02	0.147657E+07	0.367865E-02

U=49 FT/SEC GRID

NO	X	H	Rex	ST
1	2.44	0.250203E+02	0.606576E+05	0.786268E-02
2	4.50	0.205164E+02	0.111983E+06	0.644731E-02
3	6.56	0.158255E+02	0.163309E+06	0.497320E-02
4	8.63	0.146779E+02	0.214635E+06	0.461257E-02
5	10.69	0.127067E+02	0.265960E+06	0.399312E-02
6	12.75	0.118547E+02	0.317286E+06	0.372535E-02
7	14.81	0.115333E+02	0.368612E+06	0.362437E-02
8	16.88	0.110305E+02	0.419938E+06	0.346637E-02
9	18.94	0.104788E+02	0.471263E+06	0.329297E-02
10	21.00	0.104319E+02	0.522589E+06	0.327826E-02
11	23.06	0.992928E+01	0.573915E+06	0.312030E-02
12	25.13	0.994586E+01	0.625240E+06	0.312551E-02
13	27.19	0.985422E+01	0.676566E+06	0.309671E-02
14	29.25	0.943057E+01	0.727892E+06	0.296358E-02
15	31.31	0.956307E+01	0.779217E+06	0.300521E-02
16	33.38	0.963006E+01	0.830543E+06	0.302622E-02
17	35.44	0.956534E+01	0.881869E+06	0.300593E-02
18	37.50	0.930696E+01	0.933195E+06	0.292473E-02
19	39.56	0.913157E+01	0.984520E+06	0.286962E-02
20	41.63	0.927801E+01	0.103585E+07	0.291564E-02
21	43.69	0.954052E+01	0.108717E+07	0.299813E-02
22	45.75	0.976259E+01	0.113850E+07	0.306792E-02
23	47.81	0.925621E+01	0.118982E+07	0.290878E-02
24	49.88	0.914901E+01	0.124115E+07	0.287510E-02
25	51.94	0.869490E+01	0.129247E+07	0.273239E-02
26	54.00	0.877906E+01	0.134380E+07	0.275884E-02
27	56.06	0.964224E+01	0.139513E+07	0.303009E-02

DETECTOR PLACEMENT AND PARTICLE SIZE INTERPRETATION FOR A MULTIPLE RATIO SINGLE PARTICLE COUNTER

FINAL REPORT

MINI GRANT

Sponsored by the

AIR FORCE OFFICE OF SCIENTIFIC RESEARCH

Conducted by the

UNIVERSAL ENERGY SYSTEMS, INC.

Prepared by

Robert P. Howard

and

Carl A. Ventrice, Ph. D.

January 23, 1987

Contract Number

SB 5851/-0360

AN ABSTRACT OF A DISSERTATION

A MULTIPLE RATIO SINGLE PARTICLE COUNTER TECHNIQUE FOR PARTICLE SIZE MEASUREMENTS

Robert P. Howard

Doctor of Philosophy in Engineering

A Multiple Ratio Single Particle Counter (MRSPC) has been proposed by Sverdrup Technology, Inc. (AEDC) for size measurements of spherical particles of known refractive index with diameters between 0.1 and 10.0 micrometers (particle size parameter between 0.64 and 64 for an incident wavelength of 0.4880 micrometers). A Monte Carlo simulation program that incorporates measurement errors has been developed for analyzing the sizing system performance and selecting detector placement angles for the MRSPC.

Detector placement angles were selected for particles with refractive indices 1.33 and 1.776, respectively, assuming an incident light wavelength of 0.4880 micrometers. Particle size distribution errors predicted by the simulation program are presented assuming scattered intensity measurement errors of up to ±20 percent for different numbers of detectors up to eight detectors. Methods were discussed and compared for particle size interpretation for scattered intensity measurements.

The results of this study indicated that particle diameters can be adequately distinguished within the given size range, using as few as eight detectors if intensity measurement errors are within ±20 percent. Fewer detectors are needed for smaller measurement errors. Also, the results indicate that placing detectors in the back scattering region offers no advantages in distinguishing particle sizes over placing all detectors within the forward scattering region.

ACKNOWLEDGEMENTS

Robert P. Howard was project director for this study. He was assisted in this work by Dr. Carl A. Ventrice whose expert advice and suggestions were invaluable. Because of his contributions, Dr. Ventrice is listed as a co-author of this report.

Appreciation is extended to Dr. Nicholas G. Demas whose helpful suggestions and discussions gave greater insight to the problem.

Robert Howard would like to express his appreciation to the Air Force Systems Command, Air Force Office of Scientific Research and Universal Energy Systems for allowing him the opportunity to participate in the Mini Grant Program. Thanks are also conveyed to Mr. P.J. Murphy, Dr. W.K. McGregor and Dr. R.A. Reed of the EL-3 test group of Sverdrup Technology for their technical assistance and advice throughout this research, and to Mr. Marshall Kingery (AEDC), and Mr. Rodney Darrah and Ms. Sue Espy of Universal Energy Systems for their assistance in obtaining this grant and administering the Mini Grant Program.

Thanks is also extended to the Center for Manufacturing Research and Technology Utilization at Tennessee Technological University and the University for making available facilities necessary for this research.

INTRODUCTION

Since the development of electromagnetic wave theory, the interaction of electromagnetic waves with material bodies has been investigated. Lord Rayleigh in 1881 published a derivation of electromagnetic wave scattering by a small dielectric sphere to explain the blueness of the sky [1]. This derivation, however, was limited to cases for which the electromagnetic wavelength was much greater than the particle diameter. In 1908, Mie [2] published an exposition on the general solution of electromagnetic scattering by a sphere. Although this phenomenon of scattering is often referred to as light scattering by particles, the general scattering laws apply with equal validity to all wavelengths. The solutions to the scattering equations depend upon the ratio of a characteristic dimension of the particle to the wavelength of the incident electromagnetic wave rather than explicitly upon the particle size. This allows the general scattering theory to be applicable to seemingly different types of problems. For example, the scattering of microwaves by raindrops, the scattering of radiowaves by artificial earth satellites, and the scattering of light by aerosols are similar phenomena because in each case the wavelengths of the electromagnetic waves are of the same order of magnitude as the dimensions of the scatterer.

Two classes of problems exist in the scattering of electromagnetic waves by a system of particles. One class involves the theoretical or

experimental determination of the scattered radiation by a known, well-defined system. The other is to characterize the system of scatterers (by such properties as particle size, for example) from a knowledge of the scattered radiation, usually obtained by experiment [1]. There are a wide range of problems encountered in many areas of physical science that require particle size analysis. These include studies pertaining to communication links through the atmosphere and environmental effects of particulate matter in pollution. The increased demand for additional satellite communications capacity has stimulated the design of microwave systems that operate at higher frequencies and maintain dual orthogonal polarizations to allow two simultaneous signal transmissions on the same channel. At frequencies above 10 Gigahertz, attenuation and depolarization caused by atmospheric particles can reduce the performance of radar and space communication links. Such particles include ice crystals, rain, fog and snow [3].

Effects of pollution on the environment is determined primarily by the characteristics of the particulate matter released into the atmosphere. For example, the sizes of particles in city smog affect the haziness of city air, the depth of penetration of the particles into human lungs and the amount of deposition of the particles on various surfaces before winds disperse the smog [4].

A very important and immediate application to scattering theory is the determination of the size distribution of the particulates in the exhaust plume of rocket motors. In this case, the particle size distribution must be known in order to determine the effect of the exhaust plume on the performance of solid propellant rocket motors. The particle sizing technique must be adaptable for use in the testing

environment of rocket motor test cells. Mie theory is well suited for fiber optics systems proposed for use in an optical measuring device to perform this task.

Progress in space travel, the increasing use of manmade satellites, the Defense Department's concern for identifying rocket propelled vehicles and the Strategic Defense Initiative has stimulated the need for understanding the physics of solid-propellant rocket motors. Rocket-propulsion scientists have developed computer codes that predict with great accuracy the thrusts and some other performance characteristics of these motors. One of the major uncertainties in these codes is the size distribution of particulates within the plume. The size distribution is important in the flow rate and radiation equations. The development of these codes relied heavily upon test data from rocket motor test facilities, rather than a complete theoretical understanding of the physical principles involved in the rocket motors. The test facilities can simulate earth's atmosphere to about 100,000 feet. The design of rocket motors with specific performance characteristics for higher altitudes requires a more in-depth understanding of the physics of rocket motors. An extensive experimental analysis of the exhaust plume is necessary in formulating the physical theory.

Among the more important measures is the size distribution of particulates within the plume. The measurement is difficult owing to the "optical thickness" of the plume. Thus far, attempts to determine the properties and size of the particulates have led to extracting particle samples from the plume for analysis in a laboratory. This technique consisted of mounting a particle extracting probe into the plume and catching a sample of particles before the probe was destroyed by the high

temperature of the plume. The type of particles were determined, but the size measurements were unreliable due to the effects on the particle sample in collection. There is the possibility of coagulation [5], condensation, and deposition processes that would alter the state of the system of particles during sample collection.

To overcome the problem of "optical thickness," a probe device is under construction that will be used to redirect and dilute a representative sample of particles from the plume, so that a single particle counter, an optical measuring technique, may be employed to measure the particle size distribution. The optical measuring scheme [6], a multiple ratio single particle counter (MRSPC), proposed by the Sverdrup Technology Group at Arnold Engineering Development Center (AEDC) is illustrated schematically in Figure 1.1. Light from a laser passes through a quarter wave plate, used to control the polarization, and is focused into a single mode optical fiber that preserves the light polarization. The optical fiber guides the laser beam to the mounting ring where it is focused to the center of the ring by a second lens as it exits the fiber. Light scattered by a particle near the beam focus into the fiber optic probes is transmitted to photomultiplier tubes where the intensities are measured and stored by a computerized data acquisition system. Polarization filters may be placed in front of the fiber optic probes if such measurements are desired. The theoretical basis for determining particle sizes from scattered radiation in most optical particle sizing systems is Mie theory for spherically shaped particles. The intensity scattered from a spherical particle of known refractive index into a detector (fiber optics probe) is dependent on the particle diameter, the detector placement angle θ, the polarization component(s)

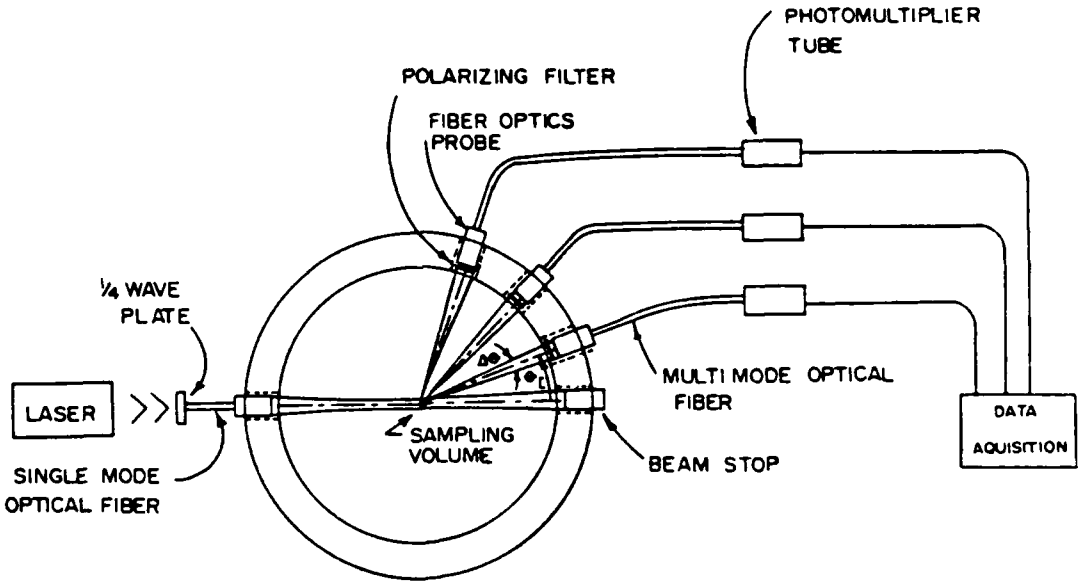

Figure 1.1. Schematic of a MRSPC Proposed by Sverdrup Technology, Inc. (AEDC) for Particle Size Measurements.

accepted by the detector and the wavelength of the electromagnetic wave incident on the particle.

In many applications involving light scattering measurements from individual submicron particles, only lasers can provide adequate light intensity for detection above the background noise levels [7]. Usually a continuous wave (cw) gas laser operating in the fundamental (TEM_{00}) mode is used as the light source for optical measurements of this type. Lasers operating in the fundamental mode maintain at all cross-sections along the beam a Gaussian intensity distribution [8] as illustrated in Figure 1.2. Under conditions usually attainable in laser particulate systems, the Gaussian distribution can be maintained [9] throughout diffraction limited optical systems. Use of fiber optics for transmitting the laser beam is a convenience, not a necessity. For rocket plume measurements, the fiber optics allow delicate instrumentation to be located away from the harsh environments of the measurement sight.

Typically the receiving optics of optical single particle counters have a narrow field of view receiving scattered light only from a particle transversing the beam near the beam focus. A particle passing through the beam continuously scatters light proportional to the incident intensity along the particle trajectory through the beam. Since the radial intensity distribution of the cross-section of the beam is Gaussian, the intensity scattered into a detector by a particle of constant velocity transversing the beam perpendicular to the beam axis will be a Gaussian temporal profile as shown in Figure 1.3, assuming the particle cross-section is much smaller than the beam diameter. The amplitude of the scattered profile for a given particle size is dependent

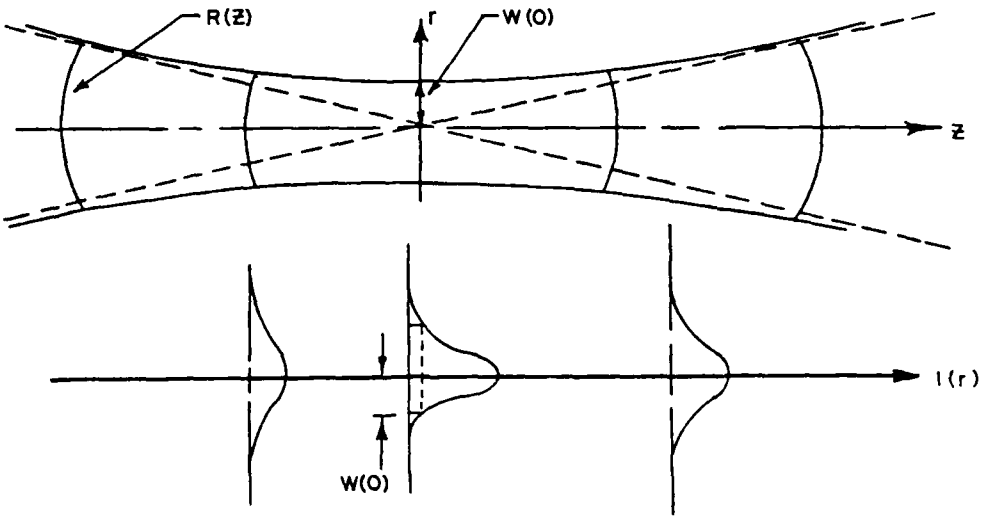

Figure 1.2. Properties of a Gaussian Beam Near a Beam Waist.

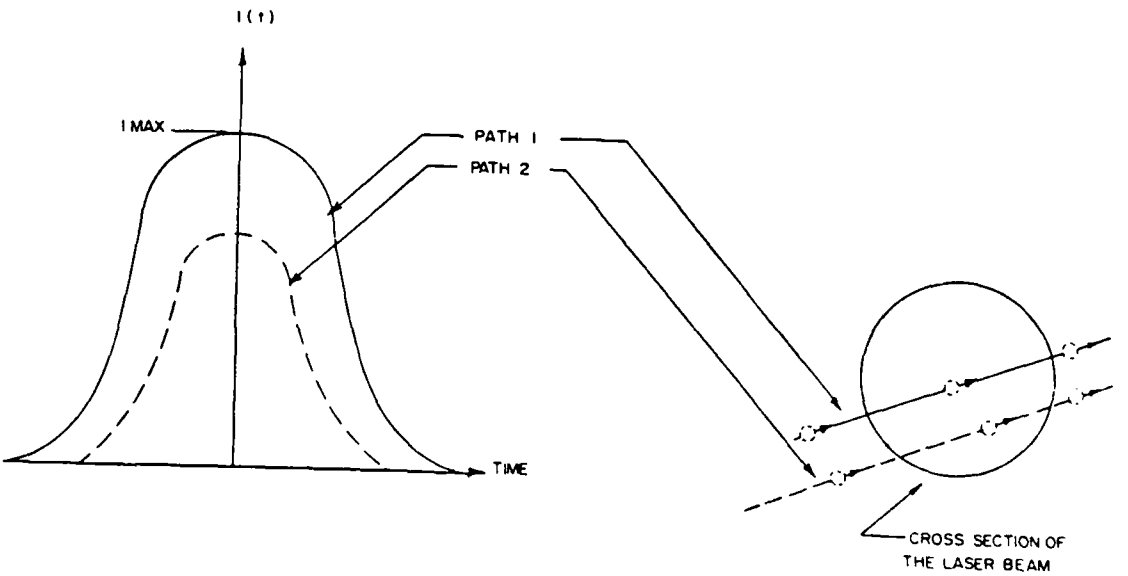

Figure 1.3. Relative Intensity Profiles Scattered into a Detector of the MRSPC as a Particle Transverses the Cross-section of a Gaussian Laser Beam Through Different Paths.

upon its path through the beam. The width of the Gaussian profile depends on the particle velocity vector and the beam width at the position at which the particle transverses the beam.

Direct correlation of measured intensities to theoretical calculations to determine particle size depends upon an accurate knowledge of not only the incident beam intensity and the intensities scattered into the detectors of the instrument, but also the path of the particle through the beam as shown in Figure 1.3. For example, a large particle transversing the Gaussian beam off axis through the lower intensity region may scatter the same amount of light (either maximum or integrated) into a detector as a smaller particle transversing near the beam axis [10]. To alleviate this problem, Hodkinson [11] suggested and Gravatt [12] investigated a technique of ratioed intensities of light scattered into two angles in the forward scatter region. This technique, called a single ratio single particle counter (SRSPC), provides a measure of particle size independent of the incident intensity and the position of the particle in the beam. However, as seen in Figure 1.4 the ratio of intensities versus particle diameter scattered from spherically shaped particles has a one-to-one correspondence only over a narrow range of small particle sizes. Over the size range of interest, diameters $.1\mu < d < 10.0\mu$, the ratio of intensities for two scattering angles is a multivalued function of particle diameter. Thus, particle size measurements over a wide size interval using a SRSPC would result in large errors due to ambiguity in particle size.

Hirleman [13] suggested that multiple ratios could be used to extend the range of particle sizes that could be measured. Figure 1.5 is a schematic of a ratio apparatus Hirleman used for particle size

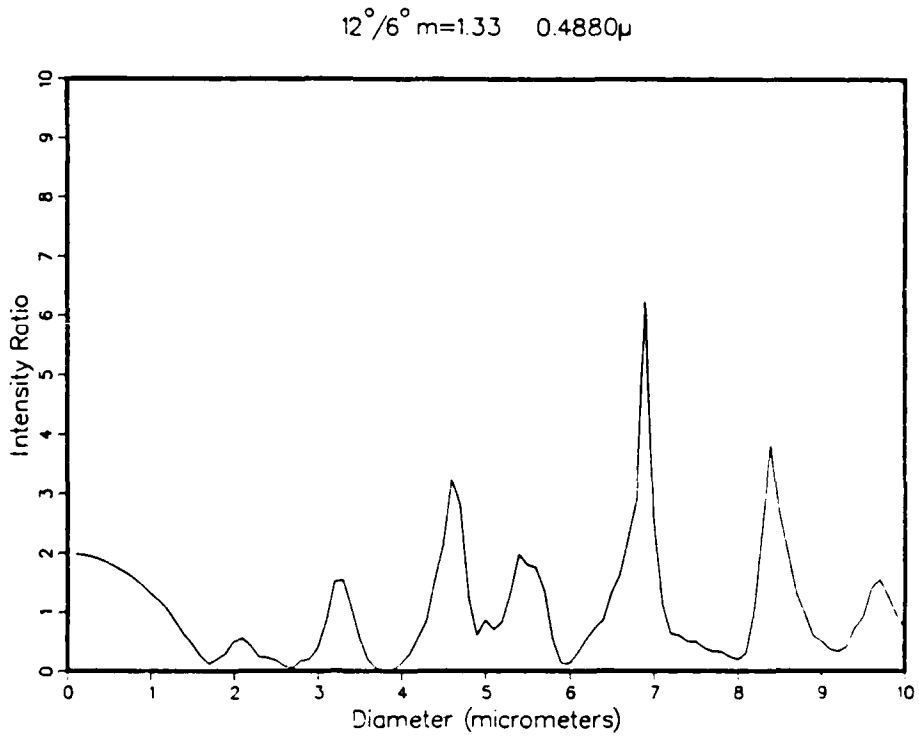

Figure 1.4. A Typical Intensity Ratio Versus Diameter Scattered into Two Detectors of the MRSPC of Figure 1.1.

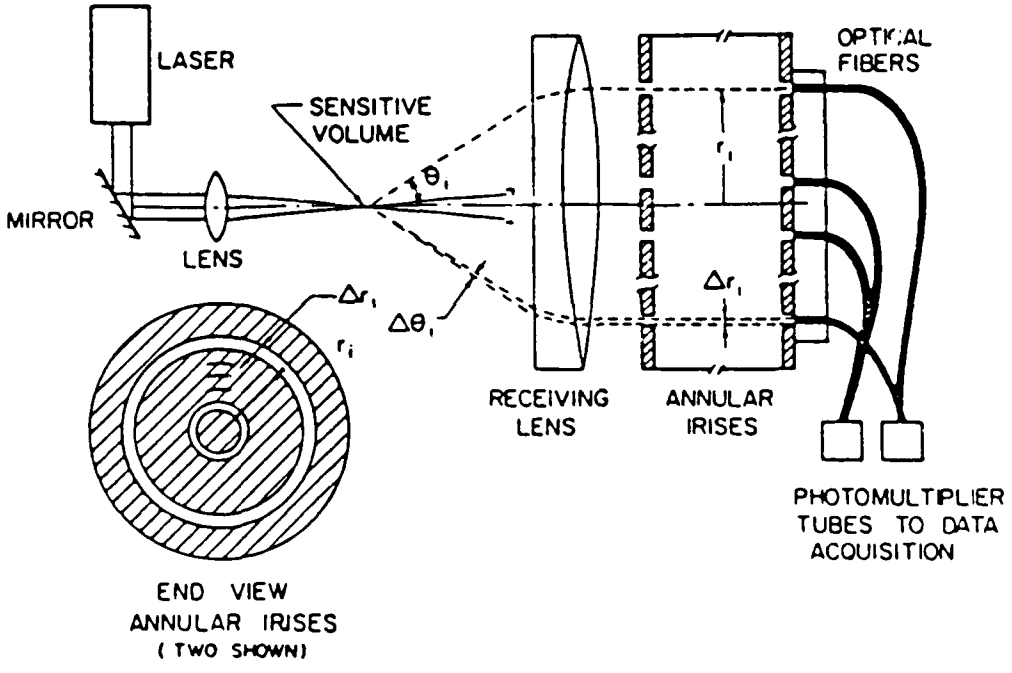

Figure 1.5. Hirleman's Size Measurement Apparatus.

analysis. A lens focused the laser beam to a beam waist as shown. A f/2 receiving lens placed at one focal length from the beam waist collimates light scattered by individual particles passing near the focus. Scattered light enters nine annular irises (Δr = 0.1 - 0.3mm). The nine center radii correspond to the scattering angles measured from the laser beam propagation direction θ_i = 1.5°, 3°, 6°, 9°, 12°, 15°, 18°, 21°, 24° given by:

$$r_i = f \tan\theta_i,$$

where f is the primary focal length of the receiving lens and r_i and θ_i are, respectively, the center radius and the scattering angle of the i^{th} detector. The annular iris tube assembly was constructed to allow only axis-parallel light to be transmitted to the optical fibers. Light scattered into an angular ring at θ_i by an individual particle near the beam focus is collimated by the receiving lens and transmitted to a ring of optical fibers. The optical fibers corresponding to each ring transmits the light to a respective photomultiplier tube. Utilizing many scattering angles would result in several ratio curves similar to Figure 1.4.

For any given ratio-to-diameter curve, a measured ratio value could correspond to several diameters. However, all measured intensity ratios for a single particle scattering event must simultaneously correspond to the same diameter. For elimination of ambiguity in particle size within a certain size range, an ideal set of ratio curves $\{R_1(d), R_2(d), \ldots, R_{NR}(d)\}$ corresponding to n scattering angles, would be one in which there is a unique set of ratio values for any diameter d. Of course this is an "ideal" definition in that it does not take into

account measurement errors, which as discussed in Chapter 3, also affects ambiguity.

The sizing scheme of Figure 1.1 allows scattered radiation measurements at any scattering angle (outside the incident beam) without interfering with the particle flow field. Strategically selecting the scattering angles should minimize the number of detectors required to sufficiently reduce particle size ambiguity in size distribution measurements. The general Mie scattering equations are very complicated. Any analysis requires that scattering data be generated for the detectors of the MRSPC as a function of diameter.

There are complications working directly with calculated intensity ratios. Two detectors are required for one ratio curve. There are many combinations of the detectors even if the scattering angles are made discrete and limited to a relatively small range of detector angles. It is not difficult to determine if two diameters are distinguishable on a given ratio curve. If two ratio values corresponding to diameters d_i and d_j are equal, or close in value since measurement errors must be accounted for, the diameters are not distinguishable. The difficulty is quantifying ambiguity over the entire size range so that effective comparisons can be made for different angles.

As seen from a typical ratio curve in Figure 1.4, it is obvious that more than one curve is necessary to distinguish all particles sizes. For two ratio curves, it is not the intersections of the curves, as one might suspect, that determines ambiguity between two diameters. The intersections are irrelevant. Two diameters are distinguishable if the two corresponding ratio values on at least one curve are not close in value. Each ratio curve has its own set of ambiguous diameters. Each

possible second curve used in conjunction with the first ratio curve, eliminates ambiguity for different diameters. Again, quantifying ambiguity directly from the curves such that detector placement comparisons can be made effectively is very difficult.

Due to the width of the size range of interest, the behavior of the ratio curves as a function of diameter and associated measurement errors that can affect ambiguity, the only feasible means of quantifying ambiguity and analyzing the sizing performance for a given set of detector angles is through a computer simulation of the sizing system.

The objective of this research was to develop methods for analyzing the sizing system and selecting a minimum number of detector scattering angles that sufficiently reduces particle size ambiguity. To analyze the sizing system, a computer simulation program was developed that incorporates measurement errors to get a realistic assessment of the sizing performance. This program was also used in a search technique both to quantify particle size ambiguity for angle comparisons and predict the sizing performance of the MRSPC as each detector angle was added to the system. Detector angles were selected and analyzed for water and aluminum oxide particles. Methods of correlating scattered intensity ratio measurements to Mie theory calculations for particle size interpretation were also developed and compared using the simulation program.

SCATTERED INTENSITY CALCULATIONS FOR THE DETECTORS OF THE MRSPC

The theoretical basis for determining particle sizes from scattered radiation in most particle sizing systems is Mie theory for spherically shaped particles. The prediction of light scattering by irregular particles is in general impossible [10]. To emphasize the approximations and behavior of the solutions of Mie theory, the Mie scattering equations are presented in this chapter followed by a discussion of scattered intensity calculations of the detectors of the MRSPC of Figure 1.1. The scattering intensity equations are given in the form presented by Kerker [1].

Scattering from a Sphere (MIE Theory)

A scattered wave is generated when a plane monochromatic wave is incident on an object possessing a discrete boundary and with optical constants different from those of the medium. The scattering object in this case is an isotropic homogenous sphere characterized by a complex propagation constant k^{II}, diameter d and a complex index of refraction m^{II}. The particle is contained in an isotropic homogeneous medium that is assumed to be a dielectric with a real propagation constant k^{I} and real refracture index m^{I}.

The electromagnetic properties of space must be determined for the incident wave, transmitted wave (inside the object), and the scattered wave. The field vectors ($\vec{E}^{i}$, $\vec{H}^{i}$ for the incident wave; $\vec{E}^{T}$, $\vec{H}^{T}$ for the transmitted wave; $\vec{E}^{s}$, $\vec{H}^{s}$ for the scattered wave) associated with the wave, must obey the Maxwell field equations, the homogeneous wave equations, and the boundary conditions that follow from Maxwell's equations.

The scattering of an electromagnetic wave by a sphere is [illegible] with respect to a spherical coordinate system, figure [illegible]. As shown in figure [illegible], the z-axis is chosen to coincide with the direction of propagation $\hat{k}^i$ of the incident wave. The center of the spherical object coincides with the origin of the coordinate system. The incident plane wave is linearly polarized along the x-axis. The scattering angle is defined as the angle measured from the z-axis to the direction of scattered light given by the propagation vector $\hat{k}^s$. The angle ϕ is measured from the x-axis to the projection of scattered light onto the xy plane. The coordinate r is the distance from the center of the particle to a point of observation.

Light scattering observations at optical wavelengths are, in practice, carried out in the far-field zone. Only the far-field solutions scattered radiation polarized in the θ and ϕ azimuths is given by

$$I_\phi = \frac{\lambda^2}{4\pi^2 r^2} |S_1|^2 \sin^2\phi = \frac{\lambda^2}{4\pi^2 r^2} i_1 \sin^2\phi, \qquad (2.1)$$

$$I_\theta = \frac{\lambda^2}{4\pi^2 r^2} |S_2|^2 \cos^2\phi = \frac{\lambda^2}{4\pi^2 r^2} i_2 \cos^2\phi, \qquad (2.2)$$

where i_1 and i_2 are called the intensity functions and λ is the wavelength of the incident light. The quantities i_1 and i_2 correspond to the polarized components of scattered light perpendicular and parallel, respectively, to the scattering plane. The scattering plane is defined as the plane that contains the direction of propagation of the incident light and direction (θ, ϕ) of observation. The quantities S_1 and S_2, called the amplitude functions, are defined as

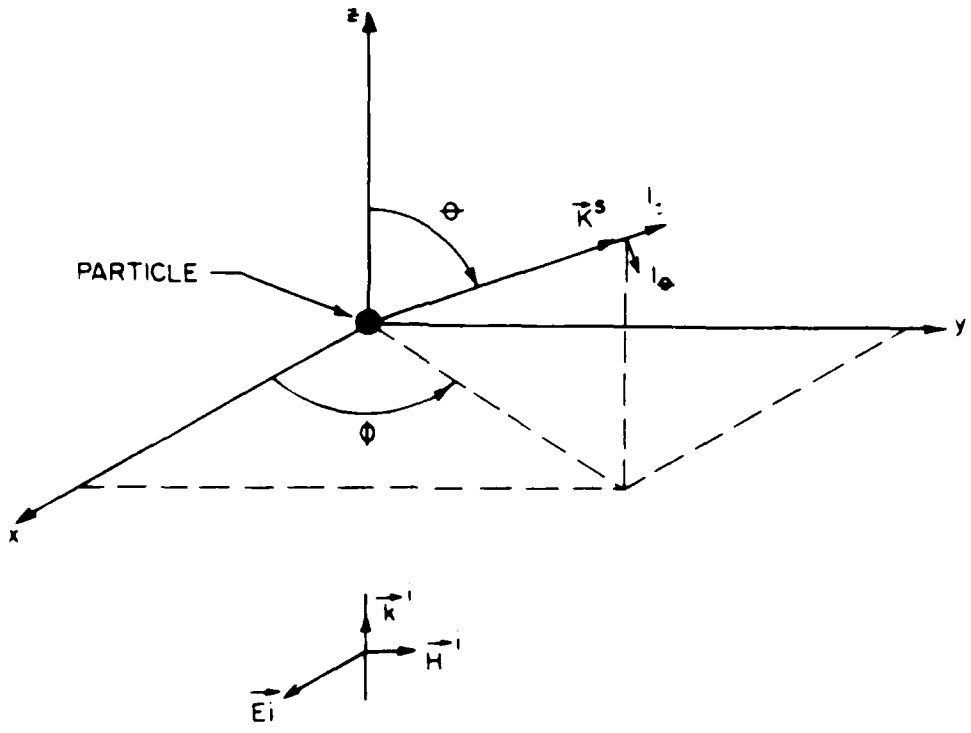

Figure 2.1. Spherical Coordinate System for Electromagnetic Scattering by a Spherical Object.

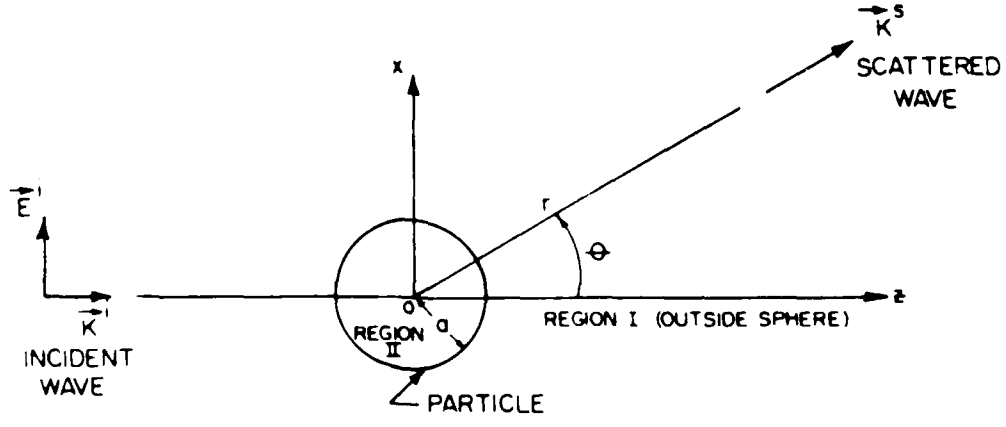

Figure 2.2. Coordinate System and Notation for Light Scattering by a Spherical Object.

$$\cdots \sum \cdots \left\{ \cdots \right\} \cdots \tag{2.3}$$

$$\cdots \sum \cdots \left\{ \cdots \right\} \cdots \tag{2.4}$$

where the angular functions are

$$\cdots = \frac{P_\ell^1(\cos\theta)}{\sin\theta} \tag{2.5}$$

$$\cdots = \frac{d}{d\theta} P_\ell^1(\cos\theta) \tag{2.6}$$

The angular function $P_\ell^1(\cos\theta)$ is the associated Legendre function of the first kind and c_ℓ and d_ℓ are the scattering coefficients given by

$$\cdots = \frac{\cdots}{\int_\ell^{(2)}(x)\cdots - \cdots \int_\ell^{(2)}(x)} \tag{2.7}$$

$$\cdots = \frac{\cdots}{\int \cdots} \tag{2.8}$$

where

$$\cdots \tag{2.9}$$

$$\cdots \tag{2.10}$$

where $\cdots$ is the wavelength in the vacuum and $\cdots$ are the Ricatti-Bessel

$$\cdots \tag{2.11}$$

where $J_{\ell+\frac{1}{2}}(\rho)$ and $N_{\ell+\frac{1}{2}}(\rho)$ are the half interger order Bessel and Neumann functions. The function $\zeta_\ell^{(2)}$ is the linear combination of these functions given by:

$$\zeta_\ell^{(2)}(\rho) = \psi_\ell(\rho) + i\chi_\ell(\rho) = \sqrt{\frac{\pi\rho}{2}}\, H^{(2)}_{\ell+\frac{1}{2}}(\rho). \tag{2.12}$$

$H^{(2)}_{\ell+\frac{1}{2}}$ is the half integral order Hankel function of the second kind.

There are two special cases of interest. Referring to Figure 2.1, if yz is chosen as the scattering plane, the incident light is polarized perpendicular to this plane, $\phi = 90°$, $I_\theta = 0°$ and

$$I_\phi = \frac{\lambda^2}{4\pi^2 r^2} i_1. \tag{2.13}$$

However, if xz is chosen as the scattering plane, the incident light polarization is parallel to this plane, $\phi = 0°$, $I_\perp = 0$ and

$$I_\theta = \frac{\lambda^2}{4\pi^2 r^2} i_2. \tag{2.14}$$

The intensity equations (2.80) and (2.81) are functions of

$$\alpha = \frac{\pi d}{\lambda}, \tag{2.15}$$

called the particle size parameter. For both small α, $\alpha \lesssim .3$, and large α, $\alpha \gtrsim \frac{3}{m-1}$, the scattered intensities may be approximated by simpler expressions. However, for α within the range

$$0.3 \lesssim \alpha \lesssim \frac{3}{m-1}, \tag{2.16}$$

full Mie calculations are necessary.

To gain a perspective on the behavior of the scattered intensity functions, polar plots are shown in Figures 2.3 to 2.5 for various values of α. The plots represent the magnitude of intensity scattered as a function of scattering angle θ for the two special cases, I_θ for $\phi = 90°$ and I_ϕ for $\phi = 0°$. Figure 2.3 shows the scattering pattern for small α, called the Rayleigh scattering region. For Rayleigh scattering, [illegible]d and the particle behaves as a radiating dipole antenna. For increasing sizes of α, Figure 2.4 shows that the scattering pattern becomes more forward directed until, as in Figure 2.5, the forward (diffraction) lobe dominates and side-lobes appear.

Scattered Intensity Calculations for the Detectors of the MRSPC of Figure 1.1

For particle scattering measurements, the spatial extent of the optical sampling volume, simply defined as that portion of the beam from which a particle scatters light into the detectors, is determined by the intensity distribution in the field of view of the detectors. The field of view of each detector is in the shape of a cone with apexes overlapping at the laser beam focus. The optical sampling volume, also called the measurement or sensitive volume, is small for detectors with narrow fields of view.

In calculating the intensity scattered into a detector of the MRSPC of Figure 1.1, it is convenient to use the coordinate system of Figure 2.1 with the origin at the center of the sampling volume. The radiant flux F, described by van de Hulst [14], scattered by a particle at the origin into the solid angle subtended by a detector is

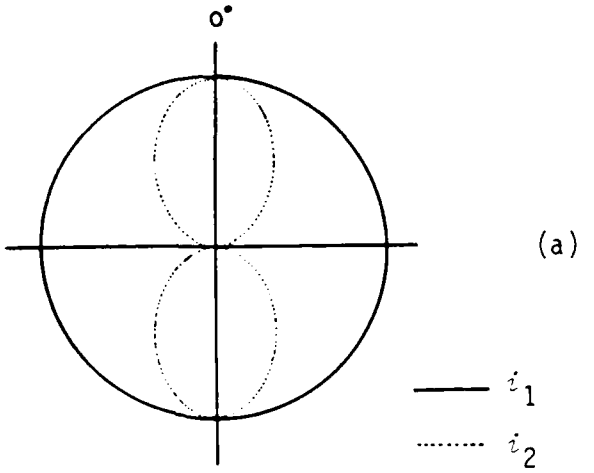

$\alpha = 0.1$

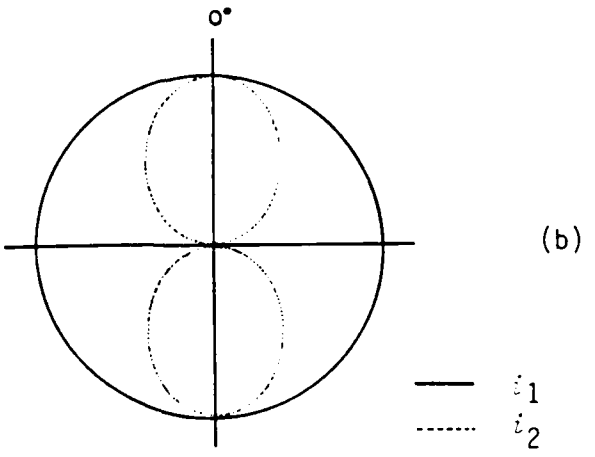

$\alpha = 0.3$

Figure 2.3. Polar Plots of i_1 for $\phi = 90°$ and i_2 for $\phi = 0°$ for Small α, the Rayleigh Scattering Region.

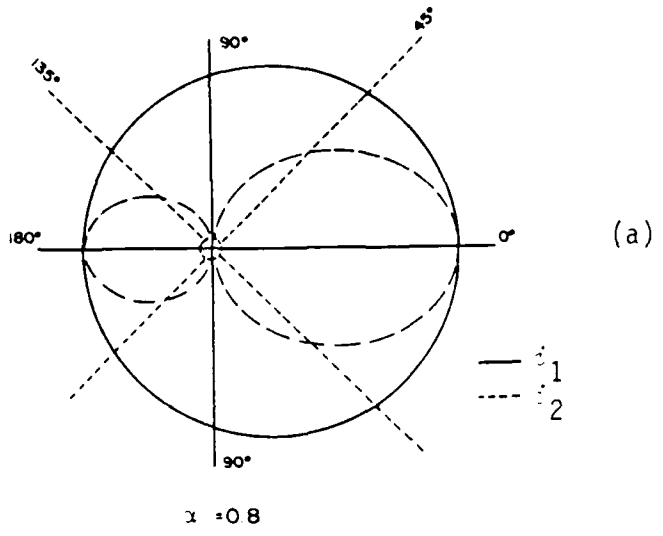

(a)

$\alpha = 0.8$

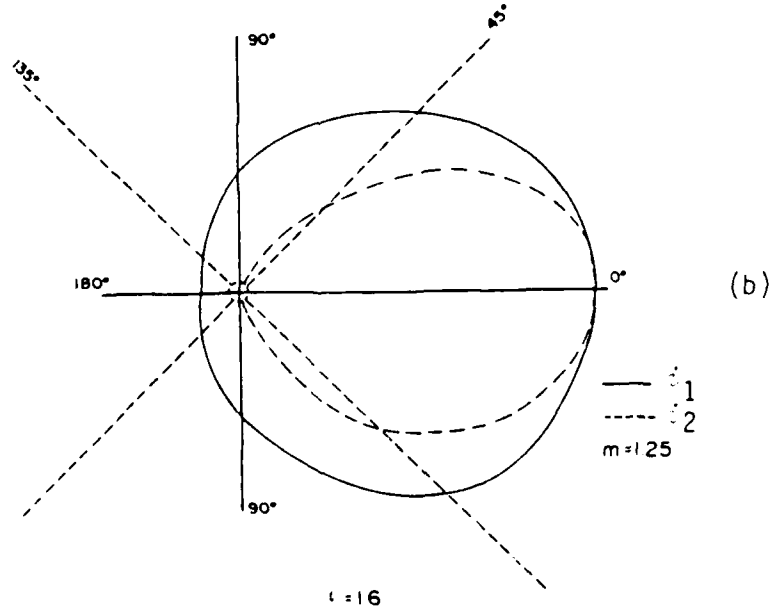

(b)

$\alpha = 1.6$

Figure 2.4. Polar Plots of f_1 for $\phi = 90°$ and f_2 for $\phi = 0°$ for Intermediate α Values.

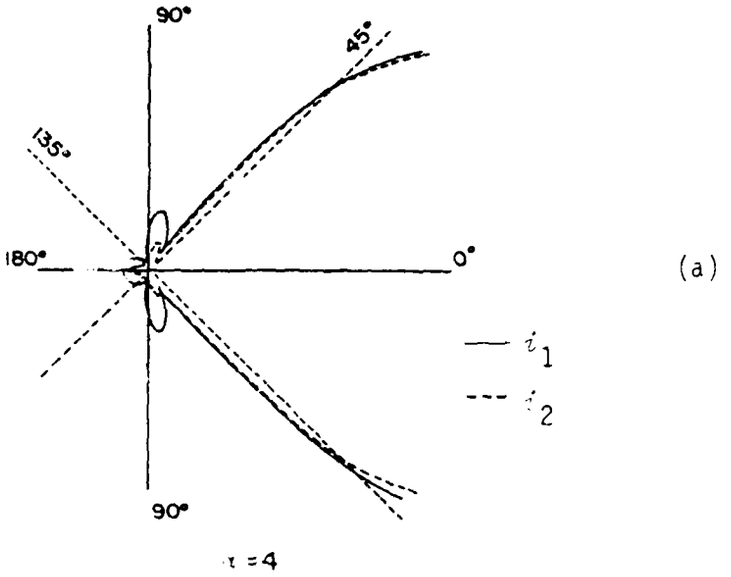

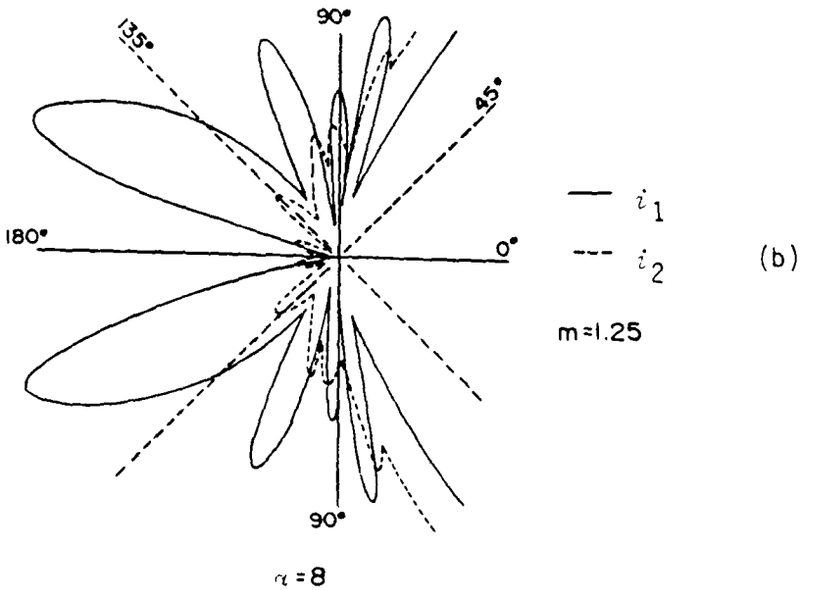

Figure 2.5. Polar Plots of i_1 for $\phi = 90°$ and i_2 for $\phi = 0°$ for Large α Values.

$$F = \frac{I_{inc}\lambda^2}{4\pi^2} \int_{\theta_j - \frac{\Delta\theta}{2}}^{\theta_j + \frac{\Delta\theta}{2}} \int_{\phi_j - \frac{\Delta\phi}{2}}^{\phi_j + \frac{\Delta\phi}{2}} \left[i_1(\theta, \alpha, m)\sin^2\phi + i_2(\theta, \alpha, m)\cos^2\phi \right] \sin\theta d\theta d\phi, \quad (2.84)$$

where I_{inc} is the incident intensity and the angles θ_j and ϕ_j identify the location of the center of the j^{th} detector. This analysis assumes negligible variation in incident laser intensity over the particle dimensions. The angle ϕ_j and the subtended angle $\Delta\phi$ are the same for each detector leaving F a function of only θ_j for a given refractive index, particle size, and wavelength.

A polarizing filter, placed in front of each detector, allows the selective measurement of scattered light polarized either perpendicular P_1 or parallel P_2 to the plane of observation. For the respective polarized components of scattered radiation, equation (2.17) reduces to either

$$F_1(\theta_j) = \frac{I_{inc}\lambda^2}{4\pi^2} \int_{\phi_j - \frac{\Delta\phi}{2}}^{\phi_j + \frac{\Delta\phi}{2}} \sin^2\phi d\phi \int_{\theta_j - \frac{\Delta\theta}{2}}^{\theta_j + \frac{\Delta\theta}{2}} i_1(\theta,\alpha, m)\sin\theta d\theta, \quad (2.85)$$

or

$$F_2(\theta_j) = \frac{I_{inc}\lambda^2}{4\pi^2} \int_{\phi_j - \frac{\Delta\phi}{2}}^{\phi_j + \frac{\Delta\phi}{2}} \cos^2\phi d\phi \int_{\theta_j - \frac{\Delta\theta}{2}}^{\theta_j + \frac{\Delta\theta}{2}} i_2(\theta,\alpha, m)\sin\theta d\theta. \quad (2.86)$$

The ratio of two fluxes collected by two detectors (P_1) at angles θ_k ...

θ_j is

$$\frac{F_1(\theta_k)}{F_1(\theta_j)} = \frac{\int_{\theta_k - \frac{\Delta\theta}{2}}^{\theta_k + \frac{\Delta\theta}{2}} i_1(\theta,\alpha, m)\sin\theta d\theta}{\int_{\theta_j - \frac{\Delta\theta}{2}}^{\theta_j + \frac{\Delta\theta}{2}} i_1(\theta,\alpha, m)\sin\theta d\theta} = \frac{I_1(d, \theta_k)}{I_1(d, \theta_j)}. \qquad (2.87)$$

A similar relationship exists for P_2 components. The ratio for one polarization component to another is also similar except that the integration over Φ does not necessarily divide out. For the ratio sizing technique, calculations of the intensities $I_1(d, \theta_j)$ and/or $I_2(d, \theta_j)$ for a given particle refractive index and incident wavelength are sufficient.

The computer program to calculate the scattering functions i_1 and i_2 integrated over a $\Delta\theta$ was provided by the Arnold Engineering Development Center. A sample output is included in Appendix A. A typical plot of equation (2.20) versus particle diameter d is given in Figure 1.4. This curve is referred to as a characteristic, calibration, or sizing curve.

The numerical search technique described in Chapter 3 requires Mie theory calculations over a wide range of scattering angles $\theta_{min} \leq \theta_j \leq \theta_{max}$, where θ_{min} and θ_{max} are the limits on the range of detector angle selection. For each θ_j, scattered intensities, $I(d_i, \theta_j)$ for either P_1 or P_2, are calculated for discrete diameters within a desired sizing interval $dmin \leq d_i \leq dmax$ in incremental steps of $\Delta d = d_{j+1} - d_j$. Table 2.1 summarizes the calculations for the intensities.

Table 2.1. Summary of Mie Calculations for the Search Technique of Chapter 3.

	θ_{min}	θ_{min+1}	...	θ_{max}
d_1	$I(d_1, \theta_{min})$	$I(d_1, \theta_{min+1})$	...	$I(d_1, \theta_{max})$
d_2	$I(d_2, \theta_{min})$	$I(d_2, \theta_{min+1})$	...	$I(d_2, \theta_{max})$
.	.	.		.
.	.	.		.
.	.	.		.
d_N	$I(d_N, \theta_{min})$	$I(d_N, \theta_{min+1})$	...	$I(d_N, \theta_{max})$

DETECTOR ANGLE SELECTION TECHNIQUE AND A SIMULATION OF SYSTEM PERFORMANCE

The problem of particle size ambiguity was addressed in Chapter 1. As illustrated in Figure 1.4, a two-detector system (or a Single Ratio Single Particle Counter) is incapable of distinguishing particle sizes over a wide or general particle size range. Thus, it is desirable to strategically locate a minimum number of detectors that sufficiently decreases particle size ambiguity for a size range of interest. However, before this can be achieved, it is necessary to quantify the amount of particle size ambiguity existing for any arbitrary choice of n-detector placement angles.

In this chapter, a simulation program is described that simulates the performance of the n-detector MRSPC of Figure 1.1 incorporating measurement errors that are expected in scattered intensity measurements. Using this for quantifying particle size ambiguity, a technique is discussed for selecting a set of n-detector placement angles that sufficiently reduces particle size ambiguity over a desired particle size range, in this case 0.1 to 10.0μ (micrometers). In a later section, another technique is described for selecting detector angles. This technique has a significantly shorter computer time but does not take into account measurement errors that might bias the selection process.

In actual and simulated measurements, scattered intensities must be correlated to Mie theory in order to interpret the particle size. Two

methods are discussed and compared using the simulation program.

Interpretation of Particle Size from Measured Intensities

Intensity measurements scattered from individual particles into the n detectors of the MRSPC allow a histogram of particle sizes to be constructed over a statistically large number of particle scattering events. To ease experimental requirements (Chapter 2), measurements are correlated to theoretical Mie data through intensity ratios. It should be noted that any means of correlation that reduces the data to the form of equation (2.20) is acceptable. Calculated Mie data of Table 2.1, for a specified number of scattering angles put into correct form (ratioed or other) serves as a look-up table for measured intensities. The first method of correlation discussed, called the ratio method, literally ratios the intensities for combinations of two detector scattering angles. The second method mathematically treats the set of scattered intensities from one scattering event as components of a normalized n-dimensional vector, assuming n detectors. This method is referred to as the vector method of correlation.

In the ratio method, first, the intensities of Table 2.1 corresponding to a particular set of n scattering angles are put into matrix form as shown in Table 3.1. The intensities of Table 3.1 are row-wise ratioed into a ratio look-up table, Table 3.2, resulting in a total number of ratios given by

$$NR = n(n-1)/2. \tag{3.1}$$

For example, if n = 3, there are three columns in Table 3.2 calculated according to

Table 3.1. Tabled Mie Data for n Selected Detector Scattering Angles.

	θ_1	θ_2	...	θ_n
d_1	$I(d_1, \theta_1)$	$I(d_1, \theta_2)$	...	$I(d_1, \theta_n)$
d_2	$I(d_2, \theta_1)$	$I(d_2, \theta_2)$	...	$I(d_2, \theta_n)$
.	.	.		.
.	.	.		.
.	.	.		.
d_N	$I(d_N, \theta_1)$	$I(d_N, \theta_2)$	...	$I(d_N, \theta_n)$

Table 3.2. Ratioed Intensities of Table 3.1.

d_1	$R_1(d_1)$	$R_2(d_1)$	...	$R_{NR}(d_1)$
d_2	$R_1(d_2)$	$R_2(d_2)$	...	$R_{NR}(d_2)$
.	.	.		.
.	.	.		.
.	.	.		.
d_N	$R_1(d_N)$	$R_2(d_N)$	...	$R_{NR}(d_N)$

$$R_1(d_j) = I(d_j, \theta_2)/I(d_j, \theta_1),$$
$$R_2(d_j) = I(d_j, \theta_3)/I(d_j, \theta_1), \qquad (3.2)$$
$$R_3(d_j) = I(d_j, \theta_3)/I(d_j, \theta_2).$$

The n measured intensities for a particle scattering event are ratioed according to equation (3.2) giving a set of NR measured ratios, $\{R^M, R^M, \ldots, {}^{R}_{NR}\}$, to be correlated to the ratioed look-up table, Table 3.2. In this work, it is assumed that no particle diameters exist outside the size range of interest. The diameter, d_k, of Table 3.2 producing the least squared error,

$$\text{Error}(d_k) = \sum_{i=1}^{NR} [R_i(d_k) - R_i^M]^2, \qquad (3.3)$$

is accepted as the measured diameter corresponding to the measured ratios. In this manner every set of measured ratios produces a measured diameter. For actual measurements, a consistency check [13] for all ratios would aid in excluding particle sizes outside the size range of interest that might pass through the sensitive volume. A consistency check is comparing each measured intensity ratio to the corresponding theoretical ratio. If the values are not reasonably close, the particle is assumed to be outside the size range of interest.

There are techniques other than intensity ratios for correlating measured data to a look-up table of theoretical calculations to determine the particle size. One such alternative is to row-wise vector-normalize the intensities of Table 3.1 as illustrated in Table 3.3. An element, $\bar{I}_i(d_j)$, of the vector look-up table, Table 3.3, denotes the i^{th} component of a unit vector corresponding to diameter d_j. Each intensity of Table

Table 3.3. Mie Intensities of Table 3.1 in Vector-Normalized Form.

	θ_1	θ_2	...	θ_n
d_1	$\bar{I}_1(d_1)$	$\bar{I}_2(d_1)$	...	$\bar{I}_n(d_1)$
d_2	$\bar{I}_1(d_2)$	$\bar{I}_2(d_2)$	...	$\bar{I}_n(d_2)$
.	.	.		.
.	.	.		.
.	.	.		.
d_N	$\bar{I}_1(d_N)$	$\bar{I}_2(d_N)$	...	$\bar{I}_n(d_N)$

3.1 corresponding to diameter d_j becomes a component of a normalized vector calculated according to

$$\bar{I}_i(d_j) = \frac{I(d_j, \theta_i)}{\left\{\sum_{i=1}^{n} [I(d_j, \theta_i)]^2\right\}^{\frac{1}{2}}}. \tag{3.4}$$

A set of n measured intensities, scattered into the detectors for a particle scattering event, form a vector which must be normalized according to equation (3.4). The measured unit vector corresponds to a diameter yet to be determined and may be written as

$$\vec{\bar{I}}^M = \langle \bar{I}_1^M \ \bar{I}_2^M \ \ldots \ \bar{I}_n^M \rangle, \tag{3.5}$$

where the superscript M denotes "measured" as before. The measured vector $\vec{\bar{I}}^M$ is compared to each row of Table 3.3 (vector $\vec{\bar{I}}(d_j)$) by forming the dot product

$$\vec{\bar{I}}^{M} \cdot \vec{\bar{I}}(d_j) = \sum_{i=1}^{n} \bar{I}_i^{M} \bar{I}_i(d_j). \qquad (3.6)$$

The measured diameter, d^M, is the diameter d_j of Table 3.3 for which the dot product of equation (3.6) is the greatest (maximum = 1).

Simulation Program for the Particle Sizing System

To effectively quantify ambiguity, a Monte Carlo simulation program was developed for the sizing scheme of Figure 1.1. Measurement errors affect the amount of ambiguity as demonstrated in Figure 3.1. The ratio value R = 2.25 corresponds to the diameters 4.4, 4.75, 6.7, 7.0, 8.25 and 8.6μ. However, with uncertainty in the ratio measurement (shaded region), possible diameters are in the neighborhood of 0.2, 4.4, 4.75, 5.5, 6.7, 7.0, 8.25, and 8.6μ. To effectively model the sizing system, these errors should be representative of errors generally encountered in actual intensity measurements. The simulation technique is outlined as follows:

1. The scattering angles are selected for an n-detector system.

2. The calculated Mie intensities of Table 2.1 corresponding to the n scattering angles are ratioed or vector-normalized.

3. Measured scattered intensities are simulated for each particle of an input distribution by introducing errors onto the calculated intensities scattered into the detectors for that particle size.

4. The "measured" intensities for each input particle are ratioed or vector-normalized and compared to the calculated Mie intensities constructing an interpreted size distribution, for convenience called the "measured" distribution.

5. The "measured" and input distributions are compared for a

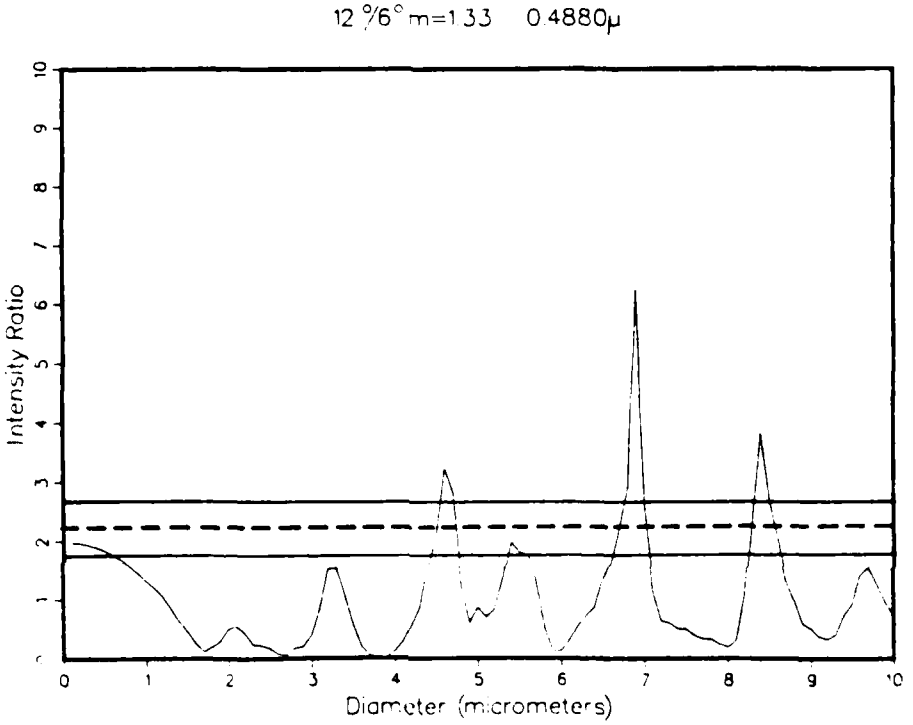

Figure 3.1. Ratio Plot Versus Diameter for Perpendicularly Polarized Components of Intensities Scattered into Detectors Located at 6° and 12°.

quantitative amount of error.

The techniques for selecting the scattering angles are discussed in later sections, although, any choice and number of angles may be used in the simulation program.

An input distribution of particle sizes is generated over a subinterval of the particle size range [dmin, dmax] by either systematically, or randomly selecting a statistically large number of particle diameters according to an input distribution function $n^i(d)$. This selected input diameter can, in general, take on any value within the continuous size subinterval. For each d, the Mie intensities $\{I(d, \theta_1), I(d, \theta_2), \ldots, I(d, \theta_n)\}$ are obtained from Table 3.1, interpolating as necessary.

A simple, yet effective, means of simulating measured intensities is to assume that a "measured" intensity scattered into a detector is the calculated value in error by a percentage of the calculated value. A number E_i is randomly selected within the interval [Emin, Emax], where E_i may be a function of the scattered intensity. Measured intensities are simulated for a diameter d by introducing errors onto each Mie intensity according to

$$I^M(d, \theta_i) = I(d, \theta_i) + E_i \, I(d, \theta_i), \tag{3.7}$$

where E_i is the error randomly selected for the i^{th} detector for each particle processed. The interval [Emin, Emax] is referred to as the error interval.

The "measured" intensity values are compared to the look-up table yielding a "measured" diameter d^M. The particle size range [dmin, dmax] is divided into size bins. As each input particle size is analyzed, the

input and "measured" diameters are stored in respective size bins (different distributions), thus constructing input, $n^i(d_j)$, and "measured," $n^M(d_j)$, distributions of discrete diameters that can be numerically compared. For this study, the size interval [0.1μ, 10.0μ] is divided into 100 size bins denoted by d_j. Particle diameters within a subinterval $[d_j - 0.05\mu, d_j + 0.05\mu]$ are grouped into the size bin d_j, except for bins $d_1 = 0.1\mu$ and $d_{100} = 10.0\mu$, which span half this size subinterval. The distribution $n(d_j)$, for either input or "measured," is defined by $\Delta n = n(d_j)\Delta d$, where Δn is the number of particles within the size interval of the bin.

The amount of ambiguity is quantitatively determined from the error in the "measured" to input distributions, calculated by

$$Err = \sum_{j=1}^{100} [n^i(d_j) - n^M(d_j)]^2. \qquad (3.8)$$

Monte Carlo Search Technique

Detectors for the sizing scheme of Figure 1.1. may be placed at scattering angles $\theta_{min} \leq \theta \leq \theta_{max}$. There are cases for which the range of placement should be restricted. For example, Hodkinson [11] suggested and Gravatt [12] offered evidence that the forward lobe region (diffraction dominated) is least affected by the index of refraction. Thus, if the particles being sized are of unknown composition or of variable refractive index, detectors should be located, if reduction of ambiguity permits, only at forward scattering angles. If the refractive index and particle shape are known and reasonably constant, the full range of θ might allow sufficient reduction of ambiguity with a lesser number of detectors.

For a given size range of interest, it is desirable to determine the minimum number of detectors that sufficiently reduce the particle size ambiguity. The Mie scattering equations are too complicated to allow general analytical solutions to this problem. Therefore, a comparative-type numerical analysis is required. A generalized search technique is needed that can be applied for each application of the sizing instrument. There are limitations placed on any such numerical analysis. First the scattering angles and diameters must be made discrete as illustrated in Table 2.1. Then ideally, the search would begin with a small number of scattering angles, compare existing ambiguity for all possible combinations, and continue with additional angles until sufficient ambiguity reduction is achieved. However, due to the large amounts of data, it is impractical even with the use of presently available high speed computers to compare all combinations of angles for more than two or three detectors, depending on the range of angles and diameters and their respective spacing. A good search technique can locate a minimal combination of scattering angles that work well in reducing particle size ambiguity, but to determine if the set is truly optimum is impractical.

A Monte Carlo search technique was developed because it can incorporate measurement errors which affects particle size ambiguity as explained earlier. This technique utilizes the simulation program to quantify ambiguity for a set of n detector scattering angles as the number and placements of detectors are varied. The search technique is outlined as follows:

1. The size range of interest, [0.1μ, 10.0μ], is divided into the

five subintervals shown in Table 3.4.

Table 3.4. Size Subintervals for Distributions.

	Subintervals	Input Distribution	"Measured" Distribution
1	[0.1μ, 2.0μ]	$n_1^i(d_j)$	$n_1^M(d_j)$
2	[2.0μ, 4.0μ]	$n_2^i(d_j)$	$n_2^M(d_j)$
3	[4.0μ, 6.0μ]	$n_3^i(d_j)$	$n_3^M(d_j)$
4	[6.0μ, 8.0μ]	$n_4^i(d_j)$	$n_4^M(d_j)$
5	[8.0μ, 10.0μ]	$n_5^i(d_j)$	$n_5^M(d_j)$

2. An input particle size distribution is assumed over one of the size subintervals. The Monte Carlo simulation program is applied to all combinations of two scattering angles of Table 2.1. The combination for which the ambiguity is the least, as determined from equation (3.8), is chosen as the first two detector scattering angles for the MRSPC, thus establishing a two-detector system, (θ_1, θ_2).

3. The Monte Carlo simulation is then applied independently to each of the five subintervals of Table 3.4 using the two-detector scattering angles previously selected. This determines an overall amount of ambiguity and an amount for each subinterval. The size interval with the greatest amount of ambiguity is used in selecting the next detector scattering angle.

4. The simulation program is applied to sets of three scattering angles $(\theta_1, \theta_2, \theta_t)$, where θ_t, called a trial angle, represents one of the remaining scattering angles of Table 2.1. The angle θ_t that best

complements θ_1 and θ_2 in reducing size ambiguity for the subinterval from step 3 with the maximum ambiguity, is chosen as the third detector scattering angle.

5. Additional detectors are added in this manner until sufficient reduction in particle size ambiguity is achieved.

In order not to bias a particular range of particle sizes within a subinterval during the search, a flat distribution of particle sizes was assumed over each subinterval. Rather than rely on a random number generator to generate the flat distribution, the diameters for the input distributions are generated by stepping across the size subinterval in diameter steps, ISTEP, determined by

$$\text{ISTEP} = \frac{\text{dmax} - \text{dmin}}{\text{NP}}, \tag{3.9}$$

where dmin and dmax are respectively minimum and maximum diameters of the i^{th} subinterval of Table 3.2 and NP is the number of particles making up the input distribution. Also, for uniformity throughout the search for a particular scattering angle, the same set of random numbers is used for E_i in simulating "measured" intensities by initializing the random number generator each time a new trial angle is analyzed.

The advantages of the Monte Carlo technique are obvious from the standpoint that angle selections are determined from a prediction of the MRSPC performance. Measurement errors based on the actual instrumentation can be used for simulating measured scattered intensities. However, a disadvantage is the large amount of computer time required for the search.

Normalized Vector Technique for Selecting Scatter Angles

Ambiguity in particle size as shown in Figure 1.4 exists where a given intensity ratio corresponds to more than one diameter. This concept can be extended to multiple ratio curves by examining Table 3.3. Ambiguity exists between two diameters d_j and d_k if the dot product $\vec{I}(d_j)\cdot\vec{I}(d_k)\approx 1$. This suggests that a quantitative amount of ambiguity for a given n-detector systems might be determined from the dot products of all combinations of the vectors of Table 3.3. The dot products put into matrix form are shown in Table 3.5. The resulting matrix is symmetric about the diagonal with all diagonal elements equal to one. The maximum value of any element is 1 because all vectors are unit vectors. It would be desirable, for minimum ambiguity, to find a combination of n-detectors for which all off-diagonal elements are small in value, close to zero. Since the matrix is symmetric, only the upper triangle needs to be considered. The first off-diagonal elements represent comparisons of diameters d_j and d_{j+1}, two neighboring sizes within the size range. If distinguishing these diameters is unimportant, then this off-diagonal need not be considered. The summation of the matrix values of the upper triangle,

$$\text{AREA} = \sum_{j=1}^{N-1} \sum_{k=j+1}^{N} \vec{I}(d_j) \cdot \vec{I}(d_k) \qquad (3.10)$$

serves as a quantitative measure for an amount of ambiguity for a set of n detectors, where N is the number of discrete diameters.

Table 3.5. Matrix of Dot Products for All Combinations of Vectors of Table 3.3.

	d_1	d_2	...	d_n
d_1	$\vec{I}(d_1)\cdot\vec{I}(d_1)$	$\vec{I}(d_1)\cdot\vec{I}(d_2)$	...	$\vec{I}(d_1)\cdot\vec{I}(d_n)$
d_2	$\vec{I}(d_2)\cdot\vec{I}(d_1)$	$\vec{I}(d_2)\cdot\vec{I}(d_2)$	...	$\vec{I}(d_2)\cdot\vec{I}(d_n)$
	.	.		.
	.	.		.
	.	.		.
d_n	$\vec{I}(d_n)\cdot\vec{I}(d_1)$	$\vec{I}(d_n)\cdot\vec{I}(d_2)$	...	$\vec{I}(d_n)\cdot\vec{I}(d_n)$

Use of this approach as a search technique requires significantly less computer time than the Monte Carlo search technique, but is still impractical for analyzing all combinations of n detector angles for n 2. However, using similar search strategy as before, the first two detector scattering angles can be selected by comparing all combinations of scattering angles taking two at a time. This is the combination for which the summation of dot products is minimum. Additional detector angles are added one at a time such that the new angle best complements fixed angles in minimizing the summation of the dot products. As each detector scattering angle is added, the simulation program can be used to determine if sufficient ambiguity reduction has been achieved.

The computer time required to select detector angles is significantly reduced. However, this technique does not incorporate measurement errors that might bias scattering angle selection.

RESULTS

Mie theory calculations must be performed for Table 2.1 before applying the techniques discussed in Chapter 3. This requires a knowledge of the incident light polarization and wavelength, the polarization of light accepted by the detector (if polarizing filters are used), the solid angle subtended by a detector, the refractive indices of the particles and surrounding medium, and the range and incremental steps for both the scattering angle and diameter. For the development and evaluation of the techniques, calculations were made for the following conditions.

1. The incident laser beam is polarized perpendicular to the plane of the detectors. The wavelength of the incident beam is 0.4880 .

2. Polarizing filters placed in front of the detectors transmit only scattered light polarized perpendicular to the scattering plane, thus allowing calculations from the integral of the intensity function i_1, equation (2.20).

3. A detector subtends a solid angle for which $\Delta\theta = \quad = 2.53°$ for calculations of equation (2.20).

4. The medium containing the particle is assumed to have a refractive index of 1.0. The particles are assumed to be water particles with a refractive index of 1.33.

5. Calculations were made for each scattering angle $6° \leq \theta_j \leq 174°$ in increments of 1°, for particle diameters d_j within the size $0.1 \leq d_j \leq 10.0$

in 0.01μ steps. Note: Mie equations were used to calculate the intensities in steps of 0.1μ. Table 2.1 was refined to 0.01μ steps using Newton's Forward Difference Interpolation Technique [15]. Mie calculations are plotted in Figure 4.1 with and without interpolated values. As shown in the plot, the interpolated values agree closely with the calculated values.

An evaluation of the Monte Carlo simulation program and the Monte Carlo search technique is given. The ratio method is used for particle size interpretation. The results of detector angle selections are given for water droplets assuming measurement errors described for equation (3.7). The selected scattering angles and predicted sizing performance of the MRSPC for aluminum oxide particles for each of three wavelengths, 0.4880μ, 1.06μ, and 1.32μ, are presented. A comparison of the ratio method and vector method for particle size interpretation is presented along with the angles selected for the detectors using the vector method.

Evaluation of the Simulation Program

The Monte Carlo search technique requires large amounts of computer time. Both NP, the number of particles per input distribution, and Δd, the diameter step size for the look-up table, Table 3.1, greatly affect the computer time. Scattering angles, selected arbitrarily, were analyzed using the simulation program to determine the effect of NP on the distribution errors, equation (3.3). The simulation program generates simulated scattered intensity measurements by introducing random errors, equation (3.7), onto calculated intensities. In any neighborhood of a diameter of the input distribution, there should be a sufficient number of particles generated by the simulation program

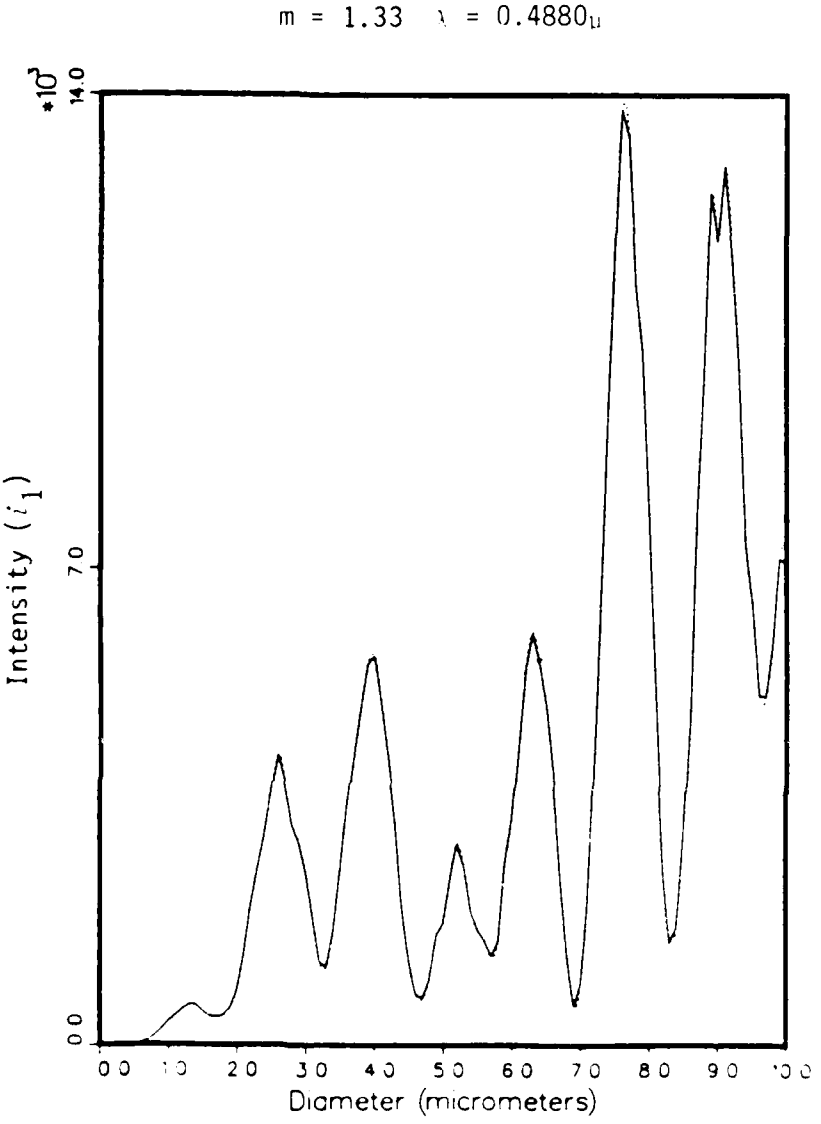

Figure 4.1. Mie Calculations, i_1, for a Detector of the MRSP Centered at 6° where the Dotted Curve Represents Interpolated Values.

to insure a representative sample of random error combinations for the simulated intensities.

To determine a minimum allowable NP, the simulation program was used to generate input-to-"measured" distribution errors for values of NP between 100 and 3000 for an arbitrary set of angles, {6°, 9°, 12°, 15°}. The diameter step size $\Delta d = 0.01\mu$ was used for this analysis. The "measured" distributions, for this set of angles as NP was varied, contained incorrectly sized particles at the same diameters for NP > 500. Particles at diameters of the "measured" distribution outside the input size interval indicate ambiguity with diameters within the input size interval. The square root of the distribution errors is proportional to NP, illustrated in Figure 4.2, if a statistical number of particles are used for the Monte Carlo simulation. Each curve represents the distribution errors for one of the five size intervals described in Table 3.4. The plots indicate that NP > 500 should be sufficient to maintain statistical results. Similar results were obtained for other combinations of four detectors and the results were even better for a larger number of detectors. For the remainder of this work, NP = 500.

To determine a maximum allowable Δd, the Monte Carlo search technique was used to select detector scattering angles and predict the performance of the sizing system for values of Δd between 0.01 and 0.1 . Detector angles selected from a restricted range of θ and the corresponding distribution errors for the diameter step sizes 0.02 , 0.03 , 0.05 , and 0.1 are given in Table 4.1. Each row of the table represents the input-to-"measured" distribution errors calculated by the search program as each detector angle is selected. Input and "measured"

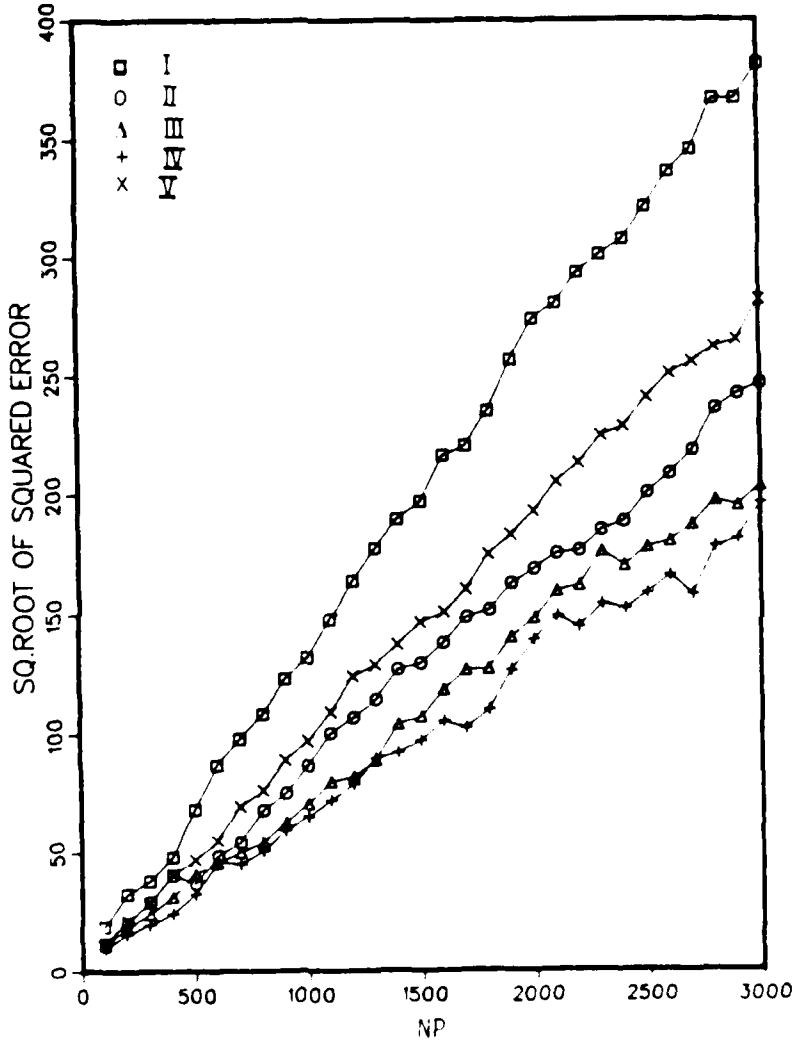

Figure 4.2. The Square Root of Distribution Errors of the Simulation Program for Values of NP.

Table 4.1. Selected Scattering Angles and Predicted Performance Errors for Water (m = 1.33 at $\lambda = 0.4880\mu$) with [θmin, θmax] = [6°, 60°], [Emin, Emax] = [-0.2, 0.2] and NP = 500.

DISTRIBUTION ERRORS					Detector Angles	Number of
I	II	III	IV	V	(degrees)	Detectors
7112	9644	10890	10674	8966	15,38	2
6254	7350	5484	8888	6548	50	3
4898	4982	5006	4312	3870	9	4
2568	2754	2194	2638	2006	18	5
1848	1134	1054	1608	970	6	6
1180	920	700	712	378	21	7
842	758	568	602	330	30	8
		$\Delta d = 0.1\mu$				
5940	10162	8548	9860	9100	13,49	2
4826	4940	6994	7804	8050	44	3
3138	3194	4604	5144	3184	52	4
1810	1902	1996	2010	1924	8	5
1042	1106	802	612	924	16	6
440	406	292	336	290	20	7
274	356	360	214	272	24	8
		$\Delta d = 0.05\mu$				
6278	9824	10314	9960	9752	17,50	2
4394	3902	4638	7060	8282	6	3
2106	3314	2980	3464	2300	13	4
956	1066	1112	1054	1480	24	5
356	764	576	872	546	10	6
418	344	400	226	414	21	7
370	346	360	246	278	41	8
		$\Delta d = 0.03\mu$				

Table 4.1 (continued)

DISTRIBUTION ERRORS					Detector Angles (degrees)	Number of Detectors
I	II	III	IV	V		
6338	9214	8568	10060	8206	14,48	2
3814	4736	4940	5442	6882	6	3
1456	1886	1524	1898	2740	11	4
716	800	672	1074	1040	39	5
162	94	350	194	612	31	6
94	182	248	190	210	32	7
222	98	74	220	224	36	8

$\Delta d = 0.02\lambda$

distributions are plotted in Figures 4.3 to 4.9 for Δd = 0.02μ to illustrate distribution errors as each detector is added. The sets of selected detector angles in Table 4.1 have several angles in common, or at least, close in value, although the angles are selected in a different order for each Δd. The set of angles for Δd = 0.05μ has two angles distinctly different from angles of the other sets.

Of importance is the effect of Δd on the distribution errors. The distribution errors are significantly smaller for a fewer number of detectors as Δd is decreased. Table 4.1 indicates that if Δd = 0.02μ, only 5 or 6 detectors are required to achieve about the same error reduction as 8 detectors for Δd = 0.1μ. In addition to Table 4.1, distribution errors for fixed sets of scattering angles showed a significant decrease in errors as Δd was decreased from 0.1μ to 0.02μ. There was little difference in the input-to-"measured" distribution errors and plots for Δd = 0.02μ and 0.01μ. Thus, the look-up table should be calculated for a maximum diameter step size of Δd = .02μ to reduce errors in particle size interpretation for a given number of detectors. Since Δd does affect the selection of the detectors, the search should incorporate the value of Δd that will be used in particle size interpretation for actual measurements.

Detector angle selections for Table 4.1 and Figures 4.3 to 4.9 assumed the error interval [-0.2, 0.2] for simulated measurements. The number of particles per distribution and diameter step size are respectively, 500 and 0.02μ for the remainder of this work. Results of scattering angle selections for the error intervals [-0.2, 0.2], [-0.1, 0.1] and [0.0, 0.0] are shown in Table 4.2 for water particles. As expected, a decrease in measurement error decreases the distribution

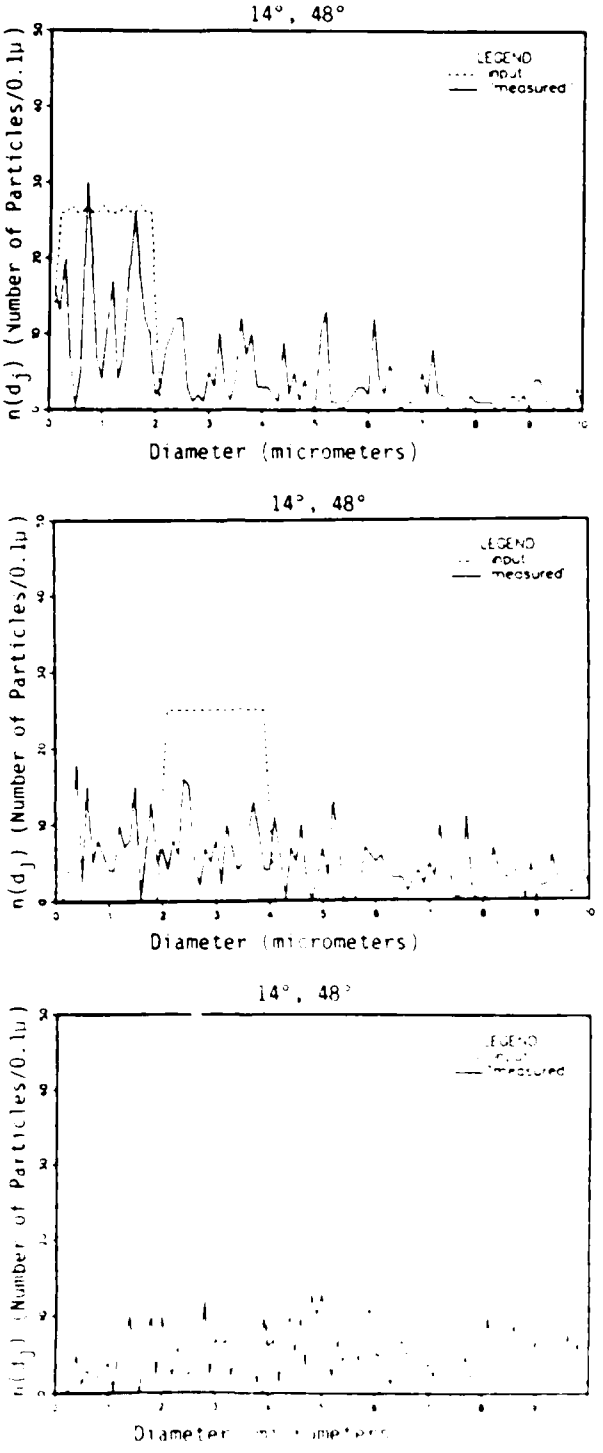

Figure 4.3. Input and Measured Distributions for a Two-Detector System for [illegible] 0.4880 μ and Error Interval [-0.2, 0.2].

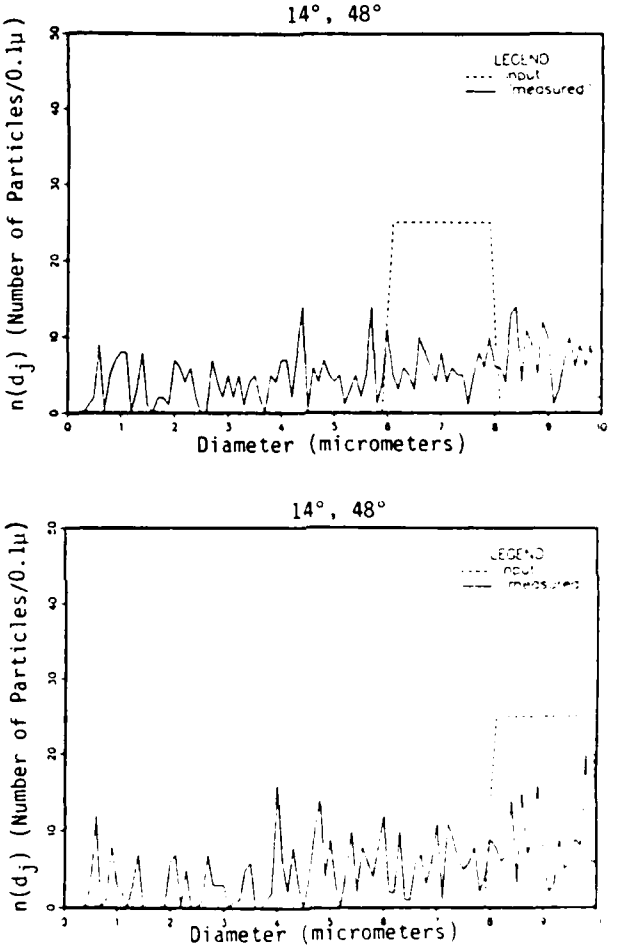

Figure 4.3. (Continued).

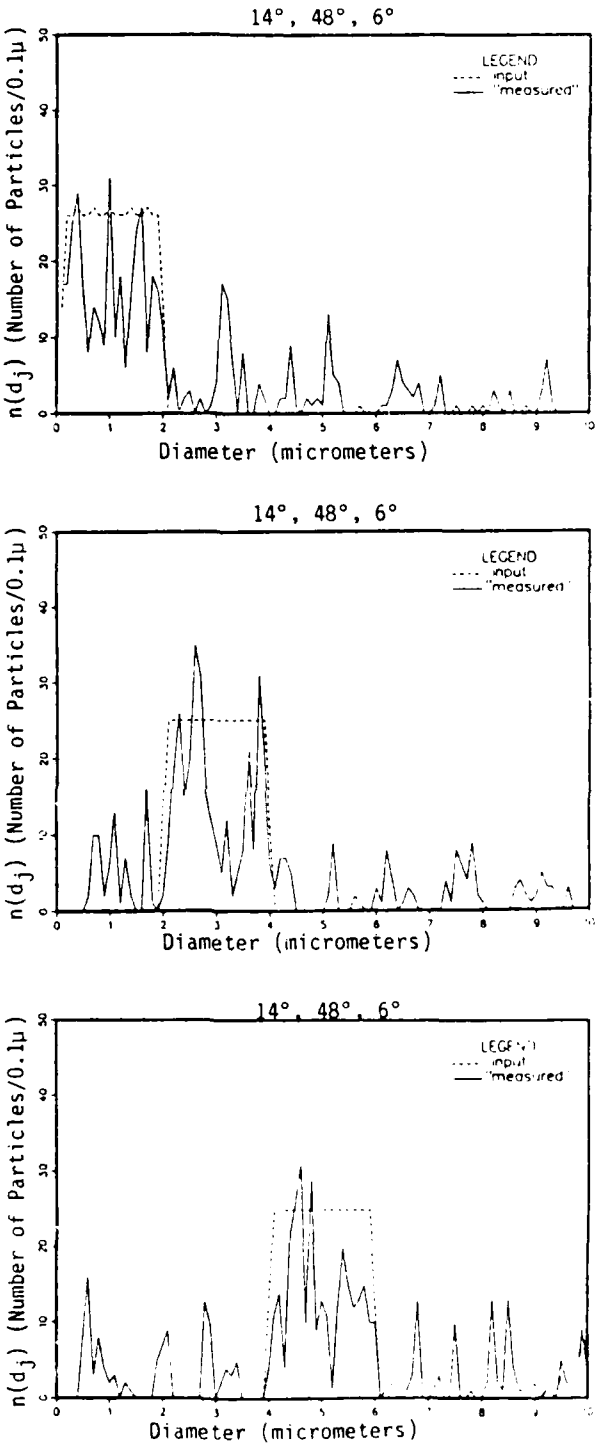

Figure 4.4. Input and "Measured" Distributions for a Three-Detector System for m = 1.33, λ = 0.4880μ and Error Interval [-0.2, 0.2].

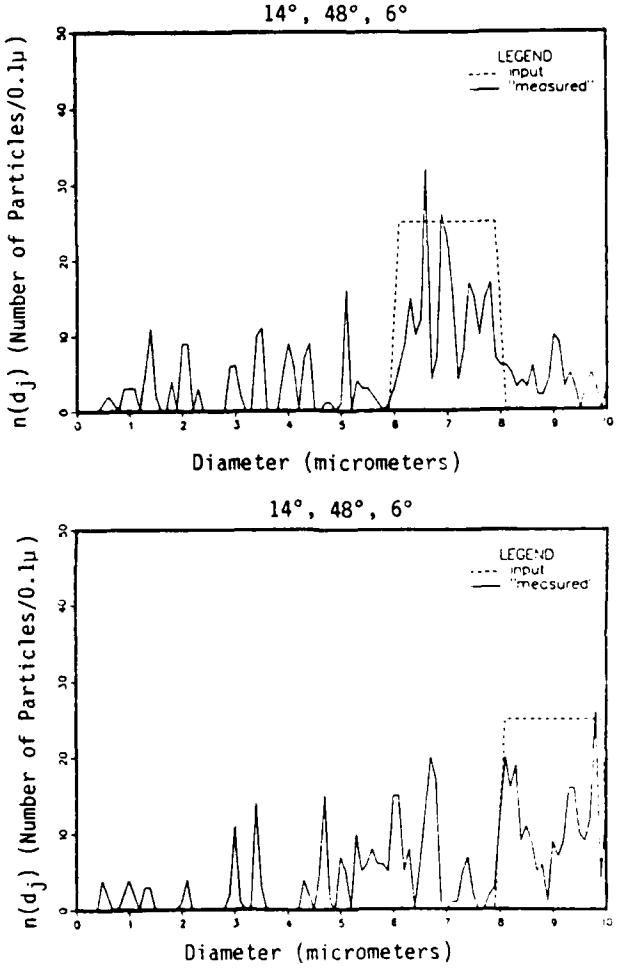

Figure 4.4. (Continued).

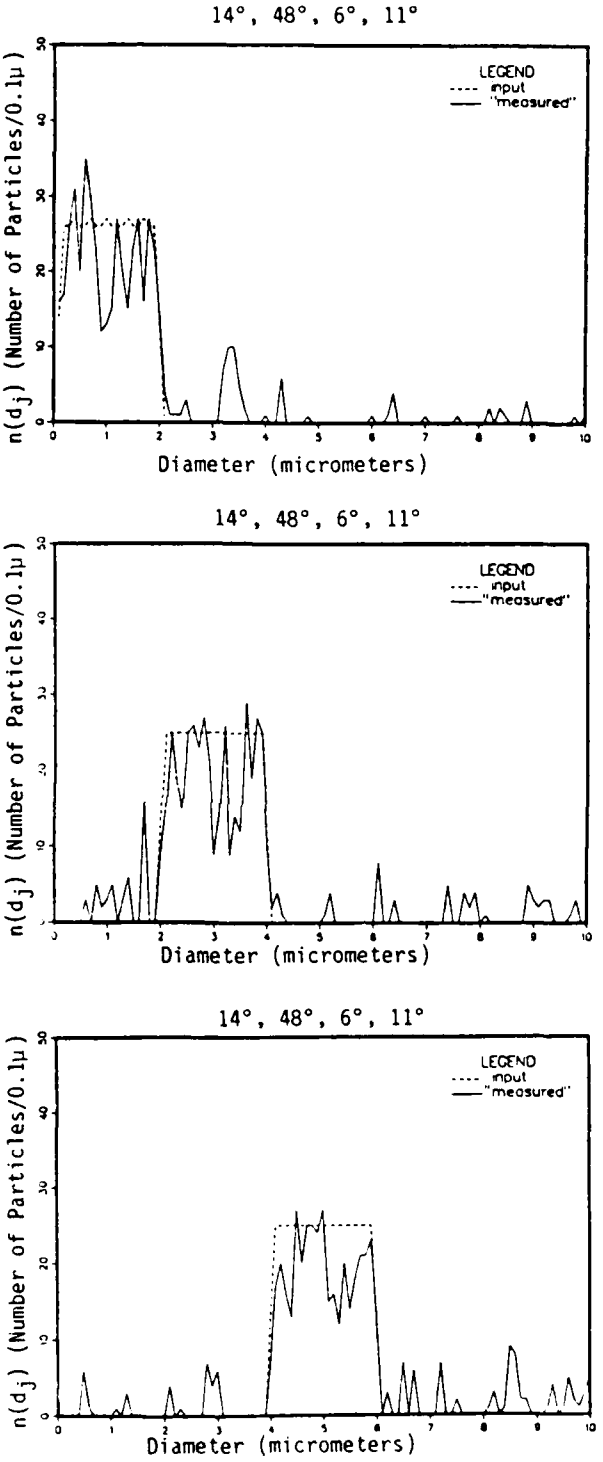

Figure 4.5. Input and "Measured" Distributions for a Four-Detector System for m = 1.33, λ = 0.4880μ and Error Interval [-0.2, 0.2].

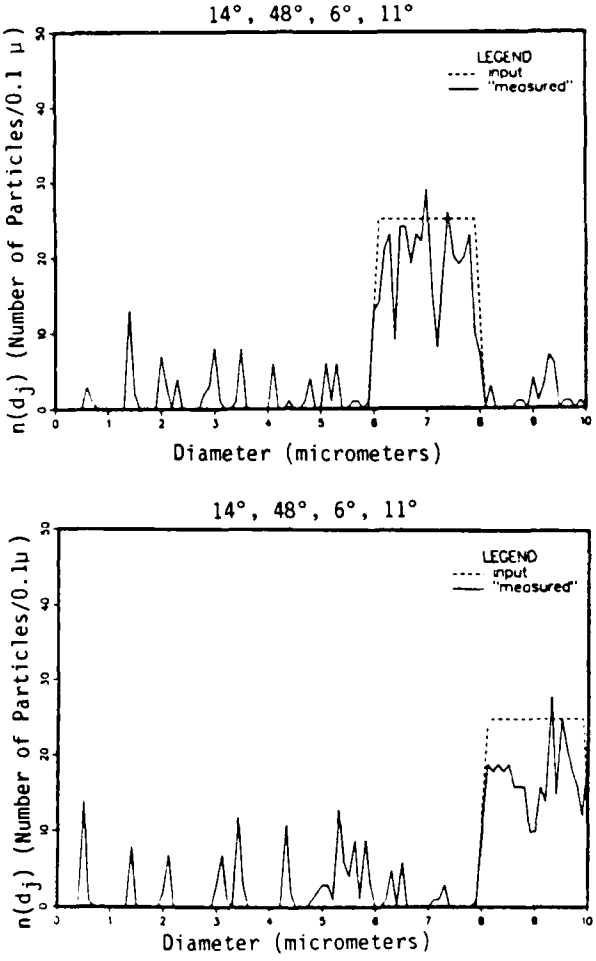

Figure 4.5. (Continued).

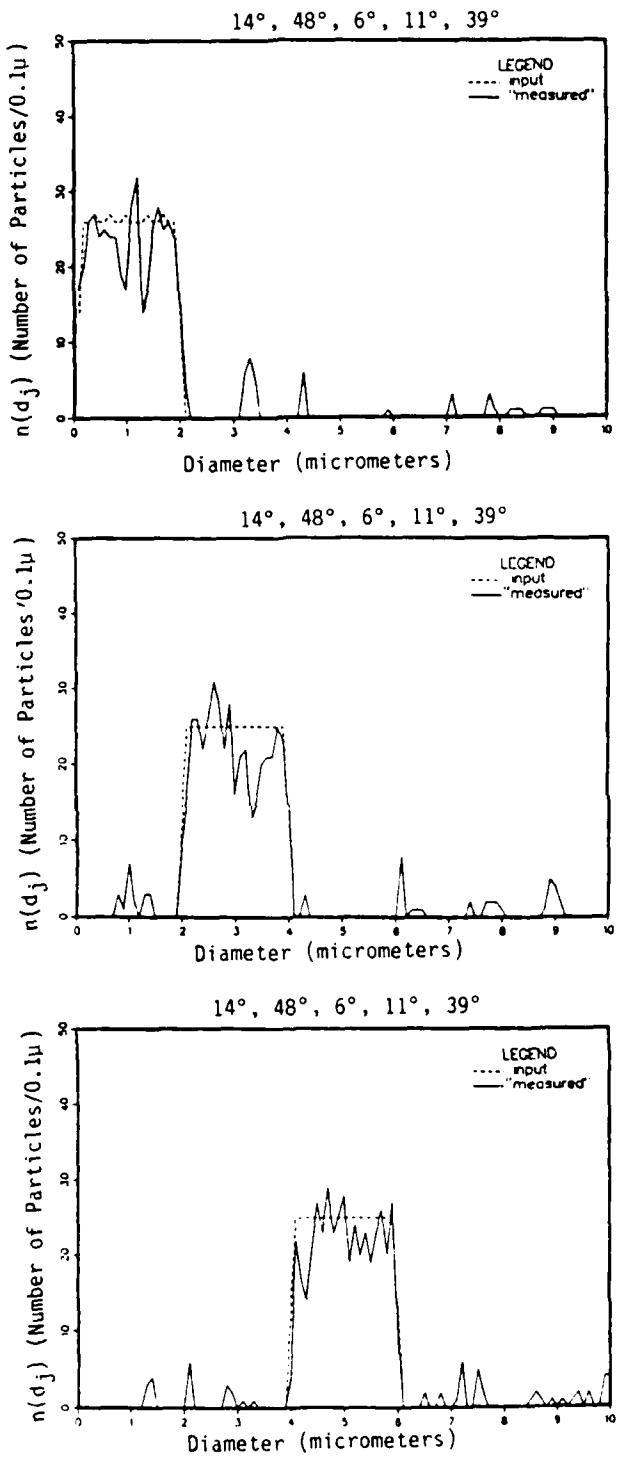

Figure 4.6. Input and "Measured" Distributions for a Five-Detector System for m = 1.33, λ = 0.4880μ and Error Interval [-0.2, 0.2].

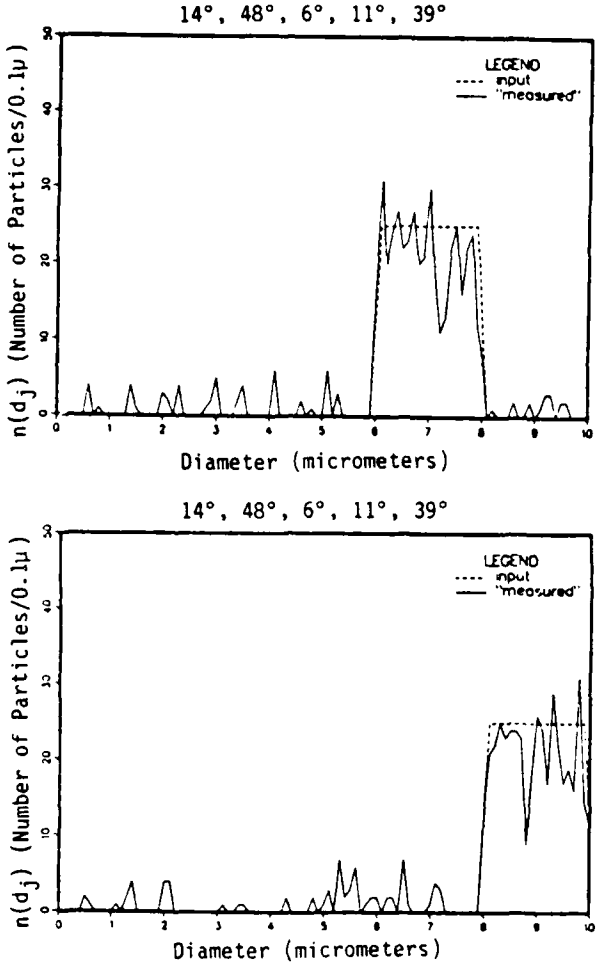

Figure 4.6. (Continued).

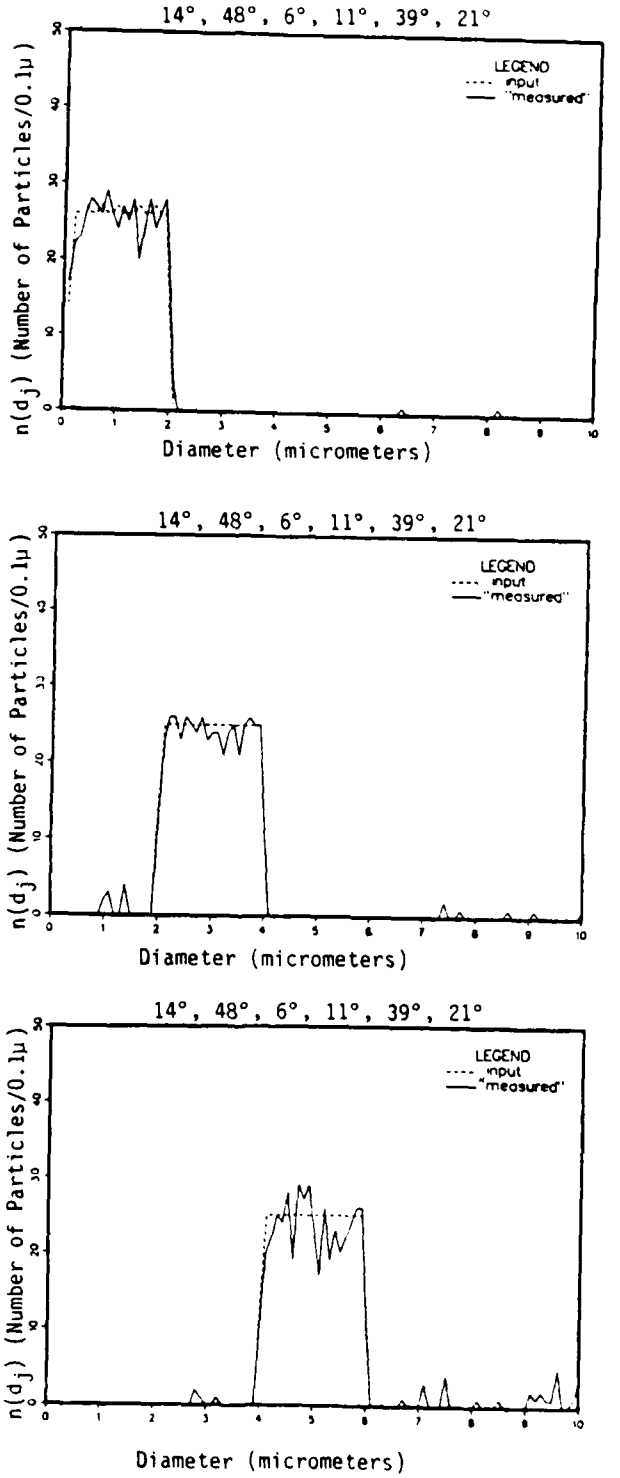

Figure 4.7. Input and "Measured" Distributions for a Six-Detector System for m = 1.33, λ = 0.4880μ and Error Interval [-0.2, 0.2].

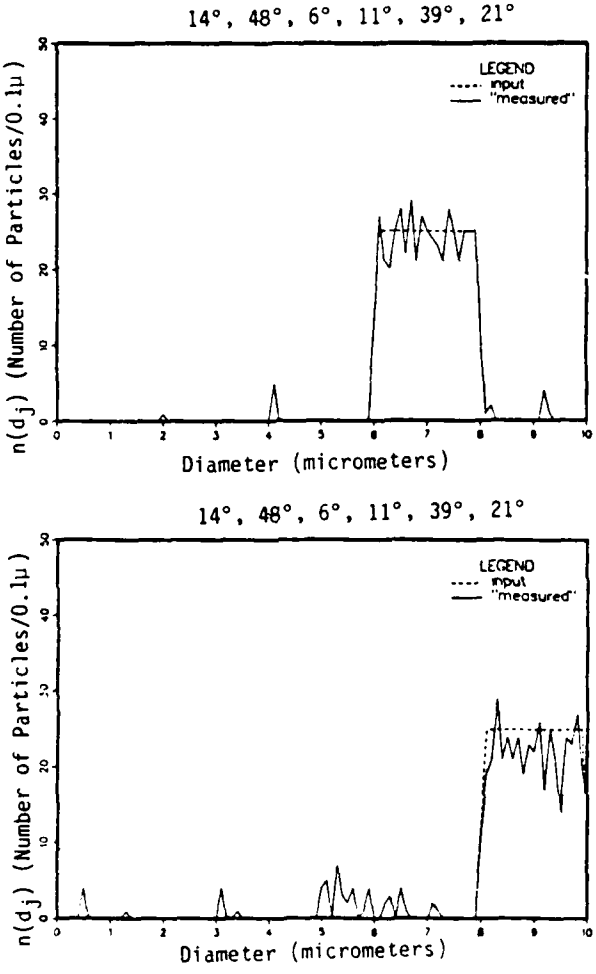

Figure 4.7. (Continued).

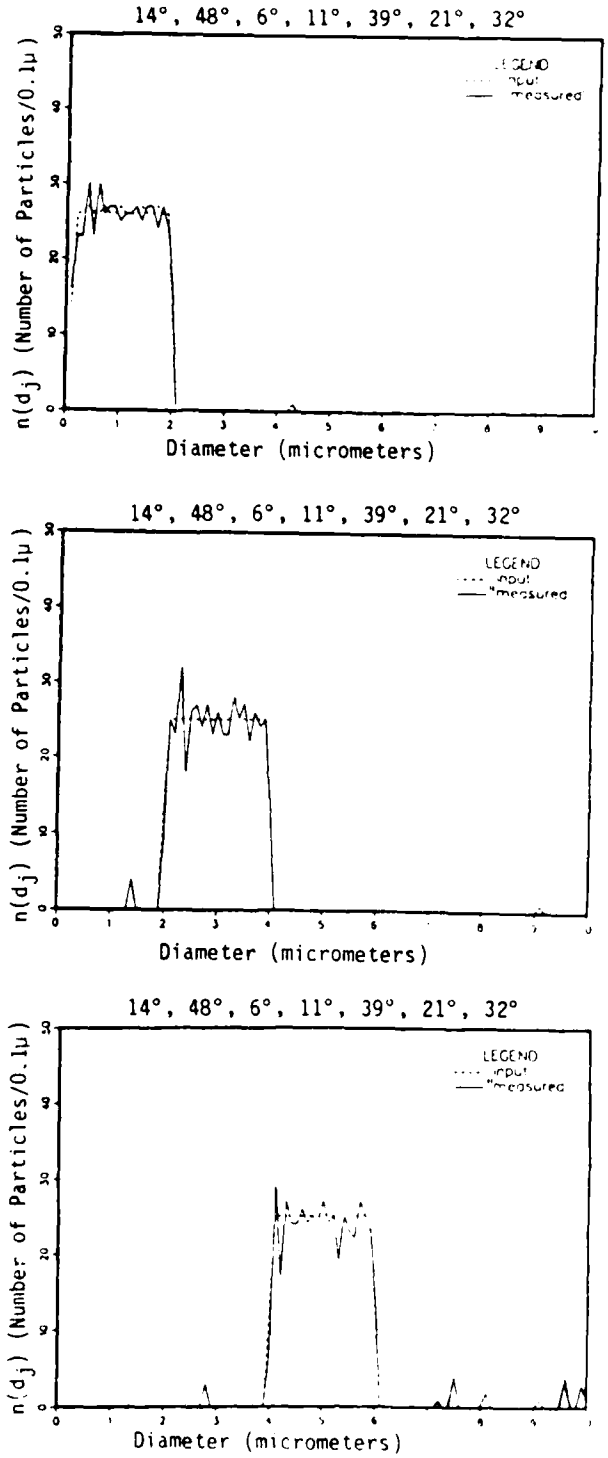

Figure 4.8. Input and "Measured" Distributions for a Seven-Detector System for m = 1.33, λ = 0.4880μ and Error Interval [-0.2, 0.2].

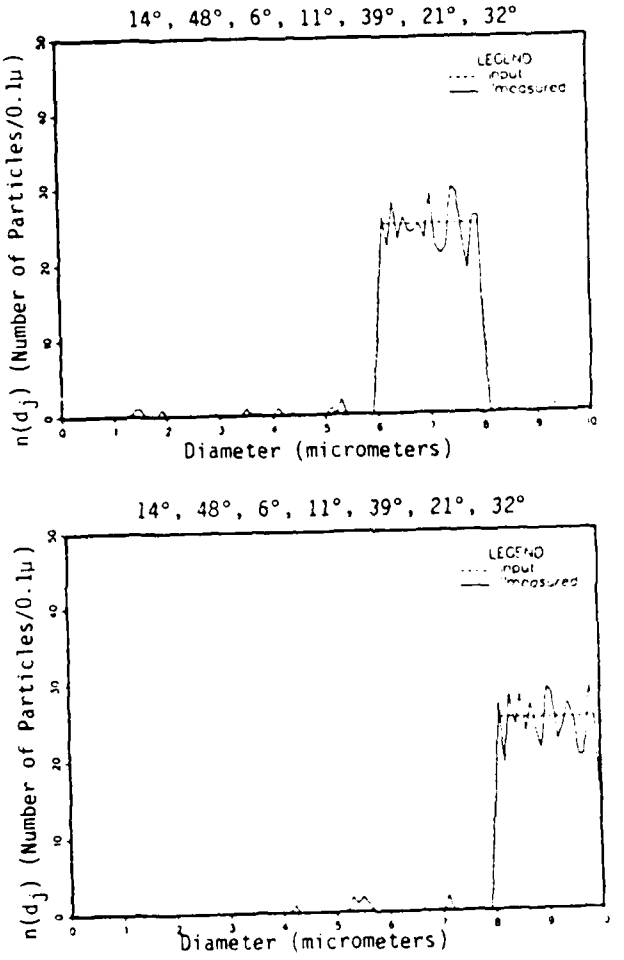

Figure 4.8. (Continued).

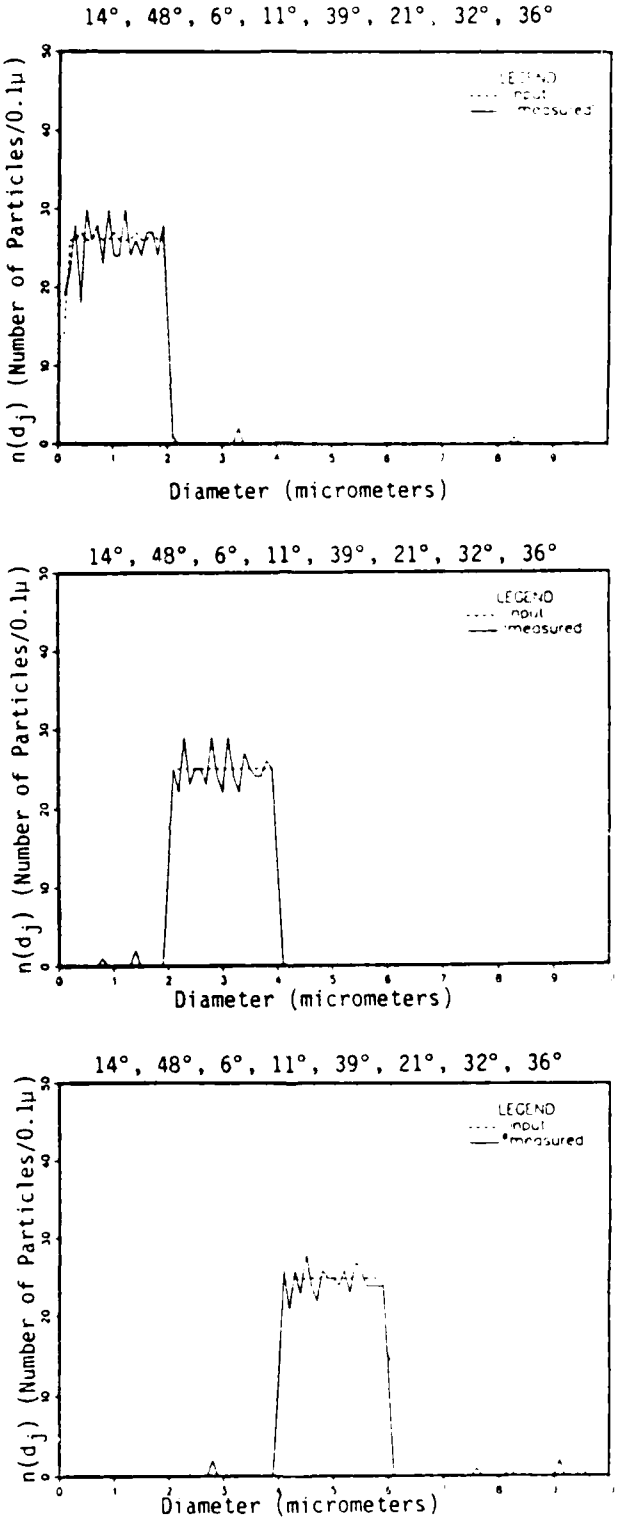

Figure 4.9. Input and "Measured" Distributions for an Eight-Detector System for m = 1.33, $\lambda = 0.4880_{\mu}$ and Error Interval [-0.2, 0.2].

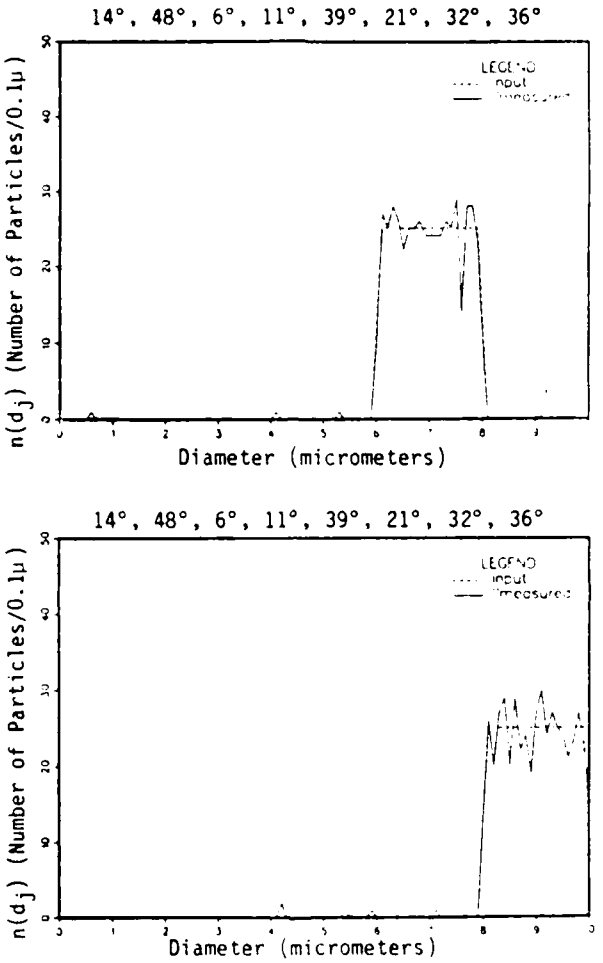

Figure 4.9. (Continued).

Table 4.2. Selected Scattering Angles and Predicted Performance Errors for Water ($m = 1.33$ at $\lambda = 0.4880\mu$) with $[\theta min, \theta max] = [6°, 60°]$, NP = 500, and $\Delta d = 0.02\mu$.

DISTRIBUTION ERRORS					Detector Angles	Number of
I	II	III	IV	V	(degrees)	Detectors
6338	9214	8568	10060	8206	14,48	2
3814	4736	4940	5442	6882	6	3
1456	1886	1524	1898	2740	11	4
716	800	672	1074	1040	39	5
162	94	350	194	612	21	6
94	182	248	190	210	32	7
222	98	74	220	224	36	8
	[Emin, Emax] = [-0.2, 0.2]					
5840	8892	9524	9766	6182	14,49	2
3650	4018	3846	3668	2730	6	3
698	434	512	356	636	11	4
112	84	108	100	294	22	5
210	46	114	72	56	19	6
98	60	44	54	166	52	7
228	70	38	26	22	32	8
	[Emin, Emax] = [-0.1, 0.1]					
3506	5340	4944	6358	6914	6,9	2
90	1040	1008	986	228	13	3
100	32	66	158	54	31	4
102	32	2	0	0	25	5
52	14	2	0	0	56	6
38	6	0	0	0	48	7
122	2	0	0	0	18	8
	[Emin, Emax] = [0.0, 0.0]					

errors for an equivalent number of detectors. Thus, for smaller measurement errors, fewer detectors are required for similar ambiguity reduction. Note that input-to-"measured" distribution errors can exist even for zero measurement errors. This is because of ambiguity and the process of making diameters discrete for the look-up table. Intensities for input diameters that fall between diameters of the look-up table are interpolated and thus have small errors with respect to intensities of the look-up table diameters without external errors being introduced. Increases in distribution errors with the addition of a detector scattering angle is attributed to ambiguity between intensity ratios for existing angles and ratios formed for the added angle.

The range in scattering angles [θmax, θmax] for Tables 4.1 and 4.2 was limited to [6°, 60°]. The range was limited for two reasons. First, to develop and present the technique, the range of detector angles is arbitrary. Secondly, semilog plots of the intensity scattering functions versus θ_j for fixed particle sizes, Figures 4.10 to 4.15, show stronger scattered intensities at the forward scattering angles over the entire range of diameters. It is favorable to locate the detectors within the highest intensity scattering region to better insure a good signal-to-noise ratio for the measurements. This is especially important for the smaller particles of the size range. Smaller particles intercept less of the incident energy and thus scatter less energy. A particle will be sized by the instrument only if scattered signals are detectable above background noise. This is a limiting factor for small particle measurements.

Detector angles selected from the full range of θ for various particles are given in Table 4.3 along with distribution

AD-A186 492 UNITED STATES AIR FORCE RESEARCH INITIATION PROGRAM 5/11
1985 TECHNICAL REPORT VOLUME 2(U) UNIVERSAL ENERGY
SYSTEMS INC DAYTON OH R C DARRAH APR 87
UNCLASSIFIED AFOSR-TR-87-1718 F49620-85-C-0013 F/G 15/3 NL

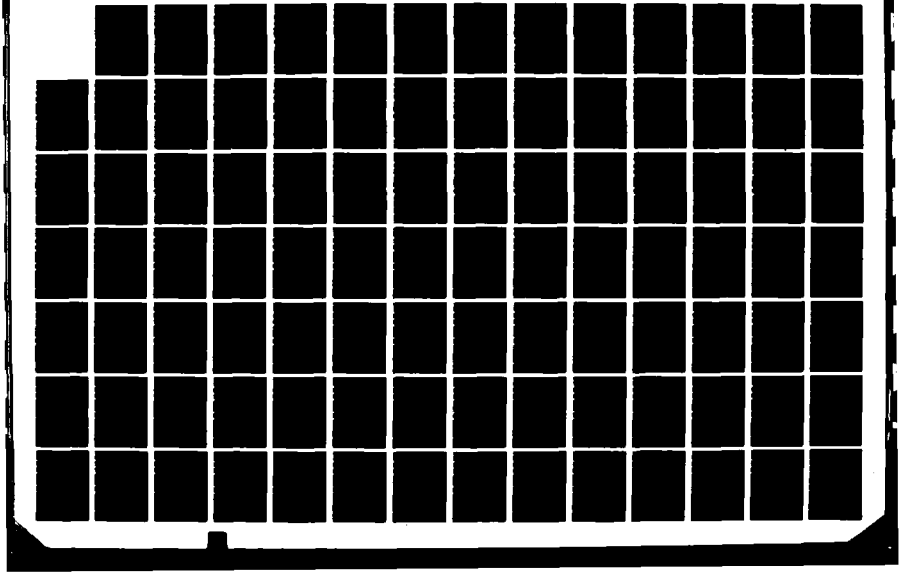

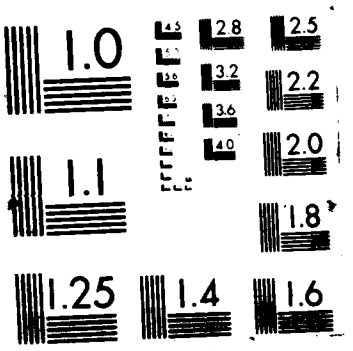
1.0
1.1
1.25
1.4
1.6
1.8
2.0
2.2
2.5
2.8
3.2
3.6
4.0

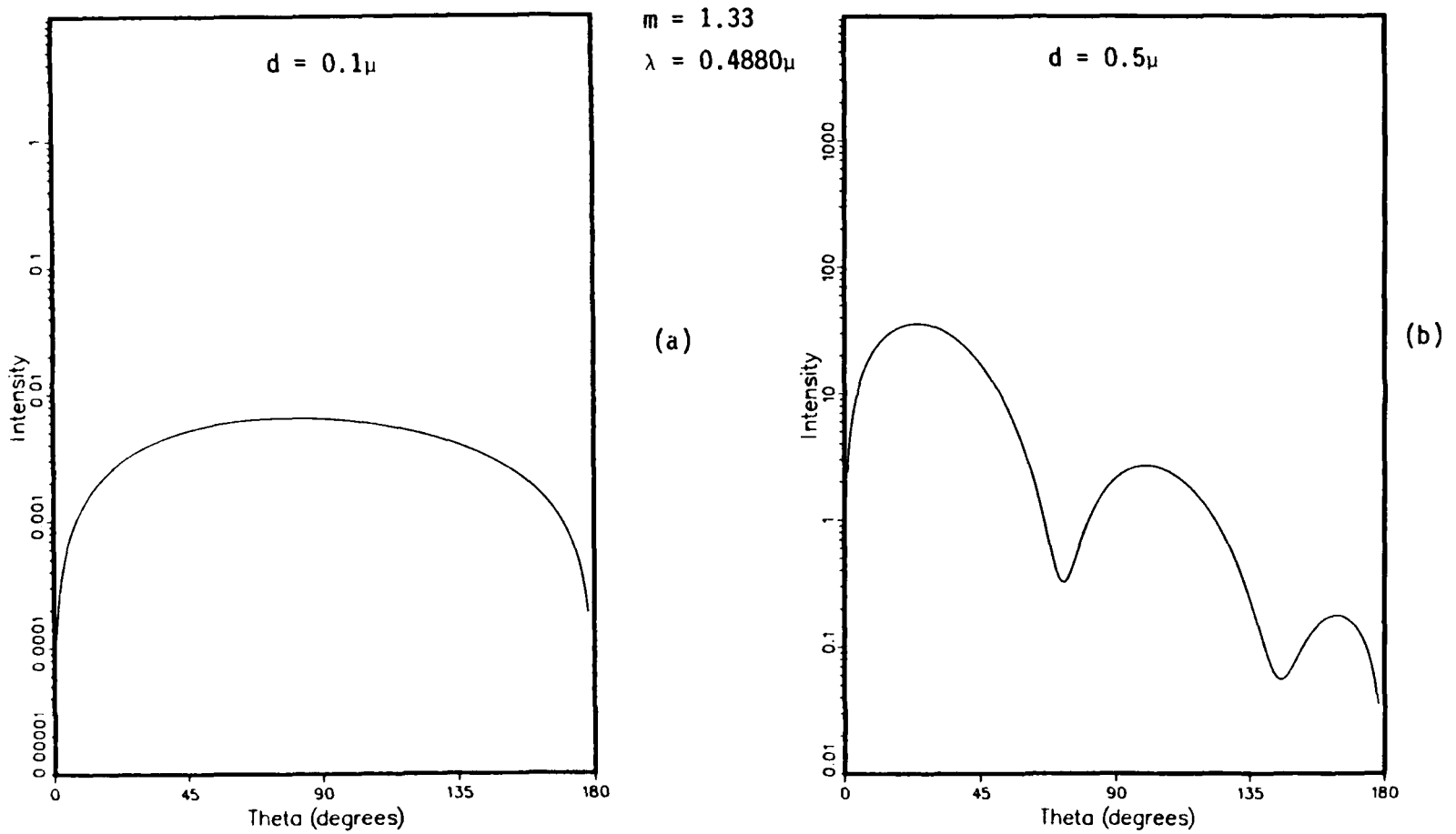

Figure 4.10. The Integrated Intensity Function i_1 Versus Theta.

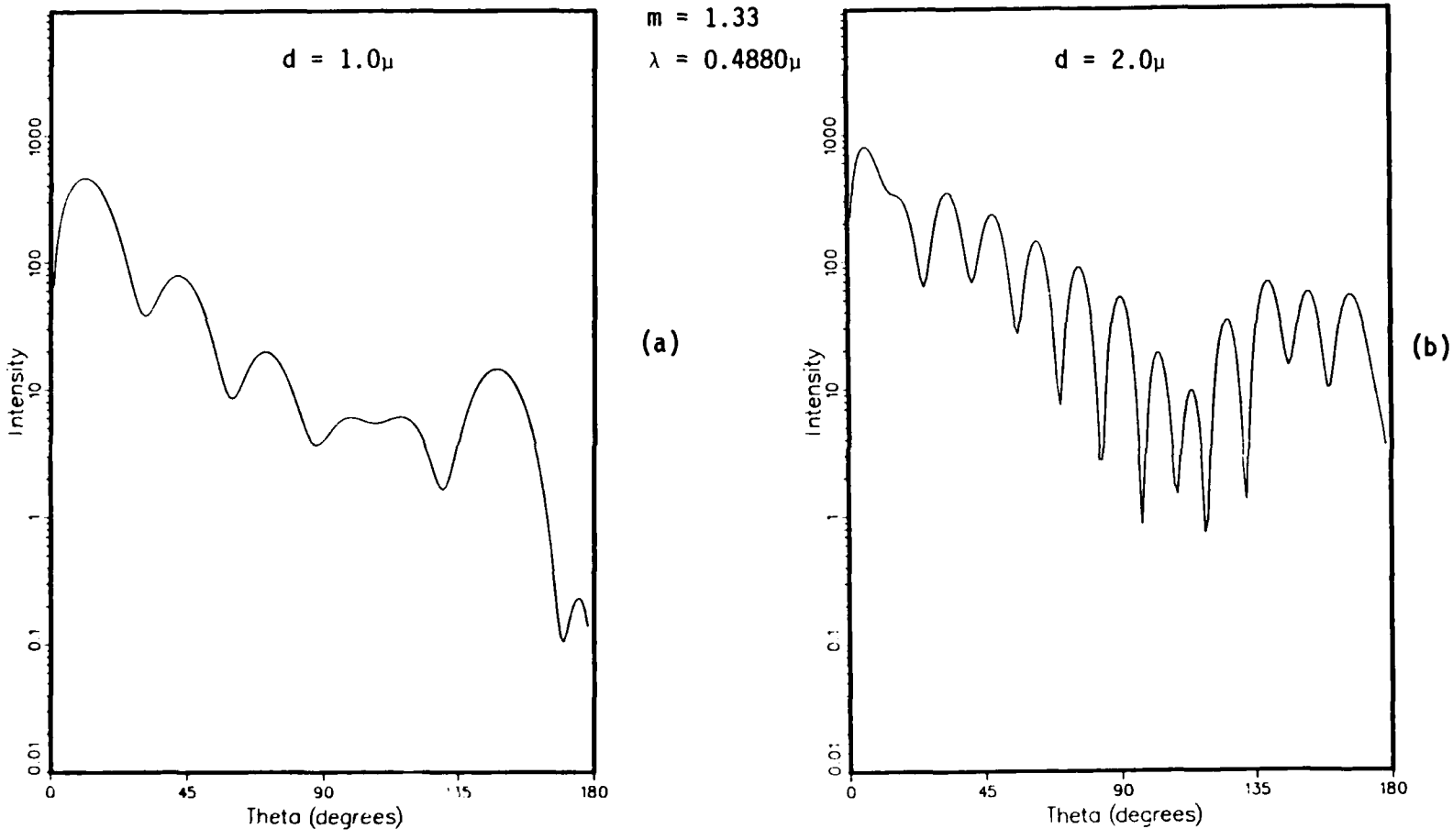

Figure 4.11. The Integrated Intensity Function i_1 Versus Theta.

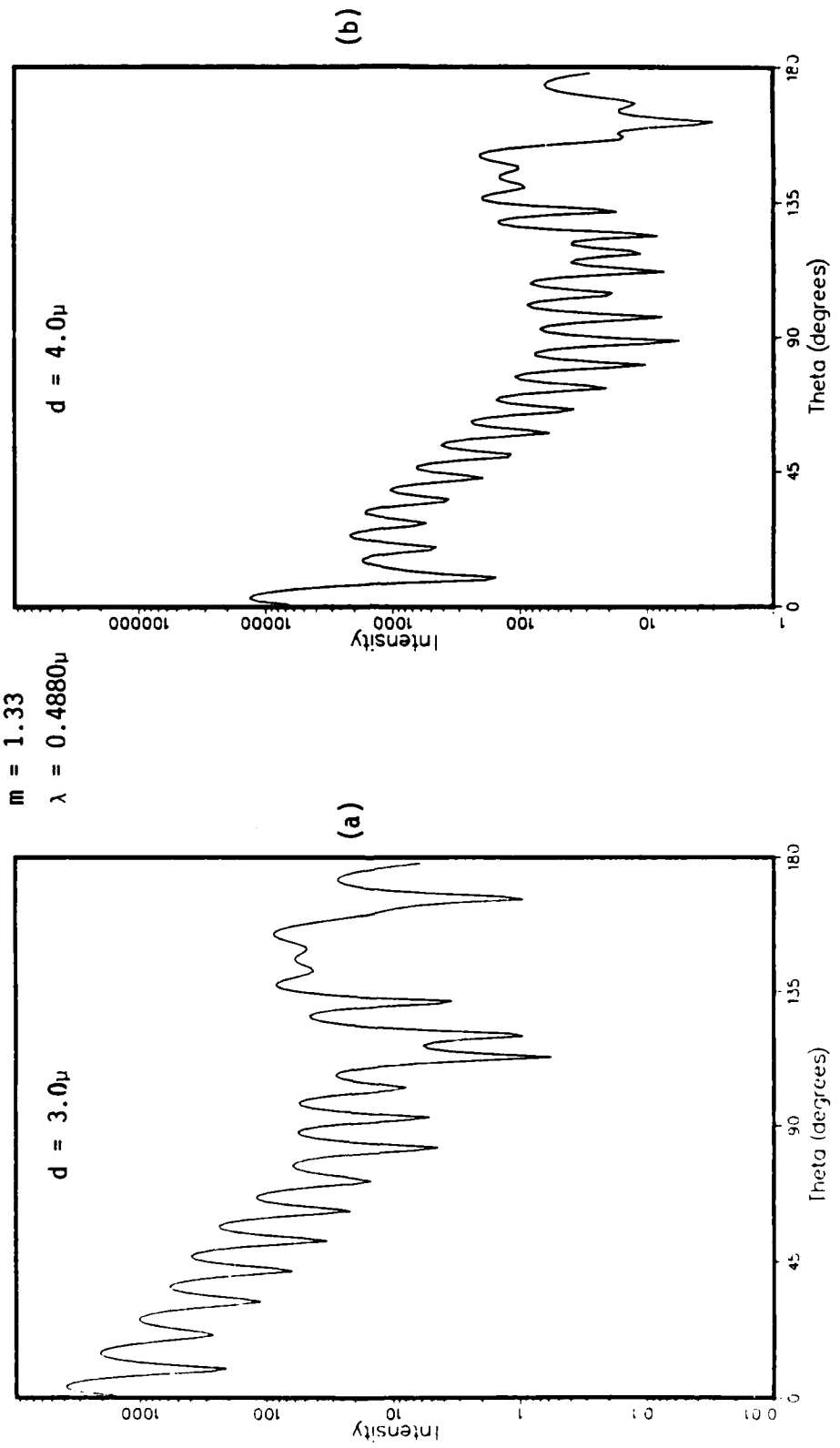

Figure 4.12. The Integrated Intensity Function i_1 Versus Theta.

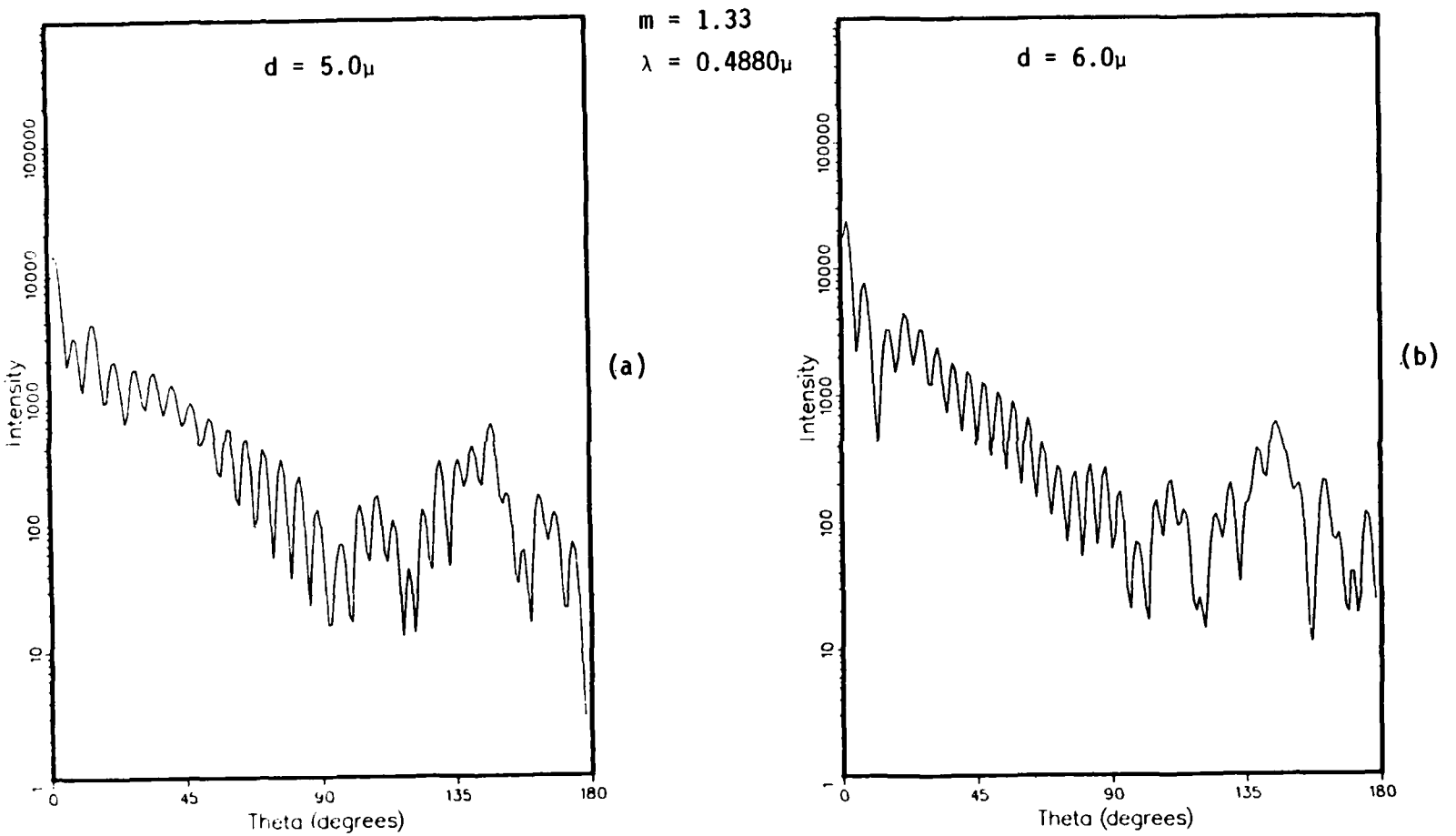

Figure 4.13. The Integrated Intensity Function i_1 Versus Theta.

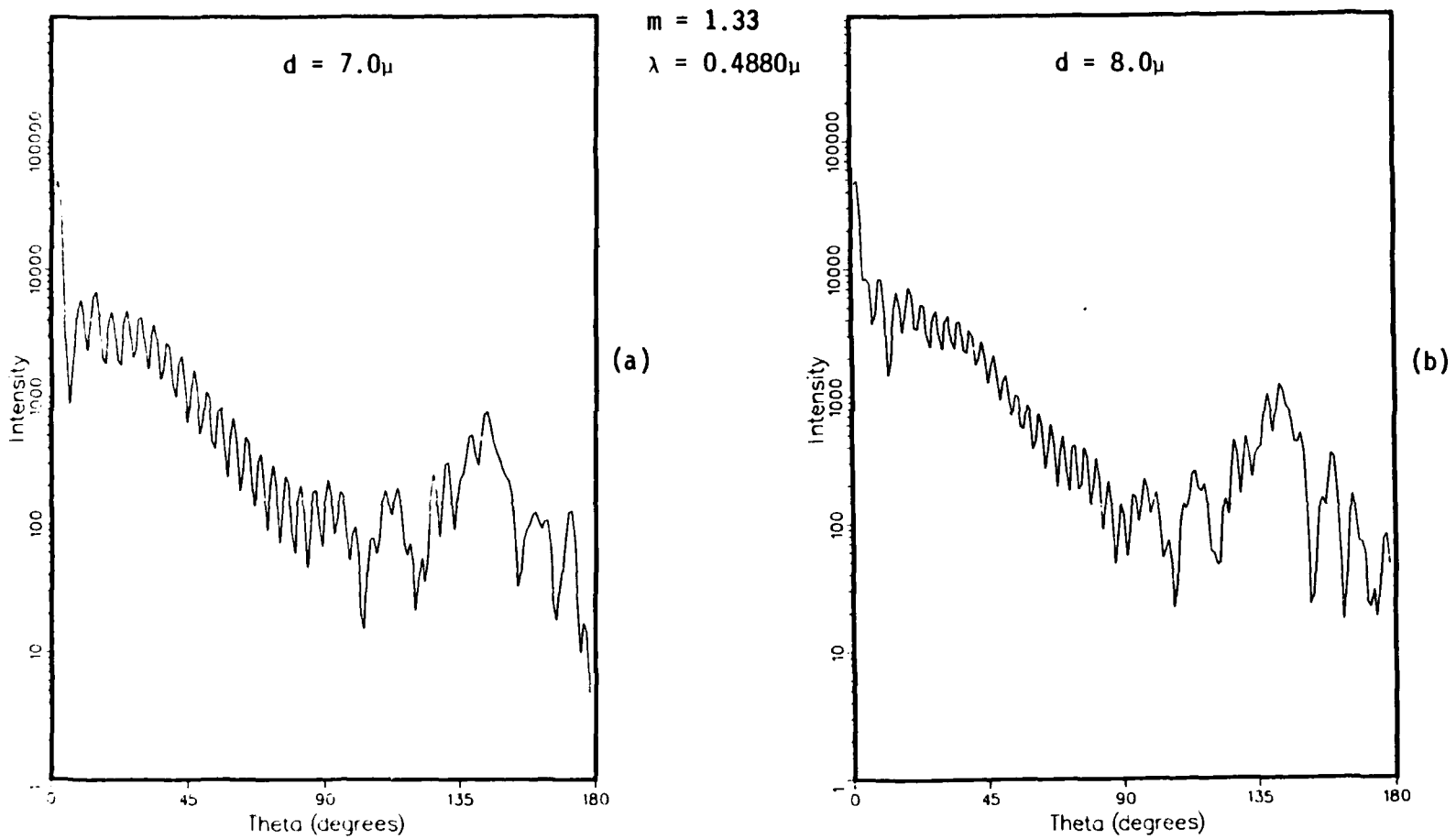

Figure 4.14. The Integrated Intensity Function i_1 Versus Theta.

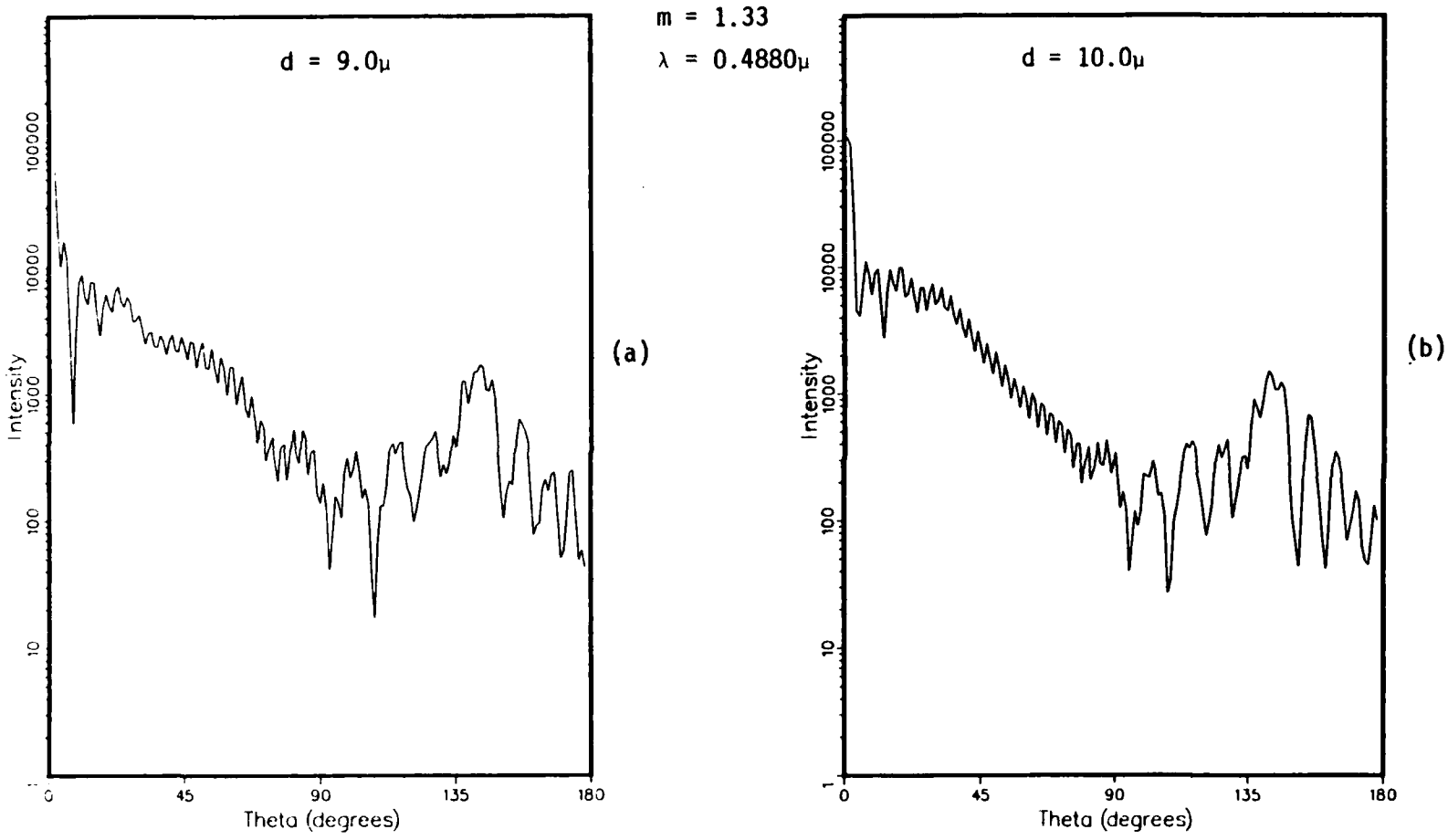

Figure 4.15. The Integrated Intensity Function i_1 Versus Theta.

Table 4.3. Selected Scattering Angles and Predicted Performance Errors for Water (m = 1.33 at λ = 0.4880μ) with NP = 500, Δd = 0.02μ, and [θmin, θmax] = [6°, 60°].

DISTRIBUTION ERRORS					Detector Angles	Number of
I	II	III	IV	V	(degrees)	Detectors
3020	8740	9788	8430	9080	81,147	2
3080	3372	3328	5544	6596	158	3
1386	1466	1260	2940	2264	151	4
650	412	806	722	480	154	5
180	160	122	318	306	70	6
176	96	140	72	120	129	7
66	80	248	218	256	12	8

[Emin, Emax] = [-0.2, 0.2]

assumed intensity error interval [-0.2, 0.2]. The distribution errors are similar in value to errors for the set of angles selected over the restricted range in θ, given in Table 4.2. Since the detector angles selected from the full range of θ afford no increase in ambiguity reduction, the detector angles for water particles should be limited to the forward scattering angles.

Detector Angle Selections for Aluminum Oxide

A proposed application for the MRSPC of Figure 1.1 is the size measurement of particulates within the plume of solid propellant rocket motors. Results of the Monte Carlo search technique for incident light wavelengths, 0.4880μ, 1.06μ, and 1.32μ, are given in Tables 4.4 to 4.6 for aluminum oxide particles. The range of selection angles was limited to [6°, 60°]. Although measurement errors for the actual instrumentation should be used in this search, the error intervals [Emin, Emax] denoted in the tables, allow an indication of the distinguishability of these particles and the number of detectors required for the measurements. The refractive indices of aluminum oxide at these wavelengths were supplied by Sverdrup Technology, Inc. at AEDC and are indicated on each table. Plots of the scattering functions i_1 for aluminum oxide, calculated from Mie theory for several particle diameters and an incident wavelength of 0.4880μ, are given in Figures 4.16 to 4.21. Larger scattered intensities are maintained at forward scattering angles for the size range of interest.

Input-to-"measured" distribution plots are given in Figures 4.22 to 4.28 for [Emin, Emax] = [-0.2, 0.2] and λ = 0.4880μ. These distributions and the distribution errors of Table 4.4 indicate that the MRSPC can distinguish particle sizes of spherically shaped aluminum oxide

Table 4.4. Selected Scattering Angles and Predicted Performance Errors for Aluminum Oxide Particles ($m = 1.776$ at $\lambda = 0.4880\mu$) with NP = 500, $\Delta d = 0.02\mu$, and [θmin, θmax] = [6°, 60°].

DISTRIBUTION ERRORS					Detector Angles (degrees)	Number of Detectors
I	II	III	IV	V		
6928	9166	9732	9280	9360	11,50	2
5008	5558	5108	7156	6828	47	3
2426	2514	3372	2378	3624	21	4
438	714	1120	1434	926	8	5
420	128	242	100	148	15	6
92	60	88	42	80	32	7
114	104	36	30	76	60	8
[Emin, Emax] = [-0.2, 0.2]						
5272	8992	9952	8558	10508	8,11	2
2618	3560	5158	5222	4114	58	3
1132	1348	1464	954	1372	28	4
346	406	110	214	196	18	5
264	90	92	64	80	33	6
80	98	18	30	34	23	7
148	12	14	38	20	40	8
[Emin, Emax] = [-0.1, 0.1]						
3078	5466	6194	5938	6854	7,10	2
308	1460	2296	2248	1316	45	3
382	880	222	400	102	39	4
322	68	66	24	22	22	5
178	34	46	0.	0	28	6
120	28	8	0	0	57	7
144	8	0	0	0	25	8
[Emin, Emax] = [0.0, 0.0]						

Table 4.5. Selected Scattering Angles and Predicted Performance Errors for Aluminum Oxide Particles (m = 1.75463 at λ = 1.06μ) with NP = 500, Δd = 0.02μ, and [θmin, θmax] = [6°, 60°].

DISTRIBUTION ERRORS					Detector Angles	Number of
I	II	III	IV	V	(degrees)	Detectors
2964	8546	10066	8428	8648	6,42	2
1540	6670	4502	5428	4992	15	3
1376	1302	2934	1820	2052	9	4
1260	808	874	588	482	19	5
354	302	348	374	240	59	6
628	202	460	120	176	49	7
266	114	250	164	118	23	8
	[Emin, Emax] = [-0.2, 0.2]					
2350	9394	8878	7590	8034	6,40	2
1394	1436	2768	2458	2844	9	3
742	710	788	492	298	21	4
486	538	96	138	176	45	5
342	128	130	158	50	12	6
274	150	236	48	60	48	7
130	148	116	66	34	57	8
	[Emin, Emax] = [-0.1, 0.1]					
1074	1490	2496	3042	3486	7,10	2
300	134	516	350	294	33	3
474	240	40	46	96	19	4
88	356	346	24	24	53	5
156	134	174	56	4	42	6
130	66	34	132	2	25	7
136	70	26	10	4	38	8
	[Emin, Emax] = [0.0, 0.0]					

Table 4.6. Selected Scattering Angles and Predicted Performance Errors for Aluminum Oxide Particles (m = 1.750159 at λ = 1.32μ) with NP = 500, Δd = 0.02μ, and [θmin, θmax] = [6°, 60°].

DISTRIBUTION ERRORS					Detector Angles (degrees)	Number of Detectors
I	II	III	IV	V		
2906	7362	8918	9318	10152	6,58	2
3338	3366	4550	5080	3472	10	3
1512	1834	2292	1764	2432	48	4
1360	1804	1514	748	400	53	5
650	526	498	320	402	20	6
660	600	522	208	248	59	7
538	448	228	374	330	42	8
	[Emin, Emax] = [-0.2, 0.2]					
2552	6522	8416	8622	8516	6,56	2
864	2802	4742	2516	3940	31	3
666	990	1212	1300	1534	11	4
538	356	286	334	208	36	5
390	434	212	92	106	23	6
618	200	182	74	108	51	7
516	266	56	34	150	59	8
	[Emin, Emax] = [-0.1, 0.1]					
910	3608	5498	5296	3870	6,18	2
196	1748	606	2750	1542	38	3
998	704	404	88	364	13	4
230	210	114	72	98	54	5
174	60	152	72	16	57	6
184	66	104	112	36	60	7
204	212	58	104	8	22	8
	[Emin, Emax] = [-0.1, 0.1]					

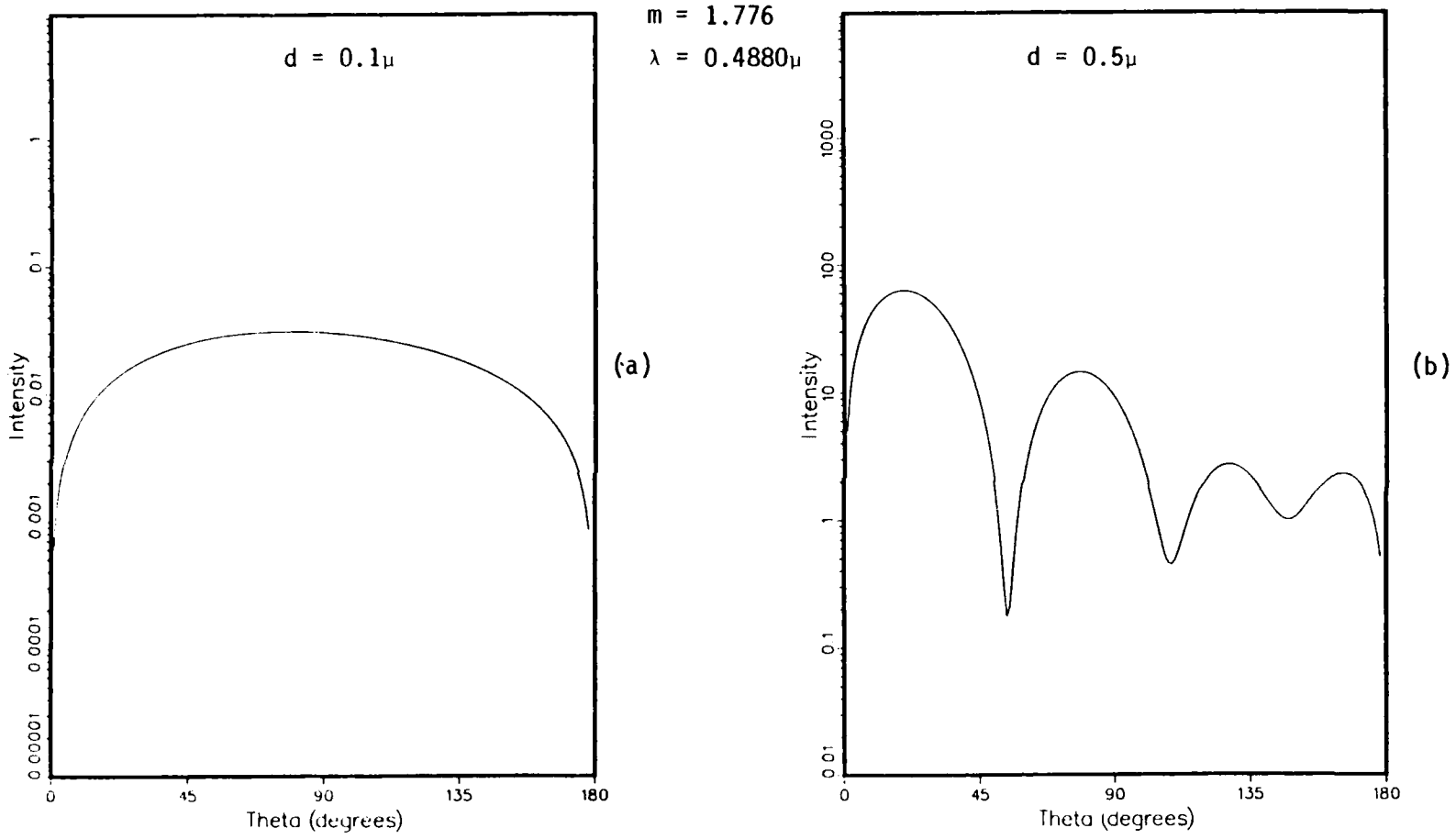

Figure 4.16. The Integrated Intensity Function i_1 Versus Theta.

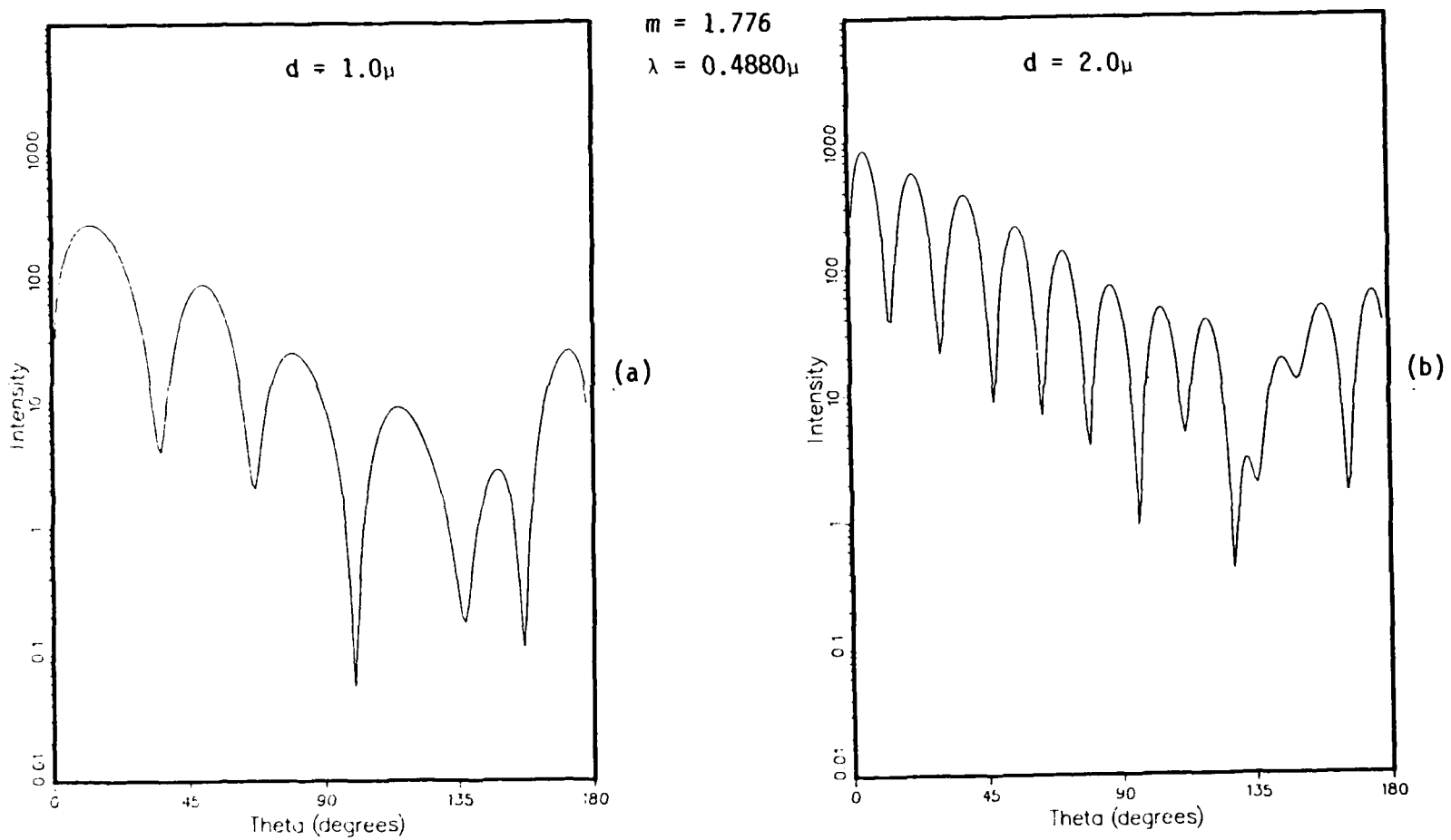

Figure 4.17. The Integrated Intensity Function i_1 Versus Theta.

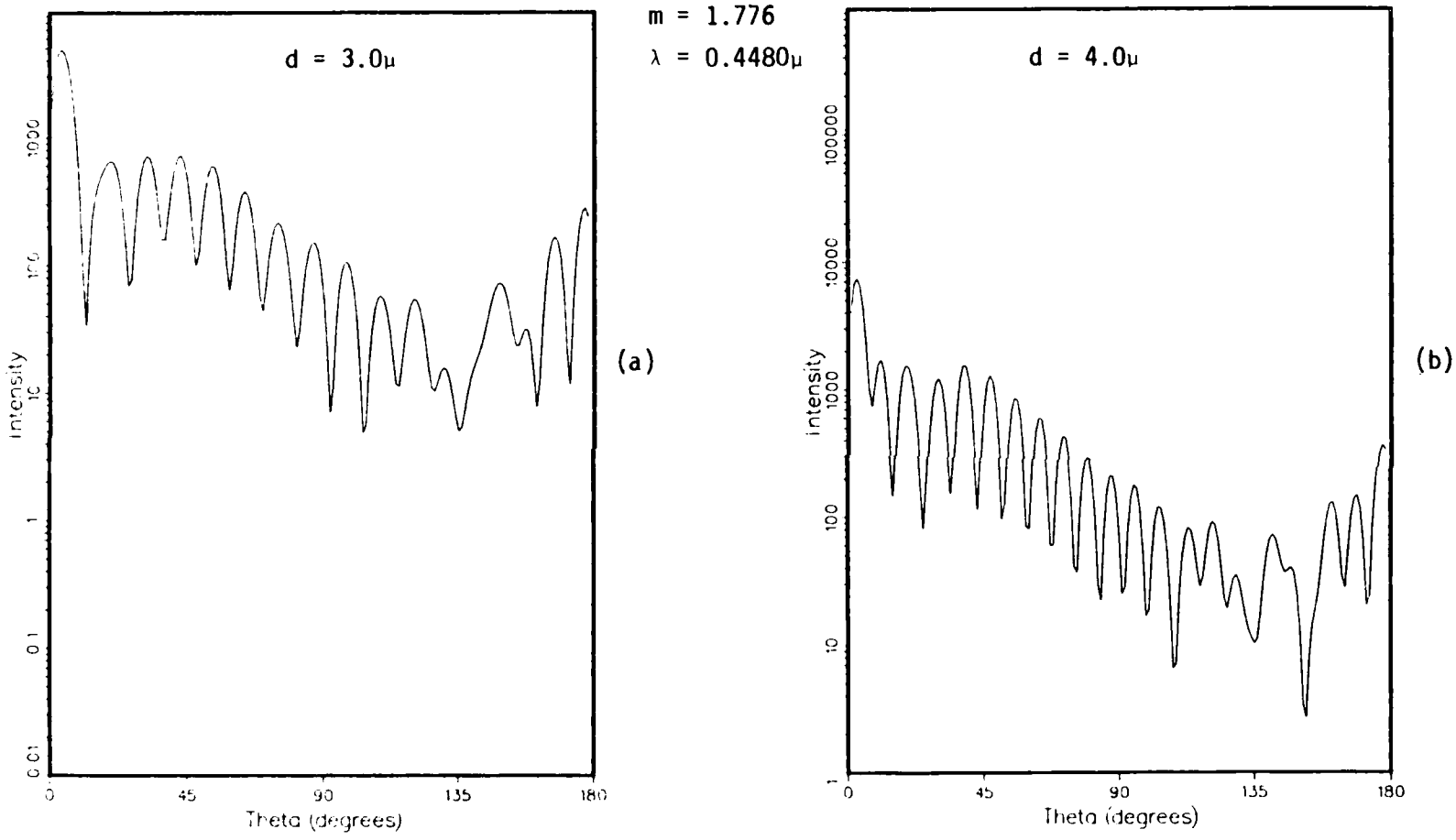

Figure 4.18. The Integrated Intensity Function i_1 Versus Theta.

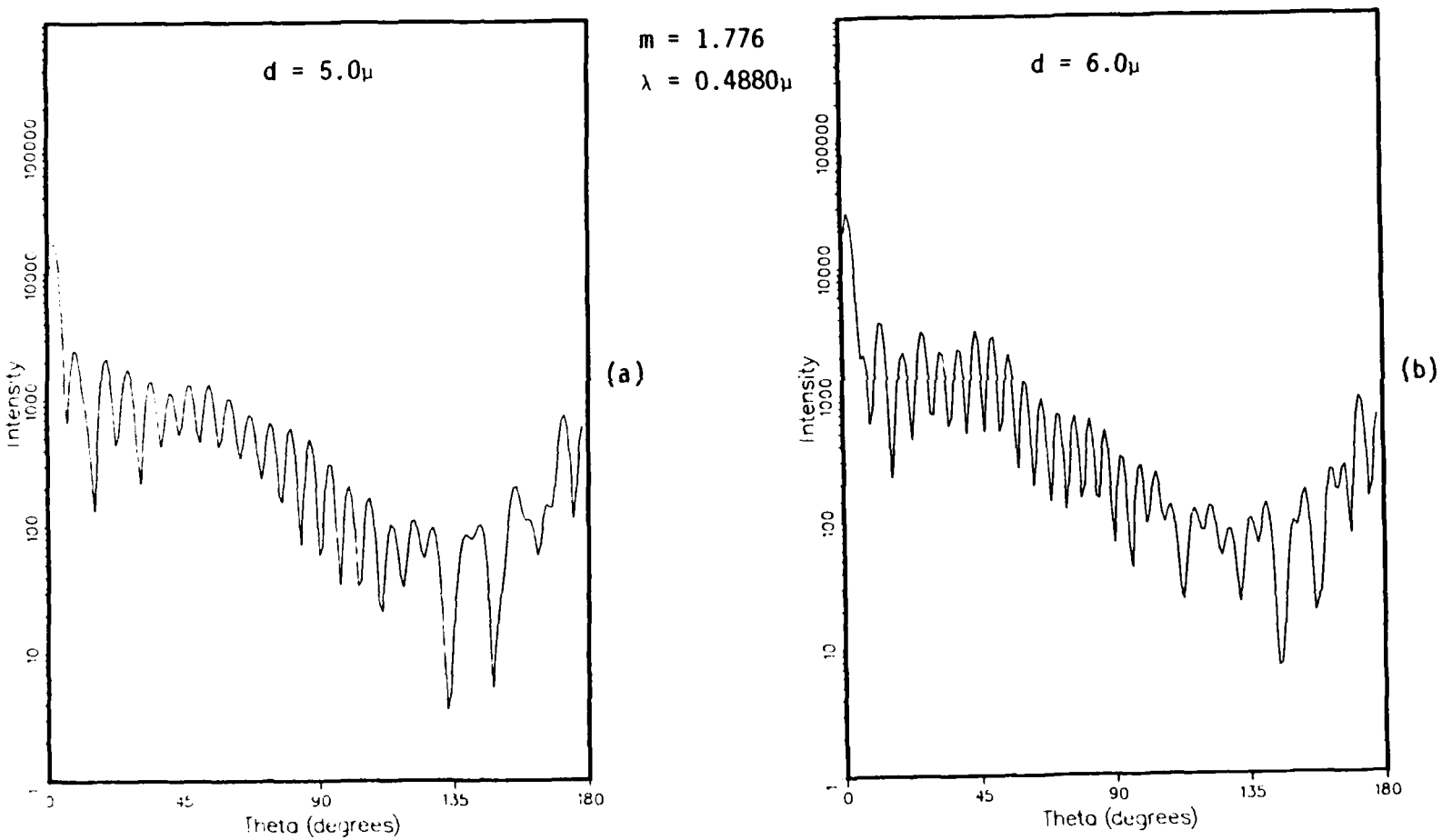

Figure 4.19. The Integrated Intensity Function i_1 Versus Theta.

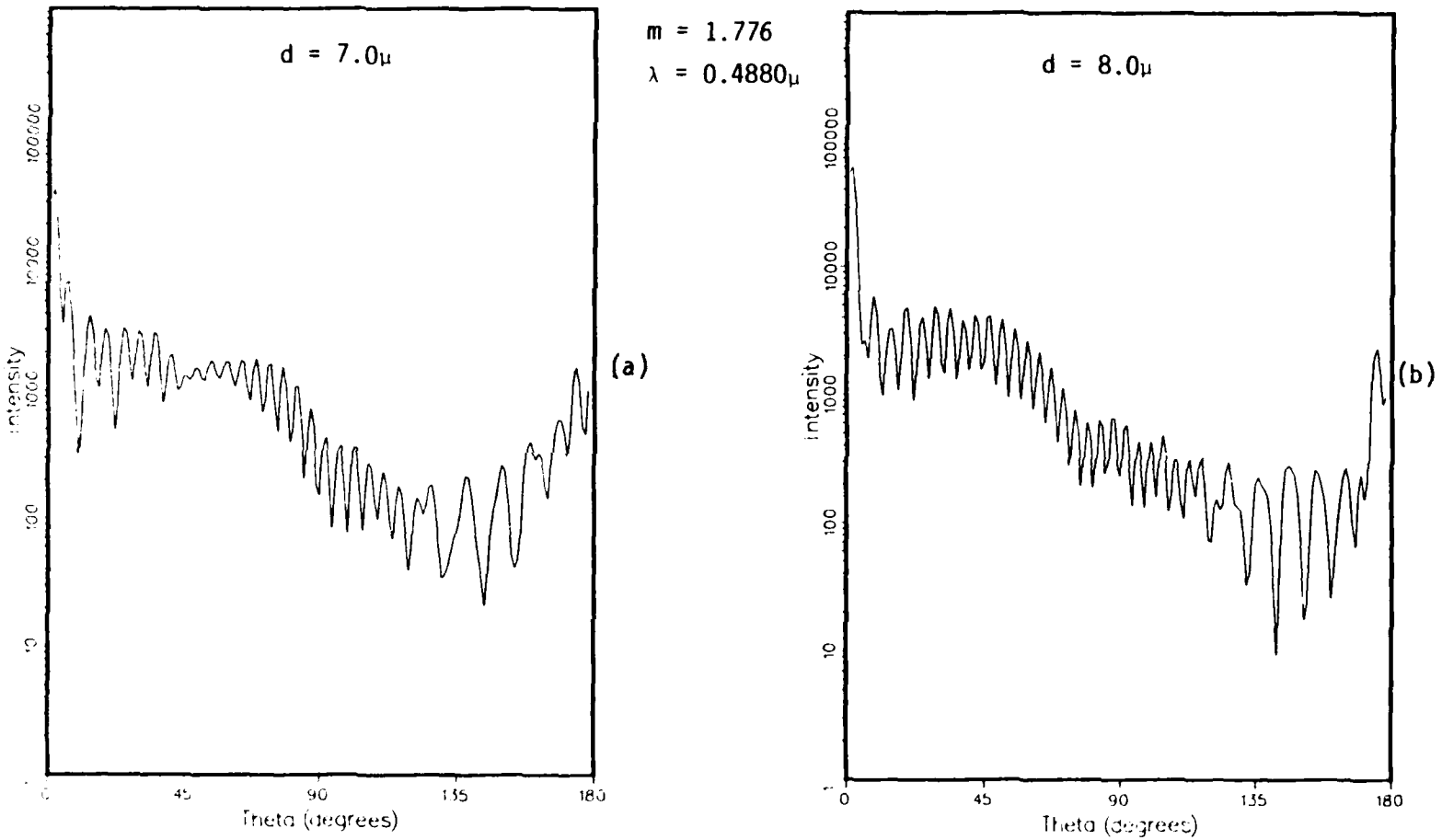

Figure 4.20. The Integrated Intensity Function i_1 Versus Theta.

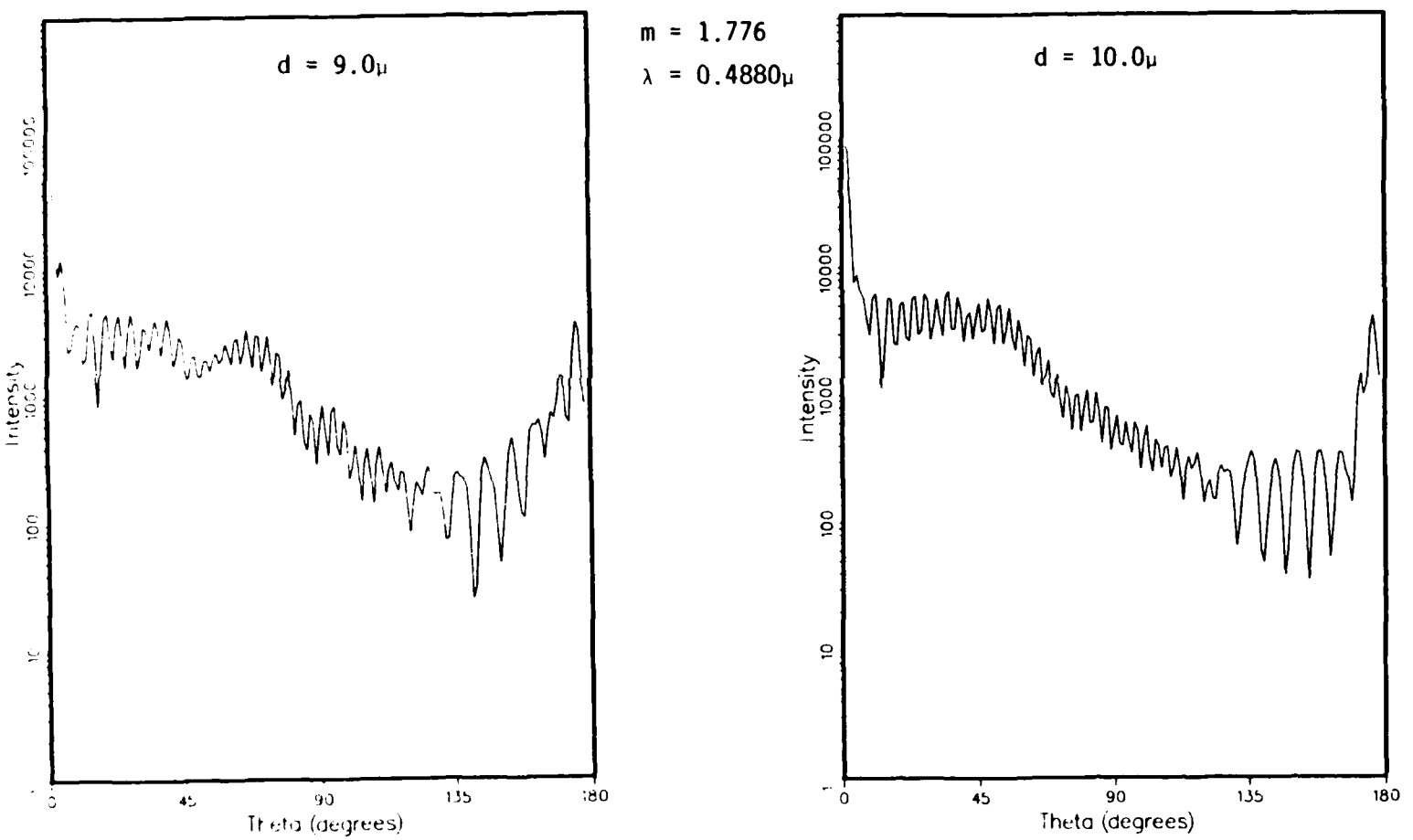

Figure 4.21. The Integrated Intensity Function i_1 Versus Theta.

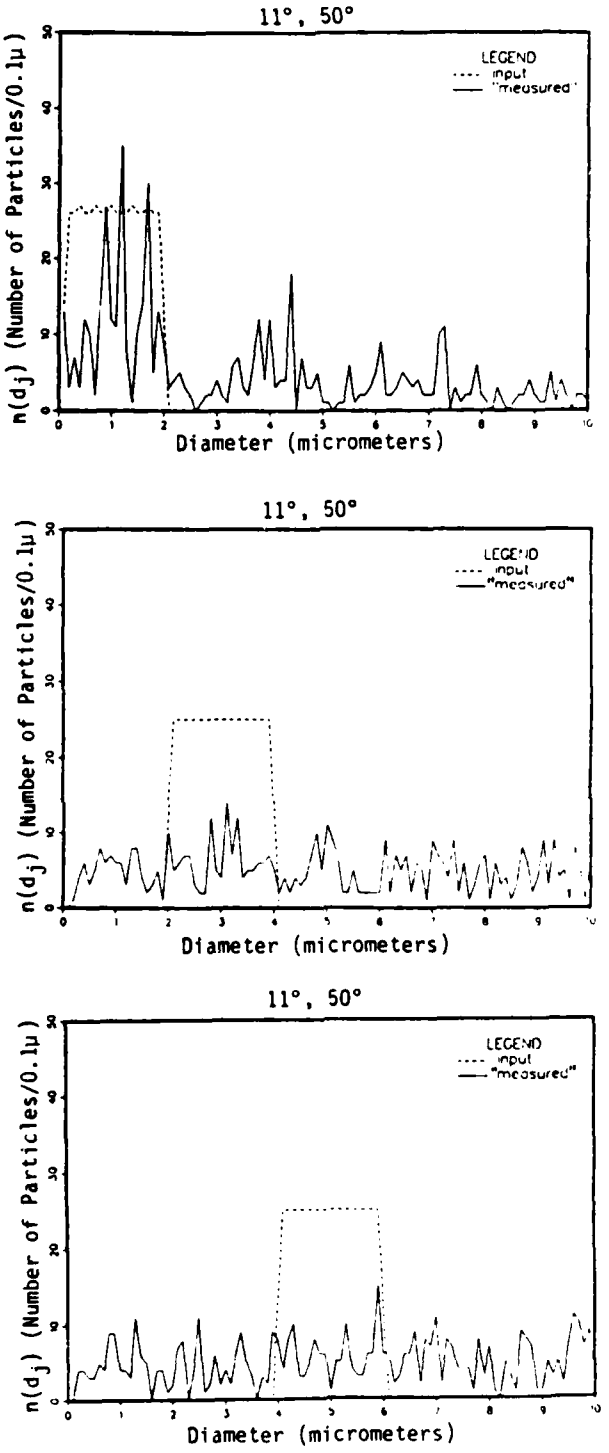

Figure 4.22. Input and "Measured" Distributions for a Two-Detector System for m = 1.776, $\lambda = 0.4880_{\mu}$ and Error Interval [-0.2, 0.2].

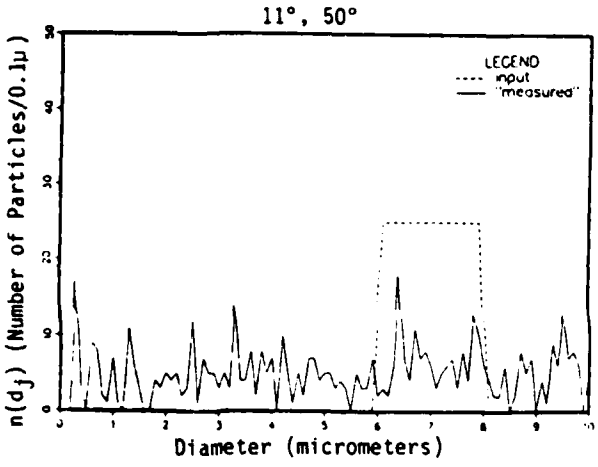

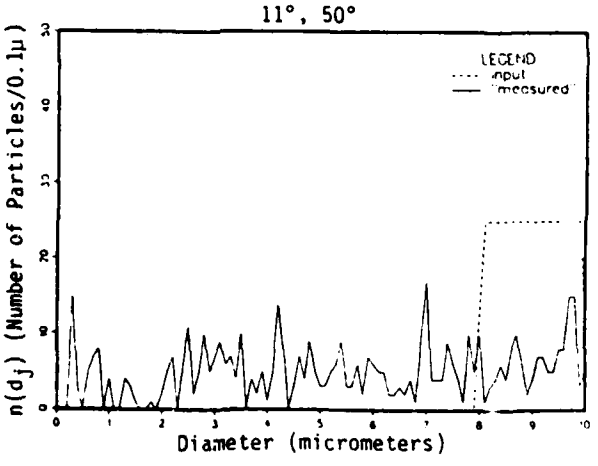

Figure 4.22. (Continued).

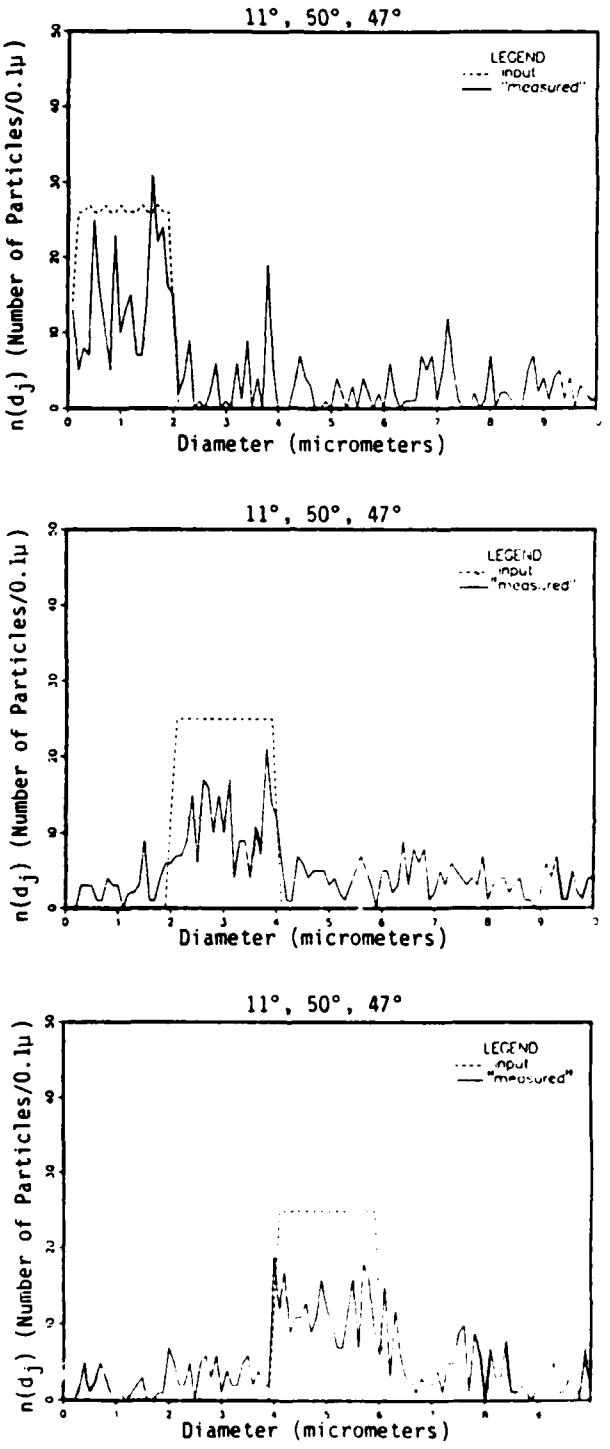

Figure 4.23. Input and "Measured" Distributions for a Three-Detector System for m = 1.776, λ = 0.4880μ and Error Interval [-0.2, 0.2].

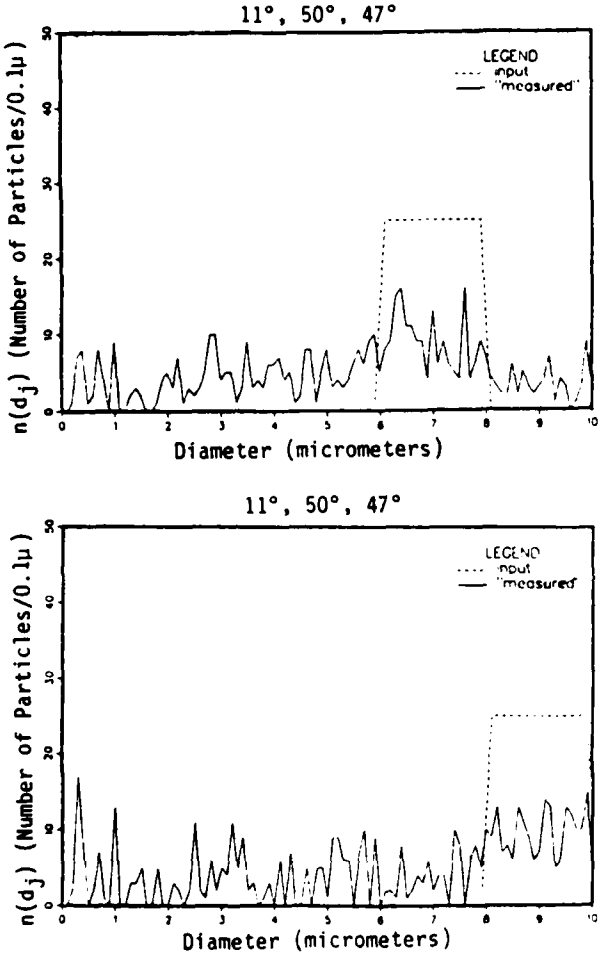

Figure 4.23. (Continued).

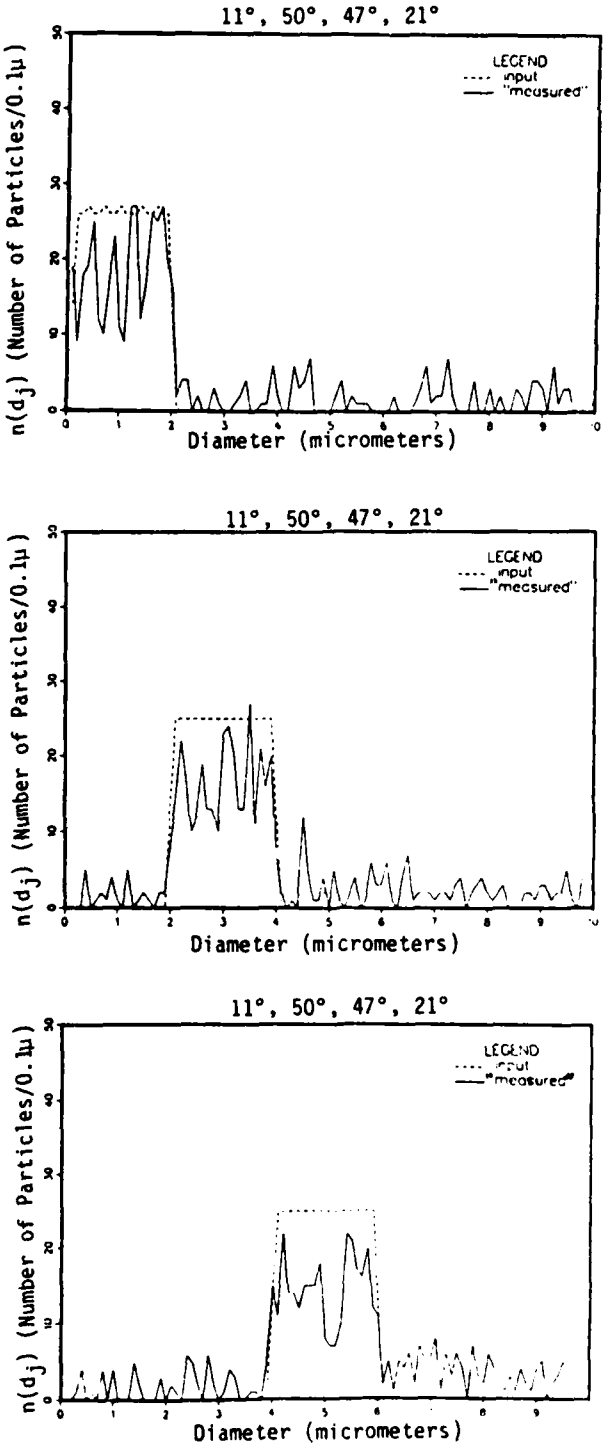

Figure 4.24. Input and "Measured" Distribution for a Four-Detector System for m = 1.776, λ = 0.4880μ and Error Interval [-0.2, 0.2].

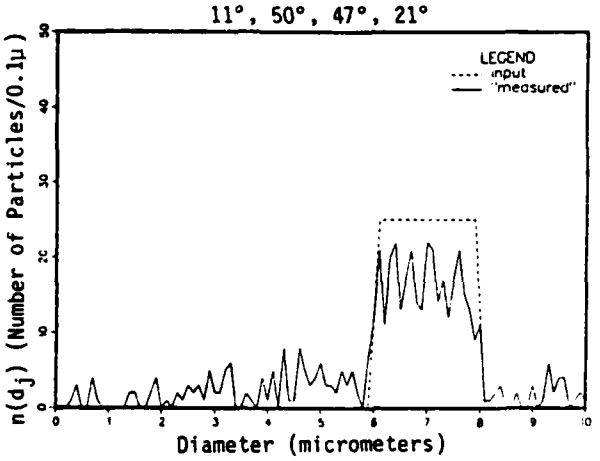

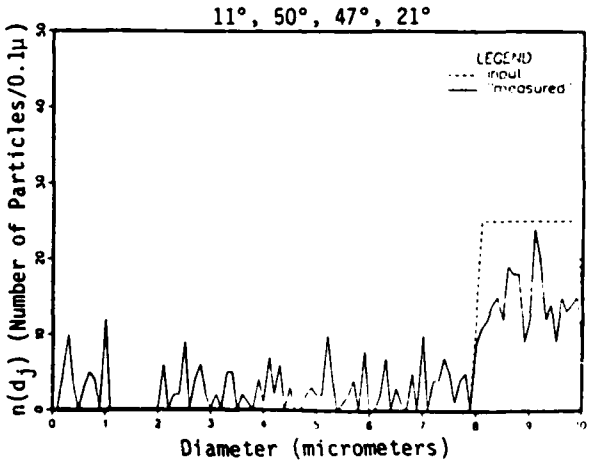

Figure 4.24. (Continued).

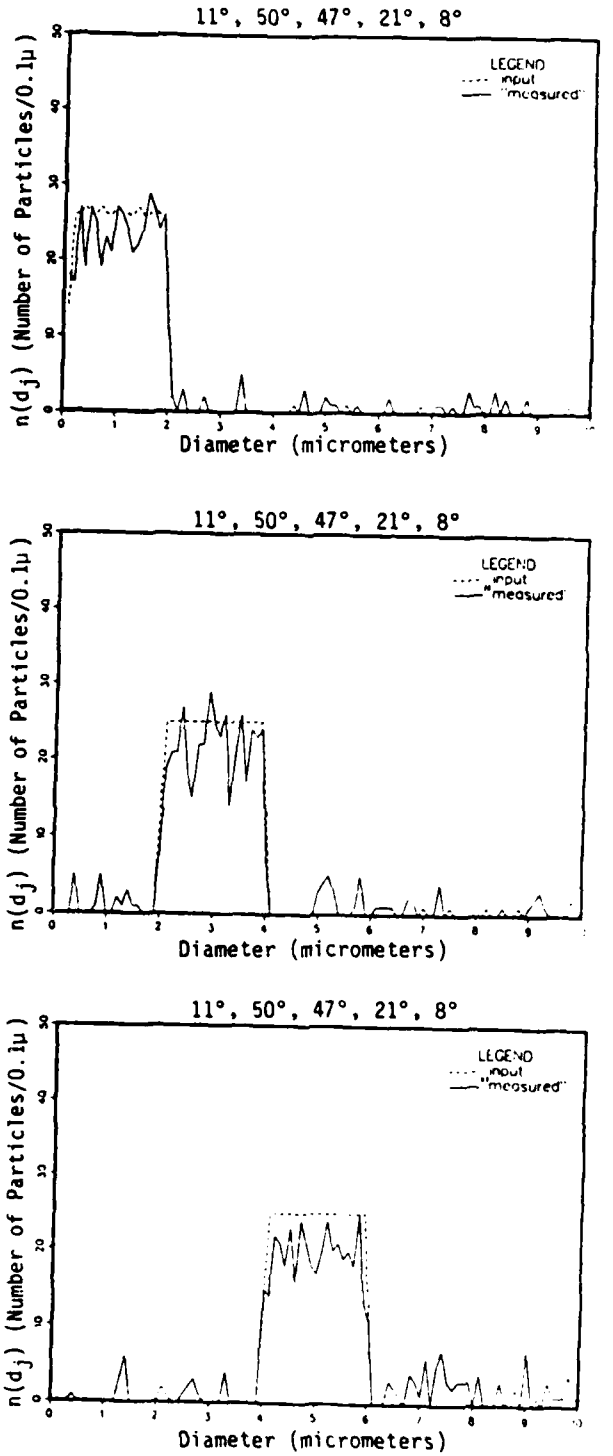

Figure 4.25. Input and "Measured" Distributions for a Five-Detector System for m = 1.776, λ = 0.4480μ and Error Interval [-0.2, 0.2].

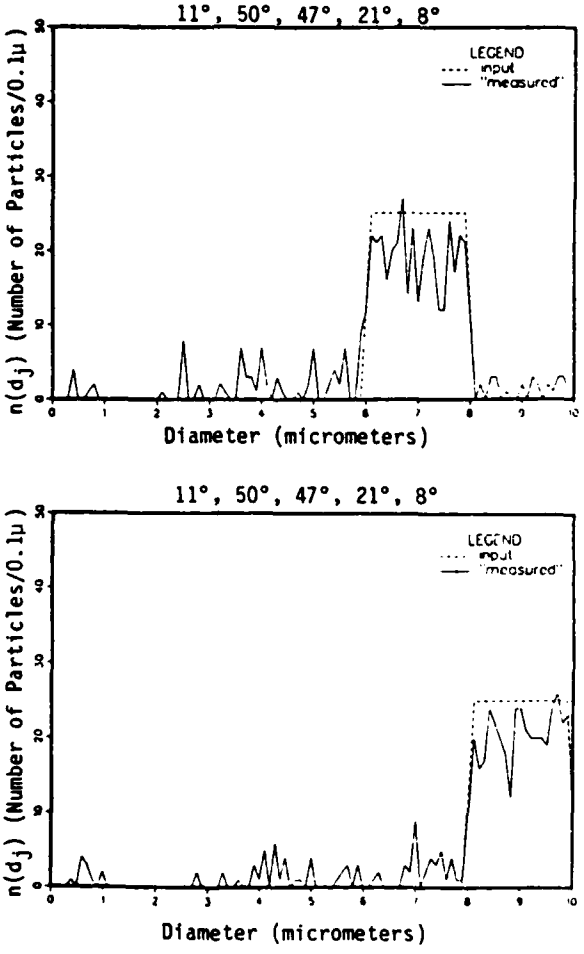

Figure 4.25. (Continued).

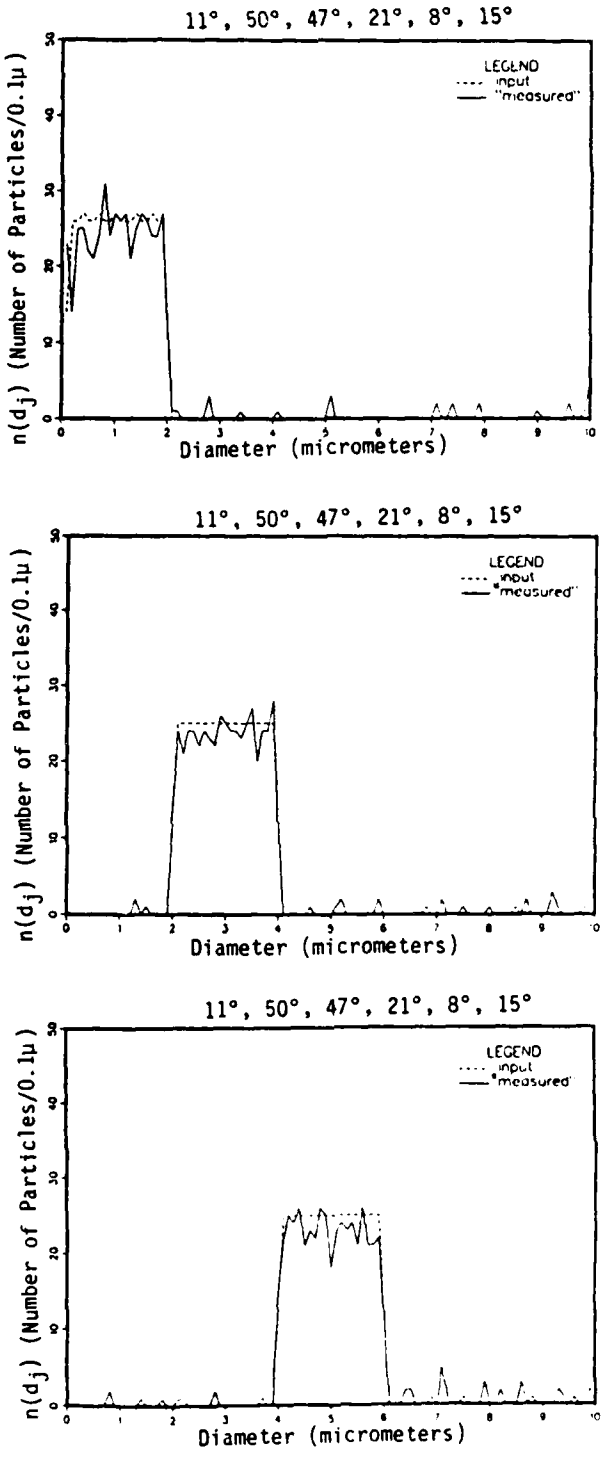

Figure 4.26. Input and "Measured" Distributions for a Six-Detector System for m = 1.776, λ = 0.4880μ and Error Interval [-0.2, 0.2].

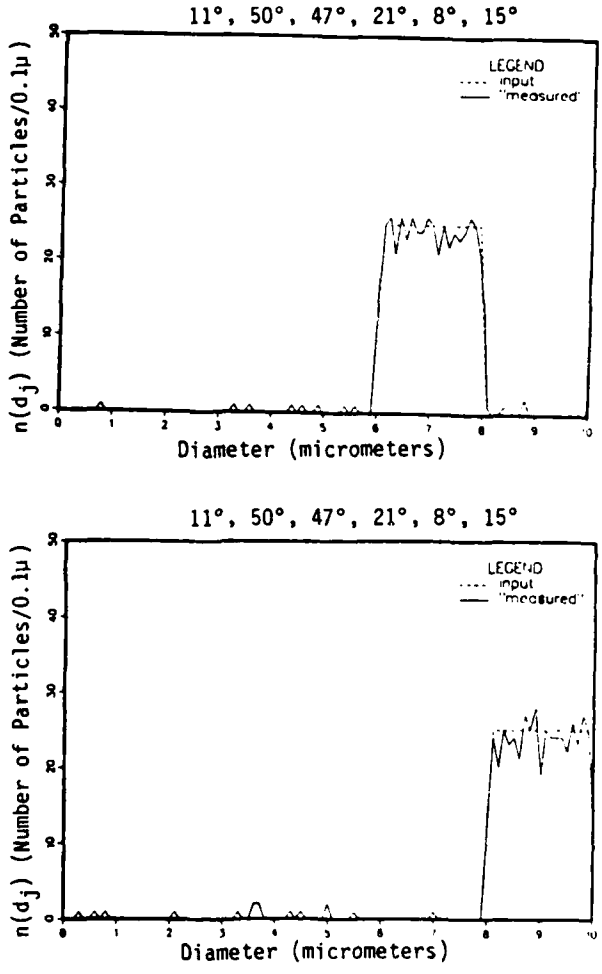

Figure 4.26. (Continued).

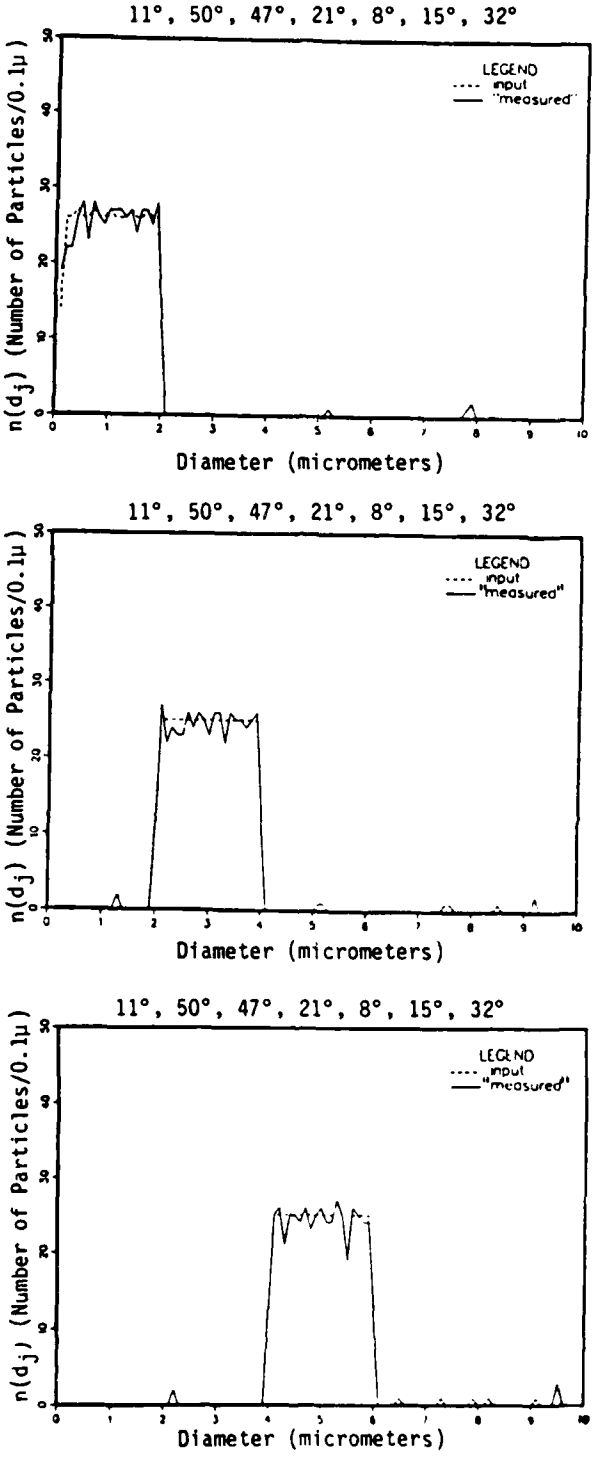

Figure 4.27. Input and "Measured" Distributions for a Seven-Detector System for m = 1.776, λ = 0.4880μ and Error Interval [-0.2, 0.2].

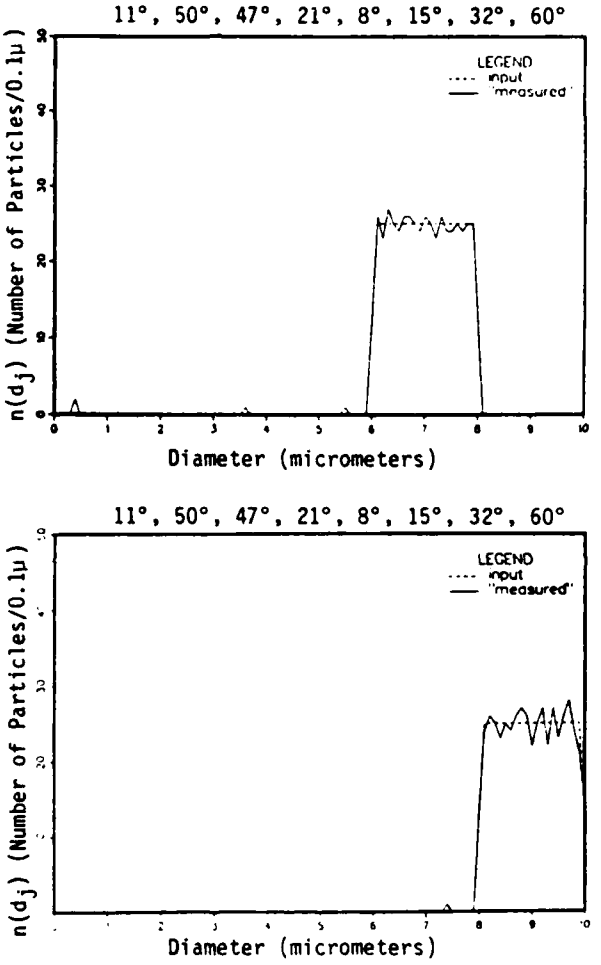

Figure 4.27. (Continued).

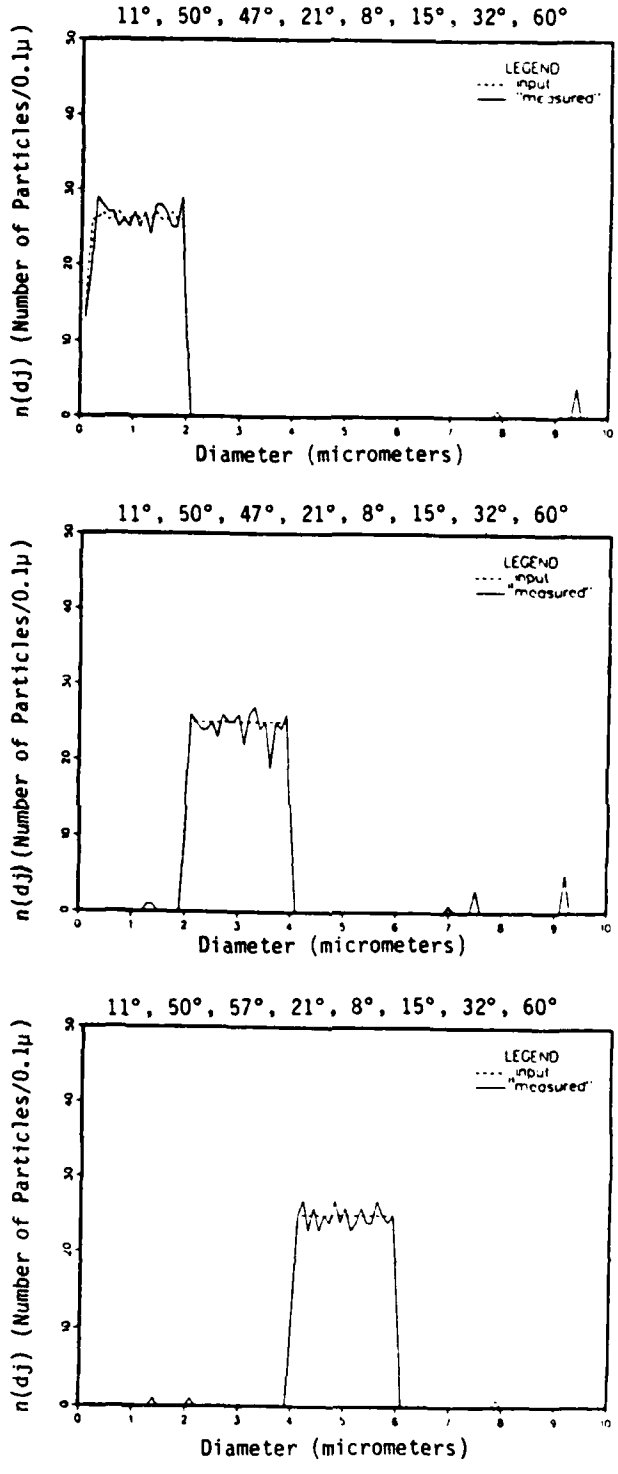

Figure 4.28. Input and "Measured" Distributions for an Eight-Detector System for m = 1.776, λ = 0.4480μ and Error Interval [-0.2, 0.2].

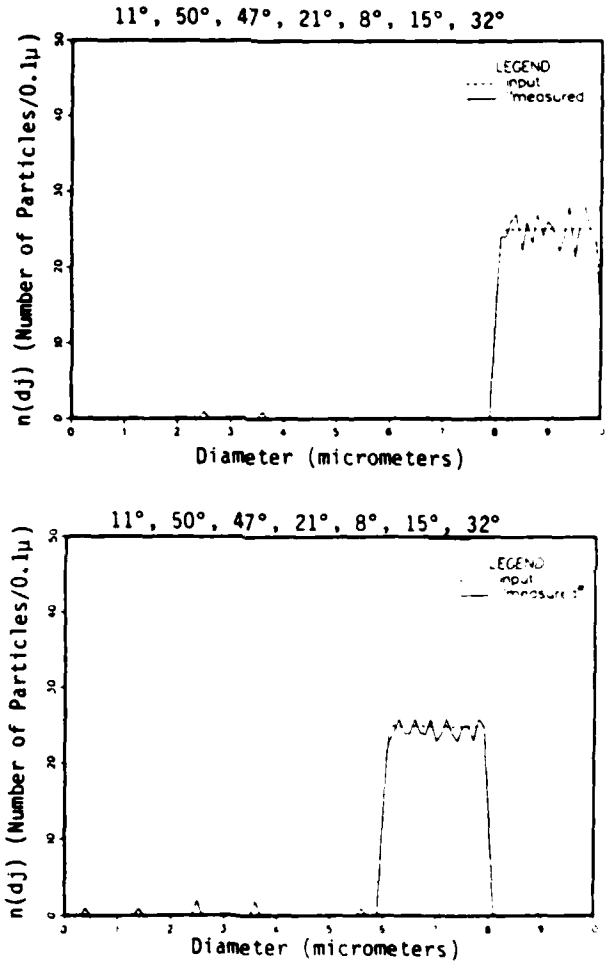

Figure 4.28. (Continued).

particles within the size range [dmin, dmax] = [0.1μ, 10.0μ].

The distribution errors increase for longer incident wavelengths as seen from Tables 4.5 to 4.6, especially for the first size subinterval. The intensity ratio plots of Figures 4.29 to 4.32 show that for longer wavelengths the ratios are only slightly sloped for smaller diameters making diameter resolution poor within this size range. Distribution errors are smaller for 0.4880μ wavelength for an equivalent number of detectors making it a better choice for measuring aluminum oxide particles.

Detector Angle Selections Using the Vector Search Method

Distribution errors were generated for the sets of angles of Table 4.2 using the vector method of particle size interpretation in the simulation program keeping the parameters NP, Δd, and [Emin, Emax] the same. Also the same random numbers were used to simulate the measured intensities. The results, Table 4.7, in comparison to Table 4.2, show no overall significant differences.

Still, there are reasons for preference of methods of size interpretation. It is much easier to incorporate a consistency check into the ratio method to help discriminate particles outside the size range of interest. However, as the number of detectors becomes large, the number of ratios, taking all combinations as described in equation 3.1, becomes very large. The vector method always has the same number of columns in the look-up table as there are detectors for the sizing system.

The vector search method was used to select detector angles for the MRSPC of Figure 1.1. The detector angles are given in Table 4.8 for water and aluminum oxide for the light wavelength 0.4880μ. The AREA represents the figure of merit as described in equation 3.10.

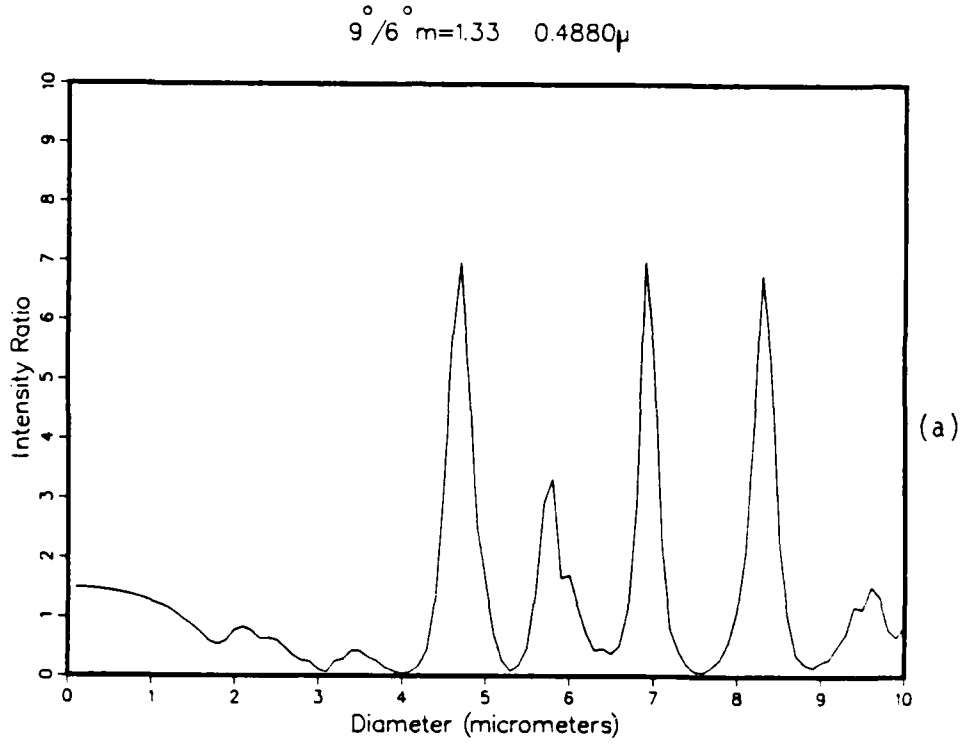

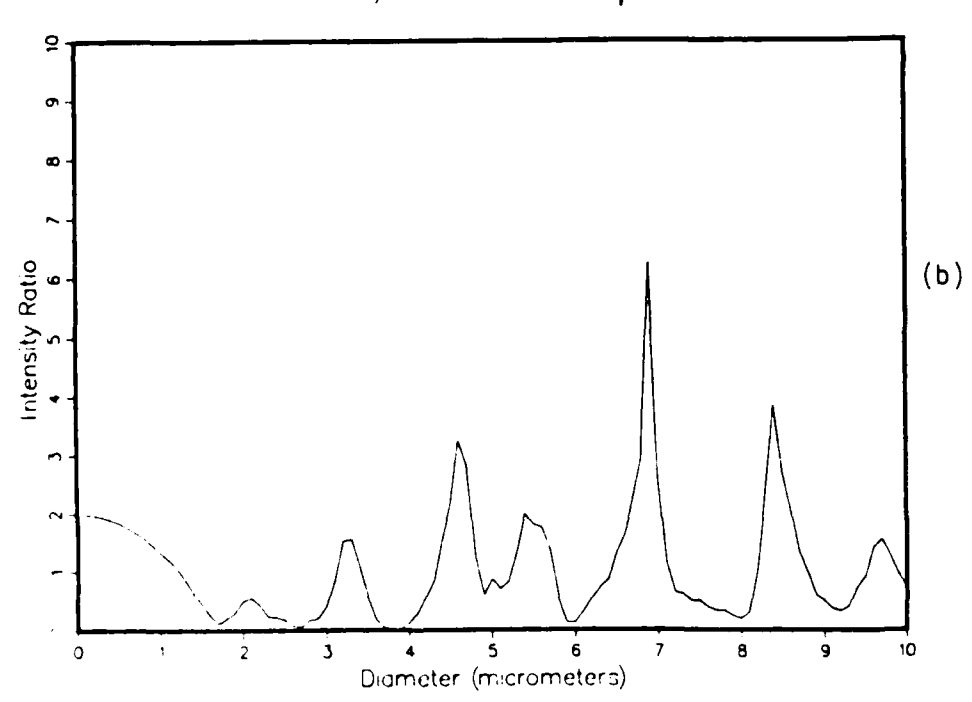

Figure 4.29. Sample Intensity Ratio Plots for Water Particles for $\lambda = 0.4880\mu$.

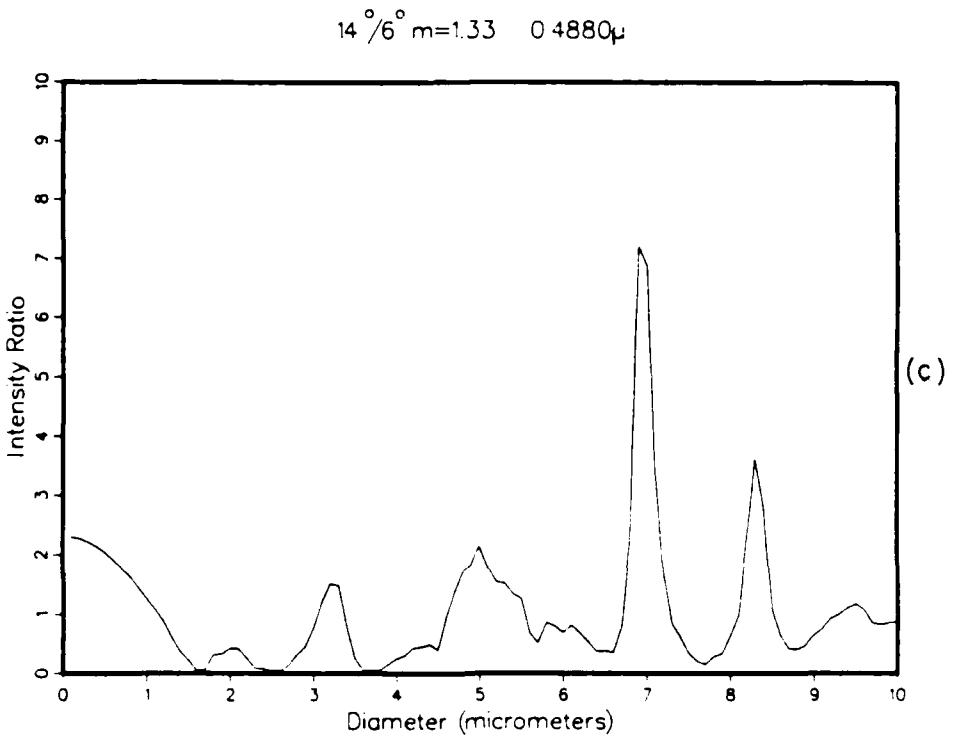

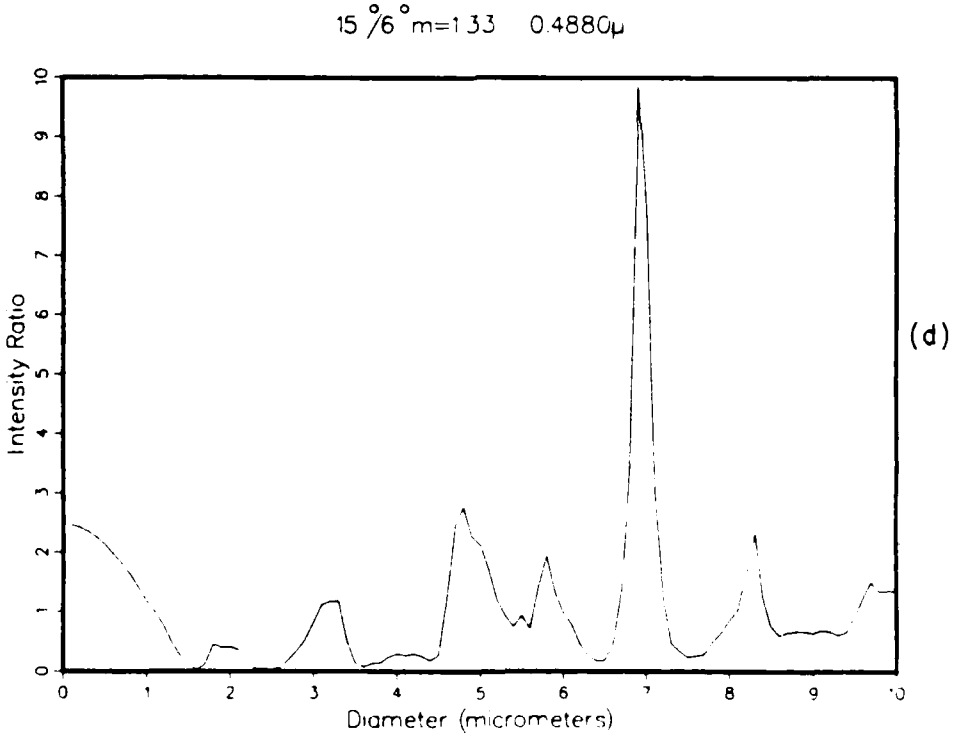

Figure 4.29. (Continued)

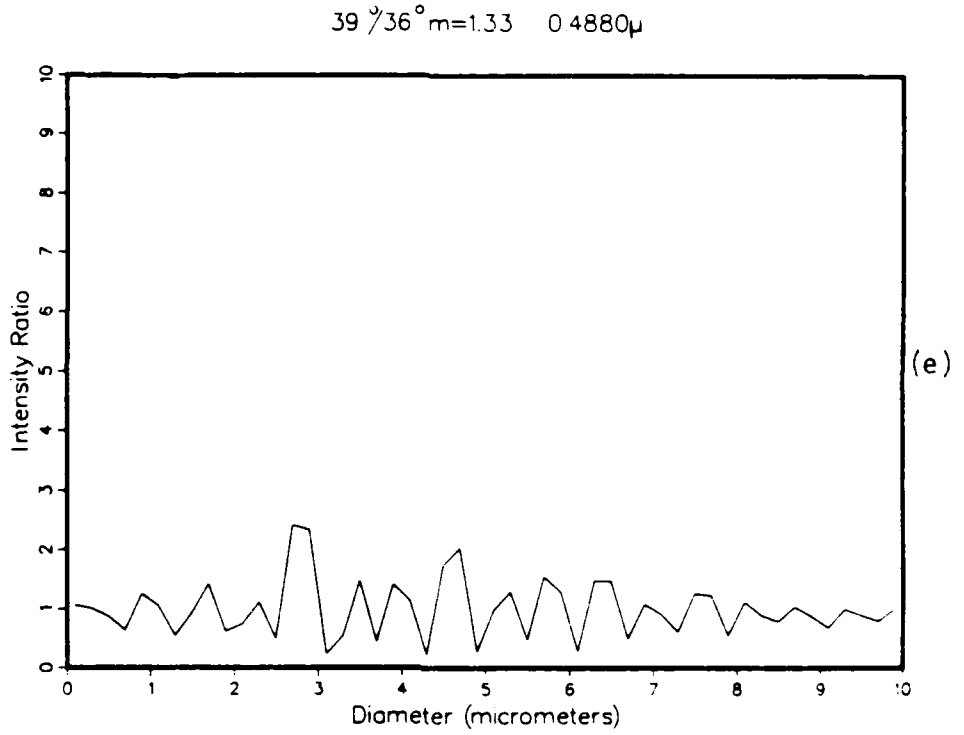

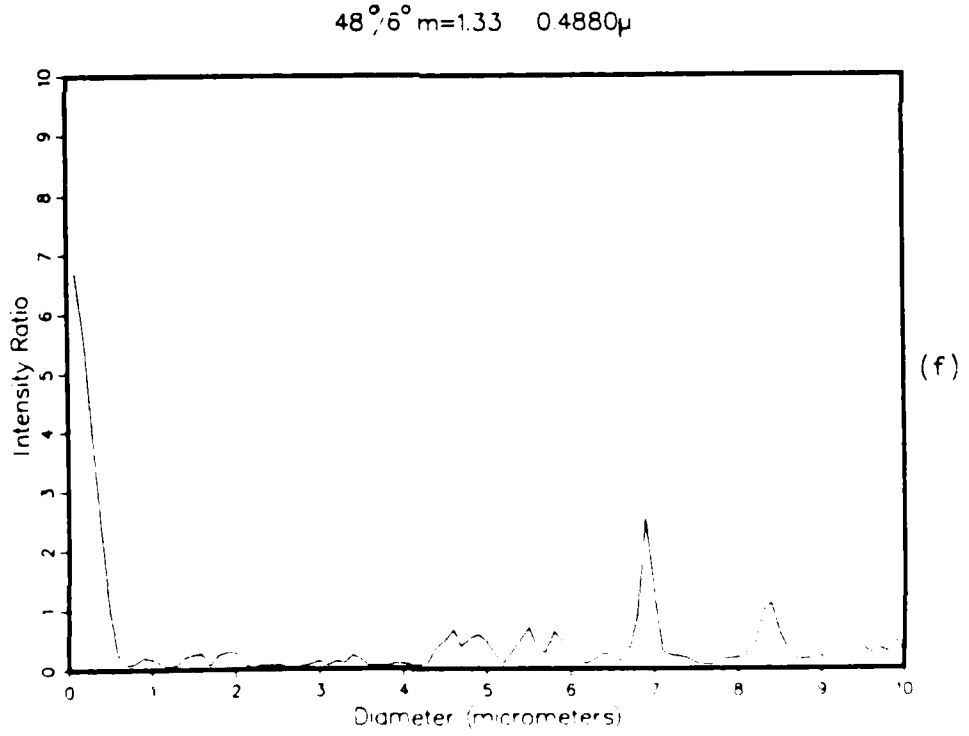

Figure 4.29. (Continued).

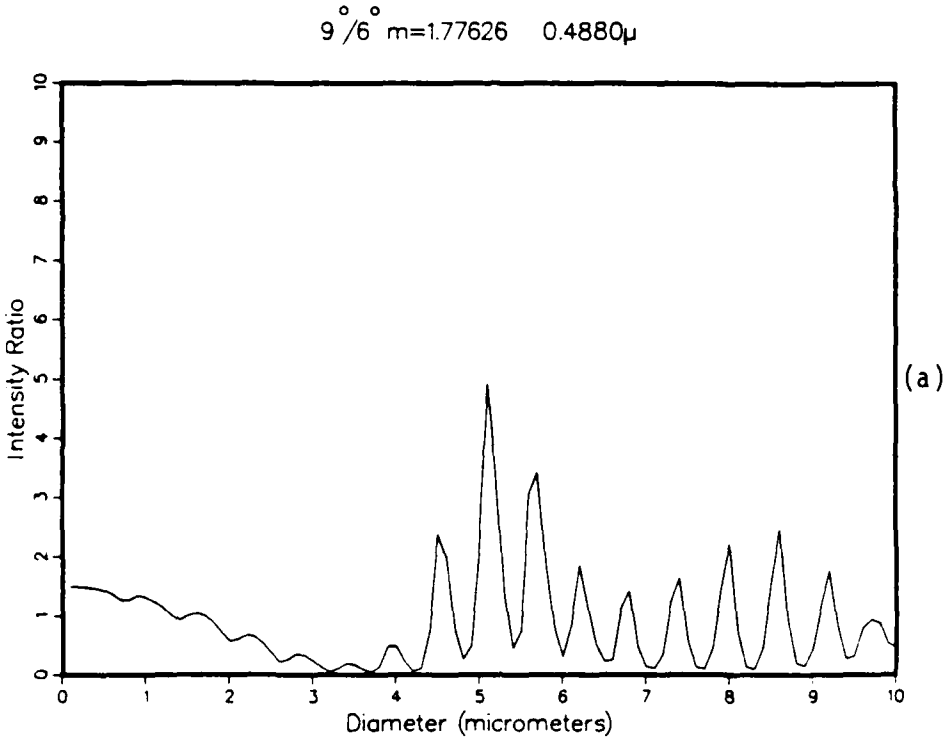

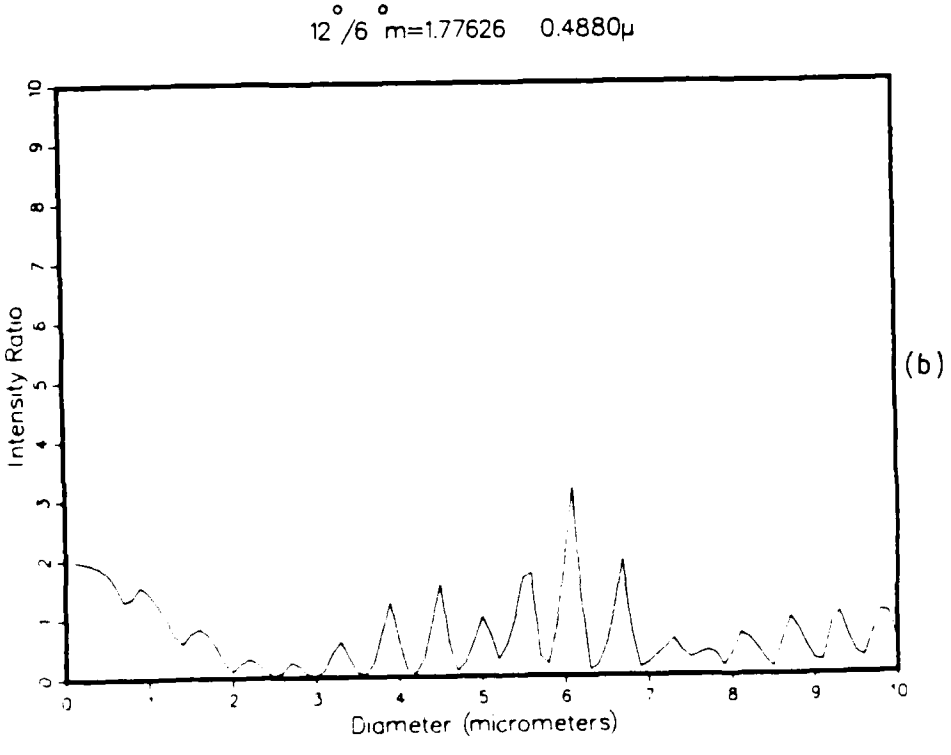

Figure 4.30. Sample Intensity Ratio Plots for Aluminum Oxide Particles for λ = 0.4880u.

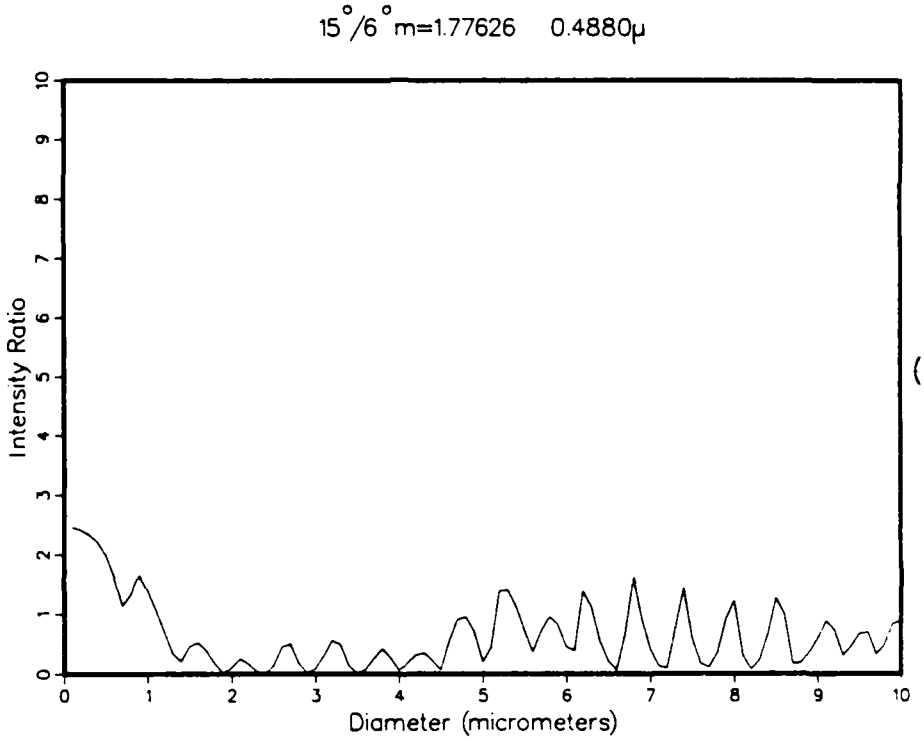

(c)

Figure 4.30. (Continued).

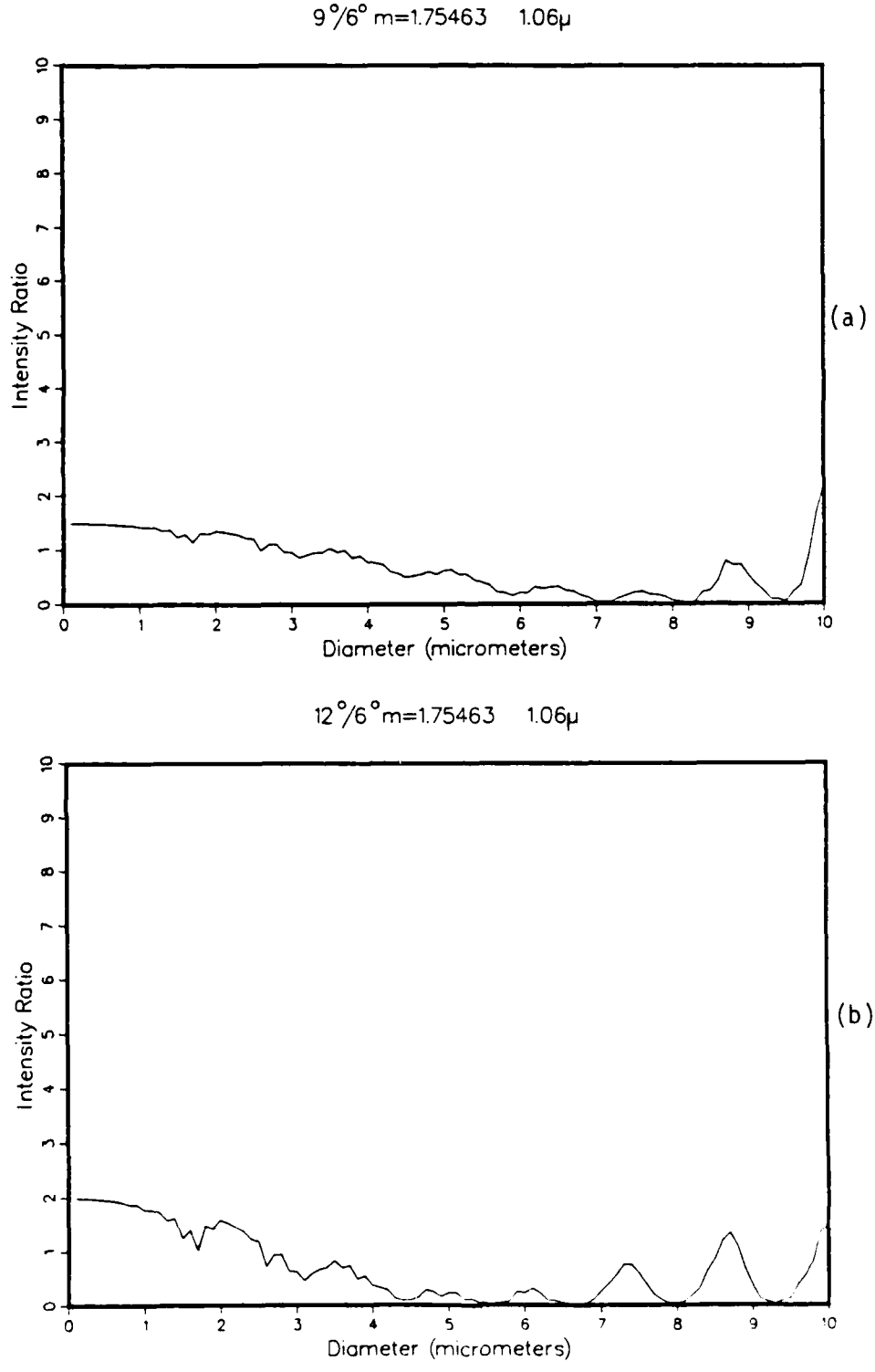

Figure 4.31. Sample Intensity Ratio Plots for Aluminum Oxide Particles for λ = 1.06μ.

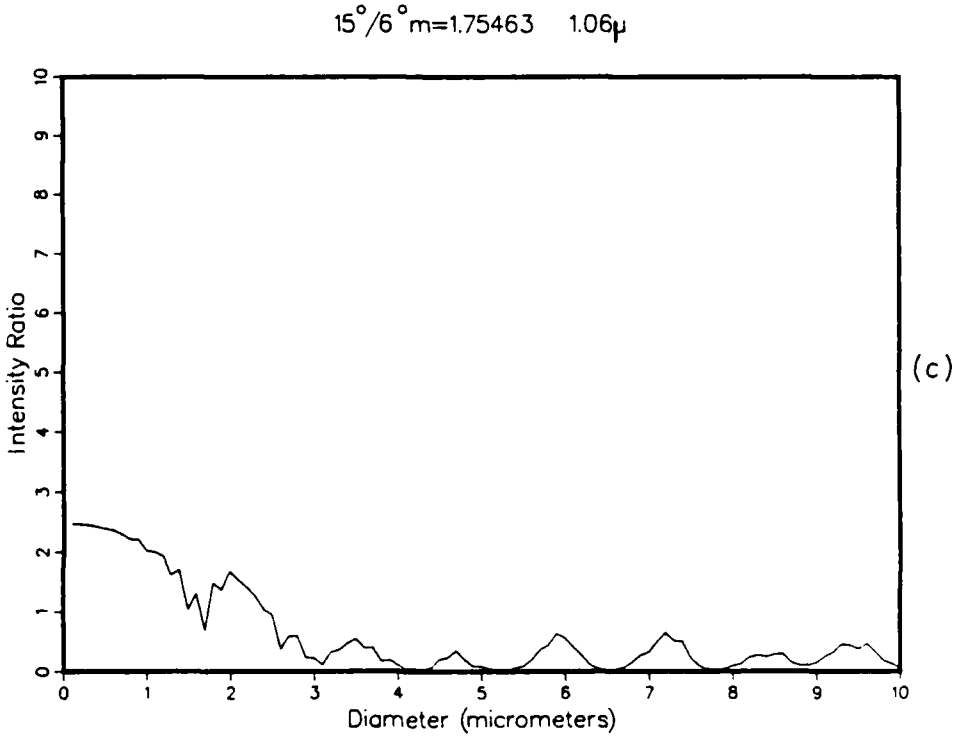

Figure 4.31. (Continued).

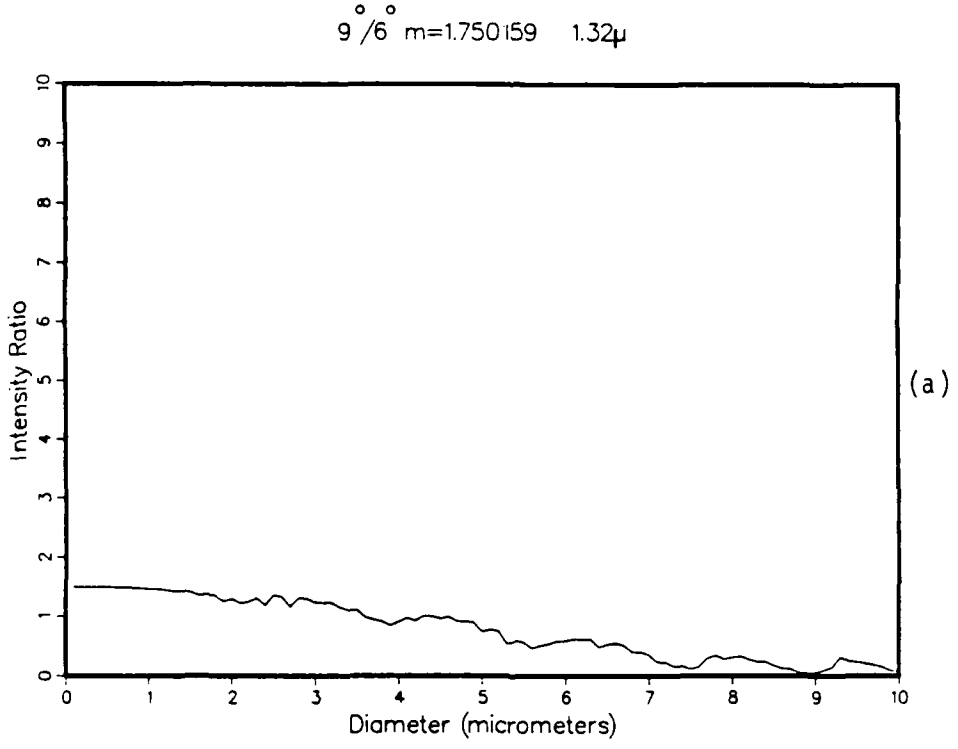

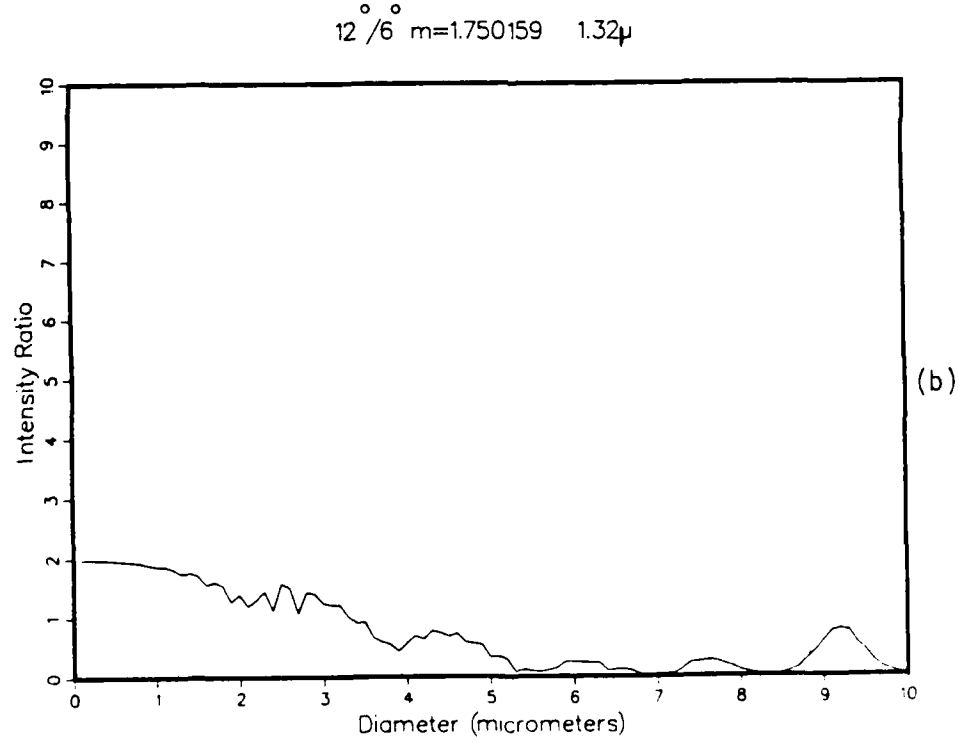

Figure 4.32. Sample Intensity Ratio Plots for Aluminum Oxide Particles for $\lambda = 1.32\mu$.

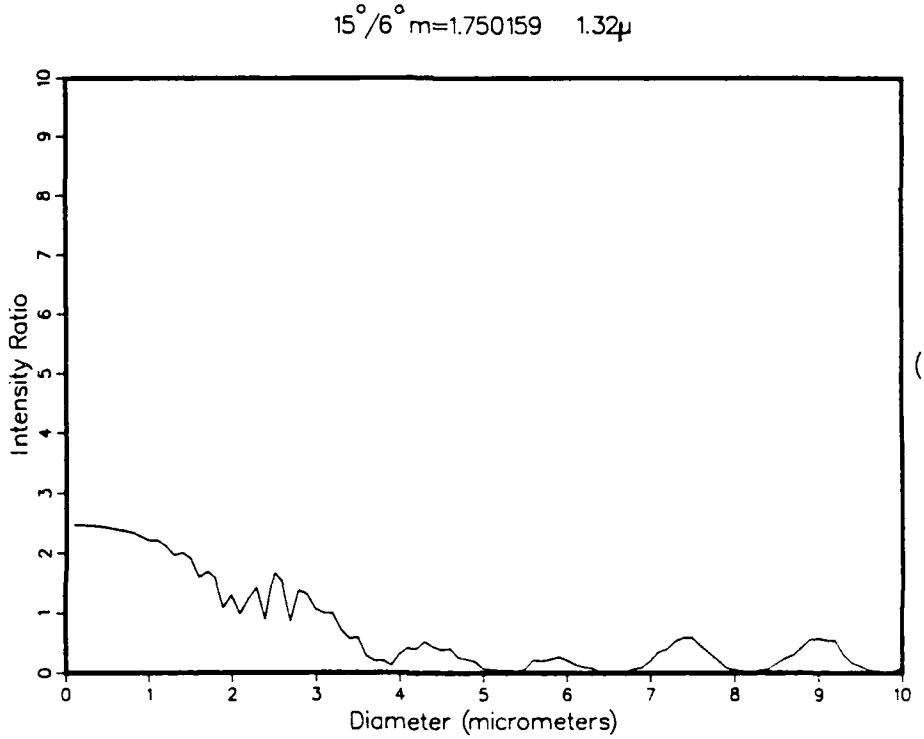

(c)

Figure 4.32. (Continued).

Table 4.7. Distribution Errors Using the Vector Method of Interpretation in the Simulation Program for Comparisons to Table 4.2.

DISTRIBUTION ERRORS					Detector Angles	Number of
I	II	III	IV	V	(degrees)	Detectors
6456	9490	8444	10176	9102	14,48	2
3102	4072	5594	4272	7008	6	3
2382	1558	2512	2032	2878	11	4
1742	1118	636	1028	960	39	5
430	488	288	176	424	21	6
376	216	154	74	174	32	7
474	166	58	50	96	36	8
	[Emin, Emax] = [-0.2, 0.2]					
5802	8690	9484	10064	6960	14,49	2
2296	2860	4306	3606	3596	6	3
376	240	544	656	752	11	4
124	148	86	38	252	22	5
94	54	34	122	100	19	6
162	32	58	40	52	52	7
186	16	42	62	74	32	8
	[Emin, Emax] = [-0.1, 0.1]					
3274	5250	4864	6924	7924	6,9	2
84	230	540	534	190	13	3
72	14	32	32	16	31	4
56	0	0	0	0	25	5
64	0	0	0	0	56	6
62	0	0	0	0	48	7
62	0	0	0	0	18	8
	[Emin, Emax] = [-0.0, 0.0]					

Table 4.8. Scattering Angles Selected Using the Vector Search Method, $\lambda = 0.4880\mu$.

Particle	[θmin, θmax]	Number of Detectors	Detector Angles (Degrees)	Area
Water	[6°, 174°]	2	109,166	3799.27
		3	162	3349.18
		4	157	3217.35
		5	172	3152.00
		6	97	3133.50
		7	169	3109.94
		8	117	3112.77
Water	[6°, 60°]	2	8,11	4088.76
		3	14	3759.56
		4	53	3678.06
		5	57	3662.55
		6	60	3657.12
		7	50	3655.20
		8	39	3654.74
Aluminum Oxide	[6°, 60°]	2	15,18	3988.77
		3	9	3845.48
		4	6	3759.61
		5	57	3695.07
		6	12	3662.81
		7	53	3637.70
		8	60	3630.94

SUMMARY AND CONCLUSIONS

A Multiple Ratio Single Particle Counter (MRSPC) has been proposed by Sverdrup Technology, Inc. (AEDC) for size measurements of spherical particles of known refractive index within the range of diameters $0.1\mu \leq d \leq 10.0\mu$ ($0.64 \leq \alpha \leq 64.0$ for $\lambda = 0.4880\mu$). This optical sizing technique is well suited to fiber optics for noninterfering remote measurements, especially useful in harsh environments. Particle size interpretation is performed through correlation of measured intensity ratios to theoretically calculated ratios, thus, eliminating both the need for reference measurements of the incident beam intensity and a knowledge of the particle position within the Gaussian beam. However, the intensity ratios are multivalued functions of diameter making it difficult to correctly interpret particle size.

To overcome the problem of particle size ambiguity, several intensity ratios are measured for a single particle scattering event. The measured ratio values must simultaneously correspond to respective theoretical calculations. Two techniques, a least squared fit to actual ratioed data and a vector method, were considered for particle size interpretation. The ratio method seems to offer better size resolution and should be better suited to consistency checks for discriminating particles that might lie outside the size range of interest.

The basic objective of this investigation was to develop methods for analyzing the sizing system and selecting a minimum number of

detector placement angles that sufficiently reduces particle size ambiguity. To quantify ambiguity and predict sizing system performance for a given set of scattering angles, a Monte Carlo simulation program was developed that incorporates measurement errors which affect particle size ambiguity. Measurement errors used in this study were generalized, but the program can be easily modified to include specific instrumentation errors for a particular sizing system.

Preliminary studies, using the simulation program, indicated that particle sizes can be distinguished over the size range of interest using a practical number of detectors. Ambiguity was found to be very dependent upon the measurement errors.

The minimum number of particles per distribution in the simulation program that maintains statistical results was found to be 500 over a size subinterval of 2.0μ. The maximum diameter step size for the theoretical look-up table, for size interpretation, was found to be 0.02μ. A step size of 0.1μ in the simulation program produced much larger distribution errors than for 0.02μ.

The simulation program was developed into a search technique for selecting detector placement angles. The first two angles were selected simultaneously forming a two-detector system. Additional detectors were added one at a time. As each detector angle was selected, the current set of n-detector angles were analyzed to determine the amount of ambiguity remaining. This technique allowed a minimum number of detectors to be selected that sufficiently reduces particle size ambiguity.

Mie calculations of the intensity functions versus scattering angle, for certain diameters throughout the size range, indicate that

stronger intensities are scattered into the forward angles throughout the entire size range. Detectors placed within this region should maintain the best signal-to-noise ratios and detect scattered signals from smaller particles. Small particle measurements are limited to sizes that scatter intensity signals detectable above background noise. Also, the forward scattering angle (diffraction lobe) intensities are less sensitive to nonsphericity and variable refractive index [12].

Detector placement angles were selected for water and aluminum oxide particles with refractive indices 1.33 and 1.776, respectively, assuming an incident wavelength of 0.4880μ. In each case, eight detector angles were selected from the forward scattering angles [6°, 60°] and distribution errors presented for three cases of intensity measurement errors. The distribution errors decrease significantly with a decrease in measurement errors. Also, a change in measurement errors was shown to affect the detector angle selections.

The distribution errors for the detector scattering angles selected from [6°, 60°] were not significantly different from distribution errors for the set of detector angles selected from the full range of scattering angles [6°, 174°]. Thus, for the measurement errors assumed, placing detectors outside this restricted range of scattering angles offers no advantage in reducing particle size ambiguity.

Detector placement angles were also selected for aluminum oxide particles assuming incident wavelengths of 1.06 and 1.32μ. The distribution errors were larger for these wavelengths than for 0.4880μ wavelength.

A disadvantage of the Monte Carlo search technique for selecting detector angles is lengthy computer time. Another technique, referred

to as the vector search method, was presented and used to select scattering angles for water and aluminum oxide particles for the 0.4880μ wavelength. The computer time is much less, but the method does not incorporate measurement errors that should bias detector angle selection, especially if measurement errors are expressed as a function of intensity.

Input and simulated measured distributions are given in Figures 4.3 to 4.9 and Figures 4.22 to 4.28 for the water and aluminum oxide particles, respectively, assuming intensity measurement errors to be random within ±20 percent. These distributions give an indication of particle size interpretation errors in actual measurements. Future work is proposed to investigate a technique for recovering the input (or actual size distribution) using the simulation program to predict errors in the measured distributions.

The instrumentation for the MRSPC is currently being developed by Sverdrup Technology, Inc. (AEDC). The MRSPC is to be tested in the laboratory by measuring the size distribution of water particles generated by a commercial atomizer and the results compared to similar measurements by commercial sizing systems. If the experimental results are promising, then further performance studies should be performed for this sizing technique. These include effects of size interpretation for non-spherical particle shapes and/or a group of particles with varying refractive indices.

Due to the complexity of the general scattering theory, exact solutions are possible only for a few simple particle geometries such as spheres and infinite cylinders. Usually scattered intensity measurements are correlated to Mie theory for spheres for particle size interpretation.

The scattering pattern of the spherical diameter that most resembles that of the measured intensities (for the given set of detectors) is interpreted as the particle size. This could result in large sizing errors especially for single particle counters. Therefore, a study should be performed to determine the sizing response to scattering from non-spherical particles. Such an investigation would be impractical except for special limiting cases due to the number of possible shapes and orientations within the sample volume. A special case of importance, if feasible, would be a study of effects of size interpretation for slightly non-spherical particles. This might be achieved by assuming spheroids that are almost spherical. Approximate scattering solutions for a given orientation could be calculated for a particle refractive index of particles that are to be measured. Using these calculations for "measured" intensities in the Monte Carlo simulation program, interpreted size distributions could be compared for an input distribution of spherical particles and spheroids.

REFERENCES

REFERENCES

1. Kerker, M., The Scattering of Light and other Electromagnetic Radiation, Academic Press, New York, 1969.

2. Mie, G., Ann. Phys., Vol. 25, p. 377, 1908.

3. Sadiku, M., Theoretical Calculations of Attenuation and Phase Shift of Electromagnetic Wave Propagation Through Snow, Ph.D. Dissertation, Tennessee Technological University, Cookeville, Tennessee, Dec. 1981.

4. Cadle, R. D., Particle Size, Reinhold Publishing Corporation, New York, 1965.

5. Davies, C. N., Aerosol Science, Academic Press, New York, 1966.

6. Belz, R. A., "Particle Diagnostics for Propulsion," AEDC-TR-85-19, Research and Technology Program Synopsis, pp. 175-176, July 1985.

7. Hirleman, E. D. and S. L. K. Wittig, Sixteenth Symposium (International) on Combustion, The Combustion Institute, Pittsburgh, p. 245, 1977.

8. Siegman, A. E., An Introduction to Lasers and Masers, McGraw-Hill Book Company, Inc., New York, 1971.

9. Dickson, L. D., Applied Optics, Vol. 9, p. 1854, 1970.

10. Hirleman, E. Dan, "Laser-Based Single Particle Counters for in-situ Particulate Diagnostics," Optical Engineering, Vol. 19(6), pp. 854-860, Nov./Dec. 1980.

11. Hodkinson, J. R., "Particle Sizing by Means for the Forward Scattering Lobe," Applied Optics, Vol. 5, p. 839, 1966.

12. Gravatt, C. C., "Real Time Measurement of the Size Distribution of Particulate Matter by a Light Scattering Method," APCA Journal, Vol. 23, p. 1035, 1973.

13. Hirleman, E. D. and H. K. Moon, "Response Characteristics of the Multiple Ratio Single Particle Counter," Journal of Colloid and Interface Science, Arizona State University, Tempe, Arizona, June 12, 1981.

14. van de Hulst, H., Light Scattering by Small Particles, Wiley, New York, 1957.

15. Wendell, E. Grove, Brief Numerical Methods, Prentice Hall, N. J., 1966.

ADDITIONAL REFERENCES

Hardy, A. C., and F. H. Perrin, The Principles of Optics, McGraw-Hill Book Company, Inc., New York, 1932.

Hirleman, E. D., "Laser Technique for Simultaneous Particle-Size and -Velocity Measurements," Optics Letters, Vol. 3, p. 19, July 1978.

Hirleman, E. D., and W. H. Stevenson, "Intensity Distribution Properties of a Gaussian Laser Beam Focus," Applied Optics, Vol. 17, No. 21, Nov. 1978.

Jenkins, F. A., and H. E. White, Fundamentals of Optics, McGraw-Hill Book Company, Inc., New York, 1957.

Verdeyen, Joseph T., Laser Electronics, Prentice-Hall, New Jersey, 1981.

Walker, Jr., H. C., P. J. Murphy, R. A. Belz, and J. H. Bridges, "Fiber Optical Light Transmission for Electro-Optical Instrumentation," AEDC-TMR-85-E8, April 1985.

Watson, G. N., Theory of Bessel Functions, University Press, Cambridge, 1962.

APPENDIX A

SAMPLE MIE SCATTERING PROGRAM OUTPUT

```
&DATA
JW=          0.,THETA=   50.000000000000000     ,DIAM= 0.10000000000000006     ,STEP= 0.10000000000000006     ,FINAL=
   10.000000000000000     ,M2=( 0.10000000000000000D+01, 0.00000000000000000D+00),M1=
( 0.13300000000000007D+01, 0.00000000000000000D+00),THETA1=  1.12799999999999989     ,THETA2=  1.12799999999999989
                          LAMDA= 0.48800000000000003     ,INTSWT=          1
&END
```

THETA	DIAMETER	INT1	INT2	WAVELENGTH	QEXT
5.000000D+01	1.000000D-01	5.459370D-03	2.307446D-03	4.880000D-01	1.820745D-02
5.000000D+01	2.000000D-01	3.356597D-01	1.554735D-01	4.880000D-01	2.117134D-01
5.000000D+01	3.000000D-01	2.833267D+00	1.653078D+00	4.880000D-01	6.425665D-01
5.000000D+01	4.000000D-01	8.203001D+00	5.366615D+00	4.880000D-01	1.279730D+00
5.000000D+01	5.000000D-01	1.137361D+01	1.037279D+01	4.880000D-01	2.009914D+00
5.000000D+01	6.000000D-01	6.156047D+00	1.041981D+01	4.880000D-01	2.671490D+00
5.000000D+01	7.000000D-01	5.302943D+00	1.170072D+01	4.880000D-01	3.218276D+00
5.000000D+01	8.000000D-01	1.881365D+01	2.039696D+01	4.880000D-01	3.634329D+00
5.000000D+01	9.000000D-01	4.798756D+01	4.062038D+01	4.880000D-01	3.930015D+00
5.000000D+01	1.000000D+00	4.600437D+01	5.179109D+01	4.880000D-01	3.973704D+00
5.000000D+01	1.100000D+00	3.151390D+01	4.983477D+01	4.880000D-01	3.729444D+00
5.000000D+01	1.200000D+00	1.569402D+01	4.635792D+01	4.880000D-01	3.432508D+00
5.000000D+01	1.300000D+00	6.378090D+01	7.144605D+01	4.880000D-01	3.142519D+00
5.000000D+01	1.400000D+00	1.147791D+02	1.047743D+02	4.880000D-01	2.778422D+00
5.000000D+01	1.500000D+00	1.008348D+02	1.189090D+02	4.880000D-01	2.281045D+00
5.000000D+01	1.600000D+00	6.384012D+01	9.538841D+01	4.880000D-01	1.911725D+00
5.000000D+01	1.700000D+00	2.699105D+01	9.933771D+01	4.880000D-01	1.822873D+00
5.000000D+01	1.800000D+00	1.538553D+02	1.372612D+02	4.880000D-01	1.852958D+00
5.000000D+01	1.900000D+00	1.603839D+02	1.670040D+02	4.880000D-01	1.823645D+00
5.000000D+01	2.000000D+00	1.959848D+02	1.755192D+02	4.880000D-01	1.834697D+00
5.000000D+01	2.100000D+00	4.605229D+01	1.214847D+02	4.880000D-01	2.117179D+00
5.000000D+01	2.200000D+00	8.482925D+01	1.902805D+02	4.880000D-01	2.453075D+00
5.000000D+01	2.300000D+00	2.088594D+02	1.457708D+02	4.880000D-01	2.682396D+00
5.000000D+01	2.400000D+00	2.804986D+02	2.392552D+02	4.880000D-01	2.649826D+00
5.000000D+01	2.500000D+00	1.893632D+02	1.611481D+02	4.880000D-01	2.727171D+00
5.000000D+01	2.600000D+00	3.313850D+01	2.600931D+02	4.880000D-01	2.855992D+00
5.000000D+01	2.700000D+00	1.726811D+02	1.275620D+02	4.880000D-01	2.733344D+00
5.000000D+01	2.800000D+00	2.356485D+02	2.223402D+02	4.880000D-01	2.618319D+00
5.000000D+01	2.900000D+00	3.491653D+02	2.529204D+02	4.880000D-01	2.263581D+00
5.000000D+01	3.000000D+00	1.572682D+02	2.258235D+02	4.880000D-01	2.181848D+00
5.000000D+01	3.100000D+00	5.848341D+01	2.973825D+02	4.880000D-01	2.116971D+00
5.000000D+01	3.200000D+00	2.522343D+02	1.608386D+02	4.880000D-01	1.917399D+00
5.000000D+01	3.300000D+00	3.995764D+02	3.104288D+02	4.880000D-01	1.873589D+00
5.000000D+01	3.400000D+00	3.613909D+02	2.899354D+02	4.880000D-01	1.857794D+00
5.000000D+01	3.500000D+00	1.262899D+02	4.531163D+02	4.880000D-01	2.073111D+00
5.000000D+01	3.600000D+00	1.291148D+02	1.331109D+02	4.880000D-01	2.138390D+00
5.000000D+01	3.700000D+00	3.345338D+02	3.291868D+02	4.880000D-01	2.235230D+00

5.0000000D+01	3.8000000D+00	4.912323D+02	4.102547D+02	4.8800000D-01	2.344009D+00
5.0000000D+01	3.9000000D+00	4.096113D+02	4.299882D+02	4.8800000D-01	2.462089D+00
5.0000000D+01	4.0000000D+00	1.236894D+02	6.779635D+02	4.8800000D-01	2.641061D+00
5.0000000D+01	4.1000000D+00	2.597623D+02	3.073166D+02	4.8800000D-01	2.504420D+00
5.0000000D+01	4.2000000D+00	4.066958D+02	4.622589D+02	4.8800000D-01	2.411271D+00
5.0000000D+01	4.3000000D+00	6.522601D+02	5.993443D+02	4.8800000D-01	2.334969D+00
5.0000000D+01	4.4000000D+00	3.808834D+02	5.640195D+02	4.8800000D-01	2.256124D+00
5.0000000D+01	4.5000000D+00	2.299743D+02	8.171977D+02	4.8800000D-01	2.234315D+00
5.0000000D+01	4.6000000D+00	3.187698D+02	4.528913D+02	4.8800000D-01	1.992948D+00
5.0000000D+01	4.7000000D+00	6.211496D+02	6.677976D+02	4.8800000D-01	1.919531D+00
5.0000000D+01	4.8000000D+00	7.134427D+02	7.370536D+02	4.8800000D-01	1.948162D+00
5.0000000D+01	4.9000000D+00	3.767592D+02	7.790216D+02	4.8800000D-01	2.009042D+00
5.0000000D+01	5.0000000D+00	4.245437D+02	7.299424D+02	4.8800000D-01	2.067256D+00
5.0000000D+01	5.1000000D+00	3.477093D+02	5.797908D+02	4.8800000D-01	2.077761D+00
5.0000000D+01	5.2000000D+00	8.895320D+02	8.714427D+02	4.8800000D-01	2.202946D+00
5.0000000D+01	5.3000000D+00	6.633452D+02	8.680906D+02	4.8800000D-01	2.345088D+00
5.0000000D+01	5.4000000D+00	5.353892D+02	9.672747D+02	4.8800000D-01	2.419377D+00
5.0000000D+01	5.5000000D+00	3.901259D+02	5.578323D+02	4.8800000D-01	2.379165D+00
5.0000000D+01	5.6000000D+00	5.636198D+02	8.158838D+02	4.8800000D-01	2.352573D+00
5.0000000D+01	5.7000000D+00	9.886426D+02	9.418814D+02	4.8800000D-01	2.352169D+00
5.0000000D+01	5.8000000D+00	8.144481D+02	1.219856D+03	4.8800000D-01	2.309180D+00
5.0000000D+01	5.9000000D+00	8.924968D+02	7.407684D+02	4.8800000D-01	2.217632D+00
5.0000000D+01	6.0000000D+00	3.335938D+02	6.832117D+02	4.8800000D-01	2.048416D+00
5.0000000D+01	6.1000000D+00	7.539014D+02	9.673928D+02	4.8800000D-01	2.003904D+00
5.0000000D+01	6.2000000D+00	1.097663D+03	1.176921D+03	4.8800000D-01	2.023453D+00
5.0000000D+01	6.3000000D+00	9.086986D+02	1.104654D+03	4.8800000D-01	1.981765D+00
5.0000000D+01	6.4000000D+00	7.907868D+02	7.185546D+02	4.8800000D-01	2.000407D+00
5.0000000D+01	6.5000000D+00	4.318954D+02	9.081192D+02	4.8800000D-01	2.017243D+00
5.0000000D+01	6.6000000D+00	1.035009D+03	1.200957D+03	4.8800000D-01	2.128903D+00
5.0000000D+01	6.7000000D+00	1.126028D+03	1.492724D+03	4.8800000D-01	2.253913D+00
5.0000000D+01	6.8000000D+00	1.398998D+03	9.698248D+02	4.8800000D-01	2.263607D+00
5.0000000D+01	6.9000000D+00	4.658316D+02	9.173150D+02	4.8800000D-01	2.283511D+00
5.0000000D+01	7.0000000D+00	6.454429D+02	1.160158D+03	4.8800000D-01	2.310855D+00
5.0000000D+01	7.1000000D+00	1.278323D+03	1.457677D+03	4.8800000D-01	2.348400D+00
5.0000000D+01	7.2000000D+00	1.393805D+03	1.262653D+03	4.8800000D-01	2.273418D+00
5.0000000D+01	7.3000000D+00	1.845048D+03	1.178903D+03	4.8800000D-01	2.225381D+00
5.0000000D+01	7.4000000D+00	4.900087D+02	1.155344D+03	4.8800000D-01	2.114776D+00
5.0000000D+01	7.5000000D+00	1.041707D+03	1.476841D+03	4.8800000D-01	2.073048D+00
5.0000000D+01	7.6000000D+00	1.435824D+03	1.885482D+03	4.8800000D-01	2.095987D+00
5.0000000D+01	7.7000000D+00	1.883535D+03	1.510603D+03	4.8800000D-01	1.965377D+00
5.0000000D+01	7.8000000D+00	1.354562D+03	1.326463D+03	4.8800000D-01	2.040446D+00
5.0000000D+01	7.9000000D+00	6.990481D+02	1.523601D+03	4.8800000D-01	2.005828D+00
5.0000000D+01	8.0000000D+00	1.313827D+03	1.684177D+03	4.8800000D-01	2.084183D+00
5.0000000D+01	8.1000000D+00	1.906251D+03	1.556102D+03	4.8800000D-01	2.180628D+00
5.0000000D+01	8.2000000D+00	1.876812D+03	1.662877D+03	4.8800000D-01	2.148965D+00
5.0000000D+01	8.3000000D+00	6.117231D+02	1.589961D+03	4.8800000D-01	2.244595D+00
5.0000000D+01	8.4000000D+00	9.832202D+02	1.830701D+03	4.8800000D-01	2.284131D+00
5.0000000D+01	8.5000000D+00	1.635696D+03	1.929254D+03	4.8800000D-01	2.312265D+00
5.0000000D+01	8.6000000D+00	2.281209D+03	1.729490D+03	4.8800000D-01	2.248392D+00

5.0000000D+01	8.7000000D+00	1.697796D+03	1.789225D+03	4.8800000D-01	2.192642D+00
5.0000000D+01	8.8000000D+00	7.738188D+02	1.971571D+03	4.8800000D-01	2.177866D+00
5.0000000D+01	8.9000000D+00	1.338125D+03	1.969944D+03	4.8800000D-01	2.142238D+00
5.0000000D+01	9.0000000D+00	2.166379D+03	2.062870D+03	4.8800000D-01	2.081275D+00
5.0000000D+01	9.1000000D+00	2.114689D+03	1.952315D+03	4.8800000D-01	1.981325D+00
5.0000000D+01	9.2000000D+00	1.437544D+03	2.062566D+03	4.8800000D-01	1.979055D+00
5.0000000D+01	9.3000000D+00	1.075212D+03	2.350935D+03	4.8800000D-01	2.030456D+00
5.0000000D+01	9.4000000D+00	1.731984D+03	1.922920D+03	4.8800000D-01	2.043539D+00
5.0000000D+01	9.5000000D+00	2.238917D+03	2.073324D+03	4.8800000D-01	2.056678D+00
5.0000000D+01	9.6000000D+00	2.035934D+03	2.250666D+03	4.8800000D-01	2.092094D+00
5.0000000D+01	9.7000000D+00	1.385118D+03	2.480708D+03	4.8800000D-01	2.176969D+00
5.0000000D+01	9.8000000D+00	1.061873D+03	2.313896D+03	4.8800000D-01	2.315288D+00
5.0000000D+01	9.9000000D+00	2.293679D+03	1.983982D+03	4.8800000D-01	2.246596D+00
5.0000000D+01	1.0000000D+01	2.141518D+03	2.378938D+03	4.8800000D-01	2.213702D+00

APPENDIX B

MONTE CARLO DETECTOR PLACEMENT ANGLE PROGRAM

```
C  THIS PROGRAM PREDICTS THE SIZING PERFORMANCE FOR AN INPUT SET
C  OF DETECTOR PLACEMENT ANGLES AND SELECTS ADDITIONAL ANGLES
C  THAT BEST COMPLIMENTS THE INPUT SET IN REDUCING PARTICLE SIZE
C  AMBIGUITY.
C
C*****************************************************************
C
C  DESCRIPTION OF VARIABLES AND SUBROUTINES:
C
C  INPUT:    AN INPUT DATA FILE WITH NUMBER OF FIXED DETECTOR,
C            ANGLES THE FIXED ANGLES, EMIN, EMAX, NUMPART AND
C            NUMDET.
C  IH20488:  AN INPUT DATA FILE WITH MIE INTENSITIES USING AN
C            EXTENDED RECORD LENGTH.
C  OUTPUT:   OUTPUT DATA FILE THAT RESULTS ARE WRITTEN TO.
C  INTEN:    MATRIX OF MIE INTENSITIES FOR A DIAMETER STEP OF 0.1
C            MICROMETERS.
C  INTER:    MATRIX OF INTERPOLATED MIE INTENSITIES FOR A
C            DIAMETER STEP OF 0.01 MICROMETERS.
C  NTHETA:   NUMBER OF MIE INTENSITY SCATTERING ANGLES TO BE
C            INPUT INTO THIS PROGRAM.
C  MINTH:    MINIMUM THETA (IN INTEGER FORM) OF THE DETECTOR
C            PLACEMENT ANGLE SELECTION RANGE.
C  MAXTH:    MAXIMUM THETA (IN INTEGER FORM) OF THE DETECTOR
C            PLACEMENT ANGLE SELECTION RANGE.
C  NUMFIX:   NUMBER OF FIXED DETECTOR ANGLES INPUT INTO THIS
C            PROGRAM.
C  FIXTH:    MATRIX OF FIXED DETECTOR ANGLES INPUT INTO THIS
C            PROGRAM.
C  INTERP:   SUBROUTINE TO EXPAND THE MATRIX INTEN TO MATRIX
C            INTER USING NEWTON'S FORWARD DIFFERENCE
C            INTERPOLATION TECHNIQUE.
C  EMIN:     THE MINIMUM FRACTIONAL ERROR FOR "MEASURED"
C            SCATTERING INTENSITY SIMULATION.
C  EMAX:     THE MAXIMUM FRACTIONAL ERROR FOR "MEASURED"
C            SCATTERING INTENSITY SIMULATION.
C  NUMDET:   NUMBER OF DETECTOR PLACEMENT ANGLES TO BE FOUND.
C  HOLDINT:  MATRIX OF MIE INTENSITIES FOR FIXED DETECTOR ANGLES.
C  NUMRAT:   NUMBER OF INTENSITY RATIOS FOR NUMDET.
C  RATFIX:   MATRIX OF INTENSITY RATIOS FOR INTENSITIES OF
C            HOLDINT.
C  DISTRIB:  A SUBROUTINE THAT GENERATES INPUT-TO-"MEASURED"
C            DISTRIBUTIONS AND CALCULATES DISTRIBUTION ERRORS FOR
C            FIVE SIZE SUBINTERVALS FOR THE SET OF FIXED DETECTOR
C            ANGLES.
C  INTERV:   AN INTEGER (1 TO 5) THAT DENOTES A RESPECTIVE SIZE
C            SUBINTERVAL.
C  MAXERR:   THE MAXIMUM DISTRIBUTION ERROR FOR THE FIVE SIZE
C            SUBINTERVALS.
```

```
C  NUMPART:  THE NUMBER OF PARTICLES PER SIZE SUBINTERVAL FOR
C            AN INPUT SIZE DISTRIBUTION.  (CALLED NR IN THE TEXT)
C  DIST:     A SUBROUTINE THAT GENERATES AN INPUT-TO-"MEASURED"
C            DISTRIBUTION AN DISTRIBUTION ERROR FOR A PARTICULAR
C            SIZE SUBINTERVAL.
C  D1:       A DIAMETER OF THE CONTINUOUS FIRST SIZE SUBINTERVAL.
C  D:        A DIAMETER OF A CONTINUOUS SIZE SUBINTERVAL (EITHER
C            OF THE SUBINTERVALS 2 THROUGH 5).
C  MEAINT:   MATRIX OF INTENSITIES FOR A GIVEN DIAMETER WITH
C            INTENSITY ERRORS INTRODUCED TO SIMULATE "MEASURED"
C            INTENSITIES.
C  MEARAT:   MATRIX OF RATIOED "MEASURED" INTENSITIES.
C  INTVL:    DENOTES THE SIZE SUBINTERVAL (1 TO 5) WITH THE
C            LARGEST DISTRIBUTION ERROR FOR THE FIXED SET OF
C            ANGLES.
C  RDIST:    MATRIX STORAGE OF AN INPUT SIZE DISTRIBUTION FOR A
C            GIVEN SIZE SUBINTERVAL.
C  MDIST:    MATRIX STORAGE OF THE RESULTING "MEASURED" SIZE
C            SUBINTERVAL FOR AN INPUT SIZE DISTRIBUTION.
C  LSERR:    DISTRIBUTION ERROR FOR AN INPUT-TO-"MEASURED" PAIR
C            FOR A SIZE SUBINTERVAL.
C  ISEED2:   SEED VALUE FOR A RANDOM NUMBER GENERATOR.
C  NSTEP:    FIRST, ROWS OF RATFIX REPRESENT DIAMETERS.  NSTEP
C            DETERMINES A DIAMETER STEP VALUE FOR COMPARING
C            "MEASURED" INTENSITY VALUES TO THE LOOK-UP TABLE,
C            MATRIX RATFIX.
C
C*****************************************************************
C
C  THIS PROGRAM IS WRITTEN IN FORTRAN
C
      REAL INTEN(100,180),INTER(1000,180),MEAINT(5,8)
      REAL MEARAT(5,28),RATFIX(1000,28),HOLDINT(1000,8)
      INTEGER FIXTH(8),RDIST(100,5),MDIST(100,5),LSERR(5)
      COMMON INTEN,INTER,MINTH,MAXTH
      COMMON /BLK1/ HOLDINT,RDIST,MDIST,RATFIX,LSERR
      NSTEP=2
      NTHETA=178
      MINTH=6
      MAXTH=174
      M=10
      N=11
      K=20

      OPEN(UNIT=M,FILE='IH20488.DAT',RECL=3800,STATUS='OLD')

      READ(M,*)
      READ(M,*)
      DO 2000 IDIAM=1,100
        READ(M,*)(INTEN(IDIAM,ITHETA),ITHETA=1,NTHETA)
2000  CONTINUE
```

```
      CLOSE(M)

      OPEN(UNIT=N,FILE='INPUT.DAT',STATUS='OLD')
      OPEN(UNIT=12,FILE='OUTPUT.DAT',STATUS='NEW')
      WRITE(12,*)' H2O (1.33,0.0) WAVELENGTH=.4880 MICROMETERS'

      READ(N,*)NUMFIX
      READ(N,*)(FIXTH(I),I=1,NUMFIX)
      DO 1990 I=1,NUMFIX
        DO 1980 J=-2,2
          IF(J.EQ.0)GO TO 1980
          INTEN(1,FIXTH(I)+J)=-1.0
1980    CONTINUE
1990  CONTINUE

      CALL INTERP

      DO 1975 I=1,NUMFIX
        INTEN(1,FIXTH(I))=-1.0
1975  CONTINUE

      READ(N,*)EMIN,EMAX
      READ(N,*)NUMPART
      READ(N,*)NUMDET

      CLOSE(N)

      DO 1970 I=1,NUMFIX
        DO 1960 IDIAM=10,1000
          HOLDINT(IDIAM,I)=INTER(IDIAM,FIXTH(I))
1960    CONTINUE
1970  CONTINUE

      NUMRAT=NUMFIX*(NUMFIX-1)/2
1949  DO 1950 IDIAM=10,1000
        I=0
        DO 1940 IDEN=1,NUMFIX-1
          HOLDDEN=HOLDINT(IDIAM,IDEN)
          DO 1930 ICOL=IDEN+1,NUMFIX
            I=I+1
            RATFIX(IDIAM,I)=HOLDINT(IDIAM,ICOL)/HOLDDEN
1930      CONTINUE
1940    CONTINUE
1950  CONTINUE

      DO 1925 I=1,100
        DO 1924 J=1,5
          RDIST(I,J)=0
          MDIST(I,J)=0
1924    CONTINUE
1925  CONTINUE

      CALL DISTRIB(ND,NUMPART,NUMFIX,EMIN,EMAX,NUMRAT,NSTEP)
```

```
      MAXERR=LSERR(1)
      INTERV=1
      DO 1923 I=2,5
        IF(LSERR(I).GT.MAXERR)THEN
          MAXERR=LSERR(I)
          INTERV=I
        ENDIF
1923  CONTINUE
      GO TO 80

1945  CONTINUE

      NUMFIX=NUMFIX+1
      NR=NUMFIX*(NUMFIX-1)/2
      LSERRH=99999999
      DO 1920 ITHETA=MINTH,MAXTH
        IF(INTEN(1,ITHETA).EQ.-1.0)GO TO 1920
        DO 1910 IDIAM=10,1000
          HOLDINT(IDIAM,NUMFIX)=INTER(IDIAM,ITHETA)
1910    CONTINUE
        DO 1900 IDIAM=10,1000
          I=0
          DO 1890 IDEN=1,NUMFIX-1
            HOLDDEN=HOLDINT(IDIAM,IDEN)
            DO 1885 ICOL=IDEN+1,NUMFIX
              I=I+1
              RATFIX(IDIAM,I)=HOLDINT(IDIAM,ICOL)/HOLDDEN
1885        CONTINUE
1890      CONTINUE
1900    CONTINUE
        NUMRAT=NR
        DO 1884 I=1,100
          RDIST(I,INTERV)=0
          MDIST(I,INTERV)=0
1884    CONTINUE

        CALL DIST(NUMPART,NUMFIX,EMIN,EMAX,NUMRAT,INTERV,NSTEP)

        IF(LSERR(INTERV).LT.LSERRH)THEN
          LSERRH=LSERR(INTERV)
          ITHETAH=ITHETA
        ENDIF

        WRITE(12,1879)ITHETA,INTERV,LSERR(INTERV)
1879    FORMAT(X,'THETA=',I4,' INTERVAL=',I2,
     1    '   LSERR(INTERVAL)=',I10)

1920  CONTINUE

      FIXTH(NUMFIX)=ITHETAH
      DO 1870 I=-2,2
        INTEN(1,ITHETAH+I)=-1.0
1870  CONTINUE
```

```
      WRITE(12,1878)ITHETAH,INTERV,LSERRH
1878  FORMAT(X,'NEXT DET. ANGLE=',I3,'  INTERVAL=',I2,
     1       '  LSERR=',I8)
      DO 1876 IDIAM=10,1000
        HOLDINT(IDIAM,NUMFIX)=INTER(IDIAM,ITHETAH)
1876  CONTINUE
      GO TO 1949


80    K=K+1
      OPEN(UNIT=K,STATUS='NEW')
      WRITE(K,*)' FIXED DETECTOR ANGLES'
      WRITE(K,79)(FIXTH(I),I=1,NUMFIX)
79    FORMAT(X,8I5)
      WRITE(K,*)' EMIN=',EMIN,'   EMAX=',EMAX,'   NSTEP=',NSTEP
      WRITE(K,*)' NUMBER OF PARTICLES PER DIST.=',ND,NUMPART
      WRITE(K,*)' H2O (1.33,0.0)  WAVELENGTH=.4880 MICROMETERS'
      WRITE(K,*)' REAL-TO-MEASURED DISTRIBUTION ERRORS'
      WRITE(K,70)(LSERR(I),I=1,5)
70    FORMAT(6X,5I10)
      WRITE(K,*)' SIZE   IR    IIR  IIIR   IVR   VR    IM   IIM
     1   IIIM   IVM   VM'
      DO 50 I=1,100
        DIA=I/10.
        WRITE(K,60)DIA,(RDIST(I,J),J=1,5),(MDIST(I,J),J=1,5)
60      FORMAT(X,F4.1,10I6)
50    CONTINUE
      CLOSE(K)
      IF(NUMFIX.LT.NUMDET)GO TO 1945

      CLOSE(K)
      STOP
      END
C***END OF MAIN PROGRAM*********************************************

C***SUBROUTINE TO CREATE DISTRIBUTIONS OVER SIZE SUBINTERVALS.***
      SUBROUTINE DISTRIB(ND,NUMPART,NUMFIX,EMIN,EMAX,NUMRAT,
     1     NSTEP)
      REAL HOLDINT(1000,8),RATFIX(1000,28),MEAINT(5,8)
      REAL MEARAT(5,28)
      INTEGER RDIST(100,5),MDIST(100,5),LSERR(5)
      COMMON /BLK1/ HOLDINT,RDIST,MDIST,RATFIX,LSERR

      ISEED2=77777
      ND=0
      D1=0.1-1.9/NUMPART
      D=2.0-2.0/NUMPART

8995  CONTINUE

      D1=D1+1.9/NUMPART
      D=D+2.0/NUMPART

      ID1=INT(D1*10.)
```

```
      ID=INT(D*10.)

      RD=RD+1
      J=1
      IF((D1*10.-ID1/1.0).LT.0.5)J=0
      RDIST(ID1+J,1)=RDIST(ID1+J,1)+1
      J=1
      IF((D*10.-ID/1.0).LT.0.5)J=0
      RDIST(ID+J,2)=RDIST(ID+J,2)+1
      RDIST(ID+20+J,3)=RDIST(ID+20+J,3)+1
      RDIST(ID+40+J,4)=RDIST(ID+40+J,4)+1
      RDIST(ID+60+J,5)=RDIST(ID+60+J,5)+1

      ID1=INT(D1*100.0)
      ID=INT(D*100.0)
      DT1=ID1/100.0
      DT=ID/100.0

      DO 9000 ICOL=1,NUMFIX
        MEAINT(1,ICOL)=(D1-DT1)*(HOLDINT(ID1+1,ICOL)
     1       -HOLDINT(ID1,ICOL))/.01+HOLDINT(ID1,ICOL)
        I=1
        DO 8990 J=0,400,200
          I=I+1
          MEAINT(I,ICOL)=(D-DT)*(HOLDINT(ID+J+1,ICOL)
     1         -HOLDINT(ID+J,ICOL))/.01+HOLDINT(ID+J,ICOL)
8990    CONTINUE
        IF(ID+600.EQ.1000)THEN
          MEAINT(5,ICOL)=HOLDINT(1000,ICOL)
        ELSE
          MEAINT(5,ICOL)=(D-DT)*(HOLDINT(ID+600+1,ICOL)
     1         -HOLDINT(ID+600,ICOL))/.01 +HOLDINT(ID+600,ICOL)
        ENDIF
9000    CONTINUE

      DO 8980 ICOL=1,NUMFIX
        R2=RAN(ISEED2)
        ERR=R2*(EMAX+EMIN)-EMIN
        DO 8970 J=1,5
          MEAINT(J,ICOL)=MEAINT(J,ICOL)+ERR*MEAINT(J,ICOL)
8970    CONTINUE
8980  CONTINUE

      DO 8960 J=1,5
        I=0
        DO 8950 IDEN=1,NUMFIX-1
          HOLDDEN=MEAINT(J,IDEN)
          DO 8940 ICOL=IDEN+1,NUMFIX
            I=I+1
            MEARAT(J,I)=MEAINT(J,ICOL)/HOLDDEN
8940      CONTINUE
8950    CONTINUE
8960  CONTINUE
      DO 8930 INTVL=1,5
```

```
          ERRHOLD=0.0
          DO 8920 IDIAM=10,1000,NSTEP
            ERROR=0.0
            DO 8910 I=1,NUMRAT
              ERROR=(MEARAT(INTVL,I)-RATFIX(IDIAM,I))**2+ERROR
8910        CONTINUE
            IF(IDIAM.EQ.10)THEN
              ERRHOLD=ERROR
              IDHOLD=IDIAM
            ELSE
              IF(ERROR.LT.ERRHOLD)THEN
                ERRHOLD=ERROR
                IDHOLD=IDIAM
              ENDIF
            ENDIF
8920      CONTINUE

          A=IDHOLD/10.0
          IB=INT(A)
          C=(A-IB/1.0)*10.0
          ID=INT(C)
          J=0
          IF(ID.GE.5)J=1
          MTRXDIA=IB+J
          MDIST(MTRXDIA,INTVL)=MDIST(MTRXDIA,INTVL)+1
8930    CONTINUE

        ND=ND+1
        IF(ND.LT.NUMPART)GO TO 8995

        DO 8900 J=1,5
          LSERR(J)=0
          DO 8890 IDIAM=1,100
            LSERR(J)=LSERR(J)+(RDIST(IDIAM,J)-MDIST(IDIAM,J))**2
8890      CONTINUE
8900    CONTINUE
        RETURN
        END
C   ******END OF SUBROUTINE DISTRIB*********************************

C   ******SUBROUTINE DIST*******************************************
        SUBROUTINE DIST(NUMPART,NUMFIX,EMIN,EMAX,NUMRAT,INTERV,
     1         NSTEP)
        REAL HOLDINT(1000,8),RATFIX(1000,28),MEAINT(5,8)
        REAL MEARAT(5,28)
        INTEGER RDIST(100,5),MDIST(100,5),LSERR(5)
        COMMON /BLK1/ HOLDINT,RDIST,MDIST,RATFIX,LSERR

        ISEED2=77777
        NP=0
        IF(INTERV.EQ.1)THEN
          D=0.1-1.9/NUMPART
        ELSE
          D=2.0-2.0/NUMPART
```

```
      ENDIF
      JJ=0
      IF(INTERV.EQ.3)JJ=200
      IF(INTERV.EQ.4)JJ=400
      IF(INTERV.EQ.5)JJ=600
      II=JJ/10

7955  CONTINUE

      IF(INTERV.EQ.1)THEN
        D=D+1.9/NUMPART
      ELSE
        D=D+2.0/NUMPART
      ENDIF

      ID=INT(D*10.0)
      J=1
      IF((D*10.-ID/1.0).LT.0.5)J=0
      RDIST(ID+II+J,INTERV)=RDIST(ID+II+J,INTERV)+1
      ID=INT(D*100.0)
      DT=ID/100.0
      DO 7830 ICOL=1,NUMFIX
        IF(ID+JJ.EQ.1000)THEN
          MEAINT(INTERV,ICOL)=HOLDINT(1000,ICOL)
        ELSE
          MEAINT(INTERV,ICOL)=(D-DT)*(HOLDINT(ID+JJ+1,ICOL)
     1        -HOLDINT(ID+JJ,ICOL))/.01+HOLDINT(ID+JJ,ICOL)
        ENDIF
7830  CONTINUE
      DO 7820 ICOL=1,NUMFIX
        R2=RAN(ISEED2)
        ERR=R2*(EMAX+EMIN)-EMIN
        MEAINT(INTERV,ICOL)=MEAINT(INTERV,ICOL)+
     1          ERR*MEAINT(INTERV,ICOL)
7820  CONTINUE
      I=0
      DO 7810 IDEN=1,NUMFIX-1
        HOLDDEN=MEAINT(INTERV,IDEN)
        DO 7800 ICOL=IDEN+1,NUMFIX
          I=I+1
          MEARAT(INTERV,I)=MEAINT(INTERV,ICOL)/HOLDDEN
7800    CONTINUE
7810  CONTINUE
      ERRHOLD=0.0
      DO 7790 IDIAM=10,1000,NSTEP
        ERROR=0.0
        DO 7780 I=1,NUMRAT
          ERROR=(MEARAT(INTERV,I)-RATFIX(IDIAM,I))**2+ERROR
7780    CONTINUE
        IF(IDIAM.EQ.10)THEN
          ERRHOLD=ERROR
          IDHOLD=IDIAM
        ELSE
          IF(ERROR.LT.ERRHOLD)THEN
```

```
              ERRHOLD=ERROR
              IDHOLD=IDIAM
            ENDIF
          ENDIF
7790      CONTINUE
          A=IDHOLD/10.0
          IB=INT(A)
          C=(A-IB/1.0)*10.0
          ID=INT(C)
          J=0
          IF(ID.GE.5)J=1
          MDIAM=IB+J
          MDIST(MDIAM,INTERV)=MDIST(MDIAM,INTERV)+1
          NP=NP+1
          IF(NP.LT.NUMPART)GO TO 7955
          LSERR(INTERV)=0
          DO 7769 IDIAM=1,100
            LSERR(INTERV)=LSERR(INTERV)+(RDIST(IDIAM,INTERV)
     1        -MDIST(IDIAM,INTERV))**2
7769      CONTINUE
          RETURN
          END
C************END OF SUBROUTINE DIST*********************************

C************INTERPOLATION SUBROUTINE*******************************
          SUBROUTINE INTERP
          REAL INTEN(100,180),INTER(1000,180),HOLD(100,4)
          COMMON INTEN,INTER,MINTH,MAXTH
          DO 3000 ITHE=MINTH,MAXTH
            IF(INTEN(1,ITHE).EQ.-1.0)THEN
              INTER(1,ITHE)=-1.0
              GO TO 3000
            ENDIF
            DO 2090 IDIAM=1,100
              HOLD(IDIAM,1)=INTEN(IDIAM,ITHE)
2090        CONTINUE

            DO 2080 ICOL=2,4
              DO 2070 IDIAM=1,100-ICOL+1
                HOLD(IDIAM,ICOL)=HOLD(IDIAM+1,ICOL-1)-
     1              HOLD(IDIAM,ICOL-1)
2070          CONTINUE
2080        CONTINUE

            DO 940 IDIAM=1,97
              IF(IDIAM.EQ.1)THEN
                DO 930 IDX=1,9
                  X1=IDIAM/10.0
                  X=IDIAM/10.0+IDX/100.0
                  U=(X-X1)/.1
                  T1=HOLD(IDIAM,1)
                  T2=U*HOLD(IDIAM,2)
                  T3=U*(U-1.0)*HOLD(IDIAM,3)/2.0
                  T4=U*(U-1.0)*(U-2.0)*HOLD(IDIAM,4)/6.0
```

```
                INTER(IDX+10,ITHE)=T1+T2+T3+T4
930           CONTINUE
            ENDIF
            DO 920 IDX=1,9
              X1=IDIAM/10.0
              X=(IDIAM+1)/10.+IDX/100.0
              U=(X-X1)/.1
              T1=HOLD(IDIAM,1)
              T2=U*HOLD(IDIAM,2)
              T3=U*(U-1.0)*HOLD(IDIAM,3)/2.0
              T4=U*(U-1.0)*(U-2.0)*HOLD(IDIAM,4)/6.0
              INTER((IDIAM+1)*10+IDX,ITHE)=T1+T2+T3+T4
920         CONTINUE
            IF(IDIAM.EQ.97)THEN
              DO 910 IDX=1,9
                X1=IDIAM/10.0
                X=(IDIAM+2)/10.0+IDX/100.0
                U=(X-X1)/.1
                T1=HOLD(IDIAM,1)
                T2=U*HOLD(IDIAM,2)
                T3=U*(U-1.0)*HOLD(IDIAM,3)/2.0
                T4=U*(U-1.0)*(U-2.0)*HOLD(IDIAM,4)/6.0
                INTER((IDIAM+2)*10+IDX,ITHE)=T1+T2+T3+T4
910           CONTINUE
            ENDIF
940       CONTINUE
          DO 900 IDIAM=1,100
            INTER(IDIAM*10,ITHE)=HOLD(IDIAM,1)
900       CONTINUE
3000    CONTINUE
        RETURN
        END
C**********THIS CONCLUDES THE INTERPOLATION SUBROUTINE**********
```

1986 USAF-UES Mini Grant

Sponsored by the

AIR FORCE OFFICE OF SCIENTIFIC RESEARCH

Conducted by the

UNIVERSAL ENERGY SYSTEMS, INC.

FINAL REPORT

SOME REMARKS ON THE MANTLE FLOW STRUCTURE BENEATH PASSIVE CONTINENT MARGINS AND THE ASSOCIATED SURFACE GEOID RESPONSES

Prepared by : Albert T. Hsui

Academic Rank : Associate Professor

Department and University :

Department of Geology
University of Illinois at Urbana-Champaign

Date : March 19, 1987

CONTRACT NO : AF-UES-S-760-OMG-054

Abstract

In this project, there are three tasks that have been accomplished. First, a detailed study to understand the origin of numerical diffusion has been carried out. There are two possible sources for the generation of artificial diffusion in most of numerical simulation studies. One is due to the Taylor series truncation in the construction of a first order finite difference approximation. Its effects can generally be eliminated when higher order approximations are utilized. Another source arises through the discretization of computational domains. Due to the averaging of dependent variables within a grid volume, diffusion can be created artificially. It is suggested that discretization diffusion can be suppressed through grid refinement and the incorporation of actual physical diffusion processes.

Secondly, the mantle flow structure beneath passive continental margins has been studied. The viscous forces are found to be too strong such that the production of a secondary cell immediately adjacent to a continental root is not observed even when the wall of the continental root is vertical. This appears to be consistent with the SEASAT altimetry data which indicate that geoid anomaly contours are mostly perpendicular to the axis of continental slopes.

Finally, two dimensional formulas for geoid and gravity modelling have been examined in details. It is found that most of the formulas provide an accurate shape of anomaly curves but not the amplitude of the anomaly. In order to model the anomalies to be detected, it is suggested that appropriately truncated mass anomaly bodies should be considered instead.

Introduction

The main objective of this project is to study the mechanical structure of mantle flows beneath passive margins and to determine if such structure can produce geoid anomalies that are strong enough to be observed at the surface. If the theoretically predicted signals are sufficiently strong, efforts will be made to analyze the SEASAT altimetry data to verify if such signals are present.

Within the framework of the modern plate tectonic theory, some form of solid state thermal convection is postulated to be the main driving mechanism that drives surface plates in motion. However, the details about the flow patterns within the mantle are elusive. It is generally accepted today that flows within the mantle can be described in terms of at least two different length scales. The large scale motion is represented by the surface plate motions. Superposed upon this large scale circulation, there exist various small scale motions which may or may not be directly observable at the surface. One of those that are directly observable is evidenced by mid-plate volcanism. Sea mounts and hot spots are the direct manifestations of such a geological process. They are postulated to be some form of mantle upwellings that penetrate through the large scale circulations. Other small scale circulations can also be inferred through other geophysical observations. For example, back arc spreading and high heat flow within the back arc basins indicate the existence of an induced flow immediately above the descending plate associated with the basin (Toksöz and Hsui, 1978). Recent studies of geoid undulations near oceanic ridges also suggest the

possible existence of small scale longitudinal rolls beneath young oceanic plates (Buck, 1985). It is hypothesized in this project that small scale convective cells also exist beneath passive continental margins. Their presence is hypothesized based on the assumption that lithospheric thicknesses are discontinuous across the bottom of the ocean-continent transition. Based on seismic studies, continental lithospheres are found to be thicker than oceanic lithospheres by an amount ranging from 100 km (Anderson, 1979) to over 300 km (Jordan, 1978). If such a discontinuity does exist, the induction of a corner flow by the mantle dynamics at this corner is highly likely (Roache, 1976). This induced flow will alter the local thermal structure from a pattern presumably varies only in the radial direction. The altered thermal structure in turn will produce density anomalies to generate surface geoid undulations. To test if this hypothesis is valid, a research program has been formulated. It is first to simulate numerically the mantle flow beneath passive continental margins. After the flow patterns are determined, theoretical analyses of the expected geoid anomalies will be carried out. If the predicted geoid undulations are sufficiently strong, SEASAT altimetry data will be examined to verify if such small scale flow structures are observable.

Finite Difference Models for Mantle Flows

The Earth's mantle beneath passive margins is modelled utilizing a two dimensional rectangular domain with a step geometry at the upper boundary (figure 1). Since the focus of our interest is only within the top several hundred kilometers, a two dimensional model is quite adequate in resolving the structure of local mantle dynamics. It is recognized that a step like boundary is highly idealized. It nevertheless represents one end member of the complete range of possibilities. Therefore, in order to determine if a small scale convective cell is possible, such a model is utilized as a starting point for our investigation. The governing equations for mantle dynamics have been discussed by many investigators (e.g. Turcotte et al. 1973). This set of equations represents a non-linear system even at the large Prandtl number limit (i.e. the inertia forces are negligibly small when compared with the viscous forces). Together with an irregular upper boundary, such a nonlinear system can only be resolved through numerical techniques.

The numerical scheme chosen for this study follows that described by Torrance et al. (1973). The scheme utilizes a forward difference in time, a second order central difference in space and a special upwind differencing procedure to treat the non-linear convective terms. It has been recognized that artificial diffusion can arise in some upwind difference schemes. To understand the possible effect of numerical diffusion on our simulation, a more in depth study to analyze the origin of numerical diffusion has been undertaken.

Diffusion processes are generally described mathematically

as second order space derivatives. Therefore, it is well known that due to the truncation of Taylor series expansion associated with finite difference approximations, second derivative terms can be introduced for most if not all of the first order approximations. Hence, artificial diffusion is created. However, when higher order approximations are used for finite differencing, this problem will disappear. This type of numerical diffusion is, therefore, designated as truncation diffusion here to distinguish it from another type of numerical diffusion to be discussed. In our simulation, truncation diffusion poses no difficulties since the upwind differencing scheme used is derived based on the conservation principles. Such a formulation has been demonstrated to possess second order accuracy (Roache, 1976). Consequently, numerical diffusion due to truncation errors will not be present.

Besides truncation diffusion, another class of numerical diffusion has also been identified. It arises through discretization of the computational domain. To demonstrate how discretization diffusion can occur, following example will be examined. Consider two immiscible fluids that are enclosed within a circular tube. The two fluids are separated by two sharp interfaces perpendicular to the wall. Through some external forces such as the electromagnetic forces, the fluids in the tube are induced into a solid body rotation. Since the fluids are immiscible and non-diffusive, the interfaces will in principle rotate without losing their sharp definition. The dynamics of the solid body rotation is simulated with a finite difference

technique identical to the one used here for the vortex dynamic simulation. In this simulation, the fluids are identified with a binary concentration of 0 and 1. The calculated results indicate that as the rotation continues, the fluids gradually diffuse into each other and the initially sharp interfaces are gradually being smoothed out and eventually lose their identities. When the rotation continues for a long period of time, the two fluids will be completely mixed together and form a homogenous fluid with a concentration represented by the averaged value of the initial concentrations. The evolution of the maximum magnitude of concentration is plotted in figure 8. As evidenced in this diagram, the initial concentration of 1 is rapidly being diffused into the other fluid even though the fluids are non-diffusive and immiscible. It clearly demonstrates the existence of numerical diffusion. However, how can it be certain that the diffusion is caused by discretization and not by truncation? Another example has been run to demonstrate the origin of this diffusion. In this run, time steps are chosen such that $\omega \Delta t = \omega \Delta r$ where ω is the rotational velocity, Δt is the time step, r is the radius of the tube and Δr is the grid spacing. The results of the evolution of the maximum concentration is also given in figure 8 by the dashed curve. It is apparent that in this case, the maximum concentration remains unchanged as time advances. Indeed, the results indicate that the high concentration fluid possesses the same amount of value as it initially does even after many revolutions. Because of this observation, it is obvious that the numerical diffusion can not be caused by truncation since identical truncation errors exist in both runs. The only

understand how discretization diffusion occurs, one must slow down the rotational motion and examine the behavior of the interface at successive time steps. Now, let us focus on the two grid volumes located on either side of an interface. The up-stream grid is indexed as grid i while the down stream grid is designated as grid i+1. It is further assumed that grid i has a concentration of 1 while grid i+1 has a concentration of 0. When rotation begins, the interface first moves in a clockwise direction. Let us assume that time steps are chosen such that $v * \Delta t = 0.5 * r * \Delta\theta$, where v again is the rotational velocity. After the first time step, the interface will reach the mid-point of grid i+1. Since in finite difference studies, concentration within a grid volume is represented by an averaged value, grid i+1 will thus possess a concentration of 1/2 after the first time step. Physically, it represents material diffusion of half a grid point within this time interval. For a constant time step situation, the next time step will cause the concentration to diffuse to grid element i+2. For each subsequent time steps, diffusion will migrate one more grid element in the direction of the flow. However, if time step is chosen such that $v * \Delta t = r * \Delta\theta$, numerical diffusion will not occur because the interface will always reach the surface of an element such that a uniform concentration within the grid volume will [illegible] grid concentrations. Therefore, it can be said that discretization diffusion will arise as a result of the [illegible] rotational velocity and the time step size. The [illegible] reasons. The inability to suit a different [illegible]

size of the grid elements. It is about one grid distance per time step. Thus, $v_d = r * \Delta B / \Delta t$.

It should be pointed out that the discretization diffusion is intrinsic to all finite difference schemes since it is caused by the averaging process within a grid volume. Although the origin of this diffusive process is understood, there exist no practical methods at present to treat the problem. However, in most of the realistic mantle dynamics simulations, actual physical diffusion will produce an effect that is generally more significant than the one due to discretization diffusion. As a result, the effects of numerical diffusion will not be very important. Since thermal diffusion is being incorporated in our simulations, we are satisfied that the effects of discretization diffusion do not play an significant role.

Dynamic Structure of the Mantle beneath Passive Margins

To simulate a flow model for the Earth's mantle, it is necessary to define a computational domain that has a length scale equivalent to that of the mantle. Since our interest is mostly in a region that surrounds the step corner beneath the ocean-continent transition with a length scale of no more than about a few hundred kilometers, a simulation with a mantle-wide scale will not provide sufficient resolution for the secondary cell that is being sought. Consequently, a regional kinematic model is used following an approach as described by Hsui et al. (1983). The computational domain is sketched in figure 1. Following a general practice, the problem is scaled by the thickness of the step which can vary from 100 to 300 km. The vertical boundaries of the computational domain are located at a distance about four times the step thickness from the step corner. The total thickness of the box is about four times the step thickness. This is believed to be adequate to resolve the flow patterns surrounding the step corner.

If the mantle flows are assumed to drive surface plates into motion, it follows that the mantle will flow faster than the lithospheres. Consequently, the viscous tractions will drag the lithospheres into relative motions. Since motions between the crust and the mantle are relative, it is assumed that the lithosphere is stationary while the mantle is flowing toward the ridge. This relative motion can be imposed [illegible]

to be about 10 cm/s. The resultant flow structure is given in Figure 3. It is apparent from the diagram that no secondary cells are produced within the step corner. It suggests that the viscous forces are so dominant that flows will adhere to the boundaries without flow separation that is necessary in the generation of secondary cells. In numerical simulations, small perturbations that are responsible for the production of secondary cells can often can be suppressed by truncation damping. This possibility has been investigated through grid refinement, when grid spacings are reduced by a factor a two, identical results are obtained. It indicates that truncation damping is not the explanation for the absence of the secondary cells. This is a rather discouraging result since a vertical step like boundary is the most favorable condition for secondary cells to be produced. If boundary geometries are sloping toward the northeast, it will be even more unlikely for the rarefie flow to produce a secondary cell.

Water studies of the Mississippi River Estuary relative to baroclinic effects. The secondary cells in the Mississippi River estuary have been studied by a different group. The flow field is similar to the previous one except in this case, the bottom boundary is taken to be sloping toward the northeast. Again, the

In light of the failure of the earthflow to disturb stable structures beneath passive continental margins, one of the original objectives of the project included the mid-Pleistocene horizon. Although existing BEMEM data do not penetrate this deep, some general remarks about mantle flow beneath the earthflow can be made based on heterogeneous earthquake density distributions that have been derived from the studies associated with this project. These will be discussed in the following sections.

SEASAT Altimetry and Geoid Anomalies

In this section, we shall first examine the global sea surface undulations as expressed by the SEASAT altimetry measurements to see if any consistent pattern exists between the geoid anomalies and the location of passive margins. Thereafter, some problems associated with the two dimensional modeling of [illegible] geoid anomalies will be discussed.

Averaged deviations of the sea surface from a reference ellipsoid have been measured by the GEOS-3 and the SEASAT missions during [illegible]. The results of these two observations have been combined and interpolated to produce a 1.0 x 1.0 degree map (Marsh, personal communication). A careful examination of the map indicates that a [illegible] correlation between the geoid anomalies and the [illegible] edge of continental [illegible]. For example, [illegible]

wavelength geoid anomaly contours seem to run parallel to the margin. Therefore, it is apparent that anomalies along continental margins can not be explained by one single tectonic process. Instead, they must be analyzed individually.

To analyze regional geoid anomalies, it is a common practice to model the regional density structure utilizing two dimensional models. This is especially true if the anomalies have total wavelengths that are shorter than a few thousand kilometers. However, intrinsic to all two dimensional models is the assumption that all mass anomalies extend to infinity in the third dimension. Because of this assumption, ambiguity arises in the correct interpretation of geoid observations according to two dimensional models.

If a density anomaly is isolated and uncompensated, two dimensional calculations will give a geoid anomaly that possesses a correct shape but incorrect magnitude as pointed out by Chapman [ ]. Therefore, if relative geoid differences between [illegible] are significant in a [illegible] map, the [illegible] that the geoid height due to a particular density [illegible] might be determined incorrectly when two dimensional [illegible]

Conclusions

[illegible] numerical modeling of mantle flow [illegible] continental margins has been carried [illegible] test numerical simulations, there exist [illegible] due to the production of artificial [illegible] of numerical diffusion has been carefully [illegible] two possible sources exist to produce [illegible] is that due to the truncation of the [illegible] the construction of the finite difference [illegible] well documented that for all first [illegible] the truncated second order terms generally [illegible] behave identical to a diffusion [illegible] problem, a typical approach is to [illegible] difference approximations such that [illegible] second derivatives. Since [illegible] sphere chosen for our model [illegible] finite difference approximation, the [illegible] present. Another [illegible] artificial diffusion can be [illegible] the computational [illegible] numerical diffusion [illegible] boundaries [illegible] to all finite [illegible] techniques to [illegible] grid refinement [illegible] can be [illegible] not used

Mantle dynamics immediately beneath the passive margins have been simulated. It is found that the viscous forces within the mantle are so dominant that mantle flows simply adhere to the boundary of a continental root without any flow separation. Consequently, small scale secondary convective cells are not realizable in these regions. In the absence of any characteristic mantle structure beneath passive margins, surface geoid anomalies can not be used to study the deep structure of continents at present. However, we shall continue our examination of the geoid maps (produced by combining the GEOS-3 and SEASAT altimetry data) to see if any common patterns along passive continental margins can be realized. If no common patterns can be identified, the mantle structure beneath passive margins will be studied individually.

Finally, applicability of geoid anomaly formulas derived from two dimensional models has also been examined. Intrinsic to all two dimensional models, predictions on the magnitude of geoid and gravity anomalies are found to be independent of burial depth. This non-physical result is basically due to the existence of infinite mass associated with the infinite extent of sources in the third dimension. Therefore, cautions must be exercised when using these formulas to compute model geoids. It will be more advisable to calculate geoid and gravity anomalies from first principles utilizing a truncated two dimensional model such that the infinite mass problem can be suppressed.

Although results produced thus far appear to indicate that [illegible] be a negative experiment. However, we have recently

found a new approach to simulate mantle flows which may produce more realistic mantle dynamic structures. Therefore, our efforts to pursue the original objectives of this project will continue despite the termination of the mini-grant. AFOSR support will be acknowledged for all of our future publications that are related to this project.

References

Anderson, D. L., The deep structure of continents, J. Geophys. Res., 84, 7555-7560, 1979.

Buck, W. R., When does small scale convection begin beneath oceanic lithosphere? Nature, 313, 775-777, 1985.

Chapman, M. E., Techniques for interpretation of geoid anomalies, J. Geophys. Res., 84, 3793-3801, 1979.

Haxby, W. F. and D. L. Turcotte, On isostatic geoid anomalies, J. Geophys. Res., 83, 5473-5478, 1978.

Hsui, A. T., B. D. Marsh and M. N. Toksoz, On melting of the subducted oceanic crust: effects of subduction induced mantle flow, Tectonophysics, 99, 207-220, 1983.

Jordan, T. H., Composition and development of the continental tectosphere, Nature, 274, 544-548, 1978.

Roache, P. J., Computational fluid dynamics, Hermosa Publishers, Albuquerque, N.M. 87108, U.S.A. 446pp. 1976.

Telford, W. M., L. P. Geldart, R. E. Sheriff and D. A. Keys, Applied Geophysics, Cambridge University Press, Cambridge, 860pp., 1976.

Toksoz, M. N. and A. T. Hsui, Numerical studies of back arc convection and the formation of marginal basins, Tectonophysics, 50, 177-196, 1978.

Torrance, K. E., R. Davies, K. Eakes, P. Gill, D. Gutman, A. Hsui, S. Lyons and H. Zien, Cavity flows driven by buoyancy and shear, J. Fluid Mech., 51, pt. 2, 221-231, 1972.

Turcotte, D. L., K. E. Torrance and A. T. Hsui, Convection in the earth's mantle, in: Editors Bolt, B. A., B. Alder, S. Fernbach and M. Rotenberg, Methods in Computational Physics, Vol. 13, Academic Press, New York, 431-454, 1973.

Figure Captions

Figure 1. Geometry of the two dimensional computational domain for mantle flows beneath passive continental margins. The top step boundary represents the bottom of the lithospheres with the continental root inserting into the mantle.

Figure 2. Evolution of the maximum magnitude of concentration of fluids within a circular tube undergoing a solid body rotation. The solid line represents the results when time steps are chosen such that the fluids can only move half a grid point over one time interval. The dashed line represents the case when fluids are able to move the full grid point at every time step.

Figure 3. Simulated mantle flows beneath a passive margin. Because of the strong viscous forces, flow appears to adhere closely to the boundary without separation. Consequently, the existence of small scale secondary cells is not expected.

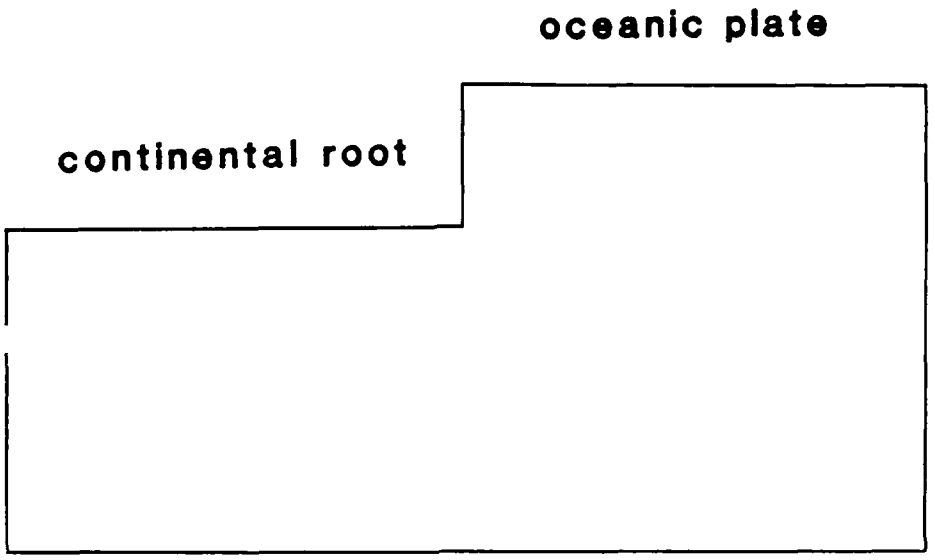

Figure 1

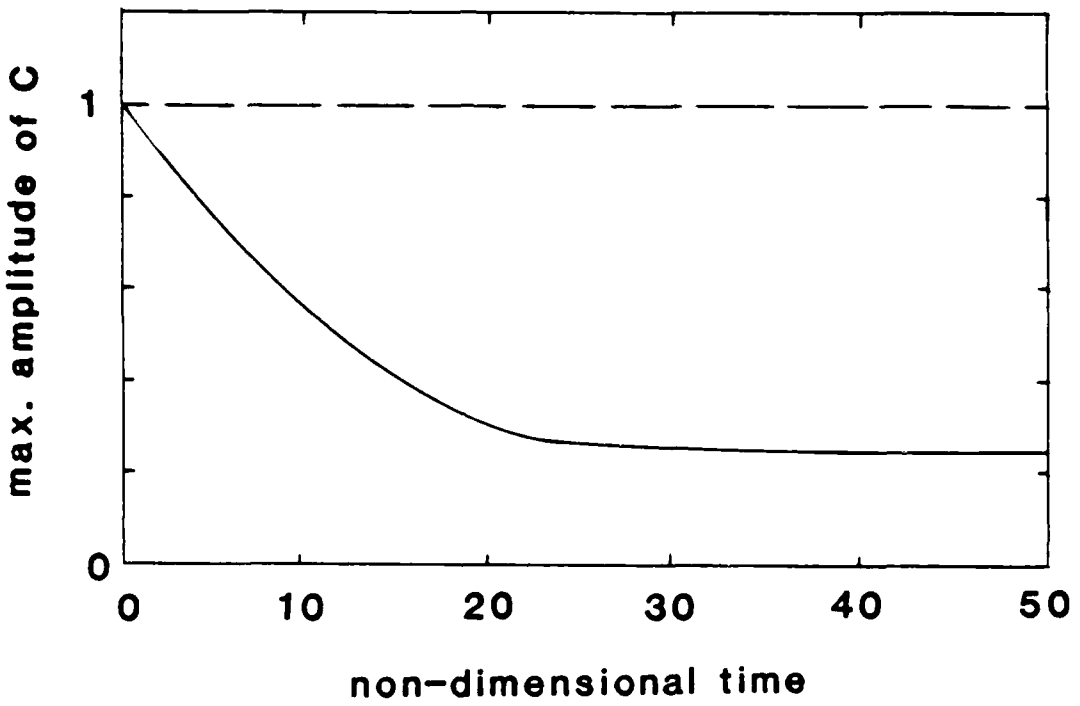

Figure 2

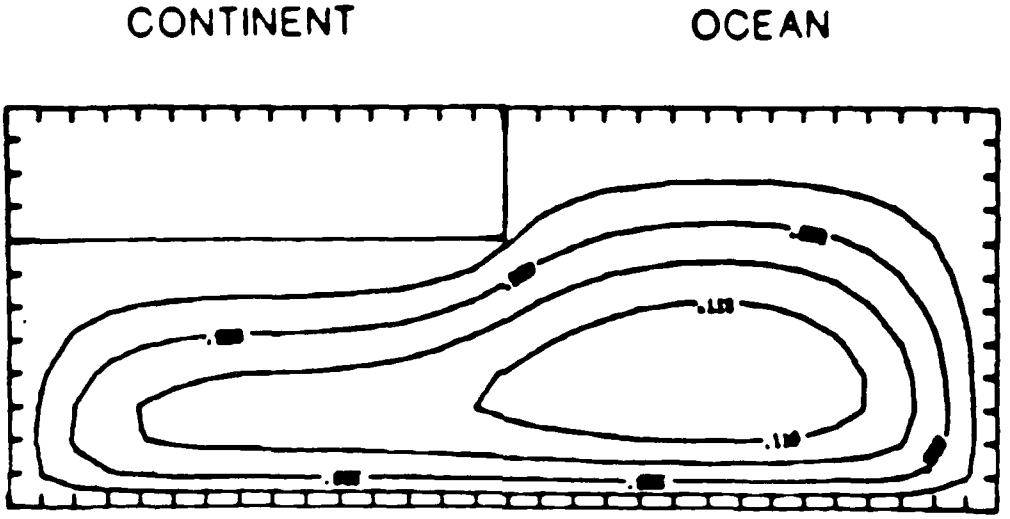

STREAM LINES

Figure 2

FINAL REPORT NUMBER 38
APPOINTMENT MADE TOO LATE
FOR RESEARCH TO BE COMPLETED
Dr. Clifford T. Johnston
760-OMG-077

Final Report

RF Project: 718035 **Master Project**: 66205

Entitled

Photoluminescence Excitation Spectroscopy

for

III-V Semiconductor Characterization

Principal Investigator: Dr Patrick L Jones

Sponsored by: Universal Energy Systems, Inc and the Air Force Office of Scientific Research under contract number F[illegible]

attainable so far. The heavy hole [illegible] and light hole [illegible] transitions near the GaAs band edge are clearly visible in this test case. In comparison to standard methods of doing PR spectroscopy, this data compares favorably and in principle will give better signal to noise. However many test samples we have examined exhibit a large sensitivity to laser amplitude noise. Figure 1 shows another sample which exhibits such large scale noise. We feel this noise is primarily noise introduced by the laser dye jet and are presently investigating an inexpensive passive approach to solving this problem rather than the expensive electronic servo system currently employed by some of us. We are also trying to correlate the characteristics of these materials with the sensitivity of the PR spectrum for this case. In addition we have returned recently to investigate the behavior of structures in GaAs materials using PLE spectroscopy.

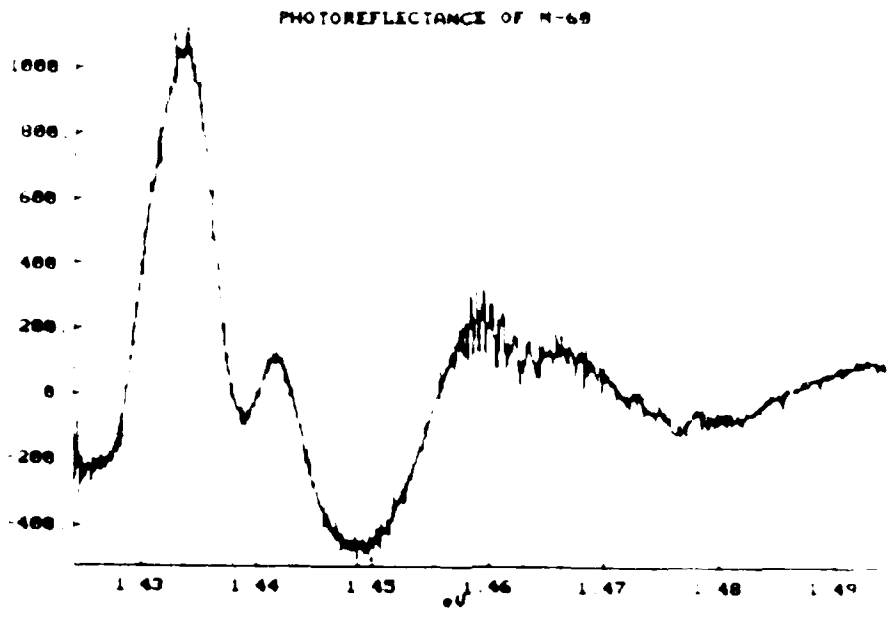

Figure ... Photoreflectance spectrum of AlGaAs/GaAs multiquantum well material. The features 1.434 ev and 1.441 ev are the ... transitions respectively.

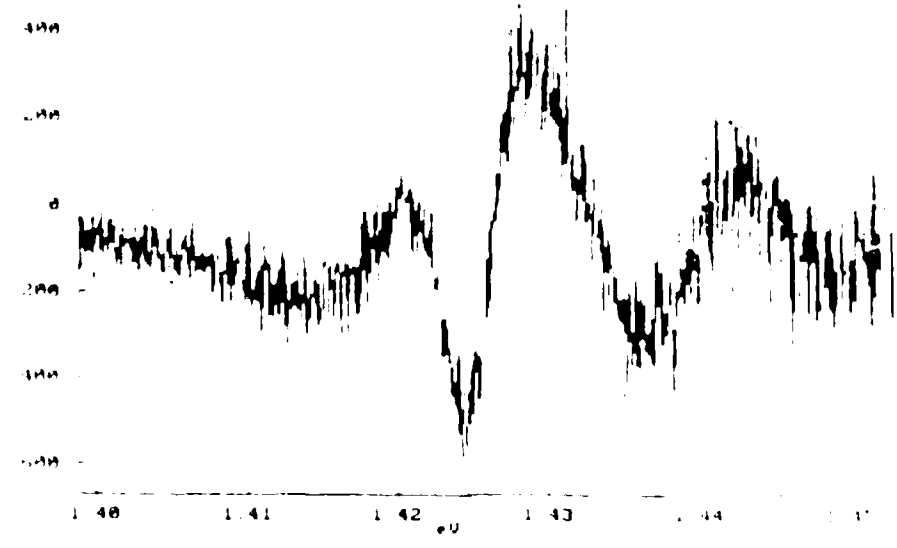

Acknowledgements

[illegible] particular the assistance of Dr. Bill Dobbs in the [illegible] of Wright-Patterson AFB and also by Dr. Ivan Goldfarb [illegible] Materials Laboratory (AFWAL-) during the progress of the pro- [illegible] the award of the contract by the Air Force Office of Scientific [illegible] Universal Energy Systems.

AD-A186 492 UNITED STATES AIR FORCE RESEARCH INITIATION PROGRAM 6/11
1985 TECHNICAL REPORT VOLUME 2(U) UNIVERSAL ENERGY
SYSTEMS INC DAYTON OH R C DARRAH APR 87
UNCLASSIFIED AFOSR-TR-87-1718 F49620-85-C-0013 F/G 15/3 NL

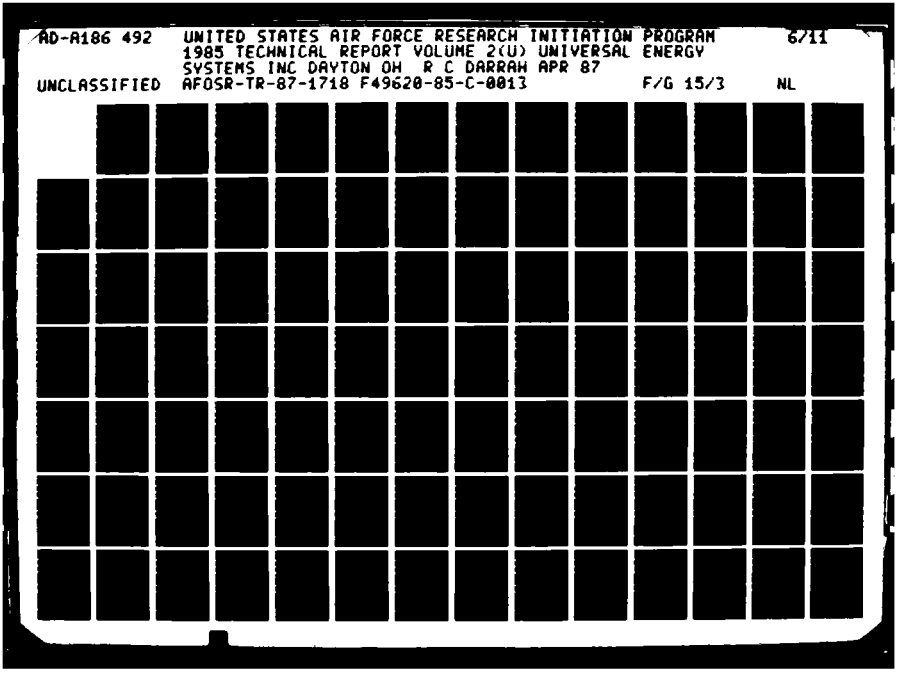

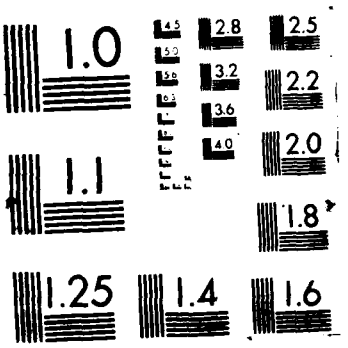
1.0
1.1
1.25
1.4
1.6
1.8
2.0
2.2
2.5
2.8
3.2
3.6
4.0

Abstract

The study of the electrical and optical characterization of ion-implanted Polyphenylene-benzo-bis-thiazole (PBT) has been undertaken. Iodine ions are chosen for implantation. The samples have been annealed in argon atmosphere at 200° C before data was taken. Useful information concerning the nature of charge transport, structure of the density of states and the type of charge defects that play a major role in the conduction mechanism is possible from the investigation.

It has been observed that the d.c. electrical conductivity of the iodine doped PBT increases with temperature and follows the Arrheneus equation yielding an activation energy of 0.39 ev. The variation of conductivity with temperature suggests Mott-conduction mechanism. The 9.89 GH_z microwave data suggests that the microwave conductivity may be higher than the d.c. conductivity. Preliminary esr data leads to an interesting observation, namely, no signal in the undoped PBT where as a strong signal was observed in the I_2-doped sample. The IR – absorption data suggest the I_2-association with the benzene rings resulting in the dampening of the skeletal modes and yielding some vibration of its own association.

Introduction

The application of polymers in electronics and computers is expected to grow rapidly during the next decade. The study undertaken has been restricted to electrical and optical characterization of doped poly-p-phenylene-benzo-bis-thiazole (PBT) polymer film (Fig. 1). Samples of this polymer were obtained from the polymer branch (MLBP) through Dr. Ivan Goldfarb at WPAFB. The doping of these samples was done by ion implantation rather than by chemical means. The chemical method of doping may not be feasible for lack of suitable solvents. Studies undertaken by other researchers [1] have indicated that the introduction of dopants into the polymer chain by ion implantation results in more stable polymers than the chemically doped polymers. By ion-implantation, the energetic ions after penetration into the target material initiate a large number of atomic collisions in the material, forming a collision cascade. Inside the material these collisions can result in the mixing of atomic species. The impact on a lattice atom in a compound frequently results not only in lattice position change but also leads to bond breakage and chemical state changes. The energy of the bombarding ions and the temperature of the polymer surface could affect the delocalization of the electrons along the chain of the polymer.

Data using the following physical techniques were planned:

1. Implantation of PBT samples with iodine ions
2. D. C. Conductivity vs. temperature
3. Microwave conductivity vs. temperature
4. ESR studies (Pauli Susceptibility)
5. Infrared Studies
6. Laser Raman Studies

The completion of the above study should lead to a better understanding of the charge transport mechanism. With doped conjugated polymers, the possibility exists to achieve high conductivities (conductive polymer) with a host of applications. The results obtained, have been presented at International scientific conferences. [2].

and from the definition of $z = \exp(-j\omega d/c\sqrt{\mu^*_r\epsilon^*_r})$, define

$$C_2 = \mu^*_r\epsilon^*_r = -\{\frac{c}{\omega d}\ln(\frac{1}{z})\}^2 \tag{8}$$

Then,

$$\mu^*_r = \sqrt{C_1C_2} \tag{9}$$

$$\epsilon^*_r = \sqrt{\frac{C_2}{C_1}} \tag{10}$$

This pair of relations permits easy determination of the complex permittivity and permeability.

2. Objectives

The objectives of the effort on doped PBT are:

(i) Understanding the charge transport mechanism in this polymer sample

(ii) Determination of the nature of the charge carriers

(iii) Evaluation of the d.c. and microwave conductivity data in the light of existing theories. The deviations of the theory from measured a.c. and d.c. conductivities should yield information on the structure of the density of states in the samples investigated [3].

(iv) Investigation of the Raman spectrum of the ion-implanted samples and the study of the effect of the energy of the bombarding ions and temperature of the substrate. Investigation also by absorption in the near infrared as well as far-infrared regions.

3. Details of the Study:

The PBT samples were implanted with 335 KeV iodine ions to various fluences and the D.C. and microwave conductivities were measured.

D.C. and Microwave Conductivity of Iodine-Doped PBT

The d.c. conductivity of the PBT film was measured by a two probe method using a voltage source (241, regulated high voltage supply Keithley Instruments) and an electrometer (610C Keithley Instruments). Gold, electrical contacts were prepared at the two ends of the film by an evaporation technique. The conductivity measurements were performed as a function of temperature between 20° C to -55° C. The sample was kept at least for 20 minutes at every desired temperature. Low temperatures were obtained by blowing cold nitrogen vapor from a liquid N_2 dewar.

Figure 2 shows the log ρ versus $\frac{1}{T}$ plot of the PBT film. The d.c. conductivity increases with increasing temperature. Electrical conductivity is a negative exponential function of inverse temperature and can be represented by the relation:

$$\sigma = \sigma_0 \exp(-E_a/kT)$$

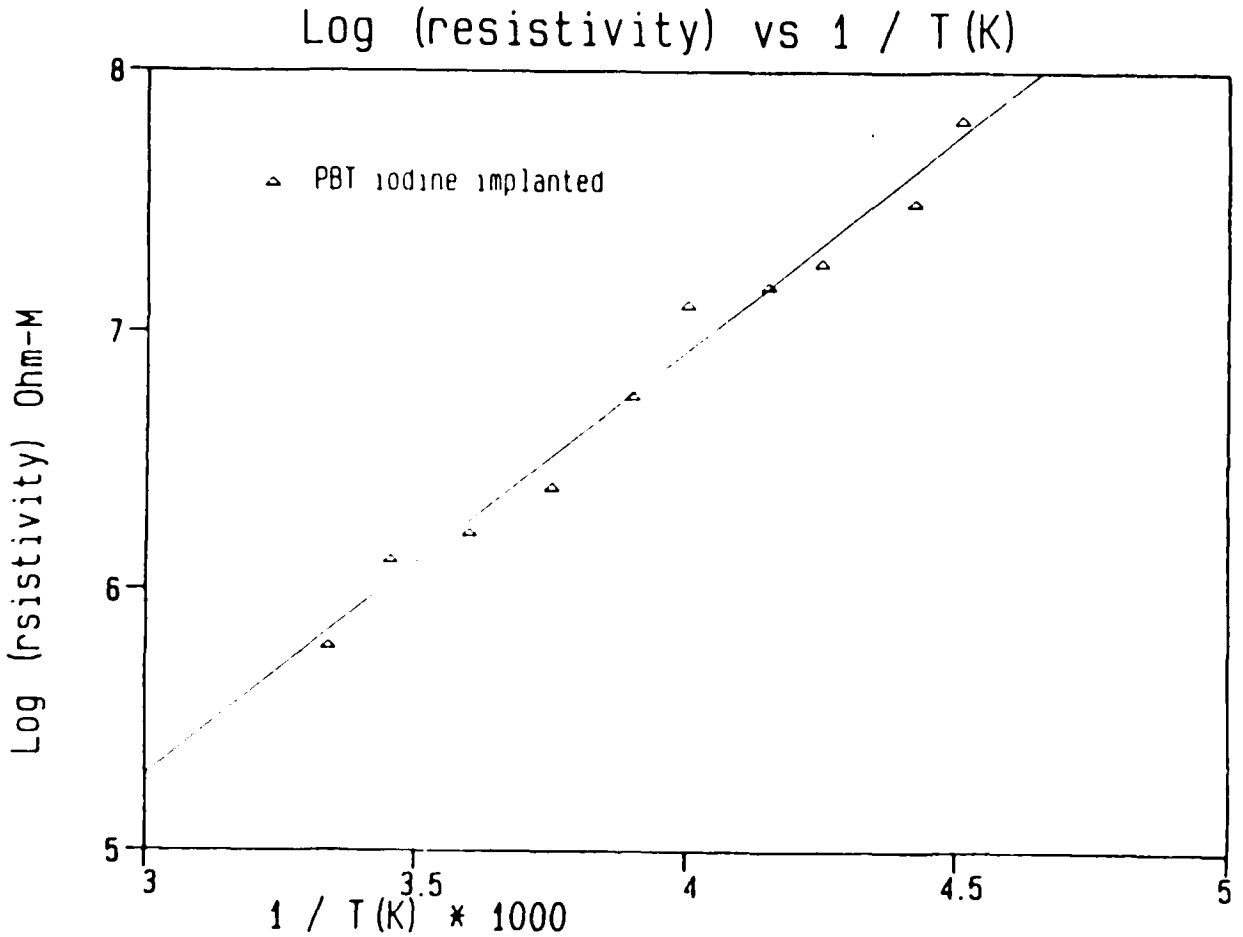
Log (resistivity) vs 1 / T(K)
PBT iodine implanted
Log (rsistivity) Ohm-M
8
7
6
5
3
3.5
4
4.5
5
1 / T(K) * 1000

FIGURE 2

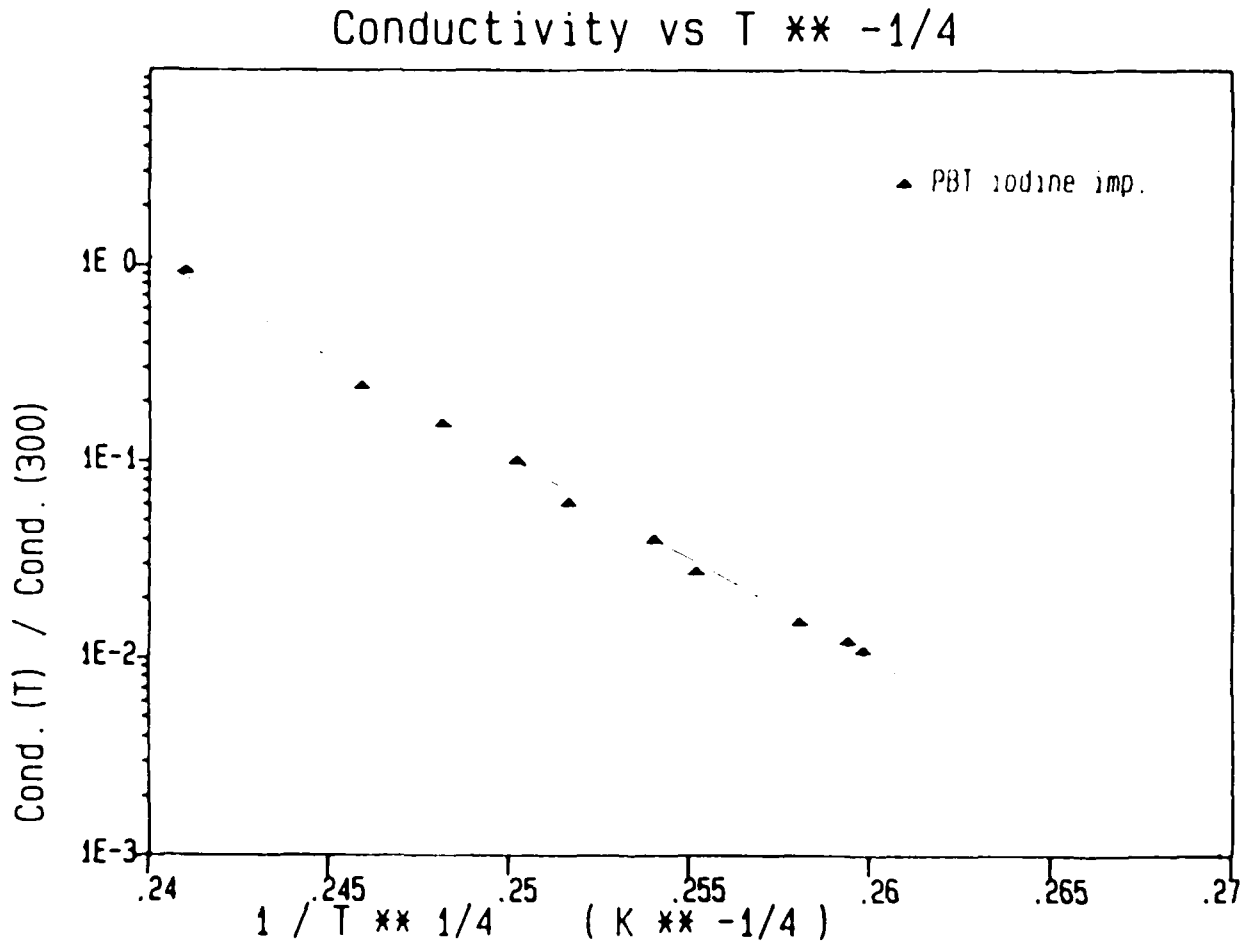
Conductivity vs T ** -1/4
PBT iodine imp.
1E 0
1E-1
1E-2
1E-3
Cond. (T) / Cond. (300)
.24
.245
.25
.255
.26
.265
.27
1 / T ** 1/4 (K ** -1/4)

FIGURE 3

or

$$\rho = \rho_0 \exp(+E_a/kT)$$

where σ is the conductivity, ρ is the resistivity, E_a is the activation energy for conduction, k is the Boltzmann constant and T is the absolute temperature. The preexponential parameters σ_0 and ρ_0 are constants.

The activation energy from the slope of log ρ against $\frac{1}{T}$ plot was found to be 0.39 ev. for the implanted sample.

Figure 3 shows the $\sigma_{(T)}/\sigma_{(RT)}$ versus $T^{-\frac{1}{4}}$ plot of PBT over the temperature region 23° C to -55° C. The theoretical model of hopping conduction in disordered materials predicts a temperature dependence of logσ vs. T^{-x} where σ is the conductivity, T is the temperature and x is a constant ranging from $\frac{1}{4}$ to 1. (N. F. Mott, Philos. Mag. **19**, 835 (1969)). A good fit of the experimental data was obtained, which is evidence of variable range hopping conduction process. Present experimental data are in good agreement with the Mott hopping mechanism of conduction. This typical behavior has also been observed in other polymers such as polypyrole (H. S. Nalwa et.al. Polymer Communications, **26**, 240 (1985)).

The time dependence of the electrical current in the undoped sample at a fixed voltage was also studied. Current decreases very slowly as a function of time from 1.2×10^{-9} amps to 7.3×10^{-10} amps at 3 kv over a period of 6 h at room temperature indicating a polarization effect. This is characteristic of an insulating material. The sample was maintained in a nitrogen atmosphere during this measurement.

Determination of the Permittivity of the PBT Film in the Microwave Region

Two methods were used in the measurements. One involved the use of the HP 8510 network analyzer system to measure the scattering parameters $S_{11}(\omega)$ and $S_{21}(\omega)$ which are related to the reflection and transmission of microwave energy that result when the microwave beam is incident on the sample contained in a waveguide. Actually, $S_{11}(\omega)$ and $S_{21}(\omega)$ are related to the

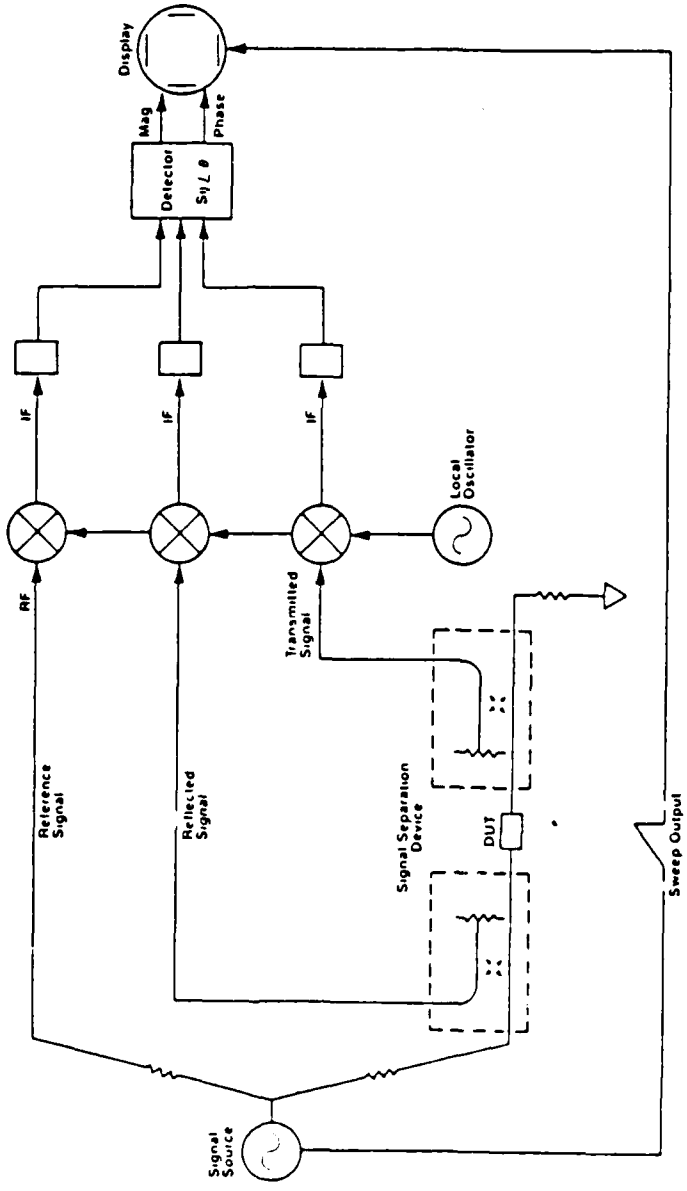

Figure 4(a): Schematic diagram of the network analyzer.

Sample mount for reflection – transmission data

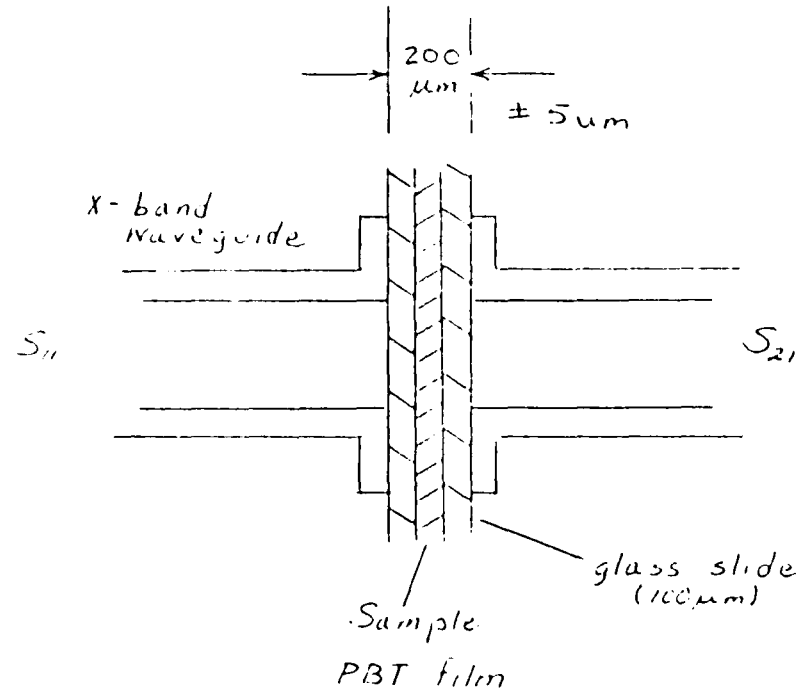

FIGURE 4(b)

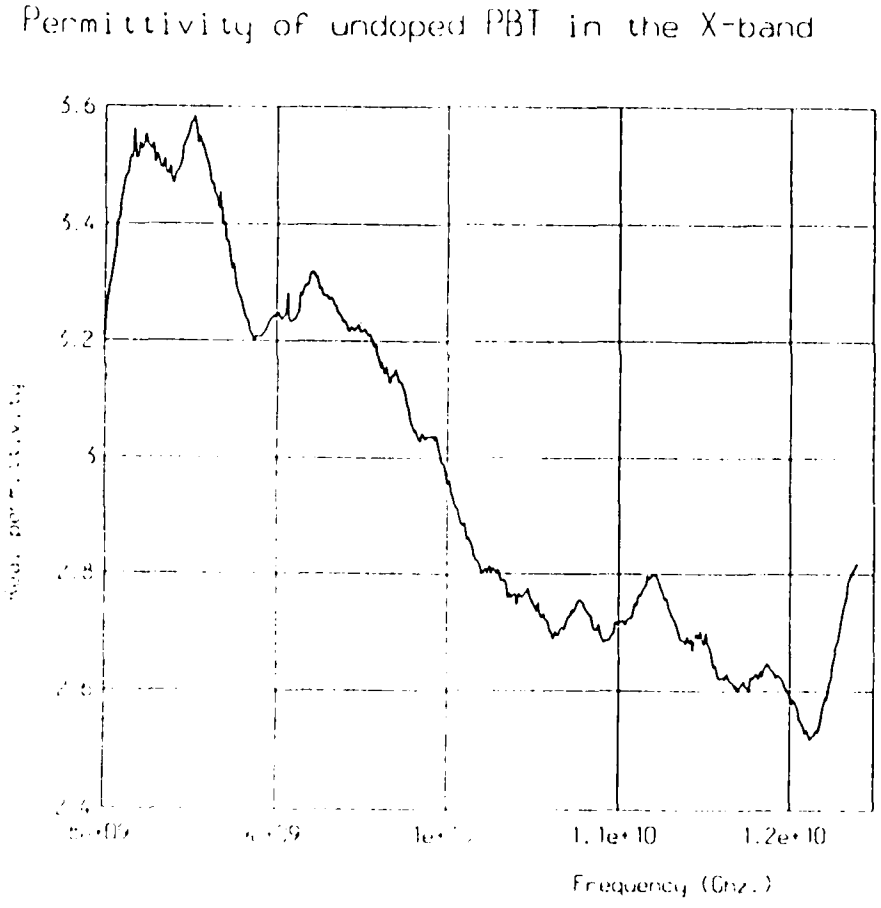
Permittivity of undoped PBT in the X-band
5.6
5.4
5.2
5
1.1e+10
1.2e+10
Frequency (Ghz.)

FIGURE 5

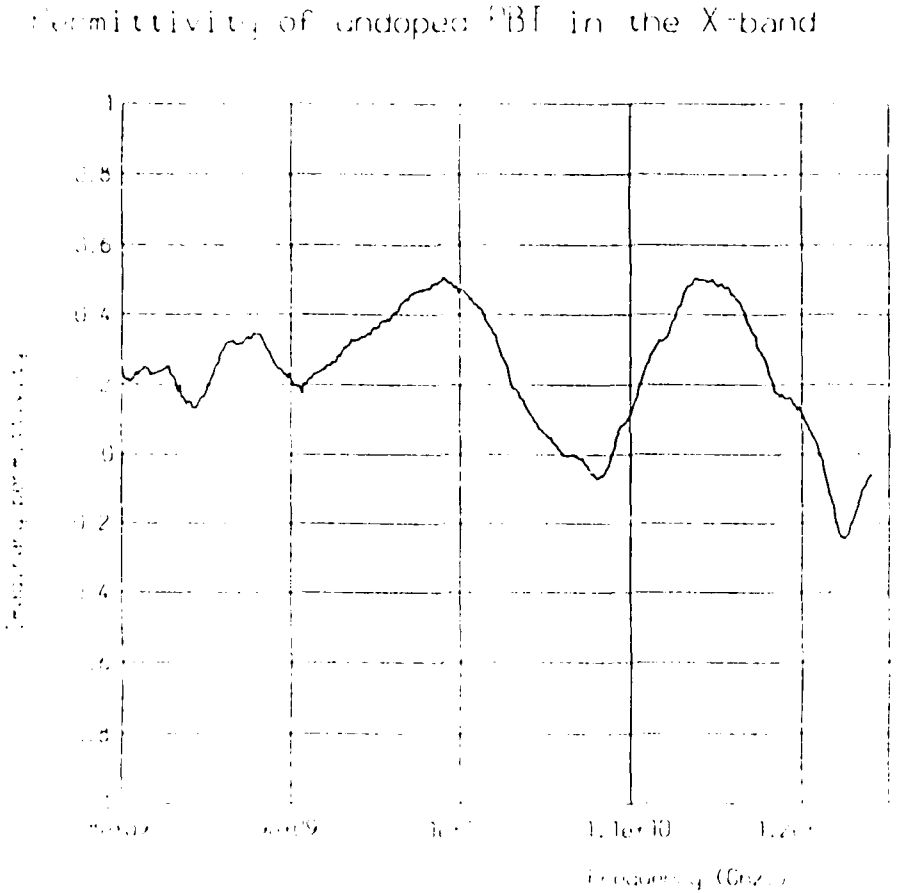
Permittivity of undoped PBI in the X-band
1
0.8
0.6
0.4
0
-0.2
-0.4
1.1e+10

FIGURE 6

reflection coefficient (Γ) and transmission coefficient (T). The latter quantities can then be used to calculate the complex permittivity (ϵ^*_r). The second method involved the use of the microwave cavity perturbation technique which has been used by several workers in the past.

i) Details of the network analyzer method

Figure 4(a) shows the network analyzer simplified block diagram. The HP 8510 network analyzer system consists of the HP 8510A network analyzer and the HP 8515A S-parameter test set. The full 2-port calibration with step sweep mode and averaging was used to obtain accurate measurement of S_{11} (ω) and S_{21} (ω). Conversion from S-parameter data measured by the HP 8510A to dielectric properties is accomplished by reading trace data into a computer, performing the required conversion and then plotting or listing the results. The computer used here is an AT&T 3B20 with the conversion software written in the C programming language. Appendix I gives the measurement flow chart used for ϵ^*_r and μ^*_r measurements. In our measurement the polymer film was sandwiched between two thin glass cover slides. This made it easier to insert the sample between the ends (flanges) of two waveguide sections. Figure 4(b) gives the details of the sample mounting scheme. In order to eliminate the effects of the glass slides, one glass slide was first measured, then two slides were measured and the results stored. Then the film was placed between the glass slides and measurements made. The S-parameters due to the glass slides were subtracted from the film sandwich readings. It should be noted that the sample is offset from the normalized reference plane by a distance of one glass cover slide thickness. The nonlinear phase rotation that results was determined and removed following a procedure suggested in reference [4]. Appendix II gives the equations relating the measured S_{11} (ω) and S_{21} (ω) to the ϵ^*_r of the polymer sample.

Figures 5 and 6 show respectively the real and imaginary part of ϵ^*_r for the undoped PBT in the X-band. It should be noted, however, that the measurement of low-loss samples ($\tan \delta \lesssim 0.01$) is difficult using this technique as indicated in reference [4]. The cavity perturbation technique is to be preferred for low loss samples in the measurement of the imaginary part of ϵ^*_r.

ii) Details of the cavity perturbation method:

The details of the cavity perturbation technique can be found in the literature [5,6]. Inserting a small sample into a microwave cavity changes its resonant frequency f_0' by

$$\delta = (f_0' - f_0'')/f_0'$$

and its loss $1/Q'$ by

$$\Delta = \frac{1}{Q''} - \frac{1}{Q'} = \frac{1}{Q_s}$$

where f_0'' and Q'' denote the parameters of the perturbed cavity and $1/Q_s$ the loss due to the sample. In the quasi-static approximation these two measurable quantities are related to the complex dielectric constant $\epsilon^* = (\epsilon' + j\epsilon'')$ of the sample by the following two equations:

$$\delta = \frac{\alpha}{N}\left[1 - \frac{1 + N(\epsilon' - 1)}{[1 + N(\epsilon' - 1)]^2 + (N\epsilon'')^2}\right] \quad (1)$$

$$\Delta = \frac{2\alpha}{N}\,\frac{N\epsilon''}{[1 + N(\epsilon' - 1)]^2 + (N\epsilon'')^2} \quad (2)$$

In the above equations α is the filling factor and N is the sample depolarization factor. An accurate determination of N is possible for a sphere or an ellipsoid [3]. Ambiguities in evaluating the conductivity due to less well defined depolarization factors N of samples of arbitrary shape can be overcome with the help of a fitting procedure [4,5]. The final formula given in reference [6] is:

$$\epsilon''(T) = \{1 \pm [1 - (\Delta(T)/\Delta_{max})^2]^{\frac{1}{2}}\}/(\alpha_F \Delta(T)/\delta^2_{max}) \quad (3)$$

where the positive sign of the square root is valid for $T \geq T(\Delta_{max})$ and the negative sign otherwise. In equation (3), only the measured parameters $\alpha, \Delta(T)$, Δ_{max} and δ_{max} appear and not the depolarization factor N, which, if not known exactly, induces large errors in the calculation of ϵ''.

The details of the experimental technique are similar to the one reported in reference [6]. The experimental data Δ and δ have been obtained from room temperature down to 100° K and these are shown in Table I. Additional data needs to be obtained at lower temperatures in order to evaluate Δ_{max} and δ_{max} so that ϵ'' can be obtained by the use of Eq. (3) without having to evaluate N. This work is in progress.

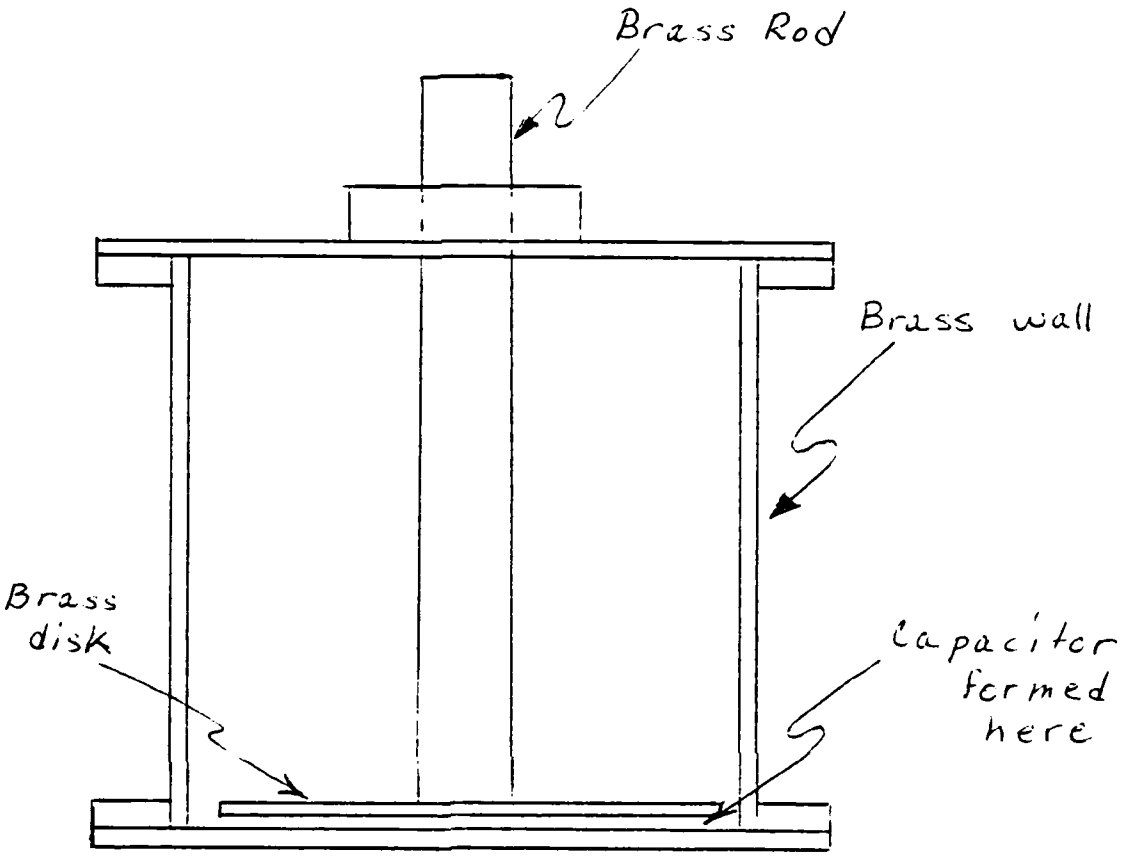

FIGURE 7: A cylindrical cavity modified to form a coaxial line terminated by a capacitor. Samples are placed between the capacitor plates.

Table I. Variation of the relative resonance frequency shift (δ) and the microwave loss (Δ) as a function of temperature (T). Frequency of measurement = 9.89 GHz. Sample: Iodine-doped (PBT).

T°K	$\Delta x10^{-4}$	$\delta x10^{-4}$
100	1.4	3.6
119	1.1	4.08
138	0.9	4.35
155	0.7	4.52
176	0.52	4.68
195	0.45	4.7
210	0.4	4.8
221	0.35	4.85
240	0.3	4.9
255	0.28	4.92
276	0.25	4.95
285	0.22	5.0
300	0.20	5.05

A cylindrical reentrant cavity similar to the one suggested in the literature [7] is under construction and will be used for the measurement of ϵ' and ϵ'' around 3 GHz. A schematic of the above cavity is shown in Figure 7.

Preliminary results have been obtained by esr technique on both the undoped and iodine doped PBT samples at room temperature. It is interesting to note that while there is a strong esr signal in the doped sample, no signal appears in the undoped sample. The esr signal of the doped sample is shown in Figure 8. Our results appear to be different from that reported by Scott et al. [8] in the case of pyrrole polymers where they found relatively intense esr signals in both the neutral and oxidized states of the polymers.

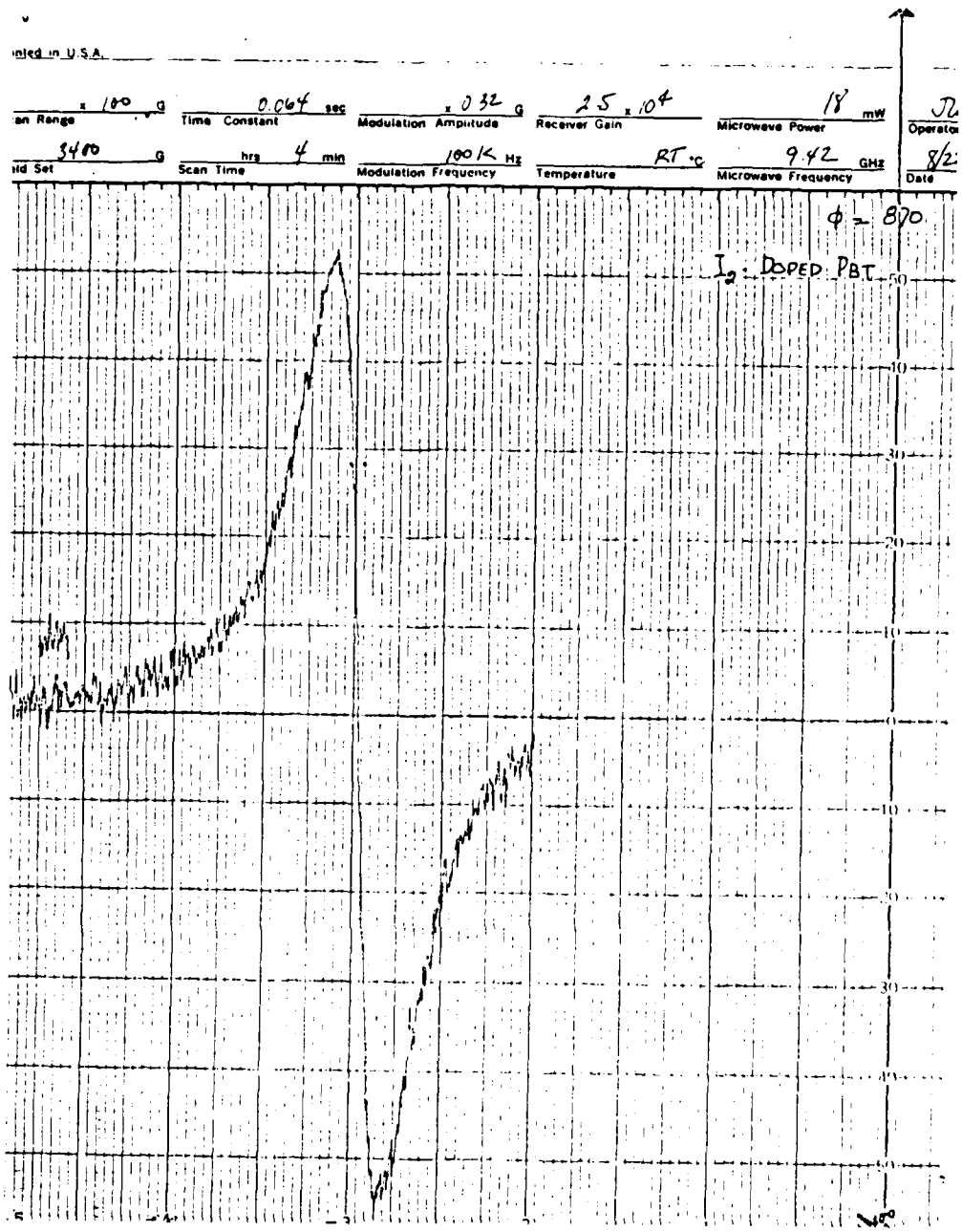

FIGURE 8: esr signal of the I_2-doped PBT

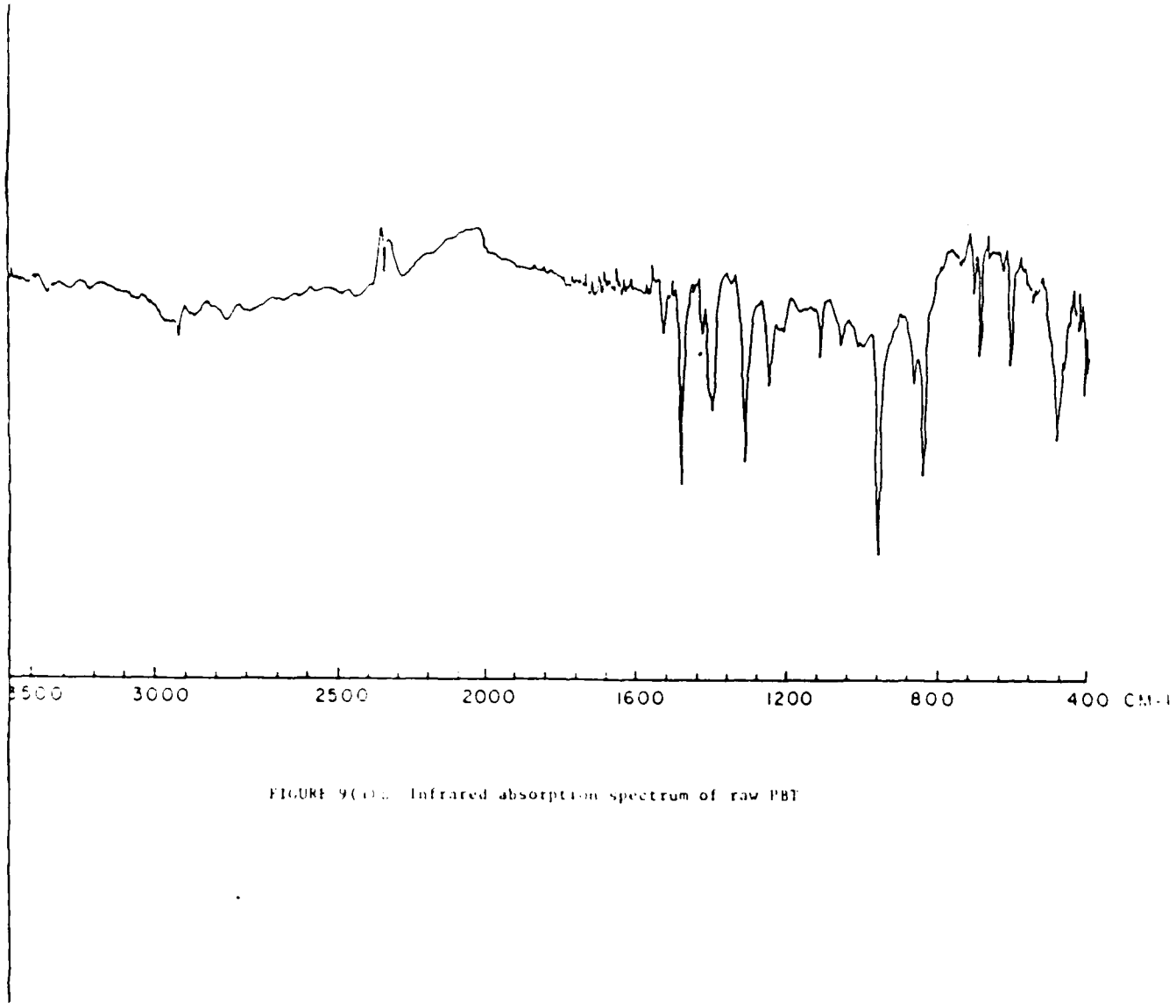

FIGURE 9(c). Infrared absorption spectrum of raw PBT

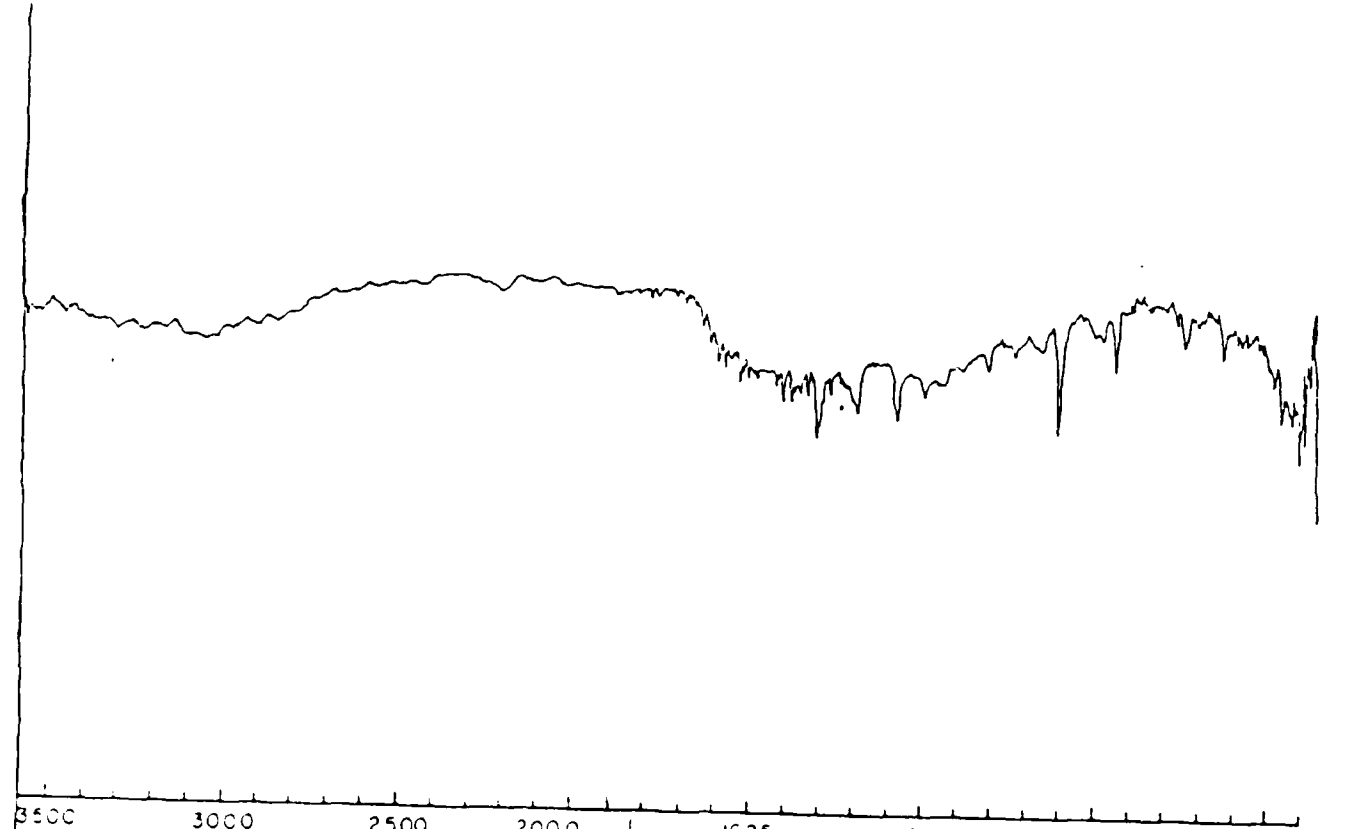

FIGURE 9(b). Infrared absorption spectrum of I_2-doped PBT

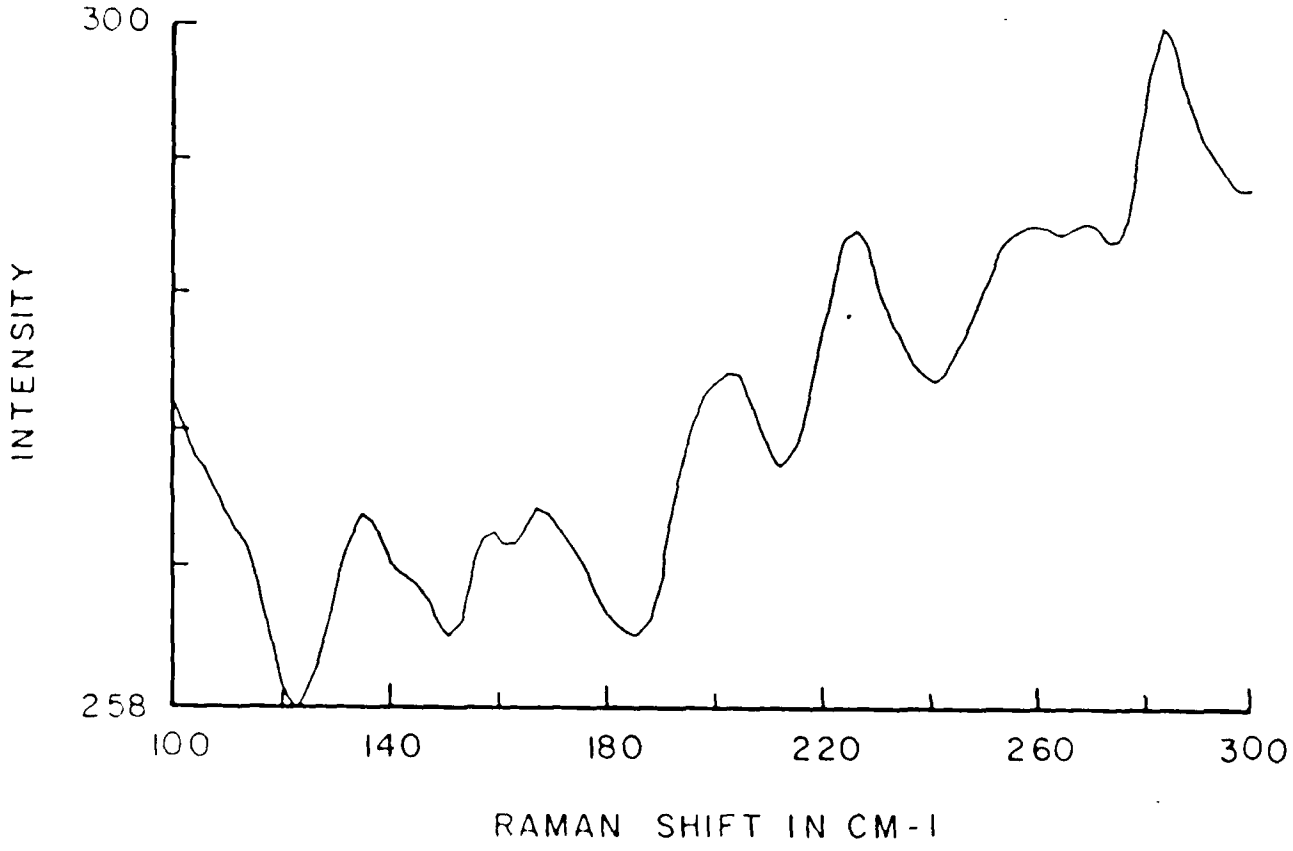

Figure 1 (a): Raman spectrum of Y_2-doped PBI

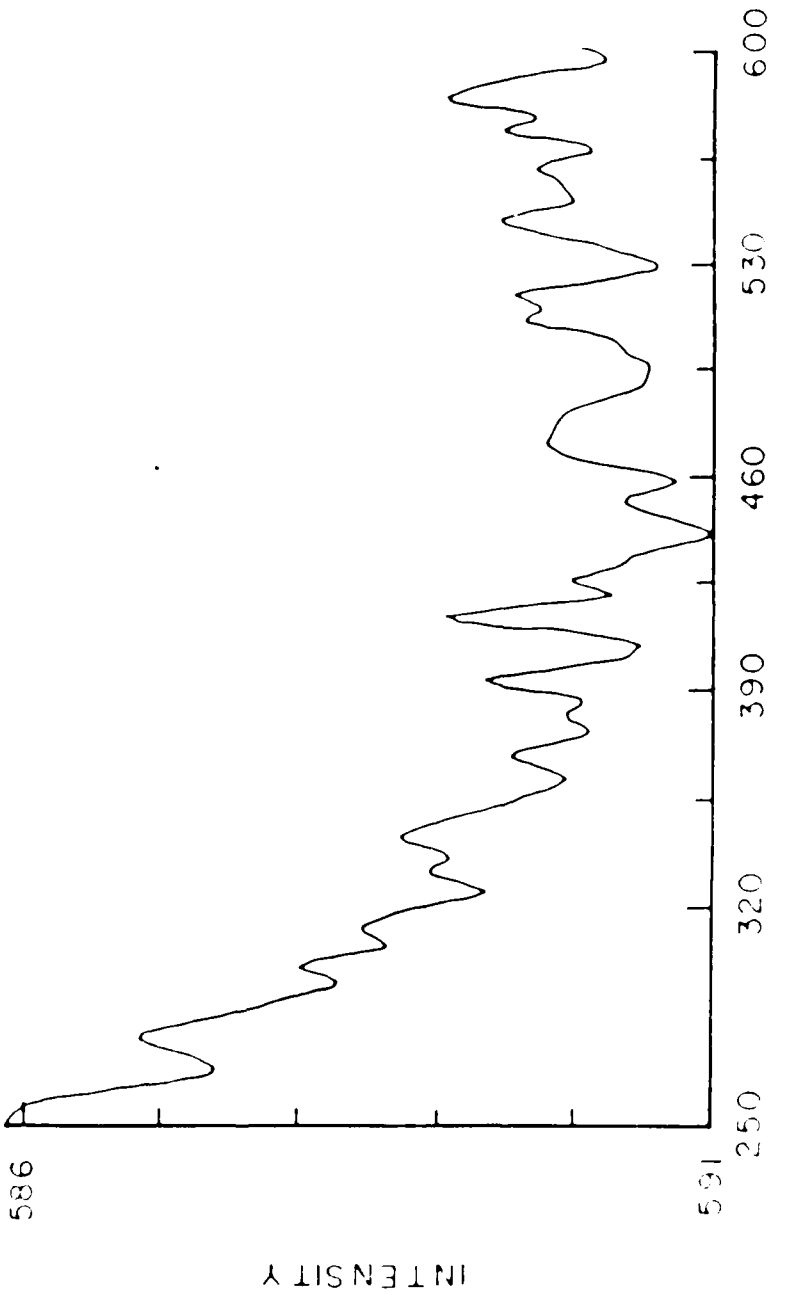
586
591
250
320
390
460
530
600
INTENSITY
RAMAN SHIFT IN CM-1

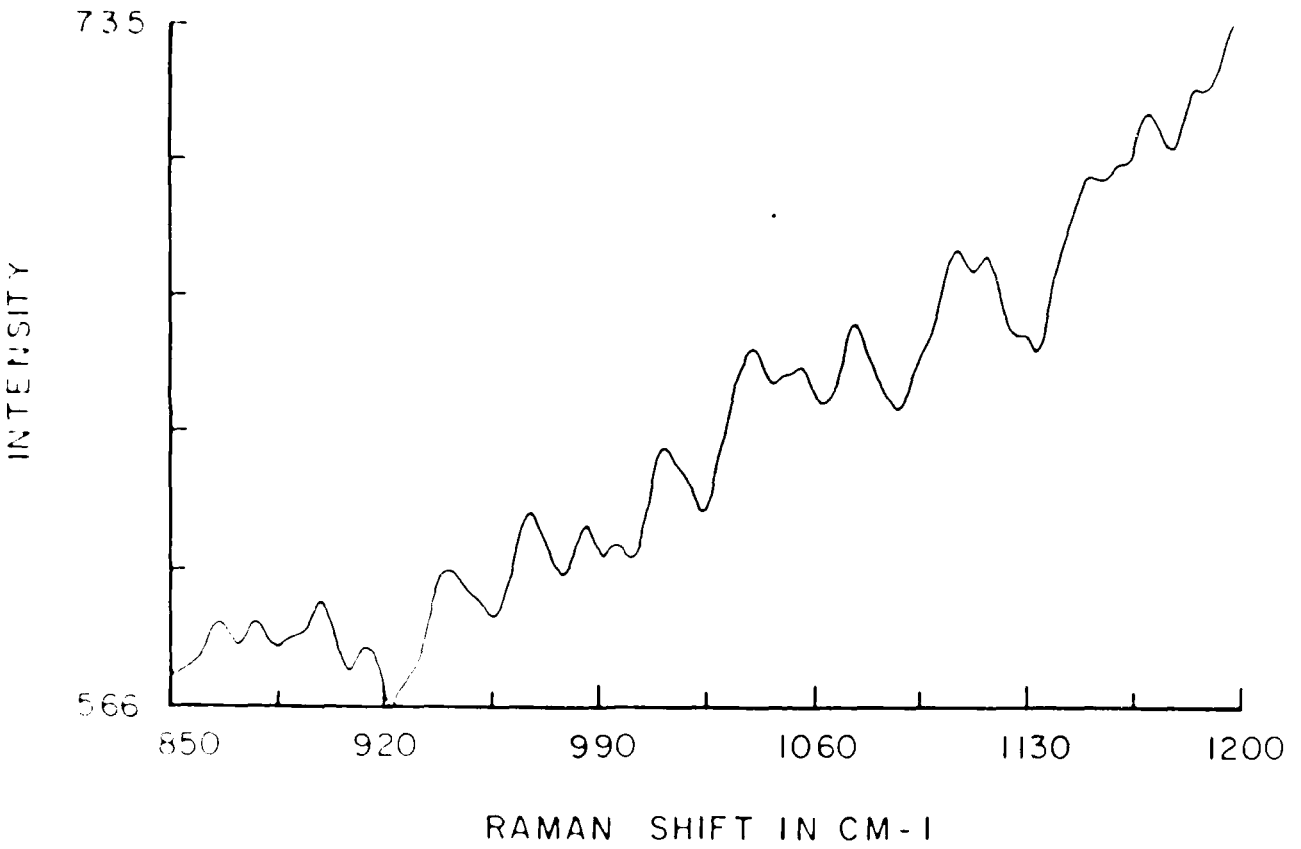
735
566
INTENSITY
850
920
990
1060
1130
1200
RAMAN SHIFT IN CM-1

FIGURE 30(c)

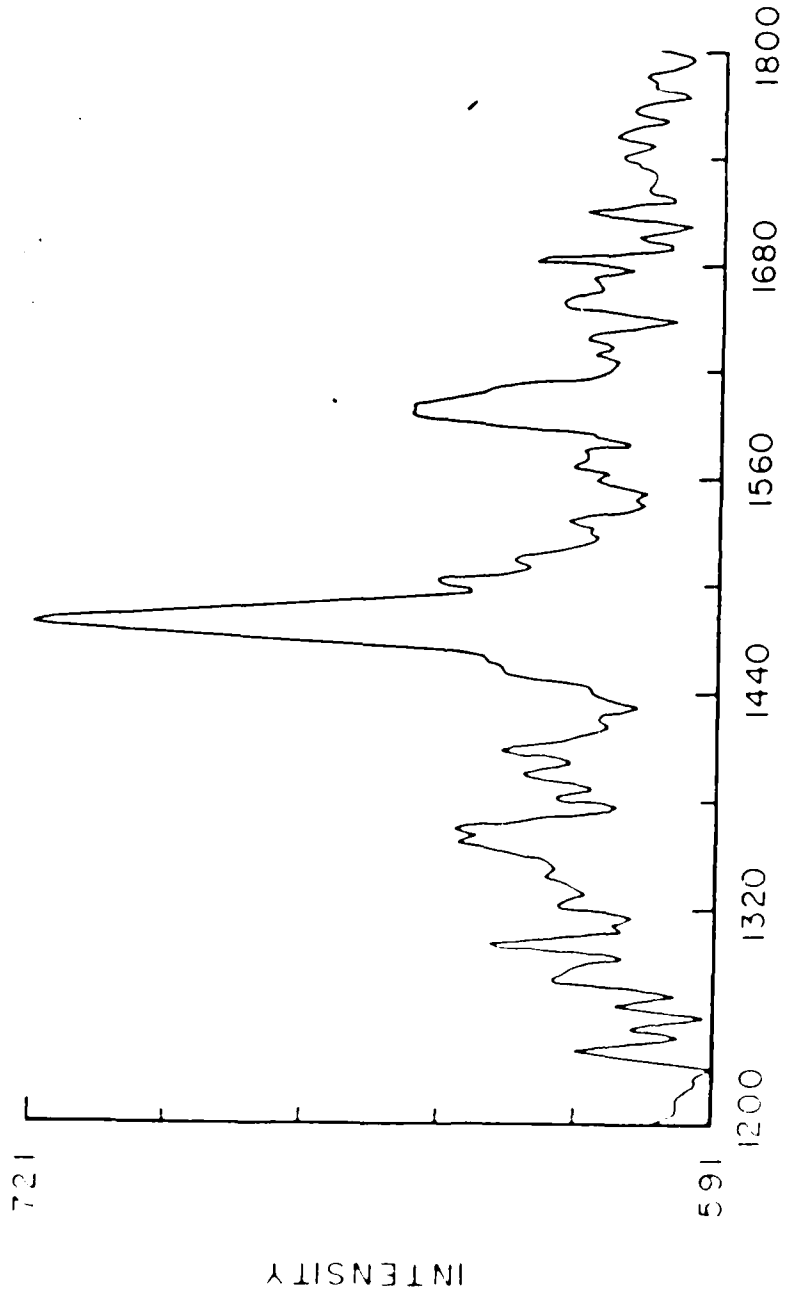
INTENSITY
721
591
1200
1320
1440
1560
1680
1800
RAMAN SHIFT IN CM-1

FIGURE [illegible]

Infrared absorption and Raman scattering measurements

The infrared absorption studies on the raw PBT samples and the iodine doped PBT samples were undertaken over the region 400 - 4500 cm^{-1} on a Bomen Fourier - transform infrared spectrometer. No infrared absorptions were observed above 2000 cm^{-1}. Both for raw as well as iodine implanted samples the bulk of the infrared absorption occurs in the 400 - 2000 cm^{-1} region. These observation are illustrated in Fig. 9 and the observed bands are collected in Table 2. The Raman data on these samples were taken on a Jarrell-Ash double monochromator using Ar^+ laser as a source. The grating drive of the monochromator has been replaced by Burleigh Inch-worm resulting in better resolution. The two lines of the Ar^+ laser at 4880 and 5145 $\mathring{A}$ were used as the incident light on the samples. The Raman bands consistent in both these observations were taken to be the real bands. A very large number of Raman bands have been observed, and this is consistent with the observation on other polymer samples. One observation we did make, and it is worth mentioning here, that is the inconsistencies in the Raman observations. The data taken at the same spot of the sample under two observations, without altering any parameter does not come out consistent. The profile and the resolutions of the bands change from one run to the other. This is indicative of the fact that the microstructure of the sample at the point of observation may not be staying consistent. Since Raman observations are undertaken over a very small area of the sample, equal to the cross-section of the laser beam incident on the sample, the inconsistencies appear much pronounced. In the case of IR absorption, the studies are undertaken over a much larger area and these uncertainties statistically average out. In other words, for the PBT samples provided to us, the IR data is reproducible for the entire sample where as the Raman data appears changing. The most consistent Raman bands for both the raw and implanted PBT are reported in Fig. 10 and the infrared and Raman bands are collected in Table 2.

The fundamental difference between the IR and Raman data of the raw and iodine implanted PBT appears to be the absence of the 300 cm^{-1} band and the presence of the 1000 cm^{-1} absorption band in the IR spectrum of the implanted PBT over that of the unimplanted PBT. This simply suggest the dampening out of some low frequency tortional mode, (for example the

TABLE II(a)

PBT Raw			
IR	Raman		
138	132	723	1377
157	153	746	1389
212	173	768	1405
225	193	788	1422
240	212	802	1450
270	238	831	1478
280	242	845	1498
307	278	865	1511
336	302	878	1568
370	314	910	1570
396	334	925	1629
490	346	938	1638
540	370	965	1656
580	383	992	1671
608	395	1008	1682
630	416	1038	1696
690	428	1054	1710
708	453	1072	1723
837	474	1105	1741
865	483	1115	1751
960	513	1166	1766
1030	521	1184	1785
1060	545	1195	1802
1115	561	1206	1817
1180	574	1235	-
1210	586	1245	-
1250	606	1260	-
1350	616	1277	-
1408	653	1290	-
1430	680	1315	-
1485	691	1333	-
1530	715	1351	-

TABLE II(b)

PHT Implemented			
IR	Ramon		
103	132	580	1092
121	145	600	1102
139	157	612	1121
166	166	624	1134
175	178	635	1164
193	200	642	1170
205	224	665	1182
223	231	673	1194
246	244	690	1206
259	260	709	1229
	267	723	1248
	279	741	1254
	290	756	1266
(not shown)	299	785	1290
610	317	803	1306
625	325	816	1333
	339	830	1348
710	353	843	1358
815	367	864	1377
860	383	879	1391
960	395	896	1407
1000(new)	417	906	1436
1025	430	914	1442
1060	442	937	1448
1115	456	946	1474
1180	466	958	1502
1255	485	972	1516
1320	505	982	1535
1400	517	998	1557
1480	535	1030	1569
	545	1038	1592
1550	558	1081	1620
			1626
			1648
			1658
			1680
			1687
			1709
			1714
			1719
			1741
			1746
			1770
			1778
			1784
			1811

absorption due the non coplanarity of the benzene rings resulting in a tortional mode in which both rings rotate slightly in the opposite direction along a C-C bond). The addition of I_2, may result in iodine associating with one of the benzene rings and stopping this motion. On the other hand, this association of iodine may result in some vibrations associated with the PBT components. The IR band at 1000 cm^{-1} may be one such vibration. This activity may not be Raman active.

4. Conclusions

The d.c. electrical conductivity of iodine doped poly-p-phenylene-benzo-bis-thiazole (PBT) increases with increasing temperature and follows the Arrheneus equation yielding an activation energy of 0.39ev. A plot of conductivity versus $T^{-\frac{1}{4}}$ gives a straight line, indicating the Mott-conduction mechanism. The time dependence of the electrical current in the undoped sample at a fixed voltage indicates a slow decrease characteristic of a polarization effect in insulating materials.

The study of the microwave conductivity of iodine doped PBT could not be carried to low temperatures beyond liquid nitrogen temperature for lack of liquid helium facility and associated microwave equipment. Hence, no definite conclusions could be drawn. The available data at a frequency of 9.89 GH_z seems to indicate that the microwave conductivity is higher than the d.c. conductivity. Preliminary results of the esr data leads to an interesting observation, namely, no signal in the undoped sample where as a strong signal was observed in the iodine doped sample.

The infrared absorption studies of the raw and I_2-doped PBT yeild consistent results about the structure of the samples. Not much change was observed except the fact that I_2 association with the benzene rings retards 300 cm^{-1} torsional made in which both rings rotate slightly in the opposite directions along a C-C bond. This association of iodine might also be responsible for the IR band at 1000 cm^{+}, which may not be Raman active. The Raman scattering data lacks consistency as explained earlier. Though some reliable data has been observed, it is hereby suggested that for undertaking such Raman studies a technique should be developed whereby scattering from a broad area of the sample can be studied for Raman data. This can be accomplished by using a ray-detector, thus averaging out the micro-structural changes, responsible for the difficulties

encountered. In order to study these micro-structural changes, a Raman micro-probe should be incorporated in future studies.

APPENDIX I

The measurement procedure for ϵ_r and μ_r measurements.

Setup 8510 System

↓

Input Cutoff Frequency

↓

Perform Full 2-Port Cal (Coaxial or Waveguide)

↓

Insert Sample Material

↓

Input the Material Length

↓

Input Reference Plane Rotation

↓

Measure $S_{11}(\omega)$, $S_{21}(\omega)$

↓

Calculate Γ

↓

Calculate T

↓

Calculate μ_r

↓

Calculate ϵ_r

↓

Print ϵ_r and μ_r

↓

Plot ϵ_r and μ_r

↓

End

$$\Gamma = K \pm \sqrt{K^2 - 1}, \text{ where } K = \frac{\{S_{11}^2(\omega) - S_{21}^2(\omega)\} + 2S_{11}(\omega)}{2S_{11}(\omega)}$$

$$T = \frac{\{S_{11}(\omega) = S_{21}(\omega)\} - \Gamma}{1 - \{S_{11}(\omega) + S_{21}(\omega)\}\Gamma}$$

$$\mu_r = \frac{1 + \Gamma}{\Lambda}(1 - \Gamma)\sqrt{\frac{1}{\lambda_0^2} - \frac{1}{\lambda_c^2}}$$

$$\epsilon_r = \frac{(\frac{1}{\Lambda^2} + \frac{1}{\lambda_c^2})\lambda_0^2}{\mu_r}$$

$$\text{where } \frac{1}{\Lambda^2} = -\{\frac{1}{2\pi d} \ln(\frac{1}{T})\}^2$$

APPENDIX II

The following equations rel[illegible] the scattering parameters to complex relative permittivity. (Excerpt from [9,10]).

The sum and difference of the scattering coefficients are found as

$$V_1 = S_{21} + S_{11} \tag{1}$$

$$V_2 = S_{21} - S_{11} \tag{2}$$

A variable x will be define[illegible]s the ratio of $1 - V_1V_2$ and A variable x will be defined as the ratio of $(1 - V_1V_2)$ and $(V_1 - V$[illegible]

$$x = \frac{1 - V_1V_2}{V_1 - V_2} \tag{3}$$

By direct substitu[illegible]on of the defining expressions for the scattering coefficients into Eq. (3) yields the following equation:

$$x = \frac{(1 + \Gamma^2)(1 - z^2)}{2(1 - z^2)} = \frac{\Gamma^2 + 1}{2} \tag{4}$$

This equation can be solved for Γ.

$$\Gamma = x \pm \sqrt{x^2 - 1} \tag{5}$$

where the plus or minus sign is chosen to restrict the Γ magnitude to less than one in absolute value

Again, direct substitution of the defining expressions for the scattering coefficients, in Eq. (1), yields and equation for z in ter[illegible]as of V_1 and Γ.

$$z = \frac{V_1 - \Gamma}{1 - V_1\Gamma} \tag{6}$$

Now, from

$$\Gamma = \frac{z - z_0}{z + z_0}$$

define

$$C_1 = \frac{\mu^*_r}{\epsilon^*_r} = \left(\frac{1 + \Gamma}{1 - \Gamma}\right)^2 \tag{7}$$

APPENDIX III

i) Titles of papers presented at Scientific Meetings:

1. "Raman Characterization of an implanted conducting Polymer", A. Bidarian, M. S. Mathur, P. K. Kadaba and E. B. Bradley, Xth International Conference on Raman Spectroscopy, Eugene (OR), 31st August, 1986.

2. "Conduction Mechanism in Implanted PBT: A Raman, IR and ESR Study", M. S. Mathur, A. Bidarian, P. K. Kadaba and E. B. Bradley, Annual Fall Meeting Division of Atomic and Molecular Physics (Canadian Associates of Physicists), October 24-25, 1986.

3. "Microwave Permittivity and Optical Absorption in the Polymer Film, Poly-p-phenylene benzobisthiazole (PBT)," M. L. Smith and P. K. Kadaba, South-Eastern Meeting of the American Physical Society, Williamsburg, VA, November 20-22, 1986.

ii) List of graduate students research assistants involved in the program.

Abe Bidarian: Graduate Student and Research Assistant working towards his PhD in electrical engineering.

Michael L. Smith: Graduate Student working towards M.S. degree in electrical engineering.

Lynn Kilcoyne: Graduate Student working towards M. S. degree in electrical engineering.

Pramed Harzal: Graduate Student working for M.S. in Metallurgy.

REFERENCES

1. Aldissi M., "Review of the Synthesis of Polyacetylene and Its Stabilization To Ambient Atmosphere", Synthetic Metals, **9**, 131, 1984

2. (See Appendix III 1)

3. Ehinger K., **et. al.:** J. Phys. C., Solid State Phys., **17**, 3753 (1984).

4. H. P. Product Note No. 8510-. "Measuring Dielectric Constant with the HP8510 Network Analyzer", August, 1985.

5. Buranov, L.I. and Shchegolev, I. F., Prip. Tekh. Eskp. **2**, 171 (1971).

6. Bauhofer, W., J. Phys. E, Sci. Instrum., **14**, 931 (1981)

7. Sen, S., **et. al.:** Rev. Sci. Instrum., **50**, 1594 (1979)

8. Scott, J. C., **et. al.:** Synthetic Metals, **9**, 165 (1984).

9. Aguirre, D. G.,. "Frequency Domain Measurements of Microwave Absorber Design Materials," M. S. Thesis, Air Force Institute of Technology (AFIT), Dec. 1980, WPAFB, OH

10. Kadaba, P. K., IEEE Transactions on I and M, **IM-33**, No. 4, 336 (1984)

Final Report

to

Universal Energy Systems, Inc.

and

The Air Force Office of Scientific Research

Synthesis of Novel Polybenzimidazoles

by

James J. Kane, Naim Akmal and Lee A. Rider

Contract No. F49620-85-C-0013/SC-0013/SB5851-0360

Subcontract No. S-760-0MG-025/James J. Kane,
Principal Investigator
Chemistry Department
Wright State University
Dayton, Ohio

Abstract

Synthetic routes to a novel polybenzimidazole tetraamine monomer, N(1),N(4)-diphenyl-1,2,4,5-tetraaminobenzene were explored. One route, a modified Curtius reaction on N,N'-diphenyl-2,5-diaminoterephthalic acid, gave 1,5-diphenylbenzo(1,2-d:4,5-d')diimidazole-2,6-dione which , on hydrolysis, should provide the desired tetraamine. However, this intermediate exhibited remarkable resistance to hydrolysis.

The second synthetic route, synthesis of 2,5-difluoro-1,4-dinitrobenzene followed by nucleophilic aromatic substitution of fluoride with aniline gave N,N'-diphenyl-1,4-diamino-2,5-dinitrobenzene which on reduction with sodium sulfide gave the desired tetraamine.

Acknowledgement

The authors would like to express their appreciation to the Air Force Systems Command, the Air Force Office of Scientific Research and Universal Energy Systems, Inc. for supporting this program. We would also like to thank Dr. R. C. Evers, AFWAL, Materials Lab, WPAFB for helpful suggestions and discussions and Mr. George Moore of the same location for supplying N,N'-diphenyl-2,5-diaminoterephthalic acid.

I Introduction

The synthesis of novel polybenzimidazoles is motivated by the current need for ultra-high strength, thermo-oxidatively stable polymers for use as structural materials in aerospace vehicles. More specifically, the need is for production of materials with mechanical properties comparable to the current fiber reinforced composites but with significantly improved enviornmental tolerance and without the use of fiber reinforcement.

The rigid-rod aromatic heterocyclic polymers are the materials chosen for this effort. Their physical and chemical properties show promise for fulfilling program objectives but they do present certain processing and fabrication problems because of their "all para" rigid rod character. Thus, continuing Materials Laboratory in house research as well as related contractual programs in academic and industrial laboratories are addressing aspects of the processing and fabrication of these polymers which possess improved processing characteristics and or enhanced mechanical physical properties.

The current project involves the synthesis of certain monomers which would be expected to undergo condensation polymerization reactions to yield the novel rigid rod polybenzimidazoles, poly-1,7-diphenylbenzo[1,2-d:4,5-d']bisimidazole-2,6-diyl, I and poly-1,7-diphenylbenzo[1,2-d:4,5-d']bisimidazole-2,6-diyl, II

II Objectives

The immediate objective of this program is the synthesis of the tetramine, N,N'-diphenyl-1,2,4,5-tetraminobenzene, III and the evaluation of reaction conditions for the preparation of

appropriate di- or tetra- amine with oxamide.

The condensation reaction of dicarboxylic acids with aromatic tetraamines is one of the classical methods for preparation of polybenzimidazoles (1) However, the reaction of 1,2,4,5-tetraaminobenzene with oxalic acid yields the six membered heterocyclic polydihydroisoquinoxaline rather than the desired benzimidazole(2). Similarly, Lane (3) reported the reaction of o-phenylenediamine with oxalic acid or diethyl oxalate yielded 2,3-dihydroxyquinoxaline. However, the same author reported formation of the desired 2,2'-bisbenzimidazole by reaction of o-phenylenediamine with oxamide (3) This result suggests the synthesis of Polymer I and II by direct condensation of the appropriate tetraamine with oxamide.

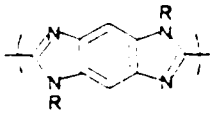

I, R = H
II, R = O

The tetraamine III precursor for polybenzimidazole II has not been reported in the literature. Two possible synthetic routes to this tetraamine have been chosen for exploration. One route involves the [illegible] of related polymers from the readily available N,N'-diphenyl 2,5 diaminoterephthalic acid, IV. The second route starts with oxidation of 2,5 difluoro 4-nitroaniline, V, to 2,5-difluoro-1,4-dinitrobenzene, VI, followed by displacement of fluoride by aniline [illegible] N,N' diphenyl 2,5 dinitro 1,4 phenylenediamine, VIII. The [illegible] of the nitro functions to amines followed by [illegible] III

III Results and Discussion

A Synthesis of Polymer I by condensation of 1,2,4,5-tetraaminobenzene with oxamide.

It has been reported (3) that oxamide condenses with o-phenylene to give the bis-benzimidazole. Extension of this reaction to reaction of oxamide with tetraamino benzene would provide a convenient synthesis for Polymer I.

1 Attempted synthesis of 2,2'-bisbenzimidazole.

The condensation reaction of o-phenylene diamine and oxamide was run in an attempt to repeat the work of Lane who reported (3) that the reaction of one mole of oxamide with two moles of o-phenylene diamine yields 2,2'-bisbenzimidazole. In our hands, this reaction yielded a solid product whose infra-red spectrum was not similar to that of an authentic sample of 2,2'bisbenzimidazole. The product obtained was assumed to be 2,3-dihydroxyquinoxaline. (Rx. 1)

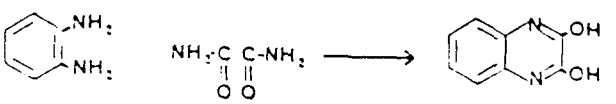

Rx. 1

B. Synthesis of N(1),N(4)-diphenyl-1,2,4,5-tetraaminobenzene, III, from N,N'-diphenyl-2,5-diaminoterephthalic acid, IV.

N,N'-diphenyl-2,5-diaminoterephthalic acid is readily available by condensation of aniline with 2,5-dicarbethoxy cyclohexane 1,4 dione and subsequent oxidation. Finally, hydrolysis of the diethyl ester provides the free diamino-diacid. A variety of related reactions are available for conversion of the carboxylic acid functions to the primary amines.

2. Reaction of N,N'-diphenyl-2,5-diaminoterephthalic acid with hydrazoic acid.

Attempted conversion of the title compound directly to N(1),N(4)-diphenyl-1,2,4,5-tetraaminobenzene by hydrazoic acid in concentrated sulfuric (Schmidt Reaction) gave only starting material. Apparently protonation of the amine functions in the acid medium deactivated the carboxylic acid toward protonation, a necessary first step in the Schmidt reaction.

3. Reaction of N,N'-diphenyl-2,5-diaminoterephthalic acid with diphenylphosphoryl azide.

Diphenylphosphoryl azide, a reagent useful for effecting modified Curtius reactions reacted with the title dicarboxylic acid to produce 1,5-diphenylbenzo(1,2-d:4,5-d')diimidazole-2,6-dione (IX) rather than the expected diurethane derivative of the tetraamine (III). This result is explicable when one considers the competing reactions between the isocyanate intermediate with the t-butyl alcohol solvent or with the secondary amine in the ortho position (Rx. 2). The reaction was repeated using ethanol and then with methanol in hopes that the lesser steric requirements of these alcohols would lead to urethane rather than ring closure. Unfortunately ring closure prevailed.

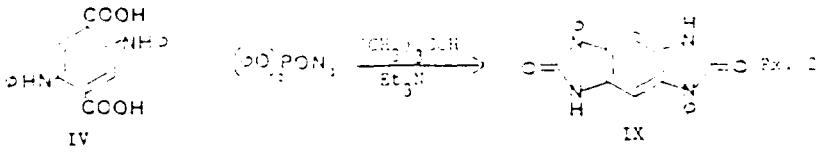

IV IX

Hydrolysis of 1,5-diphenylbenzo(1,2-d:4,5-d')diimidazole-2,6-dione should provide the desired tetraamine, III, (Rx. 3).

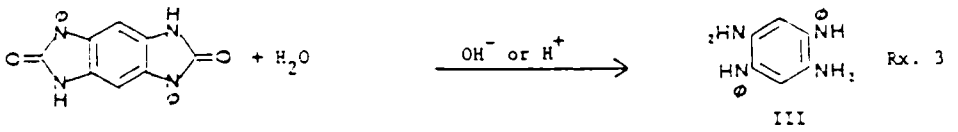

III

4. Synthesis of 1-phenylbenzimidazol-2-one.

1-Phenylbenzimidazol-2-one was prepared from N-phenylanthranilic acid and diphenylphosphoryl azide in order to provide a substrate for hydrolyses experiments.

5. Attempted hydrolysis of 1-phenylbenzimidazol-2-one.

The title compound was subjected to the following hydrolysis experiments. In each case starting material was recovered quantitatively.

a. 2% KOH in ethylene glycol for 24 hours at 120°C.

b. 85% phosphoric acid at 60°C for 20 hours.

c. 100% phosphoric acid at 60°C for 20 hours.

d. methanesulfonic acid at 60°C for 20 hours.

e. 50% KOH in ethylene glycol at 120°C for 24 hours.

f. 50% KOH in glycerol at 150°C for 34 hours.

The hydrolytic stability of this heterocyclic system is remarkable.

B. Synthesis of N(1),N(3)-diphenyl-1,2,4,5-tetraminobenzene (III) by nucleophilic aromatic substitution with aniline on an appropriately substituted dinitro-dihalo benzene.

The isomeric tetraamine, N(1),N(3)-diphenyl-1,2,4,5-tetraminobenzene is prepared (5) by reaction of aniline with 1,3-dichloro 4,6-dinitro benzene followed by reduction of the nitro functions to primary amines.

It has been reported (6) that reaction of 2,5-dichloro or 2,5-dibromo-1,4-dinitrobenzene with aniline gives a variety of products but not the desired N,N'-diphenyl-1,4-diamino-2,5-dinitrobenzene. This result is probably due to the fact that the nitro groups which are better leaving groups than chloride or bromide are activated with respect to nucleophilic aromatic substitution by virtue of their para position to one another.

Since fluoride is as good and sometimes a better leaving group than nitro (7), it was decided to examine the reaction of aniline with 2,5-difluoro-1,4-dinitrobenzene.

1. Synthesis of 2,5-difluoro-1,4-dinitrobenzene, VI.

The title compound was synthesized in over all 79 percent yield by nitration of 2,5-difluoroacetanilide, hydrolysis of the amide and finally oxidation of the 2,5-difluoro-4-nitroaniline with hydrogen peroxide (Rx. 4).

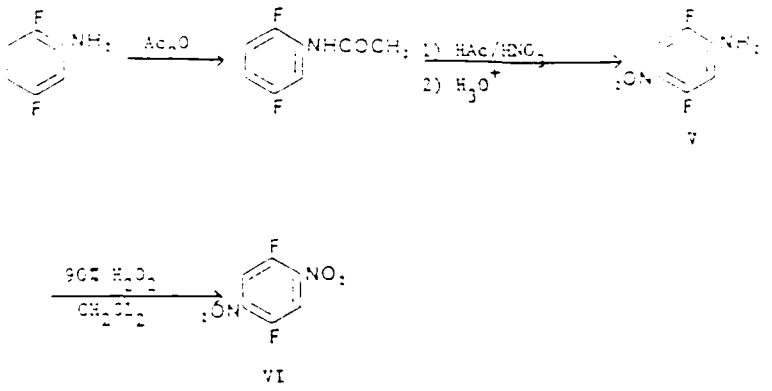

Rx. 4

2. Synthesis of 2,5-dinitro-4-fluorodiphenylamine, VII.

When 2,5-difluoro-1,4-dinitrobenzene was refluxed in tetrahydrofuran (THF), with two equivalents of aniline for 10 hours, it gave, surprisingly, an 89 percent yield of 2,5-dinitro-4-fluorodiphenylamine (Rx. 5) The lack of reactivity of the second fluorine is probably due to the electron donating effect of the amine in its para position. Subsequent reaction of the title compound with aniline in dimethyl sulfoxide (DMSO) gave the desired N,N'-diphenyl-1,4-diamino-2,5-dinitrobenzene in moderate yield. This reaction will be re-examined further in the future as a route to unsymmetrical

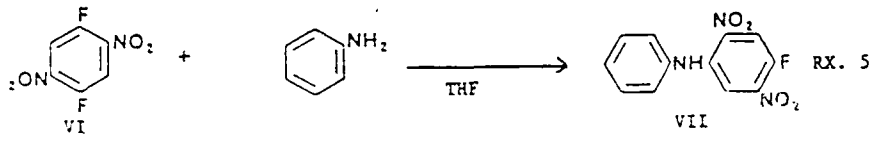

tetraamines.

3. Synthesis of N,N'-diphenyl-1,4-diamino-2,5-dinitrobenzene, VIII.

The title compound was prepared in 17 percent yield by reaction of 2,5-difluoro-1,4-dinitrobenzene with two equivalents of aniline in DMSO at 155 C for 12 hours. The other reaction products have not been identified (Rx. 6).

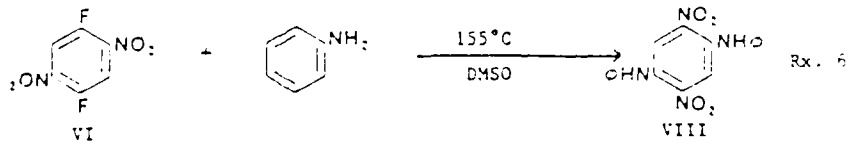

4. Reduction of N,N'-diphenyl-1,4-diamino-2,5-dinitrobenzene.

Reduction of the title compound in ethanol-water with sodium sulfide provided a colorless solid tentatively assigned the structure N(1),N(4)-diphenyl-1,2,4,5-tetraaminobenzene on the basis of its IR spectrum. Verification of this structure is awaiting elemental, mass spectral and PMR spectral analysis (Rx. 7).

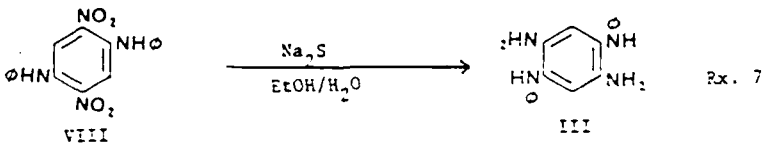

VIII III Rx. 7

IV. Conclusions

Although analytical data was not available at the writing of this report to verify the structure of tetraamine III, it seems reasonable to conclude that a viable synthesis of the target compound, N(1),N(4)-diphenyl-1,2,4,5-tetraaminobenzene, III, has been accomplished as described in Reactions 4-7.

It has also been confirmed that Polymer I and II cannot be directly synthesized by reaction of the tetraamine with oxamide.

V. Suggestions for Future Work.

It remains yet to develop a purification technique for the tetraamine III and to improve the yield for synthesis of its precursor, N,N'-diphenyl-1,4-diamino-2,5-dinitrobenzene, VIII, by investigating use of alternative solvents and reaction conditions for the double nucleophilic aromatic substitution reaction outlined in Rx. 6.

The intermediate substitution product, 2,5-dinitro-4-fluorodiphenylamine, VII, is of potential utility as previously mentioned as a precursor to a variety of tetraamine monomers for preparation of an

In addition, the compound VII could be subjected to selective reduction experiments to give 2-amino-4-fluoro-5-nitrodiphenylamine, X, which would be more likely to exhibit selective substitution of fluoride on reaction with aniline.

The alternative route for synthesis of II by starting with N,N'-diphenyl-2,5-diaminoterephthalic acid should also be further investigated. Discovery of a convenient one step method for conversion of the benzimidazolone IX to tetraamine III would provide a tetraamine precursor which is stable and which could be safely stored.

VI. Experimental

1. 2,5-Difluoroacetanilide. 2,5-Difluoroaniline was acetylated with acetic anhydride. m.p. 122-3°C (lit.(8) m.p. 122°C).

2. 4-Nitro-2,5-difluoroaniline. 4-Nitro-2,5-difluoroaniline was made by the method of Finger et al. in 80% yield, recrystallized from ethanol to give golden needles, mp 152-3°C (lit.(8) mp 152°C)

3. 1,4-Difluoro-2,5-dinitrobenzene, VI. To 6.7 mL (0.12 mol) of 90% hydrogen peroxide in 200 mL methylene chloride was added 40.4 mL trifluoroacetic anhydride at room temperature. After an induction period of several minutes, an exothermic reaction occurred. A slurry of 10.5 g of 4-nitro-2,5-difluoroaniline in 40 mL methylene chlorode was added over 10 m. After cooling, the reaction mixture was washed with 100 mL water, dried and stripped of solvent to yield 12.2g (99% yield) of 1,4-difluoro-2,5-dinitrobenzene. Recrystallization from ethanol gave yellow crystals, mp 104-5°C. Anal. calcd for $C_6H_2F_2N_2O_4$: C, 35.29; H, 0.90; N, 13.73. Found C, 35.46; H, 0.96; N, 13.56. EI mass spectrum, m/e 204 (M+). PMR (60 MHz) 8.35 ppm (overlapping dd). IR 1340, 1545 cm^{-1}.

4. 2,5-Dinitro-4-fluorodiphenylamine, VII. To a solution of 2.55 g (12.5 mmol) of 1,4-difluoro-2,5-dinitrobenzene in 10 mL distilled THF at 60°C and under nitrogen was added 2.32 g (25.0 mmol) of freshly distilled aniline over 1.5 h. The reaction mixture was then refluxed for 10 h, cooled to room temperature and poured into water. The solid product was filtered and dried to yield 3.14 g (89% yield) of deep red crystals of VII. Recrystallized from ethanol, mp 143.0-143.5°C. Anal. calcd for $C_{12}H_7FN_2O_4$: C, 51.99; H, 2.89; N, 15.15. Found C, 51.82; H, 2,69; N, 15.38. EI mass spectrum, m/e 277 (M+). PMR (60 MHz, $CDCl_3$) 7.3 ppm(m, 5 H, arom.), 7.8 ppm(d, 1 H, H-6), 8.15 ppm(d, 1 H, H-3), 9.3 ppm(br. s, 1 H, NH). IR 3370, 1541, 1350 cm^{-1}.

5. N,N'-Diphenyl-1,4-diamino-2,5-dinitrobenzene, VIII. A solution of 12.75 g (62.5 mmol) of 1,4-difluoro-2,5-dinitrobenzene in 30 mL freshly distilled DMSO was purged with nitrogen at 80°C. To this was added [illegible] freshly distilled aniline over 1.5 h. The mixture was

heated at 155 C for 12 h, cooled to room temp., poured into water and filtered. The product was isolated from the black amorphous residue by column chromatography by eluting with methylene chloride. The resulting solid was continuously extracted with pet. ether, leaving a deep blue solid, 3.65 g (17% yield) of VIII, mp 195-6 C. Anal. calcd for $C_{16}H_{14}N_4O_4$: C, 61.71; H, 4.00; N, 16.00. Found C, 61.78; H, 3.92; N, 15.42. EI mass spectrum, m/e 350 (M-). PMR (60 MHz, $CDCl_3$) 7.3 ppm (m, 10 H, arom), 8.2 ppm (s, 2 H, H-3,H-6), 8.55 ppm(br s, 2 H, NH). IR 3360, 1240, 1510 cm^{-1}.

6. N(1),N(4)-Diphenyl-1,2,4,5-tetraaminobenzene, III. A mixture of 0.6 g (1.71 mmol) of VIII, 3.0 g sodium sulfide monohydrate, 9 mL of ethanol and 1.2 mL water was stirred at reflux for 10 h. The alcohol was stripped and the residue diluted with 10 mL water (all work-up manipulations were done under nitrogen). The resulting precipitate was collected, washed with aqueous ethanol and recrystallized from benzene to give 0.14 g (28.1% yield) of III, a white solid, mp 253-4°C. IR 3420, 3340 cm^{-1}. (primary amine), 3220 cm (secondary amine), no indication of nitro absorptions.

7. 1,5-Diphenylbenzo(1,2-d:4,5-d')diimidazole-2,6-dione, IX. A mixture of 4.35 g (12.5 mmol) N,N'-diphenyl-2,5-diaminoterephthalic acid, 6.87g (25 mmol) of diphenylphosphoryl azide and 1.86 g (25 mmol) of t-butanol in 45 mL of triethyl amine was heated at reflux for 20 h. The reaction mixture was concentrated, dissolved in 75 mL toluene, washed with 5% citric acid, sat'd sodium bicarbonate and water. The organic layer was dried and stripped to yield IX, a tan solid, mp over 340 C. Anal. calcd for $C_{20}H_{14}N_4O_2$: C, 70.2; H, 4.1; N, 16.4. Found C, 69.35; H, 4.42; N, 15.3. EI mass spectrum, m/e 342 (M-). IR broad 3200-3400 cm^{-1}, 1740 cm^{-1}.

8. 1-Phenylbenzimidazol-2-one. This compound was synthesized from n-phenylanthranilic acid by the above procedure to give an off-white solid, mp 195°C.

VII. Bibliography

1. E. W. Neuse, Adv. in Polym. Sci. 47 1 (1982).

2. U. Prabhu and R. C. Evers, AFWAL, Materials Laboratory, WPAFB, OH. Unpublished Results.

3. H. S. Lunn, J. Chem. Soc. 2088 (1913).

4. M. S. Newman and K. Rutherford, J. Amer. Chem. Soc. 79 213 (1957).

5. C. S. Marvel and D. Vogel, J. Polym. Sci., Part A 1 1531 (1963).

6. F. E. Arnold, J. Wolfe, AFWAL, Materials Laboratory, WPAFB, OH. Unpublished Results.

7. J. F. Bunnett, Chem. Rev. 49, 273 (1951).

8. [illegible] J. Chem. Soc. 73 148 (1951).

FINAL REPORT NUMBER 42
REPORT NOT RECEIVED IN TIME
WILL BE PROVIDED WHEN AVAILABLE
Dr. Amir Karimi
760-OMG-110

Sponsored by the

AIR FORCE OFFICE OF SCIENTIFIC RESEARCH

Conducted by the

UNIVERSAL ENERGY SYSTEMS, INC.

GRANT REPORT

The Multi-Weapon Multi-Target Multi-Phase Assignment Problem

Prepared by:	Stephan E. Kolitz
Academic Rank:	Assistant Professor
Department and University:	Management Sciences Dept. University of Massachusetts/Boston

Date:	April 17, 1987
Contract No:	F49620-85-C-0013

The Multi-Weapon Multi-Target Multi-Phase Assignment Problem

by

Stephan E. Kolitz

ABSTRACT

In the Strategic Defense Initiative Battle Management and Command, Control, and Communications (SDI BM/C^3), one of the problems that arises is the multi-weapon, multi-target, multi-phase assignment problem. Weapon platforms are satellites in orbit containing kinetic kill vehicles (projectiles) which can be sent to targets (boosters/missiles). A given weapon platform's projectiles have a known probability of hitting any particular target. A ballistic missile's trajectory is typically described as consisting of four phases; three phases are studied here: boost, post-boost, and midcourse. This assignment problem was formulated as a large-scale non-linear integer programming problem. Efficient near-optimal algorithms were found. The most promising algorithm was studied in depth, using analytic and simulation techniques.

I. INTRODUCTION

In th Strategic Defense Initiative Battle Management and Command, Control, and Communications (SDI BM/C^3), one of the problems that arises is the multi-weapon, multi-target, multi-phase assignment problem. Weapons (or weapon platforms) are satellites in orbit containing kinetic kill vehicles (projectiles) which can be sent to targets (boosters/missiles) in hopes of hitting them.

It is assumed that:

1) a given weapon platform's projectiles have a known probability of hitting any particular target,

2) the value of each target is known,

3) there is not enough time for information about whether a hit or miss actually takes place to get back to the assigner of projectiles and

4) each projectile is probabilistically independent of any other.

A ballistic missile's trajectory is typically described as consisting of four phases; the problem studied here can be used to model the first three phases: boost, post-boost, and midcourse. Boost phase is defined to be the phase during which the target is firing its rocket motors. Post-boost is the phase after boost in which the post-boost vehicle (target) releases reentry vehicles. Midcourse phase starts when the

reentry vehicle has left the post-boost vehicle and ends when the reentry vehicle enters the atmosphere. The problem studied here is to assign projectiles to targets in order to minimize the surviving target value, subject to the available supply of projectiles.

This assignment problem can be formulated as a large-scale non-linear integer programming problem. Efficient near-optimal algorithms have been found. The most promising algorithm was studied in depth, using analytic and simulation techniques. This algorithm assigns projectiles sequentially using a maximum marginal return criterion.

Sufficient conditions for optimality of the algorithm were found; in addition, it is shown that the algorithm is optimal in the limit for a broad range of weapon-target single shot probabilities of hit (kill). A closed-form expression for the expected number of hits is derived.

II. PROBLEM I

Let

$x(i,j)$ = the number of projectiles sent from weapon platform i and aimed at target j,

$p(i,j)$ = the maximum (over time from now) probability of hitting target j with a projectile sent from weapon platform i,

a = the number of available projectiles on each weapon platform,

$v(j)$ = the initial value of target j,

n = the number of targets, and

m = the number of weapon platforms.

Let

$$H(j) = \begin{cases} 1 & \text{if target } j \text{ is hit} \\ 0 & \text{if target } j \text{ is not hit} \end{cases}$$

Denote the probability of target j surviving by

$$P\ (\ H(j) = 0\ ) = q\hat{}(j).$$

Clearly $$q\hat{}(j) = \prod_{i=1}^{m} (\ 1 - p(i,j))^{x(i,j)}$$

and $$P\ (\ H(j) = 1\ ) = p\hat{}(j) = 1 - q\hat{}(j).$$

Let T be the total number of hits, i.e.

$$T = \sum_{j=1}^{n} H(j)$$

and V be the value of the targets hit,

$$V = \sum_{j=1}^{n} v(j)H(j).$$

V can be thought of as the weighted sum of independent non-identical Bernoulli trials, with success probability p^(j) for the jth trial. Thus,

$$E[V] = \sum_{j=1}^{n} v(j)p^{\wedge}(j)$$

and

$$VAR[V] = \sum_{j=1}^{n} v(j)^2 p^{\wedge}(j)q^{\wedge}(j).$$

Since the H(j) are uniformly bounded, the Central Limit Theorem holds; as n increases, V becomes normally distributed with mean and variance given above. See Feller [1968].

An interesting problem, henceforth called Problem I, is to

$$\max \quad E[V]$$

subject to

$$\sum_{j=1}^{n} x(i,j) <= a \qquad \text{for all } i$$

$$x(i,j) >= 0 \text{ and integer.}$$

Letting SV = the value of the surving targets, we get

$$SV = \sum_{j=1}^{n} v(j)(1 - H(j)).$$

The objective function above could thus be written equivalently as min E [SV] where

$$E[\,SV\,] = \sum_{j=1}^{n} \prod_{i=1}^{m} (\,1 - p(i,j)\,)^{x(i,j)}$$

Problem I appeared as a suggested formulation by Dantzig in Manne [1958], where a similar problem was approximated by a transportation problem. Problem I is a non-linear integer programming problem and complete enumeration would require looking at

$$\left[\frac{(a + n - 1)!}{a!(n - 1)!} \right]^{m}$$

different ways to assign the projectiles to the targets. See Bogart [1983]. When the problem is large, complete enumeration is clearly out of the question. For example, with 10 weapon platforms, 100 targets and 10 projectiles per platform, there are approximately 4×10^{130} different ways to assign the projectiles to the targets.

III. ALGORITHM I

Let X(s) = a matrix of { x(i,j) } such that

$$\sum_{i=1}^{m} \sum_{j=1}^{n} x(i,j) = s \quad \text{and}$$

$$\sum_{j=1}^{n} x(i,j) <= a.$$

X(s) is a feasible assignment matrix with exactly s projectiles assigned to targets.

Let P = the matrix of { p(i,j) },

Q(s) = diag ({ q(j) }) for { x(i,j) } from some X(s),

V' = diag ({ v(j) }), and

R(s) = PV'Q(s), consisting of elements

{ r(i,j) = p(i,j)v(j)q(j) }.

The product v(j)q(j) is the expected value of target j, given X(s). Thus, the element r(i,j) is the expected decrease in target j's value by sending one additional projectile from weapon platform i.

Let

$$r(i(s),j(s))$$

$$= \max_{i,j} \{ r(i,j) \text{ in } R(s) \text{ such that } \sum_{j=1}^{n} x(i(s),j) < a \}.$$

The best marginal feasible assignment of the next projectile, given the s projectiles already assigned, is from platform i(s) to target j(s).

Algorithm I

Step 1. Set s = 0.

Step 2. Calculate R(s).

Step 3. Find i(s),j(s).

Step 4. Increment x(i(s),j(s)) by one, forming X(s+1).

Step 5. Increment s by one, to s+1.

Step 6. If s = a*m, stop; otherwise go to step 2.

Algorithm I can be thought of as trying, within the limits of integer values of x(i,j), to equalize the expected value of the targets.

An equivalent algorithm first appeared in denBroeder, et.al. [1959]. Algorithm I does not always find an optimal solution as the following example will illustrate.

Example

$$P = \begin{bmatrix} 0.6 & 0.9 \\ 0.0 & 0.7 \end{bmatrix}$$

$$V' = \begin{bmatrix} 1 & 0 \\ 0 & 1 \end{bmatrix}$$

$a = 1$ $\quad m = 2$ $\quad n = 2$

Step 1. $s = 0$.

Step 2. $R(0) = P$.

Step 3. $i(0) = 1$, $j(0) = 2$

Step 4. $X(1) = \begin{bmatrix} 0 & 1 \\ 0 & 0 \end{bmatrix}$

Step 5. $s = 1$.

Step 6. $1 < 2$; go back to Step 2.

$$\text{Step 2. } R(1) = \begin{bmatrix} 0.6 & 0.9 \\ 0.0 & 0.7 \end{bmatrix} \begin{bmatrix} 1 & 0 \\ 0 & 1 \end{bmatrix} \begin{bmatrix} 1 & 0 \\ 0 & 0.1 \end{bmatrix}$$

$$= \begin{bmatrix} 0.6 & 0.09 \\ 0.0 & 0.07 \end{bmatrix}.$$

Step 3. $i(1) = 2$, $j(1) = 2$ (remembering that it is not feasible to send any more projectiles from weapon platform 1)

$$\text{Step 4. } X(2) = \begin{bmatrix} 0 & 1 \\ 0 & 1 \end{bmatrix}$$

$$V'Q(2) = \begin{bmatrix} 1 & 0 \\ 0 & 0.03 \end{bmatrix}$$

Step 5. $s = 2$.

Step 6. $2 = 2$, so stop.

For this solution E [SV] = 1 + (0.1)(0.3) = 1.03, but

clearly,

$$X(2) = \begin{bmatrix} 1 & 0 \\ 0 & 1 \end{bmatrix}$$

is optimal with E[SV] = 0.4 + 0.3 = 0.7.

Note that since V'Q(s) is a diagonal matrix, the eigenvalues are the expected values of the targets, given X(s); thus the trace of V'Q(s) is E [SV].

IV. OPTIMALITY OF ALGORITHM I

Algorithm I finds an optimal solution for Problem I under some conditions. A general result which provides sufficient conditions for optimality was found; a number of special cases of interest are also given.

Let

$$m(j) = \max_i \{ p(i,j) \} \quad \text{for all } j$$

and

$$I^*(j) = \{ i : p(i,j) = m(j) \}.$$

$m(j)$ represents the best probability of hitting target j; $I^*(j)$ is the set of weapons which can achieve this.

Suppose for a given problem Algorithm I has picked weapons for each target j out of $I^*(j)$. Now, for a given set of $p(i,j)$, for any set of

x(i,j), the objective function of Problem I

$$E\,[\,SV\,] \;=\; \sum_{j=1}^{n} \prod_{i=1}^{m} \left(\,1 - p(i,j)\,\right)^{x(i,j)}$$

$$>= \;\; \sum_{j=1}^{n} \prod_{i=1}^{m} \left(\,1 - m(j)\,\right)^{x(i,j)}$$

So we have

1) Algorithm I finds the locally best feasible reduction in E [SV] as each projectile is assigned (by the structure of the algorithm) and

2) the locally best feasible reduction in E [SV] is globally best (by the inequality above).

That is, if at any stage of the assignment it were possible for each target to be attacked by weapons which have the best chance of hitting it, the assignment is optimal at that stage.

Thus the following holds.

RESULT I

If, for all j, Algorithm I results in $\{ x(i,j) \}$ such that

if i is not in $I^*(j)$ then $x(i,j) = 0$

and

if $x(i,j) > 0$ implies i is in $I^*(j)$

then $\{ x(i,j) \}$ is an optimal assignment of weapons to targets for Problem I.

As a direct consequence of Result I, there are many special cases where Algorithm I is optimal for Problem I. The cases listed below are of particular interest.

Case I.

If $p(i,j) = p(j)$ for all i, then Algorithm I finds an optimal solution.

Since for every j all i are in $I^*(j)$, Result I holds. A much less intuitive proof of Case I can be found in denBroeder [1959].

Case II.

If m = 1, then Algorithm I finds an optimal solution.

This can be regarded as a special case of Case I.

Case III.

If the constraints in Problem I are replaced by a global constraint,

$$\sum_{i=1}^{m} \sum_{j=1}^{n} x(i,j) <= a'$$

then Algorithm I finds the optimal solution.

Algorithm I will continue to choose a maximum p(i,j) for every j until the global constraint has no slack, hence it finds an optimal solution.

Case IV.

Suppose there exists a partition (a set of disjoint completely exhaustive sets) of the weapons which results in a partion of the targets. Then if each set of the weapon partition satisfies one of the Cases above, Algorithm I is optimal.

Within each element of the weapon partition, the sum of the terms in the objective function coming from the corresponding element of the target partition is minimized. The total value of the objective function is the sum of minimal terms and is then itself minimized.

When $p(i,j) = p$ for all i and j and $v(j) = v$ for all j, the objective function is

$$v\ (1-p)^{x(i,j)}.$$

Note that there are diminishing marginal returns from additional projectiles sent at the same target.

That is, for any integer k,

$$v\ [(1-p)^{k} - (1-p)^{(k+1)}] <= v\ [\ (1-p)^{(k-1)} - (1-p)^{k}].$$

Thus Algorithm I will cycle through the targets, assigning one projectile to all the targets, then two and so on, until running out of projectiles. Since the conditions here are a special case of Case II above, this solution is optimal. Note that in general, the effect of Algorithm I is to equalize the expected value of the targets at each step of the allocation process. This fact is critical in subsequent derivations in this paper.

Therefore, to minimize the expected surviving value, the projectiles should be "dealt out" to the targets like a whole deck of cards to card players. If there are 52 projectiles (cards) dealt out to 7 targets (players), three targets (players) will get 8 projectiles (cards) and four will get 7. Thus, the number of projectiles (cards) dealt out to any of the weapons (players) differs by at most one and we have the following result.

Result II.

If $p(i,j) = p$ for all i and j and $v(j) = v$ for all j, then the optimal assignment is to assign the projectiles so that the total number of projectiles directed at any two targets differs by no more than one.

Result II proves very useful in later Sections in finding closed form approximations which describe the performance of Algorithm I.

V. PERFORMANCE OF ALGORITHM I

This section examines the performance of Algorithm I under more general conditions than those in section IV.

.double

Suppose each p(i,j) is regarded as a random variable, each generated independently from a probability distribution function

$$F(i,j,x) = P(p(i,j) <= x).$$

Note that

$$M(j) = \max_i \{ p(i,j) \},$$

the maximum probability of hitting j, is now itself a random variable.

Result I of Section IV says that if Algorithm I assigns weapons with maximum hit probability for each target, the assignment is optimal. These sufficient conditions for optimality are not true in general. Suppose in some cases, these conditions hold in the limit as the number of weapons increases. Then, Algorithm I is optimal in the limit for these cases.

There is an interesting parallel between the sufficient conditions in Section IV and the situation here.
For a given fixed matrix, the condition "p(i,j) = p(j) for all i" guarantees that Algorithm I is optimal.
The equivalent here is "F(i,j,x) = F(j,x)" for all i" guarantees that in the limit, Algorithm I is optimal. If the distributions of the p(i,j)'s
for all the weapons are the same, then with independence each weapon is equally likely to be the one with maximal p(i,j) for a given j. If the maximal p(i,j)'s are exactly uniformly spread out throughout a matrix, then Algorithm I will be able to use them for each target, satisfying the conditions for Result I to hold. Since in the limit the observed result will
approach the expected result of uniformity with probability one, Algorithm I is optimal in the limit.

RESULT III

If the p(i,j)'s are generated from distributions which only depend upon j, then Algorithm I is optimal in the limit.

This broad range of cases is characterized by having the maximal probabilities of hitting different targets spread out over the weapons as the number of weapons increases and could certainly be generalized to a probability equivalent of Result I.

RESULT IV

If, for all j, Algorithm I results, with probability one, in $\{ x(i,j) \}$ such that

$$\text{if } i \text{ is not in } I^*(j) \text{ then } x(i,j) = 0$$

and

$$\text{if } x(i,j) > 0 \text{ implies } i \text{ is in } I^*(j)$$

then with probability one Algorithm I solves Problem I optimally.

The more useful result is Result III, which has sufficient conditions which can be more readily checked.

The "worst case" situation is that there is one weapon which is the expected best for all targets, no matter how many other weapons are available. Then the sufficient conditions would not be true in the limit. Note that the number of targets does not have to increase for optimality.

Denote the probability distribution function of M(j) by

$$F\hat{}(j,x)$$

$$= \quad P \ (\ M(j) <= x \ )$$

$$= \quad P \ (\ p(1,j) <= x, \ p(2,j) <= x, \ \ldots \ , p(m,j) <= x \ ), \text{ since}$$

for fixed j, the event "the maximum of the p(i,j)'s is less than or equal to x " is equivalent to "all the p(i,j)'s are less than or equal to x ".

By independence,

$$F\hat{}(j,x) \quad = \quad \prod_{i} \quad F(i,j,x).$$

and since

$$E \ [\ Y \ ] = \int_{0}^{1} P \ (\ Y >= y) \ dy \qquad \text{for any random variable Y,}$$

the expected largest p(i,j) is

$$M(j) = \int_0^1 (1 - F^{\wedge}(j,x)) \, dx.$$

As noted in Section IV, the effect of Algorithm I is to equalize, as much as possible, the expected surviving value of each target at every step of the allocation process. Using this fact, it is possible to derive closed form expressions for an expected bound for the performance of Algorithm I.

Suppose that the targets are numbered so that equal valued targets are clumped together in classes and, that the expected maximal p(i,j) is the same for equal valued targets and that the conditions of Result III hold. That is, for j = 1 to n(1), v(j) = w(1) and E [M(j)] = m'(1); for j = (n(1) + 1) to (n(1) + n(2)), v(j) = w(2) and E [M(j)] = m'(2); and so on, where n(s) = the number of targets with value w(s) and m'(s) is the expected maximal p(i,j). Let x'(s) be the number of projectiles sent to one of the targets with value w(s) and N_t the number of classes

of different valued targets. It is assumed temporarily that the discrete nature of projectiles is relaxed mathematically; i.e. x'(s) can take on non-integer values.

The total number of projectiles available can be written in a "conservation of projectiles" formula:

$$n(1)x'(1) + \sum_{s=2}^{N_t} n(s)x'(s) = am$$

After Algorithm I has been run, the approximate equality of the expected surviving target values leads to the following. (The symbol $\underset{\sim}{=}$ will be used to approximate equality.

For targets with v(j) = w(s),

$$w(s)\ (1 - m'(s))^{x'(s)} \underset{\sim}{=} w(1)\ (1 - m'(1))^{x'(1)}.$$

Thus by taking the natural log of both sides and solving for x'(s) the following is derived:

$$x'(s) \underset{\sim}{=} \frac{\ln\ (\ w(1)/w(s)\ ) + x'(1)\ \ln\ (1 - m'(1))}{\ln\ (1 - m'(s))}$$

After multiplication by n(s), summation from s = 2 to N_t and simultaneous solution for x'(1) with the "conservation of projectiles" expression, the result is:

$$x'(1) \underset{\sim}{=} \frac{am - \sum_{s=2}^{N_t} \frac{n(s)\ \ln(w(1)/w(s))}{\ln(1 - m'(s))}}{\ln(1 - m'(1)) \sum_{s=2}^{N_t} \frac{n(s)}{\ln(1 - m'(s))} + n(1)}$$

For any s, x'(s) can be calculated using the two previous approximate equalities.

The expression simplifies when m'(s) = m' for all s.

$$x'(1) \underset{\sim}{=} \frac{am - \sum_{s=2}^{N_t} \frac{n(s)\ \ln(w(1)/w(s))}{\ln(1 - m'))}}{n}$$

When in addition w(s) = 1 for all s, the expression reduces to

$$\underset{\sim}{x'(1)} = \frac{am}{n}$$

and in addition x'(s) = x'(1) for all s; i.e. send the same number of projectiles to each target. This number is the average number of projectiles available for each target.

Since only discrete numbers of projectiles can actually be sent in practice, the number of projectiles assigned to any target j within a given class of targets would differ by at most one; call x(j) this number sent to target j.

To calculate x(j):

1) multiply the relevent x'(s) by n(s) and round; this is the approximate number of projectiles allocated to the class

2) "deal out" all the projectiles to each target within the class as evenly as possible.

The predicted expected value of surviving targets (PEV) can then be calculated by

$$PEV = \sum_{j=1}^{m} \left(1 - E\,[M(j)] \right)^{x(j)} \qquad (5.1)$$

This optimal solution to Problem I will have an expected surviving target value no less than this and will approach it in the limit as the number of weapons increases. Under the conditions of Result III, Algorithm I's solution should converge toward this also. The rate of convergence has not been estimated analytically, but simulation results noted in the what follows indicate that, at least for one type of situation, convergence is fairly rapid.

Under simplifying assumptions and for a specific class of distributions of F(i,j,x), calculations were done and compared with simulated results.

Suppose that E [M(j)] is the same for all j, v(j) = 1 for all j and let a' = am. Then following the procedures above, x(j) for all j will be the following solution.

The solution is to assign

$$g = \text{trunc}\left(\frac{a'}{n} \right)$$

projectiles to (n - a'mod n) targets and (g + 1) projectiles to the other a'mod n targets.

Suppose each p(i,j) is chosen from the following distribution

$$P (X <= x) = \begin{cases} 1 - d & \text{for } x < b \\ (1 - d) + d (x - b)/(u - b) & \text{for } b <= x <= u \\ 1 & \text{for } x > u \end{cases}$$

where $0 <= b <= u <= 1$ and $0 < d <= 1$.

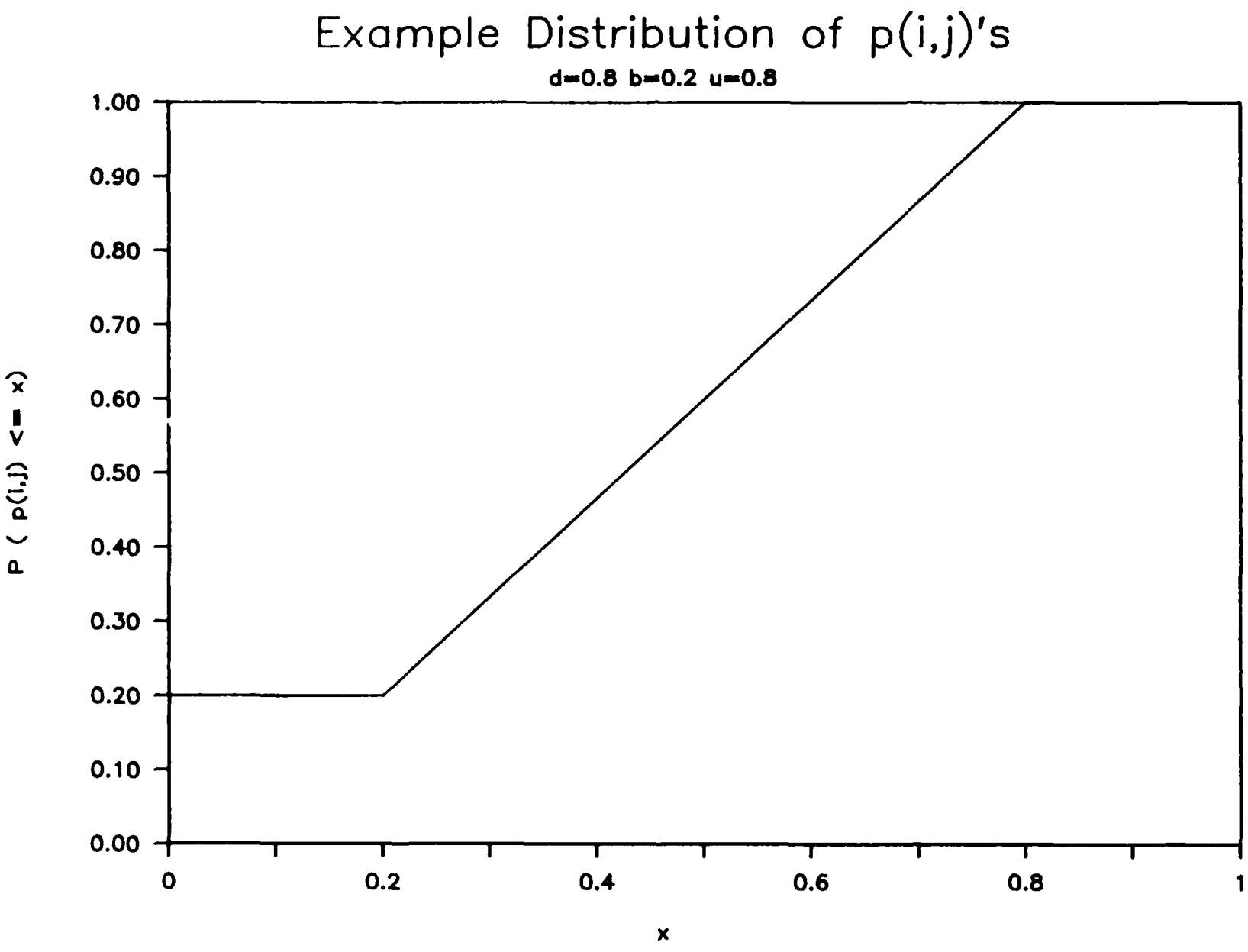
Example Distribution of p(i,j)'s
d=0.8 b=0.2 u=0.8
P (p(i,j) <= x)
1.00
0.90
0.80
0.70
0.60
0.50
0.40
0.30
0.20
0.10
0.00
0
0.2
0.4
0.6
0.8
1
x

Each p(i,j) can be thought of as being generated in the following way. With probability d (for density) p(i,j) is positive, otherwise it is zero. If it is positive, then it is selected from a uniform distribution from b (lower bound) to u (upper bound).

Let $Y = \max (X_1, X_2, \ldots, X_m)$ where each X_i is independent and has the distribution defined for X.

Then

$$P (Y <= y) = P (\max (X_i) <= y)$$

$$= P (X_1 <= y, X_2 <= y, \ldots, X_m <= y)$$

$$= [P(X <= y)]^m$$

$$= \begin{cases} (1 - d)^m & \text{for } y < b \\ [(1 - d) + d\,(y - b)/(u - b)]^m & \text{for } b <= y <= u \\ 1 & \text{for } y > u \end{cases}$$

$$\text{Thus } E[\,Y\,] = \int_0^1 P\,(\,Y >= y)$$

$$= \int_0^b [\,1 - (\,1 - d\,)^m$$

$$+ \int_b^u 1 - [\,(1-d) + d\,(y-b)/(u-b)\,]^m$$

$$+ \int_u^1 [\,1 - 1]$$

Thus $E[Y] =$

$$[1 - (1 - d)^m]\, b$$

$$+ (u - b) - \frac{(u - b)\,(1 - (1 - d)^{(m+1)})}{d\,(m + 1)}$$

This value is the maximum expected p(i,j) that can be used to attack any target; that is, it is equal to $E[M(j)]$ for all j.

Let $w = a' \bmod n$. Then PEV is the predicted expected surviving target value as in (5.1) where here

$$PEV = (n - w)(1 - E[M(j)])^g + w(1 - E[M(j)])^{(g+1)} \qquad (5.2)$$

Simulations were run with p(i,j) matrices generated from the class of distribution as described above. The range of parameter values are given below; not all possible combinations of density and number of weapons and projectiles were run for each number of targets case. All possible mean values of p(i,j) were run for chosen values of the other parameters.

Number of targets:	100,200,500 1000
Number of weapons:	5,10,20,25,40,80,100,200
Number of projectiles:	5,10,20,25,40,80,100,200
Density:	0.05,0.10,0.25,0.50,0.75,1.0
Mean p(i,j):	0.1 to 0.9 in increments of 0.1
Variance p(i,j):	For each mean p(i,j), by range from 0 to maximum feasible, keeping the distribution symmetrical

The output was voluminous; the summary is given in the following graph. The horizontal axis represents the product of density and number of weapons, the expected number of weapons with positive p(i,j) for any target, called the number of useable weapons. The vertical axis is the percentage deviation from equation (5.2) observed in the simulations.

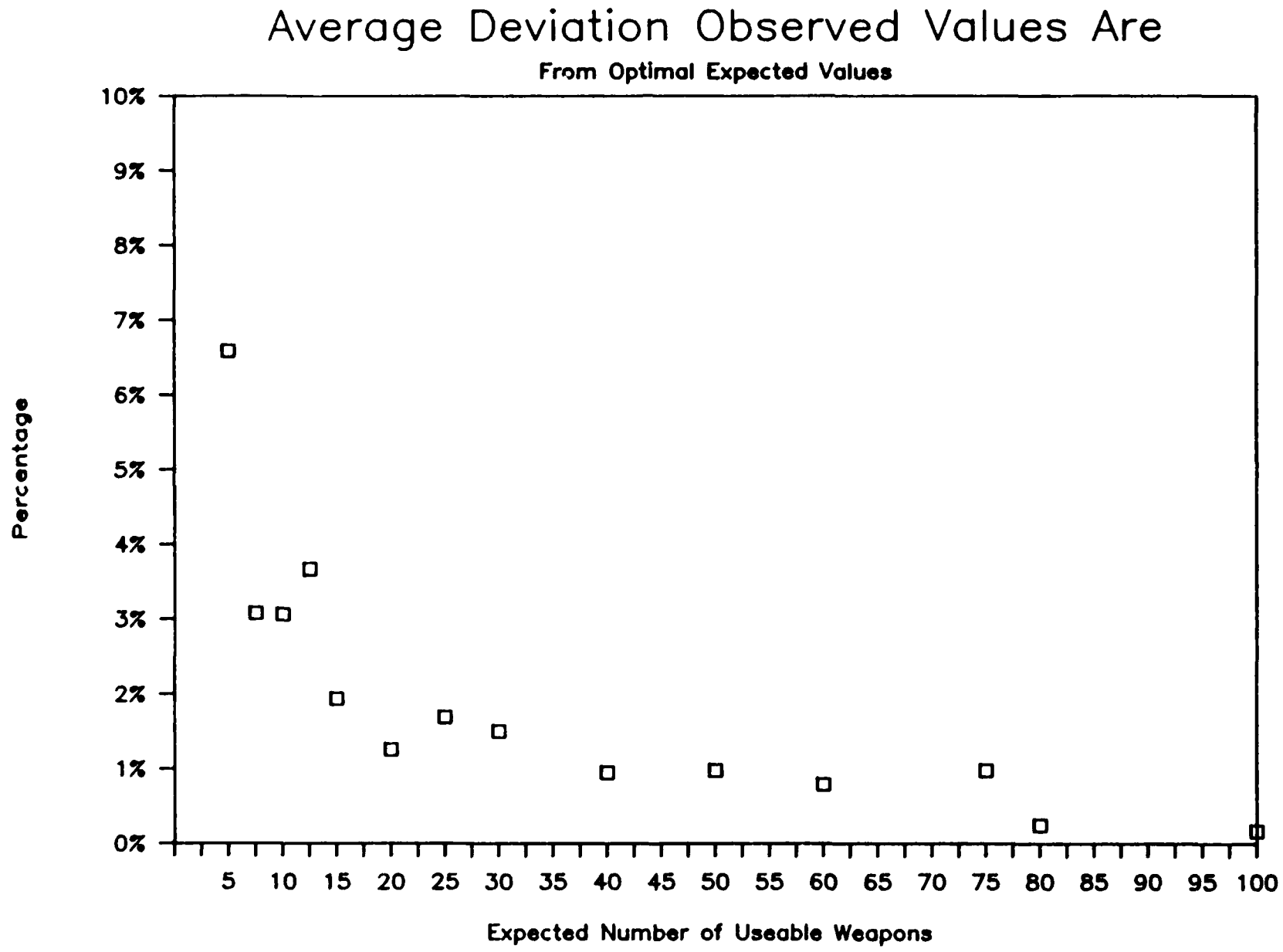
Average Deviation Observed Values Are
From Optimal Expected Values
Percentage
10%
9%
8%
7%
6%
5%
4%
3%
2%
1%
0%
5 10 15 20 25 30 35 40 45 50 55 60 65 70 75 80 85 90 95 100
Expected Number of Useable Weapons

As seen in the graph, equation (5.2) is not only a bound for the performance of Algorithm I, but can be used as a closed-form approximation for the number of surviving targets for even relatively small matrices of the type studied here; for large matrices, the error should approach zero and was observed to do so in the simulations.

A reasonable rule based on the empirical data would be to apply the approximation when the expected number of useable weapons (those with positive p(i,j)) is over 5. The overall average percentage deviation observed from equation (5.2) in all runs with five or more expected useable weapons is less than 3%.

In addition to checking Algorithm I against optimality, it is interesting to compare its performance with a different Algorithm, Algorithm D. Algorithm D assigns projectiles independently of the (positive) value of p(i,j). It simply searches for the next available positive p(i,j) and assigns a projectile from i to j. Algorithm D is a proxy for the policy of estimating whether a given p(i,j) is positive or zero, but not estimating the magnitude. The result of using Algorithm D is to use on average the average p(i,j). From the results of this Section, it is evident that Algorithm I on average ends up

using the maximal elements of the p(i,j) matrix. When there is no variance in the distribution of the p(i,j)'s, the two Algorithms will perform essentially the same. But when the variance is non-zero, the considerable difference in their performance is directly related to the size of the variance. The following graphs will illustrate this. The first shows what the expected number of hits would be for the two Algorithms when an equal number of projectiles is available for both. The second shows how many projectiles Algorithm D must have at its disposal to equal the performance of Algorithm I; the number of projectiles Algorithm I can use is held constant.

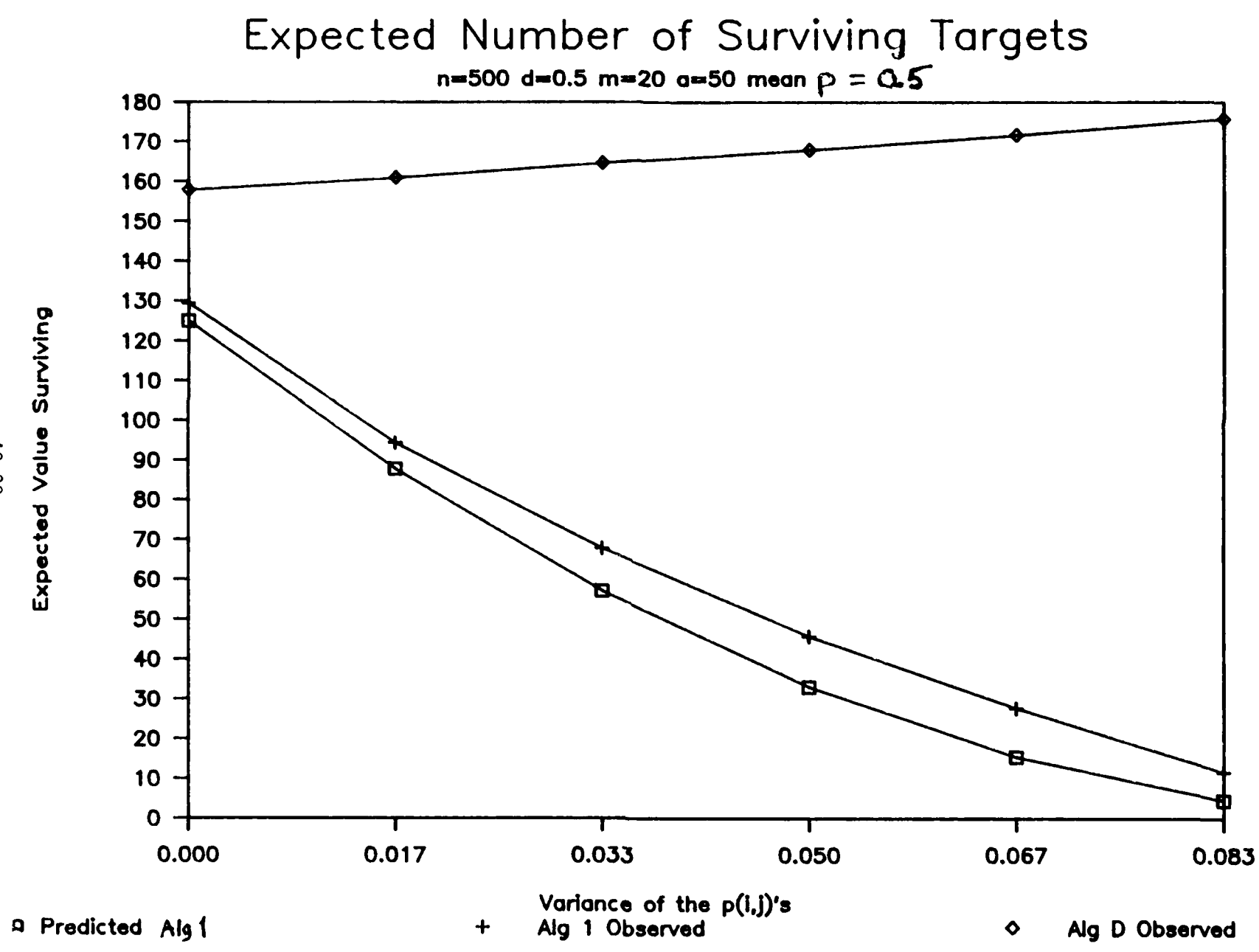
Expected Number of Surviving Targets
n=500 d=0.5 m=20 a=50 mean p = 0.5
Expected Value Surviving
180
170
160
150
140
130
120
110
100
90
80
70
60
50
40
30
20
10
0
0.000
0.017
0.033
0.050
0.067
0.083
Variance of the p(i,j)'s
Predicted Alg 1
Alg 1 Observed
Alg D Observed

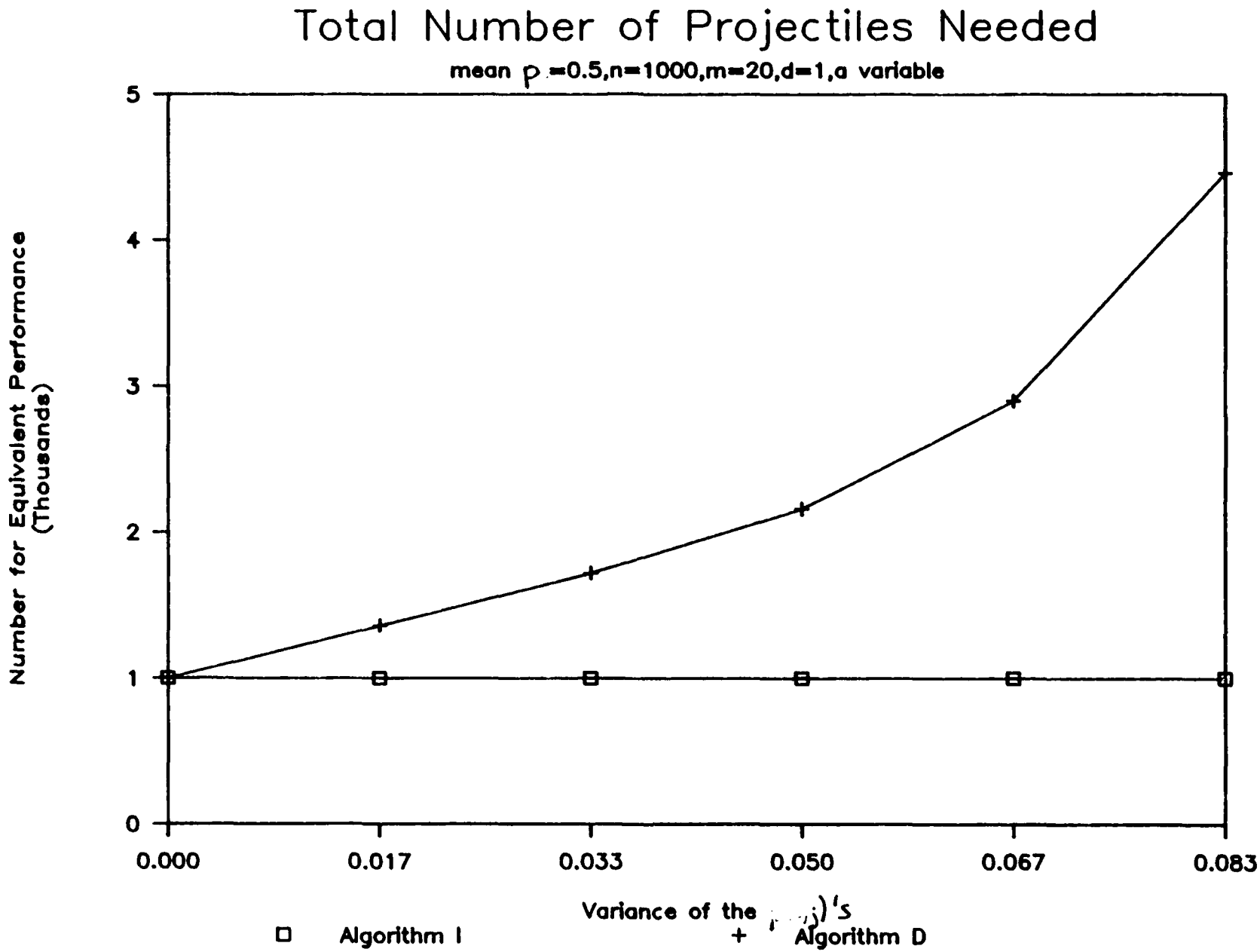
Total Number of Projectiles Needed
mean p =0.5,n=1000,m=20,d=1,a variable
Number for Equivalent Performance (Thousands)
5
4
3
2
1
0
0.000
0.017
0.033
0.050
0.067
0.083
Variance of the
Algorithm I
Algorithm D

VI. SMALL CASE RESULTS

The performance of Algorithm I has been shown to approach optimality for large problems. In small problems, empirical results indicate that while Algorithm I does very well, improvement is possible.

Some of the distributions for the p(i,j)'s discussed in Section V were used to generate small matrices. Algorithm I was run on 100 matrices for each set of parameter values. The results are given below. While these runs were made with the uniform distribution from [0.2,0.8] and density = 1, runs were made on distributions with other parameters of the range. Those runs were not done in nearly as many cases as those below, but similar results were obtained.

COMPARISON OF ALGORITHM I WITH COMPLETE ENUMERATION FOR SMALL CASES

Weapons	Targets	Projectiles	Algorithm I No. of hits	Complete Enumeration	Average % Off
2	4	2	2.29	2.32	1.25%
2	4	3	2.80	2.81	0.41%
2	4	4	3.18	3.21	1.05%
2	4	5	3.42	3.45	0.89%
2	5	3	3.19	3.22	1.14%
2	5	4	3.62	3.64	0.48%
2	5	5	3.98	4.02	1.03%
2	6	3	3.45	3.50	1.52%
2	6	4	4.04	4.07	0.72%
2	6	5	4.47	4.50	0.60%
2	6	6	4.83	4.88	1.05%
2	7	4	4.40	4.43	0.70%
2	7	5	4.89	4.91	0.29%
2	7	6	5.30	5.34	0.60%
2	7	7	5.65	5.70	0.94%
2	8	3	3.87	3.92	1.12%
2	8	4	4.73	4.80	1.42%
2	8	5	5.30	5.33	0.53%
2	8	6	5.77	5.79	0.29%
3	4	1	1.96	2.01	2.45%
3	4	2	3.00	3.03	1.06%
3	4	3	3.47	3.52	1.37%
3	5	2	3.35	3.40	1.50%
3	5	3	3.99	4.03	0.93%
3	6	2	3.73	3.81	2.01%
3	6	3	4.53	4.56	0.62%
3	6	4	5.07	5.12	1.11%
3	7	3	4.88	4.93	0.97%
3	7	4	5.51	5.57	0.98%
3	8	3	5.30	5.38	1.57%

There were 100 runs for each case. The PK's were drawn from a uniform distribution in the range 0.2 to 0.8.

VII. OTHER ALGORITHMS

There is another algorithm which has proved useful in solving Problem I.

Let X(s) = a matrix of { x(i,j) } such that

$$\sum_{i=1}^{m} \sum_{j=1}^{n} x(i,j) = s \quad \text{and}$$

$$\sum_{j=1}^{n} x(i,j) >= a \quad \text{for all } i.$$

X(s) is an assignment of exactly s weapon projectiles to targets; this assignment is infeasible for a given weapon when the inequality holds, and reaches feasiblity at equality.

Let

$$P\hat{} = \left\{ \frac{p(i,j)}{q(i,j)} \right\}$$

and

$$R(s) = P\hat{}V'Q(s).$$

Let

$r(i(s),j(s))$ = the minimum entry of R(s) such that

$$\sum_{j=1}^{n} x(i(s),j) >= a$$

and $x (i(s),j(s)) > 0.$

Elements of R(s) are

$$\frac{p(i,j)v(j)q(j)}{q(i,j)}$$

$$= v(j)q(j) \left[\frac{1}{q(i,j)} - 1 \right]$$

$$= - (v(j)q(j)) + \left[\frac{v(j)q(j)}{q(i,j)} \right].$$

The first term is the negative of the expected value of target j when the s projectiles described by X(s) have been fired. The second term is the expected value of target j if one projectile from weapon i is removed from X(s). Thus element (i,j) of R(s) is the expected increase in target j's value which results from sending one less projectile to it from weapon platform i. The least effective projectile currently sent is from weapon i(s) to target j(s).

Algorithm II

Step 1. Set s

= a * (m * n - the number of zero entries in P).

Step 2. Set X(s) = (a) for all i,j such that p(i,j) >0.

Step 3. Calculate R(s).

Step 4. Find i(s),j(s).

Step 5. Decrease x(i(s),j(s)) by one, forming X(s-1).

Step 6. Decrease s by one to s-1.

Step 7. If s = a * m, stop; otherwise go to Step 3.

With the same values as the example used to illustrate Algorithm I, Algorith II does find the optimal solution.

$$P = \begin{bmatrix} 0.6 & 0.9 \\ 0.0 & 0.7 \end{bmatrix}$$

$$V' = \begin{bmatrix} 1 & 0 \\ 0 & 1 \end{bmatrix}$$

a = 1 m = 2 n = 2

Step 1. s = 3.

Step 2. $X(3) = \begin{bmatrix} 1 & 1 \\ 0 & 1 \end{bmatrix}$

$$Q(3) = \begin{bmatrix} 0.4 & 0 \\ 0 & 0.03 \end{bmatrix}$$

Step 3. R(3)

$$R(3) = P^{\wedge}V'Q(3)$$

$$= \begin{bmatrix} 1.5 & 9.0 \\ 0.0 & 2.33 \end{bmatrix} \begin{bmatrix} 1 & 0 \\ 0 & 1 \end{bmatrix} \begin{bmatrix} 0.4 & 0 \\ 0 & 0.03 \end{bmatrix}$$

$$= \begin{bmatrix} 0.6 & 0.027 \\ 0.0 & 0.70 \end{bmatrix}.$$

Step 4. i(3) = 1, j(3) = 2 (since weapon platform 2 is already feasible).

Step 5. $$X(2) = \begin{bmatrix} 1 & 0 \\ 0 & 1 \end{bmatrix}$$

$$Q(2) = \begin{bmatrix} 0.4 & 0 \\ 0 & 0.3 \end{bmatrix}$$

is optimal with E[SV] = 0.4 + 0.3 = 0.7.

Algorithm II does not reach the optimal solution always and it is slower than Algorithm I to run. However, as the example above illustrated, there are times when Algorithm II is superior to Algorithm

I. Since Algorithm I has been shown to be optimal in the limit, it would be useful only in small cases, where run times would not be prohibitive.

If there is some special structure to the p(i,j) matrix, then it is quite possible for a variation of either Algorithm I or II to be superior to the original. As an example, suppose the matrix looks like the following, with numerical values a > b

Targets	1	2	3	4	5	6	7	8	9	10
Weapons										
1	a	a	a	a	a	b	b	b	b	b
2	b	b	b	b	b	0	0	0	0	0

Algorithm I would have weapon 1 first attack targets 1 through 5. If weapon 1 ran out of projectiles before being able to atack targets 5 through 10,then it would have been better to attack targets 6 through 10 with weapon 1 and targets 1 through 5 with weapon 2. The problem is that projectile resources are limited relative to targets; for if there were enough projectiles on weapon 1 to attack all ten targets, that would be optimal. A variation that would be better would be to attack targets in order from least number of possible weapon-target pairs to most, using Algorithm I within each set of targets. Here that means attacking targets 6 through 10 with weapon 1 first and then going on to targets 1 through 5.

This example could be generalized to include a larger number of weapons and targets and a range of p(i,j)'s which would cause similar behavior of Algorithm I.

There are many other special structures which the author, in collaboration with John Kattar, has examined. See Kattar [1985]. For many of the structures, variations of Algorithm I are useful. But, without information about the actual structure of a system, Algorithm I has been shown to have many desirable properties.

Whether Algorithms I or II or a variation of them is used, it would be done in a single pass through the problem leading to a solution. There are a number of algorithms which can be used after a solution is found by any one of these single pass algorithms; they will be called second pass algorithms.

One second pass algorithm would be to take away one weapon's assignments at the end and then run a single pass algorithm assigning the newly available projectiles. One interesting version of this is to randomly pick a weapon and allow the new solution to be somewhat worse than the previous solution without discarding it and going back to the previous solution. This can continue, with the size of the allowable penalty from the previous solution shrinking as a function of the number of iterations. In some sense, this is in the spirit of simulated annealing, which allows for the possibility of leaving the trap of a local optimum and going to the global optimum or at least a

better local optimum. This was not examined thoroughly; again some information about the structure of the p(i,j) matrix should be available before looking at this or any type of second pass algorithm. The author and John Kattar looked at some of these types of algorithms, but not in a completely systematic manner.

AD-A186 492 UNITED STATES AIR FORCE RESEARCH INITIATION PROGRAM 7/11
1985 TECHNICAL REPORT VOLUME 2(U) UNIVERSAL ENERGY
SYSTEMS INC DAYTON OH R C DARRAH APR 87
UNCLASSIFIED AFOSR-TR-87-1718 F49620-85-C-0013 F/G 15/3 NL

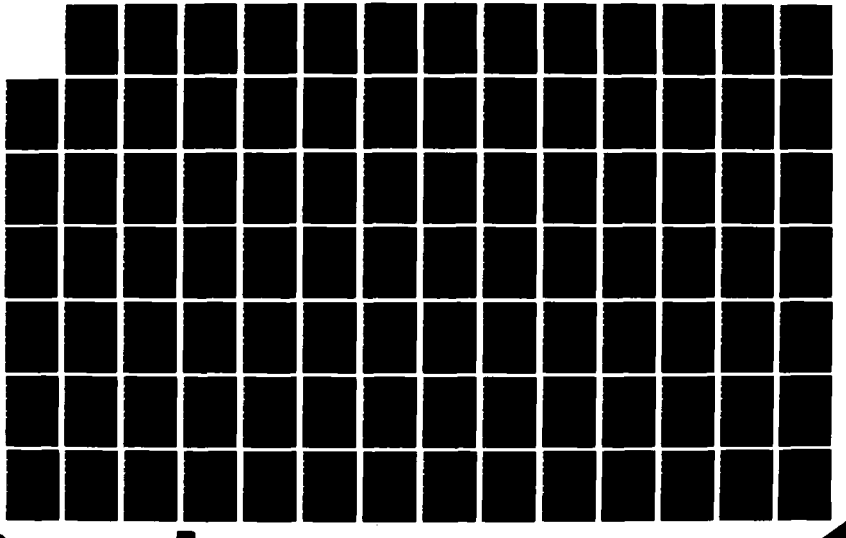

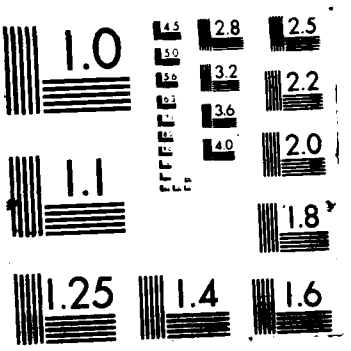
1.0
1.1
1.25
1.4
1.6
1.8
2.0
2.2
2.5
2.8
3.2
3.6
4.0

VIII. THE MULTI-PHASE PROBLEM

There are three phases or layers under consideration in this section: boost, post-boost, and midcourse. All targets which survive boost phase are single targets in post-boost phase; all targets which survive post-boost phase become multiple targets in midcourse phase. It is assumed that there is enough time to see the actual results in the previous phase when beginning a new phase.

Let

n = the number of targets (boosters) at the beginning,

S(1) = the surviving number of targets after phase 1 (Boost),

S(2) = the surviving number of targets after phase 2 (Post-Boost),

S(3) = the surviving number of targets after phase 3 (Midcourse).

There are m weapon platforms; each weapon has a(k) projectiles available at the start of phase k.

Let

u(i,k) = the number of projectiles on weapon i used on phase k;

x(i,j,k) = the number of weapons allocated from platform i to target j on phase k (these are the decision variables) and

It is very difficult to try to solve a problem similar to Problem I, that is, where the objective is to minimize the expected surviving target value. A more obtainable goal is to find:

1. { a(1) } = an initial supply of weapons on every weapon platform and

2. for all i,j,k, {x(i,j,k)} = a set of weapon to target assignments such that

P (S(i) <= g(i)) >= 1 - e for i=1,2,3 where g(i)

is a predetermined goal and e is a small positive number. Note that a probability is being controlled here, rather than the more usual expected value. The constraint then would have been stated "such that E[SBV] <= C, where C is a predetermined level".

One way to solve the last formulation, called Problem II, is to follow

the algorithm described below.

Algorithm III

The algorithm is stated as follows:

Step 1. Use Algorithm I and allocate the next weapon on the first phase.

Step 2. Calculate P (S(1) <= g(1)) = p(1).

Step 3. If p(1) >= (1 - e) go to step 4,otherwise go to step 1.

Step 4. Use Algorithm I and allocate the next weapon optimally on the second phase.

Step 5. Calculate P (S(2) <= g(2)) = p(2).

Step 6. If p(2) >= (1 - e) go to step 7, otherwise go to step 4.

Step 7. Allocate the next weapon optimally on the third phase.

Step 8. Calculate P (S(3) <= g(3)) = p(3).

Step 9. If p(3) >= (1 - e) done, otherwise go to step 7.

Note that there are assumed to be an infinite number of weapons available on each platform to start. One result of the algorithm is how many weapons are actually needed. Calculation of steps 2,5 and 8 is straightforward but tedious for exact calulations. As was noted in Section II, the Central Limit Theorem is appropriate and makes approximate calculations very easy. The calculations reduce to checking until the z-value of the goal number of hits is less than or equal to $- z_e$, the z-value with area under the normal curve to the left equal to e.

By substituting "value of targets" for "number of targets" above, the same analysis could be used to find a solution which satisfies goals based on value of targets hit rather than on number of targets hit.

IX. RESOURCE REQUIREMENTS

In this section a closed form approximation is developed which relates the following variables: number of targets, total number of projectiles, average single-shot probability of hit, goal number of hits, total cost, and the probability of achieving the goal number of hits. Using this approximation, it is straightforward to determine resource requirements (the number of projectiles) necessary to achieve overall system goals (getting the goal number of hits with a given probability). This approximation can be used in any phase (boost,post-boost or midcourse). This is a different and simpler approach than that of Section V. This approximation is useful in examining confidence and cost issues.

Let

g = the goal number of hits,

and e = the probability that $T < g$. (T is the total of hits.)

Let $v(j) = 1$ for all j; this is assumed because the emphasis here is to hit a certain number of targets, without regard to their value. Global confidence is defined to be the probability of hitting at least the goal number of targets, i.e. $P (T >= g)$; thus global confidence is numberically equal to $1 - e$. Getting the goal number of hits with a given global confidence will be called "achieving the goal of the system" in what follows.

Form a matrix of p(k,j)'s where each element is p^. Without loss of generality (since all the p(k,j)'s are the same) assume that there is one weapon platform (m = 1).

Then for any value of total projectiles a', an optimal assignment

$$x(1,j) = \begin{cases} ((a' - a' \bmod n) / n) + 1 & \text{for } j = 1 \text{ to } a' \bmod n \\ (a' - a' \bmod n) / n & \text{for } j = (a' \bmod n) + 1 \text{ to } n. \end{cases}$$

Suppose that a'= n; then x(1,j) = 1 is optimal.

Since T is approximately normally distributed (see Section II.)

$$\frac{g - np\hat{}}{\sqrt{(np\hat{}(1-p\hat{}))}} = -z_e \quad \text{(the z-score with probability e at or below)}$$

holds approximately.

This can be solved for p^; by simple manipulation the quadratic equation

$$p\hat{}^2(n^2 + z_e{}^2 n) - p\hat{}(2ng + z_e{}^2 n) + g^2 = 0$$

is derived.

The solution to use is:

$$p\hat{} = \frac{(2ng + z_e{}^2 n) + \sqrt{(2ng + z_e{}^2 n)^2 - 4g^2(n^2 + z_e{}^2 n)}}{2(n^2 + z_e{}^2 n)}$$

(The other solution gives z_e instead of $-z_e$.)
Note that a lower bound for p^ is g/n (the value of p^ when $z_e = 0$).

Thus, for the allocation (x(1,j) = 1 for all j) to achieve the goal of the system implies a uniform single shot probability of p^ above. The probability of any single projectile missing a target in this situation is (1 - p^).

Now suppose that a matrix of unequal p(k,j)'s is given. Let p be the average of all the non-zero p(k,j)'s. Form a new matrix: p(k,j) = p for all k and j. (The values p and p^ are not necessarily the same; in fact, it's very unlikely that they would be equal.) That is, all the projectiles are assumed to be identical in performance, but their single-shot probability of hitting any target is most likely different than what is needed to achieve the goal of the system with one shot at each target. Again, we can assume one weapon platform (m = 1) without loss of generality. If a continuous number of projectiles could be sent from a weapon platform, an equivalent way to guarantee achieving

the goal of the system is to have each weapon platform send out a projectiles, where a is the solution to the following:

$$(1 - p)^a = (1 - p\hat{}) \text{ for } a > 1.$$

The value a must be larger than one, else (1 - p) will be raised to a fractional power increasing the left hand side instead of decreasing it.

The solution is $a = \ln (1-p\hat{}) / \ln (1-p)$. The condition $a > 1$ implies $p\hat{} > p$. Since the lower bound of $p\hat{}$ is g/n, the approximation should definitely not be used unless $p < g/n$.

Since there are n targets, a' = the smallest integer larger than (na) gives an approximate value for the overall global requirement of projectiles needed to achieve the criterion

$$P (H > g) = 1 - e,$$

and hence to achieve the goal of the system.

Clearly, this solution a'is only an approximation of the actual number of projectiles needed to achieve the goal of the system. It should be emphasized that if there is one known matrix { p(k,j) }, the calculation of the number of needed projectiles to achieve the goal of the system, using what is an optimal or near optimal assignment, is not an onerous one.

The approximation is least accurate for values of p, the actual average single-shot probability of hitting a target, close to one. This is as a result of the skewness of the distribution of the number of hits (H); the closer p is to one, the more skewed the distribution of H will be. The Central Limit Theorem does guarantee that in the limit, as the number of targets gets very large, the approximation becomes more accurate. Thus, the predictions from the approximation should become better on average as the number of targets increases. Also, for the same reason the predictions from the approximation should become better on average as the proportion of goal hits decreases.

Table 1: Comparison of predicted and actual number of projectiles needed to achieve the goal of the system

Number of Targets	Goal Number of Hits	Global Confidence	Single Shot Hit Probability	Projectiles Needed- Actual	Predicted	Per Cent Error
500	450	0.99	0.8	895	813	-9.2%
500	450	0.99	0.6	1453	1429	-1.7%
500	450	0.99	0.4	2577	2563	-0.5%
500	450	0.99	0.2	5877	5866	-0.2%
500	450	0.75	0.8	839	744	-11.3%
500	450	0.75	0.6	1358	1306	-3.8%
500	450	0.75	0.4	2370	2343	-1.1%
500	450	0.75	0.2	5374	5363	-0.2%
500	400	0.99	0.8	618	566	-8.4%
500	400	0.99	0.6	997	994	-0.3%
500	400	0.99	0.4	1813	1783	-1.7%
500	400	0.99	0.2	4091	4083	-0.2%
500	400	0.75	0.8	537	519	-3.4%
500	400	0.75	0.6	941	911	-3.2%
500	400	0.75	0.4	1661	1635	-1.6%
500	400	0.75	0.2	3757	3743	-0.4%

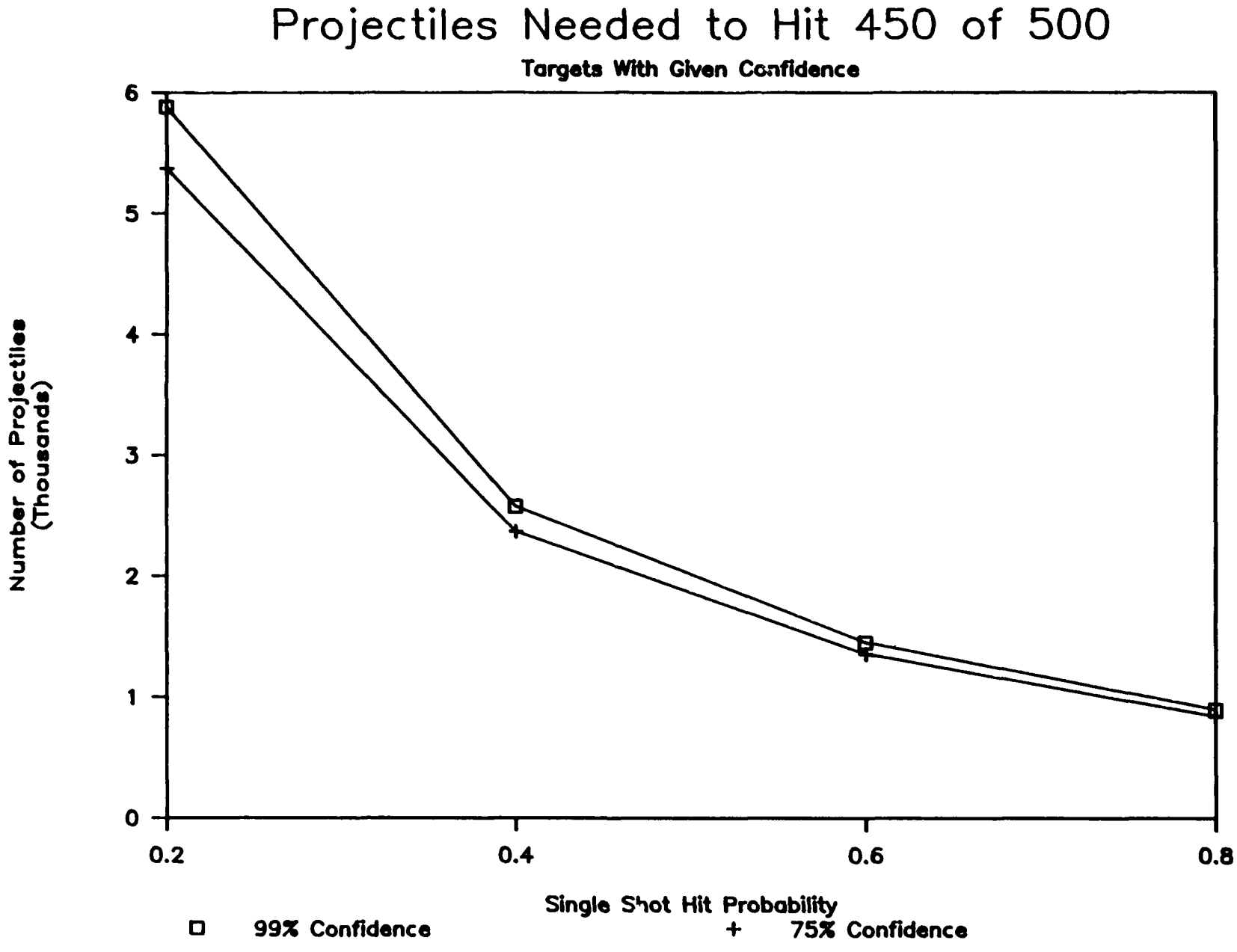
Projectiles Needed to Hit 450 of 500
Targets With Given Confidence
Number of Projectiles (Thousands)
6
5
4
3
2
1
0
0.2
0.4
0.6
0.8
Single Shot Hit Probability
99% Confidence
75% Confidence

Though much more sophisticated approximations were developed in Section V, the approximation in the Section has a number of uses. First of all, it indicates that to achieve much higher global confidence, it is not necessary to use many more projectiles. Secondly, while the total number of projectiles necessary to achieve the goals of the system increases as a function of p (the average single-shot probability of hit), the total cost of the projectiles does not necessarily increase.

Suppose the cost of firing an individual projectile is only a function of the single-shot probability of hit. This cost could include the actual cost of making the projectile, sending it into space and controlling it once in space. It seems reasonable that the higher the probability of hit, the more expensive the projectile would be. Using the following notation,

c(p) = the cost of firing an individual projectile, with single shot probability of hit equal to p,

let

$$c(p) = C_0 \, (-\ln (1-p)).$$

If this cost function is assumed then the total cost of all projectiles necessary to achieve the goals of the system (TCS) is

$$TCS = a \; n \; c(p)$$

$$= n \; C_0 \; (\ln(1-p\hat{}\,)).$$

Thus TCS is not a function of p, when c(p) is as above. If the cost of a projectile increases as a function of p more rapidly than c(p), it would be less costly to use many relatively cheap projectiles to achieve the goal of the system. If the cost of a projectile increases less rapidly than c(p), it would be less costly to use few relatively expensive projectiles.

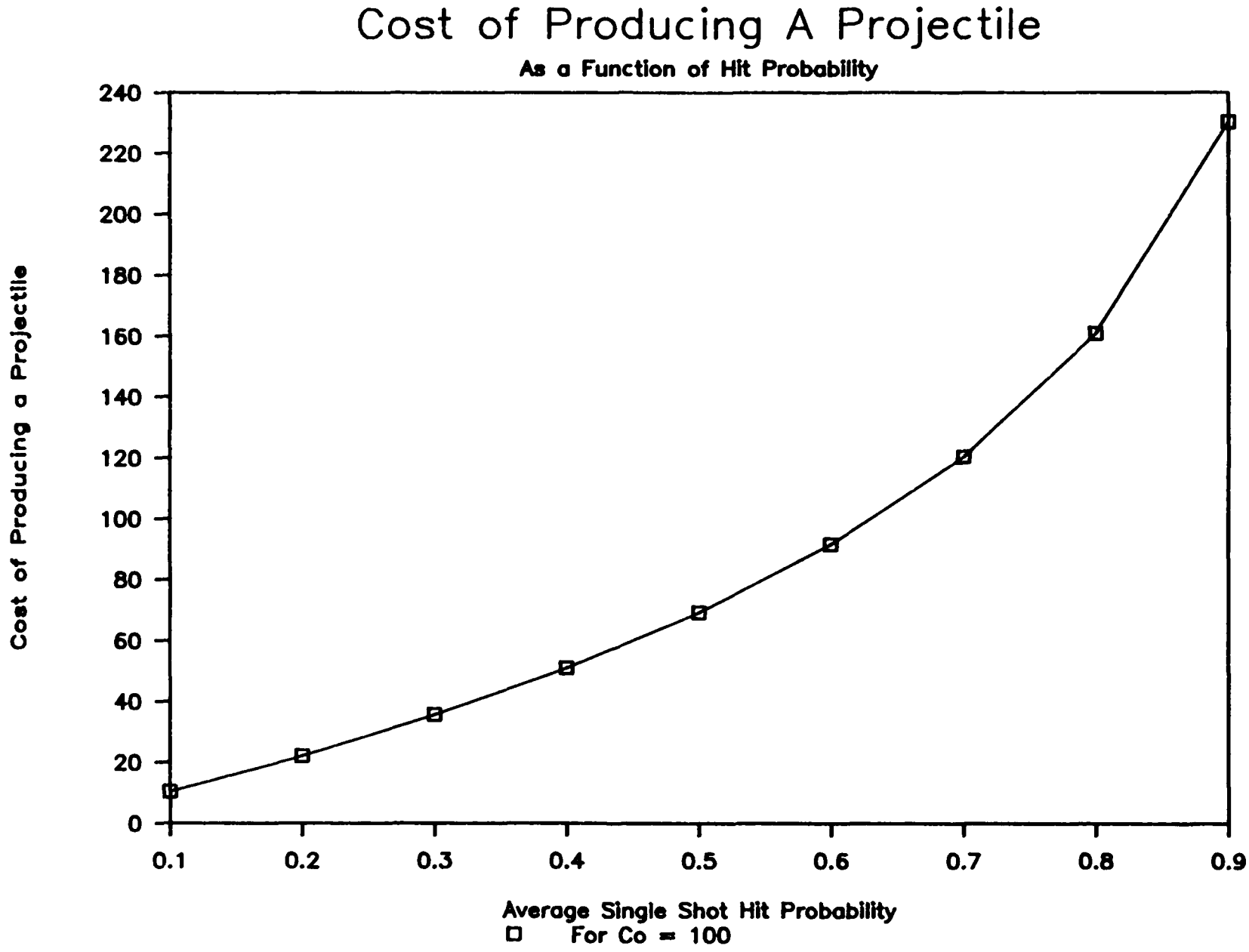
Cost of Producing A Projectile
As a Function of Hit Probability
Cost of Producing a Projectile
240
220
200
180
160
140
120
100
80
60
40
20
0
0.1
0.2
0.3
0.4
0.5
0.6
0.7
0.8
0.9
Average Single Shot Hit Probability
For Co = 100

X. CONCLUSIONS

Much is now known about the the performance of Algorithm I. Without specific information about the structure of the p(i,j), Algorithm I is the Algorithm of choice.

The method of analysis used is as important as the analysis. Whether or not the problem's formulation in this report is the best one, it is hard to imagine that there will not be diminishing marginal returns of some type when assigning projectiles sequentially.

The analysis shows the importance of trying to measure the p(i,j)'s. If the problem is formulated differently, it is reasonable to conclude that it would be just as important to estimate the return function components in the different formulation as the p(i,j)'s in this formulation.

Finally, insight gained from thinking about the problem formulated this way aids in understanding any other type of formulation.

XI. SUMMARY

THE PROBLEM

- Weapon platforms are satellites containing projectiles.
- Targets are boosters or reentry vehicles.
- The problem is to assign projectiles to targets in order to minimize the surviving target value, subject to the available supply of projectiles.

ASSUMPTIONS

- The value of each target is known.
- The maximum probability over time of hitting a given target with a projectile from a given weapon platform is known for all targets and weapon platforms.
- There is probabilistic independence among projectiles.

RESULTS

- One way to solve the problem optimally is to use complete enumeration. However with 100 targets, 10 weapon platforms and 10 projectiles per weapon platform, there are approximately 10^{130} different possibilities.

- There is an algorithm, named Algorithm I, which assigns projectiles sequentially using a maximum marginal return criterion which seems to work reasonably well, based on preliminary data.

- There are second-pass algorithms which find solutions which improve upon those from Algorithm I.

- For any p(i,j) matrix and a given assigment of projectiles, the probability distribution of the number of hits can be calculated.

- There is a closed form approximation which relates the distribution of the number of hits to

  --the average PK

  --the number of targets

  --the total number of projectiles

  --the probability of achieving the "goal of the system" (hitting a certain number of targets)

- This approximation can be used for resource requirements for different degrees of confidence in achieving the goal of the system and in making cost calculations.

- Sufficient conditions for optimality were found.

- The algorithm is optimal in the limit as the number of weapon platforms increase.

- The algorithm is optimal at any point during the assigment process when no platform has been emptied of projectiles.

- There is a way to measure how well the algorithm performs in any given run.

- Simulation results agree with the analytic work. In practical terms, the size of the problem does not have to be extremely large for the algorithm to perform very well.

- For small problems, performance is quite good. The second pass algorithms are useful in small problems and are reasonable to use in such cases.

- There is a closed form approximation, exact in the limit, which relates the expected value of the surviving targets to

  --the distribution(s) of the p(i,j)'s

  --the number of targets

  --the number of weapon platforms

  --the number of projectiles per weapon platform

- The performance of Algorithm I was compared with that of "Algorithm D". Algorithm D assigns projectiles independently of the (positive) value of PK. Algorithm D is a proxy for the policy of estimating whether a given PK is positive or zero, but not estimating the magnitude.

WHAT IS THE VALUE OF THIS ANALYSIS?

- Much is now known about the algorithm.
- The method of analysis used is as important as the analysis.
- Shows the importance of trying to measure the p(i,j)'s.
- Insight gained from thinking about the problem formulated this way aids in understanding any other type of formulation.

XII. BIBLIOGRAPHY

1. Bellman, R. and S. Dreyfus, "On a Tactical Air-Warfare Model of Mengel," Operations Research, Vol. 6, pp. 65-78 (1958).

2. Bogart, Kenneth P., Introductory Combinatorics, Pitman Publishing, Inc., Marshfield, Mass., 1983

3. Bracken, J., J.E. Falk, and F.A. Miercort, "A Strategic Weapons Exchange Allocation Model," Operations Research, Vol 25, No. 6, pp. 968-976 (1977).

4. Burr, S.A., J.E. Falk, and A.F. Karr, "Integer Prim-Read Solutions to a Class of Target Defense Problems," Operations Research, Vol. 33, pp. 726-745 (1985).

5. Day, R.H., "Allocating Weapons to Target Complexes by Means of Nonlinear Programming," Operations Research, Vol. 14, pp. 992-1013 (1966).

6. denBroeder, G.G., Jr., R.E. Ellison and L. Emerling, "On Optimum Target Assignment," Operations Research, Vol. 7, pp. 322-326 (1959).

7. Everett, H., III, "Generalized LaGrange Multipler Method for Solving Problems of Optimum Alloction of Resources," Operations Research, Vol. 11, pp. 399-417 (1963).

8. Feller, William, An Introduction to Probability Theory and Its Applications, Volume I, Third Edition, John Wiley & Sons, Inc., New York, 1968

9. Firstman, S.I., "An Approximating Algorithn or An Optimum Aim-Points Problem," Nav Res Log Quart, Vol. 7, pp. 151-167, (1960).

10. Kattar, John D., "Solution of the Multi-Target Multi-Weapon Assignment Problem," WP 26597, The MITRE Corporation, December 1985

11. Lemus, F. and K.H. David, "An Optimum Allocation of Different Weapons to a Target Complex," Operations Research, Vol. 11, pp. 787-794 (1963).

12. Manne, A.S., "A Target-Assignemnt Problem," Operations Research, Vol. 6, pp. 346-351 (1958).

13. Matlin, S., "A Review of the Literature on the Missile-Allocation Problem," Operations Research, Vol. 18, pp. 334-373 (1970).

14. Miercort, F.A. and R.M. Soland, "Optimal Allocation of Missiles Against Area and Point Defenses," Operations Research, Vol. 19, pp. 605-617 (1971).

15. Nunn, W.R., D.V. Glass, I. Hsu, and D. Perin, "Analysis of a Layered Defense Model," Operations Research, Vol. 30, No. 3, pp. 595-599 (1982).

16. Passy, U., "Nonlinear Assignment Problems Treated by Geometric Programming," Operations Research, Vol 19, pp. 1675-1690 (1971).

17. Picariello, H.J., "A Missile Allocation Problem," Operations Research, Vol. 10, pp. 795-798, (1962).

18. Soland, R.M., "Optimal Defensive Missile Allocation: A Discrete Min-Max Problem," Operations Research, Vol. 21, pp. 590-596 (1973).

19. Walkup, D.W. and M.D. MacLaren, "A Multiple-Assignment Problem," Math Note 347, Boeing, pp. 14, Apr (1964).

ACKNOWLEDGEMENTS

I would like to acknowledge the support and assistance of the Air Force Systems Command, Air Force Office of Scientific Research and ESD/MD. Without their support, this research would not have been possible. In particular, there were a number of individuals who were extremely helpful to me and to whom I owe great thanks. In ESD/XR, Mr. Gary Grann provided help, encouragement and overall support to me. In ESD/MD, Mr. George Richardson provided excellent logistical assistance and advice and Capt. Dan Cvelbar gave me an excellent military perspective on my research. Lt. Col. Ted Mervosh, made it possible for me to enrich my own professional background, thereby simultaneously benefitting the project. Col. Richard Paul showed a great willingness to listen to my comments and concerns, in the midst of his extremely busy schedule, providing strong support and encouragement to me.

In the MITRE Corporation, I would like to thank Dr. Bill Collins, whose questioning mind caused me to think deeply about the problem; Mr. Burt Noyes, who willingly shared his vast experience, expertise and intuition about the problem; and Dr. Rajan Batta, whose insightful comments proved helpful throughout. I would especially like to thank Mr. John Kattar, my colleague in this research, whose analytical and programming skills were in no small part instrumental to the success of this project.

Route Planning Problem

Sponsored by: Air Force Office of Scientific Research
Bolling AFB, DC.

Administered by: Universal Energy Systems, Inc.
4401 Dayton - Xenia Road
Dayton, Ohio 45432

Research Location: Rome Air Development Center
Command and Control Division
Applied C2 System Branch
Decision Aid Section
Griffiss Air Force Base, NY 13441

October, 1986

Final Report

Contract No. F49620-85-0013-SFRP/SB5851-0360

Subcontract No. S-760-OMG-015

Prepared by: Dr. Benjamin Lev, Principal Investigator
Chairman, Department of Management
School of Business and Management
Temple University
Philadelphia, Pa. 19122

ABSTRACT

This report presents two models for the Route Planning Problem. The objective is to identify an Optimal Route over enemy territory containing threats, each threat having both a probability of kill and a radius. First, we compute the risk of flying over a particular grid point. Next, we identify the optimal route from Origination Point to Destination Point which minimizes overall lethality. The second model includes the additional feature of multiple flying speeds. Fuel consumption is proportional to flying speed - the faster you fly, the more fuel you consume. With a limited amount of fuel on board, the problem is now more complicated. The goal is to identify the Optimal Route and the flying speeds for each leg of the route in order to minimize total lethality and consume an amount of fuel which does not exceed the amount of fuel on board the plane. Several examples are presented for both models.

ACKNOWLEDGMENTS

We would like to acknowledge the support of Mr. Yale Smith of the Rome Air Development Center. We especially appreciate the guidance of Major Robert J. Kruchten, the stimulating discussions with Mr. Clark Mollenhauer, and the moral encouragement of Dr. Diamond, Chief Scientist, all of Rome Air Development Center, Griffiss Air Force Base.

Many thanks to Mr. Rodney C. Darrah and his Staff from Universal Energy Systems, Inc. for administering this grant. This project was funded by Air Force Office of Scientific Research, Bolling AFB DC.

The author would like also to acknowledge Mr. Jyoti Paul who assisted in the computer programming and Miss. Lori Eppright who assisted in writing the final report.

The author takes sole responsibility for the content of the report.

1. INTRODUCTION

One of the oldest aviation problems is the Route Planning Problem. In planning his flying route from Origination Point to Destination Point, a pilot takes into consideration weather, topography, distance, fuel, weight, wind and many other factors. Although the shortest route from Origination Point to Destination Point is obviously the straight line between them, the territory over which the friendly pilot flies often contains enemy threats. When flying over an enemy threat the pilot risks being shot down. In this case, when risks are involved, the pilot is searching for the shortest route that avoids the threats. If it is impossible to avoid the threats, then the problem is to determine the route that minimizes the risk even though passing through the threats. The route which minimizes the risk might not be the shortest distance, but it is the least lethal route. The lethality is a utility function which represents the risk involved. The optimal route that minimizes the utility of the lethality also minimizes the overall risk of flying from Origination Point to Destination Point.

A pilot can fly at various speeds. The faster he flies the lower the probability of a successful mission. Fast flying consumes more fuel and shortens both the total flying distance and the total flying time available. A pilot thus should optimize his fuel consumption and his flying speed throughout the route.

2. OBJECTIVES OF THE RESEARCH EFFORT

A model is a compromise between complexity and accuracy. There is a tradeoff between the addition of features and the cumbersomeness of operating the model. We can always add more features, but the cost associated with those additional features is translated through the complexity of the model. We try to keep the model as simple as possible and yet expect it to meet the accuracy required by the user.

The Route Planning Problem has been studied for a long time. A research effort has been an on-going project for several years at The Rome Air Development Center in the Decision Aid Section. Mr. Clark Mollenhauer has been leading a research effort conducted at the Georgia Institute of Technology by Gene Coleman and Barnie Jones [5]. We did not have the opportunity to test their model, but it is our understanding that the model is very detailed, requires a large computer, and has an extremely long running time.

Major Kruchten has built an alternative model which solves a similar problem. His approach is a heuristic one where good solutions are obtained, but these solutions are not necessarily the optimal solutions. A pilot's approach in real life situations to this same problem is also a heuristic approach whereby the pilot is searching for a good and feasible solution which need not be the optimal one. It is good enough if the solution is within a certain percentage from the theoretical optimal solution. This is the approach taken by Major Kruchten in modeling and solving the problem. A good detailed description of this heuristic approach is given in [2].

Integrated Sciences Corporation conducted a study for the Office of Naval Research [1] that investigated ways to allocate functions between humans and computers. Part of their study was deciding the path that an aircraft would take to get to a target. Two possibilities were considered: a nonlinear programming approach and a dynamic programming approach. One of the conclusions of their study was that the dynamic programming approach is a viable and valid tool for solving the Route Planning Problem.

The objective of our research effort is to build a Route Planning model that is accurate enough in replicating the real life problem and at the same time can be solved in relatively short computer time. Among the different existing models the one we are building is placed somewhere between the following two extreme cases. At one extreme there are the detailed, cumbersome, sophisticated, slow models and at the other extreme there are the crude, robust, simple, straightforward approaches. The model that we suggest here is in between these two extremes. Our model is a simple one, can be solved in relatively short computer time, and is accurate enough for our needs.

The goal of this research is to demonstrate that the true optimal solution can be achieved using dynamic programming in reasonable computer time. This demonstrates that from a practical point of view dynamic programming is a viable vehicle to solve the problem. The model presents concepts rather than details.

Two versions of the model were built. The first searches

for the optimal route under the assumption that the airplane can fly at a single speed with no fuel restrictions imposed on the plane. A second model, more complicated and more sophisticated, does allow for multiple flying speeds. Each flying speed has a different fuel consumption rate with a total limited on board fuel amount. The optimal solution here includes both route and speed. At each leg of the route the model determines the optimal speed for that leg (Thus, the first model is a special case of the second model).

3. METHODOLOGY

A model was written using Fortran 77 for a Cyber 750. Some of the input data are coded and are part of the structure of the model. To change them one has to modify the code. The rest of the input data is inserted interactively. The model queries for specific input, and the operator must respond. The output of the model is directed to the screen in an on-line fashion. Alternatively, the output can be directed to a hard copy printer. A simple model can be run in less then ten minutes. First, we discuss a model with a single flying speed, for which flying speed is not a decision variable. Later, we consider multiple speeds with various fuel consumptions and search for both route and flying speed for each leg.

3.1 INPUT DATA

The model expects the following input data:

a. Origination Point (start of route)

b. Destination Point (end of route)

c. Threats

Each threat is represented by the coordination (x,y) of the center of the threat; the radius within which the threat is effective; the probability of kill of the threat*.

* The assumption is that the cells are small enough and the time that the airplane flies over each cell is very short. The probability (P) of being hit over one cell is independent of the probability of being hit over another cell.

The route can be anywhere in the rectangular field which defines the flying space of the airplane. Note that no restrictions are imposed on the locations of the Origination Point and/or the Destination Point. These points can be anywhere in the field -- inside a threat or outside a threat. A typical situation is of course when the starting point is outside all threats and the Destination Point is well protected by many threats and most likely is inside several threats. Implicit input data is a rectangular flying space computed internally by the model.

The field is divided into equally spaced grids. The refinement of the model depends on the number of grid points in the model. Each cell is an area surrounded by four grid points. The dimensions of the cell (its length and width) depend on the number of grid points in the field. The greater the number of grid points, the smaller the dimensions of the cells, and the more refined the model is. The more grid points we have, the more the cells shrink, and the more we can improve the model's resolution and pinpoint properties. Thus finer resolution is achieved with more grid points.

Our model assumes that the airplane moves from the center of one cell to the center of an adjacent cell, and that each cell can be addressed by the coordinates (i,j). The only legitimate moves are from the center of one cell to the centers of eight adjacent cells as shown in Figure 1 Case (a). From the center of cell (i,j), one can move to the centers of cells (i-1,j), (i+1,j), (i,j-1), (i,j+1), (i-1,j-1), (i-1,j+1), (i+1,j+1), (i+1,j-1). Obviously, when cell (i,j) is on the boundary of the

FIGURE 1 - LEGITIMATE MOVES TO A CELL

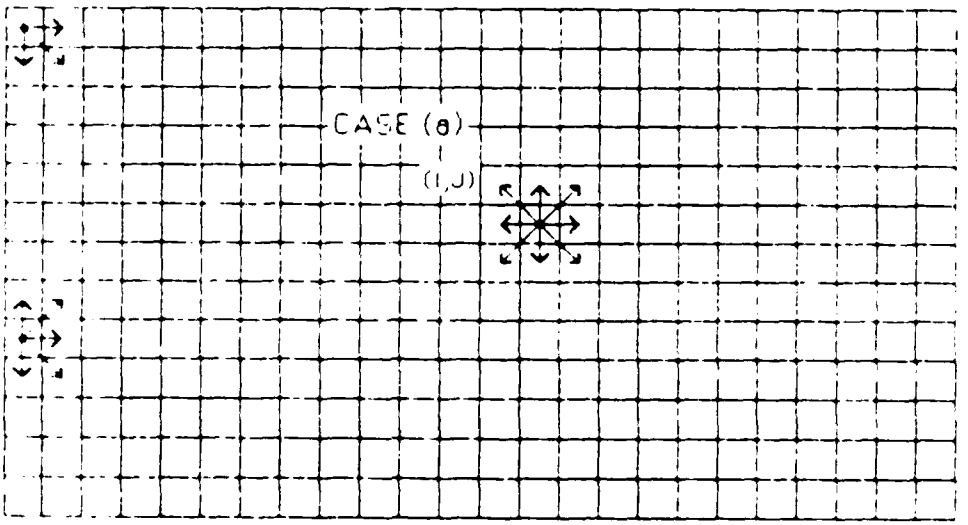

field, fewer than eight adjacent cells are legitimate moves. From side boundary point (k,l), Figure 1 Case (b) we can move to five adjacent cells. From a corner boundary point (m,n), Figure 1 Case (c), we can move to three adjacent cells.

3.2 THE SEARCH SPACE

A typical field has a grid size of 500 x 500, generating 250,000 cells. Each one of these 250,000 cells must be considered as a potential part of the optimal route, creating an enormous number of computations. It would be very advantageous to lower or to minimize the number of cells that are potentially on the optimal route. We can do this by eliminating those inferior points which could not conceivably be part of the optimal route.

For example, Figure 2 describes a field of 250,000 cells which contains four threats. Two arbitrary routes are depicted - Route A and Route B. Route A cannot be an optimal route because it is inferior to Route B. The Search Space that contains all potential cells that should be considered as part of the optimal route is the shaded envelope in Figure 2. No other point outside this shaded region can be part of the optimal solution, and therefore should not even be considered as part of the Search Space. By using this approach we can drastically reduce the number of cells to be considered by several orders of magnitude. This savings occurs in many real life situation problems.

The minimal Search Space is the convex combination generated

FIGURE 2 - SEARCH SPACE ENEVELOPE

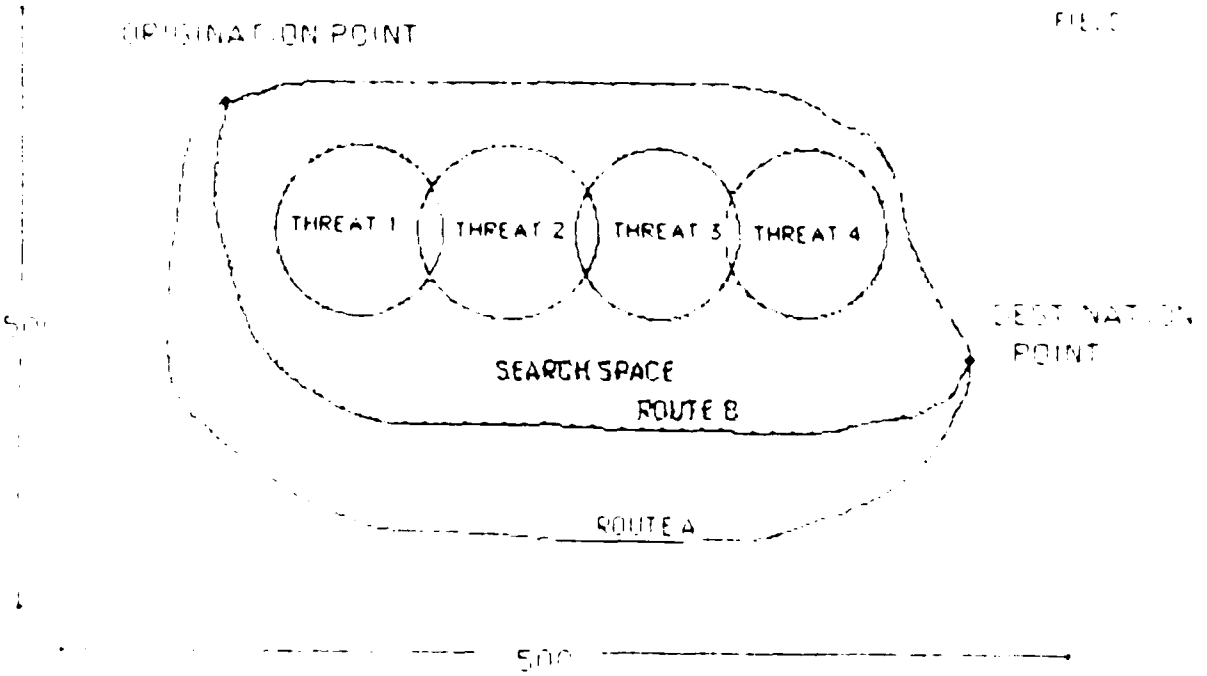

by all the threats and Origination Points and Destination Point as described in Figure 2. However, because of computer programming code simplifications, we have modified the Search Space. Figure 3 describes the Search Space considered in the model. The difference is that in Figure 2, the Search Space is a convex envelope, while in Figure 3, the Search Space is the smallest rectangle containing all threats, Origination Point and Destination Point.

One of the first matrices that we compute in solving the problem is in Table 1. Table 1 identifies every cell in the field and assigns a number to each cell. The number one means that the cell is under a single threat. For example cell (10,9) is within the range of a single threat. The number zero indicates that the cell is under no threat and is part of the Search Space. For example cell (8,11) is within the Search Space, but is not under any threat. The number two means that a cell is under two overlapping threats. For example cell (10,12) is under two threats. The OP indicates the Origination Point, and the DP indicates the Destination Point. The number -5 (an arbitrary number) indicates that this particular point is not covered by any threat and is outside the Search Space.

Notice that the Search Space is a little larger than just the threats. The model always adds an extra single column or single row allowing a safe flight around the threats. Without this the Search Space would be such that the pilot is forced to fly through the threats. With this extra column or row there is always the option of flying around threats (this of course does

FIGURE 3 SEARCH SPACE RECTANGLE

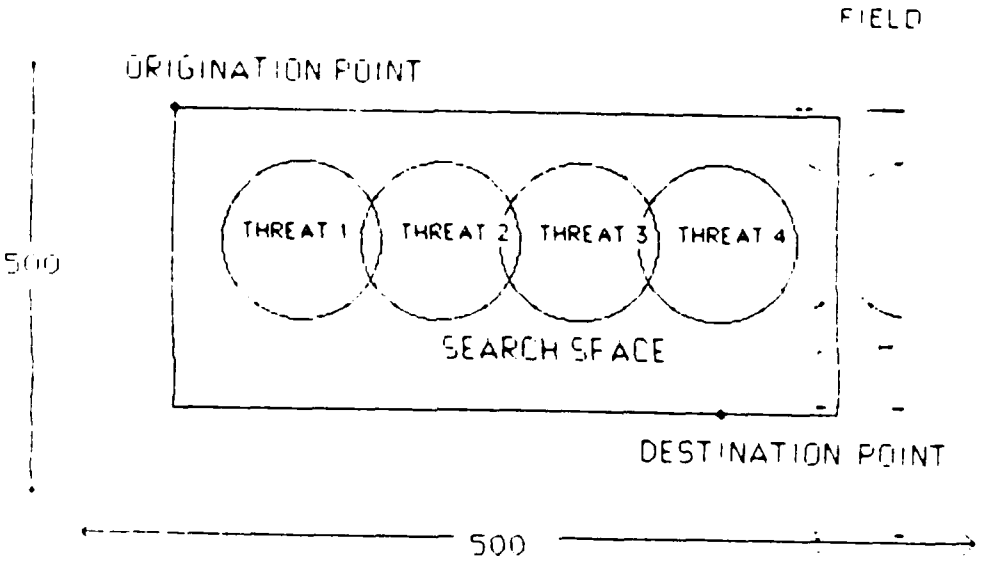

Table 1: Threat Matrix

I/J	1	2	3	4	5	6	7	8	9	10	11	12	13	14	15	16	17	18	19	20
1	-5	-5	-5	-5	-5	-5	-5	-5	-5	-5	-5	-5	-5	-5	-5	-5	-5	-5	-5	-5
2	-5	-5	-5	-5	-5	-5	-5	-5	-5	-5	-5	-5	-5	-5	-5	-5	-5	-5	-5	-5
3	-5	-5	-5	-5	-5	-5	-5	-5	-5	-5	-5	-5	-5	-5	-5	-5	-5	-5	-5	-5
4	-5	-5	-5	-5	-5	-5	-5	-5	-5	-5	-5	-5	-5	-5	-5	-5	-5	-5	-5	-5
5	-5	-5	-5	-5	-5	-5	-5	-5	-5	-5	-5	-5	-5	-5	-5	-5	-5	-5	-5	-5
6	-5	-5	-5	-5	-5	-5	-5	-5	-5	-5	-5	-5	-5	-5	-5	-5	-5	-5	-5	-5
7	-5	-5	-5	-5	-5	-5	0	0	0	0	0	0	0	0	0	-5	-5	-5	-5	-5
8	-5	-5	-5	-5	-5	-5	0	OP	0	1	0	0	0	0	0	-5	-5	-5	-5	-5
9	-5	-5	-5	-5	-5	-5	0	0	1	1	1	0	0	0	0	-5	-5	-5	-5	-5
10	-5	-5	-5	-5	-5	-5	0	1	1	1	1	2	0	0	0	-5	-5	-5	-5	-5
11	-5	-5	-5	-5	-5	-5	0	0	1	1	2	1	1	0	0	-5	-5	-5	-5	-5
12	-5	-5	-5	-5	-5	-5	0	0	0	2	1	1	1	1	0	-5	-5	-5	-5	-5
13	-5	-5	-5	-5	-5	-5	0	0	0	0	1	1	1	0	0	-5	-5	-5	-5	-5
14	-5	-5	-5	-5	-5	-5	0	0	0	0	0	1	0	DP	0	-5	-5	-5	-5	-5
15	-5	-5	-5	-5	-5	-5	0	0	0	0	0	0	0	0	0	-5	-5	-5	-5	-5
16	-5	-5	-5	-5	-5	-5	-5	-5	-5	-5	-5	-5	-5	-5	-5	-5	-5	-5	-5	-5
17	-5	-5	-5	-5	-5	-5	-5	-5	-5	-5	-5	-5	-5	-5	-5	-5	-5	-5	-5	-5
18	-5	-5	-5	-5	-5	-5	-5	-5	-5	-5	-5	-5	-5	-5	-5	-5	-5	-5	-5	-5
19	-5	-5	-5	-5	-5	-5	-5	-5	-5	-5	-5	-5	-5	-5	-5	-5	-5	-5	-5	-5
20	-5	-5	-5	-5	-5	-5	-5	-5	-5	-5	-5	-5	-5	-5	-5	-5	-5	-5	-5	-5

Legend

OP Origination Point
DP Destination Point
0 Unthreatened Cell
1 Cell Is Under One Threat
2 Cell Is Under Two Threats
-5 Not part of the Search Space

not exist if the threat reaches the boundary of the field).

For the rest of this paper we concentrate on the Search Space only and ignore the rest of the field. All future tables focus only on the non negative five (non -5) section of Table 1 which includes in this particular case columns 7 to 15 and rows 7 to 15.

3.3 THE LETHALITY FUNCTION

The objective of this model is to identify the optimal route. The optimization process is not a simple one since it combines flying over no threats, flying over a single threat and flying over multiple threats. For the purpose of the optimization process, we have to define a utility function that represents the risks involved in flying over no threats and of flying over threats. This utility function is called the lethality function. The properties of the lethality function should be that it always prefers to fly over no threats than to fly over threats, and it always prefers to fly over one threat than to fly over two threats, etc.. In addition, the lethality function should enable us to find the shortest route among all routes that pass over no threats and the shortest route among those that go over one threat and the shortest route among those that go over two threats etc. (No electronic warfare capabilities are assumed in this model).

Let $q_m(i,j)$ be the probability of kill caused by threat number m on cell (i,j). (If cell (i,j) is outside the range of threat m then obviously the probability is zero.)

An example of a lethality function is:

$P(i,j) = 10 +$ the sum over all m $(1000 \times q_m(i,j))$.

This lethality function P(i,j) is called the probability of kill (PK) and represents a case in which all cells have a minimal lethality level of 10 units per cell. In addition cell (i,j) if covered by threat m has an additional lethality of $1000q_m(i,j)$. The factor of 1000 has the effect of adding a huge penalty of $1000q_m(i,j)$ to cell (i,j) due to threat m. Finally the sum over all m simply adds penalties for all threats.

The interpretation of this lethality function is that by simply flying over a unthreatened cell, the pilot incurs a minimal lethality risk of 10 lethality units. However, if he flies over a threatened cell then the risk per cell is $10 + 1000q_m(i,j)$ lethality units which is an order of magnitude bigger.

Table 2 describes the Lethality Matrix when we have two threats, one with a probability of PK = .7 and the other with a probability of PK = .8. Some cells have a lethality level of 10. These are the unthreatened cells such as (8,11). Some cells have a lethality level of 710 which is computed by $10 + 1000(.7) = 710$ such as point (10,9). Some cells have a lethality level of 810 which is computed from $10 + 1000(.8) = 810$ such as point (12,11). Finally, there are some cells which are in the overlap of two threats, they incur a lethality level of 1510 computed from $10 + 1000(.7) + 1000(.8) = 1510$: (10,12) is such a point. Notice that Table 2 highlights only the Search Space containing columns 7 to 15 and rows 7 to 15 which is a subset of the field itself.

Table 2: Lethality Matrix

i/j	7	8	9	10	11	12	13	14	15
7	10	10	10	10	10	10	10	10	10
8	10	10	10	710	10	10	10	10	10
9	10	10	710	710	710	10	10	10	10
10	10	710	710	710	710	1510	10	10	10
11	10	10	710	710	1510	810	810	10	10
12	10	10	10	1510	810	810	810	810	10
13	10	10	10	10	810	810	810	10	10
14	10	10	10	10	10	810	10	10	10
15	10	10	10	10	10	10	10	10	10

Legend

10	Unthreatened Cell With Minimal Lethality
710	Cell is under a PK = .7 Threat
810	Cell is under a PK = .8 Threat
1510	Cell is under Two Threats, One with a PK = .7 and One with a PK = .8

A move from the center of a unthreatened cell to the center of a horizontal or vertical adjacent cell incurs a lethality of 10 units. However a diagonal move to an adjacent diagonal cell incurs a higher lethality since the distance is further. We assume that the lethality on a diagonal move is 14 units computed by the square root of($10^2 + 10^2$) = approx 14 (computed from a right triangle with all numbers truncated at the decimal points). Similarly if the horizontal or vertical lethality is 710 then the diagonal move is 710 x 1.4 = 994 and for the 810 horizontal or vertical move the diagonal move is 810 x 1.4 = 1134. Finally for the 1510 horizontal or vertical move the diagonal move is 1510 x 1.4 = 2114.

3.4 THE ALGORITHM

3.4.1 SINGLE SPEED WITH NO FUEL CONSIDERATION MODEL

Starting from the Origination Point, we first compute cumulative lethality to all cells which are under no threats. The technique we use is grid-oriented forward dynamic programming with a recursive equation explained in Appendix A. Table 3 (a) presents the cumulative lethality from the Origination Point (8,8) to all unthreatened cells.

The Origination Point is (8,8) and the cumulative lethality at (8,8) is obviously zero, but as you move to cell (7,8) the cumulative lethality is 10 (a horizontal move), or if you move to cell (7,9) the cumulative lethality is 14 (a diagonal move). The cumulative lethality from the Origination Point to cell (7,10) is 24 units consisting of a single diagonal and a single vertical

Table 3: Cumulative Lethality From Origination Point (8,8) to all Cells

(a)

i/j	7	8	9	10	11	12	13	14	15
7	14	10	14	24	34	44	54	64	74
8	10	0	10	*	38	48	58	68	78
9	14	10	*	*	*	52	62	72	82
10	24	*	*	*	*	*	66	76	86
11	34	38	*	*	*	*	*	80	90
12	44	48	52	*	*	*	*	*	94
13	54	58	62	66	*	*	*	108	104
14	64	68	72	76	80	*	108	118	114
15	74	78	82	86	90	94	104	114	124

Legend: * Area Represents Cells Under Threats

(b)

i/j	7	8	9	10	11	12	13	14	15
7	14	10	14	24	34	44	54	64	74
8	10	0	10	720	38	48	58	68	78
9	14	10	720	1004	748	52	62	72	82
10	24	720	1004	1714	1046	*	66	76	86
11	34	38	748	1046	*	1200	876	80	90
12	44	48	52	*	1200	2010	1214	890	94
13	54	58	62	66	876	1214	918	108	104
14	64	68	72	76	80	890	108	118	114
15	74	78	82	86	90	94	104	114	124

Legend: * Area Represents Cells Under Two Threats

Final Lethality Matrix Showing Cumulative Lethality From Origination Point (8,8) to All Cells

(c)

i/j	7	8	9	10	11	12	13	14	15
7	14	10	14	24	34	44	54	64	74
8	10	0	10	720	38	48	58	68	78
9	14	10	720	1004	748	52	62	72	82
10	24	720	1004	1714	1046	1562	66	76	86
11	34	38	748	1046	2556	1200	876	80	90
12	44	48	52	1562	1200	2010	1214	890	94
13	54	58	62	66	876	1214	918	108	104
14	64	68	72	76	80	890	108	118	114
15	74	78	82	86	90	94	104	114	124

move (10 + 14 = 24). The cumulative minimal lethality from the Origination Point to (14,11) is 80 units, etc.. Table 3 (a) also contains * which consists of all threatened cells.

Next, the algorithm computes penetration points. The penetration points are boundary points from which a pilot penetrates inside the threatened region. Examples of penetration points are (8,8), (8,9), (7,9), (7,10), (7,11), (8,11), and many other points. The pilot flying into the threatened area must pass through at least one of these penetration points. In fact his last "safe cell" is a penetration point, just before entering the threats.

The next step of the algorithm is to compute the cumulative lethality from the Origination Point to all cells that are covered by a single threat this step is presented in Table 3 (b). For example, the cumulative lethality from Origination Point to (9,9) is 720 (a vertical move in a cell with 710 lethality from (8,9) where lethality is 10). Cumulative lethality to point (11,10) is 1046 consisting of several legs over cells with no threats and a diagonal step over a cell with a threat. Once we have computed all cumulative lethalities to cells covered by a single threat, we compute new penetration points for the cells covered by two threats. These penetration points are (9,11), (9,12), (9,13), (10,11), (10,13), (11,10), (11,12), (12,9), (12,11), (13,9), (13,10), (13,11). The next step is to compute cumulative lethality for all cells covered by two threats. This process repeats itself until all the cells in the Search Space have cumulative lethality. The final cumulative lethality is

presented in Table 3 (c).

All that is left now is to identify the Destination Point. The cumulative lethality for the Destination Point is the minimal lethality from the Origination Point to that Destination Point. One has to backtrack the process to identify the optimal route. Some examples will be discussed in the next section.

Notice that the problem we solve here is the optimal route from point A to point B. If one wants to compute the optimal route from point A to point B and return to point A, two options are available. The first option is to solve from A to B and then from B to A. The second option is to solve the route from A to B and assume it is similar to the solution from B to A. In case of fuel consumption, the amount of fuel on board the plane must be twice as much as we use in this model (for the return trip).

3.4.2 MULTIPLE SPEEDS WITH FUEL CONSIDERATION MODEL

This model is a complicated version of the one described above. It has the additional feature that allows pilots to choose their flying speed. Obviously the pilot prefers to fly fast to minimize his risk, but flying fast consumes more fuel. If fuel is not a binding constraint, pilots will always fly fast, but often the case is that fuel quantity is a restriction. The optimization process should therefore identify over which legs of the route the pilot should go fast and over which ones the pilot should go slower.

For the sake of simplicity let us assume that a plane can fly only at three speeds: slow, average, and fast (this can be easily expanded to five speeds or more at the expense of a larger

computer memory and longer running time). Fuel consumption increases approximately quadratically with flying speed. For example, if speed is twice as fast, fuel consumption is $2^2 = 4$ times higher. If speed is 10% faster, then fuel consumption is $(1.1)^2 = 1.21$ or 21% more fuel is required. If speed is 20% less, then fuel consumption is $(.8)^2 = .64$ or fuel consumption is 36% less, etc.. We assume a simple case of fuel consumption as presented in Table 4. A move from the center of one cell to the center of an adjacent horizontal or adjacent vertical cell at an average speed requires five units of fuel. The same steps at a slow speed require only three units of fuel and at a fast speed require eight units of fuel. Diagonal moves are approximately the square root of (2) = 1.4 or 40% higher than horizontal/vertical moves. Because of truncating, fuel consumption for a diagonal move for slow, average, fast speeds are 4, 7, 11 fuel units respectively.

The risk involved over a cell decreases as flying speed increases. We assume an inverse linear relationship between flying speed and lethality. A horizontal/vertical move from one adjacent cell to another at an average speed carries an exposure of 10 lethality units. The same step at a slow speed increases the lethality by 20% to 12 units, and the same step at a fast speed decreases the exposure by 20% to 8 lethality units. Diagonal moves carry an exposure risk which is the square root of (2) = 1.4 or about 40% higher lethality. As presented in Table 4, slow, average, and fast flying speeds carry exposures of 16, 14, and 11 lethality units respectively (all

Table 4: Multiple Speeds Model With Fuel Restriction
(Fuel Consumptions and Lethalities)

Speed		Slow	Average	Fast
Fuel Consumption	Horizontal/ Vertical Step	3	5	8
	Diagonal Step	4	7	11
Lethality	Horizontal/ Vertical Step	12	10	8
	Diagonal Step	16	14	11

(Note: Diagonal Steps are 1.4 of Horizontal/Vertical Steps and are Truncated. Slow and Fast Speeds are 20% Away From Average Values.)

numbers are truncated to integers). Of course Table 4 is an arbitrary table and the user can simply change the data at will. This discussion relates to unthreatened cells with a minimal lethality level of 10. If, however, we fly over a threat with a lethality level of say, 710, all exposure values must be multiplied by 710 for the speed adjustments, but fuel consumption remains unchanged. For example, if the cell has a lethality level of 710, the slow, average, fast lethality levels are 852, 710, 568 respectively for a horizontal/vertical move and 1192, 994, 795 respectively for a diagonal move.

The grid-oriented forward dynamic programming recursive equation for the multiple speeds model is discussed in Appendix B. Basically it is very similar to the previous model except that it has three state variables, coordinations (i,j) and of the amount of fuel on board. The feasible movements from cell (i,j) are to eight adjacent cells at three different speeds for a total of 8 x 3 = 24 different combinations. Each one of the movements requires a different amount of fuel and carries a different lethality level.

4. RESULTS AND FURTHER RESEARCH

A computer program is available at Temple University that solves the Route Planning Problem. The user can submit different input data and obtain the optimal route. In this section we present some sample problems to demonstrate the various features of the model. First, we present a set of five examples for which the airplane flies with a single speed, and fuel is not a consideration. Second, we present two sets of examples for which the airplane can fly at three speeds with different fuel consumptions at each speed, and where fuel quantity is a restriction. For each one of the two sets of examples, we vary the amount of fuel on board and demonstrate how the optimal route varies with the amount of fuel available.

Finally, in this section we present some ideas for further research.

4.1 RESULTS - SINGLE SPEED WITH NO FUEL RESTRICTION

Five examples are presented whereby an airplane can fly at a single speed and plenty of fuel is on board. Thus, fuel is not a constraint, and the only objective is to determine the optimal route. In each example, we try to highlight a different special situation and the ability of the model to handle these different cases.

EXAMPLE 1:

Example 1 is a simple case where there are two threats which overlap, and the problem is such that there is an optimal route

around the threats. Because there is no fuel restriction, the optimal route does not fly over any threat. Table 5 (a) presents the problem and its solution. The Origination Point is indicated by OP; the Destination Point is indicated by DP. Zero indicated an unthreatened cell. One indicates that a cell is threatened by a single threat, and two indicates that the cell is threatened by two threats. Table 5 (b) shows the lethality levels at every cell (10 units for unthreatened cell, 710 units for a cell threatened by a PK = .7 threat, and 1510 for a cell threatened by two threats, one with a PK = .7 and the other with a PK = .8). As seen in Tables 5 (a) and 5 (b), the optimal route passes around all threats. Table 5 presents the solution and the various legs of the route. There are seven diagonal legs and two horizontal/vertical legs, and all legs are over unthreatened cells. The total lethality for this optimal route is 118 units (2x10 + 7x14 = 118).

EXAMPLE 2:

This example presents a problem where the Destination Point is inside a threat. In this case, the Destination Point (10,7) is inside a threat with a PK = .8. The model identifies a route which avoids all threats, except of course the Destination Point threat. The example and optimal route are presented in Table 6 (a) and Table 6 (b). The optimal solution consists of two horizontal/vertical legs and six diagonal legs. The legs of the route are shown in Table 6. The total lethality for this example is 904 lethality units.

Table 5: Example 1 - Single Speed Model With No Fuel Restriction

Legend: OP=Origination Point,DP=Destination Point,0=Unthreatened Cell
1=Cell Threatened By One Threat, 2=Cell Threatened By Two Threats
[ ] Indicates Cells On Optimal Route

(a) Threat Matrix

i/j	3	4	5	6	7	8	9	10	11	12	13	14	15
1													
2													
3													
4													
5													
6													
7					0	0	[0]	[0]	0	0	0	0	0
8					0	[OP]	0	1	[0]	0	0	0	0
9					0	0	1	1	1	[0]	0	0	0
10					0	1	1	1	1	2	[0]	0	0
11					0	0	1	1	2	1	1	[0]	0
12					0	0	0	2	1	1	1	1	[0]
13					0	0	0	0	1	1	1	[0]	0
14					0	0	0	0	0	1	0	[DP]	0
15					0	0	0	0	0	0	0	0	0

(b) Lethality Matrix

i/j	3	4	5	6	7	8	9	10	11	12	13	14	15
1													
2													
3													
4													
5													
6													
7					10	10	[10]	[10]	10	10	10	10	10
8					10	[10]	10	710	[10]	10	10	10	10
9					10	10	710	710	710	[10]	10	10	10
10					10	710	710	710	710	1510	[10]	10	10
11					10	10	710	710	1510	810	810	[10]	10
12					10	10	10	1510	810	810	810	810	[10]
13					10	10	10	10	810	810	810	[10]	10
14					10	10	10	10	10	810	10	[10]	10
15					10	10	10	10	10	10	10	10	10

(c) Solution

Legs	From	To	H/V/D	# of Threats	Lethality Level
1	(8,8)	(7,9)	Diagonal	0	14
2	(7,9)	(7,10)	Horizontal	0	10
3	(7,10)	(8,11)	D	0	14
4	(8,11)	(9,12)	D	0	14
5	(9,12)	(10,13)	D	0	14
6	(10,13)	(11,14)	D	0	14
7	(11,14)	(12,15)	D	0	14
8	(12,15)	(13,14)	D	0	14
9	(13,14)	(14,14)	Vertical	0	10
				Total Lethality =	118

Table 6: Example 2 - Single Speed Model With No Fuel Restriction

Legend: OP=Origination Point,DP=Destination Point,0=Unthreatened Cell
1=Cell Threatened By One Threat, 2=Cell Threatened By Two Threats
[ ] Indicates Cells On Optimal Route

(a) Threat Matrix

I/J	3	4	5	6	7	8	9	10	11	12	13	14	15
4													
5		0	0	0	0	0	0	0	0	0	0	0	0
6		0	0	0	1	0	0	0	0	0	0	0	0
7		0	0	1	1	1	0	1	0	0	0	[OP]	0
8		0	1	1	1	1	2	1	1	0	[0]	0	0
9		0	0	1	1	2	1	1	1	1	[0]	0	0
10		0	0	0	[DP]	[0]	1	1	1	[0]	0	0	0
11		0	0	0	0	0	[0]	1	[0]	0	0	0	0
12		0	0	0	0	0	0	[0]	0	0	0	0	0
13													

(b) Lethality Matrix

I/J	3	4	5	6	7	8	9	10	11	12	13	14	15
4													
5		10	10	10	10	10	10	10	10	10	10	10	10
6		10	10	10	810	10	10	10	10	10	10	10	10
7		10	10	810	810	810	10	710	10	10	10	[10]	10
8		10	810	810	810	810	1510	710	710	10	[10]	10	10
9		10	10	810	810	1510	710	710	710	710	[10]	10	10
10		10	10	10	[810]	[10]	710	710	710	[10]	10	10	10
11		10	10	10	10	10	[10]	710	[10]	10	10	10	10
12		10	10	10	10	10	10	[10]	10	10	10	10	10
13													

(c) Solution

Legs	From	To	H/V/D	# of Threats	Lethality Level
1	(7,14)	(8,13)	D	0	14
2	(8,13)	(9,13)	V	0	10
3	(9,13)	(10,12)	D	0	14
4	(10,12	(11,11)	D	0	14
5	(11,11	(12,10)	D	0	14
6	(12,10	(11,9)	D	0	14
7	(11,9)	(10,8)	D	0	14
8	(10,8)	(10,7)	H	1	810
				Total Lethality =	904

EXAMPLE 3:

This example presents the problem with five overlapping threats. The Origination Point and the Destination Point are separated by the threats. There is no possible route that can be flown that avoids all of the threats. As can be seen in Table 7, the optimal route identified flies over only two threats, but it requires 20 legs to do so. The optimal route consists of 12 horizontal/vertical legs over unthreatened cells, two horizontal/vertical legs over a threatened cell, and eight horizontal legs over unthreatened cells. Total lethality for this route is 1424 units.

EXAMPLE 4:

Example 4 presents a problem with several threats. Some of the threats overlap, but we purposely allowed for a path with no threats. As can be seen in Table 8, an optimal route exists that passes between the threats. The model does identify this route. A pilot taking this route would not pass over any threatened cells, but the final step to the Destination Point would involve passing over a cell with a PK = .8. This optimal route consists of six horizontal/vertical legs and eight diagonal legs. The total lethality for this problem is 972 units.

EXAMPLE 5:

Example 5 presents a problem in which the target is deep inside a threat. The Origination Point is at an unthreatened cell. Obviously the optimal route must go through some of the threats as shown in Table 9. The optimal route consists of two horizontal/vertical legs and five diagonal ones. One of the

Table 7: Example 3 - Single Speed Model With No Fuel Restriction

Legend: OP=Origination Point,DP=Destination Point,Ø=Unthreatened Cell
1=Cell Threatened By One Threat, 2=Cell Threatened By Two Threats
[ ] Indicates Cells On Optimal Route

(a) Threat Matrix

i/j	2	3	4	5	6	7	8	9	10	11	12	13	14	15
1														
2		Ø	Ø	1	1	1	Ø	Ø	Ø	Ø	Ø	Ø	Ø	
3		Ø	1	1	1	1	2	Ø	Ø	Ø	Ø	Ø	Ø	
4		Ø	[OP]	1	1	2	1	1	Ø	Ø	Ø	Ø	Ø	
5		Ø	[Ø]	Ø	2	1	1	1	1	1	Ø	Ø	Ø	
6		Ø	[Ø]	Ø	Ø	2	1	1	1	1	1	Ø	Ø	
7		Ø	[Ø]	Ø	1	1	2	1	1	1	1	1	Ø	
8		Ø	[Ø]	1	1	1	1	1	1	1	1	Ø	Ø	
9		Ø	[Ø]	Ø	1	1	1	1	Ø	1	Ø	Ø	Ø	
10		Ø	[Ø]	Ø	Ø	2	1	1	1	1	Ø	Ø	Ø	
11		Ø	[Ø]	Ø	Ø	1	1	1	1	[DP]	[Ø]	Ø	Ø	
12		Ø	[Ø]	Ø	1	1	1	1	1	1	1	[Ø]	Ø	
13		Ø	Ø	[Ø]	Ø	1	1	1	1	1	[Ø]	Ø	Ø	
14		Ø	Ø	Ø	[Ø]	1	1	1	1	1	[Ø]	Ø	Ø	
15		Ø	Ø	Ø	Ø	[Ø]	[Ø]	[1]	[Ø]	[Ø]	Ø	Ø	Ø	

(b) Lethality Matrix

i/j	2	3	4	5	6	7	8	9	10	11	12	13	14	15
1														
2		10	10	610	610	610	10	10	10	10	10	10	10	
3		10	610	610	610	610	1310	10	10	10	10	10	10	
4		10	[10]	610	610	1310	710	710	10	10	10	10	10	
5		10	[10]	10	1310	710	710	710	710	710	10	10	10	
6		10	[10]	10	10	1510	710	710	710	710	710	10	10	
7		10	[10]	10	810	810	1510	710	710	710	710	710	10	
8		10	[10]	810	810	810	810	810	710	710	710	10	10	
9		10	[10]	10	810	810	810	610	10	710	10	10	10	
10		10	[10]	10	10	1410	610	610	610	610	10	10	10	
11		10	[10]	10	10	610	610	610	610	[610]	[10]	10	10	
12		10	[10]	10	610	610	610	610	610	610	610	[10]	10	
13		10	10	[10	10	610	610	610	610	610	[10]	10	10	
14		10	10	10	[10]	610	610	610	610	610	[10]	10	10	
15		10	10	10	10	[10]	[10]	[610]	[10]	[10]	10	10	10	

*Note: Solution continues on the next page.

Table 7:Continued

(c) Solution

Legs	From	To	H/V/D	# of Threats	Lethality Level
1	(4,4)	(5,4)	V	0	10
2	(5,4)	(6,4)	V	0	10
3	(6,4)	(7,4)	V	0	10
4	(7,4)	(8,4)	V	0	10
5	(8,4)	(9,4)	V	0	10
6	(9,4)	(10,4)	V	0	10
7	(10,4)	(11,4)	V	0	10
8	(11,4)	(12,4)	V	0	10
9	(12,4)	(13,5)	D	0	14
10	(13,5)	(14,6)	D	0	14
11	(14,6)	(15,7)	D	0	14
12	(15,7)	(15,8)	H	0	10
13	(15,8)	(15,9)	H	1	610
14	(15,9)	(15,10)	H	0	10
15	(15,10	(15,11)	H	0	10
16	(15,11	(14,12)	D	0	14
17	(14,12	(13,12)	V	0	10
18	(13,12	(12,13)	D	0	14
19	(12,13	(11,12)	D	0	14
20	(11,12	(11,11)	H	1	610

Total Lethality = 1424

Table 8: Example 4 - Single Speed Model With No Fuel Restriction

Legend: OP=Origination Point,DP=Destination Point,0=Unthreatened Cell
1=Cell Threatened By One Threat, 2=Cell Threatened By Two Threats
[ ] Indicates Cells On Optimal Route

(a) Threat Matrix

i/j	2	3	4	5	6	7	8	9	10	11	12	13	14
2		0	0	0	1	1	1	0	0	0	0	0	
3		0	0	1	1	1	1	1	0	0	0	0	
4		0	[OP]	[0]	1	1	1	[0]	[0]	0	0	0	
5		0	0	0	[0]	1	[0]	0	1	[0]	0	0	
6		0	0	0	0	[0]	0	1	1	1	[0]	0	
7		0	0	0	0	0	1	1	1	1	1	[0]	
8		0	0	0	0	0	0	1	2	1	0	[0]	
9		0	0	0	0	0	0	1	2	1	0	[0]	
10		0	0	0	0	0	1	2	1	1	1	[0]	
11		0	0	0	0	0	1	2	2	[DP]	[0]	0	
12		0	0	0	0	1	1	1	2	1	0	0	
13		0	0	0	0	0	1	1	1	0	0	0	
14		0	0	0	0	0	0	1	0	0	0	0	
15		0	0	0	0	0	0	0	0	0	0	0	

(b) Lethality Matrix

i/j	2	3	4	5	6	7	8	9	10	11	12	13	14
2		10	10	10	710	710	710	10	10	10	10	10	
3		10	10	710	710	710	710	710	10	10	10	10	
4		10	[10]	[10]	710	710	710	[10]	[10]	10	10	10	
5		10	10	10	[10]	710	[10]	10	810	[10]	10	10	
6		10	10	10	10	[10]	10	810	810	810	[10]	10	
7		10	10	10	10	10	810	810	810	810	810	[10]	
8		10	10	10	10	10	10	810	1610	810	10	[10]	
9		10	10	10	10	10	10	810	1610	810	10	[10]	
10		10	10	10	10	10	810	1410	810	810	810	[10]	
11		10	10	10	10	10	610	1410	1410	[810]	[10]	10	
12		10	10	10	10	610	610	610	1410	610	10	10	
13		10	10	10	10	10	610	610	610	10	10	10	
14		10	10	10	10	10	10	610	10	10	10	10	
15		10	10	10	10	10	10	10	10	10	10	10	

(c) Solution

Legs	From	To	H/V/D	# of Threats	Lethality Level
1	(4,4)	(4,5)	H	0	10
2	(4,5)	(5,6)	D	0	14
3	(5,6)	(6,7)	D	0	14
4	(6,7)	(5,8)	D	0	14
5	(5,8)	(4,9)	D	0	14
6	(4,9)	(4,10)	H	0	10
7	(4,10)	(5,11)	D	0	14
8	(5,11)	(6,12)	D	0	14
9	(6,12)	(7,13)	D	0	14
10	(7,13)	(8,13)	V	0	10
11	(8,13)	(9,13)	V	0	10
12	(9,13)	(10,13)	V	0	10
13	(10,13)	(11,12)	D	0	14
14	(11,12)	(11,11)	H	1	810
				Total Lethality	972

Table 9: Example 5 - Single Speed Model With No Fuel Restriction

Legend: OP=Origination Point,DP=Destination Point,0=Unthreatened Cell
1=Cell Threatened By One Threat, 2=Cell Threatened By Two Threats
[ ] Indicates Cells On Optimal Route

(a) Threat Matrix

i/j	2	3	4	5	6	7	8	9	10	11	12
2											
3		0	0	[0]	[0]	0	0	0	0	0	
4		0	[OP]	0	1	[0]	0	0	0	0	
5		0	0	1	1	1	[0]	0	0	0	
6		0	1	1	1	1	2	[0]	0	0	
7		0	0	1	1	2	[1]	1	0	0	
8		0	0	0	2	2	[DP]	1	1	0	
9		0	0	0	1	2	2	1	0	0	
10		0	0	1	1	1	2	1	0	0	
11		0	0	0	1	1	1	0	0	0	
12		0	0	0	0	1	0	0	0	0	
13		0	0	0	0	0	0	0	0	0	
14											

(b) Lethality Matrix

i/j	2	3	4	5	6	7	8	9	10	11	12
2											
3		10	10	[10]	[10]	10	10	10	10	10	
4		10	[10]	10	710	[10]	10	10	10	10	
5		10	10	710	710	710	[10]	10	10	10	
6		10	710	710	710	710	1510	[10]	10	10	
7		10	10	710	710	1510	[810]	810	10	10	
8		10	10	10	1510	1410	[810]	810	810	10	
9		10	10	10	610	1410	1410	810	10	10	
10		10	10	610	610	610	1410	610	10	10	
11		10	10	10	610	610	610	10	10	10	
12		10	10	10	10	610	10	10	10	10	
13		10	10	10	10	10	10	10	10	10	
14											

(c) Solution

Legs	From	To	H/V/D	# of Threats	Lethality Level
1	(4,4)	(3,5)	D	0	14
2	(3,5)	(3,6)	H	0	10
3	(3,6)	(4,7)	D	0	14
4	(4,7)	(5,8)	D	0	14
5	(5,8)	(6,9)	D	0	14
6	(6,9)	(7,8)	D	1	1134
7	(7,8)	(8,8)	V	1	810

Total Lethality = 2010

diagonal legs and one of the horizontal/vertical legs are over a threat. The total lethality of this example is 2010 units.

Many more examples can be easily generated to demonstrate other capabilities of the model.

4.2 RESULTS - MULTIPLE SPEEDS AND FUEL RESTRICTIONS

In this section we present results for situations in which an airplane can fly at three different speeds, each speed having its own fuel consumption rate which increases as the speed increases. We show that the optimal route and the speeds required do change with the amount of fuel on board the airplane. We assume that if the fuel on board the airplane is 35 units, the amount of fuel that can be consumed can be only 34 units (no plane can arrive with zero fuel on board). We use Examples 1 and 5 of section 4.1 and for each Example we vary the amount of fuel on board and generate a set of examples. Examples 1.1-1.8 are all similar to Example 1, but the amount of fuel on board varies. Examples 5.1-5.6 are all similar to Example 5, but the amount of fuel on board varies.

EXAMPLES 1.1 - 1.8

Examples 1.1-1.8 are similar to Example 1 of the previous section except for the following change. In Examples 1.1-1.8, we allow the airplane to fly at three different speeds and to consume various amounts of fuel as described in Section 3.4.2 and in Table 4. In Example 1.1, the amount of fuel on board the plane is only 28 units. This is a very small amount of fuel, and the pilot is forced to fly over threats at a slow speed (worst

case). As seen in Table 10, the optimal route consists of two horizontal/vertical legs over unthreatened cells, one diagonal leg over an unthreatened cell, and four diagonal legs over threats. In order to save fuel the pilot's flying speed is always slow. The overall lethality is 5144 units.

As the amount of fuel on board the plane increases, two things happen. First, the pilot flies over unthreatened cells rather than over threatened cells, and secondly, as more and more fuel is available, the pilot increases his flying speed from slow to average and eventually to fast speeds. This is demonstrated in Examples 1.2 through 1.8, Tables 10-17. In Example 1.2, the fuel on board increases to 30 units. This is not enough to avoid the threats, but it is enough to fly somewhat faster as seen in Table 11. This allows the total lethality to decrease to 4918. In Example 1.3, the amount of fuel increases to 33 units. This amount of fuel enables the pilot to fly over only one threatened cell (down from four previous threatened cells). Flying speed is always slow and overall lethality has been drastically lowered to 1088 units. Note that there are more legs than previously (nine versus seven). In Example 1.4, fuel on board increases to 35 units, and the optimal route is over only unthreatened cells. Flying speed is still slow, but total lethality is reduced to 136 units. As the amount of fuel increases now to 37 units, flying speed increases, and lethality decreases to 134 units as shown in Example 1.5. Lethality reduces to 132 units in Example 1.6 as fuel increases to 40 units, and lethality decreases further to 110 units in Example 1.7 when fuel increases to 70 units.

Table 10: Example 1.1: Fuel=28 - Multiple Speeds Model
With Fuel Restriction

Legend: OP=Origination Point,DP=Destination Point,0=Unthreatened Cell
1=Cell Threatened By One Threat, 2=Cell Threatened By Two Threats
{}=Leg at Slow Speed,[]=Leg at Average Speed,**=Leg at Fast Speed

(a) Threat Matrix

i/j	6	7	8	9	10	11	12	13	14	15
6										
7		0	0	0	0	0	0	0	0	0
8		0	{OP}	{0}	1	0	0	0	0	0
9		0	0	1	{1}	1	0	0	0	0
10		0	1	1	1	{1}	2	0	0	0
11		0	0	1	1	2	{1}	1	0	0
12		0	0	0	2	1	1	{1}	1	0
13		0	0	0	0	1	1	1	{0}	0
14		0	0	0	0	0	1	0	{DP}	0
15		0	0	0	0	0	0	0	0	0

(b) Lethality Matrix

i/j	6	7	8	9	10	11	12	13	14	15
6										
7		10	10	10	10	10	10	10	10	10
8		10	{10}	{10}	710	10	10	10	10	10
9		10	10	710	{710}	710	10	10	10	10
10		10	710	710	710	{710}	1510	10	10	10
11		10	10	710	710	1510	{810}	810	10	10
12		10	10	10	1510	810	810	{810}	810	10
13		10	10	10	10	810	810	810	{10}	10
14		10	10	10	10	10	810	10	{10}	10
15		10	10	10	10	10	10	10	10	10

(c) Solution

Legs	From	To	H/V/D	# of Threats	Lethality	Speed	Fuel Consumed
1	(8,8)	(8,9)	H	0	12	Slow	3
2	(8,9)	(9,10)	D	1	1192	Slow	4
3	(9,10)	(10,11)	D	1	1192	Slow	4
4	(10,11)	(11,12)	D	1	1360	Slow	4
5	(11,12)	(12,13)	D	1	1360	Slow	4
6	(12,13)	(13,14)	D	0	16	Slow	4
7	(13,14)	(14,14)	V	0	12	Slow	3
					------		-----
				Total Lethality =	5144	Total Fuel =	26

Table 11: Example 1.2: Fuel=30 - Multiple Speeds Model With Fuel Restriction

Legend: OP=Origination Point,DP=Destination Point,0=Unthreatened Cell
1=Cell Threatened By One Threat, 2=Cell Threatened By Two Threats
{}=Leg at Slow Speed,[]=Leg at Average Speed,**=Leg at Fast Speed

(a) Threat Matrix

i/j	6	7	8	9	10	11	12	13	14	15
6										
7		0	0	0	0	0	0	0	0	0
8		0	{OP}	{0}	1	0	0	0	0	0
9		0	0	1	{1}	1	0	0	0	0
10		0	1	1	1	{1}	2	0	0	0
11		0	0	1	1	2	{1}	1	0	0
12		0	0	0	2	1	1	{1}	1	0
13		0	0	0	0	1	1	1	{0}	0
14		0	0	0	0	0	1	0	{DP}	0
15		0	0	0	0	0	0	0	0	0

(b) Lethality Matrix

i/j	6	7	8	9	10	11	12	13	14	15
6										
7		10	10	10	10	10	10	10	10	10
8		10	{10}	{10}	710	10	10	10	10	10
9		10	10	710	{710}	710	10	10	10	10
10		10	710	710	710	{710}	1510	10	10	10
11		10	10	710	710	1510	[810]	810	10	10
12		10	10	10	1510	810	810	{810}	810	10
13		10	10	10	10	810	810	810	{10}	10
14		10	10	10	10	10	810	10	{10}	10
15		10	10	10	10	10	10	10	10	10

(c) Solution

Legs	From	To	H/V/D	# of Threats	Lethality	Speed	Fuel Consumed
1	(8,8)	(8,9)	H	0	12	Slow	3
2	(8,9)	(9,10)	D	1	1192	Slow	4
3	(9,10)	(10,11)	D	1	1192	Slow	4
4	(10,11)	(11,12)	D	1	1134	Average	7
5	(11,12)	(12,13)	D	1	1360	Slow	4
6	(12,13)	(13,14)	D	0	16	Slow	4
7	(13,14)	(14,14)	V	0	12	Slow	3
					---		---
				Total Lethality =	4918	Total Fuel =	29

Table 12: Example 1.3: Fuel=33 - Multiple Speeds Model With Fuel Restriction

Legend: OP=Origination Point,DP=Destination Point,0=Unthreatened Cell
1=Cell Threatened By One Threat, 2=Cell Threatened By Two Threats
{}=Leg at Slow Speed,[]=Leg at Average Speed,**=Leg at Fast Speed

(a) Threat Matrix

i/j	6	7	8	9	10	11	12	13	14	15
6										
7		0	0	{0}	{0}	0	0	0	0	0
8		0	{OP}	0	1	{0}	0	0	0	0
9		0	0	1	1	1	{0}	0	0	0
10		0	1	1	1	1	2	{0}	0	0
11		0	0	1	1	2	1	1	{0}	0
12		0	0	0	2	1	1	1	{1}	0
13		0	0	0	0	1	1	1	{0}	0
14		0	0	0	0	0	1	0	{DP}	0
15		0	0	0	0	0	0	0	0	0

(b) Lethality Matrix

i/j	6	7	8	9	10	11	12	13	14	15
6										
7		10	10	{10}	{10}	10	10	10	10	10
8		10	{10}	10	710	{10}	10	10	10	10
9		10	10	710	710	710	{10}	10	10	10
10		10	710	710	710	710	1510	{10}	10	10
11		10	10	710	710	1510	810	810	{10}	10
12		10	10	10	1510	810	810	810	{810}	10
13		10	10	10	10	810	810	810	{10}	10
14		10	10	10	10	10	810	10	{10}	10
15		10	10	10	10	10	10	10	10	10

(c) Solution

Legs	From	To	H/V/D	# of Threats	Lethality	Speed	Fuel Consumed
1	(8,8)	(7,9)	D	0	16	Slow	4
2	(7,9)	(7,10)	H	0	12	Slow	3
3	(7,10)	(8,11)	D	0	16	Slow	4
4	(8,11)	(9,12)	D	0	16	Slow	4
5	(9,12)	(10,13)	D	0	16	Slow	4
6	(10,13)	(11,14)	D	0	16	Slow	4
7	(11,14)	(12,14)	V	1	972	Slow	3
8	(12,14)	(13,14)	V	0	12	Slow	3
9	(13,14)	(14,14)	V	0	12	Slow	3
					------		------

Total Lethality = 1088 Total Fuel = 33

Table 13: Example 1.4: Fuel=35 - Multiple Speeds Model With Fuel Restriction

Legend: OP=Origination Point,DP=Destination Point,0=Unthreatened Cell
1=Cell Threatened By One Threat, 2=Cell Threatened By Two Threats
{}=Leg at Slow Speed,[]=Leg at Average Speed,**=Leg at Fast Speed

(a) Threat Matrix

i/j	6	7	8	9	10	11	12	13	14	15
6										
7		0	0	{0}	{0}	0	0	0	0	0
8		0	{OP}	0	1	{0}	0	0	0	0
9		0	0	1	1	1	{0}	0	0	0
10		0	1	1	1	1	2	{0}	0	0
11		0	0	1	1	2	1	1	{0}	0
12		0	0	0	2	1	1	1	1	{0}
13		0	0	0	0	1	1	1	{0}	0
14		0	0	0	0	0	1	0	{DP}	0
15		0	0	0	0	0	0	0	0	0

(b) Lethality Matrix

i/j	6	7	8	9	10	11	12	13	14	15
6										
7		10	10	{10}	{10}	10	10	10	10	10
8		10	{10}	10	710	{10}	10	10	10	10
9		10	10	710	710	710	{10}	10	10	10
10		10	710	710	710	710	1510	{10}	10	10
11		10	10	710	710	1510	810	810	{10}	10
12		10	10	10	1510	810	810	810	810	{10}
13		10	10	10	10	810	810	810	{10}	10
14		10	10	10	10	10	810	10	{10}	10
15		10	10	10	10	10	10	10	10	10

(c) Solution

Legs	From	To	H/V/D	# of Threats	Lethality	Speed	Fuel Consumed
1	(8,8)	(7,9)	D	0	16	Slow	4
2	(7,9)	(7,10)	H	0	12	Slow	3
3	(7,10)	(8,11)	D	0	16	Slow	4
4	(8,11)	(9,12)	D	0	16	Slow	4
5	(9,12)	(10,13)	D	0	16	Slow	4
6	(10,13)	(11,14)	D	0	16	Slow	4
7	(11,14)	(12,15)	D	0	16	Slow	4
8	(12,15)	(13,14)	D	0	16	Slow	4
9	(13,14)	(14,14)	V	0	12	Slow	3
					---		---

Total Lethality = 136 Total Fuel = 34

Table 14: Example 1.5: Fuel=37 - Multiple Speeds Model With Fuel Restriction

Legend: OP=Origination Point,DP=Destination Point,Ø=Unthreatened Cell
1=Cell Threatened By One Threat, 2=Cell Threatened By Two Threats
{}=Leg at Slow Speed,[]=Leg at Average Speed,**=Leg at Fast Speed

(a) Threat Matrix

i/j	6	7	8	9	10	11	12	13	14	15
6										
7		Ø	Ø	Ø	{Ø}	Ø	Ø	Ø	Ø	Ø
8		Ø	[OP]	[Ø]	1	{Ø}	Ø	Ø	Ø	Ø
9		Ø	Ø	1	1	1	{Ø}	Ø	Ø	Ø
10		Ø	1	1	1	1	2	{Ø}	Ø	Ø
11		Ø	Ø	1	1	2	1	1	{Ø}	Ø
12		Ø	Ø	Ø	2	1	1	1	1	{Ø}
13		Ø	Ø	Ø	Ø	1	1	1	{Ø}	Ø
14		Ø	Ø	Ø	Ø	Ø	1	Ø	{DP}	Ø
15		Ø	Ø	Ø	Ø	Ø	Ø	Ø	Ø	Ø

(b) Lethality Matrix

i/j	6	7	8	9	10	11	12	13	14	15
6										
7		10	10	10	{10}	10	10	10	10	10
8		10	[10]	[10]	710	{10}	10	10	10	10
9		10	10	710	710	710	{10}	10	10	10
10		10	710	710	710	710	1510	{10}	10	10
11		10	10	710	710	1510	810	810	{10}	10
12		10	10	10	1510	810	810	810	810	{10}
13		10	10	10	10	810	810	810	{10}	10
14		10	10	10	10	10	810	10	{10}	10
15		10	10	10	10	10	10	10	10	10

(c) Solution

Legs	From	To	H/V/D	# of Threats	Lethality	Speed	Fuel Consumed
1	(8,8)	(8,9)	H	Ø	10	Average	5
2	(8,9)	(7,10)	D	Ø	16	Slow	4
3	(7,10)	(8,11)	D	Ø	16	Slow	4
4	(8,11)	(9,12)	D	Ø	16	Slow	4
5	(9,12)	(10,13)	D	Ø	16	Slow	4
6	(10,13)	(11,14)	D	Ø	16	Slow	4
7	(11,14)	(12,15)	D	Ø	16	Slow	4
8	(12,15)	(13,14)	D	Ø	16	Slow	4
9	(13,14)	(14,14)	V	Ø	12	Slow	3
					---		---

Total Lethality = 134 Total Fuel = 36

Table 15: Example 1.6: Fuel=40 - Multiple Speeds Model
With Fuel Restriction

Legend: OP=Origination Point,DP=Destination Point,0=Unthreatened Cell
1=Cell Threatened By One Threat, 2=Cell Threatened By Two Threats
{}=Leg at Slow Speed,[]=Leg at Average Speed,**=Leg at Fast Speed

(a) Threat Matrix

I/J	6	7	8	9	10	11	12	13	14	15
6										
7		0	0	0	{0}	0	0	0	0	0
8		0	[OP]	[0]	1	{0}	0	0	0	0
9		0	0	1	1	1	{0}	0	0	0
10		0	1	1	1	1	2	{0}	0	0
11		0	0	1	1	2	1	1	{0}	0
12		0	0	0	2	1	1	1	1	{0}
13		0	0	0	0	1	1	1	0	[0]
14		0	0	0	0	0	1	0	{DP}	0
15		0	0	0	0	0	0	0	0	0

(b) Lethality Matrix

I/J	6	7	8	9	10	11	12	13	14	15
6										
7		10	10	10	{10}	10	10	10	10	10
8		10	[10]	[10]	710	{10}	10	10	10	10
9		10	10	710	710	710	{10}	10	10	10
10		10	710	710	710	710	1510	{10}	10	10
11		10	10	710	710	1510	810	810	{10}	10
12		10	10	10	1510	810	810	810	810	{10}
13		10	10	10	10	810	810	810	10	[10]
14		10	10	10	10	10	810	10	{10}	10
15		10	10	10	10	10	10	10	10	10

(c) Solution

Legs	From	To	H/V/D	# of Threats	Lethality	Speed	Fuel Consumed
1	(8,8)	(8,9)	H	0	10	Average	5
2	(8,9)	(7,10)	D	0	16	Slow	4
3	(7,10)	(8,11)	D	0	16	Slow	4
4	(8,11)	(9,12)	D	0	16	Slow	4
5	(9,12)	(10,13)	D	0	16	Slow	4
6	(10,13)	(11,14)	D	0	16	Slow	4
7	(11,14)	(12,15)	D	0	16	Slow	4
8	(12,15)	(13,15)	V	0	10	Average	5
9	(13,15)	(14,14)	D	0	16	Slow	4
					------		-----

Total Lethality = 132 Total Fuel = 38

Table 16: Example 1.7: Fuel=70 - Multiple Speeds Model With Fuel Restriction

Legend: OP=Origination Point,DP=Destination Point,0=Unthreatened Cell
1=Cell Threatened By One Threat, 2=Cell Threatened By Two Threats
{}=Leg at Slow Speed,[]=Leg at Average Speed,**=Leg at Fast Speed

(a) Threat Matrix

I/J	6	7	8	9	10	11	12	13	14	15
6										
7		0	0	*0*	*0*	0	0	0	0	0
8		0	*OP*	0	1	*0*	0	0	0	0
9		0	0	1	1	1	*0*	0	0	0
10		0	1	1	1	1	2	*0*	0	0
11		0	0	1	1	2	1	1	{0}	0
12		0	0	0	2	1	1	1	1	{0}
13		0	0	0	0	1	1	1	0	[0]
14		0	0	0	0	0	1	0	{DP}	0
15		0	0	0	0	0	0	0	0	0

(b) Lethality Matrix

I/J	6	7	8	9	10	11	12	13	14	15
6										
7		10	10	*10*	*10*	10	10	10	10	10
8		10	*10*	10	710	*10*	10	10	10	10
9		10	10	710	710	710	*10*	10	10	10
10		10	710	710	710	710	1510	*10*	10	10
11		10	10	710	710	1510	810	810	{10}	10
12		10	10	10	1510	810	810	810	810	{10}
13		10	10	10	10	810	810	810	10	[10]
14		10	10	10	10	10	810	10	{10}	10
15		10	10	10	10	10	10	10	10	10

(c) Solution

Legs	From	To	H/V/D	# of Threats	Lethality	Speed	Fuel Consumed
1	(8,8)	(7,9)	D	0	11	Fast	11
2	(7,9)	(7,10)	H	0	8	Fast	8
3	(7,10)	(8,11)	D	0	11	Fast	11
4	(8,11)	(9,12)	D	0	11	Fast	11
5	(9,12)	(10,13)	D	0	11	Fast	11
6	(10,13)	(11,14)	D	0	16	Slow	4
7	(11,14)	(12,15)	D	0	16	Slow	4
8	(12,15)	(13,15)	V	0	10	Average	5
9	(13,15)	(14,14)	D	0	16	Slow	4
					---		---

Total Lethality = 110 Total Fuel = 69

Table 17: Example 1.8: Fuel=95 - Multiple Speeds Model With Fuel Restriction

Legend: OP=Origination Point,DP=Destination Point,Ø=Unthreatened Cell
1=Cell Threatened By One Threat, 2=Cell Threatened By Two Threats
{}=Leg at Slow Speed,[]=Leg at Average Speed,**=Leg at Fast Speed

(a) Threat Matrix

i/j	6	7	8	9	10	11	12	13	14	15
6										
7		Ø	Ø	*Ø*	*Ø*	Ø	Ø	Ø	Ø	Ø
8		Ø	*OP*	Ø	1	*Ø*	Ø	Ø	Ø	Ø
9		Ø	Ø	1	1	1	*Ø*	Ø	Ø	Ø
10		Ø	1	1	1	1	2	*Ø*	Ø	Ø
11		Ø	Ø	1	1	2	1	1	*Ø*	Ø
12		Ø	Ø	Ø	2	1	1	1	1	*Ø*
13		Ø	Ø	Ø	Ø	1	1	1	Ø	*Ø*
14		Ø	Ø	Ø	Ø	Ø	1	Ø	*DP*	Ø
15		Ø	Ø	Ø	Ø	Ø	Ø	Ø	Ø	Ø

(b) Lethality Matrix

i/j	6	7	8	9	10	11	12	13	14	15
6										
7		10	10	*10*	*10*	10	10	10	10	10
8		10	*10*	10	710	*10*	10	10	10	10
9		10	10	710	710	710	*10*	10	10	10
10		10	710	710	710	710	1510	*10*	10	10
11		10	10	710	710	1510	810	810	*10*	10
12		10	10	10	1510	810	810	810	810	*10*
13		10	10	10	10	810	810	810	10	*10*
14		10	10	10	10	10	810	10	*10*	10
15		10	10	10	10	10	10	10	10	10

(c) Solution

Legs	From	To	H/V/D	# of Threats	Lethality	Speed	Fuel Consumed
1	(8,8)	(7,9)	D	Ø	11	Fast	11
2	(7,9)	(7,10)	H	Ø	8	Fast	8
3	(7,10)	(8,11)	D	Ø	11	Fast	11
4	(8,11)	(9,12)	D	Ø	11	Fast	11
5	(9,12)	(10,13)	D	Ø	11	Fast	11
6	(10,13)	(11,14)	D	Ø	11	Fast	11
7	(11,14)	(12,15)	D	Ø	11	Fast	11
8	(12,15)	(13,15)	V	Ø	8	Fast	8
9	(13,15)	(14,14)	D	Ø	11	Fast	11
					------		------

Total Lethality = 93 Total Fuel = 93

Finally, in Example 1.8 there is a great deal of fuel (95 units) all legs of the route are fast and lethality is 93 units.

EXAMPLES 5.1 - 5.6

Examples 5.1-5.6, Tables 18-23 are similar to Example 5 of Section 4.1. Also, for this example the Destination Point is inside a threat and as such there is no safe route in which all threats can be avoided. With a fuel amount of 28 units the optimal route shown in Example 5.1 consists of four diagonal legs over unthreatened cells, one horizontal/vertical leg over an unthreatened cell, one diagonal leg over a threatened cell, and one horizontal/vertical leg over a threatened cell. Since the speed is slow, total lethality equals 2408 units. When fuel increases to 33 units in Example 5.2 two legs of the route can be flown at average speed (rather than the slow speeds previously). Total lethality is lowered to 2020 units. When the fuel on board increases to 35 units, Example 5.3, the speed for one leg of the route can be increased to fast, and total lethality then becomes 1858 units. In Example 5.4, fuel increases to 37 units. One leg of the route is flown at a fast speed, and one leg of the route is flown at an average speed, resulting in a total lethality level of 1793 units. When fuel rises to 40 units, as in Example 5.5, two legs of the route are flown at a fast speed, and total lethality decreases to 1631 units. In Example 5.6, fuel is now equal to 75 units. All the legs of the route are flown at a fast speed. Total lethality is lowered to 1607 units.

Table 24 summarizes the effects of the quantity of fuel on board the airplane on total lethality. For Example 1, as fuel

Table 18: Example 5.1: Fuel=28 - Multiple Speeds Model
With Fuel Restriction

Legend: OP=Origination Point,DP=Destination Point,0=Unthreatened Cell
1=Cell Threatened By One Threat, 2=Cell Threatened By Two Threats
{}=Leg at Slow Speed,[]=Leg at Average Speed,**=Leg at Fast Speed

(a) Threat Matrix

i/j	2	3	4	5	6	7	8	9	10	11	12
2											
3		0	0	{0}	{0}	0	0	0	0	0	
4		0	{OP}	0	1	{0}	0	0	0	0	
5		0	0	1	1	1	{0}	0	0	0	
6		0	1	1	1	1	2	{0}	0	0	
7		0	0	1	1	2	{1}	1	0	0	
8		0	0	0	2	2	{DP}	1	1	0	
9		0	0	0	1	2	2	1	0	0	
10		0	0	1	1	1	2	1	0	0	
11		0	0	0	1	1	1	0	0	0	
12		0	0	0	0	1	0	0	0	0	
13		0	0	0	0	0	0	0	0	0	
14											

(b) Lethality Matrix

i/j	2	3	4	5	6	7	8	9	10	11	12
2											
3		10	10	{10}	{10}	10	10	10	10	10	
4		10	{10}	10	710	{10}	10	10	10	10	
5		10	10	710	710	710	{10}	10	10	10	
6		10	710	710	710	710	1510	{10}	10	10	
7		10	10	710	710	1510	{810}	810	10	10	
8		10	10	10	1510	1410	{810}	810	810	10	
9		10	10	10	610	1410	1410	810	10	10	
10		10	10	610	610	610	1410	610	10	10	
11		10	10	10	610	610	610	10	10	10	
12		10	10	10	10	610	10	10	10	10	
13		10	10	10	10	10	10	10	10	10	
14											

(c) Solution

Legs	From	To	H/V/D	# of Threats	Lethality	Speed	Fuel Consumed
1	(4,4)	(3,5)	D	0	16	Slow	4
2	(3,5)	(3,6)	H	0	12	Slow	3
3	(3,6)	(4,7)	D	0	16	Slow	4
4	(4,7)	(5,8)	D	0	16	Slow	4
5	(5,8)	(6,9)	D	0	16	Slow	4
6	(6,9)	(7,8)	D	1	1360	Slow	4
7	(7,8)	(8,8)	V	1	972	Slow	3
					------		----

Total Lethality = 2408 Total Fuel = 26

Table 19: Example 5.2: Fuel=33 - Multiple Speeds Model
With Fuel Restriction

Legend: OP=Origination Point,DP=Destination Point,0=Unthreatened Cell
1=Cell Threatened By One Threat, 2=Cell Threatened By Two Threats
{}=Leg at Slow Speed,[]=Leg at Average Speed,**=Leg at Fast Speed

(a) Threat Matrix

i/j	2	3	4	5	6	7	8	9	10	11	12
2											
3		0	0	{0}	{0}	0	0	0	0	0	
4		0	{OP}	0	1	{0}	0	0	0	0	
5		0	0	1	1	1	{0}	0	0	0	
6		0	1	1	1	1	2	{0}	0	0	
7		0	0	1	1	2	[1]	1	0	0	
8		0	0	0	2	2	[DP]	1	1	0	
9		0	0	0	1	2	2	1	0	0	
10		0	0	1	1	1	2	1	0	0	
11		0	0	0	1	1	1	0	0	0	
12		0	0	0	0	1	0	0	0	0	
13		0	0	0	0	0	0	0	0	0	
14											

(b) Lethality Matrix

i/j	2	3	4	5	6	7	8	9	10	11	12
2											
3		10	10	{10}	{10}	10	10	10	10	10	
4		10	{10}	10	710	{10}	10	10	10	10	
5		10	10	710	710	710	{10}	10	10	10	
6		10	710	710	710	710	1510	{10}	10	10	
7		10	10	710	710	1510	[810]	810	10	10	
8		10	10	10	1510	1410	[810]	810	810	10	
9		10	10	10	610	1410	1410	810	10	10	
10		10	10	610	610	610	1410	610	10	10	
11		10	10	10	610	610	610	10	10	10	
12		10	10	10	10	610	10	10	10	10	
13		10	10	10	10	10	10	10	10	10	
14											

(c) Solution

Legs	From	To	H/V/D	# of Threats	Lethality	Speed	Fuel Consumed
1	(4,4)	(3,5)	D	0	16	Slow	4
2	(3,5)	(3,6)	H	0	12	Slow	3
3	(3,6)	(4,7)	D	0	16	Slow	4
4	(4,7)	(5,8)	D	0	16	Slow	4
5	(5,8)	(6,9)	D	0	16	Slow	4
6	(6,9)	(7,8)	D	1	1134	Average	7
7	(7,8)	(8,8)	V	1	810	Average	5
					-----		----

Total Lethality = 2020 Total Fuel = 31

Table 20: Example 5.3: Fuel=35 - Multiple Speeds Model
With Fuel Restriction

Legend: OP=Origination Point,DP=Destination Point,0=Unthreatened Cell
1=Cell Threatened By One Threat, 2=Cell Threatened By Two Threats
{}=Leg at Slow Speed,[]=Leg at Average Speed,**=Leg at Fast Speed

(a) Threat Matrix

i/j	2	3	4	5	6	7	8	9	10	11	12
2											
3		0	0	{0}	{0}	0	0	0	0	0	
4		0	{OP}	0	1	{0}	0	0	0	0	
5		0	0	1	1	1	{0}	0	0	0	
6		0	1	1	1	1	2	{0}	0	0	
7		0	0	1	1	2	1	*1*	0	0	
8		0	0	0	2	2	[DP]	1	1	0	
9		0	0	0	1	2	2	1	0	0	
10		0	0	1	1	1	2	1	0	0	
11		0	0	0	1	1	1	0	0	0	
12		0	0	0	0	1	0	0	0	0	
13		0	0	0	0	0	0	0	0	0	
14											

(b) Lethality Matrix

i/j	2	3	4	5	6	7	8	9	10	11	12
2											
3		10	10	{10}	{10}	10	10	10	10	10	
4		10	{10}	10	710	{10}	10	10	10	10	
5		10	10	710	710	710	{10}	10	10	10	
6		10	710	710	710	710	1510	{10}	10	10	
7		10	10	710	710	1510	810	*810*	10	10	
8		10	10	10	1510	1410	[810]	810	810	10	
9		10	10	10	610	1410	1410	810	10	10	
10		10	10	610	610	610	1410	610	10	10	
11		10	10	10	610	610	610	10	10	10	
12		10	10	10	10	610	10	10	10	10	
13		10	10	10	10	10	10	10	10	10	
14											

(c) Solution

Legs	From	To	H/V/D	# of Threats	Lethality	Speed	Fuel Consumed
1	(4,4)	(3,5)	D	0	16	Slow	4
2	(3,5)	(3,6)	H	0	12	Slow	3
3	(3,6)	(4,7)	D	0	16	Slow	4
4	(4,7)	(5,8)	D	0	16	Slow	4
5	(5,8)	(6,9)	D	0	16	Slow	4
6	(6,9)	(7,9)	V	1	648	Fast	8
7	(7,9)	(8,8)	D	1	1134	Average	7
					------		-----

Total Lethality = 1858 Total Fuel = 34

Table 21: Example 5.4: Fuel=37 - Multiple Speeds Model With Fuel Restriction

Legend: OP=Origination Point,DP=Destination Point,0=Unthreatened Cell
1=Cell Threatened By One Threat, 2=Cell Threatened By Two Threats
{}=Leg at Slow Speed,[]=Leg at Average Speed,**=Leg at Fast Speed

(a) Threat Matrix

i/j	2	3	4	5	6	7	8	9	10	11	12
2											
3		0	0	{0}	{0}	0	0	0	0	0	
4		0	{OP}	0	1	{0}	0	0	0	0	
5		0	0	1	1	1	{0}	0	0	0	
6		0	1	1	1	1	2	{0}	0	0	
7		0	0	1	1	2	*1*	1	0	0	
8		0	0	0	2	2	[DP]	1	1	0	
9		0	0	0	1	2	2	1	0	0	
10		0	0	1	1	1	2	1	0	0	
11		0	0	0	1	1	1	0	0	0	
12		0	0	0	0	1	0	0	0	0	
13		0	0	0	0	0	0	0	0	0	
14											

(b) Lethality Matrix

i/j	2	3	4	5	6	7	8	9	10	11	12
2											
3		10	10	{10}	{10}	10	10	10	10	10	
4		10	{10}	10	710	{10}	10	10	10	10	
5		10	10	710	710	710	{10}	10	10	10	
6		10	710	710	710	710	1510	{10}	10	10	
7		10	10	710	710	1510	*810*	810	10	10	
8		10	10	10	1510	1410	[810]	810	810	10	
9		10	10	10	610	1410	1410	810	10	10	
10		10	10	610	610	610	1410	610	10	10	
11		10	10	10	610	610	610	10	10	10	
12		10	10	10	10	610	10	10	10	10	
13		10	10	10	10	10	10	10	10	10	
14											

(c) Solution

Legs	From	To	H/V/D	# of Threats	Lethality	Speed	Fuel Consumed
1	(4,4)	(3,5)	D	0	16	Slow	4
2	(3,5)	(3,6)	H	0	12	Slow	3
3	(3,6)	(4,7)	D	0	16	Slow	4
4	(4,7)	(5,8)	D	0	16	Slow	4
5	(5,8)	(6,9)	D	0	16	Slow	4
6	(6,9)	(7,8)	D	1	907	Fast	11
7	(7,8)	(8,8)	V	1	810	Average	5
					------		-----

Total Lethality = 1793 Total Fuel = 35

Table 22: Example 5.5: Fuel=40 - Multiple Speeds Model
With Fuel Restriction

Legend: OP=Origination Point,DP=Destination Point,0=Unthreatened Cell
1=Cell Threatened By One Threat, 2=Cell Threatened By Two Threats
{}=Leg at Slow Speed,[]=Leg at Average Speed,**=Leg at Fast Speed

(a) Threat Matrix

i/j	2	3	4	5	6	7	8	9	10	11	12
2											
3		0	0	{0}	{0}	0	0	0	0	0	
4		0	{OP}	0	1	{0}	0	0	0	0	
5		0	0	1	1	1	{0}	0	0	0	
6		0	1	1	1	1	2	{0}	0	0	
7		0	0	1	1	2	*1*	1	0	0	
8		0	0	0	2	2	*DP*	1	1	0	
9		0	0	0	1	2	2	1	0	0	
10		0	0	1	1	1	2	1	0	0	
11		0	0	0	1	1	1	0	0	0	
12		0	0	0	0	1	0	0	0	0	
13		0	0	0	0	0	0	0	0	0	
14											

(b) Lethality Matrix

i/j	2	3	4	5	6	7	8	9	10	11	12
2											
3		10	10	{10}	{10}	10	10	10	10	10	
4		10	{10}	10	710	{10}	10	10	10	10	
5		10	10	710	710	710	{10}	10	10	10	
6		10	710	710	710	710	1510	{10}	10	10	
7		10	10	710	710	1510	*810*	810	10	10	
8		10	10	10	1510	1410	*810*	810	810	10	
9		10	10	10	610	1410	1410	810	10	10	
10		10	10	610	610	610	1410	610	10	10	
11		10	10	10	610	610	610	10	10	10	
12		10	10	10	10	610	10	10	10	10	
13		10	10	10	10	10	10	10	10	10	
14											

(c) Solution

Legs	From	To	H/V/D	# of Threats	Lethality	Speed	Fuel Consumed
1	(4,4)	(3,5)	D	0	16	Slow	4
2	(3,5)	(3,6)	H	0	12	Slow	3
3	(3,6)	(4,7)	D	0	16	Slow	4
4	(4,7)	(5,8)	D	0	16	Slow	4
5	(5,8)	(6,9)	D	0	16	Slow	4
6	(6,9)	(7,8)	D	1	907	Fast	11
7	(7,8)	(8,8)	V	1	648	Fast	8
					------		-----

Total Lethality = 1631 Total Fuel = 38

Table 23: Example 5.6: Fuel=75 - Multiple Speeds Model
With Fuel Restriction

Legend: OP=Origination Point,DP=Destination Point,0=Unthreatened Cell
1=Cell Threatened By One Threat, 2=Cell Threatened By Two Threats
{}=Leg at Slow Speed,[]=Leg at Average Speed,**=Leg at Fast Speed

(a) Threat Matrix

i/j	2	3	4	5	6	7	8	9	10	11	12
2											
3		0	0	*0*	*0*	0	0	0	0	0	
4		0	*OP*	0	1	*0*	0	0	0	0	
5		0	0	1	1	1	*0*	0	0	0	
6		0	1	1	1	1	2	*0*	0	0	
7		0	0	1	1	2	*1*	1	0	0	
8		0	0	0	2	2	*DP*	1	1	0	
9		0	0	0	1	2	2	1	0	0	
10		0	0	1	1	1	2	1	0	0	
11		0	0	0	1	1	1	0	0	0	
12		0	0	0	0	1	0	0	0	0	
13		0	0	0	0	0	0	0	0	0	
14											

(b) Lethality Matrix

i/j	2	3	4	5	6	7	8	9	10	11	12
2											
3		10	10	*10*	*10*	10	10	10	10	10	
4		10	*10*	10	710	*10*	10	10	10	10	
5		10	10	710	710	710	*10*	10	10	10	
6		10	710	710	710	710	1510	*10*	10	10	
7		10	10	710	710	1510	*810*	810	10	10	
8		10	10	10	1510	1410	*810*	810	810	10	
9		10	10	10	610	1410	1410	810	10	10	
10		10	10	610	610	610	1410	610	10	10	
11		10	10	10	610	610	610	10	10	10	
12		10	10	10	10	610	10	10	10	10	
13		10	10	10	10	10	10	10	10	10	
14											

(c) Solution

Legs	From	To	H/V/D	# of Threats	Lethality	Speed	Fuel Consumed
1	(4,4)	(3,5)	D	0	11	Fast	11
2	(3,5)	(3,6)	H	0	8	Fast	8
3	(3,6)	(4,7)	D	0	11	Fast	11
4	(4,7)	(5,8)	D	0	11	Fast	11
5	(5,8)	(6,9)	D	0	11	Fast	11
6	(6,9)	(7,8)	D	1	907	Fast	11
7	(7,8)	(8,8)	V	1	648	Fast	8
					------		-----

Total Lethality = 1607 Total Fuel = 71

Table 24: Summary - Multiple Speeds Model With Fuel Restrictions

Table	Example	Fuel	Lethality	Legs Over No Threats H/V	Legs Over No Threats D	Legs Over Threats H/V	Legs Over Threats D
10	1.1	28	5144	2 Slow	1 Slow		4 Slow
11	1.2	30	4918	2 Slow	1 Slow		3 Slow 1 Average
12	1.3	33	1088	3 Slow	5 Slow	1 Slow	
13	1.4	35	136	2 Slow	7 Slow		
14	1.5	37	134	1 Slow 1 Average	7 Slow		
15	1.6	40	132	2 Average	7 Slow		
16	1.7	70	110	1 Average 1 Fast	4 Fast		3 Slow
17	1.8	95	93	2 Fast	7 Fast		
18	5.1	28	2408	1 Slow	4 Slow	1 Slow	1 Slow
19	5.2	33	2020	1 Slow	4 Slow	1 Average	1 Average
20	5.3	35	1858	1 Slow	4 Slow	1 Fast	1 Average
21	5.4	37	1793	1 Slow	4 Slow	1 Average	1 Fast
22	5.5	40	1631	1 Slow	4 Slow	1 Fast	1 Fast
23	5.6	75	1607			2 Fast	5 Fast

Legend: H/V Represents A Horizontal or Vertical Leg,
D Represents A Diagonal Leg

increases from 28 to 95 units, total lethality decreases from 5144 units to 93 units. In Example 5, as fuel increases from 28 units to 75 units, total lethality decreases from 2408 down to 1607. Table 24 also presents the number of steps taken over no threats and the number of steps taken over one threat. Also it shows the diagonal and horizonta/vertical steps as well as the flying speed of each leg. It demonstrates how the optimal route changes as the amount of fuel on board the airplane changes.

4.3 FURTHER RESEARCH

In this section we propose directions for further research. Many possibilities exist, but we restrict ourselves to only a few.

4.3.1 INPUT/OUTPUT

The Input/Output portion of the model can be significantly improved to the stage where a operator sits at a terminal and easily (perhaps with the aid of a menu or a mouse) feeds in his own problem and modifies his problem on-line. The output should also have options for several different screens, and the operator should be able to select the output he desires to observe.

4.3.2 ADDITIONAL SPEEDS

The Multiple Speeds portion of the model at the moment enables us to provide three different speeds. This can be extended to 5, 7, or more different speeds.

4.3.3 TOPOGRAPHY OF THREE DIMENSIONS

The present model is a two dimensional one which might be realistic for flying over flat grounds, seas and deserts. A more realistic model would allow the pilot to fly over three dimensional topography. It is possible to expand the present model to include three dimensional topography.

4.3.4 The K-BEST ROUTES

The present model solves for the optimal (best) route. Often pilots are interested in the second best, third best route, etc.. The enemy is alert to the route used, and after a short time the route must be changed. From best route, one may want to switch to the K-best route. It is quite possible that simultaneous flights will be dispatched at the best, second best, and third best routes.

4.3.5 TARGET SELECTION

This model can be extended to assist the decision-maker in target selection. Suppose there are five potential targets, one can compute lethality to all five targets and select the target to attack based on the one with the lowest lethality. This problem becomes much more complicated when there are multiple bases as well as multiple targets.

4.3.6 MULTIPLE BASES

Assume there are multiple bases from which airplanes can be dispatched. We can extend the present model to divide the enemy field into regions. Each region will "belong" to a specific

base. When a new target has been identified, it will automatically be the responsibility of that base to which that region belongs.

4.3.7 REFUELING/NAVIGATION POINTS

The present model does not deal with the issue of refueling or navigation points. It is however possible to incorporate both refueling and navigation points into the model.

4.3.8 OTHER POTENTIAL EXTENSIONS

Additional possible extensions of the model include:

--Minimize fuel consumption over several sorties. When planning multiple flights, what set of routes minimizes total fuel consumption?

--Multiple airplanes. What is an optimal solution for say, a fleet of 24 airplanes?

--Timing of bombing. If we want to bomb a target at a specific time, what is the optimal route and speed to accomplish this goal?

--Reloading of Threats. If a threat fires its missles, it takes them say 30 minutes to reload its weapon again. For that period of time it is "safe" to fly over the threat.

--Electronic Warfare. The present model does not allow for any electronic warfare capabilities such as threat negating or lowering its PK. It is possible to extend the present model to allow for EW capabilities.

--Sensitivity Analysis. All enemy data are uncertain. It is

possible to compute the sensitivity of the optimal route as a function of enemy data changes (such as PK, radius, coordination, etc.).

--PK can be expressed as a function of the learning curve of the opponents.

REFERENCES

1. Integrated Sciences Corporation, "Experimental Investigation Of The Usefulness Of Operator Aided Optimization In A Simulated Tactical Decision Aiding Task", Report No. 215-4, January 1978.

2. Kruchten, Robert J., Major, USAF, "Decision Aid For Threat Penetration Analysis", 30 May, 1985.

3. Kruchten, Robert J. and B. Lev, "Recent Developments in Route Planning Problem", ORSA/TIMS Conference, October 1986, Miami.

4. Lev, B. and H.J. Weiss, INTRODUCTION TO MATHEMATICAL PROGRAMMING, North Holland, 1982.

5. Georgia Institute Of Technology, Gene Coleman and Barnie Jones, Final Report 1986.

APPENDIX A. DYNAMIC PROGRAMMING RECURSIVE EQUATION FOR SINGLE FLYING SPEED

In this Appendix we derive the dynamic programming recursive equation needed for the Single Flying Speed Model. Assume the following notations:

(i,j) : the coordination of cell (i,j)

f(i,j): minimal lethality from Origination Point to cell (i,j)

r(i,j): lethality level at cell (i,j)

All diagonal moves incur a lethality level of 40% more lethality than horizontal/vertical moves

(si,sj): the Origination Point

f(si,sj) = 0

The only allowable moves from cell (i,j) are to its eight adjacent cells. The forward dynamic programming recursive equation is the following:

$$
\begin{aligned}
f(i,j) = \text{minimum } \{ & [f(i,j-1) + r(i,j-1)], \\
& [f(i,j+1) + r(i,j+1)], \\
& [f(i+1,j) + r(i+1,j)], \\
& [f(i-1,j) + r(i-1,j)], \\
& [f(i-1,j-1) + 1.4r(i-1,j-1)], \\
& [f(i-1,j+1) + 1.4r(i-1,j+1)], \\
& [f(i+1,j-1) + 1.4r(i+1,j-1)], \\
& [f(i+1,j+1) + 1.4r(i+1,j+1)] \}.
\end{aligned}
$$

Using this recursive equation one can generate the data shown in Table 3. For example:

Starting with f(8,8) = 0, one determines:

f(8,7) = f(8,9) = f(7,8) = f(9,8) = 10, and

f(7,7) = f(7,9) = f(9,7) = 14

(cell (9,9) is inside a threat and is left for later computations). In this fashion one completes the construction of the entire Search Space.

APPENDIX B. DYNAMIC PROGRAMMING RECURSIVE EQUATION FOR MULTIPLE FLYING SPEEDS

In this Appendix we develop the recursive equation needed for the Multiple Speeds Model. It is very similar to Appendix A except that the state of the system is described by three state variables: the coordinations (i,j), and k, the fuel on board the plane at that particular cell.

f(i,j,k): The minimal lethality from the Origination Point to cell (i,j) arriving at (i,j) with quantity k of fuel on board.

Let l = 1, 2, 3 be the flying speed slow, average, fast respectively.

Let s(l) be the adjustment to lethality due to the flying speed. For example: s(1) = 1.2, s(2) = 1, s(3) = .8. (20% increase in lethality level for flying slow and 20% decrease in lethality level for flying fast).

Let t(l) be fuel consumption due to flying speed l. For example: t(1) = 3, t(2) = 5, t(3) = 8.

All diagonal moves incur a 40% higher fuel consumption and also a 40% higher lethality level exposure than the horizontal/vertical moves.

The forward dynamic programming recursive equation used for the Multiple Speeds Model is the following:

$$
\begin{aligned}
f(i,j,k) = \underset{l=1,2,3}{\text{minimum}} \{ & [f(i,j-1,k + t(l)) + r(i,j-1)\, s(l)], \\
& [f(i,j+1,k + t(l)) + r(i,j+1)\, s(l)], \\
& [f(i+1,j,k + t(l)) + r(i+1,j)\, s(l)], \\
& [f(i-1,j,k + t(l)) + r(i-1,j)\, s(l)], \\
& [f(i-1,j-1,k + 1.4t(l)) + r(i-1,j-1)\, 1.4s(l)], \\
& [f(i-1,j+1,k + 1.4t(l)) + r(i-1,j+1)\, 1.4s(l)], \\
& [f(i+1,j-1,k + 1.4t(l)) + r(i+1,j-1)\, 1.4s(l)], \\
& [f(i+1,j+1,k + 1.4t(l)) + r(i+1,j+1)\, 1.4s(l)] \}.
\end{aligned}
$$

The number of computations in this model is much higher than in the Single Speed Model. From eight adjacent cells and at three speeds from each adjacent cell, the number of possibilities to arrive at cell (i,j) with k fuel on board is 8 x 3 = 24 possibilities. In other words, to compute f(i,j,k) requires finding the minimum of 24 possibilities.

If (si,sj) is the Origination Point, then f(si,sj,k) = 0 for all k. One can recursively construct f(i,j,k) for all possible i, j, k and obtain the optimal minimum lethality f(i,j,k) from Origination Point to all cells (i,j).

MINIGRANT RESEARCH REPORT

FOR

AIR FORCE OFFICE OF SCIENTIFIC RESEARCH

STATISTICAL PERFORMANCE MEASURES:

RELATING AIR FORCE MISSION CAPABILITY

TO

BASE SUPPLY MEASURES

PREPARED BY: Ed Lewis, Ph.D
Professor of Management Science
Belmont College
Nashville, TN 37203

ABSTRACT

The correlation between MICAP and Seventy-eight supply performance measures were examined for all major Air Force commands in order to identify the variables (supply performance measures that are significantly correlated with mission capability within the command. Once the significant variable set for a major command was identified the variables were ranked in descending order of impact on MICAP using the MICAP elasticity to each variable. Then each variable category (e.g. Effectiveness Measures, EOQ, Recoverable Mix, Inventory Accuracy) were ranked in descending order of average absolute elasticity impact on MICAP. A model was developed which, using the performance measures identified as significant for the MAJCOM, forecasts MICAP by base within the MAJCOM. These forecasts can then be added to get a MICAP forecast for the MAJCOM and subsequently by adding the MAJCOM MICAP forecasts an Air Force wide forecast of MICAP can be developed. The forecasts thus developed were found to be accurate for short term forecasting, that is, one month ahead or at most two months ahead.

A technique was developed to identify significant differences in supply performance, between bases within a command or between major commands with respect to one or more supply performance variables or categories of variables. This latter technique allows indices to be developed with which to grade the performance of supply accounts (bases or major commands) with respect to one, some, categories of/or all supply performance variables represented in the study. Examples of the comparisons

possible were computed for bases within commands, all major commands and weapons systems within a major command.

EXECUTIVE SUMMARY

This study proposes a model that provides a means to determine the impact of supply performance measures on MICAP by MAJCOM and base within MAJCOM, and provides a means to forecast MICAP by base, by MAJCOM and Air Force wide.

Furthermore the model supplies a rank ordered list of variables in descending order of impact on MICAP and also provides for the ranking of the variable categories for a MAJCOM and base within MAJCOM.

Also presented in this study is a method for grading supply accounts (Bases, MAJCOM'S) with respect to one or many supply performance measures providing for the measurement of differences in performance between MAJCOMS or bases.

BACKGROUND

The results in this report are the result of preliminary efforts during the Summer of 1985 at Gunter AFS as part of a Summer Faculty Research Program (SFRP) and subsequently refined and completed under AFOSR minigrant 093.

OBJECTIVES

The objectives of the "Statistical Performance Measures" effort were as follows:

1. Develop a robust predictive model to predict mission capability (MICAP) from a set of supply performance measures identified as being "Salient" (highly correlated with MICAP) for a MAJCOM and all the bases in a MAJCOM.

2. Develop a technique that would identify significant differences between commands and bases within commands with respect to one or more supply performance measures.

3. To develop statistical indices with which to grade the performance of supply accounts (bases and major commands) with respect to one or more supply performance measures.

APPROACH

The approach is essentially a multistep filtering process with two stages. In stage one, which consists of three filtering steps, the variables that are "SALIENT" for the MAJCOM are identified. In the second stage, which consists of eight modelling steps, the variables identified in stage one are used in a series of regressions using a robust model to predict MICAP for each base in the MAJCOM. Only a few bases were run for SAC to demonstrate the predictive capability of the model.

For the second and third objectives dealing with determining differences in performance between bases and MAJCOMS a heuristic method called (DA) Difference Analysis was used. The method combines the influences of many performance measures by transforming the variable values to utilities, then mapping the transformed distribution of values onto a uniform distribution. From these steps emerges a distribution of values in which intervals of the utility values are associated with a percentile score or range of percentile scores. Then for any subset of the transformed values, representing a base or a MAJCOM, a percentile grade may be computed. Because the grades thusly established are percentile scores they may be interpreted in the ordinary way one looks at grades on a scale of 0 to 100 and differences computed by subtraction.

CONCLUSIONS

A model to predict MICAP was constructed that appears to be robust for all MAJCOMS and bases within MAJCOMS. The model allows all variables identified as "salient" for a MAJCOM to be used in the prediction of MICAP. The results of the model are additive over bases for the MAJCOM and these results can be summed to predict MICAP Air Force wide. Furthermore the model allows for the ranking of performance measures and categories of performance measures in descending order of impact on MICAP by base and by MAJCOM. This feature creates a priority list that can be used in operationally managing performance measures to achieve the maximum effect on MICAP.

It is possible using the DA algorithm to create an index that can be used to identify significant differences in supply performance between bases and MAJCOMS with respect to one or more supply performance measures.

DA also provides for standard based grading of supply accounts with respect to one or more performance measures.

The models developed in this study and the results achieved indicate that operational variables can be correlated to supply performance measures and that at least one operational variable MICAP can be predicted by base and MAJCOM with a respectable degree of accuracy.

Effort should continue to bring the analytical results to the base operational level to provide operational personnel with guide-lines indicating which supply performances measures should be watched closely and managed adroitly to achieve the maximium reduction of aircraft grounding incidents (MICAP).

CHAPTER 1

INTRODUCTION

The problem of relating supply performance measures to operational characteristics (variables) such as MICAP, is not new and has been the subject of many studies by the Air Force and other civilian agencies and individuals.

This study describes a method of relating supply performance measures to operational variables (MICAP) that can improve supply resource allocation and result in better allocation decisions enhancing supply performance and increasing levels of mission capability. Operational commanders at all levels can be supplied management information in the form of ordered lists of performance measures and categories of performance measures which would be the basis for base level supply management policies aimed at manipulating and watching the performance measures in priority order that have the greatest impact on operational capability (MICAP.)

Operational commanders at higher levels, base commanders and above, can be provided indices of performance, relative to the rank order of performance measures, that indicate the relative ranking of the base among bases in the MAJCOM and the establishment of the rank position as being "statistically significantly" above average, average, or "statistically significantly" below average for the MAJCOM as a whole. The indices being percentile scores can be manipulated and compared like test scores between 0 and 100 in the ordinary way.

Background

"Although a number of tools are under development to help translate logistics resources into operational capabilities, there is no existing system to link supply support given at individual bases to the operational capabilities that result from this total support effort. As a result, HQ USAF/LEYS tasked the AFLMC to examine ways to correlate existing supply performance information to operational performance factors.

As an initial examination into this area, two studies by outside activities were sponsored. An Air Command and Staff College (ACSC) study entitled "Relationship Between Wholesale Stock Fund Item Demands and Aircraft Flying Activity", Report Number 2580-81, authored by Major James C. Wendt, attempted to use simple linear regression to determine whether there existed a relationship between wholesale level demands of stock fund items and aircraft flying activity. The study was limited to the F-111 weapon system with data covering approximately two years. His results indicated there was no significant relationship between flying activity and wholesale demands. At this same time, the AFLMC contacted the faculty at Auburn University to look at possible relationships between various operational performance measures and standard supply management information. While both studies were rudimentary, this last effort with Auburn University did show some promise for further extensions into this area concerning possible correlations between supply and performance data at and across individual bases.

Following these two endeavors, the AFLMC contacted the Air Force Academy and asked the faculty to look at this area. Major Salvatore J. Monaco and Major Brian E. Esterby in "Supply Performance Indicators", Report Number USAFA TR 81-7, performed some rigorous analyses with approximately two years of data across two bases. Again, they could not arrive at a significant correlation between supply measurements and operational capabilities. However, they identified possible problems that might have prevented the successful development of a correlation model across bases: the size of the data base, the small number of variables (14 independent supply variables), and the use of different weapon systems at the bases examined.

As a result of these efforts, the AFLMC believed that a final examination of this entire area should be conducted. Basing this study on the Air Force Academy results, the AFLM sought to collect a homogeneous data base for a longer period of time and to expand the number of variables examined. This study, then, presents the finding of an effort designed to take the most favorable conditions and to develop any reasonable correlation model across more than one individual base." (The Foregoing reprinted from AFLMC Report 021029) (8)

The AFLMC study report 0212029 had as its objective "---to examine correlations between supply performance measurements and operational capability".

"---To identify supply related variables that correlate well to operational performance.

"---To identify any correlated variables applicable to more than one base."

The conclusions of this study are summarized below:

1. "The operational variable that correlated best with the supply information was the Fully Mission Capable Rate (Y2) variable".
2. "The Y2 variable was used in models that were constructed across two bases sharing a common weapons system".
3. "The key variable in all significant models was the Cause Code A (NON-MA) Supply Variable X16".
4. "Other weapons systems on any given base influence the regression results".
5. "Current aggregate measures within the standard base supply account do not provide the detailed information that would be required to support correlation effort between operational variables".

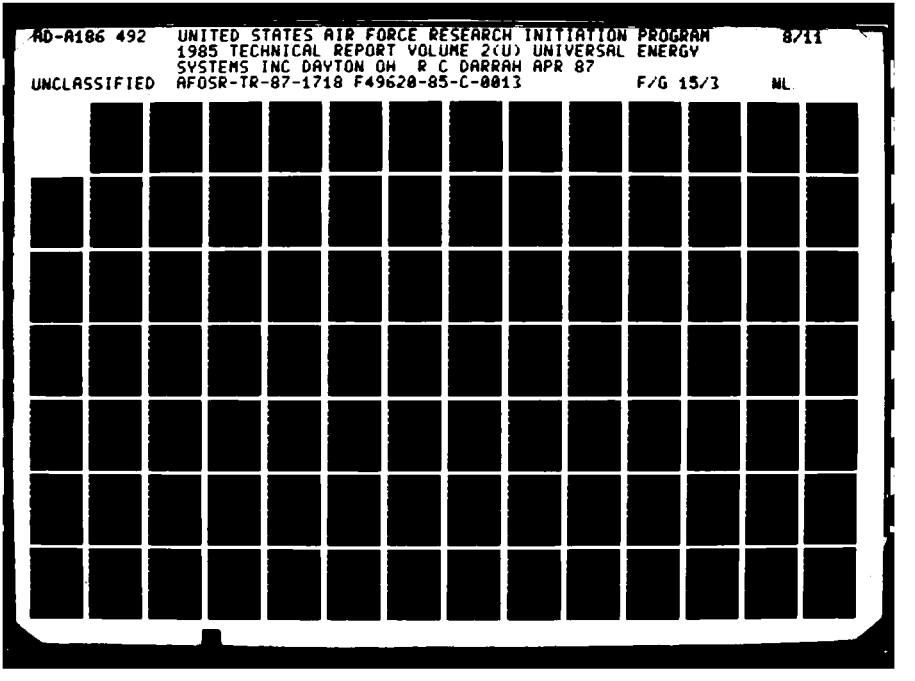
AD-A186 492 UNITED STATES AIR FORCE RESEARCH INITIATION PROGRAM 8/11
1985 TECHNICAL REPORT VOLUME 2(U) UNIVERSAL ENERGY
SYSTEMS INC DAYTON OH R C DARRAH APR 87
UNCLASSIFIED AFOSR-TR-87-1718 F49620-85-C-0013 F/G 15/3 NL

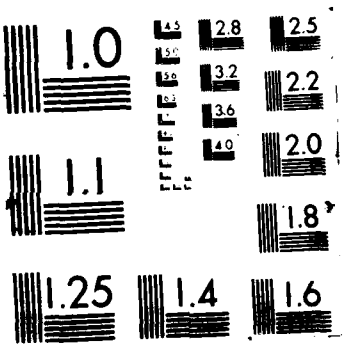
1.0
1.1
1.25
1.4
1.6
1.8
2.0
2.2
2.5
2.8
3.2
3.6
4.0

Limitations on the Methodology

The data used in this study came from Monthy Base Supply Management Report (M32) consisting of seventy-eight supply performance measures (See Appendix A). Note: the values in the M32 data have been divided by 106.

Only twelve months of data for each variable was available in the M32 data base used for this study.

CHAPTER 2

RESEARCH METHODOLOGY

The research proceeded in two stages. The first stage was concerned with finding the supply performance measures that are significantly correlated with MICAP for all bases in a major command. Considerations of "robustness" also dictate that any set of performance measures selected as "salient" (highly correlated with MICAP) for a MAJCOM should be usable in a predictive model of MICAP for every base in the MAJCOM.

The second stage of the predictive modelling research is to find a model that can be used to predict MICAP at every base in a MAJCOM using all the "salient" variables for the MAJCOM.

Knowing that MAJCOMS vary by weapons systems and types of aircraft flown and in a variety of other ways that are dictated by the unique and distinctive character of the MAJCOM, it is assumed that in stage one of the research methodology each MAJCOM would have a different set of "salient" performance measures with some measures common to all MAJCOMS. If the model developed in stage two is robust it will efficiently predict MICAP for the differing sets of Salient variables by MAJCOM.

It should be noted here that having only twelve observations of each variable by month precludes the effective use of time series analysis in stage two of the model.

The stages of the model and the steps in each are now presented in detail. Figure I depicts the model.

Stage_1_=_Step_1:_Correlating_Performance_Measures_to_MICAP

To determine for each base in a MAJCOM which performance measures have a significant correlation to MICAP it is first necessary to create from the twelve observations for each variable twelve sets of these observations but rotated in time by one month. For example, suppose the observations for a particular performance measure were as follows, called rotation zero.

Observations at Rotation (0)

1	2	3	4	5	6	7	8	9	10	11	12
4/82	5/82	6/82	7/82	8/82	9/82	10/82	11/82	12/82	1/83	2/83	3/83
10	11	12	13	14	15	16	17	18	19	20	(21)

Then Rotation (1) would be created by moving the value for 3/83 to 4/82 and pushing all the other values right one month. The result would be as follows:

Observations at Rotation (1)

1	2	3	4	5	6	7	8	9	10	11	12
4/82	5/82	6/82	7/82	8/82	9/82	10/82	11/82	12/82	1/83	2/83	3/83
(21)	10	11	12	13	14	15	16	17	18	19	20

Thus proceeding twelve rotations of the data for a performance measure (PM) are generated.

Figure I
The Performance Measures Model

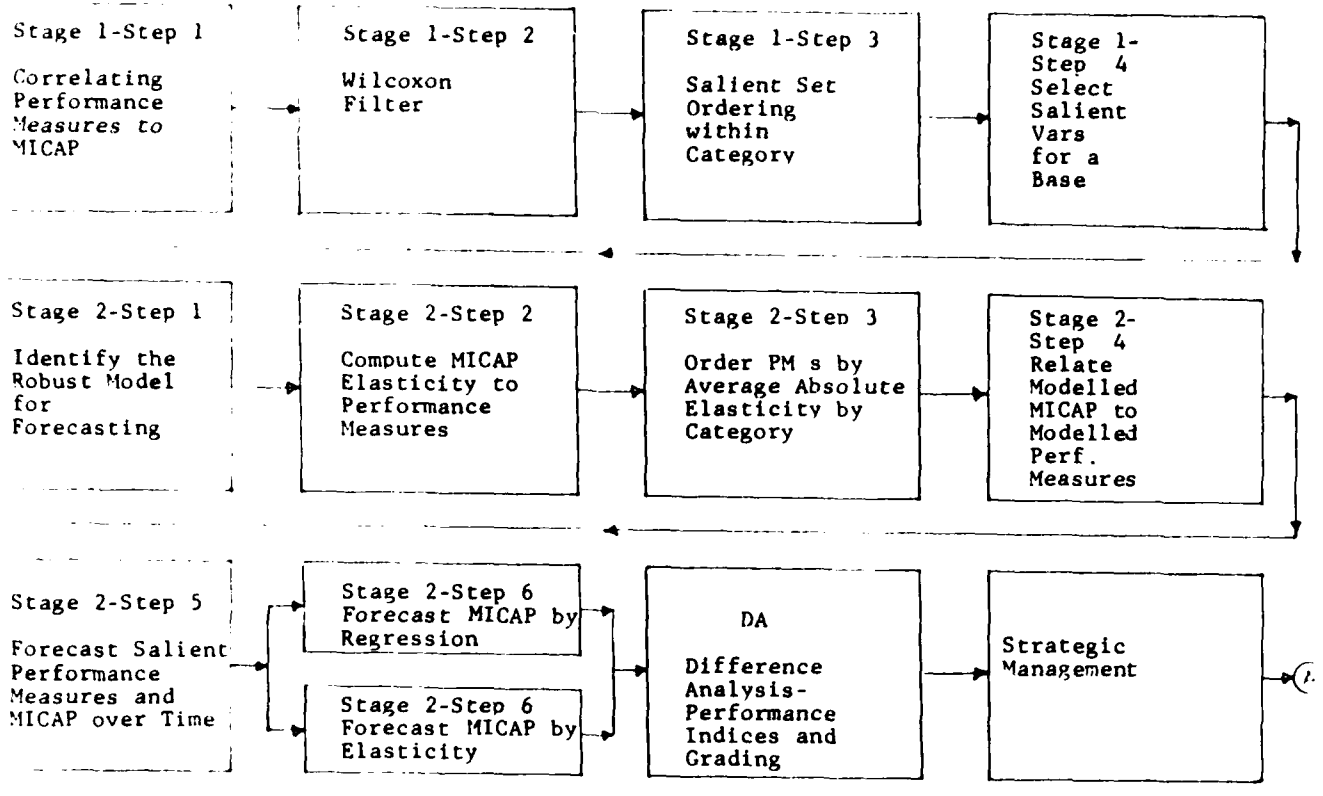

Each of the twelve rotations of the PM are now correlated with the twelve observations of MICAP for the base. One (sometimes two) of the rotations will be maximally correlated with MICAP. The rotation index of the maximally correlated rotation indicates a lag time for the correlation with MICAP. This means that if maximum correlation occurs at rotation six (6) then MICAP today is most influenced (correlated) with PM activity six (6) months ago. Appendix B contains the rotation data for all seventy eight PM's for LORING AFB in SAC.

To determine the PM rotation conmbinations that are "significantly" highly correlated with MICAP the distribution of the correlation coeffient (R) is invoked.

At the α = .001 level (two tailed) the ciritical value of (R) is 0.8230.

The correlation coefficient for every PM - rotation combination was computed for all seventy-eight PM's for SAC. Appendix C-1 contains a sample computer print out for SAC, all bases, all performances measures. Maximum significant correlations, both positive and negative, greater than 0.8230 are denoted with ***.

The justification for the above procedure is the assumption that "the past is like the present which is like the future"; in other words the general behavior of each PM and MICAP over a years period of time is essentially the same year to year.

Stage_1_-_Step_2_Selecting_The_Performance_Measure_Most_Highly Correlated_to_MICAP

From Step 1 there is found a maximum positive and a maximum negative correlation for each PM at each base in SAC. However, these maxima are not always both significant (>0.8230). The sign of the correlation also indicates the nature of the relationship between the PM and MICAP; either direct (+ correlation) or inverse (- correlation).

Using only instances (bases) for which both maximum positive correlation and the maximum negative correlation are significant a choice is made which relationship to use for the PM over all bases using the Wilcoxon Linear Two Sample Rank Correlation Test. (2).

Given that there are n_j; $j = 1, \ldots 78$ occurances for a given PM in which both the negative and positive correlations are significant then there are n_j positive correlations : n_j negative correlations. The $2n_j$ correlations are rank ordered in descending order of absolute value.

Let $w_{n_j} = \sum_{i=1}^{n_j} i z_i$; $\begin{cases} z_i = 1 \end{cases}$ if the correlation is positive and the positive correlations have the largest rank sum.

The variable w_{n_j} is distributed $\sim (n_j - 2)$ with

$$E(w_{n_j}) = \frac{n_j(2n_j+1)}{2}$$

and

$$V(w_{n_j}) = \frac{n_j^2(2n_j+1)}{12}$$

Calculated values of $t(n_j - 2)$ and the corresponding - values

and critical t values are shown in Appendix C-2. If the positive correlation rank sum significantly exceeded the negative correlation rank sum then the relationship of the PM to MICAP was assumed as direct. If the converse was true the relation of the PM to MICAP was assumed as inverse.

To insure that a statistically significant number of instances of significant positive (or negative) correlation exist for the PM at this step, the average maximum correlation, based the sample size k from which it was computed, is assumed to have a t distrubtion with k degrees of freedom. If the average maximum correlation for the determined relationship tests "not significant" at k degrees of freedom the variable is tagged as "not significant" for the MAJCOM and dropped from the salient PM set.

Consider for example PM #1 (Appendix C-2), the relation is determined as direct based on 4 instances in which positive correlation exceeded the negative correlation. The average maximum positive correlation is 0.9233 at 4 degrees of freedom. Reference to the t - distribution tables indicates that 0.9233 is significant at $\alpha = .10$. Appendix C-3 contains a table of PM'S for SAC ordered by average maximum correlation and annotated with the experimentally determined relationship to MICAP and the average time lag for the relationship. Note in Appendix C-3 a number of PM'S that exhibit significant correlation with MICAP have been ruled "not significant" based on the above test. This is a very stringent test of significance and PMs that pass it are highly significantly correlated to MICAP.

Stage_1:_Step_3:_Ordering_the_MAJCOM_"Salient_Set"_by_Significance_of_Correlation_within_Category

Appendix C-4 displays the results of the correlation filtering applied in steps 1 and 2. Here the PM's are arranged by category and significance level within category.

At this point it is clear that all variable categories are still playing a role in determining MICAP because one or more of the category PM's is statistically significantly correlated to MICAP. The variables on this display not eliminated and marked as "not significant" form the MAJCOM "salient" performance measure (PM) set. It is these variables that will be used subsequently at each base in the MAJCOM to forecast MICAP for the base.

Appendix C-5 contains a slightly different display of the same data contained in C-4 but in C-5 within each category the PM's are ordered by correlation rank and those that were identified as significant are tagged with **.

Appendix C-6 contains a summary of the above information in the form of a table of PM categories with the average rank sum for significant variables computed. (See column headed SIG R/VAR) Table C-6.1 is unsorted and table C-6.2 is sorted by SIG R/VAR. In this table the categories with the smaller average values (that is closer to the top of the table) are the categories more significantly correlated with MICAP.

The display in **Appendix C-7** shows the PM's arranged by frequency and cumulative frequency of positive, negative at total significant correlation to MICAP. It appears that there is no concentration of relationship (correlation) with MICAP in any PM or set of PMs, but rather, that there is no obvious set of PMs that are dominant in terms of freqency of significant correlation to MICAP across bases in the MAJCOM.

Stage_1-_Step_4:_Select_Salient_Variables_for_a_Specific_Base

Finally **Appendix C-8** shows the PM's at each base in SAC order by correlation, both positive and negative, with significant correlations denoted by **. When forecasting MICAP at a given base this display will be used to determine the variables in the MAJCOM salient set to delete from the forecasting set due to non-significance at the base.

Stage_2_-Step_1:_Identifying_The_Robust_Forecasting_Model

All the previous steps involved in the model were aimed at determining a "salient" PM set for a MAJCOM that could subsequently be used for every base in the MAJCOM in predicting MICAP at each base.

In developing a predictive model of MICAP the following conditions and limitations were sought and observed.

1 The model must be robust. Ideally the model should use a single "salient" set of PMs for each MAJCOM and each base in a MAJCOM.

1.1 The predictive model should use the PM's in the MAJCOM "salient" set for each base in the MAJCOM.

1.2 The predictive model should be of the same mathematical form for each base in a MAJCOM and the same for each MAJCOM.

2. Although the same PM's will be used to predict MICAP at every base in a MAJCOM, the PM's maximum correlation with MICAP from base to base will occur at different rotations (lag times).

3 The values of the PM's and MICAP over time for any base exhibit considerable random variation. The model should not be formulated to track these random variations but rather to capture the behavior underlying the random variations; that is the model should capture and represent the "essential" underlying behavior of each PM and MICAP over time.

4. The data contains only twelve (12) observations for each PM at each base. Since a MAJCOM "salient" set of PM's could contain more than twelve (12) PM's linear combinations of the PM's cannot be regressed on MICAP. Furthermore time series cannot be used effectively on so few data points.

5. The model must be capable of yielding the MICAP elasticity to each PM.

In the search for a "robust" predictive model, the limited amount of data (12 observations) is the key limitation on the methodology. It is clear that any attempt to regress linear combinations of the PM's on MICAP will fail the robustness criteria outlined above, if all the PM's in the "salient" set are to be used.

Based on the data limitation a model must be developed that relates each PM to time and MICAP to time then provides a way to relate each PM to MICAP. This model must reflect the "essential" behavior of these variables over time providing acceptable R^2 values from regressions of the variables over time.

Appendix D contains plots of the observed PM data and MICAP data for twelve months for LORING AFB, SAC, and includes the forty-one of the seventy-eight performance measures that were identified as "salient" for the MAJCOM.

Underlying the random fluctuation of MICAP and the PM's over time there are four "essential" behaviors (trends) that can be seen and which make sense in terms of the common sense relationships that can exist between MICAP and the individual PM's.

The four "essential" variable behaviors apparent in the data are shown below:

Positive Linear Trend

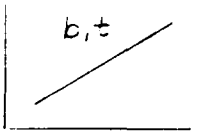

Negative Linear Trend

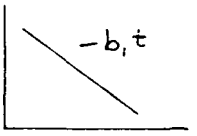

Concave Turning Point Trend

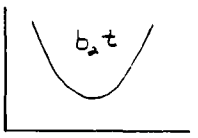

Convex Turning Point Trend

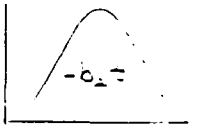

Decreasing Trend

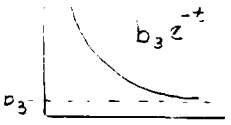

Increasing Trend

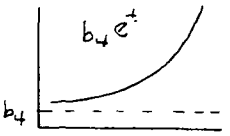

Often the observed data for a PM or MICAP will exhibit more than one of the above trends and hence the general robust model is

$$\left\{ \begin{matrix} PM_t \\ MICAP_t \end{matrix} \right\} = b_0 + b_1 t + b_2 t^2 + b_3 e^{-t} + b_4 e^{t} \qquad t = 1, \ldots, n$$

Appendix D shows the model extimates plotted with the observed data for MICAP and the PM's in the MAJCOM (SAC) "salient" set. It can be seen that the model is smooth, thus representing the complex trend in the data. Furthermore it can be seen that the model is sensitive to major upturns or downturns in the observed data.

However, MICAP is not yet related to the PM's such that MICAP can be forecast from the PM's. Also the impact of each PM as measured by the elasticity of MICAP to each PM is also not yet known.

Stage_2_-_Step_2:_The_MICAP_Elasticity_to_Performance_Measures

To establish the impact of each PM on MICAP the elasticity of MICAP to each PM is computed by regression using the following model.

$$MICAP_t = \alpha \left(PM_t^i\right)^{\beta} \qquad \begin{matrix} t = 1, \cdots, 12 \\ i = 1, \cdots, 78 \end{matrix}$$

This is a Cobbs-Douglas production-function in which the parameter is the elasticity of MICAP to the PM. To see this consider the equation

$$Y = \alpha X^{\beta}$$

then $$\frac{\partial Y}{\partial X} = \alpha \beta X^{\beta - 1}$$

which is $$\frac{\partial Y}{\partial X} = \beta \frac{Y}{X}$$

which a little algebra can show is

$$(\partial Y / Y) / (\partial X / X) = \beta$$

Replacing the infinitesimals ∂Y and ∂X with finite differences we get

$$\frac{\left(\frac{\Delta Y}{Y}\right)}{\left(\frac{\Delta X}{X}\right)} = \beta$$

in which $\Delta Y = Y_{t+1} - Y_t$ and $\Delta X = X_{t+1} - X_t$ and then

$$\beta = \frac{\left(\frac{Y_{t+1} - Y_t}{Y_t}\right)}{\left(\frac{X_{t+1} - X_t}{X_t}\right)}$$

which can be seen to be the ratio of percentage changes in the respective variables which is a definition of elasticity. The results of regression on the transformed model

$$\ln MICAP_t = \ln \alpha + \beta \ln PM_t^i \quad ; \quad \begin{matrix} t = 1, \cdots, 12 \\ i = 1, \cdots, 78 \end{matrix}$$

are found in Appendix E.. The elasticities for each regression are denoted as BETA (2.1).

Stage_2_-_Step_3:_Average_Absolute_Elasticity_by_Performance_Measure_Category

Table 2-0 displays the forty-one (41) PM's selected as salient for LORING AFB, SAC by category.

Table 2-1 shows the forty-one (41) salient MAJCOM (SAC) PM's, the maximum average correlation to MICAP, the rotation (lag) for the correlation and the elasticity of MICAP to the PM. These results were obtained using all twelve (12) months of data available for each PM. Also noted is the PM category and the category name. Table 2-2 summarizes the average absolute correlation of the salient PMs with MICAP by category including the standard deviation also the absolute elasticity of MICAP to the PM's, and the standard deviation. This table also shows the percentage of the PMs in a category that turned out significant for the MAJCOM.

In tables 2-3 and 2-4 appear the management data that would be used to draft a MICAP management strategy at the base level. In Table 2-3 the PM categories are ordered by the percentage of the variables in a category significant for the MAJCOM. Note that with exception of categories 3, 12 and 13 the ranking closely follows a ranking by average absolute elasticity. Table 2-4 shows the PM categories ranked by average absolute elasticity with MICAP in descending order. Appearing in the last column of the table is the category PM with the highest elasticity to MICAP.

From the data in Tables 2-1 to 2-4 it appears that the following PM categories are highly influential on operational capability levels.

TABLE 2-0
SAC SALIENT VARIABLES FROM MAJCOM SELECTION
FOR BASE 4678 LORING AFB

GROUP	GROUP_NAME	SIGNIFICANT VARIABLE	MAXIMUM CORRELATION ROTATION	MAXIMUM CORRELATION
1	Measures of Size	5	0	-.8436
		6	0	-.8436
		2	Not Sig	Not Sig
		1	0	-.8236
		3	Not Sig	Not Sig
		4	0	-.8471
2	Activity Measures	15	0	-.3264
		19	0	.8909
		14	9	-.8240
		17	6	-.9487
		12	11	-.8419
		11	10	-.8622
3	Effectiveness Measures	21	6	-.8474
		24	7	-.8630
		23	9	.8503
		25	2	.8694
		22	4	.8478
4	MICAP	N/A	N/A	N/A
5	Repair Cycle Information	32	10	.3202
		33	0	-.8586
		35	7	.9123
		34	3	-.8230
		39	4	.8535
6	EOQ/Recoverable Mix	42	7	.8202
7	Urgency Mix	43	7	-.8252
		44	7	.8842
8	Priority Mix	45	Not Sig	Not Sig

TABLE 2-Q (CONT)
SAC SALIENT VARIABLES FROM MAJCOM SELECTION
FOR BASE 4628 LORING (CONTINUED)

GROUP	GROUP_NAME	SIGNIFICANT VARIABLE	MAXIMUM CORRELATION ROTATION	MAXIMUM CORRELATION
9	Funding Mix	47	0	.8720
10	Bench Stock	49	5	-.9242
11	Excess	57	Not Sig	Not Sig
		55	7	.8955
		54	4	.9426
		52	4	.9393
12	Special Levels	60	2	.8680
		58	Not Sig	Not Sig
		61	Not Sig	Not Sig
		53	0	-.9379
13	Minimum Levels	63	Not Sig	Not Sig
		62	0	-.8472
		64	0	-.9436
14	MRSK/DSK	67	0	-.9348
15	Receipts on Time	70	3	.8976
		69	3	.8705
		71	3	.8288
16	Inventory Accuracy	74	6	-.8922
		76	Not Sig	Not Sig
		72	6	-.8281
		77	6	-.8996
		73	6	-.8338

TABLE 2-1
ELASTICITY WITH MICAP
ANALYSIS
WITH CORRELATIONS
SRAN 4678
LORING

VARIABLE	VARIABLE_NAME	CORRELATION	ROTATION	MICAP ELASTICITY	CAT NO.	CATEGORY _NAME__
5	$ OMB - Overall (EOQ)	-.8436	0	-1.44195	1	Cat.1 - Effectiveness Measures
6	$ OMB - Overall (Equip)	-.8463	0	- .367246	1	Cat.1 - Effectiveness Measures
1	No Item Recs - Overall	-.9236	0	-5.93254	1	Cat.2 - Activity Measures
4	$ OMB - Overall (Repair Cyc)	-.8471	0	- .492101	1	Cat.1 - Effectiveness Measures
15	Total Dor - Rec	.9264	0	1.266122	2	Cat.2 - Activity Measures
19	Tot Overall Recs - $ Total	.8909	0	1.36762	2	Cat.2 - Activity Measures
14	Total Receipts - Equip	-.8240	9	- .647362	2	Cat.2 - Activity Measures
17	Total Dor - Equip	-.9487	6	- .73521	2	Cat.2 - Activity Measures
12	Total Due - Outs - Equip	-.8419	11	- .289608	2	Cat.2 - Activity Measures
11	Total Due - Outs - Supplies	-.8672	10	- .776015	2	Cat.2 - Activity Measures
21	EOQ Issue Eff	-.8474	5	-3.07552	3	Cat.1 - Effectiveness Measures
24	Rec Rel Eff	-.8630	7	-1.73233	3	Cat.1 - Effectiveness Measures
23	EOQ Stk Eff	.8502	9	10.6282	3	Cat.1 - Effectiveness Measures
25	EOQ Rel Eff	.8394	2	6.29269	3	Cat.1 - Effectiveness Measures
22	Rec Stk Eff	.8279	4	3.68845	3	Cat.1 - Effectiveness Measures
20	Rec Issue Eff	.8477	4	4.0762	3	Cat.1 - Effectiveness Measures
37	Avg AWP. NRTS - All Org	.3202	10	.008355	5	Cat.5 - Repair Cycle Information
33	Avg RCT. Tot RTS - All Org	-.9586	0	-1.21904	5	Cat.5 - Repair Cycle Information
35	AVG RCT Condmn - All Org	.9122	7	1.0927	5	Cat.5 - Repair Cycle Information
34	Avg RCT. Total NRTS - All Org	-.8730	3	- .437352	5	Cat.5 - Repair Cycle Information
39	Total Units RTS - All Org	.8525	4	.481437	5	Cat.5 - Repair Cycle Information
42	EOQ Itms Reqst - % Tot EQ	.9701	7	6.01519	6	Cat.6 - EOQ/Recoverable Mix
43	Itms Rqsted, Urg B, % Tot	-.9259	7	-1.93023	7	Cat.7 - Urgency Mix
44	Itms Rqsted, Urg C, % Tot	.8842	7	2.72512	7	Cat.7 - Urgency Mix
47	% Tot Itms R/O - SSD	.8720	0	8.08066	9	Cat.9 - Urgency Mix
49	Bench Stk Auth - Total	-.9242	5	-1.03269	10	Cat.10- Bench Stock
55	$ Excess Equip - SSD	.8955	7	.247256	11	Cat.11- Excess
54	$ Excess Supplies - Non Stk F	.9426	4	.413365	11	Cat.11- Excess
52	$ Excess Supplies - SSD	.9392	1	.43688	11	Cat.11- Excess
60	Tot Itms - Sp Lvl Equip	.9690	2	1.13688	12	Cat.12- Special Level
59	Tot Itms - Sp Lvl EOQ	-.9379	0	-4.81902	12	Cat.12- Special Level
62	Just 0 - Life Cycle Ret	-.8472	0	-1.49975	13	Cat.13- Minimum Level
64	Just - All others	-.9436	0	-4.6694	13	Cat.13- Minimum Level
67	Tot Details - MSK	-.9349	0	- .474087	14	Cat.14- WRSK/MSK
70	Tot Pri Grp 2 - % on Time	.8476	2	3.007	15	Cat.15- Receipts on Time
69	Tot Pri Grp 1 - % on Time	.8704	3	4.02342	15	Cat.15- Receipts on Time
71	Tot Pri Grp 3 - % on Time	.2288	3	10.1738	15	Cat.15- Receipts on Time
74	Tot Itms Counted - Id Chg	-.8422	6	- .075251	16	Cat.16- Inventory Accuracy
72	Tot Itms Counted - Complete	.3291	6	- .015019	16	Cat.16- Inventory Accuracy
77	Accuracy, % Units - SP	-.8996	6	- .82954	16	Cat.16- Inventory Accuracy
73	Tot Itms Counted - SP	-.9338	6	- .02398	16	Cat.16- Inventory Accuracy

TABLE 2-2
ELASTICITY WITH MICAP
SUMMARY ANALYSIS
BY CATAGORY
SRAN 4578 LORING

CATEGORY_#	CATEGORY_NAME	CORRELATION AVG. ABS	CORRELATION STD DEV.	ELASTICITY AVG. ABS	ELASTICITY STD DEV	VARIABLE IN CAT	#CAT VARS SIG	% CAT VARS SIG
1	Measures of size	.8402	.00964	2.0611	2.2795	6	4	66.66%
2	Activity Measures	.9832	.04415	.84698	.3685	13	6	46.15
3	Effectiveness Measures	.8459	.01067	5.4322	3.4272	7	6	85.78
4	MICAP	N/A	N/A	N/A	N/A	N/A	N/A	
5	Repair Cycle Info	.8835	.02758	.6478	.4483	9	5	55.55
6	EOQ Recoverable Mix	.8701	0.0	6.0152	0	1	1	100.00
7	Urgency Mix	.8550	.02913	2.3276	.3974	2	2	100.00
8	Priority Mix	0	0	0	0	2	0	0.0
9	Funding Mix	.8720	0	8.0806	0	2	1	50.00
10	Bench Stock	.9242	0	1.03269	0	3	1	33.33
11	Excess	.9258	.02147	.3658	.0844	6	3	50.00
12	Special Levels	.9029	.03493	3.0079	1.811	4	2	50.00
13	Minimum Levels	.8954	.04817	3.0846	1.5848	4	2	50.00
14	NPSK/NSK	.9348	0	.474087	0	3	1	33.33
15	Receipts on Time	.8489	.8489	5.7347	3.1662	3	3	100.00
16	Inventory Accuracy	.8504	.8509	.2359	.3435	7	4	57.14

TABLE 2-3
CATEGORIES RANKED BY
% OF VARIABLES/CATEGORY
SIGNIFICANT
AND BY THE
AVERAGE ABSOLUTE ELASTICITY
OF VARIABLES IN THE CATEGORY

CATEGORY #	CATEGORY_NAMES	%CAT_VARS_SIG	AVG_ABS_ELASTICITY
6	EOQ Recoverable Mix	100 (1/1)	6.0152
15	Receipts on Time	100 (3/3)	5.7347
7	Urgency Mix	100 (2/2)	2.3276
3	Effectiveness Measures	85.71 (6/7)	5.4322
1	Measures of Size	66.66 (4/6)	2.0611
16	Inventory Accuracy	57.14 (4/7)	.2359
5	Repair Cycle Information	55.55 (5/9)	.6478
9	Funding Mix	50.00 (1/2)	8.0806
13	Minimum Levels	50.00 (2/4)	3.0846
12	Special Levels	50.00 (2/4)	3.0079
11	Excess	50.00 (3/6)	.3658
2	Activity Measures	46.15 (6/13)	.8470
10	Beach Stock	33.33 (1/3)	1.0327
14	MPSK/MSK	33.33 (7/3)	.47409

TABLE 2-4
CATAGORIES RANKED BY
AVERAGE ABSOLUTE ELASTICITY TO MICAP

CATEGORY #	CATEGORY_NAME	Avg Abs ELASTICITY	Avg Abs CORRELATION	VARIABLE #/ELASTICITY/VAR NAME MOST SALIENT VARIABLE (HIGHEST ABSOLUTE ELASTICITY)	
9	Funding Mix	8.0806	.8720	47/ 8.08066	% Tot Itms c R/O - SSD
6	EOQ Recoverable Mix	6.0152	.8701	42/ 6.0152	EOQ Itms Reqst - % Tot EOQ
15	Receipts on Time	5.7347	.8489	71/10.1738	Tot Itms Counted - Complete
3	Effectiveness Measures	5.4322	.8459	* 22/ 3.6884	Rec Stk Eff
13	Minimum Levels	3.0846	.8954	64/-4.6694	Just All Others
12	Special Levels	3.0079	.9029	60/ 1.1969	Tot Itms Sp Lvl - Equip
7	Urgency Mix	2.3276	.8550	44/ 2.7251	Itms Rqsted Urg C - % Total
1	Measures of Size	2.0611	.8402	1/-5.9325	No Itm Reds - Overall
10	Bench Stock	1.0327	.9242	49/-1.0327	Bench Stk Auth - Total
2	Activity Measures	.8470	.8832	19/ 1.3676	Tot Overall Reqs - $ Total
5	Repair Cycle Info	.6478	.8835	33/-1.2190	Ave RCT, Tot RTS - All Org
14	WRSK/MSK	.4741	.9348	67/- .4741	Total Det - MSK
11	Excess	.3652	.9258	52/ .4368	$ Excess Supp - GSD
16	Inventory Accuracy	.2359	.8509	77/- .8296	Accuracy % Units - SP.

Cat 6 - EOQ Recoverable Mix

Cat 15 - Receipts on Time

Cat 3 - Effectiveness Measures

Cat 7 - Urgency Mix

Cat 1 - Measures of Size

In an AFLMC report in 1981 report in 1981 Monaco and Esterby (6) concluded that due-outs, availability measures and reparable variables are highly salient in controlling MICAP. This results above appear to agree with exception of reparable variables which appear in the MAJCOM salient set but with lesser apparent influence on MICAP.

MICAP management would be exercised by reference to Table 2-4 and/or possibly Table 2-3. From Table 2-4 management attention would first focus on the category funding mix and within that category PM #47. Percent_of_Total_Items_with_BAO_=_SSD. This proceeding by category and variable action would be taken on the salient variables in the order prescribed by Table 2-4. Table 2-3 can be used as a cross-reference and at times and based on the number (percentage) of category PM's significant, one might change the management priority order as prescribed in Table 2-4.

Stage_2=_Step_4:_Relating_Modelled_MICAP_to_Modelled_Performance Measures

Returning to the issue of relating the PM's in the MAJCOM Salient set to MICAP recall that all have been regressed on time using the model

In order to use all the PM's in the MAJCOM salient set in the prediction of MICAP assume that MICAP can be functionally related to each PM and each PM is equally effective (weighted) in its forecastability of MICAP. Then the central limit theorem and the law of large numbers would lead to the assumption that the average of the forecasts of MICAP made using each PM would be a best linear unbiased estimator of future values of MICAP.

To test this hypothesis the observed PM values in the salient MAJCOM (SAC) set were normalized using the following equation.

$$\text{Eq 2.2} \quad N(PM)_t = \begin{cases} [PM_t - \min(PM)_t] / [\max(PM)_t - \min(PM)_t] & ; \; P(PM) > 0 \\ -[PM_t - \min(PM)_t] / [\max(PM)_t - \min(PM)_t] & ; \; P(PM) < 0 \end{cases}$$

$t = 1, \ldots, n \quad i = 1, \ldots, 79$

in which $N(PM)_t$ indicates a normalized value of PM Appendix F contains the result of these calculations. The last page of the appendix shows the observed MICAP values and the estimated MICAP values. The estimated MICAP values are calculated as shown below

$$\overline{MICAP}_t = \frac{\sum_{i=1}^{n} PM_{i,t}}{n} = \min(MICAP)_t + \max(MICAP)_t$$

in which $\overline{MICAP}_t$ is the estimated MICAP computed from the average of the normed values of all the PM's in the salient set at time t.

Reference to the summary (last page) of Appendix F indicates that an averaging process results in a maximum percentage error of 22%.

This very rough averaging process, though indicative that averaging of estimates is feasible, but the process must be cast in terms of the robust model already found. (Eq 2.1 above).

The averaging can be affected as follows. Since

$$\widehat{MICAP}_t = f(t)$$

and

$$\widehat{PM}_t^i = g(t)$$

MICAP and the PM's are both functions of time using the same model form MICAP can be expressed in a modelled normalized form similar to Eq 2.2 above by regressing the model (regression estimated) values of each MICAP on the modal values (regression estimated) values of each PM in the Salient set. This is of the form

$$\text{Eq 2.3} \qquad \widehat{MICAP}_t = \alpha_0 + \alpha_1 (PM_t^i)$$

α_0 & α_1 and being estimated by regression.

Stage_2_Step_5:_Forecast_The_Salient_Performance_Measures_and MICAP

To forecast MICAP we use the individual regressions of the PM's on time to forecast each PM ahead some number of months, say one month. Then we substitute these forecast PM values in Eq 2.3 above and we get forty-one forecast values of MICAP which are then averaged to get a final forecast of MICAP one month ahead.

To test the model each PM is regressed on time over for nine months, months 10, 11 and 12 which are 1/83, 2/83 and 3/83 to be forecast. Appendix G contains these regressions.

The regressions of estimated (modelled) MICAP on modelled PM values are shown in Appendix H. Reference to the Coefficents of Determination, Multiple Correlation Coefficents and F Ratios indicate that the regressions are all highly significant. The fact that the corrected values of the coefficient of determination and multiple correlation coefficient are in some cases low is a reflection of the fact that there are five terms in a model expressed by only nine values. If the model were a tracking model as one would find in time series methodology this would indicate that the model is a case of "over-fit" that is relatively few points fitted by a model with nearly as many terms. However, since the model is a smooth trending model these values mean only that the number of terms in the model is not greatly fewer than the number of data points.

Appendix H-1 contains the same regressions as in Appendix H but using the model

Eq 2 - $\widehat{MICAP}_t = \beta_0 (PM_t)^{\beta_1}$

in which β_1 is the nine month modelled MICAP elasticity to PM. These elasticities will be used in an alternate model of MICAP in what follows.

Stage 2 - Step 6: Regression and Elasticity Forecasts of MICAP

The final step in the modelling is to compute MICAP forecasts for months 10, 11 and 12 using forecast values of the PM's for months 10, 11 and 12. This is accomplished using Eq 2.3. Appendix I-1 contains the results for month 10, 11 and 12 forecast using Eq 2.3. The results are summarized below.

MONTH	MICAP FORECAST	ACTUAL MICAP	FORECAST - ACTUAL DIFFERENCE	%_DIFFERENCE
10	.00410811	.00433000	-.00022189	- 5.124450
11	.00474079	.00336000	.00138079	41.094900
12	.00637311	.00291000	.00346311	119.007000

The forecast deteriorates badly past one month in the future. The results indicate that the method is reasonably reliable in the short term but not beyond the next period.

The steps outlined above were repeated using ten (10) months of data forecasting 11 and 12. The results appear below. (Appendix_I-2)

MONTH	MICAP FORECAST	ACTUAL MICAP	FORECAST - ACTUAL DIFFERENCE	%_DIFFERENCE
11	.00385612	.00336000	.00049612	14.765500
12	.00340055	.00291000	.00049055	16.857500

Finally the steps above were repeated using eleven (11) months of data and forecasting month 12. The results appear below. (Appendix_I-3)

MONTH	MICAP FORECAST	ACTUAL MICAP	FORECAST - ACTUAL DIFFERENCE	%_DIFFERENCE
12	.00314716	.00291000	.00023716	8.149720

The results above were computed using the regression method of Eq. 2.4. This method is based on the trend models of the form of Eq 2.1. Because these models are smooth they are not extremely sensitive to major changes in a few salient variables. Therefore, results were obtained by a different forecasting method which is sensitive to large changes in a few PM's and which is based on the elasticity of MICAP to each PM. The model is of the form shown below and was used in place of Eq 2.4 to generate the results that follow.

Given the equation for elasticity

$$\text{Eq 2.5} \qquad \beta_i = \frac{\%\ \text{CHANGE IN MICAP}}{\%\ \text{CHANGE IN PM}^i} \; ; \; i = 1, \ldots, 78$$

Then

$$\beta_i = \left(\frac{M_{t+1} - M_t}{M_t} \right) \Big/ \left(\frac{V^i_{t+1} - V^i_t}{V^i_t} \right)$$

$$\frac{M_{t+1} - M_t}{M_t} = \beta_i \left(\frac{V^i_{t+1} - V^i_t}{V^i_t} \right)$$

$$\text{Eq 2.6} \qquad M_{t+1} = \beta_i \left(\frac{V^i_{t+1} - V^i_t}{V^i_t} \right) \cdot M_t + M_t$$

Using Eq 2.6 MICAP was forecast as above and the results are as follows. See Appendix I - 4

MICAP
ELASTICITY FORECASTS
BASED ON 10 MONTHS

FORECASTING MONTHS 11 AND 12

MONTH	MICAP FORECAST	ACTUAL MICAP	FORECAST - ACTUAL DIFFERENCE	%_DIFFERENCE
10	.00455481	.0043300	.00022481	5.192010
11	.00638392	.0033600	.00302392	89.997700
12	-.03382100	.00291000	-.03673100	1262.230000

MICAP
ELASTICITY FORECASTS
BASED ON 10 MONTHS

FORECASTING MONTHS 11 AND 12

MONTH	MICAP FORECAST	ACTUAL MICAP	FORECAST_-_ACTUAL DIFFERENCE	%_DIFFERENCE
11	.00427904	.0033600	.00091904	27.352400
12	.00399758	.0029100	.00108758	37.374000

MICAP
ELASTICITY FORECAST
BASED ON 11 MONTHS

FORECASTING MONTH 12

MONTH	MICAP FORECAST	ACTUAL MICAP	FORECAST_-_ACTUAL DIFFERENCE	%_DIFFERENCE
12	.00300048	.0033600	.00009048	3.109270

Comparing the MICAP forecast results accomplished by the Regression method and the Elasticity method the latter method will be more sensitive to PM's that in many given forecast period show large changes in value. whereas the Regression method will be less effected and yield more stable results. As will be noted from the data shown above both methods appear to yield good short range forecasts (one month ahead).

Appendix_I contains the results similar to those above for some other SACs bases.

As discussed in the foregoing the MICAP forecasting model provides information about the impact of salient set PM's on MICAP that can be used to develop a base level management strategy. In the next chapter a model is discussed that provides a way to develop supply performance indices by which bases and major commands maybe compared and graded on their performance in managing MICAP using the results of the forecast model. The model developing the performance indices and grades is called DA. (Difference Analysis).

CHAPTER 3

DIFFERENCE ANALYSIS (DA)

A common paradigm in decision making and alternative evaluation is to think of the decision problem in terms of a number of alternatives each characterized, described and set apart from all others by a set of attributes common to all alternatives but differing in value or description for each alternative. For example, the decision problem may be choosing the "best" automobile. The alternatives and attributes appear below:

		Attributes		
Alternative	No._of_Doors	Color	Style	Interior
Japanese	2	Red	Coupe	Velour
European	3	Green	Sedan	Leather
American	4	Black	Wagon	Plastic

When the number of alternatives and the number of attributes gets large human decision processes are severly taxed and often simply overcome by the number of trade-offs that must be considered. This is called "Cognitive Overload". Furthermore, human decision making based on subjective considerations seldom avoids the influence of pre-dispositions, preference biases and effort reducing strategies applied to the problem itself.

Another very perplexing problem in multi-alternative, multi-attribute problem scenarios is that of determining how to combine incommensurable attributes into a value for each alternative that allows at least ordinal ranking of the alternatives from "best" to "worst".

Most troublesome, however, is the problem of having attributes, the values of which, over all alternatives are distributed differently and perhaps in non-normal fashion. For example, if we seek to compare the value of one basketball player to another, the following criteria might be considered important the player's height, average points cored per game, and frequency of injury. Of course, there may well be other criteria to consider but these three attributes are enough to illustrate a key point. The distribution of the random variable of players' heights is Normal. The distribution of the random variable of mean points scored per game is Normal, but with a standard deviation different than the first distribution. The distribution of the frequency of injury is Poisson. To compare these three attributes, we must first create a composite random variable from the three different distributions above and then discover its probabability density function so that we can establish a standard of comparison which, in this case, would be the mean of the probability density functions. While the first activity is possible, the second is an extraordinarily difficult computational task and may in fact, not always be possible. In the above case, these attributes may be referred to as incommensurable quantities by virtue of the dissimilarity of their various probability density functions.

There are then, no statistically defensible ways to add these distributions or to compare statistics drawn from them for purposes of ranking alternatives. The attribute values may also be dimensionally different and valued on different scales

complicating further any attemps at a merger of the attributes into a ranking scale for the alternatives.

Even when only one attribute is used the rank alternatives it can be unclear how much difference exists between the alternatives since the ordering based on the attribute values is essentially ordinal.

In the context of the Air Force inventory system what is sought is a technique that will develop supply performance indices for basees and major commands and sets of bases grouped by weapons systems from which a grade can be determined for bases, groups of bases and MAJCOM'S that will indicate on a common sense scale (for example percentile score) "supply performance" with respect to one or more of the PM's being managed to improve operational capability. Furthermore the "grading" indices should provide for the determination of differences in supply performance between bases, groups of bases and MAJCOMS.

The model should provide for "grading" to be done using any or all of the PM's in a MAJCOM salient set or all seventy-eight of PM's described in Appendix A.

In the context of the automobile example given above "Alternative" will always refer to a base, group of bases or MAJCOM, and "Attribute" will always refer to one or more of the seventy-eight supply performance measures given in Appendix A.

The DA model has the following functional components.

1. Utility Conversion Module (UCM)
2. Multiple Criteria Decision Analysis Module (MCDA)
3. Standardization and Comparison Module (RIDIT)

Utility_Conversion_Module (UCM)

As noted above when more than (or one) PM is used to "grade" supply performance there exists a multi-dimensional scaling problem since the PM's represent many different units of measure ($, #, etc.) and many different value scales. The UCM module converts all the attribute (PM) values to utilities on a scale 0 to 1. Utility theory is covered in detail in "Utility Theory for Decision Making" by Fishburn (3).

Multiple_Criteria_Decision_Analysis_Module (MCDA)

The MCDA stage of the DA model is concerned with:

1. A process for combining weights (if any) and attribute values to develop a composite value for each alternative.
2. A process for rank ordering the compositve values of alternatives from "best" to "worst".

The composite alternative values are formulated using utility functions of the PM utility values for the alternative. Zeleny (4) notes that establishing individual attribute utility functions is often difficult enough to make attempts at creating alternative composites impractical.

Therefore linear utility functions are used based on the assumption of utility independence between the PM's. Utility independence means that a given value of one PM (attribute) can occur given any set of values for the remaining PM's (attributes).

A non-empty independent set of PM's always exists since if any two PM's (attributes) are found to be utility dependent they are combined into a single PM (attribute) and redefined as a new attribute independent of the remaining PM's.

The independent PM's can be weighted to indicate the relative importance of the PM's or how many units of utility of one is thought to be equal to one utility unit of another.

The utility function for a given alternative (base) would ben be given as:

$$U = \alpha_1 w_1 PM^1 + \alpha_2 w_2 PM^2 + \cdots + \alpha_n w_n PM^n$$

More complex utility functions are possible as described by Zeleny however, in the context of the current problem there appears to be no motivating reason to introduce them.

Standardization_and_Comparison_Module (RIDIT)

The standardization and comparison module provides for the following capabilities:

1. A process for defining the "average" or "standard" performance level for all alternatives as a whole.
2. A process for comparing the supply performance of alternatives to the standard performance for all alternatives dividing the alternatives into three performance groups.
    - Those alternatives which exhibit "statistically significantly" above average performance.

- Those alternatives which exhibit "statistically significantly" below average performance.
- Those alternatives which exhibit "statistically" average performance.

3. A process for comparing alternatives to each other the comparisons being expressed as percentile differences. These differences may be determined to be:
   - Statistically significant
   - Statistically not significant

   Therefore two alternatives may be determined as differing significantly in supply performance regardless of where they may rank relative to the overall average for all alternatives. (i.e. above average, below average or average).
4. A process for supplying confidence limits on the performance indices and control limits about the "average" or "standard" performance value.

The RIDIT methodology was originally developed by Dr. Irwin D.J. Bross, Chief Statistician at Roswell Park Memorial Institute in Buffalo, N.Y. (7)

DA is a hybrid computerized modelling technique comprised of the three components:

- Utility Conversion Module (UCM)
- Multiple Criteria Decision Analysis (MCDA)
- Standardization and Comparison Module (RIDIT)

DA is a product developed by the author and is a copyrighte proprietary product. The product has been installed on the IBM

4341 at Gunter AFB in object code form for the use of AFLMC as described in this report. Because of the proprietary nature of the product no source listing of the code is supplied with this report.

The DA product was thoroughly tested during the summer of 1984 during the author's tensure at Gunter working on this project as a Summer Faculty Researcher. Appendix K contains a sample output which is described below.

The DA example uses all bases in SAC. the comparison and grading indices calculated for one PM only, namely, Recoverable Stockage Effectiveness. (Variable 22, Appendix A).

Recall that variable #22 is one of the variables in the salient set for SAC having an elasticity with MICAP of 3.68845 at rotation 0 and a correlation with MICAP of .8272 (See table 2-1). This means that MICAP in SAC is significantly correlated to Recoverable Stockage Effectiveness at the $\alpha = .05$ level. Furthermore reference to appendix B indicates that for variable #22 the maximum negative correlation with MICAP of -.8007 occurs at rotation 0 (the current period).

The nature of the relationship between PM #22 and MICAP that would be expected is that as Recoverable Stockage Effectiveness increases, MICAP decreases. In the early stages of the model the variables were rotated in time seeking the strongest possible correlation with MICAP in order to guarantee that the regressions used later in forecasting MICAP showed the greatest possible Multiple R and F values. However, the maximally correlated rotation of a variable with MICAP may not be related directly or

inversely as common sense would predict. The logical, common sense, relationship would occur at rotation 0.

At rotation 0 the correlation of variable #22 with MICAP is negative. The elasticity value 3.68845 indicates the maximum ratio of the rates of change of the variable and MICAP but not necessarily the logical relationship, direct or inverse.

At rotation 0 Variable #22 is almost as highly negatively correlated with MICAP as it is positively at rotation 4. In order to achieve an elasticity bearing the logical inverse relationship to MICAP multiply the elasticity by the ratio of the correlations at rotation 0 and rotation 4.

$$\varepsilon' = \varepsilon \cdot \frac{R(0)}{R(4)}$$

or

$$\varepsilon' = 3.68845 \left(\frac{-.8231}{.8277} \right)$$

and the revised elasticity is

$$\varepsilon' = -3.54769$$

The approach above can be applied to any variable which during the MAJCOM modelling stage was assigned a maximum correlation relationship antithetical to the expected relationship. The justification of the above step is as follows. The multiple correlation coefficient R indicates the presence in

[illegible]

Let the regression model for the straight line be given as

$$Y_i = a + bX_i \qquad i = 1, \ldots, n$$

Then the slope of the regression straight line is given as

$$b_1 = \frac{\sum_{i=1}^{n}(x_i - \bar{x})(Y_i - \bar{Y})}{\sum_{i=1}^{n}(x_i - \bar{x})^2} \qquad (5)$$

and

$$a_1 \sum_{i=1}^{n}(x_i - \bar{x})^2 = \sum_{i=1}^{n}(x_i - \bar{x})(Y_i - \bar{Y})$$

Then dividing each side by the denominator in Eq 3.1 we get

$$\frac{\sum (x - \bar{x})^2}{\sqrt{\sum (x - \bar{x})^2 \sum (Y - \bar{Y})^2}} = \frac{\sum (x - \bar{x})(Y - \bar{Y})}{\sqrt{\sum (x - \bar{x})^2 \sum (Y - \bar{Y})^2}} = R$$

From the above we see that

$$b_1 = \frac{R\sqrt{\sum_{i=1}^{n}(x_i - \bar{x})^2 \sum_{i=1}^{n}(Y_i - \bar{Y})^2}}{\sum (x_i - \bar{x})^2}$$

which can be rewritten as

$$b_1 = R\sqrt{\frac{\sum_{i=1}^{n}(x_i - \bar{x})^2 \sum_{i=1}^{n}(Y_i - \bar{Y})^2}{\left[\sum_{i=1}^{n}(x_i - \bar{x})^2\right]^2}}$$

or

Eq 3.2 $$b_1 = R\sqrt{\frac{\sum_{i=1}^{n}(Y_i - \bar{Y})^2}{\sum_{i=1}^{n}(x_i - \bar{x})^2}}$$

Note that the MICAP elasticity to a variable X as a function of time is

Eq 3.3 $$\varepsilon = \frac{\left(\frac{Y_{t+1} - Y_t}{Y_t}\right)}{\left(\frac{X_{t+1} - X_t}{X_t}\right)} = \frac{X_t}{Y_t} \cdot b_1$$

Since all the x_i and y_i values for any rotation of a PM are the same then for two different rotations of the PM the slopes of the regression straight lines for each rotation would be

$$b_j \neq b_k \quad \text{for rotation } j \text{ and rotation } k$$

But from the Eq. 3.2

Eq 3.4 $$b_j = \Sigma_j \sqrt{\frac{\sum_{i=1}^{n} (y_i - \bar{y})^2}{\sum_{i=1}^{n} (x_i - \bar{x})^2}}$$

Then

Eq 3.5 $$\frac{b_j}{b_k} = \frac{\Sigma_j}{\Sigma_k}$$

Since the radical expresion in Eq. 3.4 involves the same x_i, y_i values.

From Eq 3.3 $$\xi_j = b_j \left(\frac{x_i^j}{y_i^j} \right)$$

for any value of i, $i = 1, \ldots$
(N = 12 in this model)

Then $$b_j = \xi_j \left(\frac{y_i^j}{x_i^j} \right)$$

and Eq 3.5 becomes

$$\frac{\xi_j y_i^j}{\xi_k y_i^k} = \frac{\Sigma_j}{\Sigma_k} \qquad \text{since } x_i^j = x_i^k$$

Then $\xi_k y_i^j = \xi_j \Sigma_k y_i^k$ and $\sum \xi_k y_i^j = \sum \xi_j y_i^k$

and

or

$$\xi_j = \xi_{re} \left(\frac{R_j}{R_{re}} \right) \quad \text{q.e.d.}$$

Variable #22 Recoverable Stockage Effectiveness is a member of the MAJCOM (SAC) salient set and highly correlated with MICAP (-.8007 at rotation 0). Also the MICAP elasticity (at rotation 0) to variable #22 is -3.56569. Therefore from the correlation we infer that MICAP is strongly inversely influenced by changes in Recoverable Stockage Effectiveness and from the elasticity we infer that a 10% increase in Recoverable Stockage Effectiveness will result, on the average at any base in the MAJCOM, in a 35.6769% reduction in grounding incidents, all other salient variables remaining unchanged.

The DA analysis (Appendix K) contains two displays, first is a table of grading indices called RIDITS appearing on the first display entitled "Summary_of_RIDIT_Computations_for_Selected_Groups_Follows". On this display are listed the bases in SAC, in the left hand column, and the following statistics regarding each.

ALTERNATIVE GROUP/ATTRIBUTE GROUP - Alternates are SAC bases for the attribute group consisting of Variable

- SAMPLE - The number of non-zero observations of recoverable stockage effectiveness for the twelve (12) month period.
- EXCLUDED - Upper number of observations excluded from the computations.
- LCL - Lower 95% confidence limit on the grading index value (RIDIT)
- RIDIT - Grading index, a percentile score
- UCL - Upper 95%k confidence limit on the grading index value (RIDIT)
- LCNTRL - Lower control limit on the average RIDIT of 0.5 which corresponds to average value of Recoverable Stockage Effectiveness of .6668.
- UCNTRL - Upper control limit on the average RIDIT of 0.5.
- **(GT) or ** (LT) which indicates that the RIDIT grading index is above or below the upper or lower control limit respectively.

The second display is a graphic display of the data presented in the Summary table. The various statistics for each base are represented on the graphic display as follows:

- ALTERNATIVE GROUP/ATTRIBUTE GROUP - indicated along the abscissa. Note the order has been changed slightly from the order in the Summary table. On the graph the alternatives

(bases) are arranged in order of decreasing sample size.

- SAMPLE - Indicated along the abscissa
- LCL and UCL - Appear as a dotted limit around the RIDIT value
- RIDIT - Indicated by #
- LCNTRL and UNCTRL - Indicated by *** *** above and below 0.5 the average RIDIT

The control limits on the graph divide the bases in SAC into three Recoverable Stockage Effectiveness groups.

1. Those bases for which Recoverable Stockage Effectiveness is "Statistically Significantly" above average. On the graph these are indicated by a # above the upper control limit *** ***. On the RIDIT Summary indicated by **(GT).

2. Those bases for which Recoverable Stockage Effectiveness is "Statistically average" or "Statistically equal" to .6666 the average for the MAJCOM. On the graph these are indicated by a # between the control limits *** ***. On the RIDIT summary these are not tagged as either ** (GT) or ** (LT).

3. Those bases for which Recoverable Stockage Effectiveness is "Statistically Significantly" below average. On the graph these are indicated by a # below the lower control limit *** ***. On the RIDIT summary these are denoted by ** (LT).

From these DA displays a management strategy for Recoverable Stockage Effectiveness with SAC may be developed. Certainly those bases "graded" as below average (See list below) should seek to improve Recoverable Stockage Effectiveness. The bases in SAC for which an improvement Strategy in Recoverable stockage Effectiveness is indicated are seen from Appendix K as following.

Minot	Wurtsmith	Barlesdale
Plattsburg	Griffiss	Fairchild
Pease	Blytheville	Grand Fork
Castle		K/I Sawyer

The bases which exhibit above average performance in Recoverable Stockage Effectiveness are:

Peterson	F/E/Warren	McConnell
Anderson	Whiteman	Malstrom
March	Beale	Carswell

Clearly the highest scoring base on this performance measure is Anderson with a RIDIT grade of .9776. The poorest performance is at Platsburg with a score of .0250. These grades are percentile scores and my subtracted to find a difference. Anderson performs 95.26% better than Plattsburg in Recoverable Stockage effectiveness.

Differences in performance between any two bases may be computed similarly.

For a difference in performance between any two bases to be statistically significant, regardless of their position relative to the MAJCOM average the difference in their RIDIT scores must be greater than the absolute difference between 0.5 and either control limit, namely .0833 or 8.33%.

In addition to comparing bases within a MAJCOM, entire MAJCOM's can be compared with respect to a single PM or groups of PM's. Appendix L contains the displays discussed above comparing the MAJCOMS with respect to performance in Recoverable Stockage Effectiveness.

The results indicate that SAC, TAC and ATC all perform "Statistically Significantly" below average for the Air Force as a whole as represented by the MAJCOM's included. The AF wide average for Recoverable Stockage Effectivenss is .5000, corresponding to the average RIDIT value of .5000.

Similarly it can be seen that USAFE, MAC, PACAF and AAC exhibit above average performance in Recoverable Stockage Effectiveness.

Also no MAJCOM is average in this regard, but all are either above average or below average.

Many other evaluations were run during the course of the research using individual PM's and groups at PM's as attributes and bases MAJCOMS and weapons systems as alternatives. An abbreviated list of some DA analyses that were accomplished appears below.

- Bases in all MAJCOMS with respect to
  - Recoverable Stockage Effectiveness
  - EOQ Stockage Effectiveness
  - Recoverable Issue Effectiveness
  - EOQ Issue Effectiveness
- MAJCOMS with respect to
  - Recoverable Stockage Effectiveness
  - EOQ Stockage Effectiveness
  - Recoverable Issue Effectiveness
  - EOQ Issue Effectiveness

- Weapons Systems in SAC and TAC with respect to
  - Recoverable Stockage Effectiveness
  - EOQ Stockage Effectiveness
  - Recoverable Issue Effectiveness
  - EOQ Issue Effectiveness

- Bases in all MAJCOMS with respect to
  - Effectiveness Measures
  - Repair Cycle Information
  - Activity Measures

- MAJCOM's with respect to all performance measure categories

- Weapons Systems in SAC and TAC with respect to selected performance measure categories

Clearly DA provides a virtually unlimited number of ways to grade supply performance providing management visibility and flexibility at a detailed level or macro level.

CHAPTER 4

MANAGEMENT SUMMARY

CONCLUSIONS AND RECOMMENDATIONS

Management_Summary

The overall model described in this study is a hybrid involving the clustering of PM's by MAJCOM to find a salient set, forecasting of MICAP by base within MAJCOM using a robust regression model and the determination of indices to measure differencies in supply performance between bases, MAJCOM'S and weapons systems with respect to any one or more of the PM's.

At this point a summary of the management import of the results is in order, since the overriding purpose of the study is to supply results that can be translated into management strategy at the base or MAJCOM level to maximize mission capability.

The implications for MICAP management are as follows

1. The determination of a "Salient" set of PM's for each MAJCOM which form the "management" set of PM's: those that, because they are statistically significantly highly correlated to MICAP are those which if managed properly will have the greatest effect on operational capability.
2. To rank order the PM categories in descending order of average absolute elasticity of the member PM's with MICAP. This step supplies Air Force base or MAJCOM level managers with a macro management tool in the format of a rank

ordered list of sixteen (16)or fewer categories on which to focus management attention and effort in descending rank order of total impact on MICAP.

3. To rank order the PM's within a category in rank order of elasticity with MICAP, thus once a category is identified as having high impact on MICAP, this step provides the variables to be managed in descending rank order of impact on MICAP.

4. MICAP can be forecast by base within MAJCOM using a robust regression model and the same "salient" set of variables for each base.

5. The ability to grade the supply performance of bases and MAJCOMS with respect to the PM categories and individual PM's within a category already ranked by impact on MICAP. To determine which bases and/or MAJCOMS require management attention due to statistically significantly below average supply performance. This step provides the feedback control mechanism to aid management in focusing attention only on entities showing poor supply performance.

Conclusions

It appears to be possible to develop reasonably robust models to determine "Salient sets" of PM's for MAJCOM'S that have high impact on MICAP, to rank order these PM's by impact on MICAP. Furthermore, MICAP can be predicted by base using a set of robust regression models to a reasonable degree of accuracy provided the forecasts are short term.

Using the DA algorithm indices can be developed with which to "grade" the performance of supply accounts with respect to one or more of the PM's in a MAJCOM "salient set".

To make the results presented in this study generally useful at the base level some integration of the various components would be necessary.

Recommendations

As the study proceeded there were a number of places in the development at which alternative methods, procedures, levels of significance and parameter settings were left flexible and capable of manipulation and change. It is not possible, in light of the number of possible outcomes these flexibilities provide, to assert with certainty that the outcome described above in detail is the "best" of all possible outcomes, although it does seem satisfactory. If the current methodology is deemed worthy of continued scrutiny, a number of these alternative outcomes should be explored.

The nature of this effort being pure research performed in a limited length of time, mitigated against neat integrated packaging of the results. Once alternative outcomes have been explored and the inevitable improvements which will result are made to the overall model, the methodology can be integrated and packaged in such a way as to be useful at the base level for strategic management of supply performance and operational capability.

BIBLIOGRAPHY

(1) CRC_Handbook_of_Tables_for_Probability_and_Statistics; 2nd Edition, Beyer, William H. Editor; CRC Press Inc. Boca Raton, Fla. 1968; P389

(2) Non_Parametic_Statistical_Inference; Gibbons, Jean, D; McGraw Hill, 1971; pp 152-165

(3) Utility_Theory_for_Decision_Making; Fisburn, P.C. John Wiley & Sons, Inc., New York, NY; 1970

(4) Multiple_Criteria_Decision_Making; Zeleny, M.J; McGraw Hill Book Co., 1982

(5) Applied_Regression_Analysis, Draper, N.R; Smith, H; John Wiley & Sons; 1966, Pgs 9-33

(6) Supply_Performance_Indicators; Monaco, S.J. Esterby, B.C.; AFLMC Report, Project 021029; August 1981, Pgs 42-43

(7) How_to_Use_RIDIT_Analysis; Bross, Irwin, D.G.; Biometrics; March 1958 pg 18-37

(8) Supply_Performance_Measures; Ogan, A.J.; Miller, C.E.; AFLMC Report 021029

APPENDIX A

through

APPENDIX M

These are available from the Author
or Universal Energy Systems, Inc.

1986 USAF-UES Research Initiation Program

Sponsored by the
Air Force Office of Scientific Research
Bolling AFB, D.C.

Conducted by the Universal Energy Systems, Inc.
Dayton, Ohio

FINAL REPORT

Investigating the Linkages Between Family Factors and Job Attitudes in the Air Force

Principal Investigator: Philip M. Lewis
Professor of Psychology
Auburn University, AL

Subcontract No. S-760-00MG-012
Under Prime Contract No. F49620-85-C-0013/SB5851-0360

Investigating the Linkages Between Family Factors and Job Attitudes in the Air Force

Philip Lewis, Ph.D.
Auburn University

The research conducted under this Research Initiation Program subcontract is divided into three sections. Each reports on the investigation of one facet of the work-family interface in the United States Air Force. The first section focuses on the relationship between family factors and the career intent of Air Force officers and supplements work done by the principal investigator on family factors and the career intent of Air Force enlisted personnel. Important differences between the dynamics of career intent for officers and enlisted personnel are noted.

The second section focuses on the impact of women's changing work and marital roles on their attitudes toward the Air Force. These attitudes are considered important, since they have been shown to be significant predictors of their Air Force husbands' career intent.

The final section of this report focuses on the dynamics of perceived stress and satisfaction of the wives of enlisted Air Force personnel. Both environmental factors and personal attributes of the wives which are predictive of perceived stress and satisfaction are noted. There was also evidence that the level of stress experienced by these wives and their satisfaction with the Air Force are predictive of their husbands' satisfaction with their Air Force careers.

Family Factors and Job Attitudes in the Air Force I: Predicting Career Intent of Air Force Officers

Philip Lewis and Dorothy Winther

Auburn University

I. INTRODUCTION. Mowday, Porter, and Steers (1982) identified numerous work-related factors (e.g., job enrichment, job stress, ambiguity) which influence career intent in a variety of employment settings. Recently, however, researchers have begun to consider family variables along with non-family factors in order to predict career intent. Lewis (1985) found that family variables such as compatibility of work schedules, length of marriage, number of children, the spouse's view of the Air Force, stressfulness of Air Force life for the family, and Air Force member's job stress, as perceived by the spouse, were significant predictors of career intent among enlisted Air Force personnel. The purpose of this investigation is to explore the influence of family variables on the career intent of Air Force officers. It is anticipated that the family stressors influencing career intent among officers will differ from those predicting career intent of enlisted personnel.

II. METHOD. The data base utilized for this investigation consisted of 1170 Air Force members and their spouses who were participants in a census survey of certain large Air Force organizations (e.g., an entire

wing) at four different U.S. air bases. Initially, the Air Force member completed the Organizational Assessment Package (OAP), a questionnaire designed to measure work-related attitudes. Subsequently, their spouses completed the Air Force Family Survey (AFFS) which was developed to assess attitudes concerning a variety of topics including involvement in the Air Force lifestyle, marital satisfaction, career and marital role orientation, and family stress.

For purposes of the current investigation, a subsample of Air Force officers and their wives (N=164) was drawn from the larger data base. Subjects who indicated that they were expecting to retire within a year or who were married to another Air Force member were eliminated from the subsample since their perceived career intent was expected to differ from the remainder of the sample. Given these exclusion criteria, the sample was reduced to a subset of 78 matched pairs. Because of the small sample size, results generated from this study must be interpreted with caution and broad generalizations avoided. Results herein can only suggest certain trends in the data with more conclusive evidence coming from future studies in this area.

In order to assess the ability of certain family variables to predict career intent, a multiple regression analysis was conducted. The predictor variables were 12 AFFS factors identified in a previous factor analytic study (Lewis, 1985). These factors included (a) Air Force member's job stress, (b) stress of Air Force life for the family, (c) marital satisfaction, (d) positive view of the Air Force, (e) sensitivity of Air Force to family needs, (f) commitment to the Air

Force lifestyle, (g) spouse's career orientation, (h) family disengagement, (i) social isolation, and (j) help-seeking attitudes. Additional predictors were the compatibility between the marital pairs, three dummy coded variables representing family life cycle stage (i.e., those families with preschool, school age, or adolescent children), and seven demographic characteristics (i.e., TDY frequency, TDY length, length of marriage, living location, educational level, number of children, and amount of time spent doing volunteer work).

The criterion variable for the analysis was the Air Force member's stated career intent (item 16 from the OAP). In order to assess the influence of the AFFS variables in predicting career intent, each predictor was entered into the model as if it were entered last and, thus, showed the influence of each predictor after the effects of all other predictors had been accounted for.

III. RESULTS. The ability of the 23 variables to predict career intent among the Air Force officers was relatively strong (R^2=.49). However, only two of the variables were able to improve the prediction of career intent to a statistically significant degree over the predictive ability of all other predictor variables taken together. The first significant predictor was that of spouse independence, $F(1,54)=5.02$, $p=.03$. Air Force officers with independent wives were likely to indicate less commitment in continuing their career with the Air Force than were officers with more dependent wives. The second variable having a significant impact on career intent was that of

marriage length, $F(1,54)=4.03$, $p=.05$. The longer the couple was married the more likely the member was to continue his Air Force career.

IV. IMPLICATIONS. Together with findings from an earlier investigation (Lewis, 1985) where it was possible to predict the career intent of Air Force enlisted personnel from certain family factors and spouse attitudes, the present findings for Air Force officers lend further support to the general notion that family variables are importantly related to the career intent of Air Force personnel. Yet, the differences in the findings for officers and enlisted personnel underline the importance of viewing family-work linkages for the two groups separately. Previous research with the wives of enlisted Air Force personnel highlighted the important role of family size, work schedule compatibility and the perceived stressful impact of Air Force life on the Air Force member's career intent. In contrast, the only important predictor for the career intent of officers was their wife's level of independence. Officers' wives who indicated that they make personal and family decisions by themselves are more likely to have husbands whose career intent is lower than that of those officers whose wives are less "independent." Although the small sample size for officer/wife pairs makes interpretation of these differences a bit risky, it appears that the career intent dynamics of Air Force officers is related to wife personality and family structure variables to a greater extent than is the career intent dynamic of enlisted personnel. For the latter group various stressors (e.g.,family size, perceived stressful impact of Air Force life) seem more important with regard to

career intent. Overall, it would appear prudent to avoid developing programs in the Air Force that are targeted toward enlisted personnel and their families which are based on the experiences of officers.

REFERENCES

Lewis, P. (1985). Family factors and the career intent of Air Force enlisted personnel. (LMDC-TR-85-9). Maxwell AFB, AL: Leadership and Management Development Center.

Mowday, R.T., Porter, L.W., & Steers, R.M. (1982). Employee-organization linkages: The psychology of commitment, absenteeism and turnover. New York: Academic Press.

Family Factors and Job Attitudes in the Air Force II: Changing Marital Roles and the Support of Air Force Wives

Philip Lewis, Dorothy Winther, and Angela Adan
Auburn University

Mickey R. Dansby
Leadership and Management Development Center
Maxwell Air Force Base

I. INTRODUCTION The classical view of military life is that a person does not "take a job" in the military. Rather, he or she "joins" the military, becoming a part of a community and lifestyle that assumes a central role in one's life and, if married, the life of one's family (Carr, Orthner, & Brown, 1980). Although this military lifestyle can have its own special rewards, it can also make special demands, particularly on those with families. Due to temporary duty assignments away from home (TDYs), frequent moves, combat alerts, etc., the spouses of military personnel are often expected to adapt their own personal and vocational interests to the demands of military life. Spouses (typically wives) may have to assume full responsibility for household chores and child care during extended TDYs, and relinquish jobs to move with their spouses to remote or foreign duty locations where their own job opportunities may be limited. Further, in fulfilling the role of an

officer's wife one is often expected to take on volunteer responsibilities connected with their husband's career (Finlayson, 1976).

Because these multiple demands are expected to be less burdensome for a non-working wife who sees her marital role as that of a homemaker supporting her husband's military career than they are for working, career-oriented wives, there has been some concern about the impact of tne changing roles of women in American society on the support of Air Force wives for their husbands' careers. American women are increasingly likely to be employed full time, view their own careers as important, and marriage as a partnership between equals (Bernard, 1981). These changes have raised fears that these "new women" will be less involved in and less supportive of military life, with a resulting negative impact on the career commitment of their military husbands.

Are these fears warranted? Do the wives of military personnel who work and/or who have a more "modern" view of marital roles in fact have a less favorable view of the military? And are they less involved in the military lifestyle? Although a number of hypotheses are possible, the qualitative literature suggests that it is the non-working, traditionally oriented wives, and those who do not see their own career as important who will have the most favorable attitudes toward the Air Force and, concomitantly, will be the most involved in the Air Force lifestyle. They presumably have the time to be more involved in Air Force life than their modern, career-oriented, working counterparts. With regard to their attitudes toward the Air Force, the demands of Air

Force life (frequent moves, TDYs, etc.) are expected to be less disruptive of the dominant roles of the traditional wives (wife and homemaker) than they are of those wives who work and/or see a career as an important part of their identity.

Another question concerns the extent to which the changing roles of women may have a different impact on the wives of enlisted personnel than they do on officers' wives. Because of the status, education, and income differences between officers and enlisted personnel, it is quite possible that different patterns of results will be found for these two groups. In addition, the greater role that officers' wives are expected to play in their husbands' careers may leave them with less time to pursue a career and may affect their attitude and level of involvement in a manner somewhat different from that of the wives of enlisted Air Force members. Accordingly, the relationships among attitude toward and involvement in the Air Force and the wife's employment status, career orientation, and marital role orientation will be examined separately for officers and enlisted personnel in the present study.

II. METHOD The sample was drawn from a large data base consisting of 1170 Air Force members and their spouses (14% officers and 34% enlisted personnel) who were participants in a census survey of four different air bases in the continental United States. Initially, the Air Force member completed the Organizational Assessment Package (OAP), a questionnaire designed to assess work-related attitudes (Short, 1985). Subsequently, their spouses completed the Air Force Family Survey (AFFS)

which was developed to measure attitudes concerning a variety of topics influential in family adjustment to the Air Force lifestyle and, in turn, on the perceived satisfaction and commitment of the Air Force member (Flannery & Dansby, 1985).

In an effort to test the effect of a spouse's employment status, career orientation, and marital role orientation on her attitude toward the Air force and on her involvement in the military lifestyle, two samples were drawn from the larger data base. The first sample consisted of 811 enlisted men and their wives. The second sample consisted of 135 male officers and their wives. Information regarding Air Force tenure, educational status and career intent of the Air Force members are presented in Table 1. The demographic characterisics of the wives of these Air Force members are presented in Table 2 with data presented separately by emlployment status. The ages of the wives of the enlisted subsample ranged from 15 to 50; for the officers' wives the ages ranged from 20 to 52. It should be noted that due to the small sample size, especially in terms of the subsample of employed officer wives (N=37), results should be interpreted with caution.

All analyses examined two dependent measures. The first dependent variable, a factor labeled "attitude toward the Air Force," consisted of the sum of six AFFS items (2, 5, 7, 18, 26, & 32). A second dependent measure, "involvement in the Air Force lifestyle," was derived from the sum of seven AFFS items (1, 3, 4, 6, 9, 11, & 47) with the last item being reverse scored. Both dependent measures were factor scores identified by Lewis (1985) in earlier research with the AFFS.

Table 1
Air Force Tenure, Educational Status and
Career Intent of Air Force Members

Status	Male Enlisted (N=811)	Male Officers (N=135)
Twelve Years or more of Air Force Service	48%	49%
In Present AF Career Field for 36 months or more	69%	56%
Stationed at Current Base for 36 months or more	54%	37%
Earned College Degree	16%	53%
Earned Graduate Degree	5%	47%
Career Intent*		
"will continue"	43%	60%
"will most likely continue"	19%	22%
"may continue"	16%	12%
"will most likely not continue"	6%	6%
"will separate/ terminate"	5%	-

*Since the current study was concerned with factors bearing on the retention of Air Force personnel, individuals within one year of retirement were not included.

Table

Demographic Characteristics of Employed and Unemployed Wives of Air Force Members*

	Employed Wives of Enlisted AF Members (N=331)	Unemployed Wives of Enlisted AF Members (N=480)
Married Between One and Four Years	27%	28%
Completed High School	45%	51%
Some College (less than 4 years)	23%	23%
Completed College	12%	12%
Graduate Degree	10%	5%
At Least One Child Living at Home	69%	81%
At Least One Preschool Child Living at Home	37%	56%

	Employed Wives of AF Officers (N=37)	Unemployed Wives of AF Officers (N=93)
Married Between One and Four Years	27%	25%
Completed College	33%	35%
Graduate Degree	25%	4%
At Least One Child Living at Home	43%	70%
At Least One Preschool Child Living at Home	11%	45%

*Wives who were also Air Force members were not included in the current study, since their attitudes toward and support of the Air Force could be expected to be heavily influenced by their own employment experiences.

Independent measures consisted of the employment status of the wives (employed versus unemployed), reasons for working (AFFS item #134) or not working (AFFS item #132), and two factor scores from the AFFS, career orientation and marital role orientation (Lewis, 1985). Career orientation was represented by the sum of three items (24, 43, & 44), and marital role orientation was the sum of two items (45 & 46). Career orientation is the wife's attitude toward working. The AFFS item with the highest loading on this factor (#44) states "In our family, it is OK for the wife to work outside the home even if it isn't an absolute financial necessity." Marital role orientation is the wife's view of the preferred role relationship between spouses. The item with the higher loading on this factor (#46) is stated in a way which reflects a traditional marital role orientation: "The husband should have the final word in most of the important decisions in our family." For the wives of enlisted Air Force members, the correlation between career orientation and marital role orientation was -.04. For the officers' wives, the correlation was -.19.

For the enlisted subsample career orientation was differentiated into two groups. Wives with a high or positive career orientation (N=545) were defined as those responding to all three AFFS items with "slightly agree," "moderately agree," or "strongly agree." Wives endorsing responses of "strongly disagree," "moderately disagree," or "slightly disagree" on all three AFFS items were defined as having a low or negative orientation toward pursuing a career (N=54). Spouses taking a neutral stance of "neither agree nor disagree" were eliminated from

the analyses (N=112). Marital role orientation was defined in a similar fashion with responses of "slightly agree" to "strongly agree" on both items representing a traditional orientation toward marital roles (N=363), and responses of "strongly disagree" to "slightly disagree" defining a more modern orientation (N=261). Again, those responding in a neutral manner (i.e. "neither agree nor disagree") were ommited from the analyses (N=187).

Because of the small sample of officer wives, career orientation and marital role orientation were treated somewhat differently than in the enlisted subsample. In this case, high and low career orientation and modern and traditional marital role orientation were defined by a median split. Subjects scoring greater than 13 on the career orientation factor (N=105), were defined as being highly motivated toward a career, while those scoring 13 or less (N=30) were considered to have a low orientation toward a career. Similarly, a score of 9 or above represented a more traditional orientation toward marriage (N=54), and a score of 8 and below represented a more modern orientation (N=81).

III. RESULTS The first sequence of analyses dealt with the subsample of enlisted wives. Two independent one-way analyses of variance (ANOVAs) were performed to assess the relationship between a wife's employment status and her involvement in the Air Force lifestyle as well as her attitude toward the Air Force. The analyses indicated no significant differences between employed and unemployed wives in terms of involvement, but a significant difference was found in terms of attitude

[illegible] Air Force, $F(1,509)=3.76$, $p=.05$. The employed wives of enlisted Air Force members have a more positive view of the Air Force ($M=28.05$) than do the unemployed wives ($M=27.89$).

A subsequent step in the analyses involved conducting separate two-way ANOVAs to investigate the effects of career orientation and marital role orientation on attitude toward and involvement in the Air Force. In terms of attitude, significant main effects were found. Regarding career orientation, $F(1,544)=4.41$, $p=.04$, those wives of enlisted Air Force members with a high career orientation had a more positive attitude toward the Air Force ($M=28.42$) than did those with a low career orientation ($M=25.57$). Wives with a traditional marital role orientation were more favorable towards the Air Force ($M=28.34$) than the [illegible] with a non-traditional marital role orientation ($M=25.65$). Though the pattern of results was similar, neither career orientation, marital role orientation, nor the interaction between the two was significantly related to involvement.

Further analyses were performed in order to assess more precisely the differences among employed and unemployed wives of enlisted Air Force members. In the employed subsample, it was demonstrated that career orientation, marital role orientation, and the interaction between the two affected neither attitude toward the Air Force nor involvement in its lifestyle. Additionally, reasons for working were not found to be significant predictors of attitude. However, the reasons for working proved to be a significant predictor of involvement, $F(6,307)=2.28$, $p=.04$. The wives who reported being more involved in the

Air Force community tended to be those who worked to make use of their free time (M=39.57), those who wanted to maintain or use their skills (M=37.50), and those who want to earn extra money (M=37.09). Women who worked for personal and professional fulfillment tended to be least involved (M=33.46), followed closely by those who worked for financial necessity (M=33.98) and those who indicated they would rather work than be at home (M=34.73).

To answer the question of whether or not the working wives having varying marital role orientations and career orientations worked for different reasons, two separate one-way ANOVAs were performed. Results indicated that neither marital role orientation nor career orientation significantly predicted the wives' reasons for working.

Comparable analyses were conducted on the subsample of unemployed wives. Two separate two-way ANOVAs were performed to determine the effects of career orientation, marital role orientation, and their interaction on involvement and attitude. No significant effects were found in terms of involvement. However, career orientation was shown to significantly predict a wife's attitude toward the Air Force, $F(1,367)=4.33$, $p=.04$. Unemployed women with a high career orientation were found to have a more positive view of the Air Force (M=28.07) than those with a low career orientation (M=25.08). Marital role orientation and the interaction effect were not found to be significant predictors of attitude.

Reasons given by the unemployed wives of enlisted personnel for not working were not related to their attitude or their involvement.

however, their marital role orientation was found to significantly predict reasons for not working, $F(1,372)=4.15$, $p=.04$. The modern wives most often indicated that they did not work for "other reasons" (39%). A stepwise regression analysis using several demographic predictors (i.e. number of children at home, age of youngest child, marriage length, Air Force tenure, frequency of TDYs, length of TDYs, education, and involvement) indicated that some of the reasons for not working included the number of children at home ($B=.15$) and the frequency of their spouse's TDYs ($B=-.11$). On the other hand, traditional wives most often indicated that they did not work because they did not desire employment (37%).

Equivalent analyses were performed on the subsample of wives of Air Force officers. A one-way ANOVA revealed a significant difference in attitude between the employed and unemployed wives, $F(1,133)=7.03$, $p=.009$, with the unemployed wives having a more positive attitude toward the Air Force ($M=29.94$) than indicated by the employed wives ($M=25.59$). Employment status showed a similar effect on involvement, $F(1,133)=4.39$, $p=.04$. Again, unemployed wives indicated more involvement in the Air Force lifestyle ($M=40.97$) than did employed wives ($M=38.30$).

Subsequent analyses revealed that attitude of the employed wives could not be predicted from their reasons for working. However, reasons for working proved to be a significant predictor of involvement, $F(5,29)=3.46$, $p=.01$, among the employed subsample. Those indicating they worked to earn extra money ($M=44.00$), to maintain or use skills ($M=42.50$), or for personal and professional fulfillment ($M=38.84$) were

To summarize, employed wives of enlisted Air Force personnel are more positive toward the Air Force than are wives who are not employed outside of the home. A contrasting effect is seen among officer wives. That is, unemployed officer wives have a more positive attitude and demonstrate more involvement in the surrounding Air Force community than do their counterparts employed in civilian jobs. In terms of career orientation and marital role orientation, neither factor is predictive of attitude or involvement among enlisted and officer wives employed in the civilian community. In both subsamples, however, career orientation serves as a significant predictor of attitude with those desiring to pursue a career being more positive toward the Air Force. In addition, career orientation predicts involvement among the unemployed officer wives with those being highly motivated to pursue a career indicating more involvement in the Air Force lifestyle.

IV. IMPLICATIONS Previous research with the present data set (Lewis, 1985) has demonstrated a strong positive relationship between the attitude of spouses toward the Air Force and their enlisted Air Force members' career intent and job satisfaction. [illegible] strong relationship between job satisfaction and career intent (Mowday, Porter, & Steers, 1982) and between career intent and retention (Steel & Nestor, 1984), the present findings have implications for the ways in which the changing marital and work roles of women may be impacting the retention of Air Force personnel through the mediating variable of the spouse's attitude toward the Air Force. However, the present findings

also suggest that the impact of spousal employment status and role orientation is different for officers and enlisted men. Since most policy decisions in the Air Force are made by officers, it is critically important that decisions affecting enlisted personnel and their spouses not be based solely on the experiences and perceptions of officers and their wives.

The most striking difference between the findings for officer and enlisted wives concerned employment status. The wives of enlisted men who work outside the home tend to have more positive attitudes about the Air Force than do their nonworking counterparts. The opposite was true for officers' wives, where the nonworking wives had the more positive attitudes. These nonworking officer wives also felt more involved in the Air Force lifestyle than did working wives. It appears that the fear that increasing employment among Air Force wives could have a negative impact on their attitudes toward and involvement in the Air Force lifestyle is unfounded, at least for enlisted personnel. Employment status per se appears to have no overall impact on either officer or enlisted wives' involvement with the Air Force and, contrary to expectations, the wives of those enlisted personnel who work have more positive attitudes toward the Air Force than their unemployed counterparts. Similarly, rather than eroding their support for the Air Force, a favorable orientation toward having their own career was positively correlated with enlisted wives' attitudes toward the Air Force. For those wives who were currently not working, this relationship held true for both enlisted and officer wives.

What are the implications of these results? One implication is that Air Force programs designed to assist Air Force members' wives in finding employment are not likely to have a negative impact on retention. On the contrary, particularly with regard to enlisted personnel, helping those wives who wish to work find jobs may actually ennance their attitudes toward the Air Force and their support of their husband's Air Force career. Even among non- working officer wives, it is those with a positive career orientation who have a more positive attitude toward the Air Force. It seems unlikely that assisting them with their career aspirations would make them less positive in their attitudes toward the Air Force.

References

Bernard, J. (1981). Facing the future. Society, 18, 53-59.

Carr, R., Orthner, D.K., & Brown, R.J., III. (1980). Living and family patterns in the Air Force. Air University Review, 31, 75-86.

Finlayson, E.M. (1976). A study of the wife of the Army officer: Her academic and career preparations, her current employment and volunteer services. In H. I. McCubbin, B. B. Dahl, & E. J. Hunter (Eds.), Families in the military system. Beverly Hills, CA: Sage Publications.

Flannery, P.A., & Dansby, M.R. (1985). USAF Family Survey: A revision of the USAF Spouse Survey (LMDC-TR-85-3). Maxwell AFB, AL: Leadership and Management Development Center.

Lewis, P. (1985). Family factors and the career intent of Air Force enlisted personnel (LMDC-TR-85-9). Maxwell AFB, AL: Leadership and Management Development Center.

Mowday, R.T., Porter, L.W., & Steers, R.M. (1982). Employee-organization linkages: The psychology of commitment, absenteeism, and turnover. New York: Academic Press.

Short, L.O. (1985). The United States Air Force organizational assessment package (LMDC-TR-85-2). Maxwell AFB, AL: Leadership and Management Development Center.

Steel, R.P., & Nestor, K.O., 2nd. (1984). A review and meta-analysis of research on the relationship between behavioral intentions and employee turnover. Journal of Applied Psychology, 69, 673-686.

Family Factors and Job Attitudes in the Air Force III: The Impact and Prediction of Family Stress and Satisfaction

Dorothy Winther and Philip Lewis

Auburn University

I. INTRODUCTION Gone are the days of viewing the family in the traditional mold of breadwinner husband, dependent homemaker wife, and children and of considering the family environment and the workplace as separate entities. Due to the major social changes which have taken place in American society over the past 20 years (Bernard, 1981), the tremendous impact that work and family environments have on one another has become increasingly apparent. Therefore, researchers have found it necessary to jointly consider work and family factors within a single framework in order to assess the reciprocal interrelationships between the two domains (Osherson & Dill, 1983; Pleck, 1977).

One result of the past two decades of social upheaval is an increase in the stress experienced by the American family. The family, in turn, has had to develop coping strategies to deal with these stresses. Air Force families are no exception in that they too have been challenged by the same pressures as other American families, such as inadequate finances, changing marital and parental role definitions, and the erosion of viable social and family support systems (Bowen, 1985). The paradox of this modern life predicament is that American families lack many of the characteristics which might serve as buffers against the pressures of modern life (Greenhaus & Beutell, 1985). The purpose of

this investigation of Air Force famlies was to examine some of the work-family interrelationships influenced by the pressures of an Air Force lifestyle.

Many factors contribute to a stressful family environment. For instance, Beutell and Greenhaus (1980) found that parents of younger children experienced more interfamily conflict than did parents of older children. There is also evidence that the size of the family is positively related to the degree of family stress, especially for women whose husbands are highly involved in their careers (Beutell & Greenhaus, 1982; Keith & Shafer, 1980). Evidence is mixed on the issue of the effects of a wife's employment outside the home (Hall & Gordon, 1973; Locksley, 1980; Pleck, Staines, & Lang, 1980), and the results appear to depend on the wife's hierarchial level within the workplace (Greenhaus & Kopelman, 1981) and the number of hours she is employed outside the home (Hall & Gordon, 1973).

Other factors contributing to family pressure originate from the work domain. For example, there appears to be a significant positive correlation between family conflict and the number of hours worked per week and the frequency of overtime (Burke, Weir, & Duwors, 1980; Keith & Shafer, 1980) . Furthermore, family stress escalates as work schedules become more inflexible (Pleck et al., 1980). Not only must many Air Force families cope with heavy work hour demands and rigid work schedules, but the very nature of a military career places additional pressures on the family members, especially on the wife (Hunter, 1982). The military wife must assume multiple roles during her husband's absences. She must be ready to move when duty assignments change and

must endure social and cultural isolation in the case where assignments are located in remote areas. She must also live with uncertainty when her husband's duty carries him into dangerous environments. Such additional stressors experienced by military wives could have far-reaching effects on family dynamics, coping behaviors, and attitudes toward the military member's job, career, and work environment. It could be hypothesized, however, that the effects of stress on the spouse and that her reactions to this pressure might also depend on the level of satisfaction she experiences as a military spouse.

The current investigation examines several aspects of the work and family domains which may influence and be influenced by an Air Force wife's perceived level of stress and satisfaction. First, it will examine some potential stressors which might serve to predict a wife's level of stress and satisfaction. Second, the study will assess the effects of stress and satisfaction on her attitude toward her husband's Air Force job, her perceived role within the family, and the tendency for the family to develop various support systems in order to combat a stressful lifestyle. Finally, the current investigation examines the effects of the wife's level of stress and satisfaction on the Air Force member's pride in his work, perceptions of work group effectiveness, job-related satisfaction, and general organizational climate.

II. METHOD The sample was drawn from a large data base consisting of 1170 Air Force members and their spouses (14% officers and 84% enlisted personnel) who were participants in a census survey of four different air bases in the continental United States. Initially, the Air Force

member completed the Organizational Assessment Package (OAP), a questionnaire designed to assess work-related attitudes (Short, 1985). Subsequently, their spouses completed the Air Force Family Survey (AFFS) which was developed to measure attitudes concerning a variety of topics influential in family adjustment to the Air Force lifestyle and, in turn, on the perceived satisfaction and commitment of the Air Force member (Flannery & Dansby, 1985).

From the larger data base, a sample of 820 enlisted men and their wives was drawn. Demographic characteristics of the enlisted sample reveal that 48% of the Air Force members had accrued 12 or more years of Air Force service, 69% had been in their present career field for 36 months or more, 54% had been stationed at the same base for 36 months or more, and 43% of the enlisted members indicated that they had no intention of terminating their career with the Air Force. Further, 23% of the couples had been married between one and four years, 75% had at least one child living at home with 47% of these children being of preschool age, and 41% of the wives were employed in full-time civilian positions.

The current study examined the wives' perceived stress and satisfaction in two ways. First, in a stepwise regression procedure, it investigated the ability of 11 demographic variables to predict stress and satisfaction in our sample of Air Force wives. The second phase of the study used two multivariate analysis of variance designs to address the question of how various levels of perceived stress and satisfaction influence certain characteristics of the family and work domains. Therefore, discussion pertaining to the first analysis will refer to

stress and satisfaction as criterion variables, while the second set of analyses will refer to them as independent variables.

The variable of stress was represented by the sum of three AFFS items (14, 17, 36) describing disruptions in family and social life due to having a husband in an Air Force career. Item #14 states, "The special demands of my spouse's career cause problems for our family that non-Air Force families don't have." Item #17 states, "Being with the Air Force makes it difficult to make friends and socialize." Item #36 states, "My spouse's work hours disrupt our family life more than if my spouse had a non-Air Force job." The stress factor was differentiated into two groups. The high stress group (N=155) was defined by those responding with "strongly agree," "moderately agree," or "slightly agree" to all three items. All other responses characterized the low stress group (N=665).

The second variable, satisfaction, was represented by the sum of three AFFS items (2, 18, 61) and constituted a measure of overall satisfaction with the Air Force lifestyle and with life in general. Item #2 states, "I would recommend the Air Force as a career to many people I know." Item #18 states, "I am glad my spouse joined or works for the Air Force." Item #61 states, "Taking things all together, I'd say I'm very happy these days." A high satisfaction group (N=255) was defined as those wives responding to all three statements with "strongly agree" or "moderately agree." All other respondents composed a low satisfaction group (N=560). The relationship between stress and satisfaction in the sample was a moderately negative one (r=-.35) indicating that there is a tendency for satisfaction to decrease as stress increases.

The first analysis used a combination of 11 demographic variables as potential predictors of a spouse's perceived level of stess and satisfaction. These included the attained grade of the Air Force member, employment status of the wife (employed/unemployed), frequency of TDYs, length of TDYs, length of time at current base, location of residence, number of children, number of children living at home, and age of the youngest child. The last two predictors, career orientation and marital role orientation, were factor scores derived from several AFFS items (Lewis, 1985). Career orientation was represented by the sum of three AFFS items (24, 43, & 44) and can be defined as the wife's attitude toward working. Marital role orientation was the sum of two items (45 & 46) representing the wife's view of the preferred role relationship between spouses.

The second phase of the study investigated the effects of stress and satisfaction on two sets of dependent measures. The first set was composed of 17 AFFS items (40 through 56) and assessed the wife's attitude toward her husband's Air Force job, perceptions of her role within the family, and the extent to which the family had developed various support systems. The second set of dependent variables consisted of four factor scores derived from OAP items (Hightower & Short, 1982). The first factor, pride, measured the pride the Air Force member derived from his work and was represented by the sum of two OAP items (32 & 46). Work group effectiveness assessed the Air Force member's view of the quantity, quality, and efficiency of work generated by his work group and was the sum of five OAP items (77, 78, 79, 80, & 81). Job-related satisfaction was the sum of seven OAP items (101, 102, 103, 106, 107,

108, & 109) and measured the degree to which the worker was generally satisfied with factors surrounding the job. Finally, organizational climate was the sum of ten OAP items (87, 88, 89, 90, 92, 93, 94, 95, 97 & 98) and assessed perceptions of the organizational climate as a whole (e.g., team spirit and communications).

III. RESULTS The first portion of this study investigated the effectiveness of 11 demographic characteristics of the family and Air Force lifestyle for predicting the criterion variables of stress and satisfaction in the sample of Air Force wives. Results of a stepwise regression analysis identified six predictors as the best combination of variables for predicting stress. These were frequency of TDYs (B=.43), number of children (B=-.30), wife's employment status (B=.30), husband's grade (B=.28), career orientation (B=-.15), and marital role orientation (B=-.10). Therefore, it appears that a wife's level of perceived stress increases as the frequency of temporary assignments, the number of children, and her husband's grade in the Air Force increases. Further, higher levels of stress tend to be experienced by the unemployed wife who has a modern view of her marital role but has little desire to pursue a career of her own.

A second regression analysis identified four variables which significantly predicted perceived satisfaction. These included location of residence (B=-.20), number of children (B=.27), career orientation (B=.18), and marital role orientation (B=.16). In brief, on-base living quarters, fewer children, more traditional views of the marital role,

and the desire to pursue a career tended to predict a higher level of satisfaction with the Air Force lifestyle and with life in general.

The second portion of this investigation addressed the issue of the effects of the wife's level of stress and satisfaction on the family and work domains. First, a two-factor multivariate analysis of variance (MANOVA), with two levels of stress (high and low) and two levels of satisfaction (high and low), was performed with the dependent variables being the 17 AFFS items discussed previously. Examination of the results revealed a main effect for stress, $F(17,800)=3.02$, $p=.001$, using the Wilk's Lambda Criterion. Follow-up analyses of variance indicated that spouses in the high stress group felt more socially isolated, $F(1,816)=25.27$, $p=.001$, believed off-base friends more important than Air Force friendships, $F(1,816)=5.80$, $p=.02$, and had friends visit their homes less frequently, $F(1,816)=6.91$, $p=.01$, than did those spouses in the low stress group. In terms of their family and marital roles and in contrast to their low stress counterparts, the high stress group felt less able to pursue their own interests, $F(1,816)=3.88$, $p=.05$, believed their husbands should not have the final word in important family decisions, $F(1,816)=6.91$, $p=.01$, and, in fact, indicated they made important family decisions on their own, $F(1,816)=6.64$, $p=.01$. Finally, the spouses reporting a high level of stress perceived an Air Force career as less fair in terms of pay, allowances, and benefits, $F(1,816)=4.67$, $p=.03$, than did the spouses reporting less stress. Group means are presented in Table 1.

Results of the MANOVA also revealed a main effect for [illegible]faction, $F(17,800)=2.43$, $p=.001$. Univariate statistics indicated

TABLE 1
Group Means for Stress

	High Stress N=155	Low Stress N=665
"Pay & Benefits Fair"	2.90	3.40
"Able to Pursue Own Interests"	4.68	5.08
"Husband Should Have Final Word"	3.30	3.97
"Off-base Friends More Important"	3.73	3.27
"Have Friends Over to Visit"	4.36	4.91
"Make Important Family Decisions Myself"	4.04	3.48
"Feel Socially Isolated"	5.16	4.12

TABLE 2
Group Means for Satisfaction

	High Satisfasction N=253	Low Satisfaction N=567
"Able to Pursue Own Interests"	5.27	4.48
"Off-base Friends More Important"	3.28	3.72
"Solve Problems Witnout Outside Help"	5.99	6.28
"Feel Socially Isolated"	4.27	5.02
"Outside Agencies Can Help Solve Problems"	3.57	3.22

that those spouses indicating a high level of life satisfaction believed tney were more able to pursue their own interests, $F(1,816)=15.36$, $p=.001$, felt Air Force friends to be more important than off-base friends, $F(1,816)=5.25$, $p=.02$, and felt less socially isolated, $F(1,816)=13.50$, $p=.001$, than did those spouses experiencing a lower level of satisfaction. In addition, the high satisfaction group viewed outside agencies as a helpful source in solving problems, $F(1,816)=3.85$, $p=.05$, and more frequently sought outside help in solving their problems, $F(1,816)=3.84$, $p=.05$, than did the low satisfaction group. Table 2 presents group means for those dependent variables influenced by spouse satisfaction.

Although the overall stress/satisfaction interaction effect was not statistically significant, $F(17,800)=1.21$, $p=.25$, several of the univariate ANOVAs were meaningful and, therefore, worth mention. First, tnose spouses in the high stress/high satisfaction group indicated that in their families everyone went their own way, $F(1,816)=4.48$, $p=.03$, and were the group most likely to seek outside help when facing serious family problems, $F(1,816)=6.88$, $p=.01$. Those in the low stress/high satisfaction group felt the wife was primarily responsible for the home, even if she was also employed outside the home, $F(1,816)=5.56$, $p=.02$. Finally, in contrast to the other three groups, the low stress/high satisfaction spouses indicated that their family almost always did tnings together, $F(1,816)=7.01$, $p=.01$. Group means for the four dependent variables of interest are presented in Table 3.

In summary, the degree of stress an Air Force wife experiences has a significant influence on her attitude toward the Air Force, her

TABLE 3
Group Means for Stress/Satisfaction Interaction

	High Stress		Low Stress	
Satisfaction	High N=29	Low N=126	High N=224	Low N=441
"Wife Responsible for Running Household"	3.45	4.02	4.37	3.85
"Everyone in Family Goes Own Way"	2.91	2.58	2.23	2.67
"Family Almost Always Does Things Together"	5.38	5.74	6.08	5.52
"Solve Problems Without Outside Help"	5.76	6.43	6.23	6.13

support systems, and family dynamics. A spouse experiencing a high degree of stress tends to have a negative attitude toward the pay and benefits afforded by an Air Force career, has few social relationships, especially with other members of the Air Force community, and assumes an independent role in making family decisions. In contrast, an Air Force wife who experiences less stress holds a more positive view of her husband's Air Force career, has formed more social bonds within the Air Force community, and tends to play more of an interdependent role with her husband in making family decisions.

It is also clear that the effects of satisfaction impinge on the lifestyle and social relationships of the Air Force wife. Those indicating a high degree of satisfaction feel free to pursue their own interests and tend to form more social bonds within the Air Force community. On the other hand, the wife experiencing little satisfaction tends to view herself as unable to pursue her own interests and as socially isolated from others in the Air Force community. More importantly, those experiencing little satisfaction are least likely to seek outside help for family problems, a solution which has potential for increasing their level of satisfaction.

Turning to the interactive effect between stress and satisfaction, there is a distinct contrast between the family relationships of the high stress/high satisfaction spouses and the spouses in the low stress/high satisfaction spouses with family members in the latter group tending to be more cohesive. On the other hand, family members in the former group tended to be more independent. Also, the high stress/high satisfaction spouses indicated they were most likely to seek outside

help when confronted with serious family problems. This finding is in contrast to their high stress/low satisfaction counterparts who were the least likely to seek such help. Finally, a spouse experiencing a condition of low stress/high satisfaction tended to hold a more traditional view of their marital role by indicating that the wife should have primary responsibility of the home, regardless of her employment status outside the home. In contrast, the high stress/high satisfaction wife responded with the most modern perspective on the issue of responsibility for running the home.

The final question involved in this study dealt with what effect a wife's level of stress and satisfaction has on her husband's perceptions of his Air Force job. To explore this question, a second two-factor MANOVA was conducted with the dependent measures being the four factors of pride, work group effectiveness, job-related satisfaction, and organizational climate. Examination of the Wilk's Lambda Criterion showed a significant main effect for spouse satisfaction, $\underline{F}(4,813)=2.83$, $\underline{p}=.02$. Husbands of wives with a high level of life satisfaction had more pride in the work they performed, $\underline{F}(1,816)=5.81$, $\underline{p}=.02$, and were more satisfied with their Air Force job, $\underline{F}(1,816)=10.02$, $\underline{p}=.002$, and with the overall climate of their work group, $\underline{F}(1,816)=3.28$, $\underline{p}=.004$, than Air Force members having wives who experienced less satisfaction in their lives. Table 4 summarizes these results by presenting the group means.

Although there was no overall main effect evidenced for stress, univariate analyses indicated that those having wives experiencing higher levels of stress were less satisfied with their jobs, $\underline{F}(1,816)=4.59$, $\underline{p}=.03$, than were Air Force members with wives

TABLE 4
Group Means for Satisfaction and Stress

	Satisfaction	
	High N=253	Low N=567
Pride	10.46	9.63
Job-related Satisfaction	36.13	33.27
Organizational Climate	47.21	43.17

	Stress	
	High N=155	Low N=665
Job-related Satisfaction	33.73	35.67

experiencing a less stressful life. Neither multivariate nor univariate statistics showed a significant stress-satisfaction interaction effect. In brief, evidence appears to indicate a spouse's satisfaction with her lifestyle as an Air Force wife and her life in general has a significant impact on her husband's perceptions of his job and the surrounding work environment. Further, a wife's level of stress plays a role in the satisfaction her husband derives from his job.

IV. IMPLICATIONS In trying to sort out the impact of Air Force life on the wives of Air Force enlisted personnel, several interesting patterns have emerged. The experience of Air Force life as stressful appears to be a joint function of both the objective circumstances of family life and certain personal attributes of the wife. Not suprisingly, Air Force life is experienced as more stressful by those wives who have more children living at home, who are unemployed, and whose husbands have more frequent TDYs. Somewhat more suprising, given the higher income of these famlies, wives are more likely to experience stress the higher their husband's grade level in the Air Force.

With regard to their personal characteristics, it is the "modern" as opposed to the "traditional" wives and those with little interest in pursuing a career that find life in the Air Force most stressful. Other findings suggest that it is those wives who are less integrated into the Air Force community who may be experiencing the most stress. Those in the high stress group reported feeling more socially isolated, and reported that friends visit in their homes less frequently, and reported that non Air Force friends are more important than friends from the Air Force community. It further appears that those Air Force famlies who

cope with the stresses they feel in their lives are more likely to seek outside help with their problems.

Overall, these findings suggest that integration into the Air Force community may serve as a significant buffer against the predictable stresses of Air Force life. Given that earlier research (Lewis, 1985) has shown that wives' perceptions of Air Force life as stressful is a significant predictor of the career intent of their enlisted husbands, Air Force programs and policies designed to increase the involvement of famlies in the Air Force community may well have a positive impact on retention.

REFERENCES

Bernard, J. (1981). Facing the future. Society, 18, 53-59.

Beutell, N.J., & Greenhaus, J.H. (1982). Interrole conflict among married women: The influence of husband and wife characteristics on conflict and coping behavior. Journal of Vocational Behavior, 21, 99-110.

Bowen, G.L. Families in blue: Insights from Air Force families. Social Casework: The Journal of Contemporary Social work, October, 1986, 459-466.

Burke, R.J., Weir, T., & Duwors, R.E. (1980). Work demands on administrators and spouse well-being. Human Relations, 33, 253-278.

Flannery, P.A., & Dansby, M.R. (1985). USAF Family Survey: A revision of the USAF Spouse Survey (LMDC-TR-85-3). Maxwell AFB, AL: Leadership and Management Development Center.

Greenhaus, J.H., & Beutell, N.J. (1985). Sources of conflict between work and family roles. The Academy of Management Review, 10, 76-88.

Greenhaus, J.H., & Kopelman, R.E. (1981). Conflict between work and nonwork roles: Implications for the career planning process. Human Resource Planning, 4, 1-10.

Hall, D.T., & Gordon, F.E. (1973). Career choices of married women: Effects on conflict, role behavior, and satisfaction. Journal of Applied Psychology, 58, 42-48.

Hightower, J.M., & Short, L.O. (1982). Factor stability of the factor structure of the Organizational Assessment Package (LMDC-TR-82-1). Maxwell AFB, AL: Leadership and Management Development Center.

Hunter, E.J. (1982). Families under the flag. NY: Praeger.

Keith, P.M., & Schafer, R.B. (1980). Role strain and depression in two job families. Family Relations, 29, 483-488.

Lewis, P.M. (1985). Family factors and the career intent of Air Force enlisted personnel (LMDC-TR-85-9). Maxwell AFB, AL: Leadership and Management Development Center.

Locksley, A. (1980). On the effects of wives' employment on marital adjustment and companionship. Journal of Marriage and the Family, 42, 337-346.

Osnerson, S., & Dill, D. (1983). Varying work and family choices: Their impact on men's work satisfaction. Journal of Marriage and the Family, 45, 339-346.

Pleck, J.H. (1977). The work-family role system. Social Problems, 24, 417-427.

Pleck, J.H., Staines, G.L., & Lang, L. (1980). Conflicts between work and family life. Monthly Labor Review, 103, 29-32.

Short, L.O. (1985). The United States Air Force Organizational Assessment Package (LMDC-TR-85-2). Maxwell AFB, AL: Leadership and Management Development Center.

1986 USAF - UES Mini Grant Program

Sponsored by the
Air Force Office of Scientific Research
Conducted by the
Universal Energy Systems, INC.

Final Report

Dynamic Task Scheduling With Resource Requirements In Hard Real-time Distributed Computer System

Prepared By: DAR-Biau Liu

Academic Rank: Associate Professor

Department: Computer Science Department

University: Old Dominion University

USAF Research: Richard Metzger & Thomas Laurence

RADC/COTD, Griffiss AFB, New York

DATE: August 15, 1986

Contract No.: S-760-OMG-092

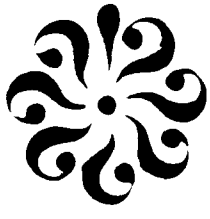

Abstract

We follow the resource management strategies in Arch OS and try to develop a general control strategy in the resource management in a decentralized distributed computer system.

A probability is considered everytime when a newly created task are going to be assigned to some processor, and a set of modified guarantee routines similar to those developed by Ramamrithm and Stankovic in (4) are introduced. The heuristic approach for solving the problem of scheduling tasks with deadlines and general resource requirements developed in (5) by Zhao and Ramamrithm, will be used, in conjunction with the guarantee algorithms and the probability selection scheme to fulfill the dynamic scheduling. The algorithms to determining the optimal paths in a stochastic network, developed by Mischandari and Soroush in (7), (8), were applied to achieve the system wide optimization when the Task is to be sent to some other node.

I *Introduction*:

This is a preliminary report of the research followed the one that developed at Rome, sponsorship of the U.S. Air Force Research Office and RADC/COTD, Griffiss AFB, New York.

We will follow the resource management strategies in Arch OS -- a decentralized distributed operating system developed at the Carnegie-Mellon University and try to develop a general control strategy in the resource management in a decentralized distributed computer system.

ArchOS has a sound theoretical base, as developed by Lui sha, Lehoczky, P., and Jenson, E.D. in (2) and (3). They used the classical set theoretical techniques to approach the concurrency control, consistency and correctness problem. The database was decomposed into the "consistency preserving" atomic data sets which are not necessary disjoint, and the notion of compound transactions was introduced. A compound transaction is defined as a partially ordered set of elementary transactions. Each elementary transaction is then independently partitioned into a partially ordered set of "correct perserving" atomic step segments according to certain modular generalized setwise and serializable scheduling rule. The optimality of concurrency control was proved based on the completeness of the fuzzy set of all modular generalized setwise and serializable scheduling rules. Some failure recovery rules were also introduced based on the notion of atomic commit segments. Although some basic techniques for the resource control strategies were developed, they seem to be not very practical as we mentioned in report (1). For example, in the Load Balance Problem, the assumption of equal probability (for assigning a newly created workload to other processors if the current processor is above the "threshold") is too strong a one, and the assumption that the assignment (to the processor) is permanent even worsens in a sense that the workloads of the new processor which were assigned to receive the new

AD-A186 492 UNITED STATES AIR FORCE RESEARCH INITIATION PROGRAM 9/11
1985 TECHNICAL REPORT VOLUME 2(U) UNIVERSAL ENERGY
SYSTEMS INC DAYTON OH R C DARRAH APR 87
UNCLASSIFIED AFOSR-TR-87-1718 F49620-85-C-0013 F/G 15/3 NL

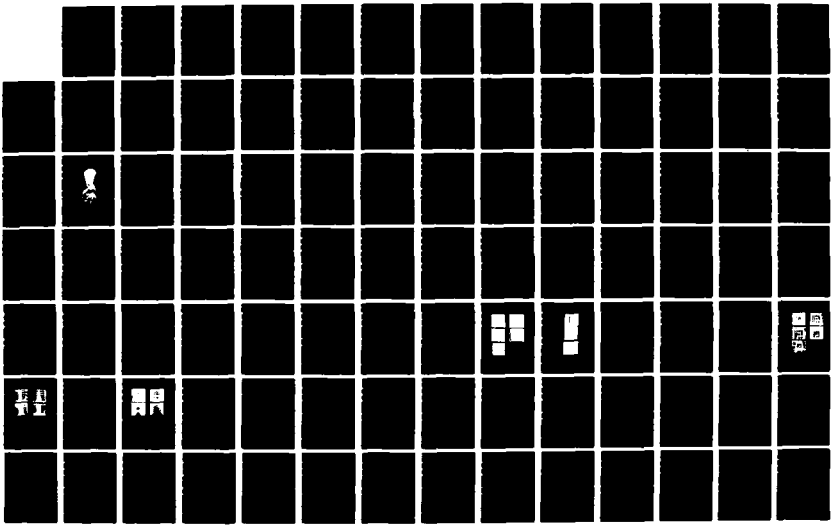

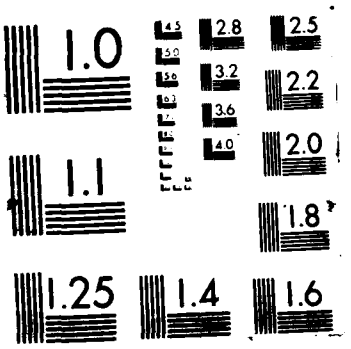
1.0
1.1
1.25
1.4
1.6
1.8
2.0
2.2
2.5
2.8
3.2
3.6
4.0

workload might itself be over the "threshold".

In this paper, a probability is considered every time when a newly created Task are going to be assigned to some processor (probabilistic selection scheme (10)), and a set of modified guarantee routines similar to those developed by Ramamrithm and Stankovic in (4) are introduced. In (4), a bidding algorithm is used in conjunction with a locally executed guarantee algorithm which either guarantees arriving tasks that they will meet their deadline or invokes the bidding algorithms to find a suitable location for the execution of the arriving task, if possible. The heuristic approach for solving the problem of scheduling tasks with deadlines and general resource requirements developed in (5) by Zhao and Ramamrithm, will be used in conjunction with the guarantee algorithms and the probabilistic selection scheme to fulfill the dynamic scheduling.

Stankovic argued in (6) that optimal decentralized control is not possible and that achievable control is based on a number of fundamental concepts including the "level of observability" that the particular system being controlled allows, the concepts of "towards", and the need for heuristics concerning entity interaction. He suggested also the use of Bayesian decision theory and estimation theory in meeting the objectives of achievable decentralized control. Although Stankovic provides a good start toward the goal for system-wide optimal decentralized control, many problems still remain. In this regards, we turn to the classical "shortest path" technique for a stochastic network. Recently, Eiger, Mischandari and Soroush had introduced the concept of "path preference" and developed an algorithm to determine the optimal path in the stochastic network for the linear and exponential utility function in (7). An algorithm for determining optimal paths in probabilistic networks for the guadratic utility functions was also developed by introducing the "temporary preference" paths in (8) by Mischandari and Soroush. We will apply this algorithm to obtain a systme-wide optimal path for the

stochastic network spanned by an initial node P_i and an end node P_{π_i}, corresponding to p_{i,π_i}, selected by the probabilistic selection scheme when a task could not be guaranteed at P_i with the resource requirements.

II. *General Assumptions:*

We will restrict ourselves to the loosely coupled distributed computer system consisting of n nodes (or processors)

P_1 , P_2 , ---, P_n .

Each node P_i (i=1,2,---,n) contains a local schedular, a dispatcher, a selection scheme, a set of guaranteed periodic tasks and a set of resources:

R_1 , R_2 ,---, R_{γ_i} (i=1,2,---,n).

Assume that each node P_i , periodically sends an update message to each of the other nodes in the system. Without of loss generality, we may assume that an update message containing load and status information's on P_i is sent at each time instant $k\tau$ for k=1,2,3,----, where τ may be taken as a number large enough to cover all periods of those fixed periodic tasks (e.g. $\tau \geq$ the l.c.m. of all periods) the time interval $I_k = (k\tau , (k+1)\tau)$ is referred to as the k-th update period, and τ is referred to as the update period length (see 10).

let $M_i(k)$ be the message sent by P_i at the instant $k\tau$, it may include any of the following observation's and estimates of load parameters on P_i :

$\mu_i(k)$ =Amount of unfinished work at $k\tau$ on P_i .

$\nu_i(k)$ =Number of jobs queued at P_i at $k\tau$.

$\alpha_i(k)$ =Number of jobs arrivals during I_{k-1}.

$\delta_i(k)$ =Number of local jobs departure during I_{k-1}.

$\beta_i(k)$=Amount of time P_i serves local jobs during I_{k-1}.

$\gamma_i(k)$=Average local job service time during I_{k-1}.

We assume also that a resource can be serially shared by tasks and that a passive resource (it has no processing power, e.g., a file) must be used with some active resources (it has processing power, like a CPU or a physical device).

A task T is a scheduling entity, the following characteristics of a task T are assumed known when it arrives at a node :

i) the worst case computation time C(T).

ii) the deadline D(T), by which the task must be completed.

iii) the resource requirements of the task T.

3. We will follow the scheme in (10) and calculate the propability $p_{ij}(k)$ for the pair of nodes P_i & P_j (j=1,2,---,), at the time instant kT:

It requires that the node P_i records the following observations during update period I_{k-1} : $\beta_i(k)$, $\delta_i(k)$, and $\nu_i(k)$ for all i=1,2,---,n. Based on these informations the node P_i estimates the average service time of its local jobs as follows:

$$\hat{\gamma}_i(1) = \beta_i(1) / \delta_i(1) ,$$

$$\hat{\gamma}_i(k) = \eta \cdot \beta_i(k)/\delta_i(k) + (1-\eta)\,\hat{\gamma}_i(k-1) \qquad (k > 1)$$

where $(0<\eta\leq 1)$ is an adjustable factor.

The estimated unfinished work on P_j , $j=1,2,\cdots,n$, $j\neq i$ is given by

$$\hat{\mu}_j(k) = \hat{Y}_j(k)\, v_j(k).$$

calculate

$$p_{ij}(k) = 1 - g_{ij}(k),$$

where

$$g_{ij}(0) = \frac{1}{n} \quad , \quad i, j = 1, 2, \cdots, n.$$

$$g_{ij}(k) = \frac{\hat{\mu}_i(k) - \hat{\mu}_j(k)}{\sum_{j=1} \left(\hat{\mu}_i(k) - \hat{\mu}_j(k) \right)} \quad , \qquad j \neq i$$

4. *General Algorithms*:

It is assumed that a task needs its resources throughout its execution and a task will request at least one resources.

STEP 1: When a non-periodic task T arrived at P_i , the "guarantee routines" will start to check to see if the task could be guaranteed to meet the deadline D(T) at P_i with the resources required for this task T.

STEP 2: If the task T could not be guaranteed at node P_i then we consider to send the task T to a remote note P_j . First we calculate $p_{i,n_i}(k) = \max_{j \neq i} p_{ij}(k)$, and select the remote note P_{n_i} which corresponds to the maximum p_{i,n_i} at the time instant k_2(Here, we assume that the time to calculate this probability can be neglected).

STEP 3: Consider the stochastic network spanned by all nodes in the distributed system with the initial node P_i and the end node P_{n_i} .

STEP 4: An optimal path can then be picked up by using the algorithm developed by Mirchandani and Soroush (8) in terms of "path preference" by maximizing the expected utility function.

STEP 5: If there exists no such node P_{π_i} which has the necessary resources requirements for the task T or if there is such a node but there does not exist paths connected to it from P_i , then, in any case, the task T could not be garanteed.

STEP 6: The local scheduler at P_i can interact with schedulers at other nodes by an appropirate communication through message updating.

Upon arriving at the destination node P_{π_i} , another attempt will be made to guarantee the task T by taking into consideration of the travel time of the optimal path from P_i to P_{π_i} and of the time to execute the optimization algorithms. (i.e. to see if $\pi\tau$ + travel-time of optimal path +executing-time of the optimization algorithm $\leq$ D(T)).

Eventually, the task will either be guaranteed or be rejected.

STEP 7:

Once the task is guaranteed at some node, then the dispatcher of that node will actually schedule the task.

5 Guarantee Routine's:

We adopt the notion of "guaranteeing a task" as in (4). A task is said to be graranteed if, under all circumstances, it will be scheduled to meet its real-time requirements and other resource requirements. Once a task has been guaranteed, we know that it will be completed before its deadline with all the resources required, but not exactly when it will be scheduled. This depends on the scheduling policy, the number of guaranteed tasks waiting to be executed, the nature of periodic tasks, new arrivals and the amount of systems overheads.

Periodic tasks are guaranteed; non-periodic tasks, after they arrive, may or may not be guaranteed. However, once guaranteed, they will definitely meet their deadlines. The intent is to guarantee all periodic tasks and as many of the non-periodic tasks as possible, utilizing the resources of the entire network.

Zhao and Ramamritham defined in (5), a feasible schedule as a list of tasks that have been guaranteed. And a schedule is "full" with respect to a set if it contains all tasks in the set, otherwise it is "partial".

They modified the guaranteed routines in (4), using a heuristic approach to select the task to be scheduled next. It is weighted three factors, each factor explicity considers information about real-time constraints of tasks and utilization of resources.

We will modify the strategy of scheduling and searching in (5) with the probabilistic selection scheme, to determine whether or not a new task can be guaranteed at a node:

1) On each node P_i , there is always a set of guaranteed tasks, say $k \geq 0$, and a current full feasible schedule for these tasks.

2) When a new task arrives at P_i ,it can be guaranteed if a *new full* feasible schedule, exists for the $k+1$ tasks. (i.e. the k tasks in the current feasible schedule remain guaranteed and the deadline of the new task also can be met).

3) If the new task is guaranteed, then the new feasible schedule, containing the new tasks, replaces the current one. the feasible schedule determines all the start times for the tasks currently on the node, and will not be changed until another new task is guaranteed.

4) If the new task cannot be guaranteed at P_i , i.e. the local schedules cannot find a full feasible schedule for all $k+1$ tasks, then the probability selection scheme and the optimal path algorithm is invoked, the new task is sent to the node P_{n_i} which has the maximum probability $P_{i,n_i}(R)$. The orginial current feasible schedule for tasks previously guaranteed on P_{n_i} remains unaltered.

The local scheduler determines a full feasible schedule for a given set of tasks in the following way:

It begins with an empty schedule and tries to extend it with one task at a time until a full feasible schedule is derived. This is, in fact, a search problem. The structure of the search space is a search tree. The root of the search tree is the empty schedule. An intermediate vertex of the search tree is a partial schedule. A descendant of a vertex is an immediate extension of the schedule corresponding to the vertex. A leaf, a terminal vertex, is a full schedule. The Goal of our algorithm is to search for a leaf that corresponds to a full feasible schedule.

The Heuristic Scheduling Algorithm in (5) introduce a vector EAT, to indicate the Earliest Available Times of resources:

EAT=(EAT1,EAT2,---,EATr),

Where EATi is the earliest time when resources R_i will become available.

I. At each level of the search-tree, the local scheduler computes (update) the EST (T), the Earliest Start Time of the task T that remains to be scheduled, EST (T)=Max{EATi | T needs Ri}, and the NEW-EAT(T) which is counting the idle factors of each resource.

II. At each level of the search-tree, the scheduler calculates:

DRUR=(DRUR1,DRUR2,---,DRURr), the Dynamic Resource Utilization Ratio, (which indicates the degree to which tasks that remains to be scheduled will use the resources), where

$$DRUR_i = \frac{(C(T) \mid T \text{ remains to be scheduled})}{\text{Max } \{D(T) \mid T \text{ remains to be scheduled}\} - EATi.}$$

In general, $DRUR_i \leq 1$.

The heuristic function which Zhao introduced is

$$H(T)=w_1 * X_1(T) + w_2 * X_2(T) + w_3 * X_3(T),$$

where $X_1(T) = D(T) - [EST(T) + C(T)]$

$X_2(T) = C(T)$

$X_3(T) = DRUR \cdot DRIF$

DRIF is the vector of Dynamic Resource Idle Factors.

The simulation result m(5) showed that, with properly chosen weight factors w_1, w_2, w_3, this heuristic algorithm is almost optimal.

We will adopt this heuristic scheduling algorithm at each node to fulfil the resource requirements.

6. Conclusions:

This is only a prelimary result of the research done in the dynamic task scheduling problem with resource requirements in a distributed computer system. Several algorithms were introduced in this area of research but this is the first one to consider the system as whole as a stochastic network in order to achieve the system wide optimization. Certainly a lot of works still remain to be done but the simulation works should be considered the very next.

References

1. Liu, D. B., "A Preliminary Investigation on Resource Control Strategies on Distributed Computer Systems, Real-Time vs Non-Real Time", Technical Report, U.S. Air Force Research Office, September, 1985.

2. Lui, Sha, Lehoczky, P., and Jensen, E. D., "Modular Concurrency Control and Failure Recovery -- Consistency, Correctness and Optimality, Part I, Concurrency Control", to appear on IEEE Transaction.

3. Lui, Sha, Lehoczky, P., and Jensen, E. D., "Modular Concurrency Control and Failure Recovery -- Consistency, Correctness and Optimality, Part II, Failure Recovery", to appear on IEEE Transaction.

4. Ramamritham, K., and Stankovic, J. A., "Dynamic Task Scheduling in Distributed Hard Real-Time Systems", IEEE Software, July, 1984.

5. Zhao, W., Ramamritham, K., and Stankovic, J. A., "Scheduling Tasks with Resource Requirements in Hard Real-Time Systems", Technical Report, University of Massachusetts, May, 1984.

6. Stankovic, J. A., "Achievable Decentralized Control for Functions of a Distributed Processing Operating System", IEEE Transactins on Computers, 1982.

7. Kiger, A., Mirchandani, P. B., and Soroush, H., "Path Preferences and Optimal Paths in Probablistic Networks", Transport Science, No. 19, 1985.

8. Mirchandani, P. B. and Soroush, H., "Optimal Paths in Probablistic Networks: A Case with Temporary Preferences", Computer & Operation Researches, Vol. 12, No. 4, April, 1985.

9. Dodin, B., "Approximating the Distributive Functions in Stochastic Networks", Computers & Operative Researches, Vol. 12, No. 3, March, 1985.

10. Hsu, C. Y. and Liu, Jane W. S., "Dynamic Load Balancing Algorithms In Homogeneous Distributed Systems", Proceedings, 6th International Conference on Distributed Computing Systems, IEEE, May, 1986.

1985-86 RESEARCH INITIATION PROGRAM

Sponsored by the

AIR FORCE OFFICE OF SCIENTIFIC RESEARCH

Conducted by the

UNIVERSAL ENERGY SYSTEMS, INC.

FINAL REPORT

THE DEVELOPMENT OF TWO AND THREE-DIMENSIONAL GRID OPTIMIZATION METHODS

Prepared by:	C. Wayne Mastin
Academic Rank:	Professor
Department and University:	Department of Mathematics and Statistics Mississippi State University
USAF Research Colleague:	Bharat Soni, Sverdrup Technology, Inc. CFD Group, AEDC, Arnold Air Force Station
Date:	October 4, 1986
Subcontract No:	S-760-OMG-004

THE DEVELOPMENT OF TWO AND THREE-DIMENSIONAL GRID OPTIMIZATION METHODS

by

C. Wayne Mastin

ABSTRACT

Optimization methods are developed and analyzed for the solution of all the popular variational problems in grid generation. Comparisons are made between the different variational methods.

I. INTRODUCTION: Variational methods in grid generation have recently become a viable alternative to the more established elliptic methods. Their appeal is likely due to the geometric foundation of the variational methods. These methods were derived using grid properties such as distances between grid points, orthogonality of grid lines, and the volumes of grid cells. Because of the earlier successes of elliptic methods, the first solution algorithms consisted of converting the variational problem to a problem of solving the elliptic Euler equations. The Euler equations were then solved using available finite difference algorithms. This approach was used by Brackbill and Saltzman [1], and Roache and Steinberg [4]. One disadvantage in this procedure is that the Euler equations are considerably more complicated than the original variational integral. Due

to the complexity of the Euler equations, they are difficult to solve and solution algorithms may not converge. These difficulties have led to the development of algorithms for the direct solution of the variational problem. This approach was followed by Kennon and Dulikravich [3] and Carcaillet et al. [2]. In these two reports, different discrete problems were formulated as unconstrained optimization problems and then solved using a conjugate gradient iterative method. There are several advantages in this alternative. The original geometric properties of the grid are stated precisely by the discrete problem. Thus there is no truncation error as there is in the numerical solution of the Euler equations. Also, the conjugate gradient and similar descent methods will always converge to a local extrema. However, the convergence rate may be very slow.

This report will present a survey of the types of integrals that may be included in a variational problem and the geometric properties that each integral imposes upon the grid. Optimization methods for the direct solution of the variational problems will also be covered. A Jacobi-Newton iterative method will be developed and compared with the Fletcher-Reeves conjugate gradient method. By combining the simpler Jacobi-Newton iteration with the direct solution of the variational problem, one has an algorithm which is easier to program than the Euler equations and requires less storage and less computer time per iteration than the conjugate gradient method.

II. VARIATIONAL INTEGRALS: Variational methods may be used to influence three geometric properties of a grid. These are the smoothness of the grid point distribution, the size of the grid cells, and the orthogonality of the grid lines. Each property, smoothness, cell volumes, and orthogonality,

can be assigned a numerical value by evaluating an integral. Most of the results will deal with three-dimensional problems, and the physical and computational variables will be denoted by x, y, z and ξ, η, ζ, respectively.

There are two basic smoothness integrals, one using the gradient of the physical variables and the other using the gradient of the computational variables. The integrals are denoted as S_1 and S_2 with D and R the computational and physical regions.

$$S_1 = \int_D |\nabla x|^2 + |\nabla y|^2 + |\nabla z|^2 \, d\xi d\eta d\zeta \tag{1}$$

$$S_2 = \int_R |\nabla \xi|^2 + |\nabla \eta|^2 + |\nabla \zeta|^2 \, dxdydz \tag{2}$$

$$= \int_D (|r_\eta x r_\zeta|^2 + |r_\zeta x r_\xi|^2 + |r_\xi x r_\eta|^2)/J \, d\xi d\eta d\zeta$$

where J is the Jacobian $\frac{\partial(x,y,z)}{\partial(\xi,\eta,\zeta)}$ and $r = (x,y,z)$.

The functions minimizing either of these integrals will define a smooth mapping between the physical and computational regions in the sense that the mapping functions are harmonic and therefore infinitely differentiable. However, the mapping defined by the minimization of S_1 may not be one-to-one. The mapping defined by the minimization of S_2 is one-to-one, but the construction of the mapping is more difficult. Current methods require the numerical solution of a system of nonlinear Euler equations.

For the two-dimensional case, there is a simple relation between the above integrals, (1) and (2), and the elliptic equations commonly used for grid generation. Often control functions are included in grid generation methods to distribute grid points in particular regions. On introducing arbitrary functions $P(\xi,\eta)$ and $Q(\xi,\eta)$ into the two-dimensional version of S_1 in (1), it follows that

$$\int_R P^2|\nabla\xi|^2 + Q^2|\nabla\eta|^2 dxdy = \int_D (P^2|r_\xi|^2 + Q^2|r_\eta|^2)/J \, d\xi d\eta,$$ where J is the Jacobian $\frac{\partial(x,y)}{\partial(\xi,\eta)}$. The Euler equations for minimizing this integral may be written as

$$\nabla^2\xi = -(\ell nQ)_\xi|\nabla\xi|^2$$

$$\nabla^2\eta = -(\ell nP)_\eta|\nabla\eta|^2$$

or in computational space, with $r = (x,y)$, as

$$|r_\eta|^2(r_{\xi\xi} - (\ell nQ)_\xi r_\xi) + |r_\xi|^2(r_{\eta\eta} - (\ell nP)_\eta r_\eta) - 2(r_\xi\cdot r_\eta)r_{\xi\eta} = 0.$$

This is the elliptic system with control functions

$$\phi = (\ell nQ)_\xi, \ \psi = (\ell nP)_\eta.$$

If ϕ and ψ are given, then the corresponding control functions for the variational integral are

$$P = \exp(\int \psi d\eta), Q = \exp(\int \phi d\xi).$$

A uniform distribution of grid cell volumes would not be appropriate in most practical applications. However a near constant value of some weighted value is often called for. The weight may depend on some desired distribution of volumes or a solution-dependent quantity used to define an adaptive grid. From a variational point of view, the optimal volume distribution could be defined by minimizing the integral

$$V_1 = \int_D G\,J\,d\xi d\eta d\zeta. \tag{3}$$

Here G is the product of a given weight function and the Jacobian, that is,

$$G = \frac{\partial(x,y,z)}{\partial(\xi,\eta,\zeta)}\, w(\xi,\eta,\zeta).$$

While there is no guarantee that the variational problem will have a solution which gives a non-singular mapping between physical and computational spaces, it can be noted that if such a solution exists, then the weighted Jacobian G will be constant. This follows from the Euler equations. The argument is simpler in the two-dimensional case. The Euler equations are then

$$G_\xi y_\eta - G_\eta y_\xi = 0$$

$$- G_\xi x_\eta + G_\eta x_\xi = 0,$$

and if it is assumed that the Jacobian $x_\xi y_\eta - x_\eta y_\xi \neq 0$, it follows that

$$G_\xi = G_\eta = 0$$

or G must be constant. The constant is determined by the physical region and the value of w since

$$\int_D G \, d\xi d\eta = \int_R w dx dy. \tag{4}$$

There is one other volume integral that should be considered. If

$$V_2 = \int_D |\nabla G|^2 d\xi d\eta d\zeta, \tag{5}$$

then the integrand is a second order differential expression in the physical variables x, y, and z. Consequently, the Euler equations are a system of fourth order equations. Now there must be two boundary conditions if a unique solution to the Euler equations is to be determined. One condition is imposed by fixing the boundary correspondence. A second condition can be motivated by considering a lower order problem where G, the integrand of V_2, is a single dependent function of the variables ξ, η, and ζ. The Euler equation would then be Laplaces equation

$$\nabla^2 G = 0.$$

The equation has a unique solution if G is given on the boundary of the computational region. The function G would be uniquely determined up to a constant value if on the boundary,

$$G_\xi = 0 \text{ for } \xi = \text{constant}$$

$$G_\eta = 0 \text{ for } \eta = \text{constant}$$

$$G_\zeta = 0 \text{ for } \zeta = \text{constant}.$$

The constant value would again be determined by (4). Either of these types of boundary conditions could be advantageous in grid generation. Being able to specify the value of G along the boundary would aid in maintaining desired distributions of grid points near boundaries such as is needed in grids for the solution of problems with boundary layers. On the other hand, the derivative boundary conditions for G would be of value when several grids are patched together and it is desired that the cell sizes vary continuously from one subregion into another. The latter condition could also be used to generate a more uniform distribution of G over a single region.

If a grid is orthogonal, then

$$r_\xi \cdot r_\eta = r_\eta \cdot r_\zeta = r_\xi \cdot r_\zeta = 0,$$

where $r = (x,y,z)$. Therefore, one measure of skewness is the integral

$$A_1 = \int_D (r_\xi \cdot r_\eta)^2 + (r_\eta \cdot r_\zeta)^2 + (r_\xi \cdot r_\zeta)^2 \, d\xi d\eta d\zeta. \tag{6}$$

The integrand depends on the size of the grid cells since, for example,

$$r_\xi \cdot r_\eta = ||r_\xi|| \; ||r_\eta|| \cos \theta$$

where θ is the angle of intersection between the ξ and η grid lines. As a result, minimizing the integral A_1 would have little effect in subregions with extremely small cells. For grids with widely varying cell volumes, the following integral would be more appropriate

$$A_2 = \int_D \left(\frac{r_\xi \cdot r_\eta}{||r_\xi||\ ||r_\eta||} \right)^2 + \left(\frac{r_\eta \cdot r_\zeta}{||r_\eta||\ ||r_\zeta||} \right)^2 + \left(\frac{r_\xi \cdot r_\zeta}{||r_\xi||\ ||r_\zeta||} \right)^2 \, d\xi d\eta d\zeta. \quad (7)$$

Irrespective of the solution algorithm selected, the minimization of A_2 is a more difficult problem since the integrand is a rational function of the physical derivatives rather than a multinomial as in A_1.

With the variational grid generation methods one selects a nonnegative linear combination of the form

$$I = \alpha S_i + \beta V_j + \gamma A_k, \quad (8)$$

where i, j, and k are either 1 or 2. Since the S_i, V_j, and A_k may be of differing magnitudes, the coefficients α, β, and γ may contain scaling factors. One method of scaling that can be used is to compute values $S_i^{(0)}$, $V_j^{(0)}$, and $A_k^{(0)}$ from an initial algebraic grid and then select nonnegative numbers a, b, and c so that

$$a + b + c = 1.$$

Now if we choose

$$\alpha = a, \ \beta = b \frac{S_i^{(0)}}{V_j^{(0)}}, \ \gamma = C \frac{S_i^{(0)}}{A_k^{(0)}},$$

then the initial value of I is the same for any combination of a, b, and c.

III. OPTIMIZATION: In the direct solution of the variational problem each integral is approximated on a square grid in computational space. Thus the continuous problem of minimizing I is reduced to the discrete problem of finding a minimum value of an objective function

$$F = \sum F_{i,j,k} \tag{9}$$

where i, j, k ranges over the indices of the grid points. The grid points on the boundary would be included although it is assumed that these points are fixed. Each term $F_{i,j,k}$ is to contain all difference approximations centered at the grid point $r_{i,j,k}$ which are used in the formation of the objective function F. The optimal grid is found by obtaining the unconstrained minimizer of the objection function F. There are many algorithms for solving optimization problems. An algorithm which has been successfully implemented in grid generation is the Fletcher-Reeves conjugate gradient method. The method can be used with any of the variational integrals of the previous section. Since the approximations of (2) and (7) involve quotients, it is possible that somewhere in the iteration scheme a division by a number close to zero may occur. This problem can be easily avoided by placing a lower bound on the denominators. Only a two-dimensional grid problem using (2) has been attempted because the three-dimensional integral becomes very complicated when transformed to computational space.

The conjugate gradient and related descent methods have the attractive feature of always converging to a grid which represents a local minimum value for the objective function. Their use in the solution of large three-dimensional grid generation problems may not be very efficient.

At each iteration a one-dimensional minimization problem must be solved to determine the optimal step-size in the descent direction. The step-size problem can not be easily solved and frequently requires several evaluations of the objective function. This is especially true when the integrals in (2) and (7) are included. Therefore, alternate solution algorithms have been investigated. The application of Newton or quasi-Newton methods for nonlinear minimization problems in grid generation does not appear to be practical because of the number of matrix operations. Motivated by algorithms which are used to solve the discretized Euler equations, a Jacobi-Newton method has been selected as an alternate algorithm for solving the optimization problem. The following development covers the basic steps of the algorithm.

A local minimum value of F occurs at points where

$$\nabla F = 0,$$

or writing this system in component form

$$\left.\frac{\partial F}{\partial x}\right|_{i,j,k} = 0$$

$$\left.\frac{\partial F}{\partial y}\right|_{i,j,k} = 0$$

$$\left.\frac{\partial F}{\partial z}\right|_{i,j,k} = 0.$$

This system is to be satisfied at all interior grid points. Assuming that F is given in the form of (9), these three equations can be equivalently stated as

$$\frac{\partial F_{i,j,k}}{\partial x_{i,j,k}} = \sum \frac{\partial F_{\ell,m,n}}{\partial x_{i,j,k}}, \quad (\ell,m,n) \neq (i,j,k)$$

$$\frac{\partial F_{i,j,k}}{\partial y_{i,j,k}} = \Sigma \frac{\partial F_{\ell,m,n}}{\partial y_{i,j,k}}, \quad (\ell,m,n) \neq (i,j,k) \tag{10}$$

$$\frac{\partial F_{i,j,k}}{\partial z_{i,j,k}} = \Sigma \frac{\partial F_{\ell,m,n}}{\partial z_{i,j,k}}, \quad (\ell,m,n) \neq (i,j,k).$$

The sum on the right-hand sides of the equations is understood to extend over all grid point indices ℓ, m, n except i, j, k. Most of the terms would vanish since the i, j, k point would only be included in a few difference approximations at neighboring points. The exact number of non-zero terms would depend on the choice of variational integrals and the derivative approximations used in the integrands. This is the first phase of the development. The name Jacobi is attached to this phase only because of the form of equations (10). For the next step in the development, vector notation will be used and (10) will be expressed simply as

$$f(r) = g(r)$$

where $$r = (x_{i,j,k}, y_{i,j,k}, z_{i,j,k}).$$

The grid optimization procedure is an iterative process. If r_0 is the initial grid point, then each new point is computed from the equation

$$f(r_k) = g(r_{k-1}), \quad k = 1, 2, \ldots.$$

This is a nonlinear system of three equations which can be solved using Newton's method. In all of our examples only one Newton iteration was used for each value of k. In fact, for certain variational integrals, this system is linear and the exact solution is obtained in one iteration.

The Jacobi-Newton iterative method described above has been used to solve a wide range of two and three-dimensional grid generation problems. So far, it has not been used with the variational integrals S_2 and A_2 because the quotients would cause the Newton iteration equations to be very lengthy. Convergence problems have not been encountered except in some cases where the grid folded. It is often necessary to use under-relaxation for larger problems, so that actual Newton equation is of the form

$$r_k^{(S)} = r_k^{(S-1)} - \omega[f'(r_k^{(S-1)})]^{-1}(f(r_k^{(S-1)}) - g(r_{k-1})), \qquad (11)$$

where $0 < \omega \leq 1$. Unlike the conjugate gradient methods, this method may diverge for certain initial grids.

III. RESULTS: The following examples are presented to demonstrate the effect of the grid optimization procedure when applied to a large-scale three-dimensional grid. As can be seen, the success of the optimization process depends primarily on the proper choice of the variational integrals included in (8). When a decision had to be made between efficiency and robustness, it was the policy to develop a robust algorithm. A numerical step-size determination was used in the conjugate gradient iteration even though it was sometimes possible to calculate the exact optimal step-size. A conservation value of $\omega = .25$ in (11) was selected although larger values led to faster convergence in some cases. Ten iterations were run in each case.

A three-dimensional region with a portion of the boundary grid is depicted in Figure 1. The bullet-shaped indention in the end of the region causes the interpolated grid to be highly skewed. An interior surface grid constructed by transfinite interpolation is shown in Figure 2. An optimized grid appears in Figure 3. The objective function used for this grid was

$$I = \alpha S_1 + \beta V_2 + \gamma A_2$$

where

$$\alpha = 0.25, \ \beta = 0.25 \frac{S_1^{(0)}}{V_2^{(0)}}, \ \gamma = 0.5 \frac{S_1^{(0)}}{A_2^{(0)}} .$$

In an effort to maintain the same grid distribution as in the algebraic grid, the volume weight function in V_2 was chosen to be

$$w(\xi,\eta,\zeta) = ||r_\xi^{(0)}|| \ ||r_\eta^{(0)}|| \ ||r_\zeta^{(0)}|| .$$

The derivative boundary conditions were imposed on G.

The selection of the wrong objective function may result in an unusable grid. For example, if the choice $\alpha = \beta = 0$ is selected, then the grid folds over the bullet as plotted in Figure 4. Even with the same proportionality weighting of geometric properties, if A_2 is replaced by A_1, the grid of Figure 5 is produced. The near orthogonality at the boundary in Figure 3 has been lost. This last case has also been used to test convergence rates for the Jacobi-Newton and conjugate gradient iterative methods. The reduction of the objective function for both methods is plotted in Figure 6. The advantage of the Jacobi-Newton method is even greater than indicated in the plot, since a conjugate gradient iteration step typically took twice as much computer time as a Jacobi-Newton step. However, in cases where grid folding occurred, the Jacobi-Newton method was often slower or even diverged. Grid folding is less likely to occur when using S_2 rather than S_1, but the integral S_2 has not been included in our three-dimensional code. The weighting used in the volume integral is a significant factor in the success of the variational method. If the function $\omega(\xi,\eta,\zeta) = 1$ is used in V_2, then ten steps of either optimization scheme produces the grid in Figure 7. Except for the weight function, the variational integral is identical to the one which generated the grid in Figure 5.

IV. CONCLUSIONS: There are many variational integrals used in grid generation. The successful application of variational methods depends on tailoring the integral to the physical region and the distribution of the desired grid. The solution of the variational problem can be computed using the traditional optimization methods or by iterative methods similar

to those currently being used to solve elliptic partial differential equations. The convergence rate for either iterative method is generally slow when applied to large-scale three-dimensional grids.

REFERENCES

1. J. U. Brackbill and J. S. Saltzman, "Adaptive Zoning for Singular Problems in Two Dimensions," Journal of Computational Physics 46 (1982), 342-368.

2. R. Carcaillet, "Optimization of Three-Dimensional Computational Grids and Generation of Flow Adaptive Computational Grids," AIAA Paper 86-0156, AIAA 24th Aerospace Sciences Meeting, Reno, Nevada, 1986.

3. S. R. Kennon and G. S. Dulikravich," A Posteriori Optimization of Computational Grids," AIAA Paper 85-0483, AIAA 23rd Aerospace Sciences Meeting, Reno, Nevada, 1985.

4. P. J. Roache and S. Steinberg, "A New Approach to Grid Generation Using a Variational Formulation," AIAA Paper 85-1527, AIAA 7th Computational Fluid Dynamics Conference, Cincinnati, Ohio, 1985.

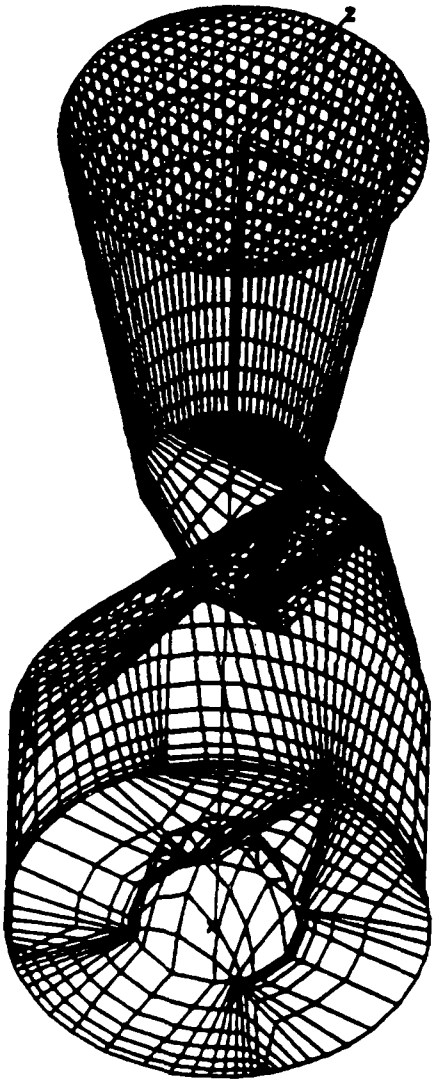

Figure 1. Original algebraically generated grid

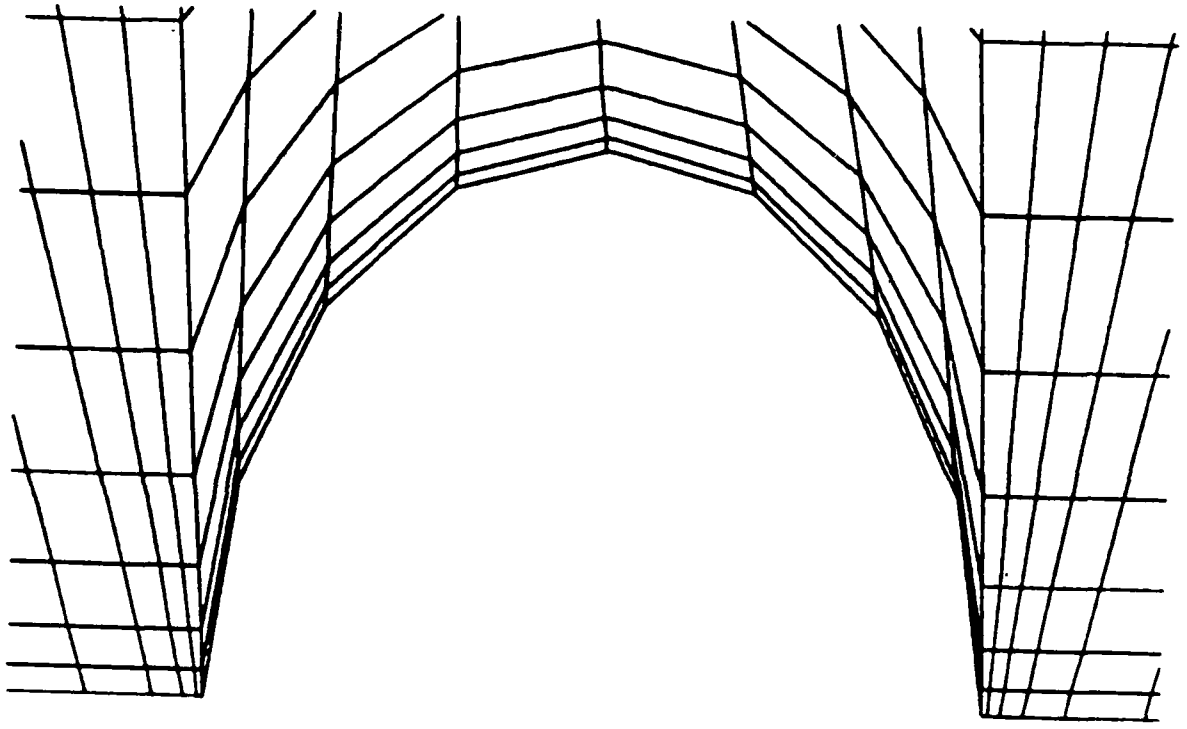

Figure 2. Grid on interior surface near bullet

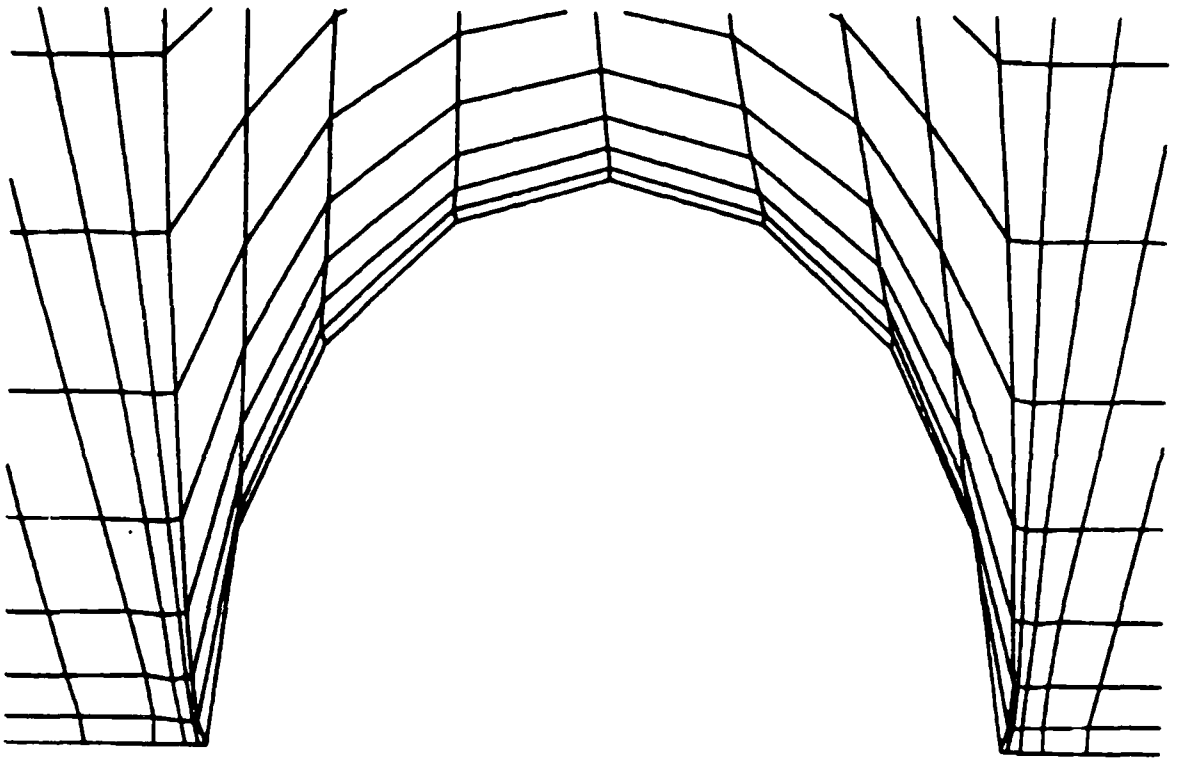

Figure 3. Optimized grid using integrals S_1, V_2, and A_2

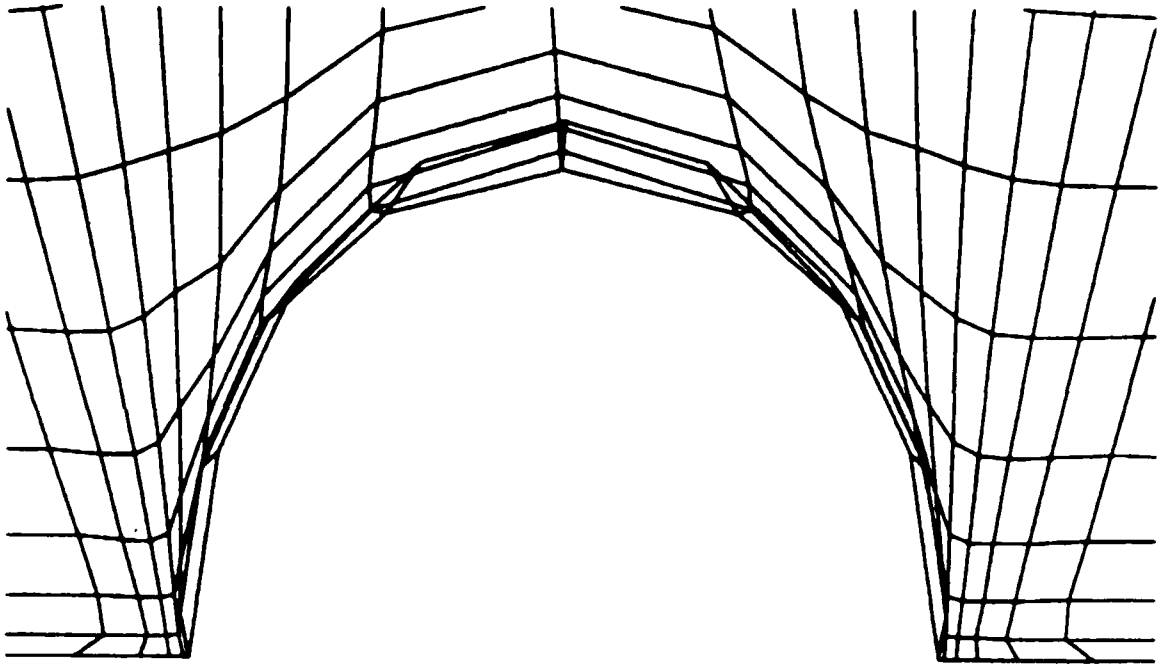

Figure 4. Optimized grid using only integral A_2

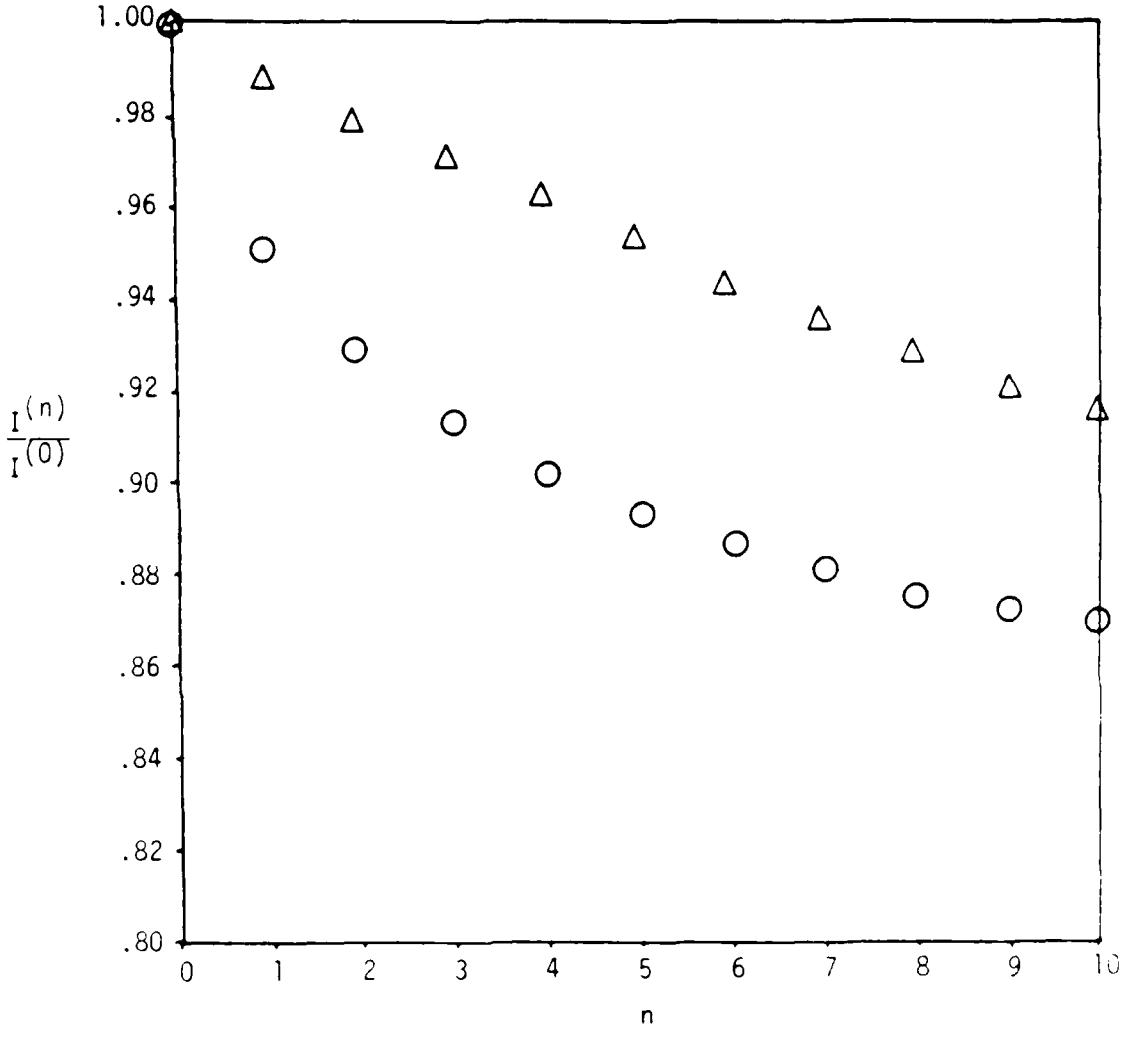

Figure 6. Reduction in objective function using the Jacobi-Newton method, ○, and the conjugate gradient method, △.

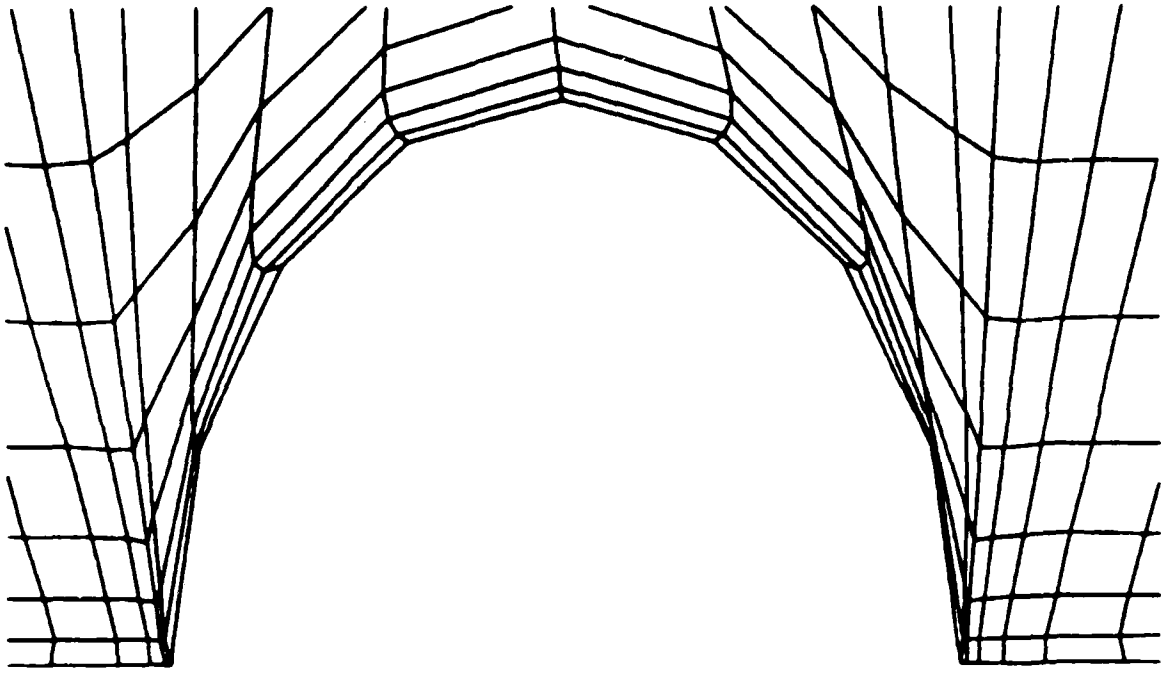

Figure 5. Optimized grid using integrals S_1, V_2, and A_1

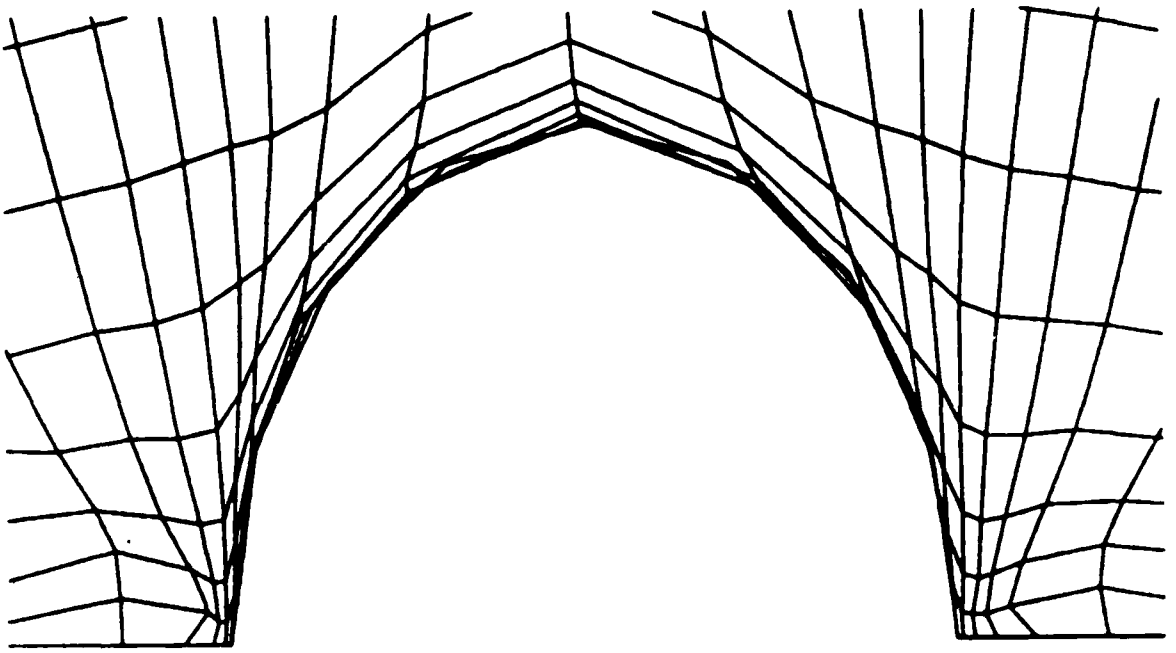

Figure 7. Optimized grid with $w = 1$ in integral V_2

FINAL REPORT

for

PLASMA SOURCE DEVELOPMENT

Bernard McIntyre

November 26, 1986

ABSTRACT

A commercial ion source was modified and used in a strong magnetic field (19-38 Gauss) so as to enhance the background ionization in a vacuum chamber. The exit grid of the 12cm ion source was covered to cut its effective area in half so as to reduce the gas flow to the chamber and allow for more variation in the chamber operating pressure--at an operating pressure of 2×10^{-4} Torr and 19 Gauss the measured electron density was 3.5×10^{7}/cc. While the source operated in this manner a 1 kev electron gun was turned on, coaxially with the ion source and the vacuum chamber. The electron density was measured at several points across the electron beam. Plasma densities were found to decrease exponentially from the center of the electron beam to the edge of its self generated plasma and then remain fairly constant out to the chamber wall. This region of constant density was that of the ionization from the ion source. The magnetic field was then doubled and the density profiles indicated that plasma diffusion outward from the center of the beam was governed by Bohm diffusion.

I. INTRODUCTION

The 12 cm electron bombardment ion source used here was previously used in small vacuum chamber applications but because of its large gas throughput a very large pumping speed was required. The usual result was that the chamber pumping system could just barely handle the minimum gas load required to initiate a discharge in the source. As a result, there was no flexibility in the variation of test parameters.

In order to reduce the required gas throughput here, the exit grid area of the source was reduced by one half. Chamber pressure could then be controlled from 1×10^{-5} to 5×10^{-4} Torr for a wide range of gas flows without losing the discharge. Measured plasma densities in the 3' x 8' chamber were $1\text{-}3 \times 10^{7}$/cc and varied by about 30% between the center of the chamber and the wall.

Having achieved a relatively high, stable plasma density which was readily controlled, our interest shifted to possible uses of this plasma. One important use of this system could be in the area of beam-plasma interactions. A 1 kev electron gun in the same chamber could produce a beam whose self generated plasma was the order of $5\text{-}8 \times 10^{7}$/cc. The background plasma from the ion source then could possibly influence interactions between the self generated plasma and the electron beam. An important contribution to the study of these interactions would be the diffusion mechanism of plasma outward from the electron beam. If the diffusion model could be identified then beam plasma interactions might be better understood at a later time. The remainder of the work discussed in this report was centered on the plasma diffusion mechanism.

II. PLASMA DIFFUSION

When a large magnetic field is applied to a group of electrons the electron motion along the field is not effected but the motion transverse to the field is constrained to circular motion about the magnetic field lines. This constraint limits the transverse conductivity of a plasma. The electrons and ions both orbit about the field lines, but the ion radii are much larger because of their larger mass. The ions in a plasma then are not as easily magnetized as the electrons and their transverse conductivity is less effected by the magnetic field.

The usual way in which electrons diffuse across the field lines is through collisions. As the electrons orbit about the field they eventually collide with other particles and undergo a random walk type of trajectory. This is not a very efficient process because of the relatively large mean free paths for the electrons. A much more efficient way to enhance the transverse diffusion of electrons is to have them interact with plasma waves. Bohm (1) showed that plasma instabilities can have high frequency plasma oscillations associated with them which interact strongly with the plasma

electrons. This interaction enhances the transverse electron diffusion by orders of magnitude over that due to collisions alone. Bohm also postulated that the form of the diffusion coeficient due to plasma oscillations (called the Bohm diffusion coeficient) should vary with magnetic field as 1/B. The collision dominated diffusion coefficient on the other hand varies as $1/B^2$, and so, in principle, the two diffusion mechanisms can be differentiated by varying the magnetic field.

The approach taken in this project was to inject an electron beam into a plasma parallel to a magnetic field. The electron beam tends to interact with the plasma and generate plasma oscillations which in turn enhance the transverse diffusion. According to Szuszczewicz(2), the plasma density should decrease exponentially from the beam center and the decay constant should vary as the inverse square root of the diffusion coefficient. By measuring the plasma density transverse to the beam for two different values of magnetic field, the field variation of the diffusion coefficient can be found. For Bohm diffusion the exponential decay constant varies directly as the square root of the field while for collision dominated diffusion it

varies with the first power of field.

III. EXPERIMENTAL CONFIGURATION

A 3′ by 8′ vacuum chamber was configured with an electron gun on one end and a plasma source on the other. Both were aligned to produce beams centered on the axis of the chamber. The plasma source utilized argon gas and resulted in a chamber pressure of 0.2 millitorr. A hot filament in the source emited electrons which were accelerated and ionized the argon atoms. Equal numbers of electrons and ions were extracted through an exit grid so as to produce a plasma density in the chamber the order of 10^7 /cc. The electron gun was operated at 1 kev energy and 3-5 ma of current, well below the threshold for initiating any beam plasma discharge. A set of magnetic coils provided an axial magnetic field of 19 and 38 gauss. A cylindrical Langmuir probe was moved in one half inch intervals across the beam region. The function of the probe was to measure the plasma electron density and temperature. The electron density measurements were ploted on semilog graph paper and

are shown in figure 1.

IV. DISCUSSION

As seen from figure 1, the density profile can be used to identify the center region of the electron beam. The ionization produced by the electron beam falls off exponentially from the center region and far from the beam, the background plasma density falls off nearly linearly to the chamber walls. For both values of the magnetic field used the background plasma density from the plasma source was nearly equal. The electron density data shows that as the field increased to 38 gauss the electron current to the probe was decreased. The ion current to the probe was the same for both magnetic field values so this decrease in electron density is a real effect due to the magnetic field constraining electron collection. The data also illustrates the effect of a larger magnetic field in compressing the electron beam diameter. Although the raw probe data is not shown here, the probe characteristic curves indicated that electron current exhibited strong saturation effects far from the central beam region, while near the beam region

they did not. The likely explaination for this behavior is that strong plasma oscillations in the central region result in Bohm diffusion and a large transverse conductivity to the probe. Outside this region the plasma oscillations are absent or of a low amplitude and the transverse conductivity to the probe is dominated by collisions and is much smaller and the electron current saturates.The slope of the density data in figure 1 increases by a factor of 1.5 as the magnetic field doubled. This implies that the slope varies as the square root of the field, the diffusion coefficient varies as the inverse of the field and Bohm diffusion dominates the transverse motion of the electrons.

REFERENCES

1. Bohm, D.,E.H.S.Burhop, H.S.W.Massey and R.M.Williams,Characteristics of Electrical Discharges in Magnetic Fields, edited by Guthrie and Wakerling, McGraw-Hill, N.Y.,1949

2. Szuszczewicz, E.P., D.N.Walker, and J.C.Holmes "Plasma Diffusion in a Space Simulation Beam Plasma Discharge",Geophysics Research Letters, 6,201,1979

FIGURE CAPTION

FIGURE 1: Semilog plot of electron plasma density vs relative position of the Langmuir probe for two values of magnetic field.

FIGURE 1

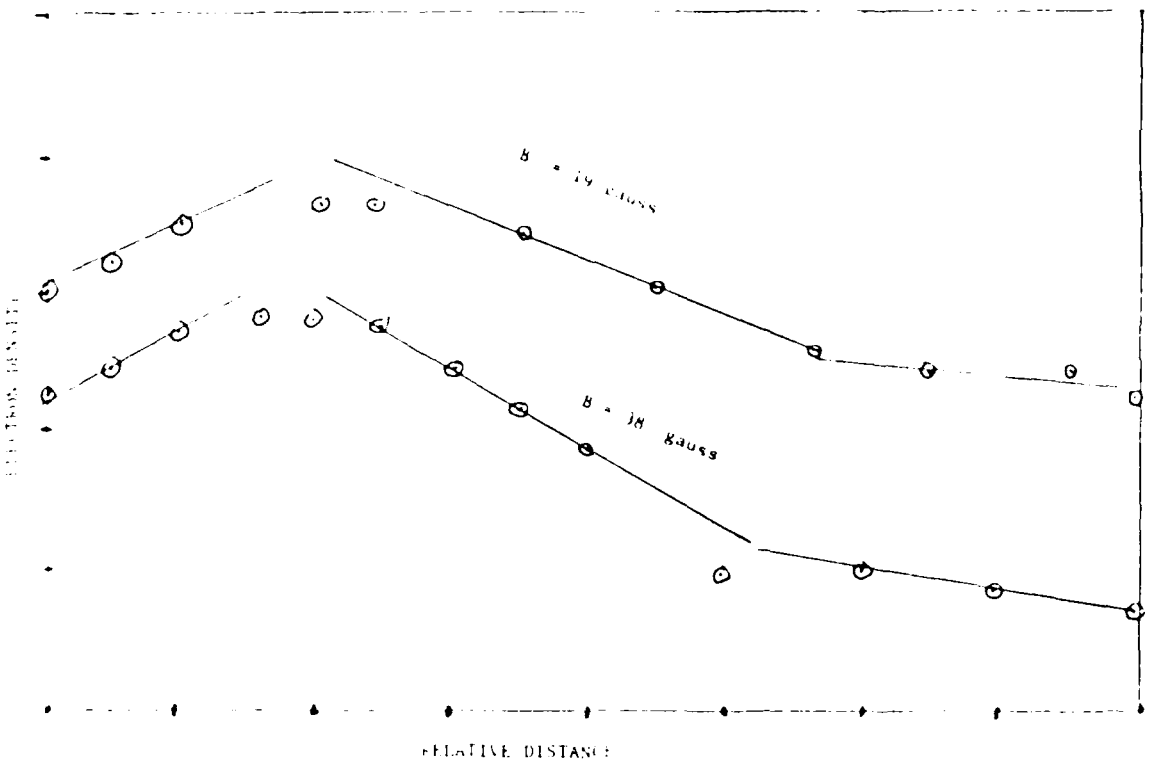

FINAL REPORT NUMBER 50
APPOINTMENT MADE TOO LATE
FOR RESEARCH TO BE COMPLETED
Dr. Rex C. Moyer
760-OMG-034

FINAL REPORT NUMBER 51
REPORT NOT RECEIVED IN TIME
WILL BE PROVIDED WHEN AVAILABLE
Dr. James Mrotek
760-OMG-101

USAF-UES RESEARCH INITIATION

PROGRAM GRANT

Sponsored by the

AIR FORCE OFFICE OF SCIENTIFIC RESEARCH

Conducted by the

UNIVERSAL ENERGY SYSTEMS, INC.

FINAL REPORT

I. HIGH PERFORMANCE LIQUID CHROMATOGRAPHY STUDIES OF THERMAL DECOMPOSITION OF 1,4-BUTANEDIAMMONIUM DINITRATE.

II. SYNTHESIS OF INSENSITIVE ENERGETIC MATERIALS.

Prepared by:	Maurice C. Neveu
Academic Rank:	Associate Professor
Department and University:	Chemistry Department State University of New York, College at Fredonia
Research Location:	Chemistry Department State University of New York, College at Fredonia Fredonia, N.Y. 14063
USAF Research Colleagues:	Robert L. McKenney, Jr. and Paul Bolduc High Explosives Research and Development Facility Air Force Armament Laboratory, Eglin AFB, FL
Date:	11 February 1987
Contract No.	S-760-OMG-072

I. HIGH PERFORMANCE LIQUID CHROMATOGRAPHY STUDIES OF THERMAL DECOMPOSITION OF 1,4-BUTANEDIAMMONIUM DINITRATE.

II. SYNTHESIS OF INSENSITIVE ENERGETIC MATERIALS.

by

Maurice C. Neveu

ABSTRACT

Samples of 1,4-butanediammonium dinitrate were thermally decomposed in the temperature range 175°C to 275°C and the decomposition products were analyzed by High Performance Liquid Chromatography (HPLC).

Several compounds with possibly insensitive high explosive properties were synthesized: 3,5-dichloro-2,4,6-trinitroanisole; 3,5-diamino-2,4,6-trinitroanisole; 3-chloro-2,4,6-trinitrobenzoic acid; 3-amino-2,4,6-trinitrobenzoic acid; 3-chloro-2,4,6-trinitroanisole; 3-amino-2,4,6-trinitroanisole; 3-chloro-2,4,6-trinitrotoluene; 3-amino-2,4,6-trinitrotoluene; 3-chloro-2,4,6-trinitrothioanisole.

INTRODUCTION

An explosives component of current interest is 1,4-butanediammonium dinitrate (BDD).Mechanistic studies on the thermal decomposition of BDD are being carried out mainly by Differential Scanning Calorimetry (DSC). It is the purpose of this work to supplement the DSC studies with High Performance Liquid Chromatography (HPLC) measurements, by detecting chemical species arising during the thermal decomposition.

Another aspect of this work is the synthesis of insensitive high explosives, especially those analogous to 3-amino-2,4,6-trinitrotoluene. It has been shown that TNT is markedly desensitized to impact and shock by its molecular modification to 3-amino-2,4,6-trinitrotoluene. Explosive yield measurements, calculated CJ pressures and detonation velocities indicate improved performance over that of 2,4,6-trinitrotoluene.[1,2] The synthetic pathway followed was generally that shown in Fig. 1. However,other pathways were followed or attempted as described in the next section.

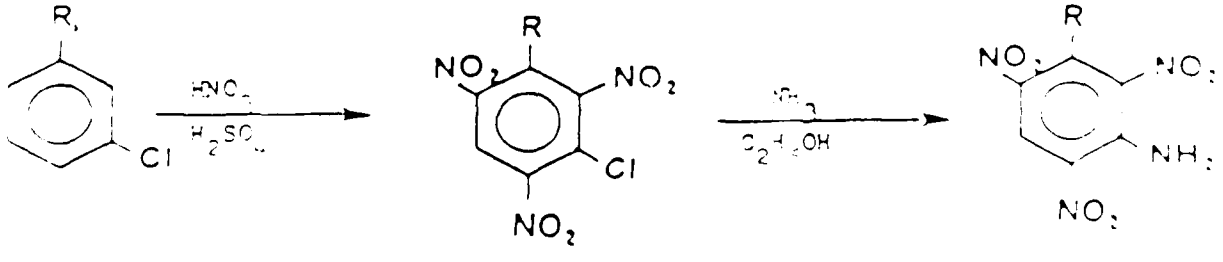

Fig. 1

EXPERIMENTAL

1. High Performance Liquid Chromatography (HPLC) Studies of Thermal Decomposition of 1,4-Butanediammonium Dinitrate (BDD)

Samples of BDD were heated in an open aluminum Perkin-Elmer Differential Scanning Calorimeter (DSC) cup on a Fisher-Johns melting point apparatus hot stage for a given period of time at a given temperature. The preweighed sample was weighed again after the heating to determine any weight loss. The cup was then dropped in a vial containing 2.0 ml of HPLC grade methanol to dissolve the residue in the cup, and an aliquot of 0.15 ml was injected into a Waters High Performance Liquid Chromatograph equipped with a refractive index detector, and the chromatogram was recorded on a Gow-Mac Model 70-990 chart recorder. The following conditions were used throughout the series of measurements: flow rate 1.5 ml/minute; pressure limit 4000 lb/in^2; attenuator 64x; chart speed 1 inch/minute. The mobile phase was HPLC grade methanol and the column used was a Waters μBONDAPAK C_{18} containing low polarity stationary phase suited for reverse partition chromatography.

BDD was prepared by the addition of 3.0 ml of 15M HNO_3 to a well-stirred solution of 2.0 g of 1,4-diaminobutane in 25 ml of absolute ethanol. A solid precipitate was collected by vacuum filtration and recrystallized three times from 95% ethanol to give the BDD product melting at 138.0-138.5°C.

BDD samples were dried in a vacuum oven at 70°C before use. Many sets of temperature and heating periods were used. Each set was run at least in duplicate. The data in Table I is a selection from the totality of runs between 175°C and 185°C chosen to give increments of 25°.

TABLE I

Temperature (°C)	Heating Period (minutes)	% Wt. Loss	Peak Position (cm) First	Second	Percent 2nd Peak
175	30	12.2	5.13	6.09	2.3
175	60	15.8	5.25	6.16	1.6
200	30	9.1	5.25	6.04	3.2
200	60	13.6	5.25	5.90	4.3
225	20	12.0	5.25	5.78	9.0
225	30	40.9	5.25	5.74	57.0
225	60	50.0	5.21	5.74	44.7
250	20	22.7	5.20	5.83	68.4
250	30	27.3	5.25	5.85	75.0
250	40	43.5	5.25	5.85	76.9
275	5	53.3	5.25	5.93	74.1
275	10	41.7	5.20	5.85	76.0
275	15	65.2	5.15	5.85	87.5
275	20	53.3	5.25	5.95	79.1
275	30	56.0	5.30	6.00	86.7
275	40	41.9	5.30	5.90	79.0
			5.23 ± 0.05	5.90 ± 0.12	

The chromatograms showed two peaks. The first one was centered at 5.23 cm from the injection position corresponding to a retention time of 124 seconds. The second peak at 5.90 cm corresponds to a retention time of 139 seconds. The intensity of the second peak increases as temperature and period of heating are increased indicating that it is due to a decomposition product. The nature of the decomposition product cannot be ascertained at this juncture without additional information such as mass spectrometric data. It had been anticipated that pyrrolidinium nitrate, formed from cyclization of BDD, might be a decomposition product. However, an authentic sample of it run in the same manner gave a peak at 5.35 cm. The first peak is the characteristic one for unreacted BDD. It might be noted that there is a fairly good correspondence between %Wt. Loss and intensity of the second peak tabulated as Percent 2nd peak. Especially to be noted is the large change in the values between the 20 and 30 minute runs at 225°C.

3,5-dichloro-2,4,6-trinitroanisole. To a nitrating mixture consisting of 4.4 ml of 30% oleum (30% SO_3 in concentrated H_2SO_4) and 4.4 ml of 90% HNO_3 was added 0.60 g of 3,5-dichloroanisole. The solution was kept in ice bath for one hour which was then allowed to warm to 25°C and kept at that temperature overnight. The temperature was raised slowly to 80°C, kept there for two hours, then again raised slowly to 97°C and kept at that temperature for four hours. The reaction mixture was then poured into 100 ml of ice water to yield 0.61 g of a light yellow solid, m.p. 85-86°C. The NMR spectrum indicated, essentially, replacement of the three aromatic protons by nitro groups.

3,5-diamino-2,4,6-trinitroanisole. Anhydrous ammonia was bubbled for 15 minutes into a solution consisting of 3,5-dichloro-2,4,6-trinitroanisole dissolved in 2 ml of absolute ethanol. The solution underwent a change from colorless to red to orange during the bubbling process, and then to yellow after a 30 minute reflux period. The reaction mixture was poured into 20 ml of ice water to yield 0.051 g of a yellow solid which did not melt when heated to 300°C.

3-chloro-2,4,6-trinitrobenzoic acid. To a nitrating mixture consisting of 1.5 ml of 30% oleum and 90% HNO_3 was added 0.270 g of 3-chlorobenzoic acid. The solution was heated at 95°C with stirring for 5 days to yield 0.116 g of white solid, m.p. 181-182°C. NMR analysis indicated placement of three nitro groups of the aromatic ring.

3-amino-2,4,6-trinitrobenzoic acid. Anhydrous ammonia was bubbled into a solution consisting of 0.034 g of 3-chloro-2,4,6-trinitrobenzoic acid in 2.0 ml of absolute ethanol for fifteen minutes. The solution was then refluxed for 50 minutes and upon cooling added to 10 ml of ice water. Extraction with ether, followed by evaporation of the ether, yielded 0.026 g of yellow solid which did not melt when heated to 300°C.

3-chloro-2,4,6-trinitroanisole. A mixture consisting of 2 ml of conc. H_2SO_4, 2 ml of conc. HNO_3 and 0.50 g of 3-chloroanisole was heated gradually to 95°C over a period of 4 hours in a water bath. The heat was then turned off and the bath allowed to stand overnight. The reaction mixture was poured into 100 ml of ice water to yield 0.59 g of orange-red solid, m.p. 75-78°C. NMR Analysis indicated placement of three nitro groups on the aromatic ring.

3-amino-2,4,6-trinitroanisole. Anhydrous ammonia was bubbled for one-half hour through a solution containing 0.051 g of 3-chloro-2,4,6-trinitroanisole dissolved in 10 ml of absolute ethanol. The solution turned brown immediately at the beginning of the bubbling process. The reaction mixture was then refluxed for one-half hour. The volume of the reaction was reduced to 3 ml. This was then poured into 10 ml of ice cold water. After centrifugation, 0.013 g of starting material, m.p. [illegible], was obtained. The supernatant was added to 20 ml of ice water. No crystals formed even after allowing it to stand in a cold-room maintained at 3°C overnight. The aqueous solution was extracted with ether to yield 0.036 g of yellow solid which did not melt when heated up to 300°C.

3-chloro-2,4,6-trinitrotoluene. To a nitrating mixture consisting of 3.0 ml of 15% oleum and 1.8 ml of 90% HNO_3 was added 0.50 g of 3-chlorotoluene. The mixture was maintained at 60°C over a period of one hour and then at 95°C for 3 hours after which it was poured into 100 ml of ice water to yield 0.83 g of light yellow crystals, m.p. 145-148°C. NMR analysis indicated the placement of three nitro groups on the aromatic ring.

3-amino-2,4,6-trinitrotoluene. Ammonia was [illegible] minutes into a mixture consisting of [illegible] g of 3-chloro-2,4,6-trinitrotoluene in [illegible] of absolute ethanol. A [illegible] to reddish [illegible] and then refluxed for 5 minutes. Solvent was [illegible] the volume [illegible] ml. This was poured in 15 ml of [illegible] precipitate was filtered to yield 0.103 g of brown solid, m.p. [illegible]. This solid may possibly be impure 3-amino-2,4,6-trinitrotoluene, m.p. 138°C.

3-chloro-2,4,6-trinitrothioanisole. To 0.48 g of KOH dissolved in 7.0 ml of absolute ethanol was added 1.00 g of 3-chlorothiophenol. The solution was stirred for one-half hour at 25°C. Methyl chloride was bubbled through the solution for fifteen minutes. A white precipitate, KCl, formed. The supernatant was poured into 140 ml of cold water. The aqueous solution was extracted with ether. The extracts were [illegible] with magnesium sulfate, filtered and evaporated to constant weight to yield 0.76 g of oily liquid. The NMR corresponded to 3-chloro-thioanisole. To a nitrating mixture consisting of 2.0 ml of 20% oleum and 2.2 ml of 90% HNO_3 was added [illegible] g of the 3-chloro-thioanisole. The mixture was stirred in an ice bath [illegible] to 25°C, stirring was continued overnight. The [illegible] refluxed for 4 hours and then poured into 125 ml of ice water. The [illegible] solid weighed 0.18 g, m.p. 120 -125°C. NMR analysis indicated the [illegible] of only one [illegible] on the aromatic ring. Attempts [illegible] the product with ammonia was not pursued.

Attempts to nitrate 3-chlorobenzaldehyde and phenylphosphonic acid were not successful even after refluxing in 90% oleum and [illegible] [illegible] with only unreacted starting material.

Preparation of 3-chloro-2,4,6-trinitrobenzoic acid was carried out *via* oxidation of 3-chloro-2,4,6-trinitrotoluene with $Na_2Cr_2O_7 \cdot 2H_2O$ in concentrated H_2SO_4. In a representative reaction 3.30 g of 3-chloro-2,4,6-trinitrotoluene was dissolved in 50.0 ml of concentrated H_2SO_4 and 4.23 g of $Na_2Cr_2O_7 \cdot 2H_2O$ was added portionwise over a period of 70 minutes. The temperature rose from 23.5°C to 33.0°C during the addition and a color change from yellow to brown was observed during that period. The reaction mixture was placed in a water bath maintained at 45-50°C and allowed to sit with stirring for 8 days by which time the color had changed to green.The reaction mixture was poured into 500 ml of ice water, and 0.49 g of solid precipitated. NMR analysis of the solid indicated it to be about 67% starting material and 33% 3-chloro-2,4,6-trinitrobenzoic acid. The aqueous layer was extracted with 350 ml of ether. After evaporation of the ether, 2.6 g of a solid was obtained. A small portion of the solid was dissolved in excess NaOH. The resulting solution was acidfied with H_2SO_4 and extracted with ether to yield a solid which melted at 176-178°C. NMR analysis of both solids corresponded to 3-chloro-2,4,6-trinitrobenzoic acid. This melting point corresponded quite well with the melting point of the product of nitration of 3-chlorobenzoic acid reported above.

Attempts were made to convert 3-aminotoluene to 3-amino-2,4,6-trinitrotoluene by converting the amino group to a carbamate with ethyl chlorocarbonate to protect it during the nitration of the aromatic ring and subsequently removing the protecting group by hydrolysis to give the desired 3-amino-2,4,6-trinitrotoluene. The scheme was successful up to the stage of the hydrolysis which yielded starting carbamate as indicated from the NMR spectrum.

REFERENCES

1. Iyer, S., "Explosive Desensitization Studies *via* Chemical Group Modification. Nitroso-derivatives of RDX and 3-Amino-TNT", Propellants, Explosives, Pyrotechnics, 7, 37-39 (1982)

2. Iyer, S., "Explosive Desensitization Studies *via* Chemical Group Modification II. 3,5-diamino- and 3,5-dichloro2,4,6-trinitrotoluene", J. Energetic Materials, 2, 151 (1984)

ACKNOWLEDGMENTS

The author would like to thank the Air Force Systems Command, the Air Force Office of Scientific Research, and the High Explosives Research and Development facility of the Armament Laboratory at Eglin AFB for their sponsorship and support.

UNIVERSAL ENERGY SYSTEMS, INC., MINI-GRANT PROGRAM

FINAL REPORT

Contract No. F49620-85-C0013/SB5851-0360
Sub Contract No. S-760-OMG-074

Project Title: An Investigation of Beam Profiling Methods with Improved Resolution and Dynamic Range.

Prepared By: Dr. Robert M. O'Connell
Associate Professor of Electrical Engineering
Electrical and Computer Engineering Department
University of Missouri, Columbia, MO 65211
(314) 882-8373

1. Introduction

This report discusses recent progress in the development of a real-time beam profiling system to be used in the Air Force Weapons Laboratory (AFWL) Laser Damage Laboratory [1]. The objectives of that development effort are real time operation with adequate spatial resolution and wide dynamic range. During the Mini-Grant period, measurements were made to evaluate the use of two solid state imaging devices (SSID) in the system. The results of those measurements are presented and discussed here.

SSID's are attractive for beam profiling because they do not contain a scanning electron beam. Thus many problems associated with conventional camera tubes, such as geometric distortion, image burn-in, and capacitive lag are eliminated or minimized [2]. The SSID's used in the present study included a frame-transfer charge-coupled-device (CCD) camera [3] and a charge-injection-device (CID) camera [4].

A brief description of the beam profiling system is presented along with the specific interfacing requirements of the SSID's used in the study. Performance of each SSID was determined by measurements of fixed pattern noise, dynamic range, and modulation transfer function. The measurements are described and their results presented and discussed. Finally, images of a CW diode laser beam, obtained with each SSID, are presented.

2. System Description

A block diagram of the beam profiling system, as it was configured for this study, is shown in figure 1. The spatial distribution of light

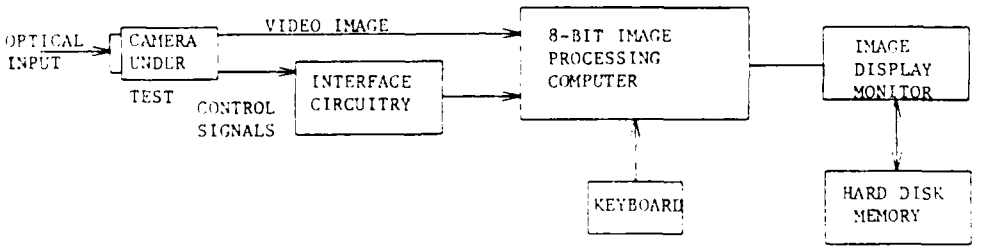

Figure 1. Block diagram of the SSID/8-bit image processor beam profiling system.

(the image) incident on the sensor under test varied depending on the specific measurements being made, but in all cases it consisted of the coherent output of a 633 nm helium-neon laser. The camera video output is digitized in the computer (an RCI Trapix 5500 image processing system) to a maximum of 256 grey levels (8 bits) and displayed on the 512 pixel X 512 pixel monitor. An external and versatile set of software programs, some of which will be described later, enable a wide variety of interactive and batch mode image analysis/processing

operations. Selected images may optionally be stored in the hard disk memory.

The 8-bit image processor can accept camera data in either RS 170/NTSC standard video, non-standard video, or even digital format. The CID camera used in this study (GE model TN 2509) outputs a non-standard video signal. For the image processor to properly receive such a signal, it must be accompanied by a pixel clock plus horizontal and vertical reset signals, all in TTL-compatible, differential form. The CID camera provides these control signals in single-ended form; thus, the interface circuitry for it (see fig. 1) consists of a simple differential line driver. The CCD camera (VSP Labs model SC 505) outputs standard video, which the image processor can format to 512 X 512 with a 1:1 aspect ratio without additional control signals. Thus no interface circuitry is needed with that camera.

The fact that it outputs standard video gives the CCD camera a significant advantage when used in the AFWL beam profiling system. This is because many of the system's image analysis/processing software programs can be used only with standard video images. For example, whereas both the gain and offset of the digitizer voltage window can be adjusted to improve the grey level range of digitized standard video images, only the offset can be adjusted with non-standard-video images.

3. Fixed Pattern Noise

Also called spatial uniformity of sensor responsivity, fixed pattern noise is the non-random pixel-to-pixel variation of sensor output, both for dark current (no illumination) and uniform illumination of the sensor. To obtain data, the grey level offset of each camera was first adjusted (using system software) for optimal suppression of background noise. Then, dark current frames were obtained and stored (in the hard disk memory) with the sensors covered, and frames for two levels of uniform illumination were obtained and stored using the optical arrangement illustrated in figure 2. Neutral density filters

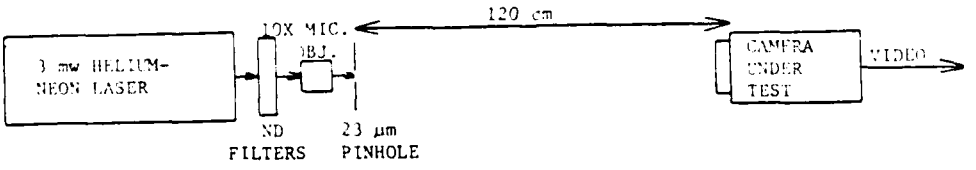

Figure 2. Optical arrangement used to measure fixed pattern noise of the SSID sensors.

were used to adjust the intensity of the laser light, which was focused with a 10X microscope objective and used to illuminate the 23 μm diameter pinhole of a spatial filter. The central lobe of the resulting Airy diffraction pattern expanded to a diameter of approximately 8 cm at the

plane of the camera sensors, whose positions were adjusted so as to be optimally centered in the beam. The dimensions of the CCD and CID camera sensors, 6.0 x 4.5 mm and 7.3 x 7.1 mm, respectively, were much smaller than that of the diffraction pattern, thereby assuring reasonably uniform illumination.

Typical data frames are shown in figure 3 for the CCD camera and in figures 4 and 5 for the CID camera. The unenlarged images in figures 4a and 5a show that the CID images do not use the full 512 X 512 monitor frame. This is because of the non-standard video nature of the CID camera output. The camera sensor has a 260 horizontal by 253 vertical square pixel format which is transmitted to the image processor one pixel at a time via the above-mentioned control signals. Thus, only the central 260 X 253 pixels of the 512 X 512 image processor (and its monitor) are used. System software also permits image enlargement up to 8X. For example, figure 4b and figures 5b and 5c are 2X enlargements of figures 4a and 5a, respectively. The fringes evident in figures 3b and 3c are due to coherent interference effects caused by a protective glass faceplate provided with the CCD camera, which could not be easily removed. The CID camera was provided with a protective faceplate also, but it was easily removed. Thus, fringing was not a problem with that camera as evidenced in figures 5b and 5c.

Analysis of the stored data frames was performed using a series of system software programs that calculate grey level statistics of any portion of an image. Thus, the superimposed histograms in figures 3, 4, and 5 indicate the distribution of pixel grey levels (from 0-255) throughout each frame. System software can also compute grey level means and standard deviations; thus, for example, in figures 3b and 5b the means/standard deviations are, respectively, 96.3/6.2 and 102.6/2.8. The profiles superimposed in the figures indicate the variation of grey levels along the line of pixels directly beneath the straight-line cursor. Except for the effects of the interference-induced fringes in figure 4, the profiles are quite flat, indicating the absence of geometric distortion, which is a problem with electron-beam scanned devices such as the silicon vidicon [1,5]. The integers 96 and 98 in figure 3c illustrate the magnitude of the interference effect caused by the faceplate on the CCD camera.

To quantify the spatial variation of sensor responsivity, the percent pattern noise, defined as the ratio of grey level standard deviation to grey level mean, was calculated for both the full sensor and the central 2.5 X 2.4 mm portion thereof for each camera using system software and the image frames shown in figures 3, 4, and 5. The results are given in table 1, from which three observations can be made. First, note that for each camera taken separately, pattern noise values for the central 2.5 x 2.4 mm portion of the sensor are very similar to those for the full sensor. This further illustrates the absence of any serious geometric distortion with these SSID cameras. Next, the dark current pattern noise of the CCD camera is significantly lower (better) than that of the CID camera. Finally, the photosensitivity pattern noise (responsivity to uniform illumination) of the CID camera appears to be better than that of the CCD camera, an apparent contradiction

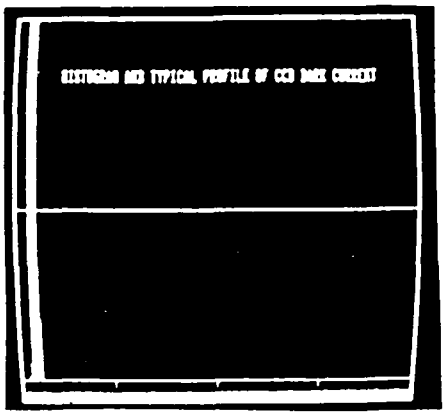

a

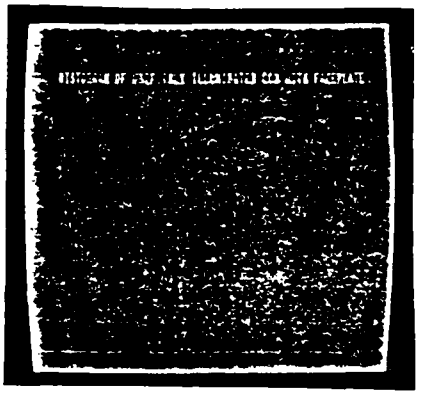

b

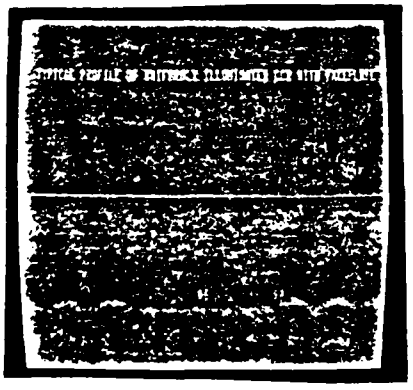

c

Figure 3. CCD camera sensor dark current [illegible]

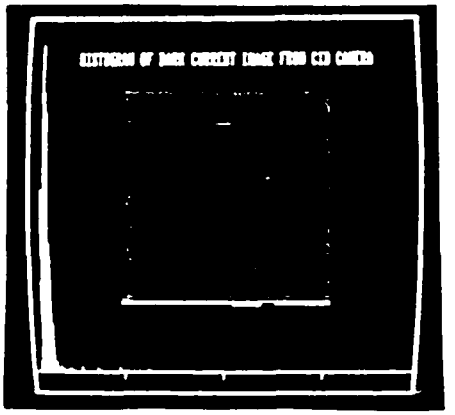

a

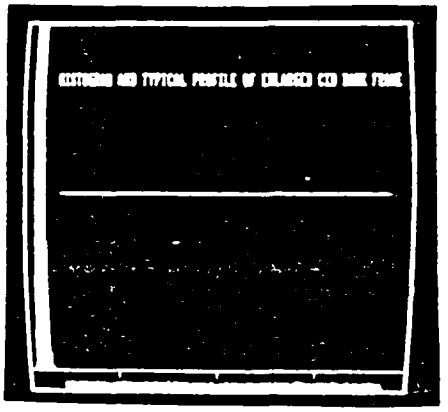

b

Figure 4. CCD camera sensor dark current. Frame b) is a 3 software enlargement of the image in frame a).

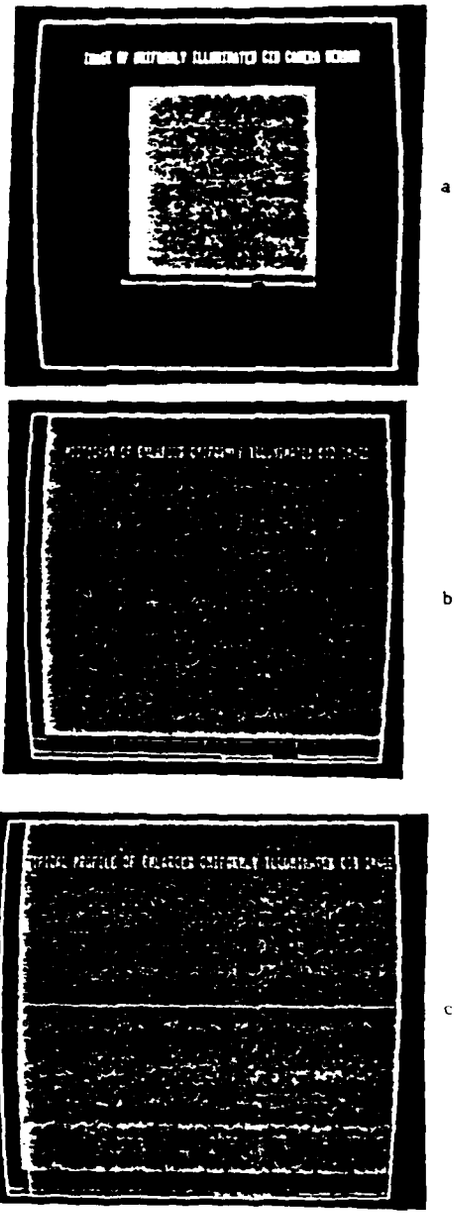

Figure 5. Response of CID camera sensor to uniform illumination. Frames b) and c) are 2X software enlargements of the image in frame a).

Table 1. Percent Pattern Noise (grey level standard deviation/grey level mean) of the two SSID sensors.

CAMERA	PORTION OF SENSOR	DARK CURRENT	UNIFORM ILLUMINATION
CCD	Full 6.0 x 4.5 mm	12.1	6.5
	Central 2.5 x 2.4 mm	11.7	6.1
CID	Full 7.5 x 7.1 mm	17.4	2.7
	Central 2.5 x 2.4 mm	17.1	2.3

since the CID camera has a higher dark current pattern noise figure. This can probably be explained in terms of the faceplate-induced interference problem observed with the CCD camera (see figure 3) but not with the CID camera. With its faceplate removed, the CCD camera's photosensitivity pattern noise may be comparable to that of the CID camera.

4. System Dynamic Range

In this study, dynamic range was defined in terms of the range of input optical intensities producing a linear variation of video voltage in one image frame. Since the beam profiling system involves two voltage windows, i.e., that of the SSID camera and that of the 8-bit digitizer, the dynamic range of the system is set by the component with the smaller voltage window. Furthermore, since the camera video signal can easily be attenuated before it enters the computer (see figure 1), the voltage window of the camera can always be made smaller than that of the digitizer, making the dynamic range of the system identical with that of the camera. Alternatively, for cameras or video signals with voltage windows much smaller than that of the digitizer, an amplifier can be used to ensure full use of the 256 level grey scale range of the digitizer.

To measure camera dynamic range, a suitable lens was added to the arrangement of figure 2 such that the pinhole was imaged onto the device sensor. The resulting video signal was monitored with an oscilloscope. Starting with the illumination level at which sensor saturation became barely evident on the oscilloscope (defined as the 100% transmittance level), the laser was attenuated with neutral density filters of various transmittances and the amplitude of the resulting video signal recorded at each transmittance level. The results were then normalized to their respective maximum values and least-squares-fitted with straight lines, as shown in figure 6. The noise level line shown in the figure

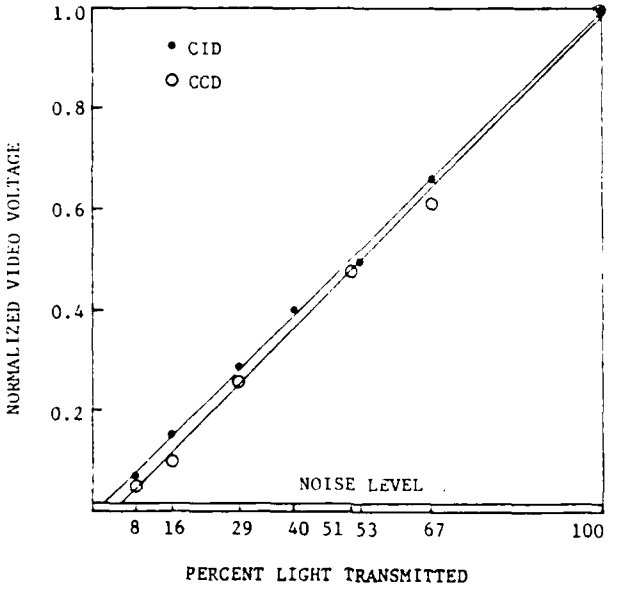

Figure 6. Results of the dynamic range measurements.

represents that of both cameras because their normalized noise values were virtually identical. Note that this result is based on the assumption that the data in figure 6 continues its linear dependence from the lowest measured transmittance level (8.4%) to the noise level. To verify this assumption, more data near the noise level would be needed.

Assuming that the data in figure 6 is linear from the saturation level (100% light transmittance) to the noise level, the dynamic range is the ratio of the maximum and minimum optical intensities above the noise level, i.e., 100% divided by the percent light transmitted at which the least-squares-fit and noise lines intersect. In figure 6, the intersections are at 5.9% and 2.1%, respectively, for the CCD and CID cameras. Therefore, their dynamic range are approximately 17 and 47, respectively.

5. Modulation Transfer Function (MTF)

The MTF of an optical sensor is the rolloff of sensor response with increasing spatial frequency. It characterizes the ability of the sensor to resolve fine detail within the object. In beam profiling, the detection of fluctuations such as hot spots would depend on this property of the sensor.

To measure the MTF's of the two subject SSID's, the optical system of figure 2 was modified as shown in figure 7. The Airy diffraction

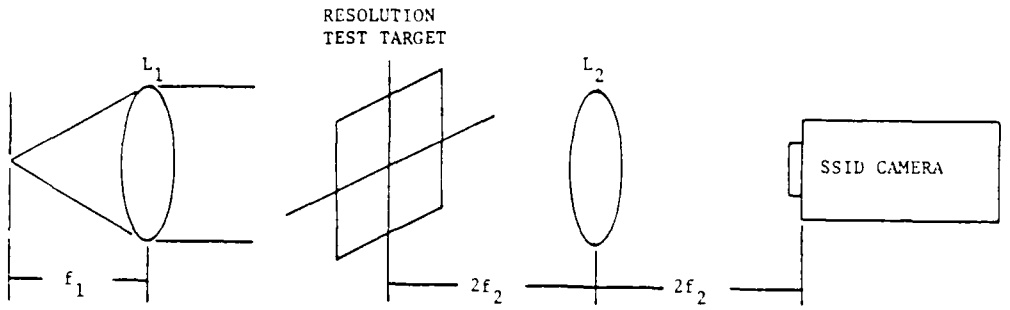

Figure 7. Optical arrangement used to measure sensor modulation transfer functions.

pattern produced by the pinhole was collimated with the first lens in the figure and used to uniformly illuminate a chromium USAF 1951 resolution test target, which uses pairs of orthogonal 3-bar patterns to synthesize a wide range of spatial frequencies. Portions of the illuminated test target were then imaged onto the camera sensor with the second lens, which was positioned for unity magnification. Typical images are shown in figures 8 and 9 for the CID and CCD cameras, respectively. Figures 8a and 9a show that the CID camera produces a much smaller image of the test target than the CCD camera. This is a result of the relative sizes of the active pixel elements in the two sensors. The pixels in the CID sensor are approximately 3 times as large on a side as those in the CCD sensor. Thus, the amount of light that illuminates one CID pixel and is transmitted to one image processor pixel will illuminate approximately 9 CCD pixels and occupy 9 image processor pixels. This point is further illustrated by figure 8b, a 3X software enlargement of figure 8a, which shows approximately the same portion of the test target as the 1X image in figure 9a. Figures 8c and 9b illustrate the relative resolution of the two cameras at spatial frequencies above 16 mm^{-1} (test target group 4 and above). The CCD camera is clearly better.

To obtain MTF curves, enlarged images of various portions (spatial frequencies) of the test target were then analyzed using system software. At each spatial frequency, the digitizer grey levels representing maximum and minimum image irradiance (g_{max} and g_{min}, respectively) were obtained from appropriate profiles and used to calculate the relative modulation M using the expression $M = (g_{max} - g_{min})/(g_{max} + g_{min})$. This was done for both vertical and horizontal spatial frequencies. For example, the images used to measure the vertical frequency responses of the CID and CCD cameras are shown in figures 10 and 11, respectively. The decreasing minimum/maximum excursion of the profiles shown in the two figures illustrate the rolloff of the vertical frequency responses of the two cameras. The results of analyzing these and similarly images are described and plotted in figures 12 and 13, respectively, for the CID and CCD cameras.

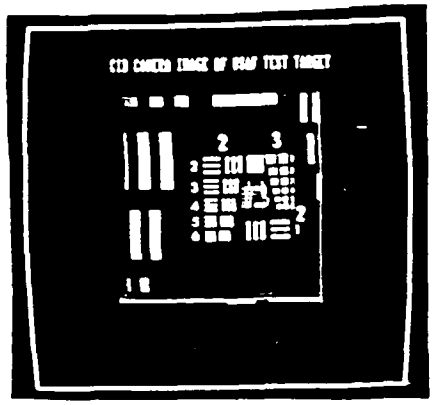

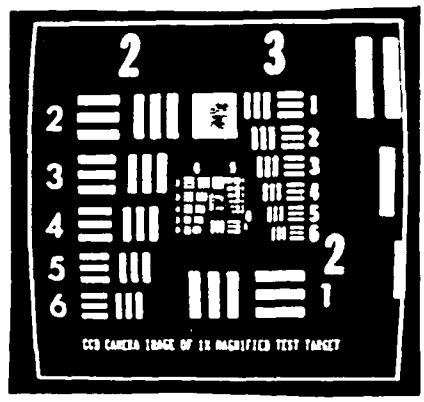

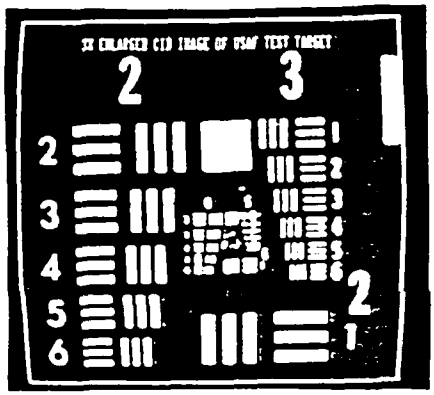

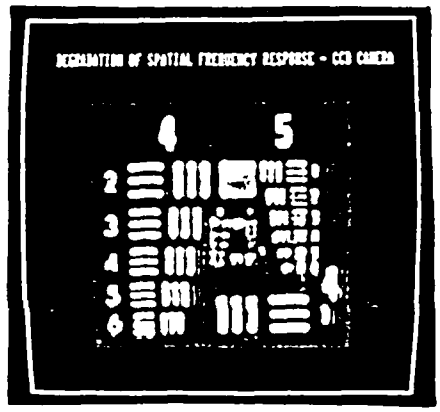

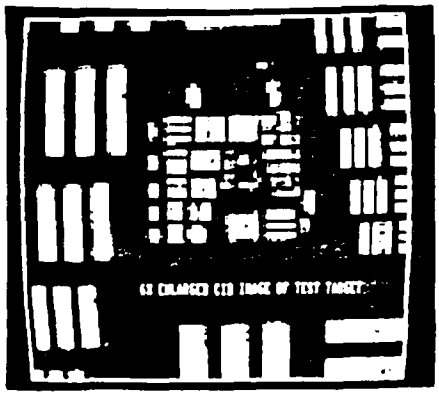

Figure 9. CCD camera image of USAF resolution test target. Frame b) is a 3X software enlargement of the image in frame a).

Figure 8. 1X, 3X, and 6X software enlargements of CCD camera image of USAF resolution test target.

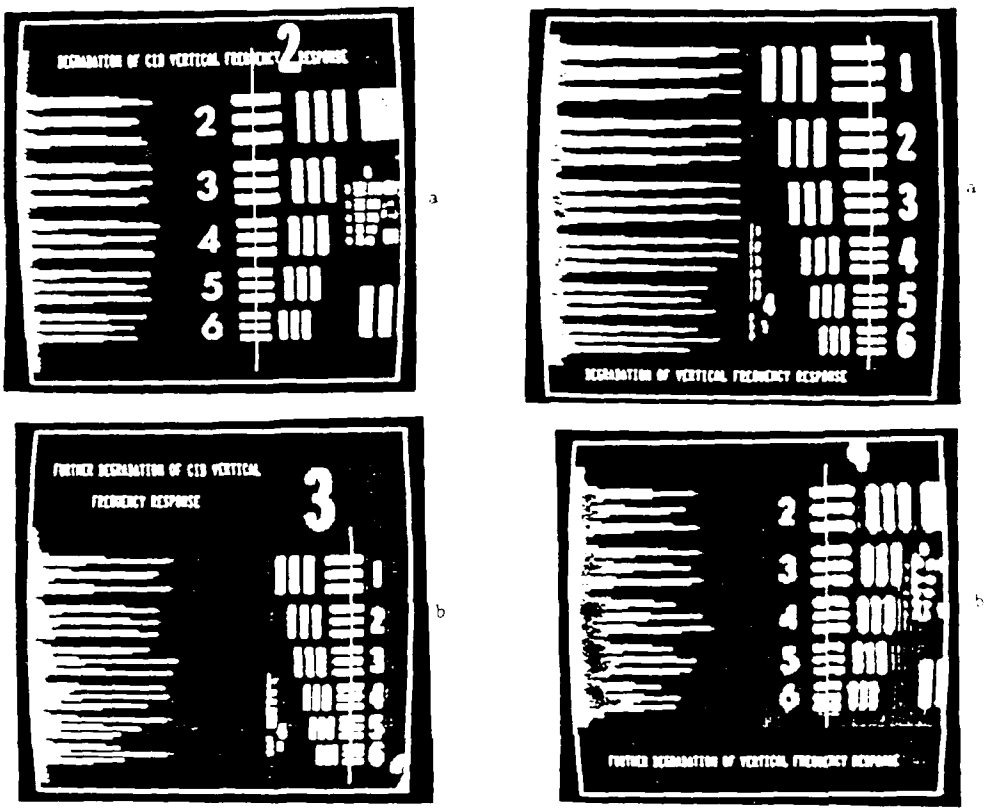
DEGRADATION OF CID VERTICAL FREQUENCY RESPONSE
2
3
4
5
6
a
DEGRADATION OF VERTICAL FREQUENCY RESPONSE
1
2
3
4
5
6
FURTHER DEGRADATION OF CID VERTICAL
FREQUENCY RESPONSE
3
1
2
3
4
5
6
b
FURTHER DEGRADATION OF VERTICAL FREQUENCY RESPONSE
2
3
4
5
6

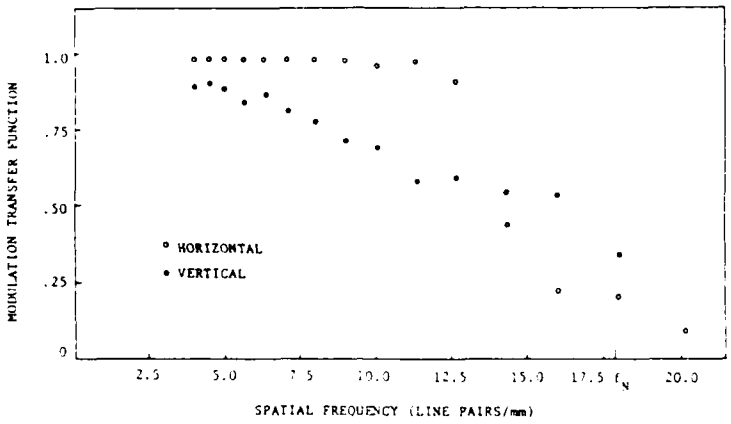

Figure 12. Measured spatial frequency response of the CID camera.

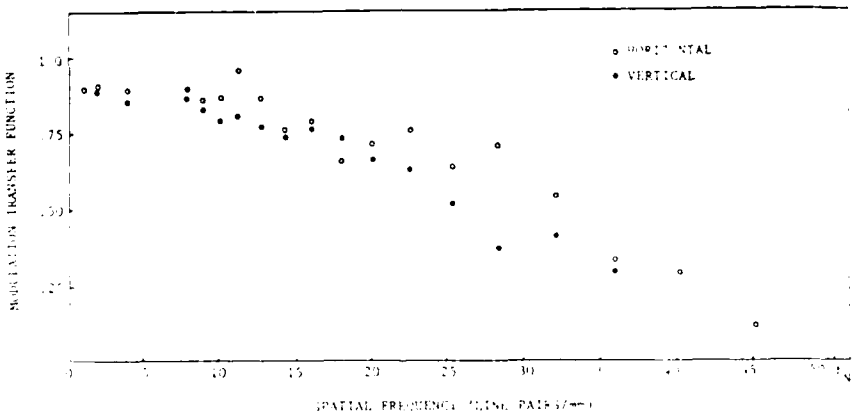

Figure 13. Measured spatial frequency response of the CCD camera.

5. CW Diode Laser Beam Images

Finally, to demonstrate the system's beam profiling capability, unity magnification images of the identical output of a 1.06 μm CW diode laser were recorded with each camera. The results, along with histograms and typical profiles, are

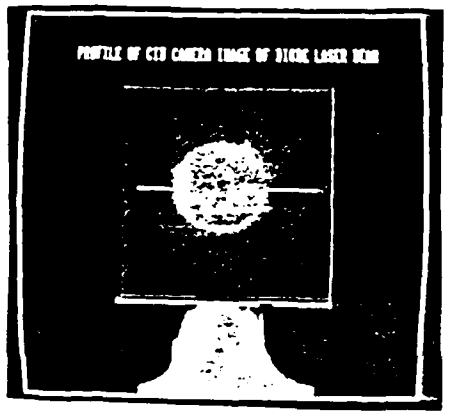

Figure 14. Histogram (a) and profile (b) of CID camera image of a 1.06 um CW diode laser beam.

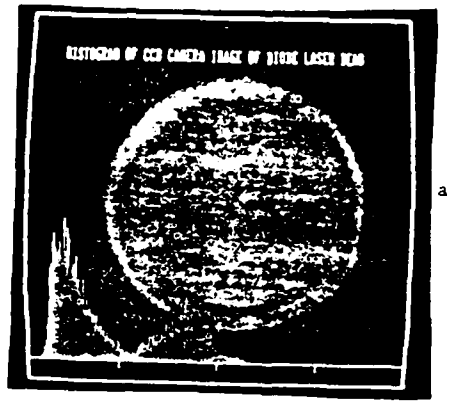

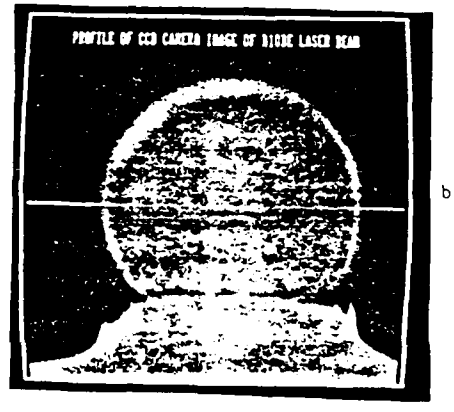

Figure 15. Histogram (a) and profile (b) of CCD camera image of a 1.06 um CW diode laser beam.

shown in figures 14 and 15, respectively, for the CID and CCD cameras. As explained above, the two cameras produce different size images on the monitor because their sensor pixels are of different sizes.

From the superimposed histograms in each figure it can be seen that the intensity of the laser diode was well below the sensor saturation level, and that the haziness surrounding the circular diode image is due to scattered diode light and not to some saturation-induced blooming effect. This latter point is supported by both the upper end of the histograms, which are well below saturation (the right edge of the image border) and the gradual decay of the distribution peak at the low end of the histogram. The component of this distribution representing dark current drops off much more rapidly, as shown in figures 3a and 4.

7. Summary and Conclusions

The AFWL beam profiling system, configured for the use of two SSID cameras and an 8-bit image processor, has been described and evaluated. The versatility of the system permits the use of a suitable video amplifier or attenuator to ensure full use of both the dynamic range of the sensor and the 256 grey levels of the digitizer.

The CID camera requires a differential line driver in order to interface with the image processor. Because the CCD camera outputs standard RS 170/NTSC video, it needs no interface circuitry. Furthermore, because of the CCD camera's standard video format, more of the system's image analysis/processing software programs can be used with it than with the CID camera.

The performance measurements showed that the CCD camera has better dark current pattern noise and wider spatial frequency bandwidth (resolution) than the CID camera. On the other hand, the CID camera appears to have a slightly wider dynamic range than the CCD device, but further measurements are needed to confirm this result. A fair comparison of the photosensitivity pattern noise of the two devices could not be made because the permanent protective faceplate on the CCD camera caused interference fringes that were not present with the CID camera.

8. REFERENCES

[1] O'Connell, R. M.; Vogel, R. A.; Stewart, A. F.; Smith, D. A. Beam Profiling Characteristics of a Sensitivity-Enhanced Silicon Vidicon System at 1.06 Microns. Proceedings of the 17th Annual Symposium on Optical Materials for High Power Lasers, Boulder, Co., 1985.

[2] Talmi, Y. TV-Type Multichannel Detectors. Anal. Chem. 47(7): 699A; 1975.

[3] Tompsett, M. F.; Amelio, G. F.; Bertram, W. J.; Buckley, R. R.; McNamara, W. J; Mikkelsen, J. C.; Sealer, D. A. Charge-Coupled Imaging Devices: Experimental Results. IEEE Trans. Electron Devices ED-18(11): 992; 1971.

[4] Burke, H. K.; Michon, G. J. Charge-Injection Imaging: Operating Techniques and Performance Characteristics. IEEE Trans. Electron Devices ED:23(2): 189; 1976.

[5] Smith W. L.; DeGroot, A. J.; Weber, M. J. Silicon Vidicon System for Measuring Laser Intensity Profiles. Appl. Opt. 17(24): 3938; 1978.

[6] Séquin, C. H. Interlacing in Charge-Coupled Imaging Devices. IEEE Trans. Electron Devices ED-70(6): 535; 1973.

[7] Barbe, D. F. Imaging Devices Using the Charge-Coupled Concept. Proc. IEEE 63(1): 38; 1975.

STUDIES OF AGE-RELATED CHANGES IN GLYCOSAMINOGLYCANS FROM CORNEA USING RAMAN SPECTROSCOPY: INSTRUMENT DEVELOPMENT

Final Technical Report for the Period:

January 1, 1986 through December 31, 1986

Submitted to:

Air Force Office of Scientific Research-Universal Energy Systems

by

Boake L. Plessy
Division of the Natural Sciences
Dillard University
New Orleans, Louisiana
Principal Investigator

I. INTRODUCTION

Recent studies have demonstrated the feasibility of using laser Raman spectroscopy as a structural probe in biophysical aspects of eye research (1,2). The success achieved in the determination of sulfhydryl concentration changes along the optical axis during aging suggests its use in determining structural changes in corneal glycosaminoglycans. No precedent for this type study exists in the biochemical literature. An extensive literature review has indicated only one publication involving Raman spectroscopy of glycosaminoglycans from commercial sources (3) and one report of spectra of intact feline corneal collagen (4). Our laboratory has been involved in a study of age related changes in corneal glycosaminoglycans using high performance liquid chromatography. The use of laser Raman spectroscopy as a structural probe for these changes is an extension of this work. We have developed a microcomputer interfaced laser Raman spectrometer for this purpose.

Biological applications of Raman spectroscopy have increased with the advent of reliable instrumentation, in particular, laser sources. Raman spectroscopy offers several advantages over traditional methods in determining structural characteristics of biomolecules. Spectra are amenable to molecular-level interpretation with accessible low frequency modes sensitive to conformational changes in the molecule. Sample size requirements are small and spectra can be determined in the liquid or solid phase or in solution. There is minimal interference by water in the spectral region from 2000-200 cm^{-1} and therefore aqueous solutions of biological systems may be studied. The primary disadvantage encountered in biological systems is the interference from fluorescent or

luminescent background which accompanies irradiation of biological systems with intense laser sources (5,6).

II. MATERIALS AND METHODS

Monochromator - The monochromator serving as the central element of the spectrometer system is the SPEX Model 1403 which was made available for this project through Los Alamos Laboratories. The 1403 is a modified Czerny-Turner 0.85-m double spectrometer. It has an aperture of f/7.8 and stray-light rejection of 10^{-14}. The spectrometer is equipped with two kinematically mounted 1800 gr/mm holographic gratings yielding a resolution of 0.15 cm^{-1} at 5791 Angstroms. The spectral region of 31000-11000 cm^{-1} is covered by a ministep drive unit allowing increments as fine as 0.0025 cm^{-1} with an accuracy of +/- 1 cm^{-1} over 10000 cm^{-1} and a repeatability of +/- 0.2 cm^{-1}. The system has four straight, bilaterally adjustable slits continuously adjustable from 3 microns to 3 mm. Scan control of the spectrometer is via a SPEX CD2A COMPUDRIVE microprocessor-based scan controller. In the present configuration, the CD2A is operated in burst mode allowing incremental scan as small as one motor step. External triggering and status lines permit communication with external peripheral devices. Shared control with a computer system is available through a two-way RS232 interface.

LASER - The laser source chosen for the spectrometer system is the Coherent INNOVA 70 series argon ion laser. The laser is a two watt multiline laser capable of supplying 800 milliwatts at 514.5 nm and 200 milliwatts at 488.0 nm. The laser uses a multiline/single line mirror holder. For multiline operation, the reflector is mounted normal to the laser bore. For single line operation, the reflector is moved and a prism

is placed intracavity. The prism allows individual wavelengths to be selected when the vertical tuning knob is turned. The wavelength selector assembly has a bimetallic design which compensates for changes in angular alignment caused by temperature, thereby stabilizing output power. The power supply provides dc power to the laser tube and head from a 208 VAC three-phase line through a silicon controlled rectifier circuit. The laser is operated in either a current or light regulated mode. In the current mode, passback current is fed back to the input to provide closed-loop regulation of laser tube current. In the light regulated mode, a signal from a photocell is used to control the current regular to maintain constant laser output power.

DETECTION - The spectrometer uses a photon-counting detector system. The system is developed around a Thorn EMI 9813A photomultiplier suitable for low-level and photon counting applications. The bialkali photocathode has low dark-current at ambient temperatures permitting use of standard non-refrigerated photomultiplier housing. The photomultiplier is powered by a Thorn EMI 3000R, 3 kv power supply. Signals are detected in a Thorn EMI APED II high speed amplifier-discriminator with pulse pair resolution of 15 ns. TTL output is available directly from this unit.

DATA ACQUISITION AND CONTROL - The ADALAB data acquisition system by Interactive Microware is used for both data acquisition and instrument control. This microcomputer based system consists of both hardware ,the ADALAB interface board, and extensive software, the QUICK I/O program, for interfacing applications of laboratory instrumentation. Each module consists of a 12 bit analog to digital (A/D) converter subsystem, a 12 bit

digital to analog (D/A) converter subsystem, 8 bit digital and parallel input/output subsystems, and a 32 bit countdown timer for a real-time clock/timer subsystem. The latter three subsystems are utilized in the spectrometer. The QUICK I/O program allows the use of short, easy to use commands from within Applesoft programs. The system used is specifically designed for use with an Apple II series microcomputer. However, the procedures are general and adaptable to other systems, particularly the IBM PC and compatibles, for which comparable hardware and software are available.

The other components of the spectrometer are standard optical hardware. Oriel mirrors with appropriate mountings are used to direct the laser beam into an unmodified Oriel sample housing. The beam is introduced through the bottom of the cell housing and collected normal to the cell surface. It is focused on the entrance slit through an Oriel X-Y-Z lens assembly. Adjustment of the image in the orthogonal X-Y plane as well as focus in the Z plane allows for ready optimizing the monochromator throughput. The sample compartment is coupled directly to the monochromator through a specially machined aluminum flange.

III. RESULTS AND DISCUSSION

The software for the control of the spectrometer is written entirely in Applesoft Basic and is a modification of the program originally written by DeBellis and Low (7). The choice of this language was dictated by the availability of the ADALAB data acquisition system and QUICK I/O software which was developed for the Apple II series computers. The normal BASIC PEEK and POKE commands which respectively return one byte from memory or place one byte into memory are replaced with Quick I/O statements

used to access counters, timers, I/O ports and other memory mapped devices. Thus, this wedge in the BASIC interpreter allows BASIC to accept special commands which address the devices on the ADALAB board. For example, the command:

```
D% = 1:&DO0
```

brings output bit 0 of the ADALAB digital output port high. All QUICK I/O commands are preceded by the ampersand. Variable D% is the byte value read from or sent to a port. DO0 stands for digital output bit zero. Similarly,

```
&AI0, &PI0, &TO2
```

mean analog input on card zero, parallel input on card zero and timer output two respectively. Card zero refers to channel zero or the first ADALAB board in the system. Timer two refers to one of four timers per board.

The spectrometer control program is completely menu driven with each item in the menu generating a specific self-explanatory command. The main menu is:

```
A. COUNT INTERVAL
B. SET SCAN PARAMETERS AND BEGIN
C. CATALOG A DISKETTE
D. SAVE DATA ON A DISKETTE
E. READ A DATA FILE
F. PLOT DATA WITH CURSOR
G. ADD CONSTANT TO DATA
H. RUN PMT TEST
I. PLOT DATA ON THE PRINTER
J. PLOT DATA ON A RECORDER
K. END
```

Selection of option "B" on the main menu brings up a submenu which addresses itself to control of the monochromator through the CD2A Compudrive. Consequently, the items on the menu generally correspond to

the CD2A keyboard. Options for data entry on either the Apple II keyboard alone or in conjunction with the CD2A keyboard are available. The latter feature was incorporated for development and testing purposes and the former for actual spectra determinations. This mode of operation is initiated when the Remote key of the CD2A is pressed and two-way RS232 communication ensues. All keys on the CD2A are then disabled and the parameters and instructions must be sent by the external device. The scan menu is:

A. START POSITION
B. END POSITION
C. SET POSITION
D. BURST INCREMENT
E. SHUTTER HIGH POSITION
F. SHUTTER LOW POSITION
G. LASER LINE
H. NUMBER OF SCANS
I. SET BURST SCAN
J. GO TO SET POSITION
K. TRIGGER SCAN
L. RETURN TO MAIN MENU

Under normal operating conditions, a spectral scan would be run by entering parameters for A, B, D, G, H, I, and K in sequence. Shutter control E and F protect the photomultiplier from intense Rayleigh scattering at the laser frequency.

Upon entering the choice "K" from the scan menu, the following sequence of events occurs. The spectrometer slews to the start position. One advantage of using the CD2A controller rather than direct drive of the stepper motor via the computer is that an anti-backlash feature is incorporated in the controller. In order to prevent data acquisition during scan operations and to synchronize mechanical movement of the spectrometer with the peripheral computer, three of the status lines of

the controller are employed. These lines are active low when the spectrometer is poised at the start position, when the spectrometer is sitting at the end of scan, and when the spectrometer is dwelling between increments in the burst scan mode respectively. Pauses in the program are introduced by using these status lines as digital inputs to the interface board and using the program line:

```
200 &DI2:IF D%>0 THEN 200
```

The program will then idle at this line until the status line becomes active low, at which point the spectrometer is poised for the next operation.

TTL pulses from the photomultiplier are coupled to the interface card through an open collector NAND gate. One of the gate inputs is simply the TTL pulses originating at the amplifier-discriminator circuit, the frequency of which are proportional to light intensity. The second input of the gate is connected to one of the digital output lines of the interface card. The time interval for which this output is high is controlled by interval timer of the interface card and is programmed in as "Count Interval". The output of the NAND gate flows to bit 6 of the digital output lines. In this case, bit 6 of the parallel output has been changed to an input with the command, POKE 49714,191, and serves as the Timer 3 input which has been configured for pulse counting with the command POKE 49723,32. The program lines performing these functions are

```
265 D%=32767:&TO3:REM SET TIMER 3 TO MAXIMUM COUNT
270 D%=0:&DO1:REM OPEN NAND GATE
275 D%=TIME*10:&TO1:REM START TIME INTERVAL
280 &TI1
285 IF D%>0 THEN 280:REM CONTINUE TIME INTERVAL TO END
290 D%=0:&DO1:REM CLOSE NAND GATE
295 &TI3:DCOUNT=D%:REM READ NUMBER OF PULSES
300 D=32767-DCOUNT
```

Two spectra are displayed during each scan, the data for the current scan and the updated average for previous scans of the same sample. The display also gives the current location in wavenumbers, the count for the particular data point as collected and the number of the scan being run. After data collection is ended, the complete spectrum is displayed on the screen. Facilities are included for changing either axis for scale expansion and a routine for finding peak intensities and positions called "plot with the cursor". Details of these features are found in DeBellis and Low (7). A complete program listing is found in Appendix I.

IV. CONCLUSION

The spectrometer system described represents a relatively inexpensive device assembled from readily available components. The principles employed in interfacing the spectrometer and computer are specific to the ADALAB board but should be adaptable to other systems with suitable modifications. Phase two of the project will involve the determination of Raman spectra on extracted proteolytic and [illegible] from [illegible]

References

1. Askren, C. C., Yu, N. T., and Kuck, J. F. R., "Variation of the Concentration of Sulfhydryl along the Visual Axis of Aging lenses by Laser Raman Optical Dissection Technique", Exp. Eye Res., Vol. 29, pp. 647-654, 1979.

2. Kuck, J. F. R., Yu, N. T., and Askren, C. C., "Total Sulfhydryl by Raman Spectroscopy in the Intact Lens of Several Species: Variations in the Nucleus and Along the Optical Axis During Aging", Exp. Eye Res., Vol. 34, pp. 23-27, 1982.

3. Bansil, R., Yannas, I. V., and Stanley, H. E., "Raman Spectroscopy: A Structural Probe for Glycosaminoglycans", Biochem. Biophys. Acta, Vol. 541, pp. 535-542, 1978.

4. Goheen, S. C., Lis, L. J., and Kauffmann, J. W., "Raman Spectra of Intact Feline Corneal Collagen", Biochem. Biophys. Acta, Vol. 536, pp. 197-204, 1978.

5. Gaber, B. P., "Biological Applications of Laser Raman Spectroscopy", American Laboratory, Vol. 8, pp. 15-24, 1977.

6. Koenig, J. L., Introduction to the Spectroscopy of Biological Polymers, edited by D. W. Jones, (Academic Press, Inc., New York), 1976.

7. DeBellis, A. D., and Low, M. J. D., "Data Acquisition and Control of a Raman Spectrometer Using an Apple Microcomputer", Analytical Instrumentation, Vol. 13, No. 3 & 4, pp. 257-267, 1984-85.

Appendix I

```
]LIST 0-275

0  HOME : VTAB 12: PRINT  TAB( 18)"RAMAN"
1  LOMEM: 24576: HIMEM: 36095:D% = 0: DIM D(2048)
2  POKE 36257,0: POKE 36273,0: POKE 36259,1
4  CALL 36096
5 D% = 255: % P00: POKE 49714,191: POKE 49723,32: REM  INITIALIZE I/O &
     TIMER
6 STX$ =  CHR$ (2):ETX$ =  CHR$ (3):CAN$ =  CHR$ (24):G$ =  CHR$ (7)
7 ACK$ =  CHR$ (6):EOT$ =  CHR$ (4):NAK$ =  CHR$ (21):NUL$ = ""
8 TIME = 2
9  GOTO 3000
10  TEXT : HOME : PRINT "***************** RAMAN ****************"
15  PRINT
20  HTAB 4: PRINT "A. COUNT INTERVAL"
25  HTAB 4: PRINT "B. SET SCAN PARAMETERS AND BEGIN"
30  HTAB 4: PRINT "C. CATALOG A DISKETTE"
35  HTAB 4: PRINT "D. SAVE DATA ON DISKETTE"
40  HTAB 4: PRINT "E. READ A DATA FILE"
45  HTAB 4: PRINT "F. PLOT DATA WITH CURSOR"
50  HTAB 4: PRINT "G. ADD A CONSTANT TO DATA"
55  HTAB 4: PRINT "H. RUN PMT TEST"
60  HTAB 4: PRINT "I. PLOT DATA ON THE PRINTER"
65  HTAB 4: PRINT "J. PLOT DATA ON A RECORDER"
70  HTAB 4: PRINT "K. END"
80  POKE  - 16368,0:CHOICE = 0
85  PRINT : PRINT "ENTER CHOICE  "
90  VTAB 15: HTAB 14
95  GET KB$:CHOICE =  ASC (KB$) - 64
100  INVERSE : FLASH
110  IF CHOICE < 1 OR CHOICE > 11 THEN 140
120  NORMAL : VTAB 15: HTAB 14: PRINT " ";KB$
130  GOTO 160
140  PRINT G$;"ILLEGAL ENTRY"
150  FOR I = 1 TO 1000: NEXT I: NORMAL
155  GOTO 10
160  ON CHOICE GOTO 21[illegible]
     0
170 NS =  VAL (NS$ :RI =  VAL  RI$):SP =  VAL (LL$) -  VAL (ST$):EP =  VAL
     (LL$) -  VAL (FN$)
175 PT =  INT ((EP - SP)    NI) + 1
180  FOR I = 1 TO PT:D( I ) = 0: NEXT I
190  FOR I = 1 TO 2[illegible]
200     I = I + 1
210     % [illegible]  HGLOBAL: HPLOT [illegible] TO [illegible]
215  HPLOT 140,0 TO 140,159
220  HOME : VTAB 2: PRINT "SCAN NO. "SS" OF "NS
270  PRINT "HIT 'ESC' TO ABORT"
280 D% = 0: % D01: REM  DISABLE NAND GATE
290  FOR II = 1 TO PT
295  D% =  D(I) + 1: REM  GET MAXIMUM COUNT
300  D% = 1: % D01: REM  OPEN NAND GATE
310  II = II + NI - 1: NEXT II
```

```
LIST 280-1090

280  % TI
285  IF D%   0 THEN 280: REM  TIME LOOP
290 D% = 0: % D01: REM  CLOSE NAND GATE
295  % TI:DCOUNT = D%
300 D = 32767 - DCOUNT
310 D(II) = D(II) + D
312  HPLOT II / PT * 140,159 - D * 159 / 65535
315  HPLOT II / PT * 139 + 140,159 - D(II) * 159 / 65535 / SS
340  VTAB 22: HTAB 25: PRINT "COUNTS=";D"     "
345  VTAB 23: HTAB 25: PRINT CL" CM-1    "
350  IF  PEEK ( - 16384) = 155 THEN 10
355  POKE  - 16368,0
356  IF CL = SP + BI * (PT - 1) THEN 375
360 D% = 0: % D00:D% = 1: % D00
365  % DI4: IF D% = 0 THEN 370
366  % DI3: IF D% = 0 THEN 365
370 CL = CL + BI
375  NEXT II
380 D% = 0: % D00:D% = 1: % D00
385  IF CL = EP THEN 390
386  % DI3: IF D% = 0 THEN 386
387 D% = 0: % D00:D% = 1: % D00
390  NEXT SS
400  HGR : HPLOT 0,0 TO 279,0 TO 279,159 TO 0,159 TO 0,0
405  FOR I = 1 TO PT
410  HPLOT I / PT * 279,159 - D(I) * 159 / 65535 / SS
415  NEXT I
420  PRINT G$;: GET A$: GOTO 10
430  GOTO 2120
900  PRINT : PRINT "DO YOU WISH TO ENTER PARAMETERS FROM THE"
905  PRINT "APPLE II KEYBOARD ONLY ? (Y/N)"
910  POKE  - 16368,0
915  GET ANS
920  IF ANS     "Y" AND ANS     "N" THEN 910
925  IF ANS = "Y" THEN 980
930  GOTO 995
980  HOME : HTAB 5: PRINT  CHR$ (7);"TURN ON THE CDIA TWO-WAY REMOTE"
985  PRINT : HTAB 4: PRINT "THEN HIT RETURN KEY ON THE APPLE"
990  INPUT "";ZZ$
995 CHOICE = 0: OL = 0
1000  PRINT  HOME : VTAB 1: PRINT "MENU": PRINT
1010  HTAB 10: PRINT "A. START POSITION"
1020  HTAB 10: PRINT "B. END POSITION"
1030  HTAB 10: PRINT "C. SET POSITION"
1040  HTAB 10: PRINT "D. BURST INCREMENT"
1050  HTAB 10: PRINT "E. SHUTTER HIGH POSITION"
1060  HTAB 10: PRINT "F. SHUTTER LOW POSITION"
1070  HTAB 10: PRINT "G. LASER LINE"
1080  HTAB 10: PRINT "H. NUMBER OF SCANS"
1090  HTAB 10: PRINT "I. [illegible]"
```

```
LIST 1100-1475

1100  HTAB 10: PRINT "J. GO TO SET POSITION"
1110  HTAB 10: PRINT "K. TRIGGER SCAN"
1120  HTAB 10: PRINT "L. RETURN TO MAIN MENU"
1130  PRINT
1140  PRINT "ENTER CHOICE "
1141  IF AN$ = "Y" THEN 1145
1142  VTAB 23: INVERSE : PRINT "ENTER PARAMETERS ON THE APPLE AND CD2A"
1145  VTAB 16: HTAB 14
1150  POKE  - 16368,0
1160  GET KB$
1170 CHOICE =  ASC (KB$) - 64
1175  INVERSE : FLASH
1180  IF CHOICE < 1 OR CHOICE > 12 THEN 1220
1190  NORMAL : VTAB 16: HTAB 14: PRINT " ";KB$
1200  GOTO 1245
1220  PRINT G$;"ILLEGAL ENTRY"
1230  FOR I = 1 TO 5000: NEXT I: NORMAL
1240  GOTO 1000
1245  PRINT : IF CHOICE = 12 THEN  GOTO 10
1250  ON CHOICE GOSUB 1400,1410,1420,1430,1440,1450,1460,1470,1480,1490,
      1500
1255  IF AN$ = "N" THEN 1284
1260 ANSWER = 0:OK = 0
1270  PR# 4: PRINT FCOMM$: PR# 0
1280  IN# 4: INPUT ANSWER$: IN# 0
1290  IF  ASC ( MID$ (ANSWER$,1,1)) =  ASC (ACK$) THEN 1330
1310  IF  ASC ( MID$ (ANSWER$,1,1)) =  ASC (NAK$) THEN 1370
1320 ANSWER = 1: GOTO 1380
1330  IF  ASC ( MID$ (ANSWER$,2,2)) =  ASC (CAN$) THEN 1360
1340  IF  ASC ( MID$ (ANSWER$,2,2)) <>  "07" THEN 1320
1350  PRINT "CD2A ERROR CODE IS:  "; RIGHT$ (ANSWER$,2):ANSWER = 1
1355  FOR I = 1 TO 5000: NEXT I: GOTO 1380
1360 ANSWER = 0: GOTO 1380
1370  PRINT "                    ": GOTO 1270
1380  IF ANSWER = 0 THEN 1284
1382  GOTO 1385
1384  PRINT "VALUE ACCEPTED": FOR I = 1 TO 2000: NEXT I: GOTO 1270
1385  PRINT "CD2A ACCEPTED": FOR I = 1 TO 3000: NEXT I
1390  IF CHOICE = 11 THEN  GOTO 10
1395  GOTO 1000
1400 COMM$ = STX$ + "SI": INPUT "ENTER VALUE ";SI$: PRINT  CHR$ (11)" "
1405  IF  LEN (SI$)  > 8 THEN 1400:FCOMM$ = COMM$ + SI$ + ETX$
1406  ANSWER = 0: RETURN
1410 COMM$ = STX$ + "SH": INPUT "ENTER VALUE ";SH$: PRINT  CHR$ (11)" "
1415  IF  LEN (SH$)  > 8 THEN 1410:FCOMM$ = COMM$ + SH$ + ETX$
1416 ANSWER = 0: RETURN
1420 COMM$ = STX$ + "SE": INPUT "ENTER VALUE ";SE$: PRINT  CHR$ (11)" "
1425  IF  LEN (SE$)  > 8 THEN 1420:FCOMM$ = COMM$ + SE$ + ETX$
1426 ANSWER = 0: RETURN
1430 COMM$ = STX$ + "BI": INPUT "ENTER VALUE ";BI$: PRINT  CHR$ (11)" "
1435  IF  LEN (BI$)  > 8 THEN 1430:FCOMM$ = COMM$ + BI$ + ETX$
```

```
LIST 1430-2190

1435 ANSWER = 0: RETURN
1440 COMM$ = STX$ + "SH": INPUT "ENTER VALUE ";SH$: PRINT CHR$ (11)"
1445  IF LEN (SH$) = 8 THEN 1440:FCOMM$ = COMM$ + SH$ + ETX$
1446 ANSWER = 0: RETURN
1450 COMM$ = STX$ + "SL": INPUT "ENTER VALUE ";SL$: PRINT CHR$ (11)" "
1455  IF LEN (SL$) = 8 THEN 1450:FCOMM$ = COMM$ + SL$ + ETX$
1456 ANSWER = 0: RETURN
1460 COMM$ = STX$ + "LL": INPUT "ENTER VALUE ";LL$: PRINT CHR$ (11)" "
1465  IF LEN (LL$) = 8 THEN 1460:FCOMM$ = COMM$ + LL$ + ETX$
1466 ANSWER = 0: RETURN
1470 COMM$ = STX$ + "NS": INPUT "ENTER VALUE ";NS$: PRINT CHR$ (11)" "
1475  IF LEN (NS$) = 3 THEN 1470:FCOMM$ = COMM$ + NS$ + ETX$
1476 ANSWER = 0: RETURN
1480 FCOMM$ = STX$ + "TYB" + ETX$:ANSWER = 0: RETURN
1490 FCOMM$ = CAN$ + "P" + ETX$:ANSWER = 0: RETURN
1500 FCOMM$ = CAN$ + "T" + ETX$:ANSWER = 0: RETURN
2100  PRINT : PRINT "NEW COUNT INTERVAL (";TIME;") ";: INPUT TIME
2102  GOTO 10
2110 D$ =  CHR$ (4): PRINT  CHR$ (4)"CATALOG,D2": GET A$: GOTO 10
2120 D$ =  CHR$ (4): INPUT "NEW FILE NAME? ";FL$
2121  PRINT D$"OPEN ";FL$: PRINT D$"WRITE ";FL$
2122  PRINT PT
2123  FOR I = 1 TO PT: PRINT D(I): NEXT I
2124  PRINT ST: PRINT NS
2125  PRINT D$"CLOSE ";FL$: GOTO 10
2130 D$ =  CHR$ (4): INPUT "OLD FILE NAME? ";FL$
2132  PRINT D$"OPEN "FL$: PRINT D$"READ "FL$
2134  INPUT PT
2136  FOR I = 1 TO PT: INPUT D(I): NEXT I
2138  INPUT SP: INPUT NS
2140  PRINT D$"CLOSE "FL$: GOTO 10
2150  REM  PLOTTING WITH CURSOR
2152 FR = 1:T1 = PT
2153 [illegible] = 1: PRINT "SCALE FACTOR ("[illegible]") = ";
2155  INPUT [illegible]
2160  HGR : HCOLOR= [illegible]: HPLOT 0,0 TO 279,0 TO 2 9,159 TO 3,159 TO 0,0
2165  HOME : VTAB 21
2170  FOR I = FR TO T1
2180  [illegible] = 159 - D(I) * 157 / 65535 / NS * F
2190  GOSUB 2500
2200  NEXT I
2210 I = FR - 1
2220  PRINT "PRESS [illegible]: FR= FOR NEW SCALE": PRINT "PRESS 'R' TO [illegible]
      [illegible]
      [illegible]
2240  GET A$
2245  IF A$ = "S" THEN  INPUT "NEW SCALE ";F: GOTO 2160
2247  IF A$ = "R" THEN  INPUT "PLOT FROM ";BE: INPUT "TO ";EN:FR = INT
      ((BE - SP) / BI) + 1:I = INT ((I - SP) / BI) + 1: GOTO 2160
2250  IF A$ = " " OR A$ = "," THEN 2310
2275  IF A$ = CHR$ (3) THEN 2320
2280  IF A$ = " " OR A$ = "," THEN 2450
```

```
LIST 2285-2860

2285  IF A$ = CHR$ (8) THEN 2440
2290  IF A$ = CHR$ ([illegible]) OR A$ = CHR$ (13) THEN 10
2295  IF A$ = "P" THEN PR# 1: PRINT I TAB( 8)SP + I * BI TAB( 20)D(I): PR#
     0: GOTO 2250
2300  PRINT "PRESS RETURN TO RETURN TO MAIN MENU": GOTO 2250
2310 I = I + 7
2320 I = I + 1
2340  IF I > T1 THEN I = FR
2360 Y = 120 - D(I) * 159 / 65535 / NS * K
2370  HCOLOR= 3: GOSUB 2500
2375  PRINT I TAB( 8)SP + I * BI TAB( 20)D(I)
2380  GOTO 2250
2430 II = I - 8: GOTO 2460
2440 II = I - 1
2460  IF II < FR THEN II = FR
2470 Y = 120 - D(I) * 159 / 65535 / NS * K
2480  HCOLOR= 0: GOSUB 2500
2487 I = II
2490  GOTO 2250
2500  IF Y < 1 THEN Y = 1
2510  IF Y > 158 THEN Y = 158
2520  HPLOT (I - FR) * 279 / (T1 - FR),Y
2540  RETURN
2600  REM  ADD A CONSTANT
2610  INPUT "CONSTANT TO BE ADDED? ";K
2615  PRINT : PRINT "COMPUTING..."
2620  FOR I = 1 TO [illegible]
2630 D(I) = D(I) + K
2640  NEXT I
2650  GOTO 10
2700  REM  RUN PMT TEST
2710  HOME
2720 D% = 0: & DO1: REM  DISABLE NAND GATE
2730  HTAB 16: PRINT "PMT TEST"
2740  HTAB 15:"********"
2750 D% = 32767: & [illegible]:REM SET MAXIMUM COUNT
2755 D% = 1: & DO1: REM  ENABLE NAND GATE
2760  FOR I = 1 TO 1000: NEXT I: DEL AYLOOP
2765 D% = 0: & DO1: REM  DISABLE NAND GATE
2770  & RII:DCOUNT = D%: REM  READ DATA
2775  IF PEEK ( - 16384) > 127 THEN  POKE  - 16368,0: GOTO 10
2780  VTAB [illegible]: PRINT "PRESS ANY KEY TO END"
[illegible]
[illegible]
2800  REM  EPSON
2810  PRINT "PREPARE PRINTER THEN PRESS RETURN"
2820  PRINT : INPUT "";A$
2830  PR# 1: PRINT CHR$ (9)"6"
2840  PRINT "STARTING POINT = "SP" ENDING POINT = "SP + BI * PT: PRINT
     "SCANS = "NS" COUNTING INTERVAL = "TIME
2850  PR# 0
2860  GOTO 10
```

```
LIST 2900-3040

2900  REM  PLOTTING
2910  PRINT "PREPARE RECORDER THEN PRESSRETURN"
2920  PRINT : INPUT "";A$
2930  FOR I = 1 TO PT
2940 D% = D(I) * 4095 * 1 / 65535 / NS + 2048
2950  FOR II = 1 TO 75: NEXT
2960  % A00
2970  NEXT I
2980  GOTO 10
2990  END
3000 NS = 1:SP = 0:PT = 1000:CL = 0
3010  POKE 768,104: POKE 769,168: POKE 770,104: POKE 771,156: POKE 772,
      0: POKE 773,154: POKE 774,32: POKE 775,15
      6
3
4
4
```

1985 USAF-UES MINI-GRANT PROGRAM

FINAL TECHNICAL REPORT

ADAPTIVE GRID GENERATION TECHNIQUES FOR TRANSONIC PROJECTILE BASE FLOW PROBLEMS

Prepared By
Chris W. Reed and Chen-Chi Hsu
Department of Engineering Sciences
University of Florida
Gainesville, Florida 32611

December 20, 1986

ABSTRACT

An adaptive grid generation technique is developed for viscous flow problems. The equations governing the grid adaptation are based on a variational statement resulting in a set of elliptic partial differential equations in which adaptation can occur independently in each coordinate direction. The method allows for control of adaptation and orthogonality while smoothness is implicit in the solution to the elliptic equations. The method has been designed specifically to provide the highly stretched grids required for adaptation to the boundary layer regions. The grid generation equations are coupled with a thin layer Navier-Stokes code to solve a transonic axisymmetric projectile flow problem. The grid is adapted to the pressure gradient in the streamwise direction and to the velocity gradient in the direction normal to the projectile surface. The results for a projectile at Mach 0.96 show that the use of a solution adapted grid can enhance the accuracy of the solution.

INTRODUCTION

The Air Force Armament Laboratory at Eglin Air Force Base is currently developing computational methods to determine the motion of stores released at transonic speeds. Critical to an accurate prediction of the store motion is an accurate calculation of the aerodynamic forces acting on the store. For a standard projectile configuration, the aerodynamic force can be divided into three components: the surface pressure drag.the viscous drag and the baseflow drag of which the baseflow

drag can be as much as 50% of the total drag. It is, therefore, important to develop an accurate and efficient solution technique for the computation of viscous transonic projectile aerodynamics with baseflow.

The published results on the application of the thin layer Navier-Stokes codes indicate that the thin layer Navier-Stokes approximation has the potential to give accurate solutions for a projectile baseflow problem at transonic speeds provided a good grid network is used. In fact, it has become evident that the grid network can have a large influence on the solution, a condition which has motivated research efforts to develop adequate grid generation techniques. Analysis of the truncation error terms arising from the discrete representation of the governing equations in the flow domain has shown that the curvilinear coordinates comprising the grid network must vary smoothly, maintain orthogonality and be well adapted to the physics of the problem in order to reduce the truncation error magnitude and subsequently increase the solution accuracy. A variety of proven methods are capable of providing grid networks with the first two grid characteristics, smoothness and orthogonality, however enhancement of the third characteristic, adaptivity, is difficult, especially if the location of the important physical gradients is not known a priori. A promising approach to this problem is that of solution adaptive grid generation techniques.

One such adaptive grid generation technique was developed during the 1985 GSSSP program at Eglin Air Force Base as reported

in reference [1]. It is the purpose of this research to continue development, testing and application of the method to solve projectile baseflow problems. During the testing phase, however, two problems were found that rendered the method insufficient for application to the viscous flow problems. First, the equations for adaptive gridding were not necessarily elliptic, which created problems in the solution procedure. Second, the extremely refined mesh required for resolving the boundary layer region had poor effects on the convergence rate of the solution to the grid generation equations. To resolve these difficulties a new set of grid generation equations were derived from a conceptually similar approach and an efficient method for increasing the convergent rate of the solution to the equations in the boundary layer regions is included. The grid generation procedure is coupled with a thin layer Navier-Stokes code to solve a transonic projectile problem with sting. Results are reported for Mach 0.96.

In preparation for tackling the transonic baseflow problem with the adaptive grid generation technique, the thin layer Navier-Stokes code has been used on a series of fixed grid networks to solve a projectile baseflow problem to gain insight on the maximum time step limitation, the required damping and to provide some results for comparison with the adaptive grid solutions. The results for a variety of grid networks are reported. Also, a detailed investigation on the application and implication of the thin-layer Navier-Stokes approximation for accurate prediction of the transonic projectile aerodynamics had

been conducted. Results obtained were presented at the 4th U.S. Army Conference on Applied Mathematics and Computing. Attached at the end of this report is a copy of the paper to appear in the proceeding of the conference.

DIFFICULTIES WITH THE ORIGINAL EQUATIONS

In an approach similar to Brackbill and Saltzman [2], the two dimensional adaptive grid generation equations, as reported in reference [1], were derived from three functionals Is, Iv, Io representing the three grid characteristics smoothness, adaptivity and orthogonality, respectively. The functionals are listed below:

$$I_s = \int [(\nabla\xi)^2 + (\nabla\eta)^2]dxdy$$

$$I_v = \int [(\bar{r}_\xi \cdot \bar{r}_\xi)P + (\bar{r}_\eta \cdot \bar{r}_\eta)Q]dxdy \qquad (1)$$

$$I_o = \int (\nabla\xi \cdot \nabla\eta)^2 dxdy$$

where ξ and η are the body fitted curvilinear coordinates, $\bar{r}$ is the position vector of the grid points and P and Q are the control functions. The resulting grid generation partial differential equations and solution technique are reported in reference [1]. The difficulty inherent in these equations is in the antagonistic roles of the two functionals Is and Iv. The extremely fine meshes in the boundary layer regions are due to a response of the grid network to the control functions of Iv,

however the portion of the equations resulting from Iv are not necessarily elliptic. The ellipticity in the equations, which is necessary to assure the existence of a unique solution, enters through the functional Is, but, unfortunately, the effect of Is is to smooth the grid spacing preventing the extreme mesh refinement necessary in the boundary layer regions. This inherent antagonism renders the equations unsuitable for generating adaptive grids for viscous flow problems.

Another problem associated with the requirement of extremely stretched grids is the convergence rate of the solution to the grid generation equations. In the areas of extreme mesh refinement the grid spacing in one coordinate direction can be up to 1000 times larger than that of the other direction creating grid cells with very large aspect ratios, up to 1000. The grid points in these regions, therefore may require 1000 times as many iterations to converge as that of grid points outside these regions. The increase in the number of iterations results in a substantial inefficiency in the procedure, again making it unsuitable as an adaptive grid generation method for viscous flow problems. Once these limitations inherent in the grid generation equations became apparent, further development and testing were terminated. The effort was then focused on finding a set of equations to govern the grid generation in which the elliptic nature of the equations did not inhibit the stringent demands of adaptation in the boundary layer regions. Such a set of equations were developed based on a similar variational approach during the 1986 GSSSP program at Eglin Air Force Base the

equations were coded in fortran and coupled with a thin layer Navier-Stokes code. Subsequently a method was developed to increase the convergence rate in the extremely fine mesh regions. A detailed description of the method as well as some initial results for a specific transonic projectile problem are reported in reference [3]. What follows here is a brief description of the method and some computed results for Mach 0.96.

THE ADAPTIVE GRID GENERATION METHOD

Following a similar variational approach, the following three functionals were used to derive the two dimensional grid generation equations.

$$I_P = \int \frac{(\nabla\xi \cdot \nabla\xi)}{P} \, dxdy$$

$$I_Q = \int \frac{(\nabla\eta \cdot \nabla\eta)}{Q} \, dxdy \qquad (2)$$

$$I_O = \int (\nabla\xi \cdot \nabla\eta)^2 dxdy$$

where P and Q are the control functions in the ξ and η [illegible] respectively. These functionals are combined to [illegible] functional I:

$$I = I_P + I_Q + \lambda I_O$$

Here λ is a parameter representing [illegible] relative to adaptation desired [illegible]

AD-A186 492 UNITED STATES AIR FORCE RESEARCH INITIATION PROGRAM 10/11
1985 TECHNICAL REPORT VOLUME 2(U) UNIVERSAL ENERGY
SYSTEMS INC DAYTON OH R C DARRAH APR 87
UNCLASSIFIED AFOSR-TR-87-1718 F49620-85-C-0013 F/G 15/3 NL

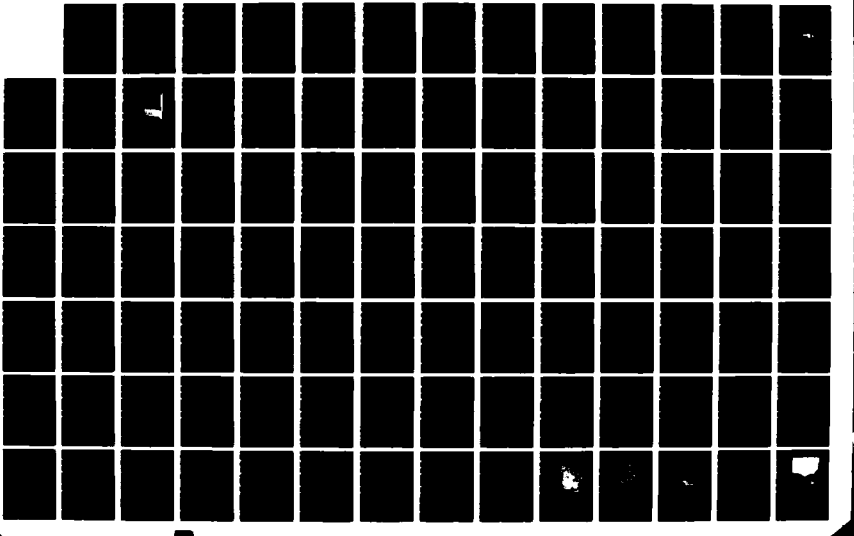

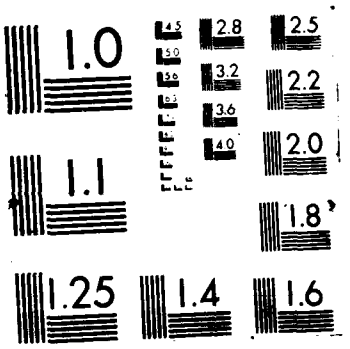
1.0
1.1
1.25
1.4
1.6
1.8
2.0
2.2
2.5
2.8
3.2
3.6
4.0
4.5
5.0
5.6
6.3

functional and employing local scaling of each functional the governing equations resulting from the Euler-Lagrange equations in the physical domain were found to be:

$$\xi_{xx} + \xi_{yy} + \frac{\lambda}{J^{-1}} (\eta_x^2\xi_{xx} + 2\eta_x\eta_y\xi_{xy} + \eta_y^2\xi_{yy})$$
$$+ \frac{\lambda}{J^{-1}} ((2\xi_x\eta_x+\xi_y\eta_y)\eta_{xx} + (\xi_x\eta_y+\xi_y\eta_x)\eta_{xy} + (\xi_x\eta_x+2\xi_y\eta_y)\eta_{yy})$$
$$= \frac{\nabla\xi\cdot\nabla P}{P}$$

(4)

$$\eta_{xx} + \eta_{yy} + \frac{\lambda}{J^{-1}} (\xi_x^2\eta_{xx} + 2\xi_x\xi_y\eta_{xy} + \xi_y^2\eta_{yy}) = \frac{\nabla\eta\cdot\nabla Q}{Q}$$
$$+ \frac{\lambda}{J^{-1}} ((2\xi_x\eta_x+\xi_y\eta_y)\xi_{xx} + (\xi_x\eta_y+\xi_y\eta_x)\xi_{xy} + (\xi_x\eta_x+2\xi_y\eta_y)\xi_{yy})$$
$$= \frac{\nabla\eta\cdot\nabla Q}{Q}$$

where J^{-1} is the inverse of the Jacobian defined as

$$J^{-1} = \xi_x\eta_y - \xi_y\eta_x \tag{5}$$

These equations will be elliptic if the terms due to the orthogonality functional are not to large. As long as λ is sufficiently small, the roots of the characteristic equation of equations (4) will always be complex, and thus, the equations will be elliptic. The smoothness of the grid then is controlled by the smoothness of the source terms containing P and Q, a condition that can be controlled through the definitions of P and

Q. Equations (4) are transformed onto the computational domain making x and y the dependent variables. The resulting equations are rather complex and are available in reference [3]. They are solved numerically using a Newton Raphson iterative scheme.

As reported earlier, the solution procedure for elliptic equations is an inefficient process when applied to grids for viscous flow problems due specifically to the large aspect ratio of the grid cells in the boundary layer regions. Movement of grid points along the projectile surface in which the grid spacing is larger is restricted by the smaller spacing of the grid points in the direction normal to the surface, increasing the number of iterations required for convergence. An efficient solution to this problem is to remove, temporarily, many of the grid points along the η coordinate (the direction normal to the surface) leaving only a few points to represent the position of the coordinate. Thus a new grid is constructed with a reduced number of grid points in which the aspect ratio of grid cells in the boundary layer region is similar in magnitude to that of the outer regions. Once the reduced grid is adapted, the points that were removed are inserted back along the η coordinates with their spacing governed by the equation

$$\eta_{ss} - \frac{\eta_s Q_s}{Q} = 0 \qquad (6)$$

which is the one dimensional analogy to the two dimensional equations. Here, s measures the arc length along the η coordinate.

When adapting along the η coordinate the control function Q which dictates the spacing along the coordinate must be modified to reflect the use of a few points to represent the spacing of the many points removed. The proper modification is derived from the equation governing one dimensional adaptivity. An analytical solution to the inverse of equation (6) yields the expression

$$S_\eta = \frac{1}{Q} \tag{7}$$

where s is the grid spacing along the coordinate. The value of Q at each of the points remaining in the boundary layer region can be modified according to equation (7) to include the spacing requirements of the surrounding points removed by summing as follows:

$$\frac{1}{Q_j^*} = \sum_i \frac{1}{Q_i} \tag{8}$$

where Q* is the modified value of the control function at a remaining point (j) and (i) spans the grid points removed from the vicinity of point (j).

The extra computations required in this procedure to remove and insert points as well as modifying the control function appear to increase the computational effort required to obtain a solution, however, the time saved in solving the elliptic equations for the reduced grid rather than the entire grid more than compensates, resulting in an efficient means of providing

the extremely refined meshes required within the framework of an elliptic grid generation procedure.

RESULTS

The adaptive grid procedure has been coupled with the thin layer Navier-Stokes code to solve an axisymmetric transonic projectile problem with sting. The projectile used is a 6 caliber secant-ogive-cylinder-boattail configuration which is shown in figure 1. The flow conditions are a Reynolds number of 710000 and Mach 0.96, a case for which experimental data are available.

In the transonic regime, the solution to the projectile flow problem is expected to contain pressure expansions at the ogive-cylinder and cylinder-boattail junctures and normal shocks are expected at locations along the projectile surface. An important physical feature due to viscous effects is the boundary layer region at the projectile surface. These phenomena require refined grid resolution for an accurate calculation of the solution and their presence motivates the choice of the control functions.

In the streamwise coordinate direction (ξ - coordinate) the control function P is defined in terms of the pressure gradient:

$$P_i = 1 + \gamma \, f_i$$

$$W_i = \left| \frac{\partial P}{\partial S} \right|_i \qquad (9)$$

$$f_i = \frac{W_i - W_{min}}{W_{max} - W_{min}}$$

where f is the normalized pressure gradient and γ is a parameter reflecting the maximum deviation from smooth spacing allowable. Here s is the physical arc length along the ξ coordinate and p is the calculated pressure.

Similarly, in the direction normal to the surface (η coordinate) a fine grid in the boundary layer region can be obtained by using the velocity gradient in the control function Q:

$$Q = 1 + \gamma f_i$$

$$W_i = \left|\frac{\partial v}{\partial s}\right|_i \qquad (10)$$

$$f_i = \frac{W_i - W_{min}}{W_{max} - W_{min}}$$

Here v is the fluid speed and s is the physical arc length in the η coordinate direction. The initial attempts at adaptive grid generation using equations (10) as the control function produced rapidly varying grid spacing along the η coordinate in the boundary layer region and consequently yielded poor results. The equation therefore has been modified to resemble the approach of Nakahashi and Deiwert [4] to include an addition parameter to control grid spacing:

$$Q_i = 1 + \gamma f_i^{\alpha} \qquad (11)$$

The value of α can be determined automatically to give a prescribed minimum spacing by solving the equation

$$(S_\eta)_{min} = \frac{L}{\Sigma\left(\frac{1}{1+\gamma f_i^\alpha}\right)} \frac{1}{(1+\gamma)} \qquad (12)$$

which is a discrete representation of the minimum spacing found when solving equation (6). Here L is the total arc length of the η coordinate and $(S_\eta)_{min}$ is the prescribed minimum spacing. Application of this method produced uniform spacing at the projectile surface and slowly varying spacing through the boundary layer.

With the control functions defined in this manner a solution for the transonic flow problem was calculated. The grid network was adapted at intervals of 10 time steps for a total of 1600 time steps at which time the solution to the thin layer Navier-Stokes equations converged. The choice of γ for the pressure gradient was 10 and for the velocity gradient it was 200000. The large value for the velocity gradient was used to obtain the extremely refined mesh required in the boundary layer region. The minimum spacing for determining α was 0.00002. The initial grid network shown in figure 2 contains 90 points in the streamwise direction and 35 points in the direction normal to the projectile. As can be seen most of the grid points along the coordinates are clustered near the surface in the boundary layer region. In the first calculation of the solution, the results agreed well with the experimental data for portions of the projectile, but deviated in on other parts. Figure 3 shows the

computed pressure coefficient along the projectile surface compared with the experimental data. As is evident, the calculations agree well along the ogive and upwind part of the cylinder but varies from the expected solution near the boattail. Figure 4 an expanded view of the grid near the projectile surface shows clearly the grid adapting to the pressure gradient. There is clustering near the junctures and in the shocks, however as shown in figure 3 the shocks' positions are not predicted accurately. The grid spacing in the coordinate direction (only those points in the reduced grid are shown) appear to vary somewhat along the surface and it is this characteristic of the grid that is thought to cause the error in the solution.

In order to isolate this problem, the case was run again with one alteration. After each grid adaptation, the points in the normal direction were redistributed according to the logarithmic distribution function used in generating the initial grid network. The computed results for this case, shown in figure 5, show excellent agreement with experimental results. The adapted grid network also shows the shocks to be in the proper locations.

These results conclude the research on the adaptive grid procedure conducted to date. The results indicate a great potential for the adaptive grid technique to provide good grid networks. Specifically, more work needs to be focused on improving the adapted grid in the boundary layer region where the extremely refined mesh is required. Experimentation with various control functions and the number of grid point used should yield

improved results. At this point, due to the problems with the adaptation in the boundary layer region, the adaptive grid procedure has not been applied to the baseflow problem. However, a series of fixed grid solutions have been obtained to begin the investigation of the transonic baseflow problem.

THE BASEFLOW PROBLEM

When solving the baseflow problem, the introduction of the sharp corner into the flow domain is expected to require special consideration. To investigate this situation a series of solutions based on fixed grids were obtained using the thin layer Navier-Stokes code. The grid networks, which ranged from 108 by 40 to 140 by 80 were generated with a hyperbolic grid generation method described in reference [5]. One grid network, 120 points in the streamwise direction and 60 points in the normal direction is shown in figure 7. The grid is an O-type network in which the streamwise coordinate wraps around the base corner and terminates at the downstream line of symmetry. The points in the normal coordinate direction are clustered near the projectile surface using a logarithmic distribution with the spacing at the surface equal to 0.00002.

For each grid network used, the maximum time step that could be used before the solution became unstable was 0.025 compared to the value of 0.10 used for the projectile with sting. Also, the explicit and implicit damping coefficients were increased from 1 and 2 times the time step for the projectile with sting problem to 4 and 8 times the time step for the baseflow problem.

The computed results for the cases run did not vary much

with the number of points in the streamwise direction. However, as the points were increased in the normal direction the solution became oscillatory. Figures 8 through 10 show the computed pressure coefficient along the projectile surface for three grid networks, 140 by 40, 140 by 60 and 140 by 80. In figures 8 and 9 the solution appears to be well behaved. There is some discrepancy between the computed and experimental solutions over the cylinder and baottail. The pressure distribution over the base is intuitively correct although some dispersive error is evident near the corner in the solution obtained in the 140 by 60 grid network. In the 140 by 80 grid, the solution, shown in Figure 10, appears to be destroyed by dispersive effects up to the cylinder-ogive juncture. At this time, insight into this phenomenon is inconclusive. Additional attempts to solve the projectile baseflow problem on this grid with various time steps and damping coefficients should yield insight into the oscillatory behavior. In general, these results will aid in solving the baseflow problem with adaptive grid techniques as information concerning the time step limitations and damping have been obtained.

It is acknowledged that the first part of calculation was performed with a Cray system at NASA Ames while the latter part of numerical experiments was conducted with the Cray X-MP/48 at Pittsburgh Supercomputing Center through an NSF computer time grant ECS-8515761.

References

1. Reed, C.W., "Adaptive Grid Generation for Viscous Flow Problems", Final Report, 1885 USAF-UES Summer Faculty Research Program/ Graduate Student Summer Support Program, July 1985.
2. Brackbill, J.U., "Coordinate System Control: Adaptive Meshes", in Numerical Grid Generation, edited by J.F. Thompson, North Holland, 1982.
3. Reed, C.W., "Adaptive Grid Generation for Viscous Flow Problems", Final Report, 1986 USAF-UES Summer Faculty Research Program/ Graduate Student Summer Support Program, July 1986.
4. Nakahashi, K. and Deiwert, G.S., "A Self-Adaptive Grid Method with Application to Airfoil Flow", AIAA paper 85-1525.
5. J.L. Steger, "A Curvilinear Grid Generation Program for Projectile Configurations", FSI Report 79-02, May 1979, Sunnyvale, California.

SOCBT

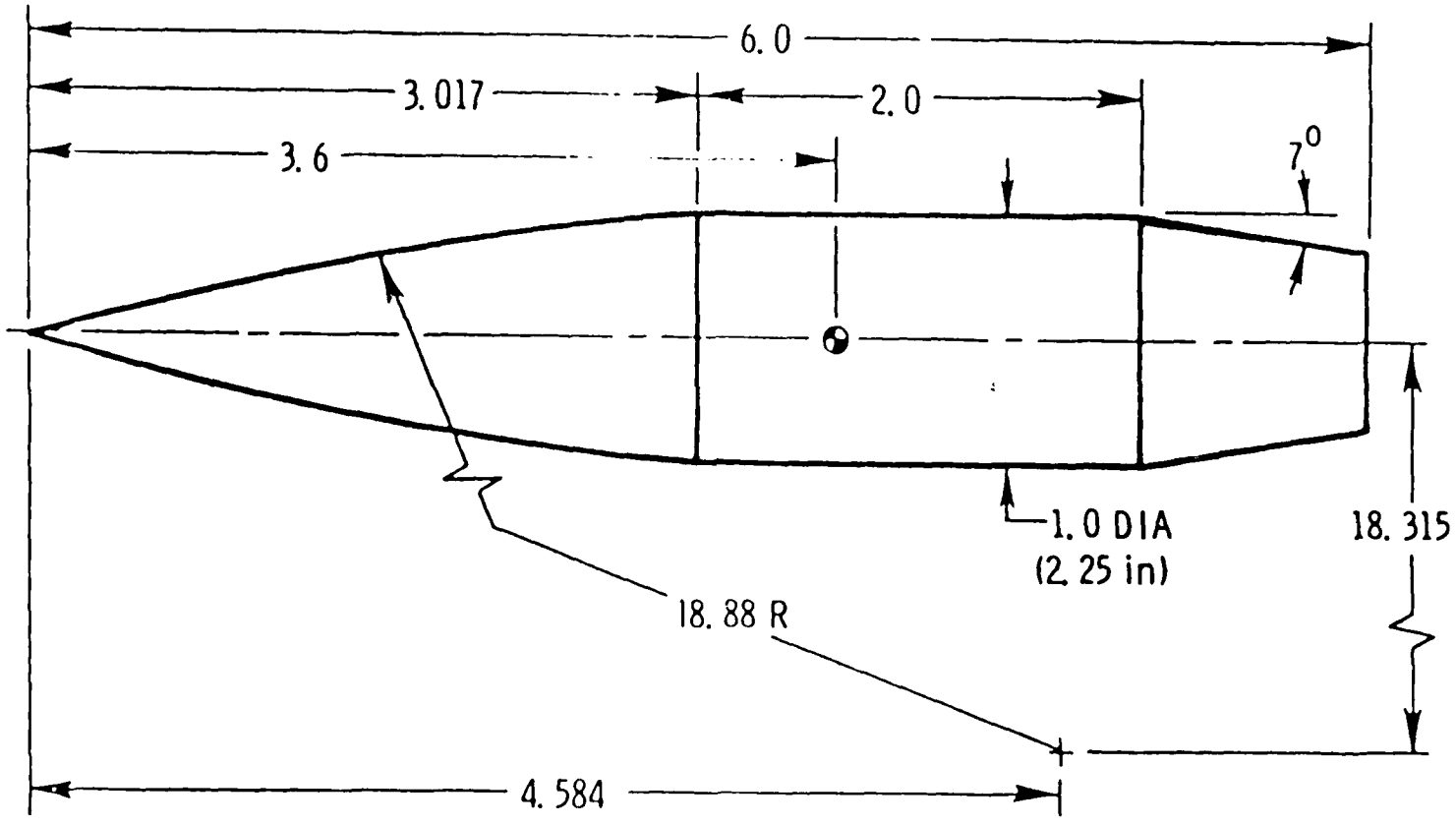

ALL DIMENSIONS IN CALIBERS

Figure 1. Projectile Shape

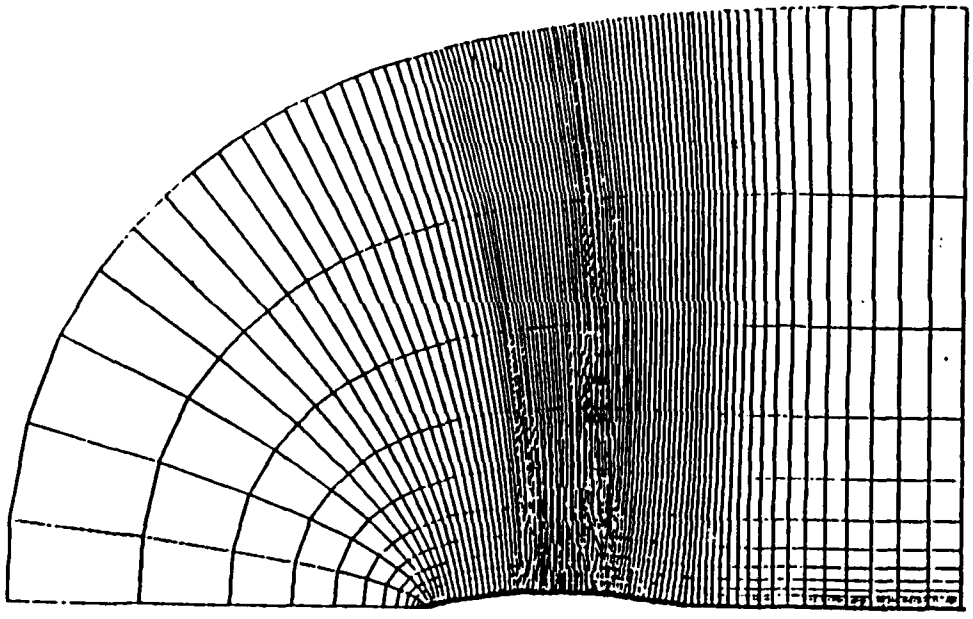

Figure 2. Initial grid configuration

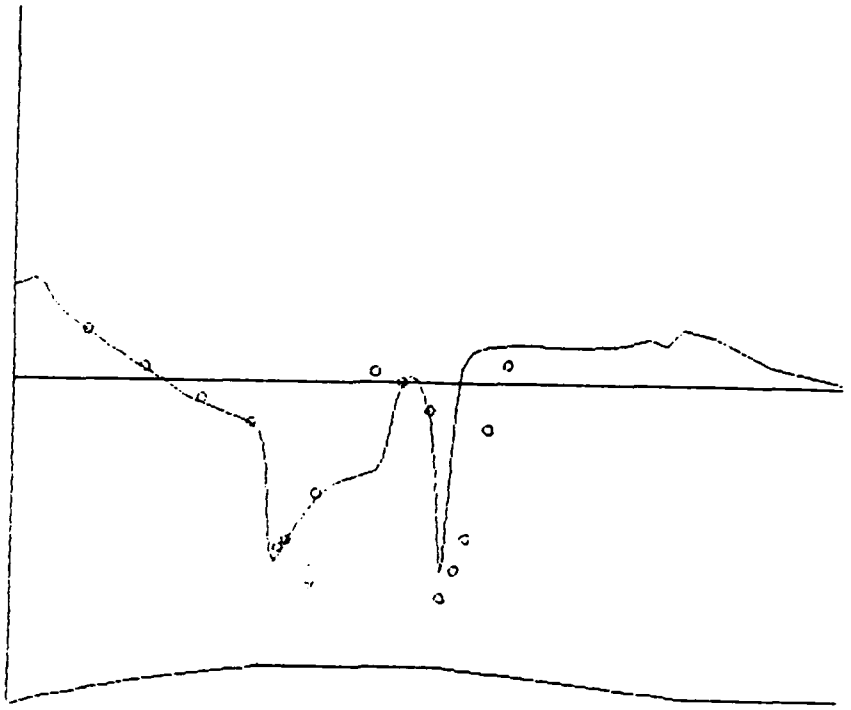

Figure 3. The surface pressure coefficient

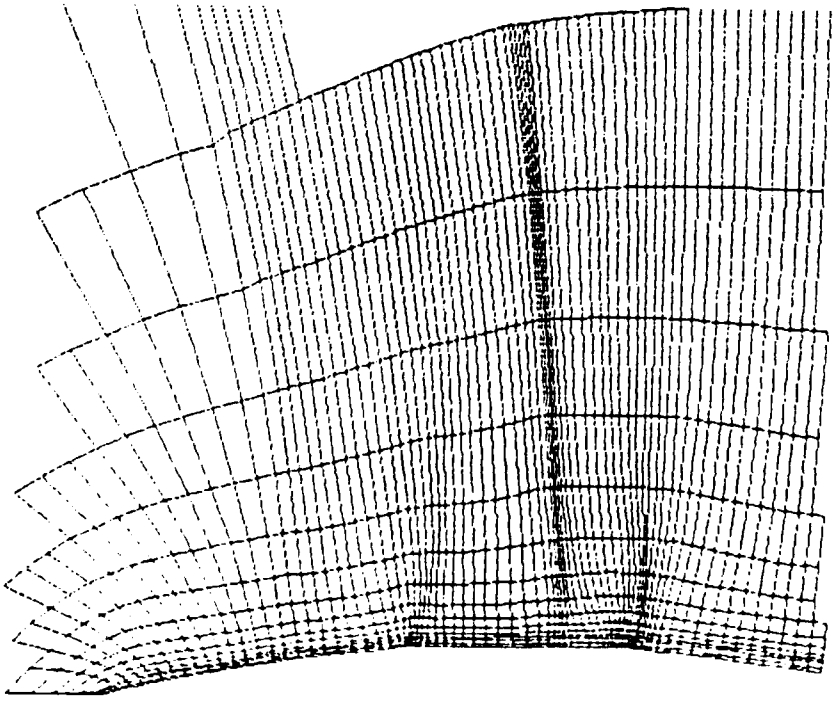

Figure 4. The adapted grid network

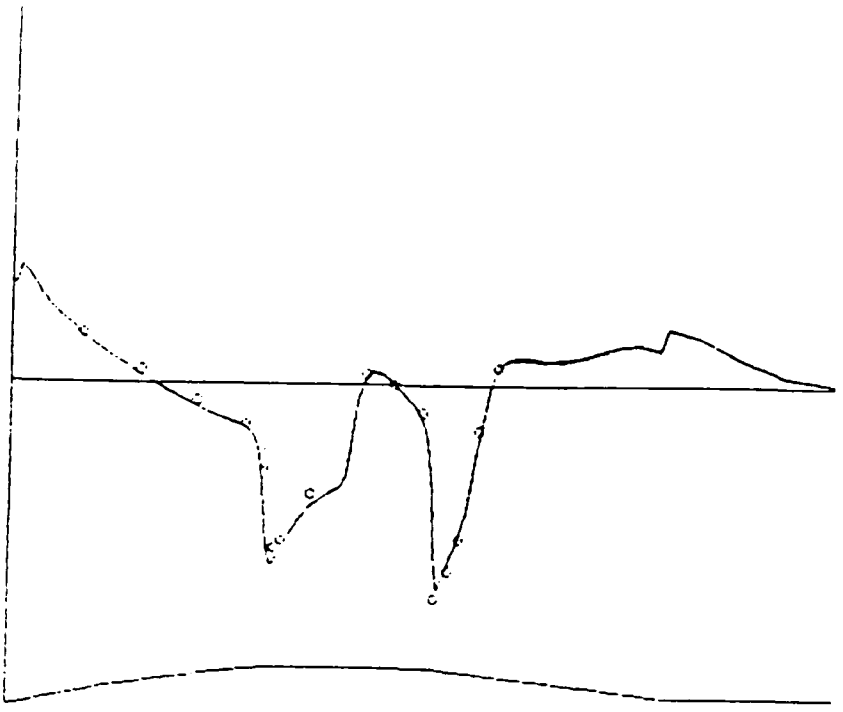

Figure 5. The surface pressure coefficient

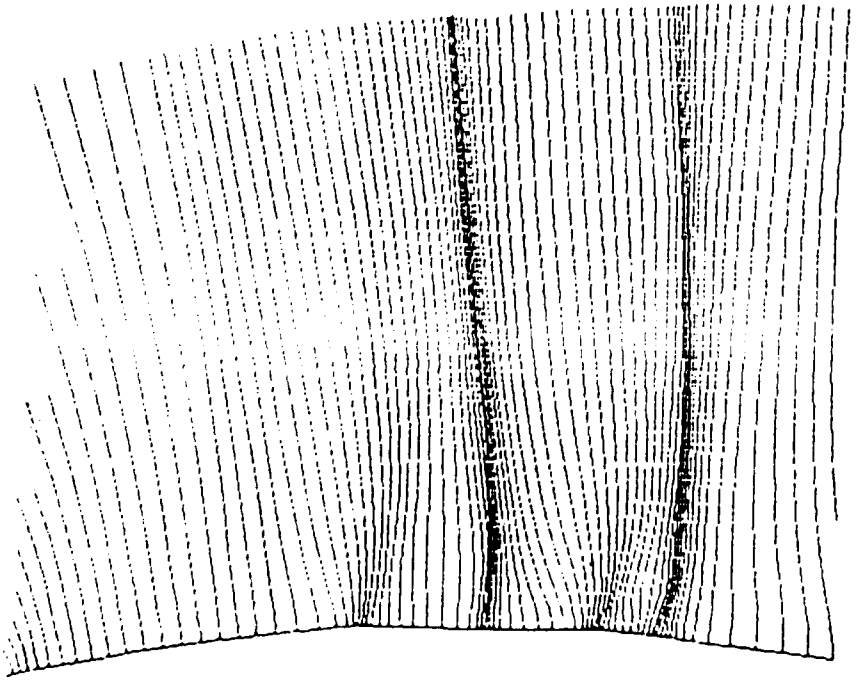

Figure 6. The adapted grid network

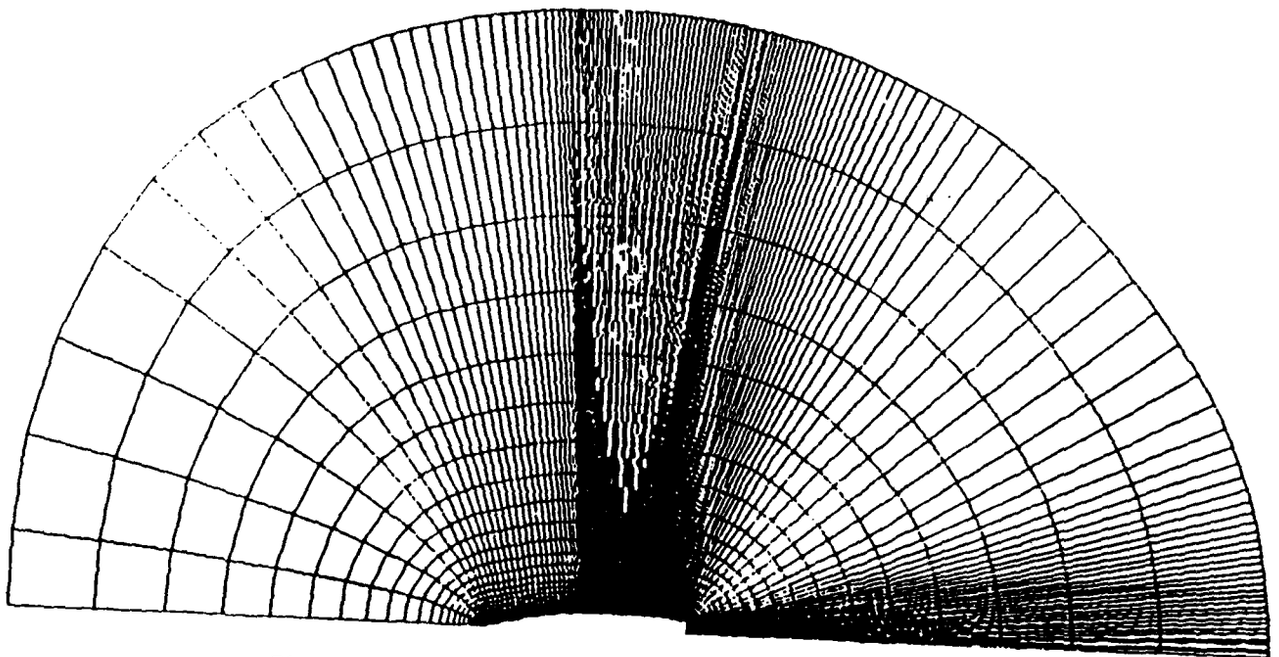

Figure 7. The grid network for the baseflow problem

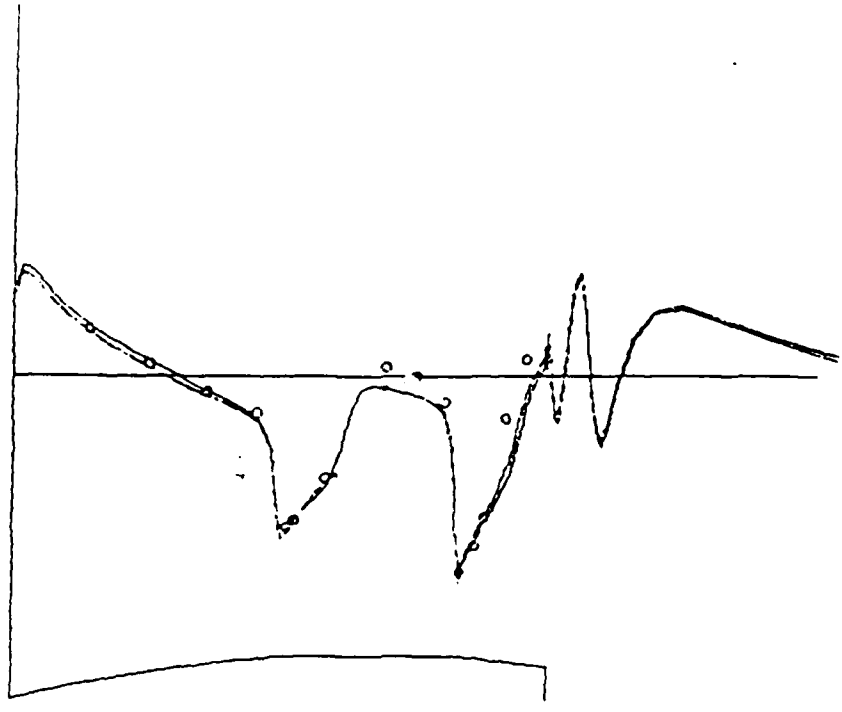

Figure 8. The surface pressure coefficint (140x40)

Figure 9. The surface pressure coefficient (140x60)

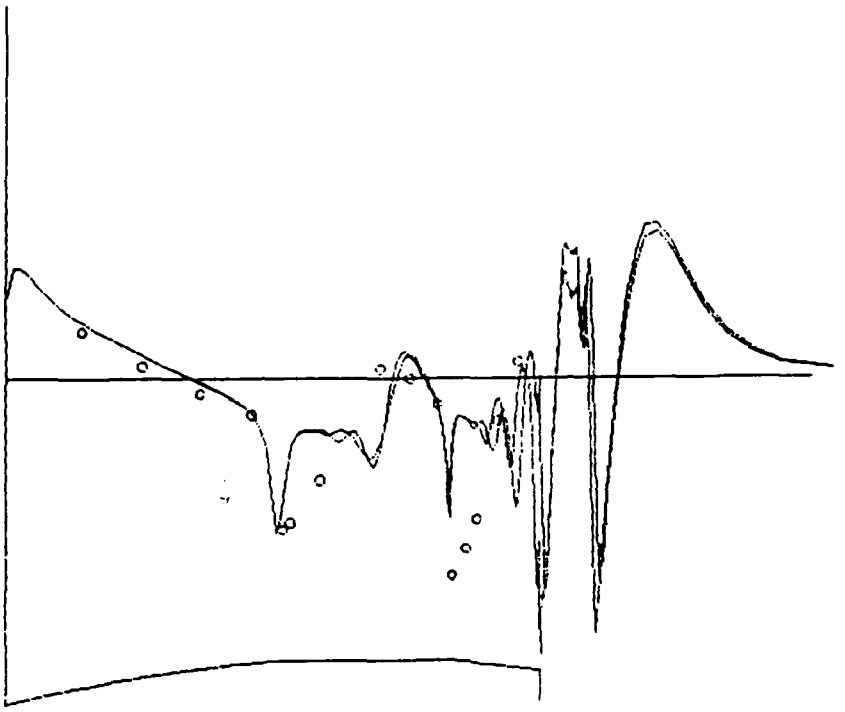

Figure 10. The surface pressure coefficient (140x80)

FINAL REPORT NUMBER 56
APPOINTMENT MADE TOO LATE
FOR RESEARCH TO BE COMPLETED
Dr. John Renie
760-OMG-112

FINAL REPORT

1985 USAF-UES SUMMER FACULTY RESEARCH PROGRAM/

RESEARCH INITIATION GRANT PROGRAM

NUMERICAL MODELING AND INVERSION OF 63μm EARTHLIMB EMISSION FROM ATOMIC OXYGEN

Prepared by:	James P. Riehl
Academic Rank:	Associate Professor
Department:	Department of Chemistry
University:	University of Missouri-St. Louis
Summer Faculty Research Location:	Air Force Geophysics Laboratory Infra-red Technology Division Infra-red Dynamics Branch
USAF Research Associate:	Dr. Ramesh D. Sharma

This report summarizes the research accomplished during the calendar year 1986, that was supported by the UES-AFOSR Minigrant Program. Additional information, including copies of the computer code, and a detailed budget summary is available upon request. The support of the UES-AFOSR has been an enormous help in the developement of our research program in atmospheric modelling, and is greatly appreciated.

I. INTRODUCTION

Atomic oxygen has long been known to play an important role in the heat balance and chemistry of the upper atmosphere. Bates [1951] suggested that the fine structure transition $O(^3P_1)$ --> $O(^3P_2)$ at 63μm plays an important part in cooling the upper thermosphere. The 5.3μm emission from vibrationally excited nitric oxide, which is produced mainly by collisions of the nitric oxide in the ground state with atomic oxygen, was shown by Kockarts [1980], Gordiets et al. [1982], Stair et al. [1985] and Zachor et al. [1985] to be the dominant cooling mechanism in the lower thermosphere. Around 100 km, 15μm emission from the bending mode of CO_2 which again is excited primarily by the collisions of oxygen atoms with ground state carbon dioxide [Sharma et al. (1981)] plays a dominant role in cooling the atmosphere [Dickinson (1980)]. We thus see that atomic oxygen, directly or indirectly, plays a vital role in the heat balance of the upper atmosphere.

Offermann, et al. [1981] have reviewed the methods used, all in situ, for the measurement of atomic oxygen densities in the upper atmosphere. Sharp [1985] has commented on results of these measurements: "The data show a variation in the concentrations by over a factor of 10 at 120 km, a factor of 40 for the peak at about 95 km and much larger factors below this. Peak concentrations range from 6×10^{10} cm^{-3} to 2×10^{12} cm^{-3}. Within any one technique there are factors of 5 variations over altitude. Some of this variation can be due to time of day, season and dynamics. However, the principal source of the variation is probably the differring measurement techniques."

In this report we describe a method of measuring the oxygen atom density and temperature by remote sensing. The method consists of simultaneous measurement of intensity in the 63 μm $^3P_1 \rightarrow {}^3P_2$ transition and the 147μm $^3P_0 \rightarrow {}^3P_1$ transition (Figure 1) between the ground state fine structure levels. We assume that these fine structure levels are in thermodynamic equilibrium with the local translational temperature (LTE), and that the atmosphere is one-dimensional. Radiance in the 63μm and 147 μm lines is calculated using a model atmosphere and a modified form of the radiation transport code of Sharma et al. [1983]. An onion-peel inversion is then carried out to show that it is possible to recover the density and temperature. Although the present inversion was performed on the data which had no noise, work in progress adds noise to the radiance data before carrying out the inversion. The principal aim of this work is to show that it is possible to develop reliable procedures for the recovery of

oxygen atom density and temperatures as a function of altitude from the limb radiance data.

The assumption that the fine structure levels are in thermodynamic equilibrium with the translational temperatures (LTE) needs some elaboration. Grossmann and Offermann [1978] concluded from their measurements at 63μm that this assumption is not a valid one and that the population of the $^3P_1$ level is less than that given by the LTE model. Iwagami and Ogawa [1980] argue that the Grossmann-Offermann results are consistent with LTE formulation if radiative transfer is properly treated. Fischer and Saha [1983] have calculated the radiative lifetime of the 63μm transition to be 3.192 hrs (11,491 seconds). Allison and Burke [1969] estimate the cross-section for transition between the fine structure levels during collisions between two oxygen atoms to be between 0.01 and 1 times the gas kinetic cross-section. At an altitude of 250 km such collisions occur about once every second or about 11,000 collisions per radiative lifetime. So it appears reasonable to assume LTE even at altitudes where the density is about .01 times the density at 250 km.

II. THEORY AND METHODOLOGY

A derivation of the radiative transfer equation has been given by Sharma et al. [1983], Sharma and Zachor [1983] and Zachor and Sharma [1985]. We present here a brief summary of the formalism. In one-dimensional models of the atmosphere, the atmospheric parameters, e.g., temperature, density, etc., depend

only on the altitude z. To calculate the emission and transmission of radiation we divide the line-of-sight (LOS) into segments of thickness (Δz) such that the atmospheric parameters over each segment may be assumed to be constant.

We express the radiance in terms of n_ν, the number of photons (of frequency νcm^{-1}) per wavenumber per unit area per steradian which are observed at a point z along the line-of-sight per unit time. The change in n_ν in a path length ds is described by

$$dn_\nu/ds = \{-n_\nu(h\nu_0/c)[n_l B(l->u)-n_u B(u->l)]+A_{ul}n_u/4\pi\}f(\nu-\nu_0) \quad (1)$$

where h and c are Planck's constant and the speed of light; n_l and n_u are the number densities of the lower and upper radiating states; B(l->u) and B(u->l) are Einstein coefficients for absorption and induced emission; A_{ul} is the Einstein coefficient for spontaneous emission, and f is a normalized lineshape function such that

$$\int f(\nu - \nu_0)d\nu = 1 \quad (2)$$

The Einstein coefficients are related by

$$g_l B(l->u) = g_u B(u->l) \quad (3)$$

and

$$A_{ul} = 8\pi h\nu_0^3 B(u->l) \quad (4)$$

where g_l and g_u are the statistical weights of the lower and upper radiating states. Through use of Eqs. (3) and (4), Eq. (1) can be cast in the form

$$dn_\nu/ds = (h\nu_0/c)B(l->u)n_l[-n_\nu(1-\gamma) + 2c\nu_0^2\gamma]f(\nu-\nu_0) \quad (5)$$

where γ is defined as

$$\gamma = g_l n_u / g_u n_l \quad (6)$$

The factor $(1-\gamma)$ corrects the simple absorption term (which is proportional to $n_l n_\nu$) for stimulated emission. The second term in brackets corresponds to spontaneous emission.

We now define the optical depth, τ_ν, by

$$d\tau/ds = (h\nu_0/c)B(l->u)f(\nu-\nu_0)n_l(1-\gamma) \quad (7)$$

Substituting Eq. (7) in Eq. (6) we get the result

$$dn_\nu/d\tau_\nu = [-n_\nu + 2c\nu_0^2\gamma/(1-\gamma)] \quad (8)$$

This equation has a very simple physical meaning. The rate of change of the number of photons with absorption depth decreases as the numbers of photons incident on the segment and increases with the source function. Under conditions of LTE the source is

equal to the black-body function when we recall that γ (Eq. 5) under these conditions equals

$$\gamma = \exp[-(E_u-E_l)/kT] = \exp[-C_2\nu_0/T] \tag{9}$$

where E_u and E_l are the energy levels of the upper and lower states; k is the Boltzmann constant; C_2 [= 1.4388 (K/cm^{-1})] is the second radiation constant, and T is the temperature.

This equation can easily be integrated across a segment. The solution is

$$n_\nu(z_{i+1}) = n_\nu(z_i)\exp(-\Delta\tau_{\nu i}) + 2c\nu_0^2[1-\exp(-\Delta\tau_{\nu i})]\gamma_i/(1-\gamma_i) \tag{10}$$

where the segment-dependence of γ has been made explicit with the subscript i. In Eq. (10), the first term represents the absorption within the ith segment of radiance incident upon it at z_i; and the second term represents the contribution from the ith segment alone.

The change in optical depth across a segment can be written as

$$\Delta\tau_\nu = (A_{ul}g_u/8\pi c\nu_0^2 g_l)n_l(1-\gamma)f(\nu-\nu_0)\Delta s \tag{11}$$

where Δs is the length of the segment.

An energy level diagram for the ground state term of atomic

oxygen $2s^2 2p^4 ({}^3P)$ is given in Figure 1. Also given in this figure are the Einstein coefficients taken from Fischer and Saha (1983).

In this study the Einstein coefficients for ground-state atomic oxygen along with assumed density, temperature, and pressure atmospheric profiles were input data for a modified form of the NLTE computer code developed at the Air Force Geophysics Laboratory (Sharma et al. [1983]). The modifications were accomplished such that the program calculates the radiance for the O^3P_2 <- O^3P_1 transition at 147μm and the O^3P_1 <- O^3P_0 transition at 63μm in the earthlimb geometry for any range of tangent heights within the range of the assumed atmospheric profile.

The atmospheric density and temperature profiles used in this study are plotted in Figure 2. This density profile was selected by comparison with previous estimates of O-atom densities, and represents a reasonable guess at the true density. Two additional density profiles corresponding to atmospheres two times and five times as dense as that given in Figure 2 were also studied in order to test the accuracy and reliability of the numerical inversion technique.

The integrated line radiances calculated from Eq. 2 are plotted versus tangent height in Figure 3 for both transitions appropriate for the atmospheric profile given in Figure 2. In these calculations it was assumed that the energy levels were in local thermodynamic equilibria. A voigt lineshape with a collisional line width equal to 0.1 cm^{-1} per amagat was assumed in

all of the work reported here. A weak $T^{-1/2}$ dependence of collisional linewidth upon temperature (Penner (1959)] was ignored. For the purpose of this initial study, it was pointed out earlier that, "exact" total integrated radiance data for the two transitions were available. Consideration of errors due to finite signal to noise and other experimental factors will be presented and discussed in a later paper.

III. Numerical Inversion of the Integrated Radiance

In order to start the inversion procedure, it was assumed that, at the highest tangent heights considered, the transitions are optically "thin". That is, no significant self-absorption takes place. In this case, the integrated radiance for the transition i<-j, N_{ij}, depends only on the excited state (O^3P_j) density profile, which is directly related to the ground state density through the temperature under the assumed conditions of thermodynamic equilibrium. Formally, we may write

$$N_{ij}(H_T) = 1/2\pi \int \varepsilon_{ij}(z) W(z,H_T) dz \qquad (12)$$

where $\varepsilon_{ij}(z)$ is the total volume emission rate at altitude z.

$$\varepsilon_{ij}(z) = n^*(z) A_{ij} \qquad (13)$$

In Eq. (12), $W(z,H_T)$ is a geometrical weighting factor corresponding to earthlimb observation geometry.

$$W(z,H_T) = (R + z)[(R+z)^2 - (R + H_T)^2]^{-1/2} \quad (14)$$

R denotes the radius of the earth.

The high altitude density profile is obtained by first assuming that the density decreases exponentially

$$n_j^*(z) = n_j^*(H_T)\exp(-\beta z) \quad (15)$$

Using Eqs. (13) and (15) in Eq. (12) we obtain the result

$$N_{ij}(H_T) = (1/2\pi)n_j^*(H_T)A_{ij}\int\exp(-\beta z)W(z,H_T)dz \quad (16)$$

The integral in Eq. (16) can be evaluated analytically with the result

$$N_{ij}(H_T) = A_{ij}n_j^*(H_T)\exp[\beta(R+H_T)](R + H_T)K_1[\beta(R+H_T)] \quad (17)$$

K_1 is the modified Bessel function. The two unknowns in this equation [n_j^* and β] can be evaluated by considering the integrated radiance at the two highest tangent heights for which radiance data is available. An approximate excited state density profile for the highest altitude regions can then be constructed from Eq. (15). We have made the additional assumption that the temperature in this region varies in a linear fashion, and can be approximated from known temperature profiles. These approximations appear to be reasonable, and, in fact, as long as the

highest measurement is far removed from the atmospheric region of interest these "starting" values have little effect on the results at lower tangent heights.

Inversion of the radiance through the lower tangent heights is accomplished by solving for the minimum in the function

$$\xi(T,n,H_T) = \frac{[N_{12}(H_T) - N^p_{12}(H_T)]^2}{N_{12}(H_T)^2} + \frac{[N_{01}(H_T) - N^p_{01}(H_T)]^2}{N_{01}(H_T)^2} \qquad (18)$$

$N^p_{ij}(H_T)$ denotes the predicted radiance at tangent height, H_T. The two terms in this equation have been separately normalized in order for them to be weighted equally. In the work described here, we have also multiplied this function by a "penalty" function in order to avoid mathematical diversions involving large temperature changes. The resultant function is given below

$$f(T,n,H_T) = \xi(T,n,H_T)\exp(0.01|\Delta T|) \qquad (19)$$

where $\Delta T = T - T_p$. T_p denotes the temperature of the previous slab, and the bar denotes that this function has been normalized.

Since for this problem functional evaluations are computationally expensive, especially for low tangent heights where the number of slabs is large, we have chosen to solve for the minimum in Eq. (19) through a combined "steepest descent" and Newton-Raphson numerical procedure. Efficiency of the solution of Eq. (19) is improved due to the insensitivity of the steepest descent

method to the initial guess, and the rapid (quadratic) convergence of the Newton-Raphson method. This numerical technique is commonly referred to as a "modified Newton method" [Bazarra (1979)]. In the work described here, this combined method is found to converge for initial guesses far from the true value, while it converges at least supralinearly for convex regions "close" to the true solution [Harlow and Riehl (to be published)].

Solution of Eq. (19) for slab j begins with an initial estimate for T_j and n_j. In this work we have employed the results from the previous slab as the initial estimates for the current slab. One cycle of the numerical procedure described above yields a next guess. For each new estimate of T_j and n_j, boundary conditions are checked, and, if exceeded, the result is reflected back into a preset allowed region. The process is repeated until convergence is obtained.

IV. Results and Conclusions

The results from the inversion procedure described above are plotted in Figures 4, 5, and 6 for the three different atmospheric profiles. The solid lines in these figures are the assumed temperature and density profiles. In Figure 4, it can be seen that the inversion was started at a tangent height of 200 km, i.e. below the highest altitude used in the calculation of the radiances (230 km), in order to simulate the kind of data that

would be available from an actual experimental measurement. In Figures 5 and 6, the numerical inversion was begun at the highest value of the assumed atmospheric profile. [In these cases the profile was extended out to 300 km.] As can be seen in these figures, the errors associated with the assumptions for the high altitude regions are not large, and are significantly reduced after a small number of inversion steps.

As is evident from the results in Figures 4-6, the inversion is quite successful for both temperature and density until the very "optically thick" regions of the atmosphere are reached. Below about 90 km (95 km for the high density atmospheres) self-absorption is so strong that the integrated radiances for the two transitions are almost constant. This can be seen, for example, in the plots of radiance versus tangent height in Figure 3. Continuation of the inversion through these regions leads to large oscillations in both temperature and density.

All three results show one or more small discontinuities in the inversion results especially in the recovered temperature values. In Figure 4, for example, these occur at approximately 120 and 130 km. These discontinuities, which are not unusual for nonlinear optimization problems of this complexity, are due to the fact that multiple solution pathways exist at these particular tangent heights. These oscillations are significantly reduced through use of the "penalty" function as described above.

Extensions of the work reported here are underway. In par-

ticular, more advanced numerical techniques are under study, and procedures to invert radiance data in which noise and finite spectral resolution have been added are under development. It is felt that measurements of atomic oxygen emission at 63μm and 147μm have enormous potential in remote sensing of this species.

ACKNOWLEDGMENTS

Research sponsored by the Air Force Office of Scientific Research/AFSC, under Contract F49620-85-c-0013. The United States Government is authorized to reproduce and distribute reprints for governmental purposes notwithstanding any copyright notation hereon. The authors are grateful to Dr. Don Ball and Dr. Frank Wodarczyk for generous support of this work. Dr. R.E. Murphy kindly provided the stimulus and environment for this work.

REFERENCES

Allison, D. C. S., and Burke, P. G., Inelastic collisions of slow atoms, J. Phys. B., 2, 941, 1969.

Bates, D.R., The temperature of the upper atmosphere, Proc. Phys. Soc., 64b, 805, 1951.

Bazaraa, M. S.; Shetty, C. M., Nonlinear Programming, John Wiley and Sons, New York, 1979.

Dickinson, P. H. G., Bain, W. C., Thomas, L., Williams, E. R., Jenkins, D. B., and Twitty, N. D., The determination of the atomic oxygen concentration and associated parameters in the lower ionosphere, Proc. R. Soc. Lond. A, 369, 379, 1980.

Fischer, C. F., and Saha, H. P., Multiconfigurational Hartree-Fock results with Breit-Pauli corrections for forbidden transitions in the $2p^4$ configuration, Phys. Rev. A, 28, 3169, 1983.

Gordiets, B.F., Yu. N. Kulikov, M. N. Markov, and M. Ya. Marov, Numerical Modeling of the thermospheric heat budget, J. Geophys. Res., 87, 4504, 1982.

Grossman, K. V., and Offerman, D., Atomic oxygen emission at 63 μm as a cooling mechanism in the thermosphere and ionosphere, Nature, 276, 594, 1978.

Iwagami, N,and Ogawa, T., Thermospheric 63 μm emission of atomic oxygen in local thermodynamic equilibrium, Nature, 298, 594, 1982.

Kockarts, G., Nitric oxide cooling in the terrestial atmosphere, Geophys. Res. Lett., 7, 137, 1980.

Offerman, D. Friedrich, V., Ross, P., and Von Zahn, U., Neutral gas composition measurements, Planet. Space Sci., 29, 747, 1981.

Penner, S. S., Quantitative Molecular Spectroscopy and Gas Emissivities, Addison-Wesley, Reading, Massachusetts 1959.

Sharma, R. D., and Nadile, R. M., Carbon Dioxide (v_2) Radiance Results using a New Non-Equilibrium Model Paper presented at the 19th Aeroscience Meeting, Am. Institute of Aeronautics and Astronautics, St. Louis, MO, Jan. 12-15, 1981.

Sharma, R. D.; Siani, R. D.; Bullit, M. K.; Wintersteiner, P. P.; A Computer Code to Calculate Emission and Transmission of Infrared Radiation Through Non-Equilibrium Atmospheres, AFGL-TR-83-0168, NTIS No. AD137162, Air Force Geophys. Lab., Hanscom AFB, Mass. 1983.

Sharma, R. D., and Zachor, A. S., Tests of an inversion algorithm for spectrally resolved limb emission, Appl. Opt., 22, 2665, 1983.

Sharp, W. E., Absolute Concentrations of $O(^3P)$ in the Lower Thermosphere at Night, Planet. Space Sci., 33, 571, 1985.

Stair, A. T., Jr.; Sharma, R. D.; Nadile, R. M.; Baker, D. J.; Greider, W. F., Observation of limb radiance with cryogenic Spectral Infrared Rocket Experiment, J. Geophys. Res., 90, 9763, 1985.

Zachor, A. S., Sharma, R. D., Nadile, R. M., and Stair, A. T., Jr., Inversion of a spectrally resolved limb radiance profile for the NO fundamental band, J. Geophys. Res., 90, 9776,, 1985.

Figure Captions

1. Schematic energy level diagram for the ground state (^3P) of atomic oxygen.

2. Assumed atmospheric temperature and density profile for atomic oxygen.

3. Calculated radiance (watts/cm^2 ster.) versus tangent height (km) for the 63 μm and 147 μm transition of atomic oxygen using the atmospheric profile given in Figure 2.

4. Oxygen atom density and temperature results obtained from numerical inversion for the atmospheric profile given in Figure 2. The solid lines are the assumed density and temperature profiles.

5. Oxygen atom density and temperature results obtained from numerical inversion for an atmospheric profile in which the density is two times that given in Figure 2. The solid lines are the assumed density and temperature profiles.

6. Oxygen atom density and temperature results obtained from numerical inversion for an atmospheric profile in which the density is five times that given in Figure 2. The solid lines are the assumed density and temperature profiles.

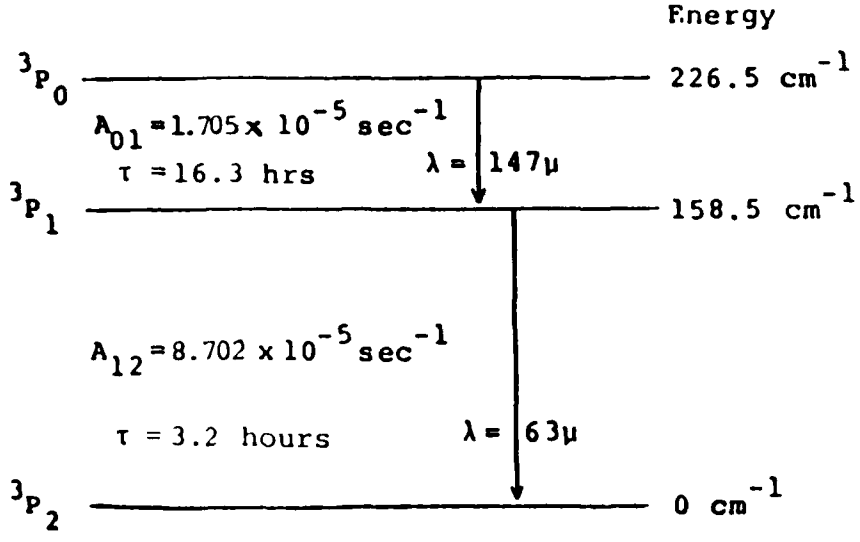

Einstein Coefficients (A's) from Fischer, C.F. and H.P. Saha, Phys. Rev. A 28, 3169 (1983)

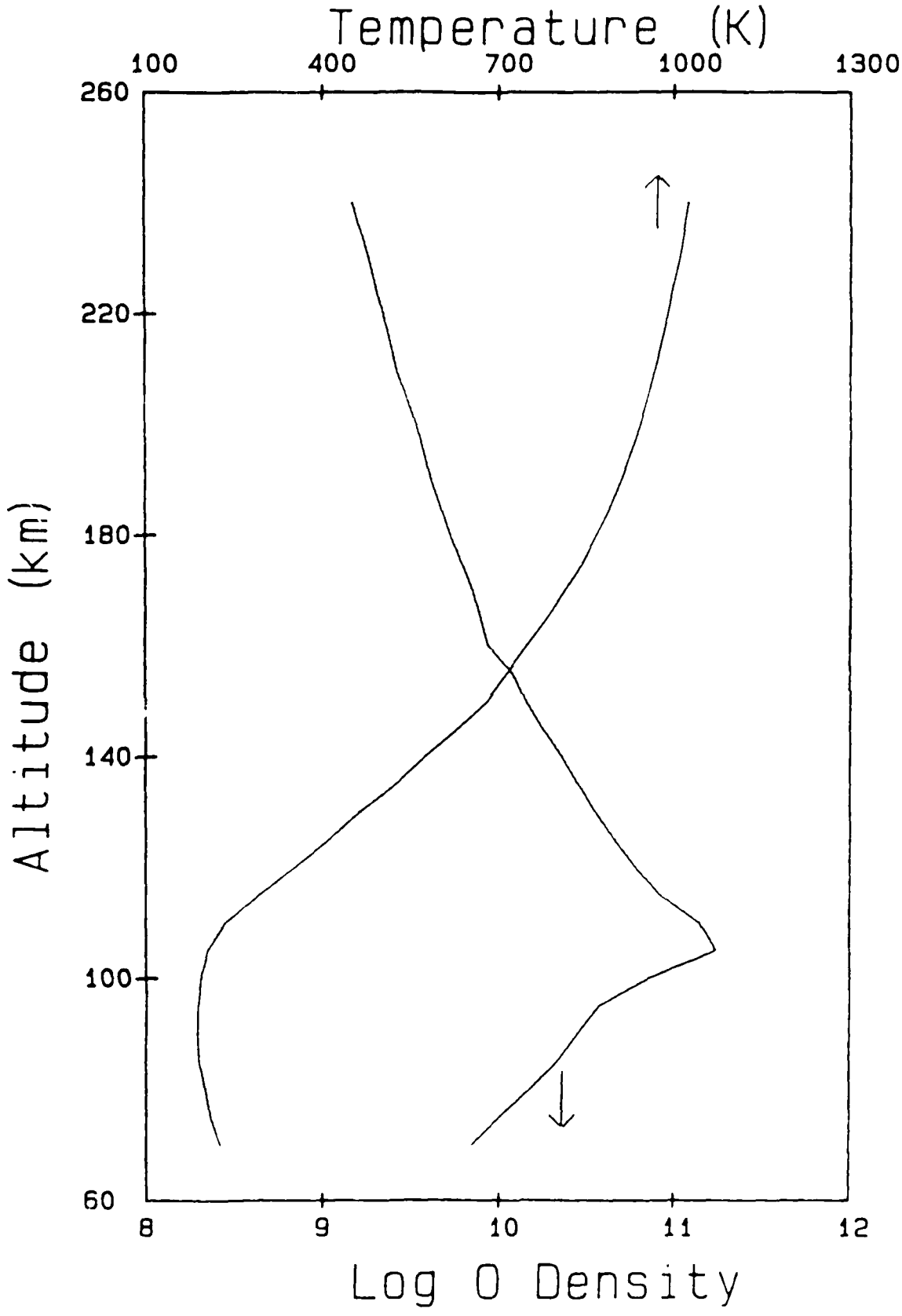
Temperature (K)
100
400
700
1000
1300
260
220
180
140
100
60
Altitude (km)
8
9
10
11
12
Log O Density

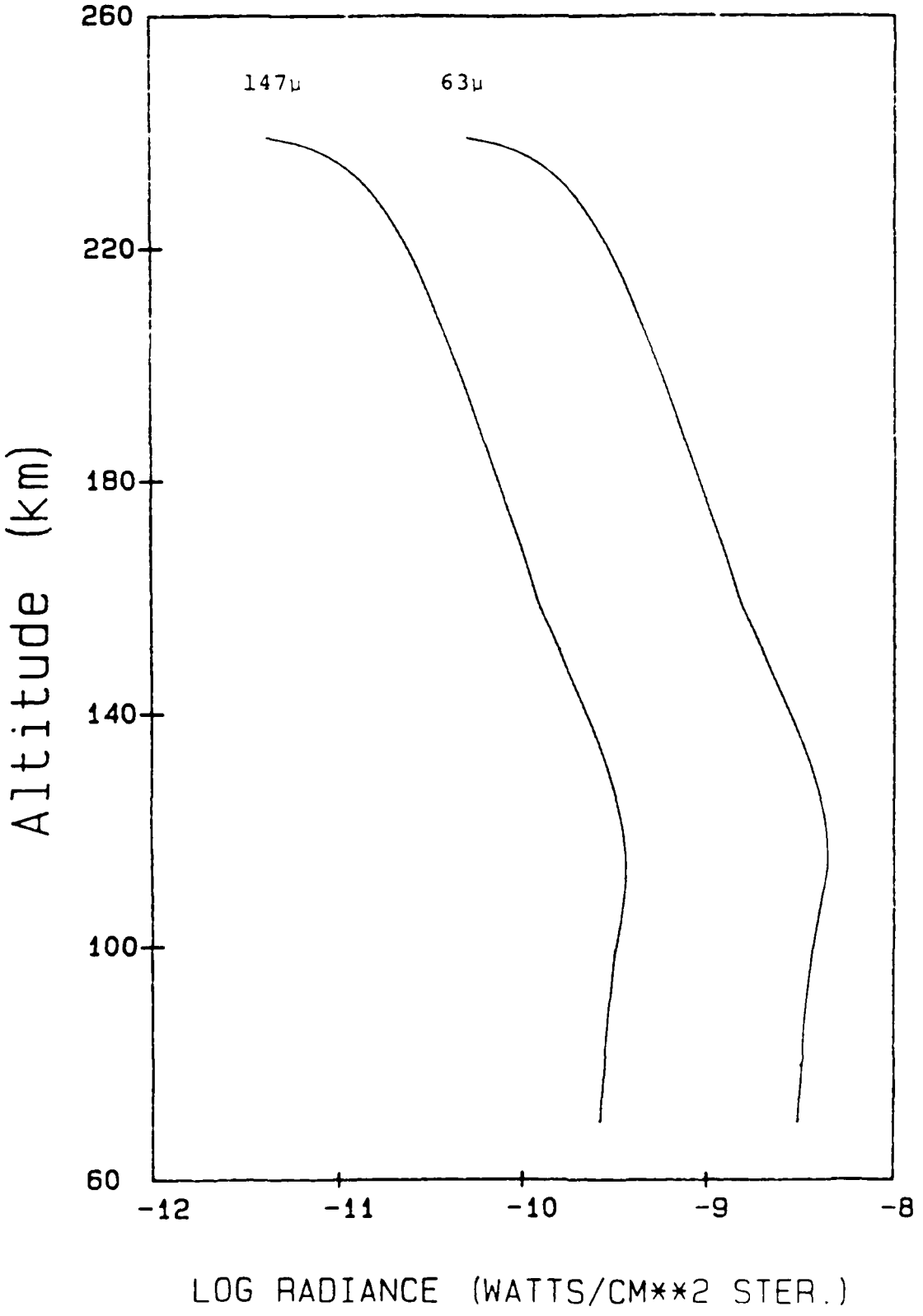
260
220
180
140
100
60
147μ
63μ
Altitude (km)
-12
-11
-10
-9
-8
LOG RADIANCE (WATTS/CM**2 STER.)

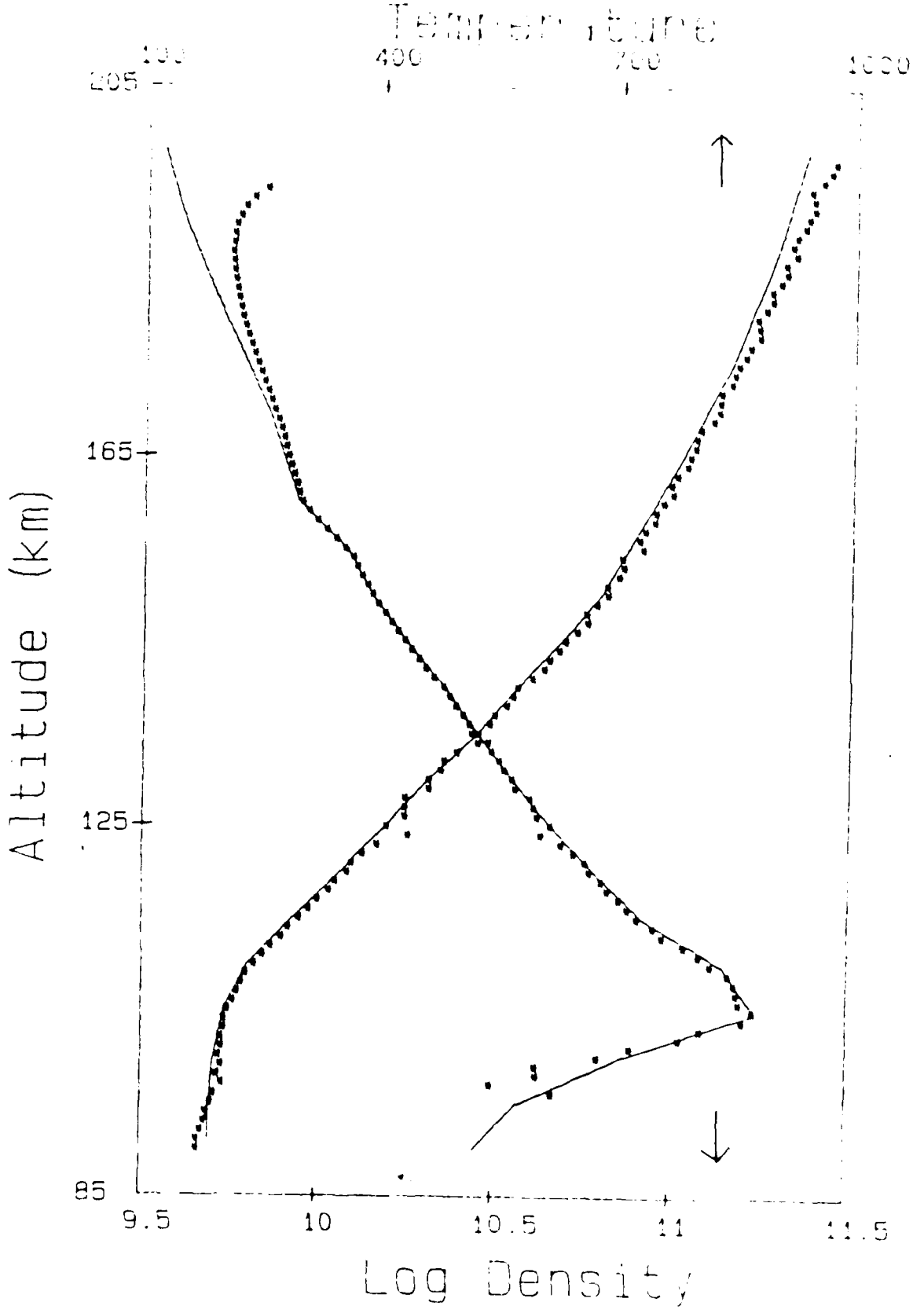
Temperature
205
400
1000
165
125
85
Altitude (km)
9.5
10
10.5
11
11.5
Log Density

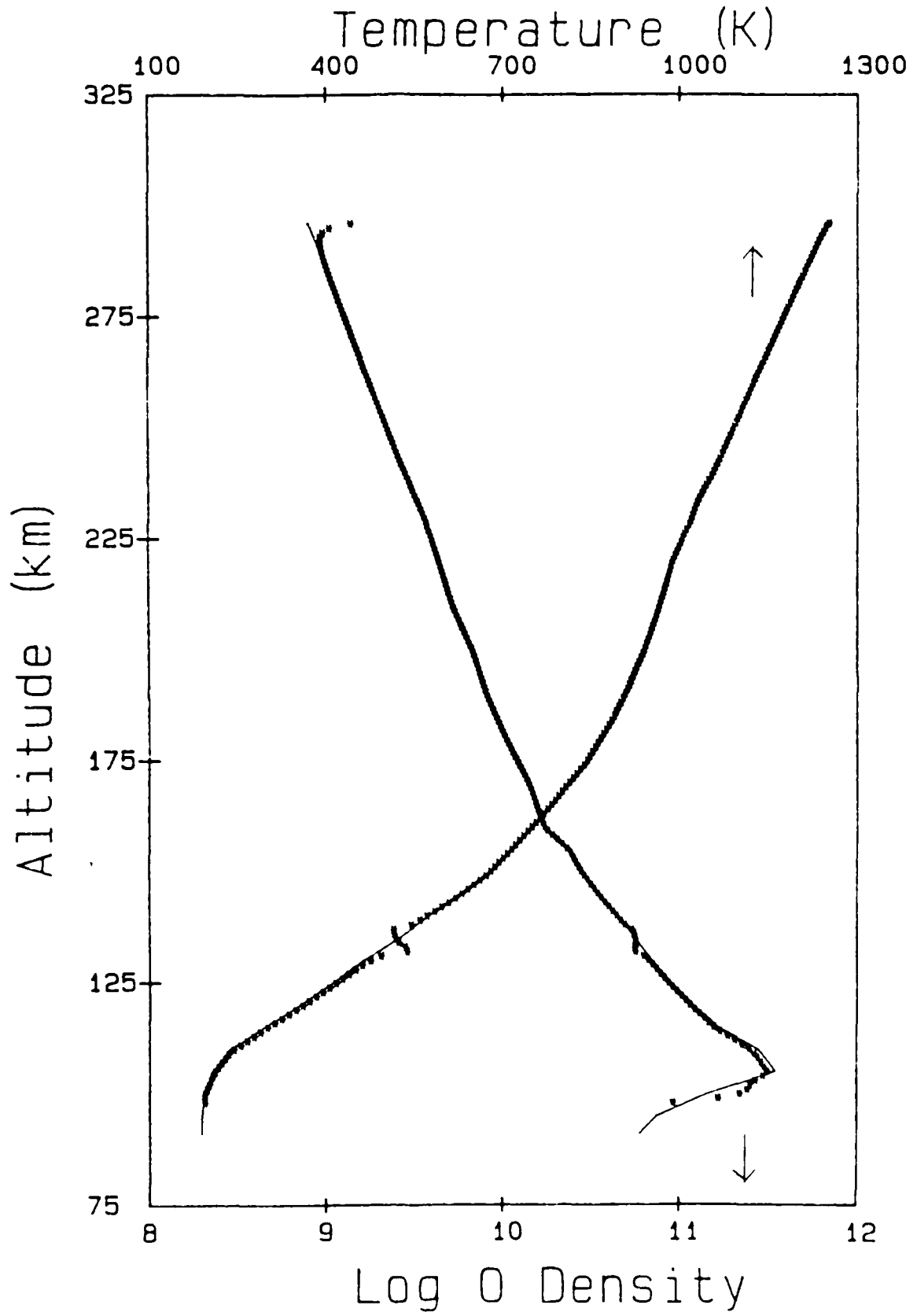
Temperature (K)
100
400
700
1000
1300
325
275
225
175
125
75
Altitude (km)
8
9
10
11
12
Log O Density

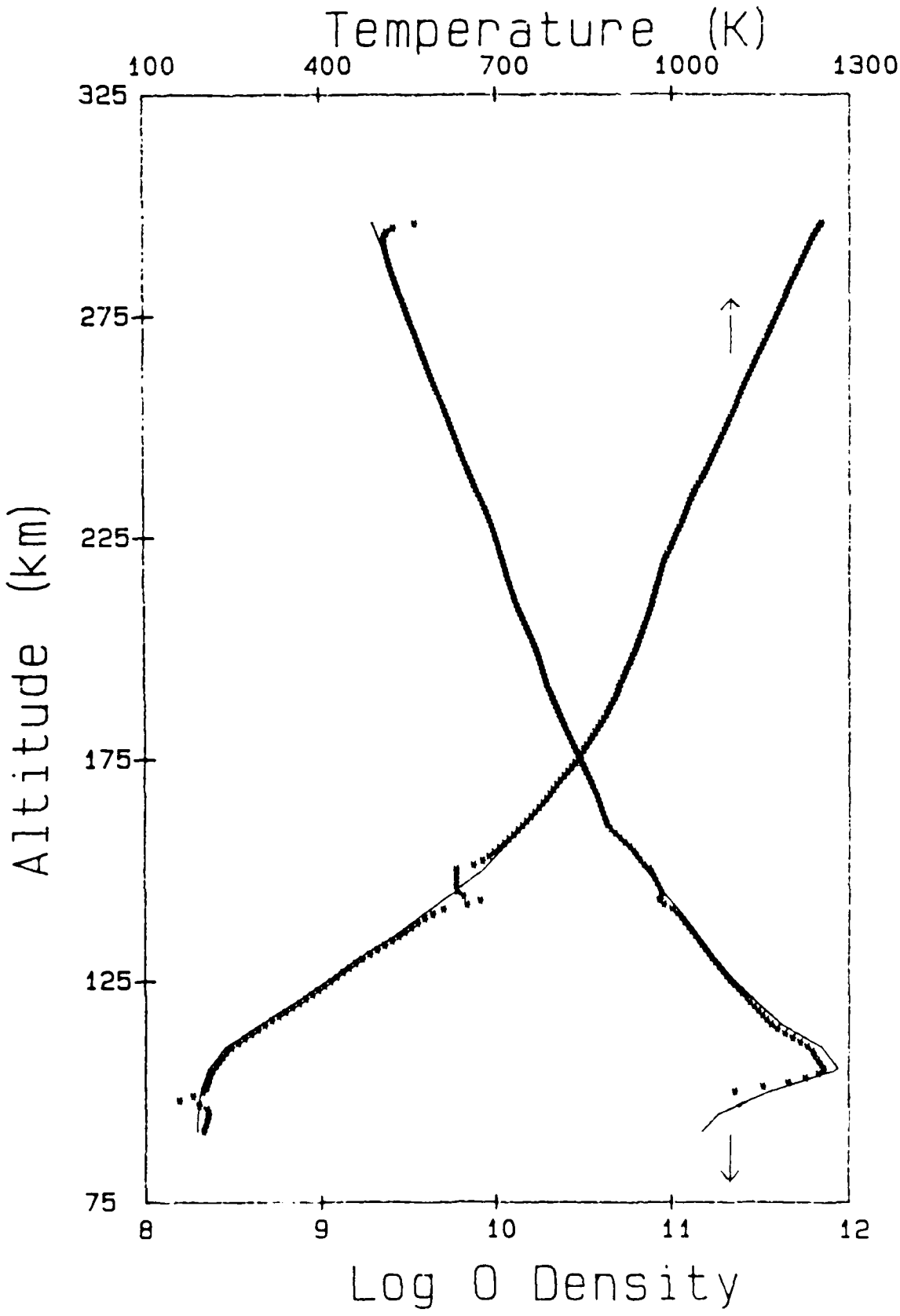
Temperature (K)
100
400
700
1000
1300
325
275
225
175
125
75
Altitude (km)
8
9
10
11
12
Log O Density

VALIDATION OF THE ELASTO-VISCOPLASTIC Finite Element Program

by

Joseph E. Saliba

Civil Engineering and Engineering
Mechanics Department
University of Dayton

to

Universal Energy Systems
4401 Dayton-Xenia Road
Dayton, Ohio 45432

December 1986

UNIVERSITY OF DAYTON
CIVIL ENGINEERING AND ENGINEERING
MECHANICS DEPARTMENT
DAYTON, OHIO 45469

I. BACKGROUND

Readiness and survivability, important United States Air Force (USAF) objectives for nonstrategic forces, must be achieved in the key area of sortie generation. Critical elements in obtaining rapid and sustained sortie generation are aircraft launch and recovery. The Air Force has many active and planned programs aimed at providing improved launch and recovery capability. The effective development, optimization, and application of many of these actions depends upon reliably predicting aircraft capability to operate on various ground surfaces.

Most USAF aircraft were designed for operation on high-strength, smooth paved surfaces, making these surfaces high priority wartime targets and subject to damage. Reliable prediction techniques exist for aircraft operation on conventional pavement surfaces. However, existing techniques for predicting aircraft operation on soil are not reliable and accurate for operation on soil surfaces having significant variations of soil strength and/or soiltype with depth. Also, techniques have not been developed for predicting aircraft operation on other contingency surfaces.

A finite element, viscoplastic analysis technique has been developed to correlate layered soils to a single strength media, and to compute tire sinkage and resulting rut depth. The

application of the analysis procedure in the form of a computer program provides a promising approach to significantly improve existing Air Force prediction techniques. It is considered that the program can be applied to significantly improve the reliability and accuracy for predicting aircraft operation on soil surfaces having large variations in strength and/or soil type with depth. Also, it is considered that the analysis procedure can be adapted for other contingency surfaces to provide a basis for the development of needed ability for predicting aircraft operation on contingency surfaces.

2. PROBLEM DESCRIPTION

The existing viscoplastic layered model uses the state of the art in both constitutive relations and numerical techniques to model soils. However, it does not have the ability to consider soil work softening/hardening, such as caused by multiple aircraft tire passes. Necessary tests have not been identified for determining the material properties needed as program input. Testing has not been done to validate the computer program. Also, simulations have not been accomplished to establish the program's applicability for improving ability to predict aircraft operation on soil and other airfield contingency surfaces. This powerful analysis tool promises to provide urgently needed improvements to Air Force ability to predict aircraft ground operation. The described work needs to be done to make the program more suitable for potential Air Force applications, and to verify its application feasibility and benefits.

3. OBJECTIVES

The objectives of the proposed research program are to:

A. Identify work softening/hardening models and include them in the finite element program demonstrating their capability to simulate the effect of cyclic loading obtained during multipass phenomena.

B. Identify the necessary tests needed to determine the material properties of soils which will be used as input data to the finite element program.

C. Validate or verify the finite element program.

4. DEVELOPMENT OF STRAIN HARDENING/SOFTENING MODELS

There are a number of materials, such as [illegible] concrete, and dense soils, which when compressed at a [illegible] strain rate under conditions of either uniaxial [illegible] axial compression exhibit a phenomenon called "[illegible]ing". Materials which exhibit such softening [illegible] characterized by a constitutive response in the axial direction in which the stress rises monotonically with strain to a peak and then decreases with further increases in strain. Under general states of small deformation, a material element is said to undergo strain softening when its stress rate multiplied by its strain rate is negative (Valanis 1984).

When subjected to a number of cycles of stress, a soil sample fails at a stress level lower than the monotonic failure stress. Five factors contribute to this behavior in varying degrees, depending upon the nature of the soil. These factors are (a) generation of pore pressures (b) [illegible] degradation or

all respects and do not take into account the rotation of principal axes of stress tensor which, in most problems, always takes place to some extent. The models do not account for the strength anisotropy induced by plastic flow, and this fault in the model causes an error of unknown magnitude which makes assessing the prediction, even in simpler benchmark problems, impossible.

This paper presents a micro-structural model which was first developed by Pande and Sharma (1980). This model was used in conjunction with our existing viscoplastic finite element program. Attention is devoted here to two aspects only: Rotation of principal axes and cyclic strain softening.

The proposed model has conceptual links with the polycrystalline models of plasticity proposed a few decades ago by Taylor (1938), Batdorf and Budiansky (1949) and Sanders (1955) and others. The model is also a numerical implementation and further extension of the "micro-structural" view of the clays as proposed by Calladine (1971). The first part of the paper sets the mathematical basis of the model; the second part describes the details of numerical implementation and solution of benchmark problems like a triaxial-axial test in monotonic loading; the third part demonstrates the characteristics of the model in cases of cyclic loading.

The influence of the rotation of principal axes in the model in comparison to the conventional Critical State Model is demonstrated.

As the software development involved in this model is extremely simple, many relatively complex models incorporating

other factors like cyclic deformation, pore pressure generation as in transient loadings can be readily incorporated.

A SIMPLE CONCEPTUAL MODEL OF PARTICULATE MEDIA

First, one must consider a solid block of arbitrary shape of homogeneous isotropic, linear elastic material intersected by K number of randomly oriented planes. The planes render the solid block into an assemblage of perfectly fitting polyhedral blocks (Fig. 1). Next one must further assume that by some process the boundaries of the microscopic polyhedral blocks are roughened, which creates asperities, and spot welded without inducing any stresses in the block. The details of justification for this rather simple conceptual model are necessary because the key to the deformational behavior of the block lies in an accurate description of the sliding phenomenon under the current effective normal and shear stresses (σ'_n , τ) along the boundaries of the polyhedral blocks and opening/closing of the inter-boundary gap (void ratio) in relation to the initial gap (initial void ratio) caused by the process of creation of asperities. Calladine (1971) employed this model to explain mechanical properties of saturated clays, obtaining remarkably good comparison with experimental data. A similar model has been used by Zienkiewicz and Pande (1977) and Pande (1977) for solving practical problems of jointed rock masses; however, their main purpose was to model strong strength anisotropy of rocks developed due to the presence of 2 or 3 sets of families of planes of weakness. As the number of contact boundaries approaches infinity, the isotropy of the material is restored.

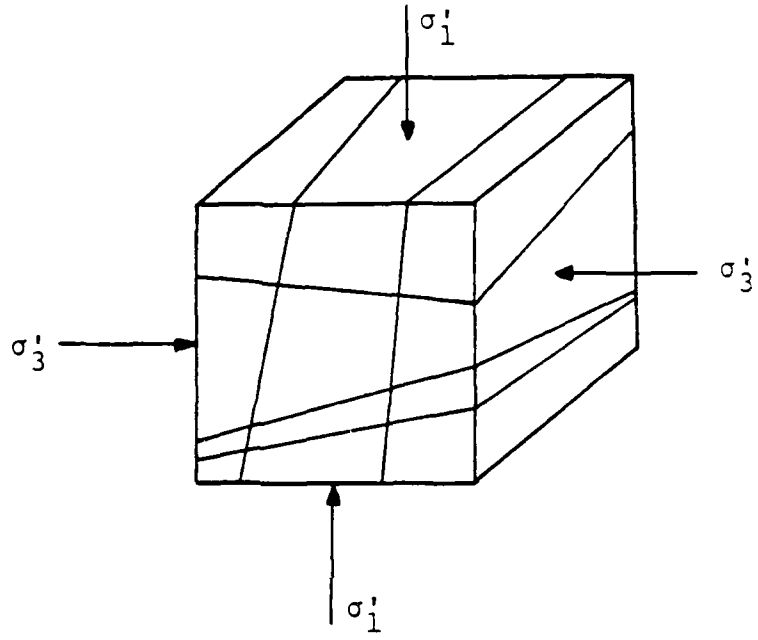

Figure 1

A block of isotropic elastic material intersected by a large number of randomly oriented planes.

The philosophy of this conceptual model is comparable to the finite element procedure. The mathematical expressions necessary to accurately describe the behavior of one contact surface are examined. The assumption is that the same relationships hold good for all contact surfaces, the global behavior being obtained by integration of contributions made by each contact surface.

ASSUMPTIONS AND MATHEMATICAL FORMULATION

Restricted to the case of small strains and deformations only, one assumes that the behavior of soil grains is purely elastic, while that of the contact boundaries is elasto/viscoplastic. This model was developed using elasto/viscoplasticity assumptions. However, the elasto/viscoplasticity assumptions are equally valid. This assumption implies that when a soil element is subjected to any load, the stresses manifested are instantaneously elastic. We further assume that total strain (ε) can be split into (a) an elastic component (ε^e), (b) a viscoplastic component (ε^{vp}) and (c) an initial strain component (ε^o) which is nonstructural in origin

$$\varepsilon = \varepsilon^e + \varepsilon^{vp} + \varepsilon^o \qquad (1)$$

and in incremental form

$$d\varepsilon = d\varepsilon^e + d\varepsilon^{vp} + d\varepsilon^o \qquad (2)$$

One develops the mathematical framework suitable for effect stress analysis, thus assuming that the total stress applied on a saturated soil element can be split into two components. One component is carried by the soil grains (effective stress (σ') and the other is carried by the pore water (pore water pressure

(p)). Thus,

$$\underset{\sim}{\sigma} = \underset{\sim}{\sigma}' + \underset{\sim}{m}p \tag{3}$$

and in incremental form

$$d\underset{\sim}{\sigma} = d\underset{\sim}{\sigma}' + \underset{\sim}{m}dp \tag{4}$$

where $\underset{\sim}{m}^T = (1,1,1,0,0,0)$ (5)

and $\underset{\sim}{\sigma}^T = (\sigma_x, \sigma_y, \sigma_z, \tau_{xy}, \tau_{yz}, \tau_{zx})$

The increments of effective stress are related to various strain components by

$$d\underset{\sim}{\sigma}' = \underset{\sim}{D}_T (d\underset{\sim}{\varepsilon} - d\underset{\sim}{\varepsilon}^{vp} - d\underset{\sim}{\varepsilon}^{o}) \tag{6}$$

where $\underset{\sim}{D}_T$ is the tangential drained elasticity matrix. If one assumes that the soil grains are incompressible, then, for the undrained condition, any volumetric strain is related to the increment (or decrement) of pore pressure by

$$dp = \frac{K_f}{\eta} d\varepsilon_y \tag{7}$$

where $d\varepsilon_y$ is the increment of volumetric strain

K_f is the bulk modulus of the fluid

η is the porosity of the soil

Equations (1) to (7) are fundamental postulates of soil plasticity and have been extensively used by many researchers (Naylor, 1975; Humpheson, 1976; and Chang, 1979). In elasto/viscoplasticity theory it is assumed that rate of viscoplastic strain is given by

$$\dot{\underset{\sim}{\varepsilon}}^{vp} = \gamma \langle \Phi(F) \rangle \frac{\partial Q}{\partial \underset{\sim}{\sigma}} \tag{8}$$

where γ is the fluidity parameter

F is the scalar yield function

Φ represents a monotonic function of F

Q is the scalar plastic potential function

$\langle\rangle$ indicates that $\Phi(F) = \phi(F)$ if $F > 0$

$= 0$ if $F \leq 0$

Most plasticity-based models assume that soil is isotropic; thus, the scalar yield function (F) is a function of principal stresses ($\sigma_1, \sigma_2, \sigma_3$) alone and not their directions. Yield functions are written in terms of invariant of stress (Nayak and Zienkiewicz, 1972; Zienkiewicz and Pande, 1977b), which precludes the possibility of anisotropic behavior. On the other hand, originally isotropic soils become strongly anisotropic after some plastic flow (Drucker, 1966). The yield function is expressed in terms of certain stress components rather than invariants to model this behavior.

One formulates the yield function for K contact boundaries encompassing a point in our conceptual model. Considering i^{th} plane, the effective normal stress (σ_n') and shear stress (τ) can be written as

$$\begin{vmatrix} \sigma'_n \\ \tau \end{vmatrix} = T_i \underset{\sim}{\sigma} \tag{9}$$

where T_i represents a transformation matrix, which is a function of the direction cosines of the unit normal to the i^{th} plane or contact boundary. The current yield function can now be expressed as

$$F_i = f(\sigma'_n, \tau, \underset{\sim}{\varepsilon}^{vp})_i = 0 \tag{10}$$

Equation (10) represents the conditions of sliding on the i^{th} contact plane. Assuming an associated form of flow, from

ideal plasticity theory (no hardening/softening) then it reduces to

$$F_i = f(\sigma_n', \tau)_i = 0 \qquad (14)$$

Once all computations can be done for randomly oriented contact boundaries, the yield function for the soil material is not required in this model. However, it can be expressed as follows

$$F = F_1 \cap F_2 \cap \ldots F_i \cap \ldots F_k = 0 \quad (15) \qquad (15)$$

This yield function is isotropic for $K \to \infty$ and for ideal plasticity (Equation 14) since, if the axes of principal stresses are rotated, values of F for each plane would change, but the sum total would remain unaltered. Preferential hardening/softening would take place, based on the direction of principal stresses and their subsequent rotation during the process of incremental loading and plastic flow, if hardening/softening is considered.

SPECIFIC FORMS OF YIELD FUNCTIONS IN σ_n'-τ SPACE

A key to the constitutive modeling in the proposed framework is the yield function in σ_n' - τ space. Much experimental as well as theoretical work (Bowden and Tabor, 1950, 1956; Tabor, 1951, 1959) has been done chiefly in tribology to explain the behavior of one metal plate sliding over the other. Here, the approach is that of simple model parameters which can be derived from conventional soil test data. The yield function in σ_n',τ space (Figure 2) can be written in the simplest form as,

$$F_1 = |\tau| + \sigma_n' \tan\phi' - c' = 0 \qquad (16)$$

equation (8) the contribution made by the i^{th} contact plane to the $\dot{\underset{\sim}{\varepsilon}}^{vp}$ vector (partial viscoplastic strain rate $\hat{\dot{\underset{\sim}{\varepsilon}}}_i^{vp}$), is

$$\hat{\dot{\underset{\sim}{\varepsilon}}}_i^{vp} = \gamma \; < \Phi \; (F_i) > \frac{\partial F_i}{\partial \underset{\sim}{\sigma}} \tag{11}$$

To obtain the expression for the viscoplastic strain rate, sum up the partial viscoplastic strain rates for all the K contact planes and let $K \to \infty$. Thus,

$$\dot{\underset{\sim}{\varepsilon}}_{i=1}^{vp} = \sum_{i=1}^{K} \gamma \; < \Phi(F_i) > \frac{\partial F_i}{\partial \underset{\sim}{\sigma}} \tag{12}$$

The discrete summation in equation (12) can be replaced by integration over the solid angle subtended by a sphere of unit radius at its center if one assumes a continuous random distribution of contact planes.

Thus,

$$\dot{\underset{\sim}{\varepsilon}}^{vp} = \int_{\Omega} \gamma < \Phi \; (F) > \frac{\partial F}{\partial \underset{\sim}{\sigma}} \, d\Omega \tag{13}$$

where $d\Omega$ represents an infinitesimal solid angle. Equations (12) and (13) show that a viscoplastic strain rate equation can be derived from the basic mechanism of sliding on the contact planes, which is more fundamental in nature. The flow equation of soil behavior is automatically defined and can be computed, once the equation (10) is specified in explicit terms of effective normal stress, shear stress and viscoplastic strains.

If the form of the equation (10) is chosen according to

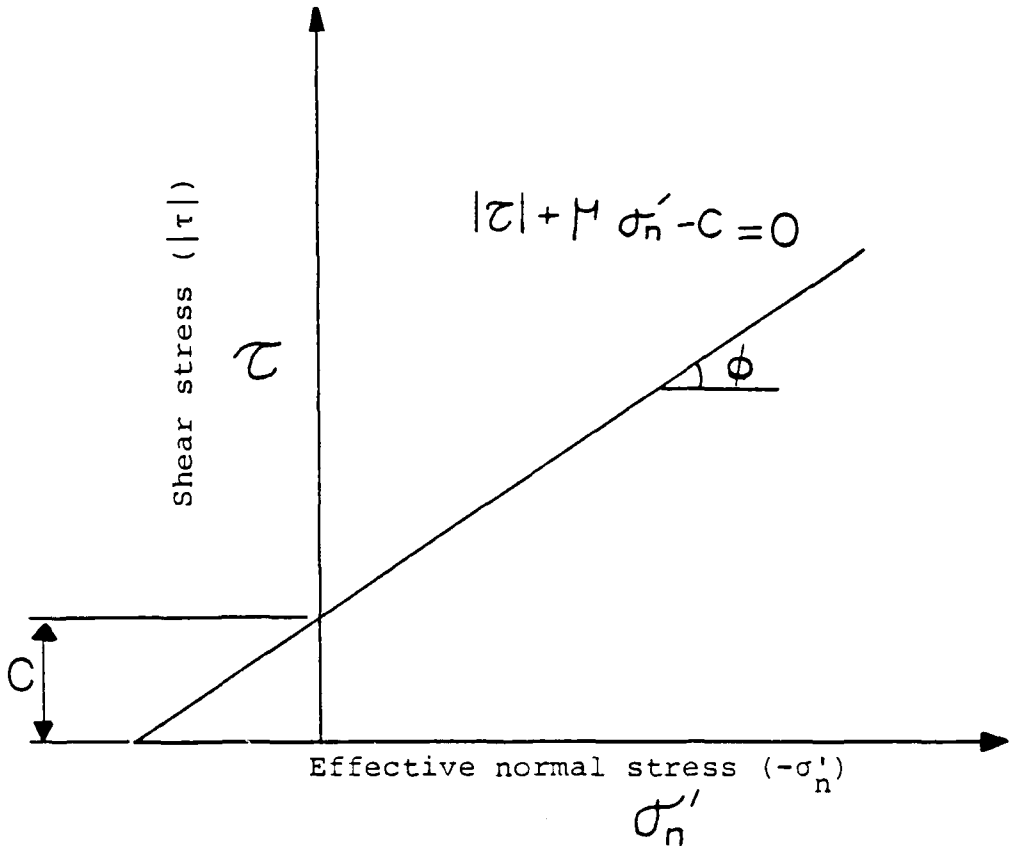

Figure 2
Mohr-Coulomb yield function in σ_n' - τ space

a representation of classical Mohr-Coulomb yield function. In equation (16) ϕ' is the apparent angle of friction and c' is the apparent cohesion. $\phi' = 0$ case is included in equation (15) when it becomes

$$F_i = |\tau| - c' = 0 \tag{17}$$

Equation (16), when substituted in equation (12), leads to

$$\dot{\underset{\sim}{\varepsilon}}^{vp} = \sum_{i=1}^{K} \gamma \langle \varphi(|\tau| + \sigma_n \tan\phi' - c')_i \rangle \frac{\partial F_i}{\partial \underset{\sim}{\sigma}} \tag{18}$$

and can be conveniently used in computation and, as others have shown (Pande and Sharma, 1979), leads to exactly the same results as are obtained by using the Mohr-Coulomb yield function in invariant form.

A critical state model accounts for rotation of principal axes and load cycling. The critical state model which interprets isotropic strain hardening was originally developed for normally consolidated clays by Schofield and Wroth (1968), and now there are a number of variants of this model (Naylor, 1975; Roscoe and Burland, 1968). Nova and Wood (1979) have extended the concepts of this model to sands. Gerogiannopoulos and Brown (1978) have attempted to prove that this model is applicable to rocks. All authors, however, have used an invariant formulation to the yield function. Here we shall specify the yield function for each randomly oriented plane in σ_n' - τ space. This would induce anisotropic hardening. Moreover, to account for the cycling of load, cyclic strain softening shall be introduced. In our model, cyclic strain softening occurs as a function of cumulative value

of absolute plastic strains on each of the planes. Thus, the yield function and strain hardening/softening rules are given by

(i) on the wet side ($-\sigma_n' - p_c^j \geq 0$)

$$F_i = \left(\frac{\tau}{\mu p_c^j}\right)^2 + \left(\frac{-\sigma_n' - p_c^j}{p_c^j}\right)^2 - 1 = 0 \qquad (19)$$

where $\mu = \tan\phi'$

$$p_c^j = p_{co}^j \, e^{\chi \varepsilon_n^{vp}}$$

in which ε_n^{vp} = normal component of the viscoplastic strain on the i^{th} plane

p_c^j = current value of pre-consolidation pressure for the j^{th} cycle

p_{co}^j = initial isotropic pre-consolidation pressure for the j^{th} cycle

χ = hardening parameter

$$= \frac{1+e_o}{\lambda - \kappa} \qquad (20a)$$

where e_o = initial void ratio

λ, κ = compression and swelling indices respectively

To account for the influence of the cyclic softening, the value of p_{co} for the j^{th} cycle (p_{co}^j) is defined as

$$p_{co}^j = p_{co}^{j-1} \left(K_1 - K_2 e^{\frac{-\varepsilon_n^{vp}}{\gamma^{vp}}}\right)^{\beta} \qquad (20b)$$

where K_1, K_2, β are constants and γ^{vp} is the absolute value of the cumulative viscoplastic shear strain on the i^{th} plane.

(ii) On the dry side ($-\sigma_n - p_c^j < 0$)

$$F_i = |\tau| + \sigma_n \tan\phi_o - \tau_o = 0 \qquad (21a)$$

where ϕ_o, τ_o are experimented constants defining peak strength and a nonassociative flow rule is used, as in

$$Q_i = |\tau| p_c^j + (-\sigma_n - p_c^j)^2 \tan\phi' = 0 \qquad (21b)$$

with Q_i representing the plastic potential function. The form of this function ensures the continuity of strain rates at $-\sigma^n = p_c^j$, which is important from a computational point of view.

Figure (3) shows the yield function represented by equations (19) and (21).

One must note the important difference between this model and the conventional critical state model. In the proposed model, the evaluation of yield loci is traced individually for each plane which is a function of effective normal stress, shear stress and a normal component of viscoplastic strain on that plane. In turn, the effective normal stress and shear stress on a plane are a function of not only magnitude of principal stresses but also of their directions. If loading is such that the direction of principal stresses stays fixed, as is the case with triaxial-axial tests, then the hardening/softening proceeds on some fixed planes and leads to isotropic hardening. On the other hand, only selective hardening/softening will take place involving anisotropy induced by plastic flow if the direction of principal stresses rotates during loading. The main advantage of the proposed model, which we shall term as "critical state model

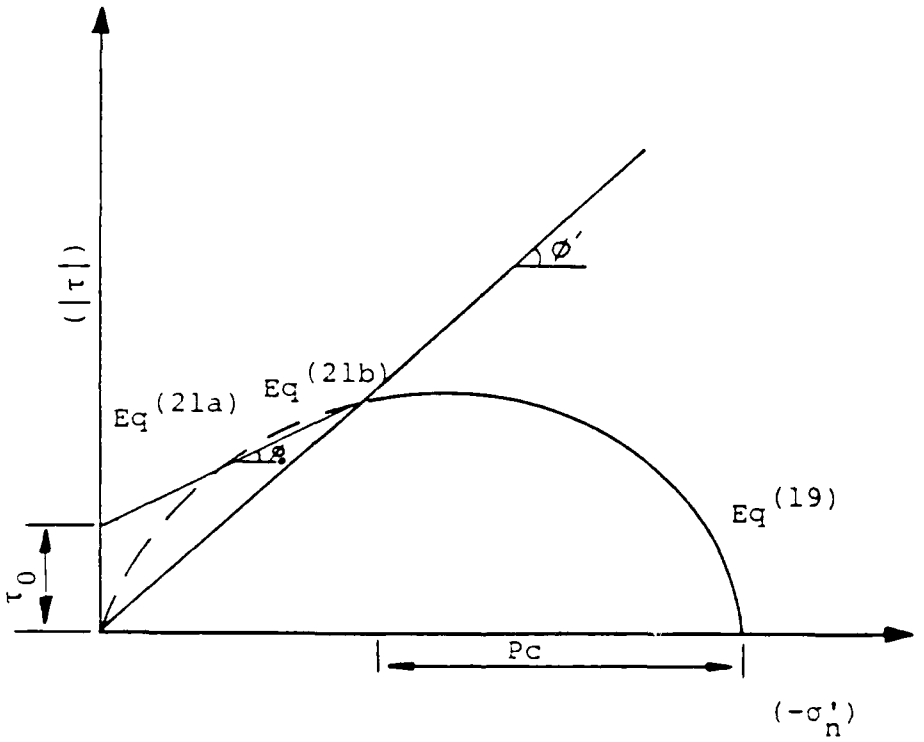

Figure 3
Critical state yield criterion in σ'_n - τ space (CSMAR)

accounting for rotation" (CSMAR) of principal stresses and cyclic softening, is its utmost simplicity.

DETERMINATION OF MATERIAL PROPERTIES

The proposed numerical framework for investigating the constitutive relationship, starting with a definition of yield surface on $\sigma_n' - \tau$ plane, flow rule and hardening rule, is extremely simple in terms of computer programming.

The summation implied by equation (12) is accomplished numerically. Several trial and error studies have led to the choice of number of contact planes surrounding a point as 10 in one octant. Another 10 planes are taken as mirror images in the adjacent octant making K = 20. Because of symmetry, only one quadrant of upper or lower hemisphere need be considered. Details of direction cosines of these planes and associated transformation matrices, etc. are indicated in Appendix I. The computations involved are made only once and are then stored. The equation (12) also involves the computations of the derivatives of σ_n' and τ with respect to the stress vector. The associated algebra is given in Appendix II. Once the $\dot{\underset{\sim}{\varepsilon}}^{vp}$ is computed for each Gauss point based on the contribution of 20 planes, the standard viscoplastic algorithm (Cormeau, 1976; Zienkiewicz, 1977) is adopted involving repeated solution of equations of the type

$$\underset{\sim}{K}\ \underset{\sim}{\delta} - \int_v \underset{\sim}{B}_T\ \underset{\sim}{D}\ \dot{\varepsilon}^{vp}\, dv = \underset{\sim}{R} \qquad (22)$$

where $\underset{\sim}{K}$ is the overall stiffness matrix of the system, $\underset{\sim}{D}$ is the drained elasticity matrix and the righthand side term $\underset{\sim}{R}$ includes

the influence of initial effective stress, initial pore water pressure, body forces, imposed tractions, etc.

$\underset{\sim}{B}$ is the strain matrix in

$$\underset{\sim}{\varepsilon} = \underset{\sim}{B}\,\underset{\sim}{\delta} \tag{23}$$

$\underset{\sim}{\delta}$ being the nodal displacement vector of the system.

The numerical examples in this section are designed keeping the following aims in mind.

(a) to show that the proposed model, with the fixed directions of principal stresses and monotonic loading, gives the same results as the conventional critical state model, but, in contrast to the critical state model, the proposed model (CSMAR) gives different results when axes of principal stresses are rotated in truly triaxial-axial situations.

(b) to show that, with proper choice of cyclic strain softening parameters, experimentally observed behavior of pore pressure generation can be simulated. At low intensities of stress, such simulation leads to purely elastic behavior, while at higher intensities, the failure occurs after a number of cycles which can be controlled by the constant β.

VALIDATION OF THE FINITE ELEMENT PROGRAM

Soils Used

One remolded soil was employed in this study. Kaolinite was used because the variation among samples can be reduced and because its engineering properties are well known.

The kaolinite used in this investigation is mined at Bath, South Carolina. In the form of dry powder, it is available commercially under the name of Peerless No. 2, supplied by R. T.

Vanderbilt Company, New York. Occurring in a pure, highly crystalline form in nature, this clay is ideal for soil mechanics research as it does not undergo extreme purification treatments such as acid washing. One important property of this clay is its high permeability. Fig. 4 shows the grain size distribution, determined from a hydrometer analysis.

Preparation of Kaolinite Samples

Device and Sample Preparation Procedure

The variations among samples should be maintained at a minimum in the experimental study of mechanical behavior of soil. Therefore the kaolinite samples were prepared using a special technique.

Fig. 5 shows the device used preparing the samples. It consists of an aluminum tube 12 inches high and 4 inches in diameter. The inside wall of the tube was lubricated with Dow Corning 200 dielectric fluid in order to reduce friction during consolidation and extrusion of the specimen. The top and bottom end caps were comprised of porous plastic discs, loading plates, and bushings for consolidating the soil. To measure pore pressure and to monitor loading rate during consolidation, a pressure transducer was mounted at the midheight of the tube. The base of the tube was connected to a burette.

A No. 20 U.S. standard sieve (0.840 mm opening) 3 inches in diameter was tied to an electric pencil vibrator to form a vibrating sieve. A procedure, called "wet up," was adopted to prepare the soil sample. Two spoonfuls of air dry kaolinite were placed in the vibrating sieve and sifted into the tube. The water level in the burette was maintained at the level of the soil surface. The soil then imbibed the water gradually

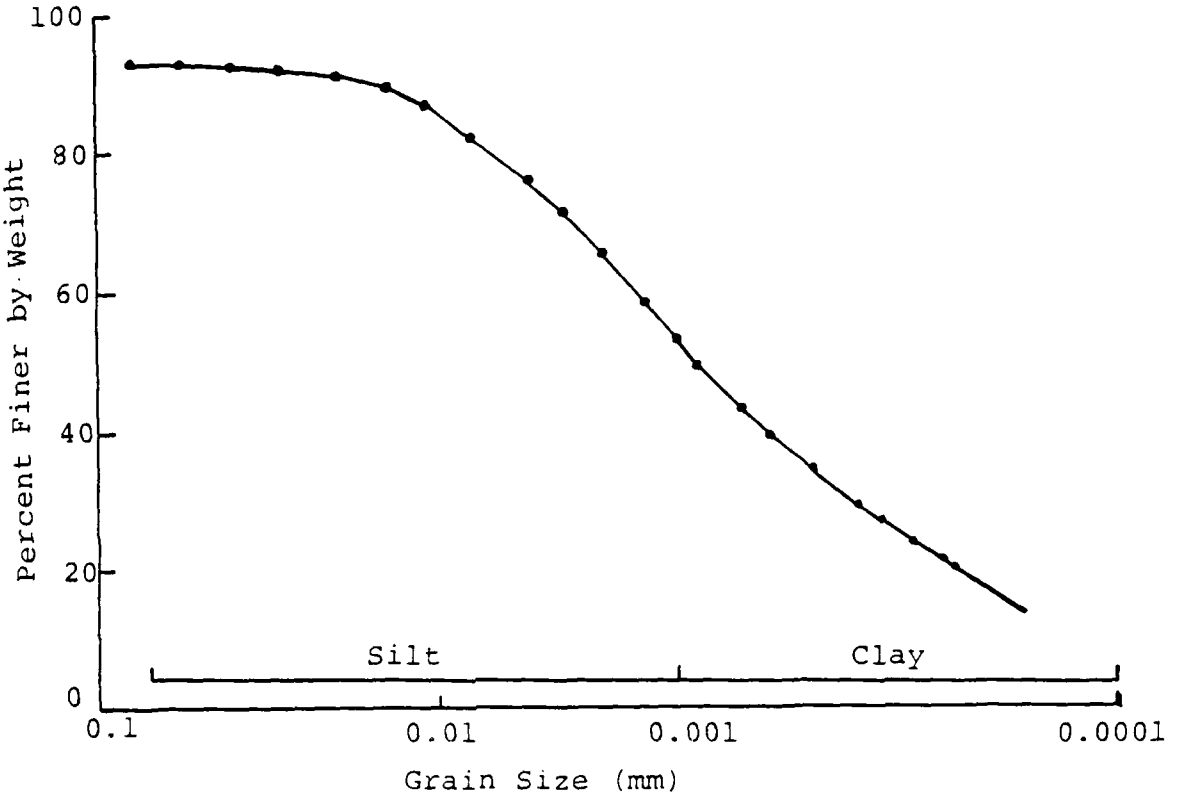

Figure 4
Grain Size Distribution of Kaolinite

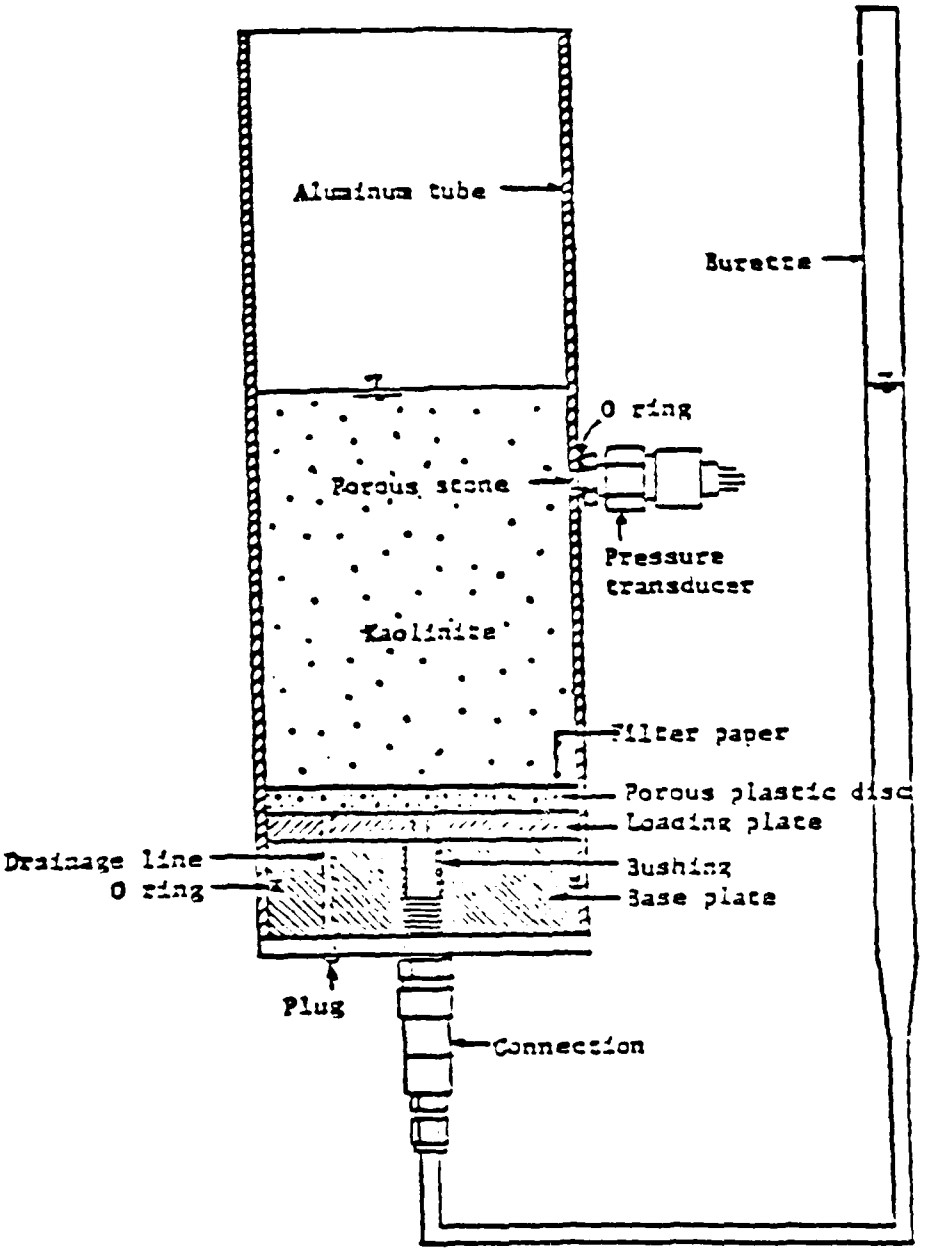

Figure 5

Device Used for Preparation of Kaolinite Samples

[illegible] bottom porous disc until the entire clay mass appeared moist. Then the water level was slowly raised until free water just appeared over the top of the clay. More kaolinite was then sifted into the tube. The procedure was repeated until the desired sample height (about 9 inches) was reached. It has been shown by Martin and Ladd (1970) that this procedure produces a randomly oriented particle structure. The initial water content is about 90 percent.

Consolidation of Slurry

Once the desired height of the soil sample was reached, a sheet of filter paper, a porous plastic disc and a loading plate were placed on the clay surface. The connection at the base was removed. Two loading rams were then inserted through the bushings in the top and the base plates and screwed on the loading plates. Thus, the tube acted as a "floating ring" consolidometer. During consolidation, displacements were directed toward the middle from both top and bottom. scatter in the data points. This may be because of the accuracies in determining the initial compression of soil*, the variations in the initial water content or the possible variations in the degree of saturation. The data could be approximated by a straight line. The water content after consolidation is about 40 percent. The time needed to consolidate the soil to a vertical predetermined pressure depends upon the height of the sample.

* During the attachment of the loading rams to the loading plates and the placment of the tube on the loading machine, the specimen compressed under its own weight and the weight of the loading ram and the plate. The amount of compression was difficult to determine.

Triaxial Test

The triaxial test is a very common soil test which is used in both research and design practice. The outstanding advantages of the triaxial test are the relative ease of preparing the undisturbed sample, the control of drainage conditions and the measurement of pore pressure.

Equipment

All triaxial compression tests were performed in E.L.E triaxial cells. The ram frictions of the triaxial cells were carefully calibrated at the various cell pressures.

The imposed pressures or deformations during the test should be kept as uniform as possible in the experimental study of mechanical behavior of soil. Therefore, the kaolinite samples were tested with enlarged lubricated end platens (Rowe and Barden, 1964; Barden and McDermott, 1965). The top cap is made of lucite and the base platen is made of stainless steel. A membrane, having a thickness of 0.015 inches, was placed between the soil sample and the end platen. The membrane was lubricated with Dow Corning high vacuum grease and was cut at intervals around the perimeter to help relieve the circumferential stress at large strains. The bottom porous stone was 0.31 inches in diameter.

For all samples, only bottom drainage was allowed. Side drains were used for tests with regular end platens.

Setup of Sample

Before the start of each test, the drainage lines were flushed with deaired water. The specimens were carefully

centered between the two end platens. Using a membrane expander, a rubber membrane (Trojan prophylactics) was slipped over the sample. A rubber band was carefully rolled around the sample, forcing out air trapped between the sample and the membrane. The membrane was secured to the platens with two O-rings, and Dow Corning 200 fluid was lightly applied to the membrane. Then the second membrane was placed over the first and fastened securely to the platens with O-rings.

EXAMPLE 1: TRIAXIAL TEST UNDER MONOTONIC LOADING

A triaxial compression test under isotropic consolidation is simulated using the following data:

$E = 210000\ kN/m^2$

$\nu = 0.3$

$P_{co} = 280\ kN/m^2$

$M = 0.772$

$\chi = 700$ (7000 for CSMAR)

$\phi' = 20^o$

Computations are made using both the conventional critical state model (CSM) and the proposed model (CSMAR). Figure 6 shows the (σ_1, σ_3) versus axial strain (ε_1) and volumetric strain versus ε_1 under drained conditions. Figure 7 shows the ($\sigma_1 - \sigma_3$) versus ε_1 and excess pore pressure versus ε_1 for the undrained case. The comparison indicates that results from the CSMAR are almost the same as those from CSM. However, if the direction of principal stress is rotated through 180°, as discussed in example 2, then at some point in the stress path (Point z in Figs. 6 and 7) the stress-strain curve for the CSMAR model would remain unchanged. Figure 8 shows the comparison of ($\sigma_1 - \sigma_3$) versus

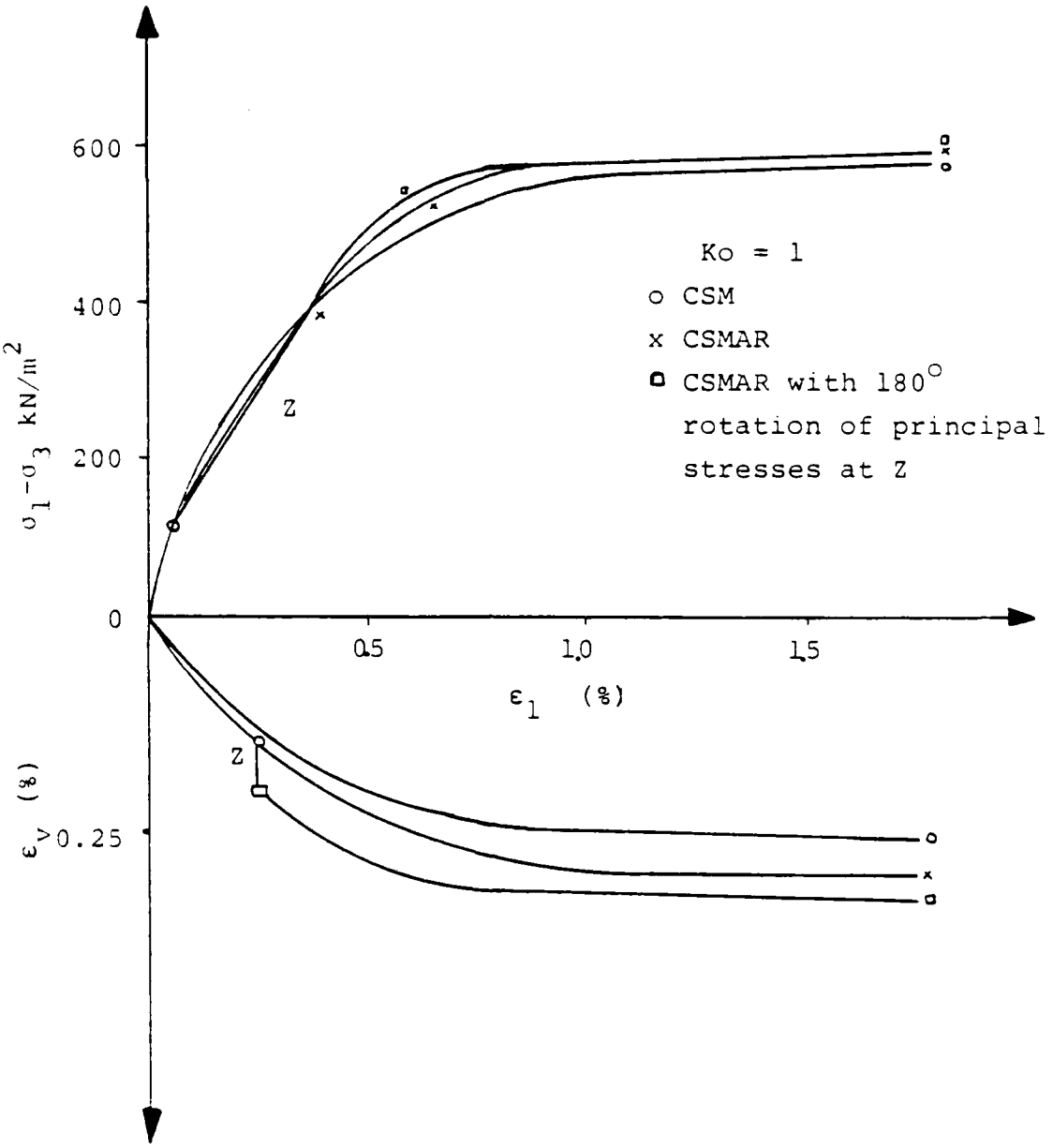

Figure 6
Isotropically consolidated drained triaxial test

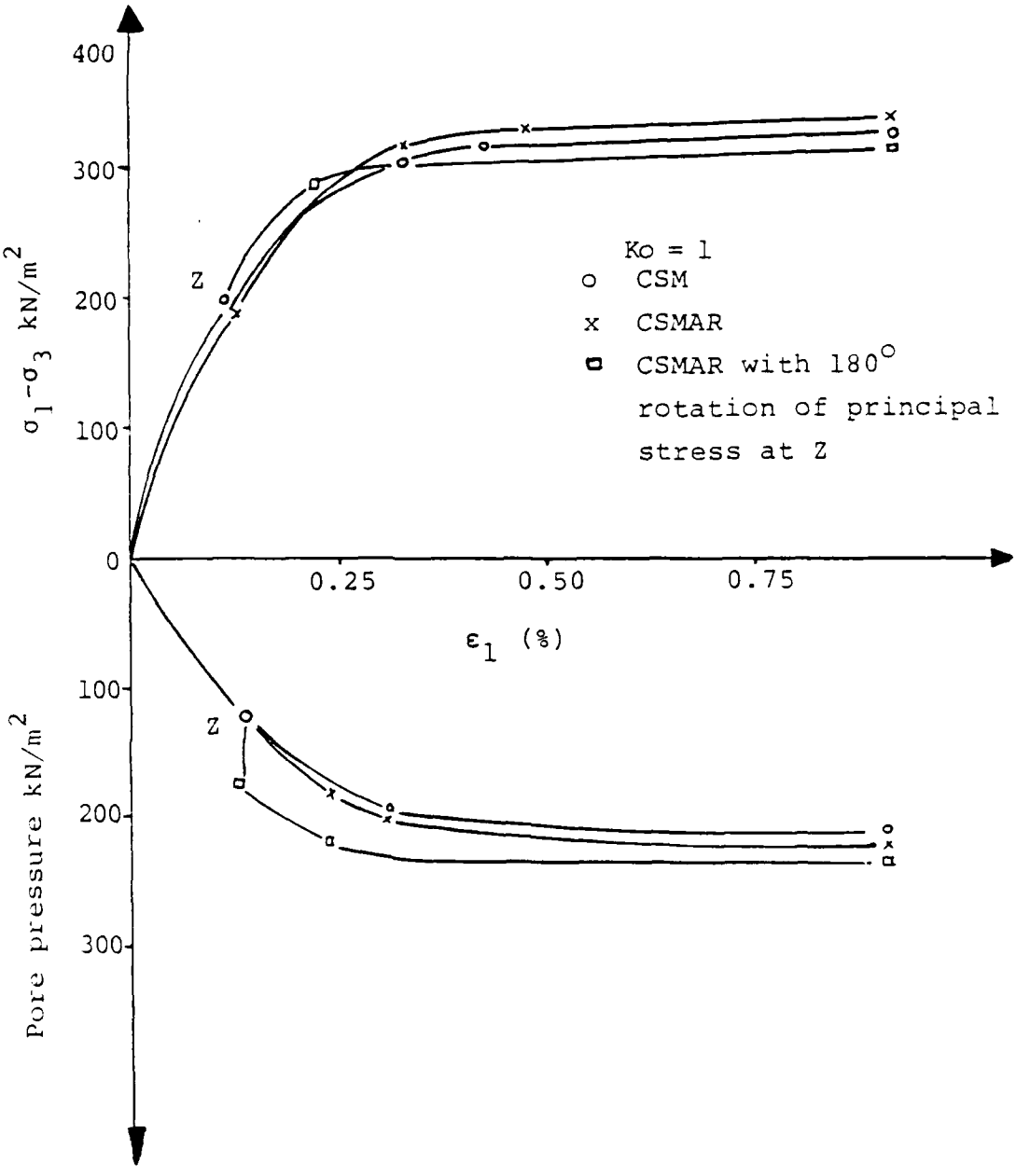

Figure 7

Isotropically consolidated undrained triaxial test

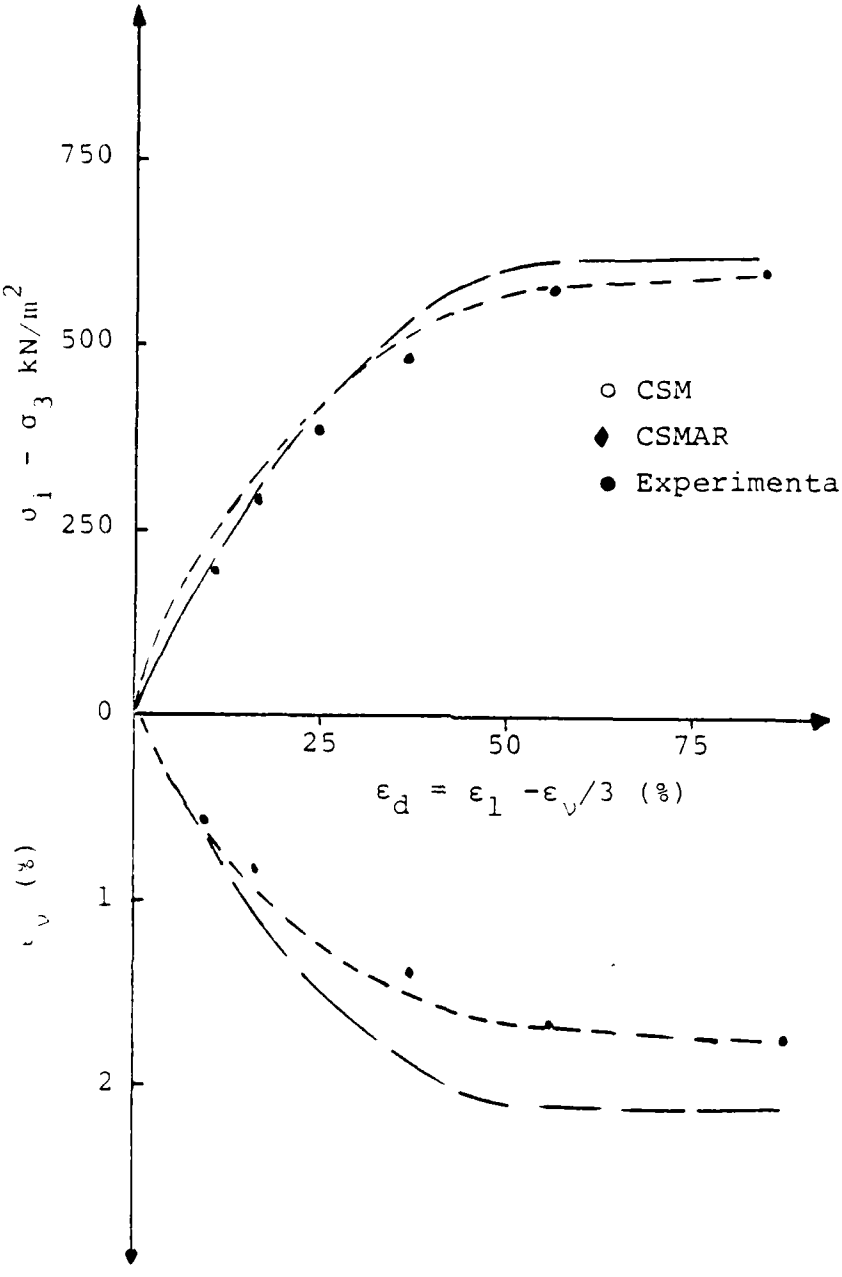

Figure 8

Consolidated drained triaxial test on Boulder Clay

$\varepsilon_d (= \varepsilon_1 - \frac{\varepsilon_v}{3})$ curves for CSM and CSMAR with experimental results of Boulder clay (Naylor, 1975; Jones, 1975). The comparison of $(\sigma_1 - \sigma_3)$ versus ε_d is very good while that of ε_v versus ε_d is reasonable.

EXAMPLE 2: A TRULY TRIAXIAL TEST

In order to illustrate the response of the model to rotation of principal axes, an imaginary truly triaxial test is devised which could, in principle, be performed in the laboratory. It is imagined that a clay specimen is isotropically or anisotropically consolidated to a specified degree. One of the principal stresses is then raised incrementally, keeping the other two principal stresses equal and unchanged. After a few increments, a system of stresses is successively applied so that the magnitude of principal stresses is unchanged but their directions are progressively rotated in the plane passing through major and minor stresses, as shown in Figure 9.

Figure 10 shows the total and effective stress paths followed by the clay element in consolidated drained and undrained tests. The final stress situation at which the rotation of principal axes is induced is shown by a large dot. Using the same data as given in Example 1, computations for plastic strains were made.

Two parameters, r and s, defined, as below were studied.

$$r = \frac{\varepsilon_{II}^{vp} \text{ at } \alpha = \theta}{\varepsilon_{II}^{vp} \text{ at } \alpha = 0} \tag{24}$$

$$s = \frac{\varepsilon_{v}^{vp} \text{ at } \alpha = \theta}{\varepsilon_{v}^{vp} \text{ at } \alpha = 0} \tag{25}$$

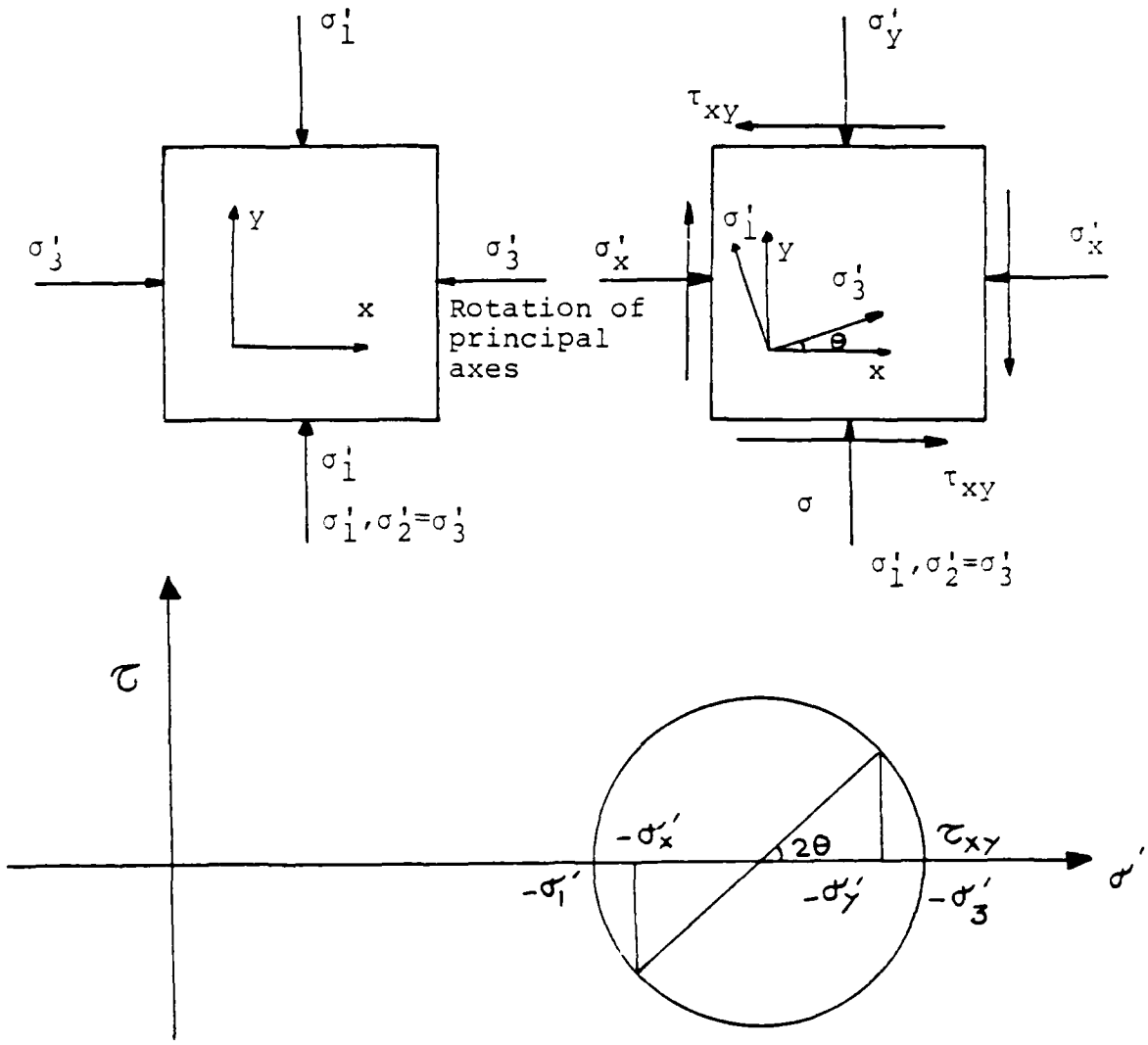

Figure 9

Rotation of principal stress system in an imaginary test

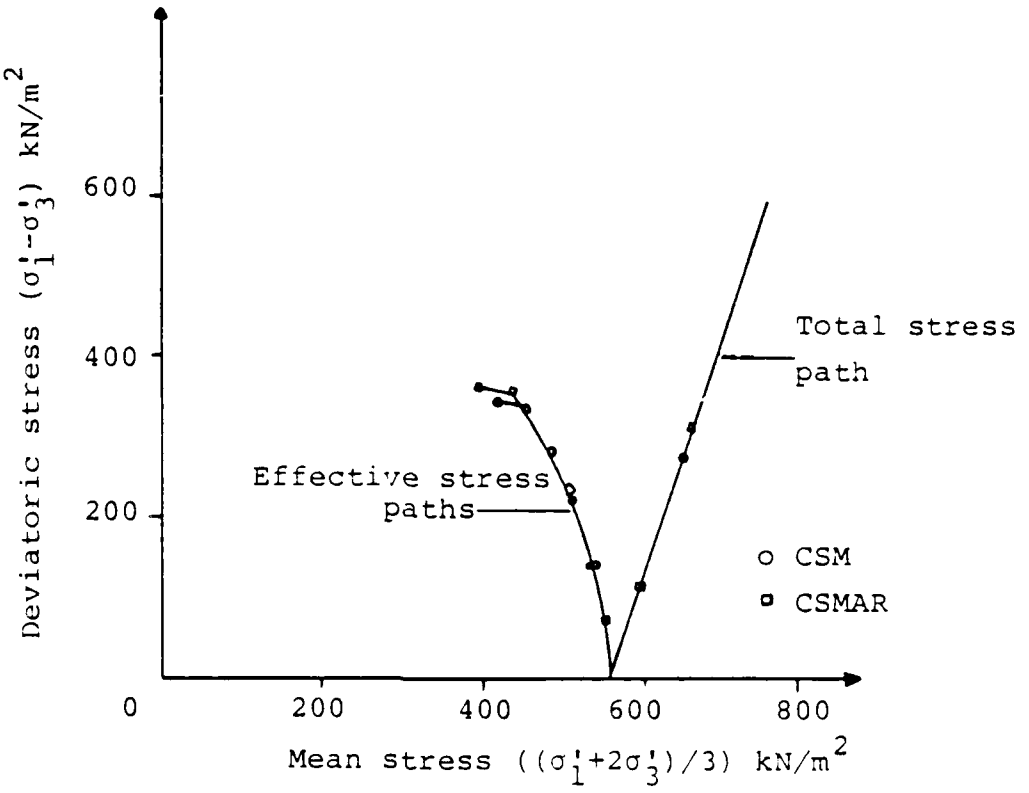

Figure 10

Total and effective stress paths for isotropically consolidated drained and undrained triaxial tests.

where ε_{II} = second invariant of deviatoric viscoplastic strains

$$= \sqrt{2[(\varepsilon_x^{vp})^2 + \varepsilon_y^{vp})^2 + (\varepsilon_z^{vp})^2] + \gamma_{xy}^2}$$

ε_v^{vp} = volumetric viscoplastic strains

θ = the angle which the current major principal stress axis makes with the initial position

Figures (11) and (12) show variation of r and s with θ for consolidated drained and undrained tests for various K_o conditions.

These results clearly indicate that the influence of rotation of principal axis could be considerable.

r and s, which are obviously constant and equal to 1 for critical state model, vary up to nearly 100% in some cases when the CSMAR model is used.

EXAMPLE 3: 'CSMAR' IN CYCLIC TRIAXIAL COMPRESSION TEST

This example shows the behavior of the model in the cyclic triaxial compression test. The parameters chosen for the soil sample are as follows:

$E = 3840$ kN/m^2

$\nu = 0.3$ $\lambda = 0.25$

$\phi' = 30^o$ $\kappa = 0.05$

$P_{co} = 40$ kN/m^2 $e_o = 1.0$

$\chi = 100$

With these parameters, the monotonic failure stress under consolidated undrained conditions is given by $q = \sigma_1'$, $-\sigma_3' = 54.0$ kN/m^2 and $p = \frac{\sigma_1 + 2\sigma_3'}{3} = 44.5$ kN/m^2. Cyclic loading test was performed with q = . The value of other constants related to cyclic loading are as follows:

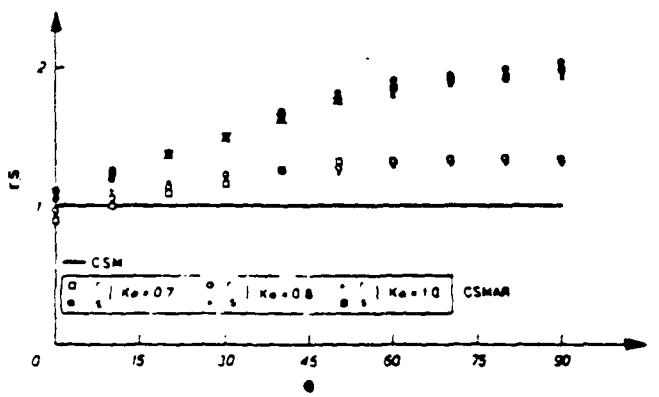

Figure 11. Variation of r and s with θ for consolidated drained triaxial tests for various K_o conditions.

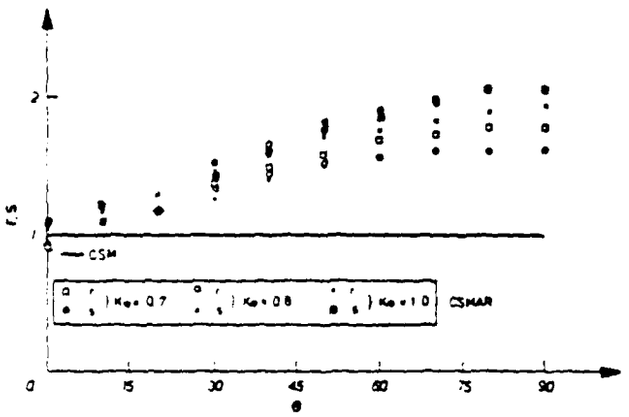

Figure 12. Variation of r and s with θ for consolidated undrained triaxial tests for various K_o conditions.

$K_1 = 0.95$ $\beta = 0.025$

$K_2 = 0.5$

The effective stress path followed by the specimen is shown on a q-p plot in Fig. 13. Fig. 14 shows the pore pressures versus the number of cycles. Fig. 15 shows the q versus deviatoric strain being defined as $\frac{2}{3}(\varepsilon_1 - \varepsilon_3)$ where ε_1 and ε_3 are axial and radial strains.

In this model the generation of pore pressures is initially very gradual. The stress-strain and pore pressure generation curves closely follow the experimentally observed pattern and the cyclic strain softening depends on the level of cumulative cyclic plastic strains on individual planes.

CONCLUSIONS

A micro-structure model which responds to the rotation of principal axes and accounts for the cyclic strain softening has been presented. The model can be further extended to account for cyclic degradation. A nonstructural autogenous strain component has been kept in the formulation to model transient loading conditions. Conceptually very simple, the proposed model can be incorporated in the finite element code very easily.

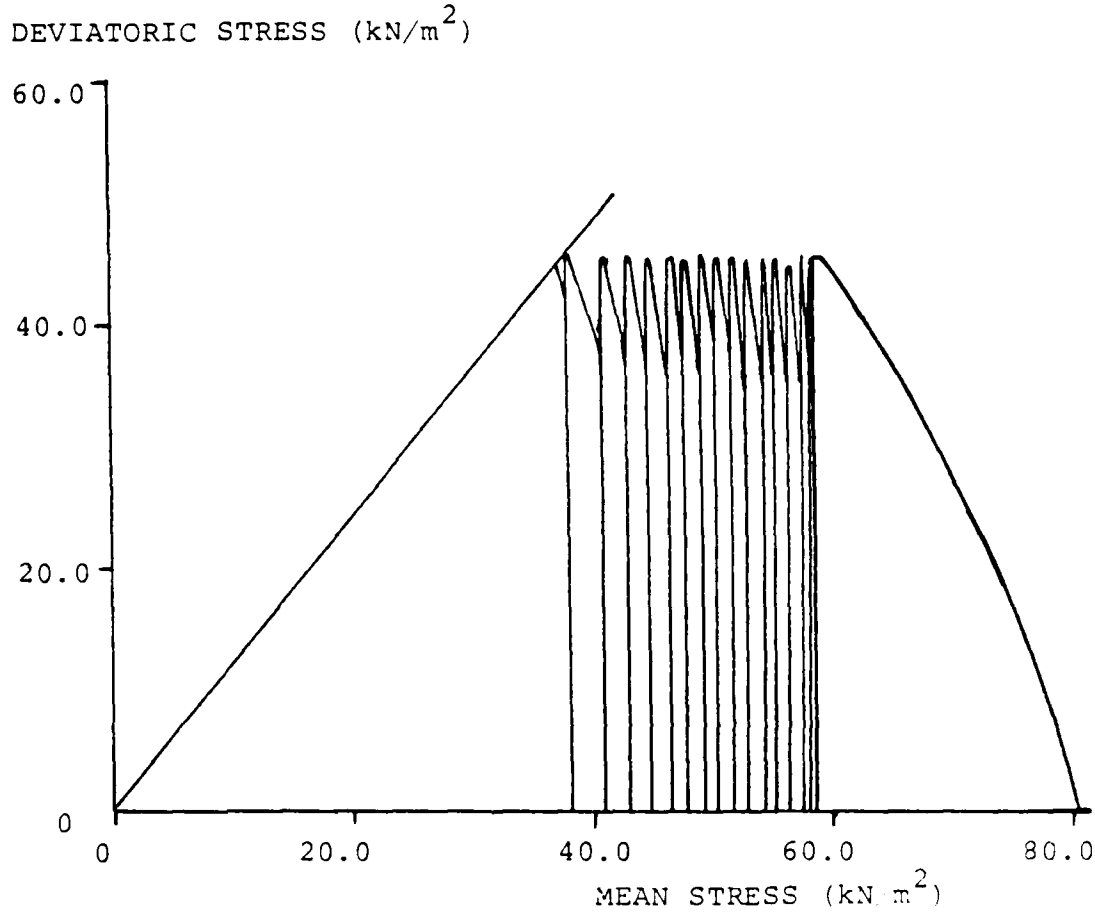

Figure 13

Cyclic Stress Path

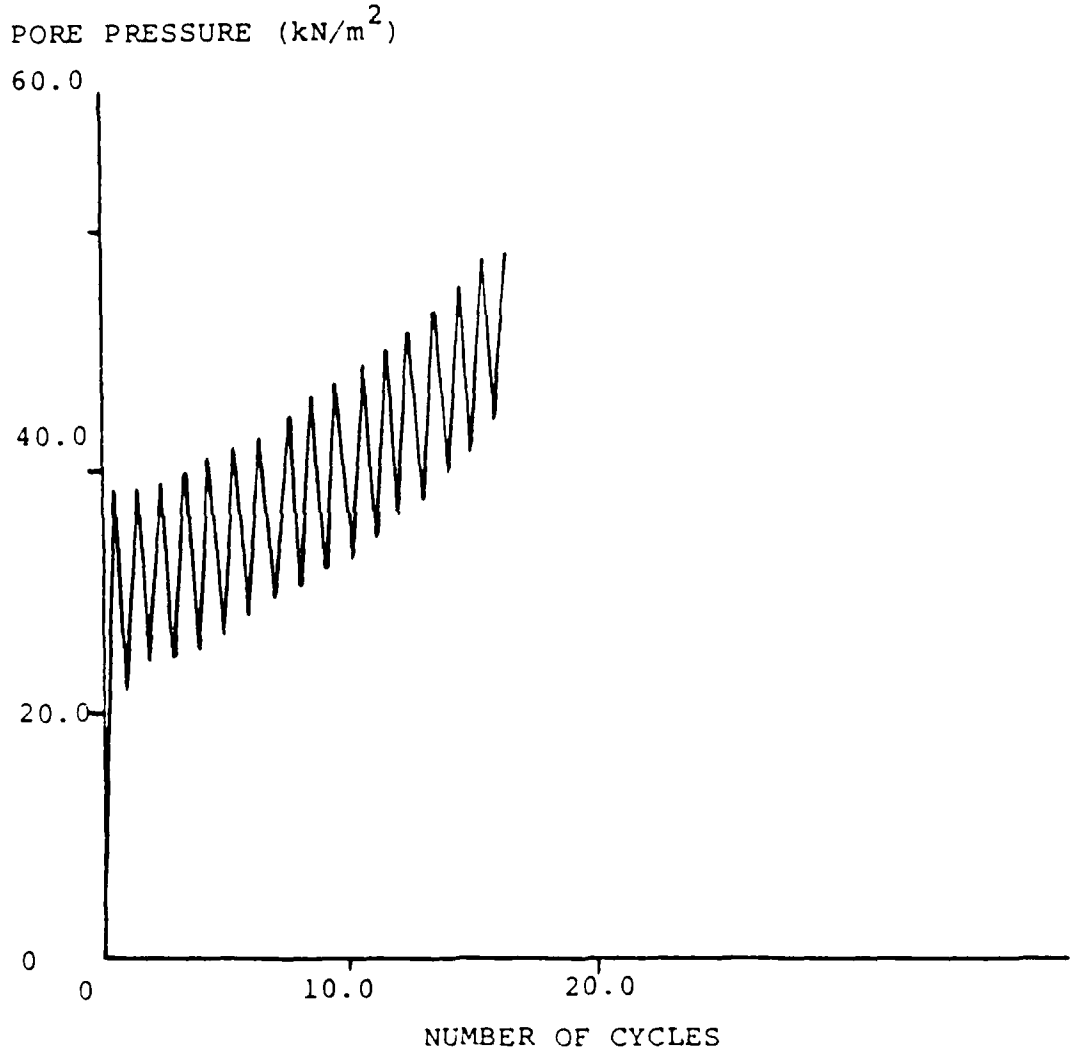

Figure 14
Pore Pressure v/s No. of Cycles

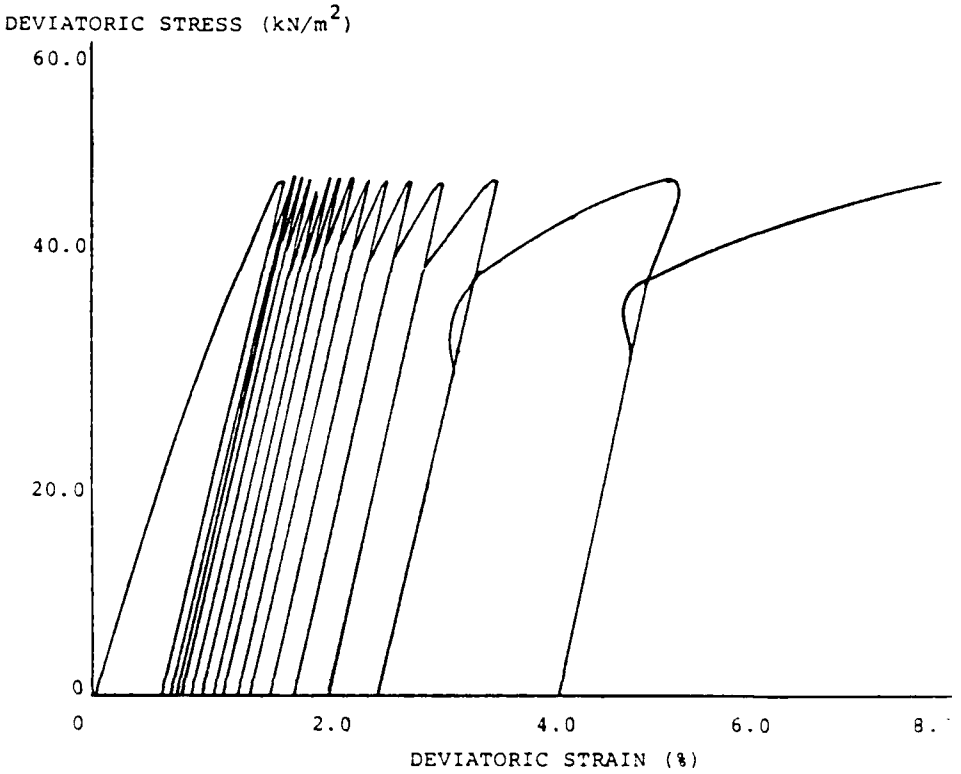

Figure 15
Cyclic Stress Strain Curve

REFERENCES

Barden, L. and McDermott, R.W. 1965, "Use of Free Ends in Triaxial Testing of Clays," Journal of the Soil Mechanics and Foundations Division, ASCE, Vol. 92, No. SM6, 1-23.

Batdorf, S.B. and Budiansky, B. 1949, "A Mathematical Theory of Plasticity Based on the Concept of Slip." National Advisory Committee for Aeronautics, TN1871.

Bowden, F.P. and Tabor, D. 1950, The Friction and Lubrication of Solids. Oxford University Press.

Bowden, F.P. and Tabor, D. 1956, Friction and Lubrication. London - Methuen.

Calladine, C.R. 1971, "A Microstructural View of the Mechanical Properties of Saturated Clay." Geotechnique, Vol. 21, 391-415.

Chang, C.T. 1979, "Nonlinear Response of Earth Dams and Foundations in Earthquakes." Ph.D. Thesis, University of Wales, Swansea.

Cormeau, I.C. 1976, "Viscoplasticity and Plasticity in the Finite Element Methods." Ph.D. Thesis, University of Wales, Swansea.

Drucker, D.C. 1966, "Concepts of Path Independence and Material Stability for Soils." Proc. IUTAM Symposium on Rheology and Soil Mechanics, Grenbole, 1964, 23-46, Springer-Verlag, Berlin.

Georgiannopoulos, N.G. and Brown, E.T. 1978. "The Critical State Concept Applied to Rock." International Journal for Rock Mechanics, Mineral Science, and Geomechanics, Vol. 15, 1-10.

Humpheson, C. 1976, "Finite Element Analysis of Elasto-Viscoplastic Soils." Ph.D. Thesis, University of Wales, Swansea.

Jones, D.B. 1975, "A Nonlinear Elastic Anisotropic Analysis of Llyn Brianne Dam by Finite Element." Ph.D. Thesis, University of Wales, Swansea.

Lade, P.V. and Duncan, J.M. 1975, "Elasto-plastic Stress-Strain Theory for Cohesionless Soil." Journal of the Geotechnical Engineering Division, ASCE, Vol. 101, No. GT10, 1037-1053.

Lee, K.L. and Vernese, F.J. 1978, "End Restraint Effects on Cyclic Triaxial Strength of Sand." Journal of the Geotechnical Engineering Division, ASCE, Vol. 104, No. GT6, 705-719.

Martin, R.T. and Ladd, C.C. 1970, "Fabric of Consolidated Kaolinite." Research Report R 70-15, Soils Publication No. 254, Department of Civil Engineering, MIT.

Mroz, Z., Norris, V.A. and Zienkiewicz, O.C. 1978, "An Anisotropic Hardening Model for Soils and its Application to Cyclic Loading." Int. J. Num. Anal. Meth. Geomech., Vol. 2, 203-221.

Mroz, Z., Norris, V.A. and Zienkiewicz, O.C. 1979, "Application of an Anisotropic Hardening Model in the Analysis of Elasto-plastic Deformation of Soils." Geotechnique, Vol. 29, 1-34.

Nayak, G.C. and Zienkiewicz, O.C. 1972, "Convenient Form of Stress Invariants for Plasticity." Proceedings, ASCE, Vol. 98, 949-954.

Naylor, D.J. 1975, "Nonlinear Finite Element Models for Soils." Ph.D. Thesis, University of Wales, Swansea.

Nova, R. and Wood, D.M. 1979, "A Constitutive Model for Sand in Triaxial Compression." Int. J. Num. Anal. Meth. Geomech., Vol.3, 255-278.

Pande, G.N. 1977, "Nonlinear Finite Element Analysis of Jointed Rock Masses." Ph.D. Thesis, University of Wales, Swansea.

Pande, G.N. and Sharma, K.G. 1979, "A Numerical Framework for the Development of Constitutive Relations of Soils." To be published.

Prevost, J.H. and Hughes, T.J.R. 1975, "Effective Stress-Strain Strength Models for Soils." J. Geotech. Engg. Div., ASCE, Vol. 101, No. GT3, 259-278.

Rowe, P.W. and Barden, L. 1964, "Importance of Free Ends in Triaxial Testing." Journal of the Soil Mechanics and Foundations Division, ASCE, Vol. 90, No. SM1, 1-27.

Roscoe, K.H. and Burland, J.B. 1968, "On the Generalized Stress-Strain Behavior of Wet Clay." Engineering Plasticity, ed. J. Heyman and F.A. Leckie, 535-605, Cambridge University Press.

Sanders, J.L. Jr. 1955, "Plastic Stress-Strain Relations Based On Linear Loading Functions." Proceedings of the 2nd National Congress of Applied Mechanics, ASME, 455-460.

Schofield, A.N. and Wroth, C.P. 1968, Critical State Soil Mechanics. McGraw-Hill, London.

Tabor, D. 1951, The Hardness of Metals. Oxford University Press.

Tabor, D. 1959, "Junction Growth in Metallic Friction: The Role of Combined Stresses and Surface Contamination." Proc. Roy. Soc., Series A251, 378-393.

Taylor, G.I. 1983, "Plastic Strains in Metals." J. Inst. Metals, Vol. 62, 307-324.

Van Eekelen, H.A.M. and Potts, D.M. 1978, "The Behavior of Drammen Clay Under Cyclic Loading." Geotechnique, Vol. 28, 173-196.

Zienkiewicz, O.C. 1977, The Finite Element Method. McGraw-Hill Book Company (U.K.) Ltd., London.

Zienkiewicz, O.C., Humpheson, C. and Lewis, R.W. 1975, "Associated and Nonassociated Viscoplasticity and Plasticity in Soil Mechanics." Geotechnique, Vol. 25, 671-689.

Zienkiewicz, O.C. and Pande, G.N. 1977a, "Time Dependent Multilaminate Model of Rocks - A Numerical Study of Deformation and Failure of Rock Masses." Int. J. Num. Anal. Meth. Geomech., Vol. 1, 219-247.

Zienkiewicz, O.C. and Pande, G.N. 1977b, "Some Useful Forms of Isotropic Yield Surfaces for Soil and Rock Mechanics." Finite Elements in Geomechanics, ed. G. Gudehus, 179-190, John Wiley & Sons, London.

1986 USAF-UES MINI-GRANT PROGRAM

Sponsored by the

AIR FORCE OFFICE OF SCIENTIFIC RESEARCH

Conducted by the

UNIVERSAL ENERGY SYSTEMS, INC.

FINAL REPORT

MICROBIOLOGY OF THE LEGIONELLAE

Prepared by:	Gordon D. Schrank
Academic Rank:	Associate Professor
Department and University:	Department of Biological Sciences St. Cloud State University

Contract No.	F49620-85-C-0013/SB5851-0360
Subcontract No.	S-760-OMG-094/Dr. Gordon D. Schrank Principal Investigator (ISU Proposal No. 86-36ERI-86148)

MICROBIOLOGY OF THE LEGIONELLAE

by

Gordon D. Schrank

ABSTRACT

Efforts were directed at a study of the flagellar antigens of the Legionellae, the recovery techniques for the isolation of the organisms from natural aquatic habitats, and the development of techniques for the isolation of bacteriophage capable of infecting Legionellae. Some differences among species were noted with regard to flagellar antigens. However, continued work is needed in order to consistently produce highly purified preparations of these antigens. Membrane-antigen contamination appears to be a major problem. The occurrence of Legionella-like organisms in natural aquatic habitats follows a seasonal pattern with a maximum number occurring in August. Standard enrichment techniques for phage isolation failed to provide for recovery of these viruses. More work is needed in this area. A lysogenic phage was demonstrated by electron microscopy after treatment of Legionella lab cultures with ultraviolet light. Methods for propagation of this virus are under study.

I. INTRODUCTION:

The family Legionellaceae contains the organism responsible for Legionnaires' Disease (Legionella pneumophila) and an additional number of species which may be associated with human disease. Currently 23 species of Legionella have been proposed (Brenner, et al., 1985). The difficulty in dealing with this large number of species is made more complex by the large number of serogroups (at least 37). This group of organisms has been characterized only recently due, in part, to the fact that Legionella pneumophila was first described in 1977. These organisms are phenotypically unique from other known bacteria. Because the scientific community has had only a short time for to study these organisms, basic research is needed in regard to the microbiology of these organisms.

Areas of study needed have included the resolution of generic designation among the various species. Also, more information is needed regarding the cell structure, composition, and antigen analysis and the methods for routine isolation and propagation of bacteriophages that might infect this group of organisms.

II. OBJECTIVES:

The objectives of this research included: 1) studies of the flagella isolated from various species of Legionella; 2) continued study of methods for improving the isolation of these organisms from potable and nonpotable water supplies; and, 3) the development of techniques for the isolation and characterization of bacteriophages capable of infecting Legionellae.

III. NOMENCLATURE:

Eight Legionella species were used in the present study. These included L. bozemanii, L. dumoffii, L. gormanii, L. micdadei, L.

pneumophila, L. jordanis, L. wadsworthii, and L. longbeachae. All species were serogroup 1 organisms.

IV. ISOLATION AND CHARACTERIZATION OF FLAGELLA:

Elliott and Johnson (1981) first ioslated flagella of Legionella pneumophila. These authors proposed the use of flagellar antigens in serogrouping of Legionellae. This work has been followed by others that have shown differences in passive hemagglutination patterns using various flagellar antigens of the Legionella (Rogers and Laverick, 1984). Therefore, the current study was undertaken to continue characterization of flagellar antigens of the various Legionella sp. An initial study was done using the procedures Elliott and Johnson (1981). Organisms were grown on buffered charcoal yeast extract agar and flagella were removed by passage of the organisms through a 27-guage needle. The flagella were then further purified by cycles of differential centrifugation. Standard polyacrylamide gel electrophoresis (PAGE) of nonsolubilized flagella showed few contaminating proteins (Figure 1). The use of solubilized flagella run on a sodium dodecyl sulfate (SDS)-PAGE gel stained with silver produced a number of unexpected bands (Figure 2). The purity of such preparations prepared by this method were then questioned.

Effort was directed toward other purification procedures. Removal of the flagella in a TRIS buffer contain the nonionic detergent Triton X-100 resulted in flagellar preparations which were then subjected to cesium chloride density gradient ultracentrifugation. Before centrifugation, flagella preparations showed considerable contamination (Figure 3). However, after centrifugation, distinct bands of contaminating vesicles (Figure 4) and flagella (Figure 5) were obtained. However, an SDS-PAGE

analysis of solubilized flagella still showed come unexpected contamination (Figure 6). It should be noted that the number of contaminating bands was smaller than using the first procedure.

These findings would indicate there are some antigenic differences among species, particularly L. pneumophila and L. bozemanii that, when using a more sensitive SDS-PAGE staining procedure (silver stain vs. Coomassie blue stain), additional protein bands exist in the gel and that some species differences exist regarding such flagellar-associated antigens. Therefore, the use of flagella or flagellar associated antigens warrants additional study. Because of species differences, such procedures may have potential for use in differentiating the various species of Legionella. Recent studies of the outer membrane of Legionella by Ehret and Ruckdeschel (1985) would indicate that both membrane and flagellar antigens are important in antigenic differentiation of species.

V. ENVIRONMENTAL ISOLATION:

Eight lakes and one old quarry in the St. Cloud area were routinely tested for the presence of Legionella or Legionella-like organisms. This aspect of the study was conducted during the period from May to September, 1986. Both culture (using concentrated water samples) and fluorescent antibody staining were used to follow the presence of presumptive-Legionella in these natural bodies of water. The term presumptive is used because the identity of isolated organisms was not confirmed using DNA homology testing. Three test sites yielded Legionella-like organisms during early August. Testing at other time periods gave negative results. These findings are similar to those reported by Braun (1982) for natural bodies of water in New York state. Apparently similar ecological factors

such as water temperature and growth of associated organisms (algae) influence the seasonal distribution of Legionella organisms in natural bodies of water in Minnesota.

VI. BACTERIOPHAGE:

Extensive efforts were devoted to the isolation of phage infective for Legionella. This was a very difficult aspect of the study due, in part, to the complex growth requirements of Legionellae in the laboratory. Attempts were made to increase the number of phage present in water from a number of sources. Water from cooling towers and a sewage treatment plant were used. An attempt was made to find host cell populations among laboratory strains as well as the presumptive organisms isolated from the environment. Enrichment was attempted at a variety of temperatures (20°C, 25°C, 30°C, and 37°C) and growth conditions (isolated cultures, shaking cultures, biphasic cultures, and aerated cultures). Several months of efforts were devoted to these studies using all eight laboratory organisms.

Results of such studies would indicate that recovery of phage is difficult; propagation is even more complex. Treatment of laboratory strains of Legionellae with ultraviolet (UV) light and mitomycin C would indicate that a small virus may be recovered after UV treatment (Figures 7 and 8). Recovery of this particle was consistent with UV treatment of Legionellae. This phase of the study must be continued to refine the isolation of both lysogenic and free virus strains. To date, no satisfactory enrichment procedures has been developed although many procdures have been tried.

A number of isolation protocols are under study. These include methods for isolation of phage associated with Streptomyces azureus (Ogata, et al.,

1985), Bacillus sp. (Seldin, et al., 1984), Yersinia ruckeri (Stevenson and Airdria, 1984) and Brucella sp. (Corbel, 1984).

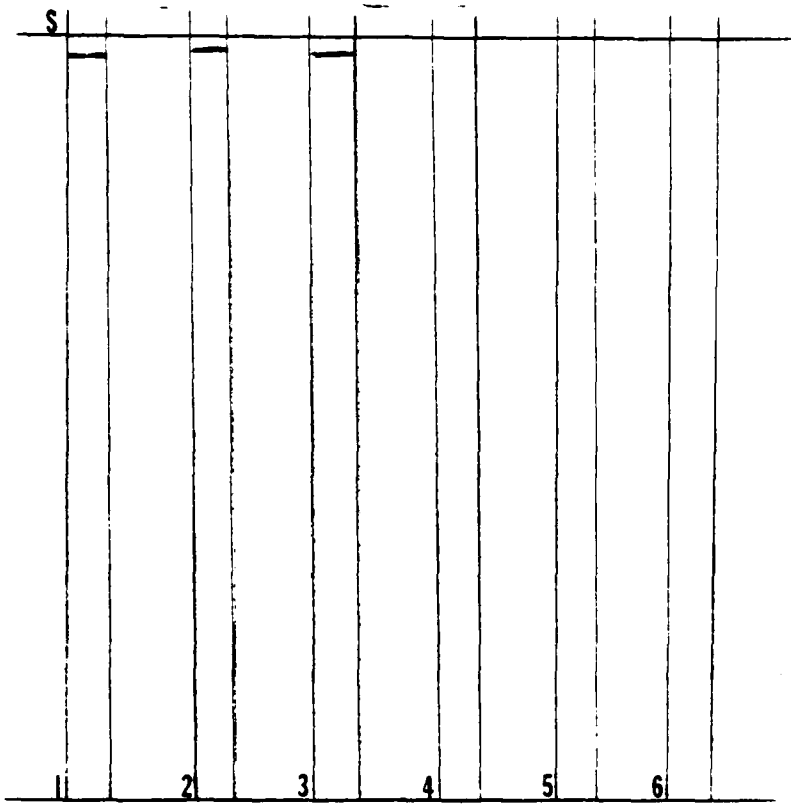

FIGURE 1. Tracing of a standard PAGE analysis of nonsolubilized flagella preparations isolated from six species of Legionellae. None of the preparations showed major contamination with unbound proteins. S = stacking gel; 1 = L. bozemanii; 2 = L. micdadei; 3 = L. longbeachae; 4 = L. gormanii; 5 = L. jordanis; 6 = L. dumoffii.

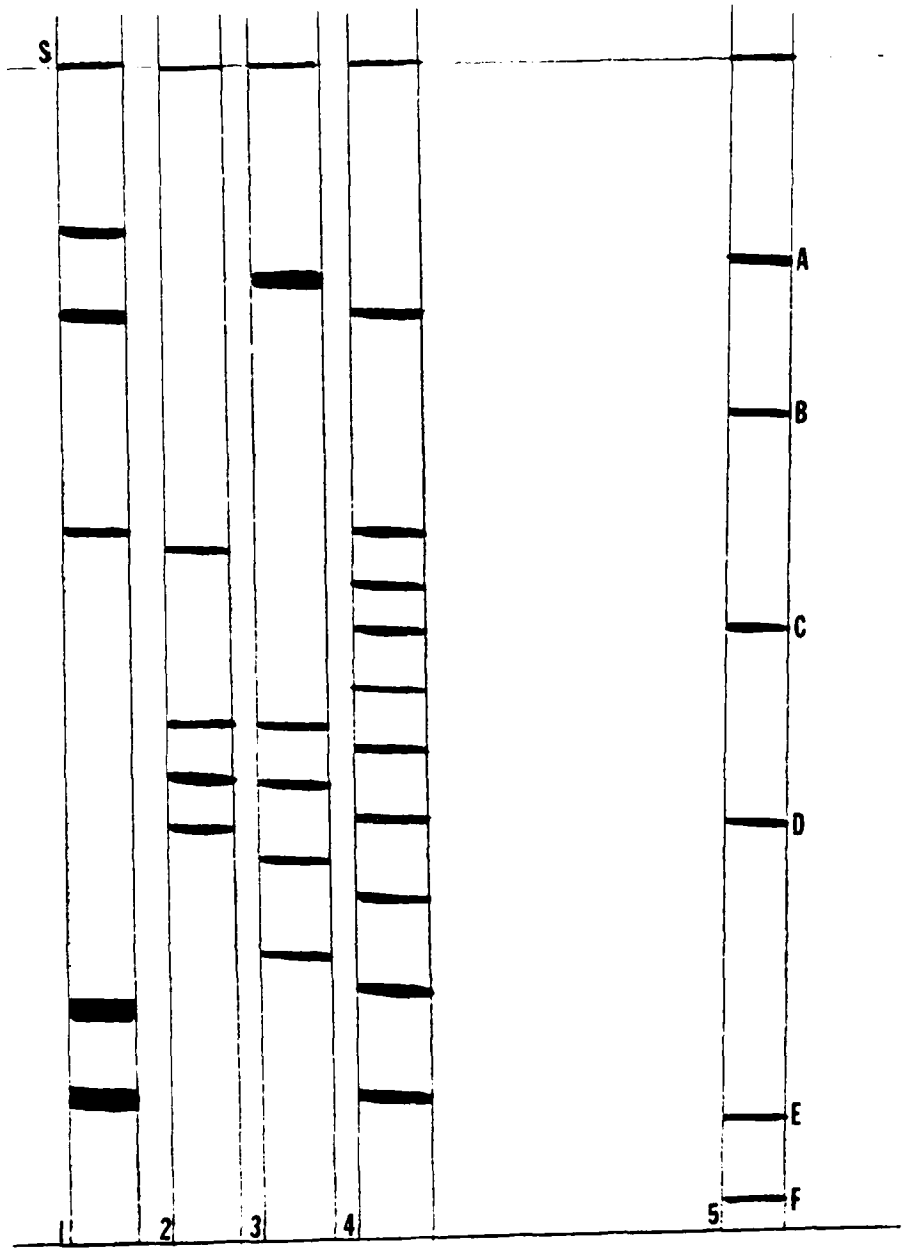

FIGURE 2. Tracing of an SDS-PAGE analysis of solubilized flagella preparations prepared by the method of Elliott and Johnson (1981). A wide distribution of unexpected proteins were observed. Lanes 1-4 represent L. bozemanii, L. micdadei, L. longbeachae, and L. gormanii. Lane 5 represents molecular weight standards with the following molecular weights from top to bottom (A-F): 92,500; 66,200; 45,000; 31,000; 21,500; and 14,400. The S represents the region of the stacking gel.

FIGURE 3. Electron micrograph of flagella prepared from L. bozemanii by the method of Elliott and Johnson (1981). Note extensive contamination with vesicular, membrane-like material. (Magnification: x40,000).

FIGURE 4. Electron micrograph of the vesicular fraction obtained after cesium chloride density gradient centrifugation. (Magnification: x27,000)

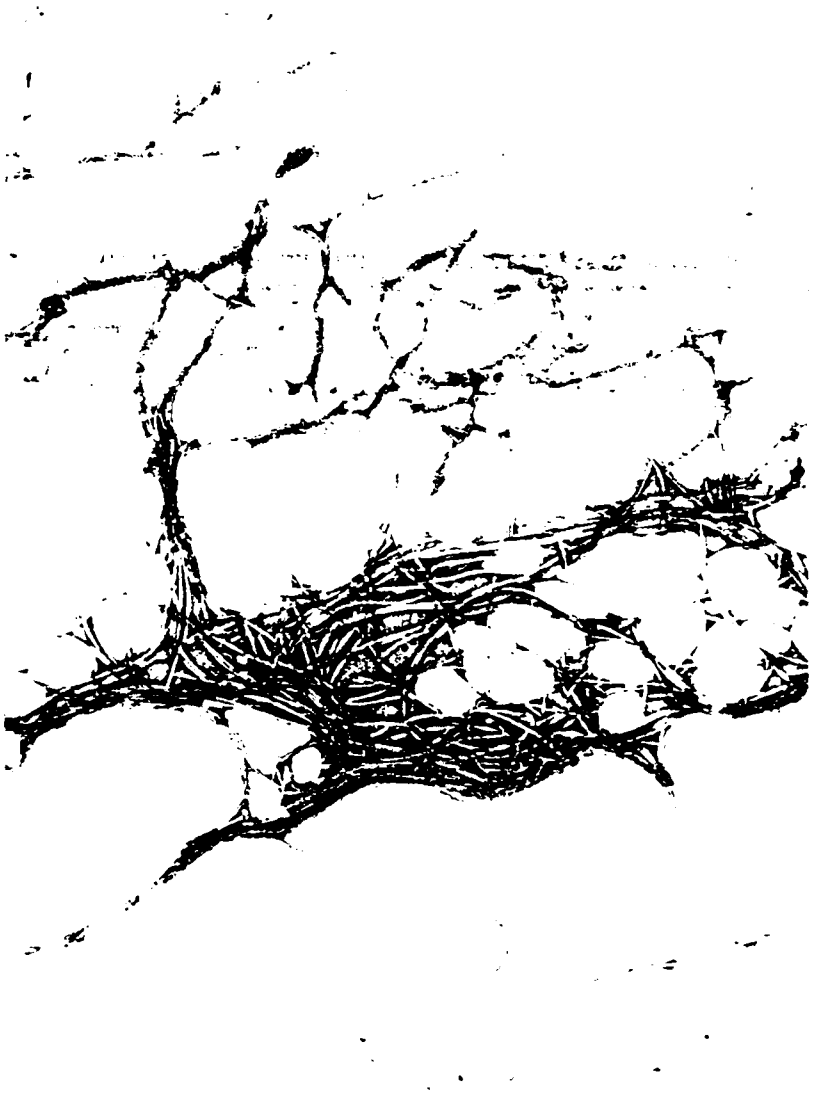

FIGURE 3. Electron micrograph of the flagellar fraction obtained from L. bozemanii after cesium chloride density gradient ultracentrifugation. Note the preparation appears to be clear of membraneous contamination. (Magnification: x20,000).

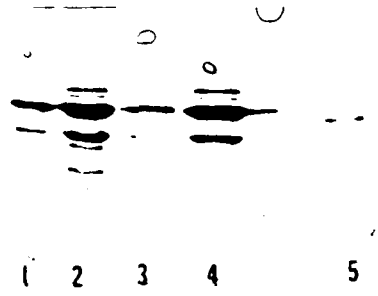

FIGURE 5. Direct photographic impression of an SDS-PAGE slab gel preparation comparing preparations of solubilized flagella from L. bozemanii (Lanes 1 and 3) and L. pneumophila (Lanes 2 and 4). The marker in Lane 5 has a molecular weight of 45,000. The preparations after density gradient centrifugation were clearly purer than earlier preparations with major bands, as expected, in the range of a molecular weight of 45,000.

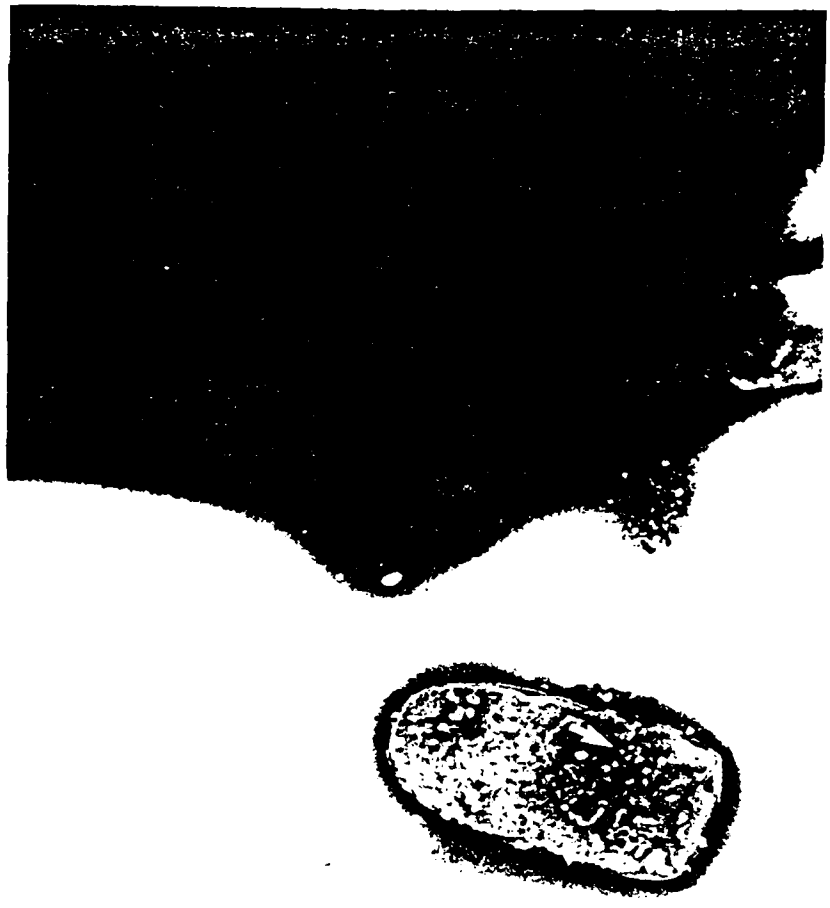

FIGURE 7. Electron micrograph of a preparation of L. pneumophila after treatment with ultraviolet light for 20 seconds. Note the appearance of small particles on the surface of the organism (arrow). (Magnification: x20,000)

AD-A186 492 UNITED STATES AIR FORCE RESEARCH INITIATION PROGRAM 11/11
1985 TECHNICAL REPORT VOLUME 2(U) UNIVERSAL ENERGY
SYSTEMS INC DAYTON OH R C DARRAH APR 87
UNCLASSIFIED AFOSR-TR-87-1718 F49620-85-C-0013 F/G 15/3 NL

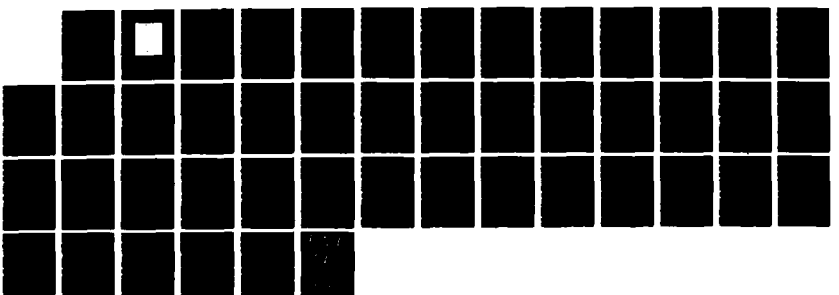

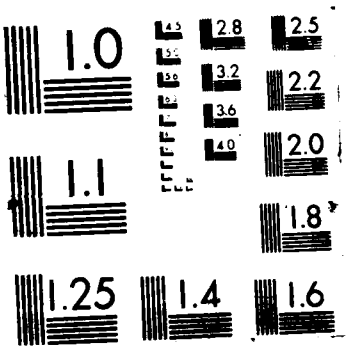
1.0
1.1
1.25
1.4
1.6
1.8
2.0
2.2
2.5
2.8
3.2
3.6
4.0

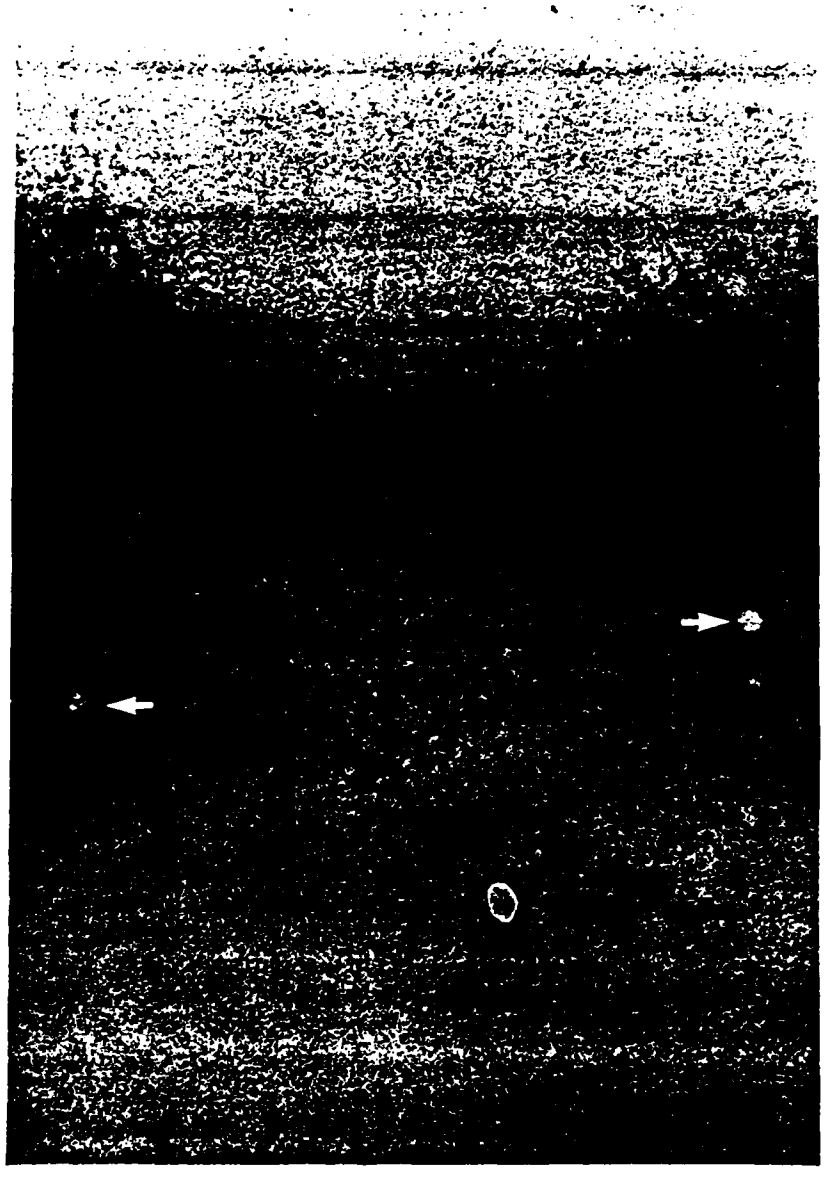

FIGURE 8. Electron micrograph of the appearance of the particles seen in the previous micrograph after partial purification by low and high speed centrifugation. (Magnification: x80,000)

REFERENCES

Braun, E. B. 1982. Factors affecting the distribution, seasonal response and control of Legionella pneumophila in aquatic environments. Ph.D. Dissertation, Rensselaer Polytechnic Institute, Troy, New York.

Brenner, D. J., et al. 1985. Ten new species of Legionella. International Journal of Systematic Bacteriology 35:50-59.

Cobel, M. J. 1984. Properties of Brucella-phages lytic for non-smooth Brucella strains. IN Development of Biological Standards, Vol. 56, S. Karger, Basel.

Ehret, W. and G. Ruckdeschel. 1985. Membrane proteins of Legionellaceae: II. Serogroup-specific and species-specific antigens in the outer membrane of Legionella pneumophila. Zentralbl. Bakteriol Mikrobiol. 260:184-196.

Elliott, J. A. and W. Johnson. 1981. Immunological and biochemical relationships among flagella isolated from Legionella pneumophila serogroups 1, 2, and 3. Infection and Immunity 33:602-610.

Ogata, S., et al. 1985. A temperate phage of Streptomyces azureus. Applied and Environmental Microbiology 49:201-204.

Rogers, F. G. and T. Laverick. 1984. Legionella pneumophila serogroup 1 flagellar antigen in a passive hemagglutination test to detect antibodies to other Legionella species. IN Legionella, proceedings of the 2nd international symposium. American Society for Microbiology, Washington D.C.

Seldin, L., et al. 1984. Bacillus polymyxa bacteriophages from Brazilian soils. Antonie van Leeuwenhoek 50:39-51.

Stevenson, R. M. W. and D. W. Airdrie. 1984. Isolation of Yersinia ruckeri bacteriophages. Applied and Environmental Microbiology 47:1201-1205.

FINAL REPORT NUMBER 60
REPORT NOT RECEIVED IN TIME
WILL BE PROVIDED WHEN AVAILABLE
Dr. Ronald Sega
760-OMG-107

MOLECULAR MODELING OF PHARMACOKINETIC DATA

A report by

Paul G. Seybold, Ph.D.
Departments of Chemistry and
Biological Chemistry
Wright State University
Dayton, Ohio 45435

to the

AIR FORCE OFFICE OF SCIENTIFIC RESEARCH
MINI GRANT PROGRAM
conducted by
UNIVERSAL ENERGY SYSTEMS, INC.
4401 Dayton-Xenia Road
Dayton, Ohio 45432

Date: November 10, 1986

USAF Laboratory: Biochemical Toxicology Branch
Aerospace Medical Research Laboratory
Wright Patterson AFB, Dayton, Ohio

USAF Investigator: Melvin E. Andersen, Ph.D.

I. INTRODUCTION

This work represents a continuation and expansion of studies originally carried out during a faculty summer research fellowship period (1). In connection with the computer-based pharmacokinetic model for inhaled vapors developed by Andersen et al. (2,3), research was begun on means for estimating the tissue solubilities and kinetic parameters of halogenated hydrocarbons based solely on the structures of the compounds. In the present work these preliminary studies have been extended and amplified. The results reported stem from the efforts of graduate students Michael L. Gargus and Steve Dixon, undergraduate student Diane E. Brooker, and the principal investigator. Reported are the extension of the structure-solubility relationships to include new compounds, the examination of new parameter approaches, computer hardware and software developments, and the status of investigations of the kinetic parameters. Only brief summaries of the major results are presented; more in-depth treatments are available in internal reports of our research group.

II. STRUCTURE-SOLUBILITY RELATIONSHIPS

In our original studies a set of 25 halocarbons was examined (1). This original set contained mostly chlorinated halocarbons and relatively few fluorinated and brominated species. To improve our understanding of the physical properties of the latter species seven fluorinated and brominated compounds were added to expand the data set to 32 compounds. Broadly speaking, no dramatic changes were observed in the forms of the resulting regression equations obtained for eight representative physical properties; on the whole the connectivity indices yielded slightly worse fits for the expanded data set and the *ad hoc* descriptors yielded slightly improved fits. As expected, error limits for the coefficients of the numbers of fluorine and

bromine atoms in the ad hoc descriptor regression equations were improved substantially, allowing more meaningful comparisons of the influences of these halogen atoms.

A number of different possible improvements in the parameterization schemes for the halocarbons were explored. In the earlier work the Wiener distance approach was found to be inadequate for description of the tissue solubilities and physical properties of the halocarbons (1). This was attributed to the failure of the original Wiener scheme to take into account the electronic differences among halogen atoms. A scheme purporting to do so has been proposed by Barysz et al. (4). This scheme was tested, but also failed to yield any significant improvement in the analysis of the physical properties and tissue solubilities. We conclude that an adequate electronic parameterization for the Wiener scheme remains to be developed.

Molecular volumes and surface areas have frequently been suggested as significant factors influencing solubility. E.g., Leo et al. (5) have argued that cavity size (molecular volume) is a key determinant of the octanol/water partition coefficient. Therefore molecular volumes and surface areas calculated by several methods were tested as modeling parameters for the halocarbon oil, water and saline solubilities. To account for electronic effects molar refraction (MR) and the polar hydrogen factor Q_H (see below) were included. In no case was a good regression fit obtained using volume or surface area, although a satisfactory fit for the oil/air partition coefficient (modeled as its logarithm, $r^2 = 0.961$) was obtained using MR and Q_H alone.

Information indices have been used successfully to model a variety of properties (6,7). The ability of such indices, using Kier's "negentrophy" definition (7), to model halocarbon solubilities was examined. The results were disappointing, and no satisfactory model for solubility was obtained using these indices.

coefficients, physical properties, and structural parameters of these compounds. Both orthogonal and oblique rotations were employed. The results were both interesting and informative. For the six partition coefficients two significant dimensions were found, accounting for 97.7% of the variation in the data. These dimensions can be interpreted as representing lipid and saline solubilities. Analysis of the physical properties indicated that the majority of these properties were heavily loaded on a factor most reasonably identified as representing dispersion forces, or in Cramer's terminology (14), a "bulk" dimension. Melting points and water solubilities appeared largely as separate dimensions. For the structural parameters, six Wiener indices accounted for 3 dimensions, eleven convectivity indices 7 dimensions, and six ad hoc descriptors, 5 dimensions. The greater dimensionalities of the connectivity indices and the ad hoc descriptors compared to the Wiener indices may explain, at least in part, the greater success of these indices in modeling the properties of the 25 halocarbons.

III. COMPUTER DEVELOPMENT

Through a separate grant from the State of Ohio it was possible to purchase several important computer hardware items, greatly enhancing our abilities to perform a variety of calculations relevant to the present project. A DEC VT 241 color graphics terminal and a Tektronics 4107A color graphics terminal were initially purchased. Both allow excellent communications with Wright State University's mainframe computers, most importantly the VAX 11/785. In conjunction with these purchases we were fortunate to acquire from colleagues at other universities two graphics software packages, PLUTO and MODEL, both of which allow simplified compound structure input and display. Other software acquisitions allow us now to perform a variety of calculations ranging from Allinger's empirical molecular

In our previous work the polar hydrogen factor Q_H developed by Di Paolo et al. (8) was employed and found to be an important descriptor for both halocarbon tissue solubilities and physical properties (1). This parameter is intended to represent the influences of the polarized carbon-hydrogen bonds arising from the inductive effects of nearby halogens. The origins of this parameter are somewhat obscure, and it was deemed useful to explore alternative ways of representing this important structural property. Alternative schemes developed by Hansch et al. (9) and Davies et al. (10) were examined in detail, but were judged to be less useful than the Q_H model of Di Paolo et al. (8). However, it was noted that a simplified form of Q_H which treats all halogens as equivalent, yields results virtually identical to those for Q_H.

In addition to the above studies, more sophisticated measures of carbon-hydrogen bond polarity were also examined. Gasteiger and co-workers (11) have developed an emperical scheme based on partial equalization of orbital electronegativities (PEOE) that appears to yield excellent values for atomic charges in atoms. A computer program was developed to perform PEOE calculations, and charges on the atoms of our basic set of 25 halocarbons were determined. Based on these charges a wide variety of potential "polarity" parameters was developed and tested. Most failed to yield improvements; however, several indices based on halogen-halogen and halogen-hydrogen interactions led to improved regression equations for both water and saline solubilities of the halocarbons. The theoretical significance of these latter indices remains to be elucidated.

Factor analysis is a statistical technique which allows one to gain insight into the inherent dimensionality of a set of properties or other variables (12,13,14). In order to better understand the properties of our set of 25 halocarbons the method of factor analysis was applied to the partition

mechanics method through semiempherical (e.g. INDO, MNDO, AM1) and ab initio molecular orbital calculations. Because of the great value of having a flexible menu of techniques at our disposal, considerable effort was expended to acquire, set up, and integrate these programs into our graphics system.

In some cases it proved desirable or necessary to write our own programs. Programs were developed for the following purposes: (1) calculation of information indices, (2) accurate calculation of molecular surface (cavity) areas, and (3) calculation of atom charges by the PEOE method (11). In addition, programs were written to interface the MOPAC (MINDO, MNDO, AM1) program and the GAUSSIAN 82 ab initio program with our PLUTO color graphics system.

IV. KINETIC PARAMETERS

Because of the time required for the new developments in structure property relationships and in the computer hardware and software areas, only a very modest amount of time could be spent on beginning to examine the observed enzyme (Michaelis-Menten) kinetic parameters. As expected, an attempt to model these kinetic parameters using the structural parameters employed previously for solubilities was not successful. A review was begun of the current state of knowledge of the mode(s) of action of the cytochrome P-450 enzymes and of previous attempts to calculate relevant behaviors of halogenated hrdrocarbon in the context of their metabolism by the P-450 enzymes. It is anticipated that rather sophisticated molecular orbital techniques will be required in order to understand the observed kinetic parameters.

REFERENCES

1. Seybold, P.G., AFOSR Summer Faculty Research Fellowship, Biochemical Toxicology Branch, AAMRL/WPAFB, Dayton, Ohio, Summer, 1985. See final report to AFOSR/Universal Energy Systems, Inc., Sept. 1985.
2. Andersen, M.E., Neurobehav. Toxicol. Teratol. 3, 383-389 (1981).
3. Ramsey, J.C., and M.E. Andersen, Toxicol. Appl. Pharmacol. 73, 159-175 (1984).
4. Barysz, M., G. Jashavi, R.S. Lall, V.A. Srivastava and N. Trinajstic, in Chemical Applications of Topology and Graph Theory, R.B. King, Ed., Elsevier, New York, 1983.
5. Leo, A., C. Hansch, and P.Y.C. Jow, J. Med. Chem. 19, 611 (1976).
6. D. Bonchev, Information Theoretic Indices for Characterization of Chemical Structures, Research Studies Press, John Wiley &Sons, New York, 1983.
7. Kier, L.B., J. Pharm. Sci. 69, 807 (1980).
8. Di Paolo, T., L.B. Kier, and L.H. Hall, J. Pharm. Sci. 68, 39 (1979).
9. Hansch, C., A. Vittorio, C. Siliko, and P.Y.C. Yow, J. Med. Chem. 18, 546 (1975).
10. Davies, R.H., R.D. Bagnoll, and W.G.M. Jones, Int. J. Quantum Chem. QBS3, 171 (1976).
11. Gasteiger, J. and M. Marsili, Tetrahedron 36, 3219 (1980).
12. Kim, J. and C.W. Mueller, Introduction to Factor Analysis, Sage Publications, Beverly Hills, 1978.
13. Kim, J. and C.W. Mueller, Factor Analysis, Sage Publications, Beverly Hills, 1978.
14. Cramer, R.D., J. Am. Chem. Soc. 102, 1837, 1849 (1980).

FINAL REPORT

DIGITAL SIMULATION OF SURFACE-TO-AIR MISSLES AND SMOOTHING OF CINETHEODOLITE AND RADAR DATA

Sponsored by the

AIR FORCE OFFICE OF SCIENTIFIC RESEARCH

Conducted by the

UNIVERSAL ENERGY SYSTEMS, INC.

Prepared by: Shawky E. Shamma

Academic Rank: Professor of Mathematics/Statistics

Department: Institute for Statistical and Mathematical Modeling

University: University of West Florida
Pensacola, FL 32514-5751

Date: August 1986

ABSTRACT

Several computer programs for numerical solution of systems of 1st order differential equations have been written for testing and implementation in the digital simulation for the dynamics of surface-to-air missiles. Another computer program for smoothing noisy data with spline functions have been developed for use in smoothing of Cinetheodolite and Radar Data for Missiles and Bombs.

The smoothing program can be modified to achieve higher degree of smoothing dependent on the nature of data. This can be accomplished by developing "automatic" methods for choosing the smoothing parameter using cross-validation methods.

I. Introduction

This report summarizes the development of more accurate methods for digital simulation of surface-to-air missiles and smoothing of cinetheodolite and radar data for missiles and bombs.

II. Methods for digital simulation of surface to air missiles:

Missile simulation models are 5 degree-of-freedom models. The missile is assumed roll stabilized and flies in the 'X' configuration. That is, the aerodynamic data base supports three lateral accelerations and only two rotational accelerations. Each of these is computed in a body coordinate system where the principal axis is coincident with the missile longitudinal axis. The other two axes are each orthogonal and lie in the planes containing the yaw and pitch control surfaces respectively.

The lateral accelerations are computed using

$$\dot{U} = f_1(C_a, C_n, C_y, C_m, C_n, P, q, A_{13}, g, W, V, S, V_m)$$

$$\dot{V} = f_2(C_y, S, V_m, U, A_{23}, g)$$

$$\dot{W} = f_3(p, V_m, S, C_n, U, q, g, A_{33}$$

and the two rotational accelerations are computed from

$$\dot{q} = f_4(P, V_m, S, d, C_m, I_{yy})$$

$$\dot{r} = f_5(p, V_m, S, d, C_n, I_{yy})$$

where $f_1, \ldots, f_5$ are defined functions of

C_a, the axial force coefficient

C_n, the normal force coefficient

C_y, the side force coefficient

C_m, the pitching movement coefficient

C_n, the yawing movement coefficient

p, the air density

S, the surface area

V_m, the total missile velocity

d, the reference diameter

g, the gravitational acceleration

A_{ij}, the elements of the body to inertial transformation matrix

I_{yy}, the pitch-yaw moment of inertia

In order to compute the missile miss distance, we must keep track of the missile in an inertial coordinate system. Using an inertial system with its origin at the missile launch point and the three axes being positive in the north, east and down directions respectively, the angular motion is expressed in the inertial system by

$$\dot{\psi} = (q \sin \phi + r \cos \phi)/\cos \phi$$

$$\dot{\theta} = q \cos \phi - r \sin \phi$$

$$\dot{\phi} = \dot{\psi} \sin \theta .$$

The initial conditions of ψ, θ, and ϕ are taken to be the angular orientation of the missile launcher at time of launch. The body velocities U, V, and W are rotated into the inertial system to obtain

$$\begin{bmatrix} \dot{X} \\ \dot{Y} \\ \dot{Z} \end{bmatrix} = (Aij) \begin{bmatrix} U \\ V \\ W \end{bmatrix}$$

Thus, in all, eleven parameters (five in the body system and six in the inertial system) are to be integrated numerically.

Let us arrange the above equations in the form $d\underline{y}/dt = \underline{f}(t,\underline{y})$ where $\underline{y}$ is the vector containing the eleven unknown parameters.

The sponsor uses a "modified Euler scheme" to integrate the above system of governing differential equations. An examination of the underlying theory of numerical integration of differential equations reveals that such a scheme is one of a larger class of solvers denoted in the literature as the class of one-step implicit methods of order one:

$$\underline{y}_{i+1} = \underline{y}_i + h\left[(1-\theta)\ \underline{f}_{i+1} + \theta \underline{f}_i\right] ,$$

such algorithm is stable if and only if $\theta \leq 1/2$.

It is known that explicit numerical methods of higher order have rather small regions of absolute stability when the system is "stiff" due to broad varying rates of some components of the system. On the other hand, implicit methods have a some what larger region of stability. However, recently developed methods combine the predictor - corrector schemes and implicit schemes for use when the system is stiff. In this option corrector's equation is replaced by implicit methods and direct iteration of the corrector is replaced by a form of Newton or fixed point iteration. Both step size and order are variables in such schemes and the computer programs can automatically change order as well as step length; the strategy here being to minimize the computational effort required for local errors to be less than a stipulated bound.

Unfortunately, it was found that variable step-size methods can not be implemented in the overall missile models used by the sponsor because the use of fixed step size is inherent in other parts of their subroutines. However since the grant calls for developing such a program, we present here a program of

higher order and variable step size that may be useful in modeling other problems that permit the use of variable step size. We also present a few programs of higher order accuracy and fixed step size. These latter programs were modified for direct incorporation in the overall missile models used by the sponsor. The computer programs for these methods are presented in appendix A, and those with fixed step size have been modified for direct implementation and integration with the mainframe programs for missile modeling at Eglin Air Force Base. These latter programs have been given to the sponsor at Eglin, for its testing and implementation.

It is appropriate that we summarize these methods and compare the accuracy, required effort, stability, and other features of these methods.

i - Implicit modified Euler method with fixed step size

The method begins the solution at i th step using the predictor formula

$$\underline{y}_{i+1} = \underline{y}_i + h\, \underline{f}(t_i, \underline{y}_i),$$

for predicting an initial approximation of the solution at the (i+1)th step, then uses the fixed point iteration formula:

$$\underline{y}_{i+1}^{(k)} = \underline{y}_i + h/2\left[\underline{f}\left(t_{i+1}, \underline{y}_{i+1}^{k-1}\right) + \underline{f}(t_i, \underline{y}_i)\right], \quad k = 1,2,3,\ldots,$$

to improve the accuracy until $\left\| \underline{y}_{i+1}^{(k)} - \underline{y}_{i+1}^{(k-1)} \right\| < \varepsilon$, where ε is a predescribed tolerence error.

ii - Hamming method with fixed step size:

The method begins the solution with obtaining the starting values using other methods such as modified Euler or Runge-Kutta method, and then continues with a predictor - corrector. The equations employed are

$$\underline{y}_{i+1,p} = \underline{y}_{i-3} + 4h/3\ (2\underline{f}_i - \underline{f}_{i-1} + 2\underline{f}_{i-2}),$$

$$\underline{y}_{i+1,m} = \underline{y}_{i+1,p} - 112/121\ (\underline{y}_{i,p} - \underline{y}_{i,c}),$$

$$\underline{y}_{i+1,c} = 1/8\left[9\underline{y}_i - \underline{y}_{i-2} + 3h(\underline{f}_{i+1,m} + 2\underline{f}_i - \underline{f}_{i-1})\right]$$

$$\underline{y}_{i+1} = \underline{y}_{i+1,c} + 9/121\ (\underline{y}_{i+1,p} - \underline{y}_{i+1,c})$$

It should be noted that the estimate of $\underline{y}_{i+1}$ is modified using the difference between the predicted and corrected values in the previous interval (this is omitted in the first interval since these are not available). Note that, while two additional equations are employed in each step, only two evaluations of the derivative functions are needed.

The special merits of Hamming's method are stability combined with good accuracy. The method has a local error of $0(h^5)$ and a global error of $0(h^4)$.

iii - Adam-Moulton Method with fixed step size

Adam-Moulton method assumes a set of starting values already calculated by some other techniques. It is usually employed in a computer program using the equations

predictor: $\underline{y}_{i+1} = \underline{y}_i + h/24\left[55\underline{f}_i - 59\underline{f}_{i-1} + 37\underline{f}_{i-2} - 9\underline{f}_{i-3}\right]$

corrector: $\underline{y}_{i+1} = y_i + h/24\left[9\underline{f}_{i+1} + d19\underline{f}_i - 5\underline{f}_{i-1} + \underline{f}_{i-2}\right]$

These fourth-order formulas are widely used, especially in combination with Runge-Kutta, because both kinds of methods have local errors of $0(h^5)$. The corrector can be modified at each step and be used as a fixed point iteration for higher accuracy using

$$\underline{y}_{i+1}^{(k)} = \underline{y}_i + h/24\left[9\underline{f}(t_{i+1}, \underline{y}_{i+1}^{(k-1)}) + 19\underline{f}_i - 5\underline{f}_{i-1} + f_{i-2}\right]$$

until $\left\| \underline{y}_{i+1}^{(k)} - \underline{y}_{i+1}^{(k-1)} \right\| < \mathcal{E}$, where $\mathcal{E}$ is a predescribed tolerence error. The computer program computes the starting values using implicit modified Euler method.

iv. Gear's method with fixed step size

Gear (1967) has proposed a predictor-corrector method that has an $0(h^6)$ local error but uses only three previous steps rather than the four previous steps employed by Adam-Moulton. It obtains its high order of error by using recorrected values of the function and derivative values. The formulas are:

$$\underset{c_1}{y_{i+1,p}} = -18y_i + 9\underset{c_1}{y_{i-1,}} + 10\underset{c_2}{y_{i-2}} + 9hy'_i + 18hy'_{i-1} + 3hy'_{i-2}$$

$$hy'_{i+1,p} = -57y_i + 24\underset{c_1}{y_{i-1,}} + 33\underset{c_2}{y_{i-2,}} + 24hy'_i + 57hy'_{i-1} + 10hy'_{i-2}$$

$$\underline{F} = hy'_{i+1,p} - h\,\underline{f}(x_{i+1}, y_{i+1,p}),$$

$$y_{i+1} = y_{i+1,p} - 95/288\underline{F},$$

$$\underset{c_1}{y_{i,}} = y_i + 3/160F,$$

$$\underset{c_2}{y_{i-1,}} = \underset{c_1}{y_{i-1,}} - 11/1440\underline{F}$$

$$hy'_{i+1} = h\,y'_{i+1,p} - \underline{F}$$

This method is stable, highly accurate and is normally used with variable order and step size. Gear (1971) has a listing and a complete description of a subroutine called DIFSUB, which includes options for stiff and non stiff systems.

v - Runge-Kutta Felberg method with variable step size

This method uses adjustable step size in a Runge-Kutta method of order four:

$$y_{i+1} = y_i + 25/216\,\underline{K}_1 + 1408/2565\,\underline{K}_3 + 2197/4104\,\underline{K}_4 - 1/5\,\underline{K}_5$$

where $\underline{K}_1 = h\underline{f}(t_i, y_i)$,

$$\underline{K}_2 = h\underline{f}(t_i, + h/4, \underline{y}_i + 1/4\ K_1)$$

$$\underline{K}_3 = h\underline{f}(t_i + 3h/8, \underline{y}_i + 3/32\ \underline{K}_1 + 9/32\ \underline{K}_2),$$

$$\underline{K}_4 = h\underline{f}(t_i + 12h/13, \underline{y}_i + 1932/2197\ \underline{K}_1 - 7200/2197\ \underline{K}_2 + 7296/2197\ \underline{K}_3$$

$$\underline{K}_5 = h\underline{f}(t_i+h, \underline{y}_i + 439/216\ \underline{K}_1 - 8\ \underline{K}_2 + 3680/513\ \underline{K}_3 - 845/4104\ \underline{K}_4)$$

$$\underline{K}_6 = h\underline{f}(t_i + h/2, \underline{y}_i - 8/27\ \underline{K}_1 + 2\underline{K}_2 - 3544/2565K_3 + 1859/4104\ \underline{K}_4 - 11/40\ \underline{K}_5)$$

The error can be estimated from:

$$\underline{E} = \underline{K}_1/360 - 128K_3/4275 - 2197\ \underline{K}_4/75240 + \underline{K}_5/50 + 2\underline{K}_6/55$$

The basis for this latter scheme is to compute two Runge-Kutta estimates for the new value of $\underline{y}_{i+1}$ but of different order of error. Thus, we compare the estimates of $\underline{y}_{i+1}$ using fourth- and fifth-order Runge-Kutta formulas and comparing the results. Moreover, both sets of equations make use of the same $\underline{K}$'s, so only six function evaluations are used. In addition, one can increase or decrease h depending on the value of $\underline{E}$ at each step.

III. Smoothing by Spline Functions

Estimation and smoothing is the process of extracting information from data-data which can be used to infer the denied information and may obtain errors. The sponsor uses "Moving Polynomial Arc Smoothing - MPAS" techniques in most cases and "Optimal Smoothing-OS" in selective cases.

Recent research work indicates that "smoothing by spline functions' is more preferable to moving polynomial arc smoothing because of the nature of the structure of splines with higher order differentiability and capability of carrying the smoothing as close as needed to the boundary points.

We discuss here the computational aspects of cubic smoothing splines. Given the approximate values $y_i = g(t_i) + \xi_i$ of some supposedly smooth function g at

data points $t_0, \ldots, tn$, a measure of the rapid local variation of the curve of g can be given by a roughness penalty such as the integrated squared second derivative. Various roughness penalties have been suggested and used but $\int (g'')^2 dt$ is most convenient. Using this measure, define the modified sum of squares

$$S(g) = \sum_i [(y_i - g(t_i)^2] + \alpha \int g''(t)^2 \, dt;$$

Minimizing S(g) over the class of all (twice-differentiable) functions g will yield an estimate g which, for the given value of α, gives the best compromise between smoothness and goodness of fit. That is, a sort of compromise between our desire to stay close to the given data and our desire to obtain a smooth function and the choice of α depends on which of these two conflicting goals we accord greater importance.

It can be shown that the curve g has the following properties:

(i) it is a cubic polynomial in each interval (t_i, t_{i+1})

(ii) at the points t_i, the curve and its first two derivatives are continuous but there may be a discontinuity in the third derivative.

Any curve which satisfies (i) and (ii) is called a cubic spline with knots t_i. It should be noted that one of the consequences of the properties of $\hat{g}$ is computational. To find $\hat{g}$, we need to find the four coeffients in the polynomial form of $\hat{g}$ in each interval. These coefficients can, essentially, be found by solving a band-limited linear system of size n. Stable and fast numerical algorithms for solving such systems are available. De Boor (1978, Chapter 14) gives a description of the way $\hat{g}$ can be found and a Fortran implementation. Silverman and collaborators (1985) have adapted De Boor's programs to yield a method which finds $\hat{g}$ using 35n multiplications/divisions for the first value of

the smoothing parameter and 25n for the others, where n is the number of data points. Thus, the computational burden in finding g goes up linearly as the number of data points.

We present here a much simpler program based on an algorithm developed by Reinsch (1967): let (t_i, y_i), $i = 0, \ldots, n$ be given and assume that $t_0 < t_1 < \ldots < t_n$. The smoothing function g to be constructed shall

$$\text{minimize} \int [g''(t)]^2 dt$$

among all functions g(t) such that

$$* \qquad \sum_{i=0}^{n} [(g(t_i) - y_i)/\delta y_i]^2 \leq S, \quad g \in C^2[t_0, t_n] .$$

Here $\delta y_i > 0, i = 0, \ldots, n$ and $S \geq 0$ are given numbers. The constant S is redundant and is introduced only for convenience. It allows for an implicit rescaling of the quantities δy_i, which control the extent of smoothing. Recommended values for S depend on the relative weights $[\delta y_i]^{-2}$. If available, one should use for δy_i an estimate of the standard deviation of the ordinate y_i. In this case, natural values of S lie within the confidence interval corresponding to the left-hand side of (*):

$$N - (2N)^{1/2} \leq S \leq N + (2N)^{1/2}, \quad N = n + 1$$

Choosing S equal to zero leads to the problem of interpolation by cubic spline functions. The extreme funtion $\hat{g}(t)$ is composed of cubic spline

$$\hat{g}(t) = a_i + b_i(t - t_i) + c_i(t - t_i)^2 + d_i(t - t_i)^3, \quad t_i \leq t \leq t_i + 1,$$

which join at their common endpoints such that $\hat{g}$, $\hat{g}'$, and $\hat{g}''$ are continuous, and $\hat{g}''(t_0) = \hat{g}''(t_n) = o$.

The computer program in Appendix B computes the parameters a_i, b_i, c_i, and d_i according to Reinsch's development of the algorithm.

IV. Summary and Conclusions

Several computer programs for numerical solution of systems of 1st order differential equations have been written for testing and implementation in the digital simulation for the dynamics of surface-to-air missiles. Another computer program for smoothing noisy data with spline functions have been developed for use in smoothing of Cinetheodolite and Radar Data for Missiles and Bombs.

The smoothing program can be modified to achieve:

a. a higher degree of smoothing dependent on the nature of data. This can be accomplished by developing "automatic" methods for choosing the smoothing parameter using cross-validation methods.

and

b. Accommodate other end (boundary) conditions

REFERENCES

A - Digital Simulation for the Dynamics of Surface-to-Air Missiles

1. Burden, R.L., and J.D. Faires, "Numerical Analysis," Third Edition, Brindle, Weber and Schmidt, 1985.

2. Dalton, O.N., and C.R. Parker, "Real-Time Flight Analysis: Fundamentals for the Generation of a Mathematical Model for a Missile in Three-Dimensional Space with Six Degrees of Freedom." Report No. 12, 1960, Flight Simulation Laboratory, White Sands Missile Range, New Mexico.

3. Gear, C.W., "Simultaneous Numerical Solution of Differential-Algebraic Equations," IEEE transactions on Circuit Theory, Vol CT-18, 1971.

4. Gear, C.W., "DIFSUB for Solution of Ordinary Differential Equations (D2)" Communication of the ACM, Vol 14, No. 3, 1971.

5. Gear, C.W., "Numerical Initial Value Problems in Ordinary Diffierential Equations," Prentice-Hall, Inc., Englewood Cliffs, New Jersey,1971.

6. Lambert, J.D., "Computational Methods in Ordinary Differential Equations," Wiley, 1973.

7. Nicolaides, J.D., "Free Flight Missile Dynamics," Lecture Notes Department of Aero-Space Engineering, University of Notre Dame, 1965.

8. Shampine, L.F., et al, "Solving non-stiff ordinary differential equations - The State of the Art," SIAM Review, Vol 18, 1976.

9. Shampine, L.F., and C.W. Gear, "A User's View of Solving Stiff Ordinary Differential Equations," SIAM Review, Vol 21, 1979, pp 1-17.

B - Smoothing of Cinetheodolite and Radar Data for Missiles and Bombs

1. Buse, A. and L. Lim, "Cubic Splines as a Special Case of Restricted Least Squares," Journal of the American Statistical Association, Vol 72, 1977.

2. Burden, R.L., and J.D. Faires, "Numerical Analysis," 3rd Edition, Brindle, Weber & Schmidt, 1985.

3. Davis, R.C., "Techniques for the Statistical Analysis of Cinetheodolite Data," U.S. Naval Ordinance Test Station, NAVORD Report No. 1299, 1951.

4. de Boor, Carl, "A Practical Guide to Spline" Springer-Verlag New York Inc. 1978.

5. Deyst, Jr., J.J., and Charles F. Price, "Optimal Stochastic Guidance Laws for Tactical Missiles," Journal Spacecraft, Vol 10, 1973.

6. Gelb, A., "Applied Optimal Estimation," MIT Press, 1984.

7. Kaminski, P.G., and A.F. Bryson, "Discrete Square Root Smoothing," AIAA Guidance and Control Conference, 1972.

8. Sterrett, J.K., "Manual for Moving Polynominal Arc Smoothing," Ballistic Research Laboratories, Report No. 840, 1952.

9. Reinsch, C.H., "Smoothing by Spline Functions," Num. Math., Vol 10, 1967.

10. Silverman, B.W., "Some Aspects of the Spline Smoothing Approach to Non-Parametric Regression Curve Fitting", J.R. Statist. Soc. B, Vol 47, No. 1, 1985.

11. Sterrett, J.K., "Manual for Moving Polynomial Arc Smoothing," Ballistic Research Laboratories, Report No. 840, 1952.

12. Wold, S., "Spline Function in Data Analysis," Technometrics, Vol 16, No 1, 1974.

ACKNOWLEDGMENTS

I would like to acknowledge the Air Force Systems Command, Air Force Office of Scientific Research, Freeman Mathematical Laboratory, and Universal Energy Systems Inc., for providing a worthy research program.

I would like to thank Ralph Duncan, George Weekly and Robert Jones of Freeman Mathematical Laboratory for providing stimulating environments and discussions. Thanks also to Rodney C. Darrah for a rewarding experience and association with Universal Energy Systems Inc.

Appendix A

Programs for solving 1st order systems of differential equations

1 - Runge-Kutta Felberg method with variable step size

```
C       TEST PROGRAM FOR SYSTEM SIMULATION

        IMPLICIT DOUBLE PRECISION(A-H,O-Z), INTEGER(I-N)
        DIMENSION HISTORY(150,4),STATE(3),RKOEF(31),VPARAM(10)
        EXTERNAL NLSYS

        N = 2
        A = 0.0
        B = 1.0
        HMIN = 0.0001
        HMAX = 0.01
        TOL = 0.0001
        TOUT = 0.01
        STATE(1) = 1.0
        STATE(2) = 0.0
        NRH = 150

        CALL RKFELB(HISTORY,NRH,N,A,B,HMIN,HMAX,TOL,TOUT,STATE,VPARAM,
     1                    NLSYS)

        WRITE(*,50) ((HISTORY(I,J), J=1,3), I=1,101)
 50     FORMAT(3F10.4,/)
        END



        SUBROUTINE RKFELB(HISTORY,NRH,N,A,B,HMIN,HMAX,TOL,TOUT,STATE,
     1           VPARAM,SYSTEM)

C-------------------------------------------------------------------------
C       HISTORY := ARRAY CONTAINING OUTPUT OF TIME SIMULATION.
C       NRH     := NUMBER OF ROWS OF THE MATRIX HISTORY.
C       N       := ORDER OF SYSTEM.
C       M       := NUMBER OF CONTROLLERS.
C       A,B     := INITIAL AND FINAL TIME.
C       HMIN    := MINIMUM STEP SIZE.
C       HMAX    := MAXIMUM STEP SIZE.
C       TOL     := ERROR TOLERANCE.
C       TOUT    := OUTPUT PERIOD.
C       STATE   := N-VECTOR CONTAINING CURRENT VALUE OF STATE.
C                        ON INPUT, IT CONTAINS THE INITIAL STATE.
C       VPARAM  := VECTOR OF VARIOUS PARAMETERS.
C       SYSTEM  := SUBROUTINE CONTAINING STATE EQUATIONS.
```

Appendix A

Programs for solving 1st order systems of differential equations

1 - Runge-Kutta Felberg method with variable step size

```
C       TEST PROGRAM FOR SYSTEM SIMULATION

        IMPLICIT DOUBLE PRECISION(A-H,O-Z), INTEGER(I-N)
        DIMENSION HISTORY(150,4),STATE(3),RKOEF(31),VPARAM(10)
        EXTERNAL NLSYS

        N = 2
        A = 0.0
        B = 1.0
        HMIN = 0.0001
        HMAX = 0.01
        TOL = 0.0001
        TOUT = 0.01
        STATE(1) = 1.0
        STATE(2) = 0.0
        NRH = 150

        CALL RKFELB(HISTORY,NRH,N,A,B,HMIN,HMAX,TOL,TOUT,STATE,VPARAM,
     1                  NLSYS)

        WRITE(*,50) ((HISTORY(I,J), J=1,3), I=1,101)
50      FORMAT(3F10.4,/)
        END



        SUBROUTINE RKFELB(HISTORY,NRH,N,A,B,HMIN,HMAX,TOL,TOUT,STATE,
     1          VPARAM,SYSTEM)

C-------------------------------------------------------------------------
C       HISTORY := ARRAY CONTAINING OUTPUT OF TIME SIMULATION.
C       NRH     := NUMBER OF ROWS OF THE MATRIX HISTORY.
C       N       := ORDER OF SYSTEM.
C       M       := NUMBER OF CONTROLLERS.
C       A,B     := INITIAL AND FINAL TIME.
C       HMIN    := MINIMUM STEP SIZE.
C       HMAX    := MAXIMUM STEP SIZE.
C       TOL     := ERROR TOLERANCE.
C       TOUT    := OUTPUT PERIOD.
C       STATE   := N-VECTOR CONTAINING CURRENT VALUE OF STATE.
C                  ON INPUT, IT CONTAINS THE INITIAL STATE.
C       VPARAM  := VECTOR OF VARIOUS PARAMETERS.
C       SYSTEM  := SUBROUTINE CONTAINING STATE EQUATIONS.
```

```
      SUBROUTINE STEP(STATE,N,T,H,TOL,HMIN,HMAX,RKOEF,SYSTEM,VPARAM)

      IMPLICIT DOUBLE PRECISION(A-H,O-Z), INTEGER(I-N)
      DIMENSION STATE(1),RKOEF(1),VPARAM(1),
     1                  RK1(15),RK2(15),RK3(15),RK4(15),RK5(15),RK6(15),
     2                  WORK(15)

C-----------------------------------------------------------------------
C       ERREST  := ERROR ESTIMATE.
C       STPMOD  := STEP SIZE MODIFICATION.
C       WORK    := DUMMY STATE VECTOR.
C       TWORK   := DUMMY TIME.
C       RK1-6   := RUNGE-KUTTA VECTORS.
C-----------------------------------------------------------------------
      ERREST = TOL + 1.0
    5 IF(ERREST.GT.TOL) THEN

              TWORK = T
              DO 10 I = 1,N
                      WORK(I) = STATE(I)
   10         CONTINUE
              CALL SYSTEM(RK1,TWORK,WORK,VPARAM)

              TWORK = T + RKOEF(2)*H
              DO 20 I = 1,N
                      RK1(I) = RK1(I) * H
                      WORK(I) = STATE(I) + RKOEF(1)*RK1(I)
   20         CONTINUE
              CALL SYSTEM(RK2,TWORK,WORK,VPARAM)

              TWORK = T + RKOEF(5)*H
              DO 30 I = 1,N
                      RK2(I) = RK2(I) * H
                      WORK(I) = STATE(I) + RKOEF(3)*RK1(I) + RKOEF(4)*RK2(I)
   30         CONTINUE
              CALL SYSTEM(RK3,TWORK,WORK,VPARAM)

              TWORK = T + RKOEF(8)*H
              DO 40 I = 1,N
                      RK3(I) = RK3(I) * H
                      WORK(I) = STATE(I) + RKOEF(6)*RK1(I) + RKOEF(7)*RK2(I)
                                         + RKOEF(8)*RK3(I)
   40         CONTINUE
              CALL SYSTEM(RK4,TWORK,WORK,VPARAM)

              TWORK = T + RKOEF(14)*H
              DO 50 I = 1,N
                      RK4(I) = RK4(I) * H
                      WORK(I) = STATE(I) + RKOEF(10)*RK1(I) + RKOEF(11)*RK2(I)
     1                                   + RKOEF(12)*RK3(I) + RKOEF(13)*RK4(I)
   50         CONTINUE
              CALL SYSTEM(RK5,TWORK,WORK,VPARAM)
```

```
                TWORK = T + RKOEF(20) * H
                DO 60 I = 1,N
                        RK5(I) = RK5(I) * H
                        WORK(I) = STATE(I)+ RKOEF(15)*RK1(I) + RKOEF(16)*RK2(I)
     1                                    + RKOEF(17)*RK3(I) + RKOEF(18)*RK4(I)
     2                                    + RKOEF(19)*RK5(I)
60              CONTINUE
                CALL SYSTEM(RK6,TWORK,WORK,VPARAM)

                DO 61 I = 1,N
                        RK6(I) = RK6(I) * H
61              CONTINUE

                ERREST = 0.0

C               ESTIMATE ERROR
                DO 100 I = 1,N
                        DUMERR =(RKOEF(25)*RK1(I) + RKOEF(26)*RK3(I) +
     1                           RKOEF(27)*RK4(I) + RKOEF(28)*RK5(I) +
     2                           RKOEF(29)*RK6(I) )/H
                DUMERR = DABS(DUMERR)
                IF(DUMERR.GT.ERREST) ERREST = DUMERR
100             CONTINUE
                STPMOD = 1.01
                IF(1.0+ERREST.NE.1.0) STPMOD = 0.5*((TOL/ERREST)**0.25)

C               RKOEF(30) CONTAINS STEP SIZE USED IN THIS ITERATION
                RKOEF(30) = H
                IF(STPMOD.LT.1.0) H = H/2

                IF(H.LT.HMIN) THEN
                        PRINT *,'*****STEP SIZE TOO SMALL******'
                        ERREST = 0.0
                        RKOEF(30) = 1.0E+20
                ENDIF

        GO TO 5
        ENDIF

        IF(H.LT.HMIN) THEN
                DO 112 I = 1,N
                        STATE(I) =STATE(I) + RKOEF(15)*RK1(I) + RKOEF(16)*RK2(I)
     1                                     + RKOEF(17)*RK3(I) + RKOEF(18)*RK4(I)
112             CONTINUE
        ENDIF

5       RKOEF(31) CONTAINS STEP SIZE RECOMMENDED FOR NEXT ITERATION.
        RKOEF(31) = H

        RETURN
        END
```

```
      SUBROUTINE COEF(RKOEF)
      DOUBLE PRECISION RKOEF(1)

C     COEF LOADS THE RUNGE-KUTTA COEFFICIENTS INTO RKOEF

      RKOEF( 1) =  1.0/4.0
      RKOEF( 2) =  1.0/4.0

      RKOEF( 3) =  3.0/32.0
      RKOEF( 4) =  9.0/32.0
      RKOEF( 5) =  3.0/8.0

      RKOEF( 6) =  1932.0/2197.0
      RKOEF( 7) = -7200.0/2197.0
      RKOEF( 8) =  7296.0/2197.0
      RKOEF( 9) =  12.0/13.0

      RKOEF(10) =  439.0/216.0
      RKOEF(11) = -8.0
      RKOEF(12) =  3680.0/513.0
      RKOEF(13) = -845.0/4104.0
      RKOEF(14) =  1.0

      RKOEF(15) = -8.0/27.0
      RKOEF(16) =  2.0
      RKOEF(17) = -3544.0/2565.0
      RKOEF(18) =  1859.0/4104.0
      RKOEF(19) = -11.0/40.0
      RKOEF(20) =  1.0/2.0

      RKOEF(21) =  25.0/216.0
      RKOEF(22) =  1408.0/2565.0
      RKOEF(23) =  2197.0/4104.0
      RKOEF(24) = -1.0/5.0

      RKOEF(25) =  1.0/360.0
      RKOEF(26) = -128.0/4275.0
      RKOEF(27) = -2197.0/75240.0
      RKOEF(28) =  1.0/50.0
      RKOEF(29) =  2.0/55.0

      RETURN
      END
```

```
C       NLSYS CONTAINS A SYSTEM OF DIFFERENTIAL EQUATIONS TO BE SOLVED VIA
C               RKFELB

        SUBROUTINE NLSYS(DX,T,X,VPARAM)
        IMPLICIT DOUBLE PRECISION(A-H,O-Z), INTEGER(I-N)
        DIMENSION DX(1),VPARAM(1),X(1),U(5)

        DX(1) = X(2)
        DX(2) = -9.0*X(1)

        RETURN
        END
```

2 - Haming method with fixed step size

```
C     TEST-HAMMING
C     MAIN PROGRAM FOR INTEGRATING A SYSTEM DX/DT=F(T,X)
C     SYSTEM IS GIVEN IN "EXTERNAL SYS" SUBROUTICNE
C     NMAX:=MAX NUMBER OF EQUATIONS
C     H:=STEP SIZE
C     N:=NUMBER OF EQUATIONS
C     TMIN:= BEGINING OF INTEGRATION TIME
C     TMAX:= END OF INTEGRATION TIME
C
      PARAMETER(NMAX=2 )
      DIMENSION E(NMAX),DE(NMAX)
      COMMON/TEMP/FOLD(3,NMAX),YOLD(4,NMAX),YPOLD(NMAX),YCOLD(NMAX)
      COMMON/DIFF/E,DE
      COMMON/STEP/T,DT4,N
      EXTERNAL AUTO
      E(1)=1.0
      E(2)=0.0
      DT4=0.01
      DO 500 JJ=1,100
      CALL INTEG
  500 CONTINUE
      END
```

```
C     INTEG-HAMMING
C     THIS SUBROUTINE CALCULATES THE STARTING VALUES OF THE SOLUTION FOR
C     HAMMING USING MODIFIED EULER'S METHOD +HAMMING
      SUBROUTINE INTEG
      EXTERNAL AUTO
C     NMAX=MAX NUMBER OF EQUATIONS THAT MAY BE CONSIDERED
      PARAMETER(NMAX=2 )
      COMMON/TEMP/FOLD(3,NMAX),YOLD(4,NMAX),YPOLD(NMAX),YCOLD(NMAX)
     1 COMMON/DIFF/E(NMAX),DE(NMAX)
     1 COMMON/STEP/T,DT4,N
     1 COMMON/AUTO/IFIRST
      DIMENSION YNEW(NMAX),YPNEW(NMAX),YCNEW(NMAX),WORK1(NMAX),ERR(NMAX)
     1,EMNEW(NMAX)
      DATA IFIRST/1/
C     N=NUMBER OF EQUATIONS IN THE SYSTEM
      N=NMAX
      DT=DT4/4.
      IF(IFIRST.EQ.1)THEN
```

```
      CALL AUTO
      DO 10 I=1,N
      YOLD(4,I)=E(I)
   10 CONTINUE
      IFIRST=2
      ENDIF
      T=T+DT4
      IF(IFIRST.LE.4)THEN
      DO 510 I=1,N
      DES(I)=DE(I)
      E(I)=E(I)+DES(I)*DT4
  510 CONTINUE
      CALL AUTO
      DO 520 I=1,N
      E(I)=E(I)+(DE(I)-DES(I))*DT8
  520 CONTINUE
      WRITE(*,7)T,E(1),E(2)
      CALL AUTO
      DO 530 I=1,N
      IF(IFIRST.EQ.2)FOLD(3,I)=DE(I)
      IF(IFIRST.EQ.2)YOLD(3,I)=E(I)
      IF(IFIRST.EQ.3) FOLD(2,I)=DE(I)
      IF(IFIRST.EQ.3)YOLD(2,I)=E(I)
      IF(IFIRST.EQ.4)FOLD(1,I)=DE(I)
      IF(IFIRST.EQ.4)YOLD(1,I)=E(I)
  530 CONTINUE
      IFIRST=IFRIST+1
      DO 540 I=1,N
      YPOLD(I)=YOLD(1,I)
      YCOLD(I)=YOLD(1,I)
  540 CONTINUE
      ELSE
      CALL HAMMING (AUTO,N,T,DT4)
      WRITE(*,7)T,E(1),E(2)
      ENDIF
    7 FORMAT(4X,3F10.4)
      RETURN
      END



C     SUBROUTINE HAMMING(SYS,N,T,H)
C
      SUBROUTINE HAMMING(AUTO,N,T,H)
      EXTERNAL AUTO
      PARAMETER (NMAX=2 )
C     N:=ORDER OF DIFFERENTIAL EQUATIONS
C     T:= CURRENT TIME
```

```
C     H:=STEP SIZE
C     SYS:= AUTO NAME OF SUBROUTINE CONTAINING DE'S
      CALL AUTO
C     FOLD:=STORAGE OF PAST F'S
C     YOLD:=STORAGE OF PAST Y'S
C     YPOLD:=STORAGE OF PAST YP'S
C     YCOLD:=STORAGE OF PAST YC'S
      COMMON/TEMP/FOLD(3,NMAX),YOLD(4,NMAX),YPOLD(NMAX),YCOLD(NMAX)
      COMMON/DIFF/E(NMAX),DE(NMAX)
      DIMENSION YNEW(NMAX),YPNEW(NMAX),YCNEW(NMAX),YMNEW(NMAX),
     & WORK1(NMAX)
C     PERFORM INTEGRATION STEPS
      DO 10 I=1,N
      YPNEW(I)=YOLD(4,I)+4.0*H*(2.0*FOLD(1,I)-FOLD(2,I)+2.0*FOLD(3,I))/3.0
      YMNEW(I)=YPNEW(I)-112.0/121.0*(YPOLD(I)-YCOLD(I))
   10 CONTINUE
      DO 11 I=1,N
      E(I)=YMNEW(I)
   11 CONTINUE
      CALL AUTO
      DO 15 I=1,N
      WORK1(I)=DE(I)
      YCNEW(I)=(9.0*YOLD(1,I)-YOLD(3,I)+3.0*H*(WORK1(I)+2.0*FOLD(1,I)
     &-FOLD(2,I)))/8.0
      YNEW(I)=YCNEW(I)+9.0*(YPNEW(I)-YCNEW(I))/121.0
   15 CONTINUE
      DO 16 I=1,N
      E(I)=YNEW(I)
   16 CONTINUE
      CALL AUTO
      DO 90 I=1,N
      YNEW(I)=E(I)
      WORK1(I)=DE(I)
      DO 50 J=1,N
      FOLD(3-J,I)=FOLD(4-J-1,I)
   50 CONTINUE
      FOLD(1,I)=WORK1(I)
      YOLD(1,I)=YNEW(I)
      YPOLD(I)=YPNEW(I)
      YCOLD(I)=YCNEW(I)
      YOLD(4,I)=YMNEW(I)
      WORK1(I)=WORK1(I)
   90 CONTINUE
      RETURN
      END
```

3 - Gear method with fixed step size

```
C     GEAR-TEST
C     MAIN PROGRAM FOR INTEGRATING A SYSTEM DX/DT=F(T,X),
C     SYSTEM IS GIVEN IN"EXTERNAL SYS" SUBROUTINE.
C     NMAX:= MAX NUMBER OF EQUATIONS
C     H:=STEP SIZE
C     N:=NUMBER OF EQUATIONS
C     TMIN:=BEGINING INTEGRATION TIME
C     TMAX:=END INTEGRATION TIME
C     DT4:= STEP SIZE
C     NOTATION FOLLOWS THAT OF THE WRITE UP
C     NMAX= MAX NUBER OF EQUATIONS THAT MAY BE CONSIDERED
      PARAMETER(NMAX=2 )
      DIMENSION E(NMAX),DE(NMAX)
      COMMON/TEMP/YOLD,FOLD    ,YC1OLD       ,YC2OLD
      COMMON/DIFF/E,DE
      COMMON/STEP/T ,DT4,N
      EXTERNAL AUTO
C     N=NUMBER OF EQUATIONS
      N=2
      E(1)=1.0
      E(2)=0.0
      DT4=0.01
      DO 500 JJ=1,100
      CALL INTEG
  500 CONTINUE
      END



C     INTEG-GEAR
C     THIS SUBROUTINE FINDS THE STARTING VALUES OF THE SOLUTION  FOR GEAR'S
C     METHOD USING MODIFIED EULER'S METHOD  +GEAR'S METHOD WITH FIXED STEP
      SUBROUTINE INTEG
      EXTERNAL AUT
      NMAX=MAX NUMBER OF EQUATIONS THAT MAY BE CONSIDERED
      PARAMETER (NMAX=2)
      COMMON/TEMP/YOLD(NMAX),FOLD(3,NMAX),YC1OLD(NMAX),YC2OLD(NMAX)
      COMMON/DIFF/E(NMAX),DE(NMAX)
      COMMON/STEP/T,DT4,N
      DIMENSION YNEW(NMAX),YPNEW(NMAX),FPNEW(NMAX),WORK1(NMAX)
      DATA IFIRST/1/
      N=NUMBER OF EQUATIONS
      DT=DT4/2.0
      IF(IFIRST.EQ.1)THEN
      CALL AUTO
```

```
      DO 10 I=1,N
      YC2OLD(I)=E(I)
      FOLD(3,I)=DE(1)
   10 CONTINUE
      WRITE(*,7) T,E(1),E(2)
    7 FORMAT(4X,3F10.4)
      IFIRST=2
      ENDIF
      T=T+DT4
      IF(IFIRST.LE.3)THEN
      DO 510 I=1,N
      DES(I)=DE(I)
      E(I)=E(I)+DES(I)*DT4
  510 CONTINUE
      CALL AUTO
      DO 520 I=1,N
      E(I)=E(I)+(DE(I)-DES(I))*DT8
  520 CONTINUE
      CALL AUTO
      DO 530 I=1,N
      IF(IFIRST.EQ.2)FOLD(2,I)=DE(I)
      IF(IFIRST.EQ.2)YC1OLD(I)=E(I)
      IF(IFIRST.EQ.3)FOLD(1,I)=DE(I)
      IF(IFIRST.EQ.3)YOLD(I)=E(I)
  530 CONTINUE
      WRITE(*,7)T,E(1),E(2)
      IFIRST=IFIRST+1
      ELSE
      CALL GEAR1(AUTO,N,T,DT4)
      WRITE(*,7)T,E(1),E(2)
C
      ENDIF
      RETURN
      END


      SUBROUTINE GEAR1 PERFORMS GEAR'S METHOD WITH FIXED STEP-SIZE
C     NOTATION FOLLOWS THAT OF WRITE UP
      SUBROUTINE GEAR1(AUTO,N,T,H)
      EXTERNAL AUTO
      PARAMETER(NMAX=2 )
      COMMON/TEMP/YOLD(NMAX),FOLD(3,NMAX),YC1OLD(NMAX),YC2OLD(NMAX)
     1,XMM(N),DIFF E(NMAX),DE NMAX)
      DIMENSION YNEW(NMAX),YPNEW(NMAX),FPNEW(NMAX),WORK(NMAX)
     &,BIDF(NMAX)
      DO 10 I=1,N
      YPNEW(I)=-18.0*YOLD(I)+9.0*YC1OLD(I)+10.0*YC2OLD(I)+
     & H*(9.0*FOLD(1,I)+18.0*FOLD(2,I)+3.0*FOLD(3,I))
      FPNEW(I)=-57.0*YOLD(I)+24.0*YC1OLD(I)+33.0*YC2OLD(I)+
     & H*(24.0*FOLD(1,I)+57.0*FOLD(2,I)+10.0*FOLD(3,I))
      FPNEW(I)=FPNEW(I)/H
```

```
   10 CONTINUE
      DO 11 I=1,N
      E(I)=YPNEW(I)
   11 CONTINUE
      T=T+DT4
      CALL AUTO
      T=T-DT4
      DO 12 I=1,N
      WORK1(I)=DE(I)
      BIGF(I)=H*(FPNEW(I)-WORK1(I))
      YNEW(I)=YPNEW(I)-95.0*BIGF(I)/288.0
   12 CONTINUE
      DO 20 I=1,N
      YC2OLD(I)=YC1OLD(I)-11.0*BIGF(I)/1440.0
      YC1OLD(I)=YOLD(I)+3.0*BIGF(I)/160.0
   20 CONTINUE
      DO 31 I=0,1
      DO 30 J=1,N
      FOLD(3-I,J)=FOLD(3-I-1,J)
   30 CONTINUE
   31 CONTINUE
      DO 40 I=1,N
      YOLD(I)=YNEW(I)
      FOLD(1,1)=FPNEW(I)-BIGF(I)/H
      E(I)=YOLD(I)
      DE(I)=FOLD(1,I)
   40 CONTINUE
      RETURN
      END
```

```
      SUBROUTINE AUTO
C     SUBROUTINE COMPUTES XDOT:=DE FROM SYSTEM OF EQUATIONS
      COMMON/DIFF/E(2),DE(2)
      COMMON/STEP/ T,DT4,N
      DE(1)=E(2)
      DE(2)= -9.0*E(1)
      RETURN
      END
```

4 - Adam-Moulton method with fixed step and iterative improvement

```
      SUBROUTINE INTEG
C     ADAM-MOULTON WITH ITERATION TO ACHIEVE A PREDESCRIBED ERROR-STARTING
C     VALUES BY MODIFIED EULER.
C     NMAX=MAX NUMBER OF EQUATIONS TO BE CONSIDERED
      PARAMETER(NMAX=2)
      COMMON /DIFF/E(NMAX),DE(NMAX)
      COMMON /STEP/ T,DT4,N
      DIMENSION DES(NMAX),F(NMAX,4),ETEMP(NMAX),ETEMP2(NMAX),ERR(NMAX)
      DATA IFIRST /1/
      DT8 = DT4/2.0
      CALL AUTO
      T=T+DT4
C     TOL=PREDESCRIBED ERROR
      DATA TOL/0.001/
      IF (IFIRST .EQ. 1 ) THEN
      DO 5 I=1,N
      F(I,1) = DE(I)
    5 CONTINUE
      IFIRST = 2
      END IF
      DO 400 I=1,N
      ETEMP(I)=E(I)
  400 CONTINUE
      IF (IFIRST .LE. 4)THEN
      DO 510 I=1,N
      DES(I)=DE(I)
      E(I)=E(I)+DES(I)*DT4
  510 CONTINUE
C     J RUNS FROM 1 TO LAST ITERATION
  515 DO 530 J=1,4
      IF(J.GT.1) GO TO 519
      DO 518 I=1,N
      ETEMP2(I)=E(I)
  518 CONTINUE
  519 CALL AUTO
      DO 520 I=1,N
      E(I)=ETEMP(I)+DT4*0.5*(DE(I)+DES(I))
      ERR(I)=E(I)-ETEMP2(I)
      ETEMP2(I)=E(I)
  520 CONTINUE
      SUMERR=0.0
      SMNORM=0.0
      DO 525 K=1,N
      SUMERR=SUMERR+ERR(K)*ERR(K)
      SMNORM=SMNORM+E(K)*E(K)
  525 CONTINUE
      IF(SUMERR/SMNORM.LE.TOL ) GO TO 531
  530 CONTINUE
  531 DO 535 I=1,N
      F(I,IFIRST) = DE(I)
```

```
  535   CONTINUE
        IFIRST = IFIRST + 1
        WRITE(*,7)T,E(1),E(2)
        ELSE
        DO 600 I=1,N
        E(I)=       (DT4/24.0)*(55.0*F(I,4)-59.0*F(I,3)+
     &  37.0*F(I,2)-9.0*F(I,1))+ETEMP(I)
  600   CONTINUE
        DO 700 I=1,N
        F(I,1)=F(I,2)
        F(I,2)=F(I,3)
        F(I,3)=F(I,4)
  700   CONTINUE
C       J RUNS FROM 1 TO LAST ITERATION
        DO 840  J=1,4
        IF(J.EQ.1) GO TO 620
        DO 610 I=1,N
        ETEMP2(I)= E(I)
  610   CONTINUE
  620   CALL AUTO
        DO 800 I=1,N
        E(I) =      (DT4/24.0)*(9.0*DE(I) +19.0*F(I,3)-
     &  5.0*F(I,2)+F(I,1)) +ETEMP(I)
        ERR(I)= E(I)-ETEMP2(I)
        ETEMP2(I)=E(I)
  800   CONTINUE
        SUMERR=0.0
        SMNORM=0.0
        DO 830 K=1,N
        SUMERR=SUMERR+ERR(K)*ERR(K)
        SUMNORM=SMNORM+E(K)*E(K)
  830   CONTINUE
        IF(SUMERR/SMNORM.LE. TOL ) GO TO 850
  840   CONTINUE
  850   DO 900 I=1,N
        F(I,4)= DE(I)
  900   CONTINUE
        WRITE(*,7)T,E(1),E(2)
        ENDIF
  7     FORMAT(4X,4F10.4)
        RETURN
        END
```

5 - Modified Euler method with iterative improvement

```
      SUBROUTINE INTEG
C     MODIFIED EULER WITH ITERATION TO ACHIEVE A PREDESCRIBED ERROR
C
C     NMAX=MAX. NUMBER OF EQUATIONS TO BE CONSIDERED
      PARAMETER(NMAX= 2)
      COMMON /DIFF/ E(NMAX),DE(NMAX)
      COMMON /STEP/ T,DT4,N
      DIMENSION ETEMP(NMAX),ETEMP2(NMAX),DES(NMAX),ERR(NMAX)
C
C     THETA IS A STABILITY PARAMETER LESS OR EQUAL 1/2
      DATA THETA/.5  /
c     TOL = PREDESCRIBED ERROR
      DATA TOL/.001/
      CALL AUTO
      T=T+DT4
      DO 510 I=1,N
      ETEMP(I)=E(I)
      DES(I)=DE(I)
      E(I)=E(I)+DES(I)*DT4
  510 CONTINUE
C     J=1 TO LAST ITERATION
  515 DO 530 J=1,4
      IF(J.GT.1) GO TO 518
      DO 516 I=1,N
      ETEMP2(I)=E(I)
  516 CONTINUE
  518 CALL AUTO
      DO 520 I=1,N
      E(I)=ETEMP(I)+DT4*((1.-THETA)*DE(I)+THETA*DES(I))
      ERR(I)=E(I)-ETEMP2(I)
      ETEMP2(I)=E(I)
  520 CONTINUE
      SUMERR=0.0
      SMNORM=0.0
      DO 525 K=1,N
       SUMERR=SUMERR+ERR(K)*ERR(K)
       SMNORM=SMNORM+E(K)*E(K)
  525  CONTINUE
       IF(SUMERR/SMNORM.LE. TOL) GO TO 531
  530 CONTINUE
  531 WRITE(*,7)T,E(1),E(2)
    7 FORMAT(4X,3F10.4)
      RETURN
      END
```

Appendix B

Program for smoothing by spline functions

```
C     SMOOTHING
C     CONSTRUCTS THE CUBIC SMOOTHING SPLINE F TO GIVEN DATA (X(I),Y(I),
C     I=1,..  N.
C       NMAX=MAX NUMBER OF DATA POINTS THAT MAY BE CONSIDERED
        PARAMETER (NMAX=100)
        REAL S,X(NMAX),Y(NMAX),DY(NMAX),A(NMAX),B(NMAX),C(NMAX),D(NMAX),J
        REAL E,F1,F2,G,H,P,R(NMAX),R1(NMAX),R2(NMAX),T(NMAX),T1(NMAX),
       &V(NMAX),XM(NMAX),Z(NMAX),W(NMAX),U(NMAX)
        INTEGER N1,N2,I
C     ..
C     ..
c       WRITE(*,1)
c     1 FORMAT(/2X,'INPUT THE INITIAL VALUES-N1,N2..FIRST & LAST DATA POINTS')
c       READ(*,2)N1,N2
c     2 FORMAT(4I3)
c       WRITE(*,3)
c     3 FORMAT(/2X,'INPUT A NON-NEGATIVE PARAMETER S, TO CONTROL',/2X,'
c      &THE EXTENT OF SMOOTHING')
C     S= UPPER BOUND ON THE DISCRETE WAIGHTED MEAN SQUARE DISTANCE OF THE
C        APPROXIMATION F FROM THE DATA. rEINSCH PROPOSED TO CHOOSE S SOME
C        WHERE WITHIN SQUARE ROOT OF (2N OF N.
c       READ(*,4) S
c     4 FORMAT(F8.3)
        N1=1
c       N2=NUMBER OF DATA POINTS
        N2=100
c       THIS PART GENERATES A DATA SET FOR THE FUNCTION Y=SIN X ON (0,1)
        DO 5 I=1,100
        X(I)=0.01*I
        Y(I)=SIN(X(I))
C     DY(I) ESTIMATES OF UNCERTAINTY IN DATA, ASSUMED TO BE POSITIVE. I.E.
C     DY(I) ESTIMATES OF STANDARD DEVIATION IN Y(I)
        DY(I)=0.01
    5   CONTINUE

C     INITIALIZE ARRAYS

        N1=N1-1
        N2=N2+1
        DO 10 I=N1,N2
        R(I)=0.
        R1(I)=0.
        R2(I)=0.
        T(I)=0.
        T1(I)=0.
   10   CONTINUE
```

```
      U(M1)=0.0
      U(N1)=0.0
      U(N2)=0.0
      U(M2)=0.0
      P=0.0
C
C   RESTORE VALUES OF M1,M2,I.E. M1=N1 AND M2=N2
      M1=N1+1
      M2=N2-1
C
C
C   SET VALUES OF X,Y,DY OR READ FILE
C
C
      H=X(M1)-X(N1)
      F=(Y(M1)-Y(N1))/H
      DO 10 I=M1,M2
      G=H
      H=X(I+1)-X(I)
      E=F
      F=(Y(I+1)-Y(I))/H
      A(I)=F-E
      T(I)=2*(G+H)/3
      T1(I)=H/3
      R2(I)=DY(I-1)/G
      R1(I)=-DY(I)/G-DY(I)/H
   10 CONTINUE
      DO 20 I=M1,M2
      B(I)=R(I)*R(I)+R1(I)*R1(I)+R2(I)*R2(I)
      C(I)=R(I)*R1(I+1)+R1(I)*R2(I+1)
      D(I)=R(I)*R2(I+2)
   20 CONTINUE
C
C   SET F2 TO -S
      F2=-S
   30 CONTINUE
      DO 40 I=M1,M2
      R1(I-1)=F*R(I-1)
      R2(I-2)=G*R(I-2)
      R(I)=1.0/(P*B(I)+T(I)-F*R1(I-1)-G*R2(I-2))
      U(I)=A(I)-R1(I-1)*U(I-1)-R2(I-2)*U(I-2)
      F=P*C(I)+T1(I)-H*R1(I-1)
      G=H
      H=DY(I)*P
   40 CONTINUE
      DO 50 I=M2,M1,-1
      U(I)=R(I)*U(I)-R1(I)*U(I+1)-R2(I)*U(I+2)
   50 CONTINUE
      E=0.0
      H=0.0
      DO 60 I=N1,M2
```

```
      G=H
      H=(U(I+1)-U(I))/(X(I+1)-X(I))
      V(1)=(H-G)*DY(1)
      E=E+V(I)*(H-G)
   60 CONTINUE
      J=-H*DY(N2)*DY(N2)
      G=J
      V(N2)=J
      G=F2
      F2=E*P*P
      IF(F2.GE.S.AND.F2.LE.G) GO TO 80
      F=0.0
      H=(V(M1)-V(N1))/(X(M1)-X(N1))
      DO 70 I=M1,M2
      G=H
      H=(V(I+1)-V(I))/(X(I+1)-X(I))
      G=H-G-R1(I-1)*R(I-1)-R2(I-2)*R(I-2)
      F=F+G*R(I)*G
      R(I)=G
   70 CONTINUE
      H=E-P*F
      IF(H.LE.P)GO TO 80
      P=P+(S-F2)/((SQRT(S/E)+P)*H)
      GO TO 30
C
C    USE NEGATIVE SQR ROOT,IF THE SEQUENCE OF ABSCISSA X(I) IS STRICTLY
C    DECREASING
C
   80 CONTINUE
      DO 90 I=N1,N2
      A(I)=Y(I)-P*V(I)
      C(I)=U(I)
   90 CONTINUE
      DO 100 I=N1,N2
      H=X(I+1)-X(I)
      D(I)=(C(I+1)-C(I))/(3.*H)
      B(I)=(A(I+1)-A(I))/H-(H*D(I)+C(I))*H
  100 CONTINUE
C     THIS PART GIVES OUTPUT FOR COEFFICIENTS IN THE CUBICS
      WRITE(*,101)(A(I),I=N1,N2)
      WRITE(*,102)(B(I),I=N1,M2)
      WRITE(*,101)(C(I),I=N1,N2)
      WRITE(*,101)(D(I),I=N1,M2)
  101 FORMAT(/5X,'A COEFFS',5X,1PE12.5)
  102 FORMAT(//5X,'B COEFFS',5X,1PE12.5//)
C     THIS PART COMPUTES THE CUBIC AT THEMIDDLE DISCRETE POINTS XM(I) AND
C     COMPAIRS RESULTS WITH ACTUAL Z(I)
      H=0.005
      DO 110 I=1,99
      XM(I)=X(I)+H
```

```
      Z(I)=SIN(X(I)+H)
      W(I)=((D(I)*H+C(I))*H+B(I))*H+A(I)
  110 CONTINUE
      DO 115 I=1,99
      WRITE(*,120) XM(I),Z(I),W(I)
  115 CONTINUE
  120 FORMAT(4X,3F15.5)
      STOP
      END
```

END

DATE

FILM

JAN

1988